Quantification des changements de la circulation océanique profonde de l'Atlantique au cours des changements climatiques rapides des derniers 40 ka

Lise Missiaen

université PARIS-SACLAY

UNIVERSITÉ DE VERSAILLES ST-QUENTIN-EN-YVELINES
université PARIS-SACLAY

NNT : 2019SACLV004

Quantification of the Atlantic deep ocean-circulation variations during the rapid climate changes of the last 40 ky

Thèse de doctorat de l'Université Paris-Saclay
préparée à Université de Versailles-Saint-Quentin-en-Yvelines

Ecole doctorale n°129 Sciences de l'Environnement d'Ile de France (SEIF)
Spécialité de doctorat : Météorologie, Océanographie Physique, Physique de l'Environnement

Thèse présentée et soutenue à Gif-sur-Yvette, le 18 Janvier 2019, par

LISE MISSIAEN

Composition du Jury :

Christophe Colin Professeur, Université Paris-Sud (GEOPS)	Président
Roger François Professor, University of British Columbia (Department of Earth, Ocean and Atmospheric Science)	Rapporteur
Kerim Hestnes Nisancioglu Professor, University of Bergen (Department of Earth Science)	Rapporteur
Samuel Jaccard Professor, University of Bern (Institute of Geological Science)	Examinateur
Andrea Burke Senior Lecturer, University of St Andrews (School of Earth and Environmental Sciences)	Examinatrice
Claire Waelbroeck Directrice de Recherches, CNRS (LSCE)	Directrice de thèse
Sylvain Pichat Maître de Conférences, ENS de Lyon (LGL-TPE)	Co-directeur de thèse

Thèse de doctorat

Ce qui compte ne peut pas toujours être compté,
et ce qui peut être compté ne compte pas forcément.

Albert Einstein

A ceux qui me sont chers,

Acknowledgments

Tout d'abord, je voudrais remercier tous ceux qui m'ont soutenue ces quatre dernières années et qui, consciemment ou inconsciemment, ont contribué, de près ou de loin, à l'élaboration de ce manuscrit. Voilà, je n'ai donc oublié personne ! Mais passons aux choses sérieuses....

Mes premiers remerciements vont évidemment à mes deux directeurs de thèse : Claire Waelbroeck et Sylvain Pichat.
Je voudrais remercier Claire pour m'avoir encadrée ces quatre dernières années, d'abord pour mon stage de Master 2, puis pendant la préparation de mon doctorat. Merci de m'avoir donné l'opportunité de participer à une campagne à bord du Marion Dufresne et à cette merveilleuse école d'été (ACDC). Merci également de m'avoir encouragée à présenter mon travail lors de nombreux congrès et d'avoir partagé ton éclairage scientifique, j'aimerais un jour en savoir autant !
Je voudrais remercier Sylvain de m'avoir fait rentrer dans la salle blanche de l'ENS de Lyon alors que je ne faisais que commencer ma licence... Merci de m'avoir transmis ton goût pour la géochimie, la paléoclimatologie quaternaire et de m'avoir fait rencontrer Claire !

Je voudrais ensuite exprimer ma gratitude à Nathaëlle (et au CNRS pour l'avoir engagée juste à temps !), Didier (R) et Jean-Claude qui m'ont encadrée, de manière non officielle certes, pour la partie modélisation de cette thèse. Grâce à vous j'ai beaucoup appris et surtout, vous m'avez donné envie de continuer !

Un grand merci également à Samuel Jaccard et à Luke Skinner pour les discussions intéressantes lors des comités de thèse. Merci à Lukas Wacker pour son accueil à Zürich et son expertise sur les analyses ^{14}C.

Merci également aux membres du jury qui ont accepté d'évaluer mon travail : Roger François, Kerim Hestnes Nisancioglu, Samuel Jaccard, Andrea Burke et Christophe Colin.

Merci d'avoir fait le déplacement jusqu'au plateau de Saclay et merci pour la discussion intéressante sur mes résultats et données.

Je voudrais aussi remercier équipes du LSCE "Paléocean" pour m'avoir d'abord accueillie dans la vallée et "CLIM" pour m'avoir adoptée en cours de route. Merci d'avoir guidé mon chemin sur le plateau de Saclay et de m'avoir ouvert les portes du monde de la modélisation. Ces années ont été enrichissantes et agréables grâce à vous tous !

Je voudrais ensuite exprimer ma reconnaissance à ceux qui ont accepté de partager leur précieux savoir (ou savoir faire) et qui m'ont aidée à résoudre les nombreux problèmes rencontrés au cours de ce travail de thèse :
Merci à Matthieu Roy-Barman ses conseils et son expertise sur les isotopes du U, Pa et Th et la bonne manière de spiker un échantillon.
Merci à François puis Arnaud pour le temps partagé sur le Neptune et d'avoir fait en sorte que tous les échantillons soient analysés à temps, malgré les caprices récurrents de la machine.
Merci à Lorna et Sandra pour leurs recettes de cuisine acides...
Merci à Eric et Louise pour leur aide lors des analyses sur le Q-ICP-MS.
Merci à Gülay de m'avoir enseigné (un peu) de son immense savoir faire avec les foraminifères.
Merci également à Elisabeth, Natalia, Bryan pour les discussions passionnantes.
Merci à Aurélien pour ses trucs et astuces, son aide assidue en cas de problème de code et les nombreuses discussions philosophiques...
Merci à Santiago pour m'avoir poussée à commencer à travailler avec R, pour sa patience lorsqu'il m'expliquait pour la quatrième fois ce que signifie cette erreur et pour sa persévérance à me faire lire la documentation R, Fortran et Python.
Merci à Jean-Yves pour son aide avec Python mais aussi pour son thé et ses conseils de bon goût, notamment sur les touches gourmandes de la cantine !

Je souhaite aussi en profiter pour remercier l'université Paris-Sud de m'avoir accordé une mission complémentaire d'enseignement ainsi que les enseignant-chercheurs qui m'ont fait confiance pour animer des séances de TP/TD : merci à Valérie Daux, Christophe Colin, Sophie Sépulcre, Stéphanie Duschamp-Alphonse, Charlotte Skonieczny. Enseigner m'a beaucoup apporté, notamment en termes de rigueur et de confiance en moi, merci de m'avoir offert cette opportunité. Je tiens également à remercier tous mes étudiants, qui, par leurs questions ou leurs réflexions m'ont également beaucoup apporté !

Je tiens ensuite à remercier mes nombreux co-bureau (et oui j'ai souvent déménagé en 4 ans) : Evelyne, Kristan, Marine, Rani, Aurélien, Anta, Thomas, Vincent et Hayoug de m'avoir supportée (dans les 2 sens du terme !). Merci Anta pour tes relectures de ce manuscrit et ton aide à l'heure de régler les questions administratives ou d'installer le pot

de thèse !

Merci également à tous les doctorants/postdoctorants/techniciens/stagiaires : Kristan, Laurine, Rana, Laurie, Martin, Romain, Shaoley, Marion, Virginie, Laetitia, Claire, Naoufel, Anouk, Lucile, Nicolas, Thomas, Tristan, Aglaé, Anta, Julia, Marie, Fanny, Stella... pour votre aide, votre bonne humeur et vos bonnes blagues ! Mention spéciale à Aglaé pour ton soutien, notamment pour les questions administratives !

Je tiens aussi à remercier mes amis et ma famille :
Léane, ma LM^2, merci pour ton soutien sans faille depuis ce premier jour de BCPST où tu es devenue mon extraordinaire binôme ! Merci aussi pour le bon rhum et tous ces moments partagés, à cheval ou autour d'un bon diner !
Merci à Sandrine, Damien, Nadège, Guillaume, Flora, Yoann pour ces aprems jeux, crêpes, dégustation de thé, cartes... et tous ces bons moments passés ensembles ! Merci également pour votre soutien lors des moments de doutes.
Merci à Aaron et Laura pour Bergerac, leur bonne humeur, le unlock, le magic, la paëlla et la tortilla =)
Merci à ma belle famille pour les bons moments partagés ensembles (cousinades, mariages, réunions de famille, Noëls). Merci à toutes les petites têtes blondes d'apporter leur énergie et leur joie ! Merci à Luc pour la découverte de l'Auvergne, merci à Marie-Claude pour les confitures délicieuses et les recettes de grand mères. Merci à tous les deux de nous accueillir chaleureusement si souvent. Merci à Marc, Sienna, Vincent, Clara et leurs deux filles pour les moments conviviaux.
Merci à toi papa, d'avoir été là, de m'avoir aidée dans les moments difficiles et d'avoir toujours cru en moi (bien plus que moi i !
Merci à toi grand-père pour ta présence et tes conseils, merci à toi grand-mère pour tes coups de fils, tes cartes et tes colis remplis de bon chocolat !

Enfin, merci à toi Jean-Louis, mon amour ! Merci pour tout ! Merci pour ton soutien sans faille, tes conseils, ta patience, ta douceur, tes bons petits plats et le piment... Sans toi, je n'aurais probablement pas été au bout de ce travail... J'espère qu'une belle aventure commencera bientôt pour nous deux dans l'autre hémisphère !

List of abbreviations

AABW: Antarctic Bottom Water

ACC: Antarctic Circum Current

AAIW: Antarctic Intermediate Water

AMOC: Atlantic Meridional Overturning Circulation

AMS: Accelerator Mass Spectrometer

BA: Bolling Allerod

BP: Before Present

B-P: Benthic - Planktonic

CfCs: Chlorofluorocarbons

DO: Dansgaard Oeschger event

DSOW: Dennmark Strait Overflow Water

DWBC: Deep Western Boundary Current

DIC: Dissolved Inorganic Carbon

GCM: General Circulation Model

GtC: Giga Tons of Carbon

GNAIW: Glacial North Atlantic Intermediate Water

HS: Heinrich Stadial

ISOW: Iceland Scotland Overflow Water

IRD: Ice Rafted Debris

ka: ky cal BP

LNADW: Lower North Atlantic Water

LSW: Labrador Sea Water

LGM: Last Glacial Maximum

MICADAS: MIni CArbon DAting System

NPS: Neogloboquadrina Pachyderma Senestral

NADW: North Atlantic Deep Water

NSW: Northern Sourced Water

PDB: Pee Dee Belemnite

PI: Pre Industrial

POC: Particulate Organic Carbon

REE: Rare Earth Elements

SMOW: Standard Mean Ocean Water

SST: Sea Surface Temperature

SSW: Southern Sourced Water

XRF: X Ray Fluorescence

YD: Younger Dryas

Table of contents

Résumé détaillé en français

Introduction

Au cours de son histoire récente, et plus précisément de la période du Quaternaire (2 derniers millions d'années), le climat de la Terre a alterné entre des périodes glaciaires froides, et des périodes interglaciaires, plus chaudes. L'étude des glaces du Groenland ou de l'Antarctique, des sédiments marins et des spéléothèmes, a mis en évidence l'existence d'évènements climatiques abrupts au sein des périodes glaciaires. Dans l'hémisphère Nord, on observe des évènements, dits de Dansgaard-Oeschger, qui ne durent que quelques milliers d'années et qui sont caractérisés par un réchauffement brutal suivi par un refroidissement graduel et un retour aux conditions glaciaires. D'autres évènements, appelés évènements de Heinrich correspondent à un refroidissement dans l'hémisphère Nord associé à des débâcles d'icebergs dans l'Atlantique Nord. Ces évènements ont été découverts à la fin des années 1980 et les mécanismes en jeu sont encore débattus. S'il est à ce jour indiscutable que des changements significatifs de la circulation océanique ont eu lieu aux cours de ces évènements climatiques abrupts, aucun consensus n'est établi quand à la géométrie des masses d'eau ou à leur vitesse de circulation.

Le changement climatique actuel est caractérisé par son aspect abrupt. Or, les modèles utilisés pour réaliser les prédictions climatiques futures sont difficilement capables de simuler des évènements abrupts, tels que ceux enregistrés dans les archives climatiques. Ceci s'explique entre autres, par le fait que ces modèles n'ont été calibrés qu'avec des observations climatologiques récentes, qui ne sont pas représentatives des différents états du système climatique (et notamment en période glaciaire). Afin de mieux anticiper le changement climatique en cours, il est donc important de mieux caractériser les évènements climatiques abrupts passés, et notamment en termes de variations de la circulation océanique, l'océan étant une composante majeure du système climatique.

Objectif et stratégie de la thèse

Cette thèse a pour objectif de quantifier les variations de la circulation océanique en Atlantique Nord au cours des derniers 40 ka et comporte une partie analytique et une partie numérique. Mon travail se focalise sur les derniers 40 ka qui ont enregistré 4 évènements de Heinrich et plusieurs évènements de Dansgaard-Oeschger et sur l'Atlantique Nord, qui est une zone clé pour l'étude de la circulation océanique car c'est là que se forment une partie des eaux profondes.

Le premier objectif consiste à appliquer plusieurs outils géochimiques qui apportent des informations complémentaires sur la circulation océanique à une même carotte sédimentaire prélevée sur le flanc ouest de la ride médio-atlantique (SU90-08-43°N, 30°W). Les outils géochimiques utilisés sont les isotopes du carbone, qui apportent des informations quant au niveau de ventilation des eaux profondes et le ^{231}Pa et le ^{230}Th, qui sont utilisés comme indicateurs de la vitesse de circulation des masses d'eau.

Le second objectif consiste à implémenter les isotopes du ^{231}Pa et ^{230}Th dans le modèle de climat de complexité intermédiaire iLOVECILM. Le modèle ainsi amélioré permet de simuler directement l'évolution des traceurs mesurés dans les carottes sédimentaires.

Chapitre - $(U/Th)_{det}$, flux sédimentaires et circulation océanique

L'utilisation des isotopes issus de la désintégration de l'uranium comme indicateurs de l'intensité de la circulation océanique (Pa/Th sédimentaire) et du flux sédimentaire (flux normalisé au ^{230}Th) nécessite de calculer les fractions en excès du ^{231}Pa et du ^{230}Th (indice "xs") au moment du dépôt sédimentaire (indice "0"). $^{231}Pa_{xs,0}$ et $^{230}Th_{xs,0}$ sont calculés à partir des mesures des concentrations isotopiques en ^{231}Pa, ^{230}Th, ^{232}Th et ^{238}U du sédiment total en corrigeant de la contribution détritique et authigène. Ces contributions sont estimées à partir du rapport d'activité ($^{238}U/^{232}Th$) de la fraction détritique des sédiments ($(U/Th)_{det}$ dans la suite). La valeur de $(U/Th)_{det}$ choisie correspond généralement à une moyenne régionale ou, plus récemment à une estimation locale. Dans le cas de SU90-08, les valeurs du flux normalisé au ^{230}Th et du Pa/Th diffèrent de façon significative en fonction de la valeur de $(U/Th)_{det}$ choisie pendant les évènements de Heinrich. Il a donc été nécessaire de mieux contraindre la valeur du $(U/Th)_{det}$.

La première partie du travail a consisté à extraire la fraction détritique des sédiments afin de pouvoir directement mesurer le $(U/Th)_{det}$. Pour cela, j'ai d'une part extrait chimiquement la fraction détritique des sédiments à l'aide d'un protocole de lixiviations séquentielles et d'autre part isolé des grains détritiques sur la fraction grossière (>150 μm). L'analyse des compositions en ^{238}U et ^{232}Th a montré que le $(U/Th)_{det}$ a varié au cours du temps pour la carotte SU90-08 entre 0.4 (Holocène) et 0.7 (dernier maximum glaciaire). Par conséquent, considérer une valeur constante de $(U/Th)_{det}$ associée à une

incertitude de $\pm$ 0.1 (2 σ), comme cela a été fait dans la littérature ne permet pas de tenir compte de la variabilité observée dans les échantillons de la carotte SU90-08.

La deuxième partie du travail a consisté à évaluer l'impact du choix de la valeur du $(U/Th)_{det}$ sur le flux normalisé au ^{230}Th et le Pa/Th. Pour cela, j'ai calculé le flux normalisé au ^{230}Th et/ou le Pa/Th pour une gamme de $(U/Th)_{det}$ allant de 0.3 à 0.8 pour la carotte SU90-08 et trois autres carottes de l'Atlantique Nord. Trois types de comportements sont observés :

— le flux normalisé au ^{230}Th et le Pa/Th ne sont pas significativement affectés par les variations du $(U/Th)_{det}$

— le flux normalisé au ^{230}Th et le Pa/Th sont significativement affectés par la valeur du $(U/Th)_{det}$ appliquée mais seulement pour certaines périodes telles que les évènements de Heinrich

— le flux normalisé au ^{230}Th et le Pa/Th sont significativement affectés sur la totalité de l'enregistrement

Ces différents comportements sont fortement corrélés à la localisation des carottes et à leurs apports en éléments d'origine détritique. Lorsque les apports détritiques sont importants ($>$ 30%), la fraction en excès est en proportion réduite, la façon dont est calculée la correction détritique devient alors cruciale pour le calcul du Pa/Th et du flux normalisé au ^{230}Th. Dans ces cas particuliers, une mauvaise appréciation des variations du $(U/Th)_{det}$ peut conduire à une mauvaise interprétation des amplitudes des changements de flux sédimentaires ou de circulation. De plus, si les variations temporelles du $(U/Th)_{det}$ ne sont pas correctement prises en compte, la variabilité temporelle des flux sédimentaires ou des changements de circulation pourrait ne pas être correctement reconstruite. Par conséquent, lorsque le $^{231}Pa_{xs}$ et le $^{230}Th_{xs}$ sont utilisés, il est nécessaire de tester leur sensibilité à des changements de la valeur du $(U/Th)_{det}$. Par ailleurs, il est important de ne pas utiliser des incertitudes sur le $(U/Th)_{det}$ inférieures aux incertitudes de mesure (qui correspondent à une erreur relative de 10% - 2 σ dans cette étude) et d'évaluer les incertitudes sur le Pa/Th et le flux normalisé au ^{230}Th en fonction des incertitudes sur la valeur du $(U/Th)_{det}$ pour la localisation étudiée.

Chapitre - Datation des carottes sédimentaires par normalisation au ^{230}Th

L'interprétation des données paléocéanographiques de la carotte SU90-08, nécessite d'établir une relation profondeur-âge fiable, précise et indépendante. Cette étape s'avère cruciale pour l'étude d'évènements climatiques d'une durée de l'ordre du millénaire tels que les évènements de Dansgaard-Oeschger ou de Heinrich, en particulier lorsqu'on souhaite

étudier les éventuels décalages temporels entre les enregistrements marins ou terrestres provenant de différentes régions. Le ^{14}C n'est pas directement utilisable pour établir les modèles d'âge des carottes sédimentaires de l'Atlantique Nord situées au delà de $\sim$ 40°N du fait de variations spatiales et temporelles de l'âge ^{14}C des eaux de surface par rapport à l'âge ^{14}C de l'atmosphère contemporaine (âge réservoir). Le modèle d'âge de ces carottes repose alors sur l'alignement des enregistrements des températures de surface sur les variations du δ^{18}O de la glace du Groenland. Cette méthode a permis d'établir 8 marqueurs chronologiques et un premier modèle d'âge pour la carotte SU90-08. Toutefois, ce résultat n'est pas entièrement satisfaisant car i) il ne permet pas de résoudre les éventuelles augmentations de taux de sédimentation associées à la présence d'importants apports détritiques lors des évènements de Heinrich et ii) il n'y a pas d'événement climatique marqué dans l'enregistrement du δ^{18}O de la glace du Groenland entre 14.64 et 23.29 ka cal BP pouvant servir de marqueur chronologique, ce qui rend le modèle d'âge mal contraint pour cette période. J'ai donc utilisé une méthode de datation peu employée jusqu'alors (Adkins et al., 1997; Bourne et al., 2012), la normalisation au ^{230}Th pour détailler l'évolution du taux de sédimentation entre deux pointeurs chronologiques. Ainsi, j'ai révisé les relations âge-profondeurs de la carotte S90-08 et de deux autres carottes de l'Atlantique Nord : SU90-03 (Atlantique Nord-ride médio Atlantique) et SU81-18 (Marge ibérique).

Ce travail relève d'une utilisation particulière de la méthode de normalisation au ^{230}Th et de la datation à haute précision. J'ai donc dans un premier temps discuté les aspects techniques et les hypothèses sous-jacentes.

La première hypothèse consiste à négliger les variations de la redistribution latérale des sédiments sur la période considérée. Ce postulat est délicat à vérifier étant donné qu'il n'existe pas d'indicateur direct de la redistribution latérale des sédiments. Néanmoins, l'analyse des données magnétiques existantes pour les trois carottes ainsi que les calculs de "facteur de focusing" réalisés à partir des données de $^{230}Th_{xs,0}$ montrent qu'il n'y a pas eu de redistribution latérale des sédiments majeure sur la période considérée dans ces trois carottes.

Par ailleurs, j'ai montré précédemment que des variations temporelles du $(U/Th)_{det}$ pouvaient causer des variations du $^{230}Th_{xs,0}$ pour les carottes à fort apport détritiques notamment la carotte SU90-08 et celles de la marge ibérique. Il est donc nécessaire de vérifier que des variations du $(U/Th)_{det}$ (jusqu'ici non contraintes sauf pour la carotte SU90-08) ne peuvent pas significativement changer les modèles d'âges issus de la normalisation au Th. Globalement, les changements de la valeur du $(U/Th)_{det}$ impactent le modèle d'âge produit par la normalisation au Th en deçà des incertitudes sur les pointeurs, ces derniers étant la première source d'incertitude pour le modèle d'âge.

Enfin, l'accord entre les variations des taux de sédimentation reconstruits à partir des dates ^{14}C et de la normalisation au Th a été testé sur une carotte de l'Atlantique équa-

torial, qui ne subit à priori pas de variation des âges réservoirs du fait de sa localisation, loin des zones de formation des eaux profondes. Un bon accord entre les deux méthodes de datation est observé sur la première section de la carotte, mais pas sur la seconde, caractérisée par une absence de variabilité dans l'enregistrement de $^{230}Th_{xs,0}$. Les données disponibles ne permettent actuellement pas de déterminer si le désaccord entre les deux méthodes provient d'un biais dans les données de $^{230}Th_{xs,0}$ ou de ^{14}C.

Après avoir validé l'utilisation de la méthode de la normalisation au ^{230}Th pour les trois carottes de l'Atlantique Nord étudiées, j'ai examiné l'évolution des températures de surface pour ces trois carottes en fonction des nouvelles chronologies établies. L'analyse de ces températures de surface montre que, en tenant compte des incertitudes de datations, le refroidissement correspondant au début du stadiaire de Heinrich 1 est synchrone dans les trois carottes. Ce refroidissement est aussi synchrone avec un événement abrupt enregistré dans le Ca^{2+} du Groenland, traceur des flux de poussières, daté à 17.48 $\pm$ 0.21 ka cal BP. Je propose donc d'utiliser cet événement comme un nouveau marqueur chronologique permettant de remédier à l'absence de pointeur entre 14.7 et 23.3 ka cal BP dans le $\delta^{18}O$ du Groenland.

Chapitre - Enregistrements multi-proxy de la carotte SU90-08

Après avoir amélioré l'enregistrement de Pa/Th sédimentaire et le modèle d'âge de la carotte SU90-08, je me suis intéressée aux séries temporelles documentant l'évolution de la circulation océanique ($\delta^{13}C$ benthique, âges ^{14}C benthiques et planctoniques et Pa/Th) au cours des derniers 40 ka. Dans un premier temps, j'ai évalué si les enregistrements disponibles reflétaient bien les variations de la circulation océanique plutôt que des processus locaux (bioturbation, flux particulaires...).

J'ai préparé des paires d'échantillons benthiques et planctoniques pour 25 niveaux de la carotte SU90-08. Les mesures des âges ^{14}C été réalisées grâce à une technique d'analyse innovante permettant de mesurer la composition en ^{14}C d'échantillons de petite taille sous forme gazeuse (MICADAS couplé à un système d'introduction gaz). J'ai pu montrer que les mesures sont de qualité (justesse-reproductibilité). Les différences d'âge benthique - planctonique obtenues sur la période post-HS1 sont cependant négatives. J'ai montré que ces résultats ne pouvaient pas découler de processus hydrothermaux ou de dissolution/recristallisation des coquilles de foraminifères. En fait, ces âges benthique-planctoniques négatifs reflètent l'impact de la bioturbation de cette carotte dont le taux de sédimentation est relativement faible ($\sim$ 4 cm/ka). Cette interprétation est cohérente avec les reconstructions de la ventilation des eaux profondes ainsi que des simulations idéalisées de bioturbation. De ce fait, l'enregistrement de ^{14}C de la carotte SU90-08 ne reflète que des variations du premier ordre (type glaciaire-interglaciaire).

Le Pa/Th sédimentaire est sensible à la fois aux changements de circulation océanique et aux changements de la composition et du flux de particules sédimentant dans la colonne d'eau. J'ai donc testé la corrélation entre le Pa/Th sédimentaire et i) la teneur en opale, ii) le flux particulaire et enfin iii) certains éléments présents dans les fluides hydrothermaux (Al, Fe, Mn). L'absence de corrélation observée atteste que les variations du Pa/Th sédimentaire enregistrées dans la carotte SU90-08 représentent bien les variations de la circulation océanique.

Dans un second temps, j'ai analysé les séries temporelles des différents proxies et confronté les informations qu'elles apportent. De 45 ka cal BP à 33 ka cal BP et depuis la sortie de HS1, les eaux de fond ont été bien ventilées et bien oxygénées. A partir de 33 ka BP les eaux de fond ont perdu leur oxygénation progressivement ; le minimum de ventilation a été atteint au dernier maximum glaciaire et cette situation a perduré jusqu'à la sortie de HS1. Ces variations ne sont pas retrouvées dans l'enregistrement de Pa/Th sédimentaire qui indique la présence d'une circulation vigoureuse et persistante pendant les derniers 40 ka mais plus active au dernier maximum glaciaire que pendant l'Holocène. De légers ralentissements de la circulation sont visibles pendant HS4 et la deuxième moitié de HS1 mais pas pendant HS2. Ainsi, en combinant les informations apportées par le Pa/Th et les isotopes du carbone, on peut déduire la présence d'une circulation vigoureuse contemporaine d'une masse d'eau profonde peu ventilée et peu oxygénée pendant le dernier maximum glaciaire. Ces résultats, à priori contradictoires, questionnent donc quant à la nature du signal réellement enregistré par chaque proxy : enregistrent-ils la signature de la même masse d'eau ou de masses d'eau différentes ? En effet, les isotopes du carbone enregistrent la signature isotopique de l'eau dans laquelle la coquille s'est formée. En revanche, le Pa/Th intègre le signal d'une plus grande portion de la colonne d'eau (jusqu'à $\sim$ 1000 m au dessus de l'interface eau-sédiment).

Enfin, j'ai comparé les enregistrements de la carotte SU90-08 aux autres séries temporelles de Pa/Th sédimentaire et de δ^{13}C benthique disponibles dans l'Atlantique. Le δ^{13}C benthique de la carotte SU90-08 est cohérent avec les autres données de l'Atlantique. L'enregistrement de Pa/Th sédimentaire de la carotte SU90-08 possède une forme classique, avec des augmentations lors des évènements de Heinrich. Toutefois, contrairement à ce qui a pu être observé pour d'autres carottes, le Pa/Th de la carotte SU90-08 n'atteint jamais le rapport de production. Ceci est probablement lié à la profondeur de la carotte (3080 m) qui enregistre une circulation persistante autour de 2000 m alors que les autres carottes plus profondes ($>$ 4000 m) indiquent une réduction plus importante de la circulation en dessous de 3000 m pendant les évènements de Heinrich. L'enregistrement de Pa/Th de la carotte SU90-08 présente aussi de fortes ressemblances avec l'enregistrement disponible une carotte la marge ibérique située à une profondeur comparable : les deux carottes ont des valeurs similaires indiquant une circulation plus active au dernier

maximum glaciaire qu'à l'Holocène. Ces deux carottes indiquent aussi un ralentissement de la circulation pendant l'événement de Heinrich 1 remarquablement synchrone et tardif par rapport aux enregistrements de Pa/Th des Bermudes ou de la marge brésilienne. Ce décalage temporel ne peut pas s'expliquer par les incertitudes sur les modèles d'âge mais pourrait correspondre aux deux phases de l'événement de Heinrich 1, proposées dans la littérature. Finalement, l'enregistrement multi-proxy de la SU90-08 indique pour la première fois un découplage entre la ventilation des masses d'eau profondes et leur vitesse d'écoulement. Quoi qu'il en soit, les informations apportées par les proxy restent qualitatives. La quantification des changements de circulation nécessite donc de recourir à la modélisation.

Chapitre - Modélisation de la réponse du Pa/Th, δ^{13}C et Δ^{14}C à un changement abrupt de la circulation océanique

Il est tout d'abord nécessaire de disposer d'un modèle de climat capable de simuler l'évolution simultanée des trois proxies (δ^{13}C, Δ^{14}C et Pa/Th) pendant plusieurs centaines d'années en un temps de calcul raisonnable. De nombreux modèles existants sont capables de simuler les compositions isotopiques du carbone en conditions préindustrielles ou glaciaires. Par ailleurs, la production, le transport et le scavenging du Pa et du Th ont aussi été implémentés dans des modèles de climats de manière plus ou moins complexes. Les approches les plus simples utilisent un modèle 2D ou réalisent des simplifications excessives dans la représentation des champs de particules dans des modèles 3D. Les derniers développements représentent les processus affectant le Pa et le Th avec plus de détails et de réalisme mais si certains modèles ont une résolution de l'océan insuffisante, d'autres ne peuvent pas simuler 1000 ans assez rapidement. J'ai donc choisi d'implémenter le Pa et le Th dans le modèle de complexité intermédiaire iLOVECLIM qui était déjà capable de simuler les cycles du ^{13}C et du ^{14}C.

Pour cela, j'ai considéré une seule classe de taille et trois types de particules ($CaCO_3$, carbone organique particulaire et opale). iLOVECLIM ne simule pas le cycle biogéochimique de l'opale, qui est pourtant considéré comme un scavenger important pour le Pa et le Th. J'ai donc décidé de considérer des champs de particules constants qui proviennent du modèle NEMO-PISCES. J'ai ensuite considéré que le Pa et le Th avaient un coefficient de désorption identique, quel que soit le type de particule, et j'ai ajusté les 6 coefficients d'adsorption (trois types de particules - Pa et Th) en utilisant une méthode d'optimisation de l'exploration de l'espace des paramètres (Latin Hypercube). J'ai réalisé 60 simulations de 1000 ans avec des ensembles de paramètres différents en conditions préindustrielles. J'ai ensuite comparé les résultats produits par le modèle aux observations disponibles. Le nouveau module de Pa/Th simule des concentrations dissoutes et particulaires réalistes

et comparables aux résultats des études de modélisation précédentes. Dans la meilleure simulation, le Pa et le Th ont tendance à être adsorbés sur les particules et enfouis dans les sédiments trop rapidement. Les concentrations dissoutes sont donc de manière générale sous-estimées dans le modèle, particulièrement dans la ceinture d'opale de l'océan Austral. Globalement, le modèle représente bien le Pa/Th sédimentaire au milieu des bassins océaniques, les régions côtières présentant les plus grandes différences entre les résultats du modèle et les observations. Ceci peut être attribué au manque de représentation de processus tels que le "boundary scavenging" (entraînement à la marge) ou les couches néphéloïdes.

Ensuite j'ai étudié la réponse des trois proxies à une réduction abrupte de la circulation océanique que j'ai provoquée en ajoutant un flux d'eau douce de 0.3 Sv pendant 300 ans dans les mers nordiques. On observe bien une réduction de la convection de l'Atlantique Nord qui s'arrête peu de temps après le début de l'ajout du flux d'eau douce et reprend progressivement après la fin de l'ajout d'eau douce. J'ai analysé la réponse temporelle des proxy en identifiant toutes les périodes de plus de 80 ans pour lesquelles la valeur du proxy est inférieure ou supérieure à la variabilité naturelle enregistrée pendant 300 années en conditions préindustrielles (contrôle). Selon les proxy, j'observe de 0 à 4 périodes de ce type. Dans ce qui suit la "réponse d'un proxy" est définie comme l'amplitude maximum de l'écart à la moyenne de ce proxy durant une des périodes de plus de 80 ans définies ci-dessus. Les proxy ont une réponse cohérente dans le bassin Ouest alors que dans le bassin Est on observe de plus nombreuses réponses multiples. J'ai pu montrer que les différents types de réponse des proxys correspondent aux trois principales masses d'eau de l'Atlantique. Dans les eaux intermédiaires, le δ^{13}C et le Δ^{14}C augmentent ; le Pa/Th augmente avec une faible amplitude. Dans l'AABW, les trois proxy réagissent de manière synchrone et cohérente : le Pa/Th augmente alors que le δ^{13}C et le Δ^{14}C diminuent, traduisant la diminution de la circulation et de la ventilation. Finalement, dans le NADW, le Pa/Th augmente alors que le δ^{13}C et le Δ^{14}C diminuent. Toutefois, si les temps de réponse du δ^{13}C et du Δ^{14}C sont généralement similaires et augmentent avec la profondeur, le temps de réponse du Pa/Th est généralement plus rapide de quelques centaines d'années.

Le décalage entre la réponse du Pa/Th et la réponse des isotopes du carbone peut s'expliquer par les mécanismes fondamentalement différents qui régissent chaque proxy. En effet, dans le modèle, les particules sont fixées et le Pa/Th ne dépend donc que des changements de circulation. De plus, le Pa et le Th ont des temps de résidence très courts dans la colonne d'eau. Au contraire, les isotopes du carbone interagissent avec de nombreux réservoirs, notamment via les échanges atmosphère-océan ou par l'activité biologique, ce qui demande du temps. Par ailleurs, bien que les évolutions simulées pour les différents proxy ne soient pas directement comparables avec les données paléocéanographiques, on observe une cohérence entre les résultats du modèle et les observations : une réponse

cohérente correspondant à une augmentation du Pa/Th et une diminution du $\delta^{13}C$ et du $\Delta^{14}C$ dans l'Atlantique Ouest (> 1500 m).

Conclusions et perspectives

L'objectif général de cette thèse était de quantifier les variations de la circulation océanique en Atlantique Nord au cours de derniers 40 ka. Pour cela, j'ai réalisé des mesures d'isotopes du carbone (^{13}C, ^{14}C) et de Pa/Th sédimentaire pour la carotte SU90-08. Avant d'analyser ces enregistrements, deux étapes préliminaires ont été nécessaires :

— Contraindre l'amplitude des variations du Pa/Th et du flux normalisé au ^{230}Th qui montraient une forte sensibilité au rapport ($^{238}U/^{232}Th$) de la fraction détritique des sédiments ($(U/Th)_{det}$). J'ai montré que $(U/Th)_{det}$ a varié au cours du temps (entre 0.4 et 0.7) et que, de manière générale, de telles variations peuvent affecter les reconstruction de flux sédimentaires et de circulation océanique dans les régions qui reçoivent d'importants apports détritiques.

— Établir un modèle d'âge robuste pour la carotte SU90-08. J'ai appliqué une méthode jusqu'alors peu utilisée, la normalisation au ^{230}Th, afin de contraindre l'évolution du taux de sédimentation entre les repères chronologiques issus de l'alignement des signaux de température de surface à ceux du Groenland. Cette étude m'a également permis de proposer l'utilisation d'un événement abrupt dans l'enregistrement du flux de poussière du Groenland daté à 17.48 ± 0.21 ka BP comme nouveau marqueur chronologique.

L'obtention de mesures de ^{14}C pour la carotte SU90-08 a nécessité l'utilisation d'une méthode d'analyse innovante (MICADAS couplé à un système d'introduction des échantillons sous forme gazeuse) capable de mesurer des échantillons de petite taille. J'ai d'abord montré que les mesures étaient justes et reproductibles puis analysé la différence entre les âges benthiques et planctoniques (B-P). Les âges ^{14}C B-P obtenus pour l'Holocène sont négatifs mais reproductibles. J'ai montré, notamment à l'aide de simulations idéalisées que les âges ^{14}C B-P reflètent la bioturbation de cette carotte dont le taux de sédimentation est relativement faible.

Les enregistrements de la carotte SU90-08 montrent deux particularités intéressantes. Au dernier maximum glaciaire, les isotopes du carbone et le Pa/Th apportent des informations contradictoires indiquant une circulation active mais une faible ventilation des masses d'eau profondes. De plus, si la réponse des proxy pendant les évènements de Heinrich pour la carotte SU90-08 est similaire à celle observée dans d'autres carottes de l'Atlantique Nord (*i.e.* augmentation du Pa/Th et diminution du $\delta^{13}C$), le Pa/Th de SU90-08 n'atteint jamais le rapport de production. Ceci pourrait s'expliquer par la profondeur de la carotte (3080 m) et le fait que le Pa/Th intègre probablement le signal sur

plusieurs centaines de mètres de colonne d'eau au dessus de l'interface eau-sédiment. Par ailleurs, l'augmentation du Pa/Th pendant l'événement de Heinrich 1 arrive environ 1000 ans en retard dans la carotte SU90-08 et à la marge ibérique par rapport à ce qui est enregistré dans les carottes situées dans le courant de bord Ouest. Enfin, le recours à la modélisation est nécessaire afin de quantifier les changements de circulation océanique des 40 derniers ka.

La deuxième partie de cette thèse a consisté à ajouter les isotopes ^{231}Pa et ^{230}Th dans le modèle de climat de complexité intermédiaire iLOVECLIM puis à étudier la réponse des trois proxy considérés à un changement de circulation abrupt.
J'ai modélisé le savenging réversible du ^{231}Pa et ^{230}Th en considérant 3 types de particules ($CaCO_3$, carbone organique particulaire et opale) et une seule taille de particules. Suite à ce travail, Le modèle est capable de simuler l'évolution simultanée du Pa/Th, δ^{13}C et Δ^{14}C en un temps raisonnable. J'ai ensuite évalué la réponse des trois proxy à un ralentissement abrupt de circulation induit par ajout d'eau douce dans les mers nordiques. La réponse des proxy reproduit la répartition des trois principales masses d'eau de l'Atlantique. Dans l'Atlantique Ouest (NADW), le δ^{13}C et Δ^{14}C diminuent et le Pa/Th augmente en réponse au ralentissement de la circulation. De plus, la réponse des isotopes du carbone est en retard de quelques centaines d'années par rapport à la réponse du Pa/Th.

Voici quelques perspectives de ce travail de thèse :

— Le $(U/Th)_{det}$ peut varier significativement dans le temps, affectant le Pa/Th et le flux normalisé au ^{230}Th dans les régions à forts apports détritiques. Il serait donc intéressant d'évaluer les variations du $(U/Th)_{det}$ là où existent des enregistrements clés de Pa/Th, notamment sur la marge ibérique ou aux Bermudes. De plus, on pourrait envisager de développer une méthode d'évaluation du $(U/Th)_{det}$ plus rapide, basée sur des mesures réalisées en routine.

— J'ai proposé l'utilisation d'un nouveau marqueur chronologique pour les datations des carottes sédimentaires de l'Atlantique Nord. Il serait donc intéressant de tester la valeur ajoutée et la validité de ce nouveau marqueur à l'aide de nouveaux enregistrements de température des eaux de surface dans l'Atlantique Nord. Par ailleurs, il pourrait être utile d'intégrer la normalisation au Th dans des logiciels de datation des enregistrements sédimentaires permettant d'estimer les incertitudes sur ces modèles d'âges.

— Les nouvelles techniques d'analyse du ^{14}C permettent d'analyser des échantillons de petite taille, ouvrant la voie pour la génération de nouvelles données. Dans le cas de la carotte SU90-08, j'ai mis en évidence que l'état de conservation des sédiments, et en particulier le niveau de bioturbation, affecte les données ^{14}C. Dans des études précédentes, de nombreuses données ont pu être considérées comme anormales et

être rejetées. Une réévaluation de ces données, à la lumière des biais potentiels de la bioturbation sur les âges ^{14}C pourrait apporter des informations intéressantes.

— La partie modélisation de ma thèse débouche sur des perspectives dans deux directions différentes. La première consiste à améliorer la représentation du comportement du Pa et du Th dans la colonne d'eau. On pourrait par exemple améliorer les réglages des coefficients d'adsorption-désorption du Pa et du Th sur les différents types de particules ou encore ajouter la représentation de phénomènes tels que les couches néphéloïdes ou le boundary scavenging. La seconde direction consiste à utiliser le modèle dans son état actuel. On pourrait par exemple évaluer la part du signal du Pa/Th qui est due aux changements de circulation *vs* la part du signal due aux changements de nature ou flux particulaires. On pourrait également tester si la réponse des différents proxy en conditions glaciaires est identique à celle établie pour le préindustriel.

General Introduction

Within the past decades, the atmospheric concentration of greenhouse gases has increased substantially. For example, the atmospheric carbon dioxide (CO_2), for which the preindustrial concentration was 280 ppmv, surpassed the symbolic threshold of 400 ppmv in 2013. The scientific community attributes these recent atmospheric composition changes to anthropogenic activities, and in particular, to fossil fuels burning. Simultaneously with the atmospheric greenhouse gases concentration rise, other changes in the Earth climate have been observed: increase in global air temperature, sea level rise, ice-sheets and sea-ice retreat, increasing occurrence of extreme climate events such as droughts or floods. These changes may represent a threat for human societies in the future. For instance, a significant sea-level rise could result in important migrations of the population currently settled in coastal environments. Besides, the global temperature rise could enlarge the arid areas, reducing the potential for food production in a context of global population increase. These climate change consequences lead the political leaders and, to a greater extent, the human societies to become concerned about the ongoing anthropogenic climate change. The numerous international summits that occurred in the past decades such as Conferences of the Parties (COP 1-22), created after the "United Nations Conference on Sustainable Development" (Rio de Janeiro, 1992) and the ratification and entry in force of Kyoto agreement (1997), and later the Paris agreement (2015), attest for the human societies concern about climate change. Thus there is a great interest and effort for understanding this climate change and predict the possible climate trajectories for the future centuries.

Looking back into Earth history using climate archives (ice, lakes or marine cores...) showed that Earth climate has been oscillating between cold glacial periods and warmer interglacial periods for the last 2.6 Ma (Quaternary). The glacial periods are mainly characterized by the reduction of the global temperature (~ 4 °C), a decreased atmospheric CO_2 concentration (by up to 90 ppmv) and an enlarged extension of polar ice caps (cor-

responding to a sea level drop of $\sim$ 120 m) compared with Interglacial periods. The last deglaciation occurred between 21 and 10 ky BP and was followed by an interglacial period called Holocene, which corresponds to the modern time period. Since the onset of the Holocene, around 10 ky ago, the climate has been relatively stable compared to what is observed for the last glacial period, which started around 110 ky ago. The study of high-resolution ice cores of Greenland and Antarctica as well as speleothems and marine sediments revealed the occurrence of millennial scale abrupt climatic events during the last glacial period. In the Northern Hemisphere, periods characterized by abrupt warming followed by gradual cooling and return to glacial initial state after 1 to 3 ky have been identified and named Dansgaard-Oeashger (DO) events. This millennial scale climate variability is characterized by an alternation and rapid switch between cold (stadials) and warm (interstadials) conditions and is recorded by several tracers in terrestrial and marine archives (*e.g.* speleothems, ice cores, marine cores). During some of these stadials, called Heinrich stadials, massive iceberg discharges occurred in the North Atlantic, leaving coarse detrital grains layers in marine sediments located in the so-called Ruddiman belt area. This coarse material is referenced as Ice Rafted Detritus (IRD) and forms Heinrich layers in North Atlantic sediment cores. Together with the Heinrich stadial conditions in the North Atlantic, a warming trend is observed in the Southern hemisphere. Although these abrupt climate events have been documented since the 1990's, their complex underlying mechanisms are still under debate. There is evidence that these episodes involved many components including reorganisations of the ocean circulation, ocean biogeochemistry, changes in sea-ice cover and ice volume, carbon cycle, vegetation, land surface and atmosphere dynamics. It is widely accepted that the ocean is a key player in those abrupt climate events. Major changes in the ocean circulation such as water masses reorganization or changes in overturning rate related to the rapid climate changes of the last glacial have been documented. Nevertheless, there is no consensus about the disposition and the circulation strength of the major water masses across theses abrupt climate events. Besides, if some qualitative features have been identified, quantifications of the deep circulation flow changes across those events are still inexistent.

One of the main characteristics of the current anthropogenic warming is that it is particularly fast and abrupt. Yet, the current state-of-the-art climate models used to perform future climate projections can hardly reproduce abrupt climate changes observed in the last glacial cycle, such as DO and Heinrich events. To date, none of these models have been successful in simulating the amplitude, pattern and timing of the millennial scale events. The climate system exhibits fast and non-linear reactions to small perturbations. In other words, when the climate oscillates between different states (*e.g.* glacial to interglacial), the threshold and the pathway corresponding to the transition glacial to interglacial will be different from the threshold and pathway corresponding to the transition

from glacial to interglacial. An example for this climate hysteresis is the slow interglacial transition compared to the abrupt deglaciations observed in Greenland ice records. Contrarily to the climate system, the current models require much larger perturbations to simulate abrupt changes. This might be attributed to the fact that models are tuned and evaluated only against recent observations. Thus, there is a need to better explore the past abrupt climate change and better quantify the ocean circulation changes across those events as the ocean is a key player in climate transitions. Such research would help to better represent non-linear climate system response into the climate models and thus improve future climate projections.

For that purpose, I adopted a combined approach using both paleo-tracers measured on marine climate archives and a climate model. The paleo-tracers part of this work focuses on the Atlantic Ocean, a key area for deep oceanic convection because it hosts one major deep-water formation zone. The targeted study period corresponds to the last 40 ky, for which 4 Heinrich events and several DO events have been documented and which corresponds to the period of validity of ^{14}C, a powerful dating tool. For the modeling part, the aim is to bring the model outputs closer to the observed data by enabling the model to directly simulate proxy evolution instead of only computing the classical climate metrics such as temperature or salinity. The chosen model is of intermediate complexity to ensure that the computation of several thousands of years can be achieved in a reasonable time (typically 800 y simulated in ∼24h). In details, this PhD thesis is divided in five chapters:

Chapter 1 is dedicated to the description of the modern ocean circulation, and the presentation of the principal tools used in paleoceceanography to reconstruct past ocean circulation. In particular, we focus on the study of carbon isotopes, which give information about the deep-water ventilation and the isolation of the water mass from the surface and the U-series nuclides (^{231}Pa and ^{230}Th), which can be used as a kinematic circulation proxy. After a summary of past and recent studies reconstructing Atlantic Ocean circulation, we also describe the thesis strategy: the chosen study site SU90-08, (43°N, 30°W, 3080m), its relevance and the data that was available at the beginning of this thesis, the need for a multiproxy approach to reconstruct different aspects of the circulation changes and the chosen climate model.

Chapter 2 focuses on the improvement of the one of the paleo-proxy record, the sedimentary ($^{231}Pa_{xs,0}/^{230}Th_{xs,0}$). Indeed, in order to be able to compare paleo-proxies records from different regions, it is necessary to screen the data and verify that the time series primarily represent climate driven circulation changes and not only local processes. This led me to investigate about the potential variations of ($^{238}U/^{232}Th$) in the detrital fraction of the sediments (hereafter labelled $(U/Th)_{det}$), a crucial parameter for the calculation of excess fractions of ^{230}Th and ^{231}Pa. Temporal variations of $(U/Th)_{det}$ that

have never been considered before in the literature, have been evidenced and quantified. Systematical sensitivity test of excess ^{231}Pa and ^{230}Th to changes in $(U/Th)_{det}$ showed that under certain circumstances, effects of temporal variations of $(U/Th)_{det}$ should not be neglected. This work is the topic of the paper "Downcore variations of sedimentary detrital ($^{238}U/^{232}Th$) ratio: implications on the use of $^{230}Th_{xs}$ and $^{231}Pa_{xs}$ to reconstruct sediment flux and ocean circulation" published in *Geochemistry, Geophysics, Geosystems* in 2018 (Missiaen et al., 2018).

Chapter 3 focuses on age-model improvements for SU90-08 and more extensively for North Atlantic marine records. Indeed, dating is a key issue for paleoceanography, especially when it comes to study millennial scale events and compare records possibly from different regions. Moreover, above ∼40°N in the North Atlantic it is not possible to simply use ^{14}C dating because important variations in surface waters reservoir ages have been documented and are still insufficiently constrained. Hence, in the North Atlantic, the marine records are often dated using alignment of sea surface records to Greenland air temperature, an approach that suffers from the lack of climatic events between 23.3 and 14.7 ky cal BP. By combining the chronological information from radiocarbon, alignment pointers and ^{230}Th-normalization for three North-Atlantic cores, we find great consistency in the timing of sea surface temperature cooling at the onset of HS1. This cooling is also consistent with an abrupt event recorded in Greenland Ca^{2+} and dated at 17.48 ± 0.17 (1σ) ky cal BP. Thus we propose to use this event as a new tie-point to remedy the lack of chronological marker between 14.7 and 23.3 ky cal BP and better constrain North Atlantic cores dating in this crucial time interval for the study of HS1 and the last deglaciation. This work is the topic of the paper "Improving North Atlantic marine core chronologies using ^{230}Th-normalization", under revision in *Paleoceanography and Paleoclimatology*.

Chapter 4 concentrates on the interpretation of SU90-08 circulation proxy time series. First, special attention is given to the interpretation of the ^{14}C dataset, which exhibits negative benthic-planktonic ages after HS1 and during the Holocene. This work is the topic the paper "Small sized foraminifer samples radiocarbon measurements using (ETHZ) MICADAS gas introduction system: insights into sediment archive preservation" currently in preparation and to be submitted to *Radiocarbon*. Then, the information about the circulation evolution from benthic δ^{13}C, radiocarbon and Pa/Th is evaluated both separately and conjointly. One of the most interesting features of SU90-08 multi-proxy record is that carbon-based proxies and sedimentary Pa/Th contain apparently inconsistent information during the LGM: they record poor ventilation but active overturning circulation. SU90-08 time series are finally compared with other North-Atlantic records available.

Chapter 5 describes how the ^{231}Pa, ^{230}Th cycles were implemented into the climate model of intermediate complexity iLOVECLIM. Thanks to this work, it is possible to

compute the simultaneous evolution of the three proxies (Pa/Th, $\delta^{13}C$ and $\Delta^{14}C$) over thousands of years in a reasonable computation time. This tool allows to evaluate the fingerprint of the multi-proxy response to abrupt circulation slowdown obatained by freshwater addition in the North Atlantic. This work shows that i) the proxy response follow the organization of the three main Atlantic water masses (NADW, AAIW, AABW); ii) in the NADW, the proxy display coherent response with $\delta^{13}C$ and $\Delta^{14}C$ decrease while Pa/Th increases and iii) in the NADW, the carbon isotopes response lags the Pa/Th response by a few hundreds of years.

Finally, the last section summarises the main conclusions of this PhD thesis and how it contributes to better understand ocean reorganizations associated with abrupt climate events of the last 40 ky. This section is finally closed on perspectives for future research that arose from this PhD work.

Chapter 1. Reconstructing the Atlantic Meridional Overturning Circulation across the abrupt climate events of the last 40 ky

1.1 The general modern ocean circulation

1.1.1 The ocean, a major componenent of the climate system

The ocean covers roughly 70% of the Earth's surface and receives an important proportion of the incoming planetary solar radiations. According to the changes in sea-ice cover, the ocean can modulate the planetary albedo and thus the global heat budget. Because of its size (1,370 millions of km^3), the ocean has the ability to store some heat and damp a global warming (Cess & Goldenberg, 1981). As the water masses move along global patterns at both the surface and at depth, the ocean also participates to the global energy transfers and in particular from the equator to the high latitudes.

Furthermore, the ocean affects the climate system because it can modulate the atmospheric greenhouse contents. Contrarily to the lithosphere, which is the biggest carbon reservoir (∼7 000 000 GtC), the ocean (∼39 000 GtC) can rapidly exchange its carbon with the atmosphere via surface air-sea exchanges. Oceanic changes in mixed layer depth, sea surface temperature or even fluctuations of the sea-ice cover can thus modulate the air-sea gas changes (Rahmstorf, 2002) and thus the atmospheric composition. The ocean circulation is also involved in the repartition of dissolved or particulate components (*e.g.* nutrients or carbon) in the water column, influencing the biological activity. The abil-

ity of the phytoplankton to consume the dissolved inorganic carbon from the upwelling nutrient-rich deep waters and thus to control the CO_2 outgassing to the atmosphere is called the biological pump efficiency.

Thus, the world ocean interacts with the global climate in multiple ways and is considered to be one major component of the climate system. Because oceanic changes can affect the planetary energy cycle, precipitation regimes and atmospheric greenhouse gas budget, studying the water masses organization and circulation is a key topic for climatology.

1.1.2 Modern deep ocean circulation

Under modern conditions, two types of large-scale ocean circulations are observed: the gyre circulation at the surface and the deep circulation. The surface processes consist in highly turbulent mixing that requires to consider meso-scale processes. In this PhD thesis, I will focus on the deep ocean circulation patterns that can be studied at a larger scale.

The large-scale ocean circulation is due to a combination of three driving mechanisms: winds, heat and fresh waters fluxes as well as tides (gravitational pull of the Moon and Sun). These driving mechanisms interact in non-linear ways since all types of current can affect heat and salt distribution (Rahmstorf, 2002). The study of water masses pathways in the ocean interior can be achieved by combining different techniques such as measuring the water properties (temperature, salinity), their chemical content (nutrients, oxygen, trace elements, isotopes...) or later following floats (argo: http://www.argo.ucsd.edu/) or passive tracers such as chlorofluorocarbons (CFCs). Thanks to the sophistication of the Global Positioning System (GPS) and enhanced computation power, the floats enabled to establish a more precise view of the world ocean currents and their complexity. Indeed, such programs highlight the turbulent nature of ocean circulation. On a more global scale, the use of the CFCs, injected to the ocean from the atmosphere permitted to trace the newly formed deep waters along their transport into the ocean interior via the deep circulation. Such work allowed to establish a global view of the global ocean circulation, which is briefly described in the following lines.

Figure 1.1 shows a simplified cartoon of the modern global circulation also called sometimes "the great conveyor belt" (Rahmstorf, 2002). Surface waters from the Caribbean flow Northward and reach the North-Atlantic deep-water formation regions: the Labrador and the Norwegian seas. After releasing their heat, the surface waters reach a critical density, above the density of underlying water masses. Thus the surface waters become unstable and sink. In the Southern Ocean, deep waters also forms in the Ross Sea and in the Weddell sea. There, the strong winds blowing on the Antarctic ice-sheet create sea-ice free zones called polynias. In the polynias, intense sea-ice formation takes place, reject-

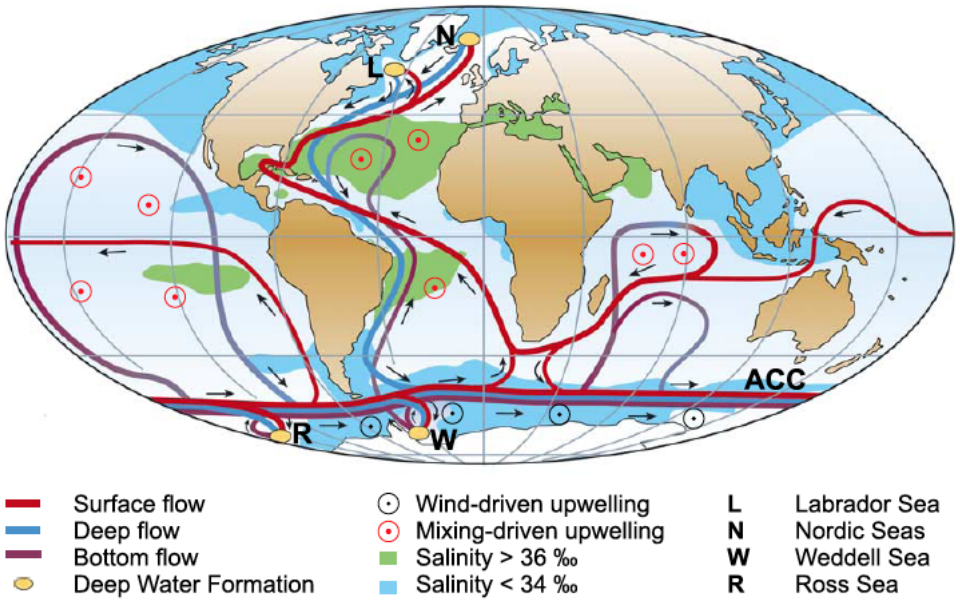

Figure 1.1 – **Highly simplified global ocean circulation cartoon (Rahmstorf, 2002)**

ing important salinity fluxes (brine rejection), the sea-ice being made of freshwater. The brines formed are very salty and very cold, participating in the formation of very dense deep-water masses (Nicholls et al., 2009). The amount of deep-water formation is estimated to 15±2 Sv (1Sv $=10^6.m^3.s^{-1}$) for the North-Atlantic and 21±6 Sv for the Southern Ocean. The export production varies at seasonal, annual and decadal time scales with an amplitude of a few Sverdrup (see Buckley & Marshall, 2016, for a review).

The deep waters formed in the North Atlantic are generally referred to North Atlantic Deep Water (NADW) and can be subdivided into several branches based on their origin and properties. The Labrador Sea Water (LSW) forms by convective processes in the relatively cold and low salinity environment of the Labrador Sea. Denser deep waters are formed by active convection in the Nordic seas and reach the Atlantic ocean by overflowing oceanic seals such as the Greenland-Iceland-Scotland Ridge or the Denmark Strait (Buckley & Marshall, 2016). Because of their respective densities, the LSW forms the upper branch of the NADW (UNADW), the overflow waters, so called Iceland Scotland Overflow waters (ISOW) or Denmark Strait Overflow Waters (DSOW) form the lower branch (LNADW) (Figure 1.2). The NADW is then mostly flowing between 2000 and 4000m depth and exported in the Atlantic by flowing in the Deep Western Boundary Current (DWBC) and other complex interior pathways. Notably, part of the NADW reaches the eastern Atlantic Basin through the Gibbs fracture in the Mid Atlantic Ridge and flows south along the eastern side of the mid Atlantic ridge, as counterpart of the DWBC (Paillet et al., 1998). Nevertheless, the DWBC is the primarily export pathway for

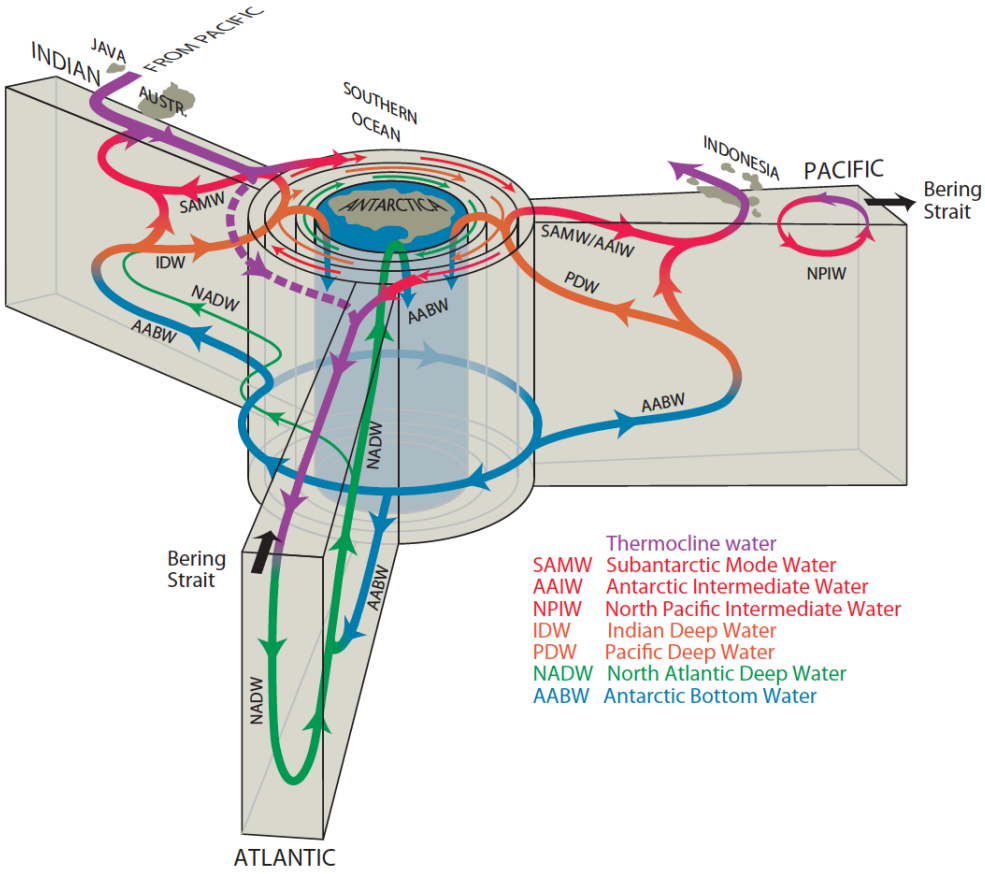

Figure 1.2 – **General ocean circulation and water masses after Talley (2013)**
This cartoon exhibits the major deep-water masses from the 3 main oceanic basins. Remarkably, in the Atlantic, the NADW flows southward in the upper 3000m of the basin; the AABW flows northward in the deep basin. The AABW circulates in the deep ACC and is distributed in the Indian and Pacific oceans where it upwells. Other general circulation patterns have been described in the Indian and Pacific Ocean but are not detailed here as this PhD project focuses on the Atlantic Ocean.

NADW. In the Southern Ocean, the dense waters upwell along isopycnals drawn by the strong winds blowing around Antarctica (Ekman pumping). Indeed, because the Earth is rotating, Coriolis force generates a wind driven surface circulation perpendicular to the wind direction. In the Southern Ocean, the surface waters are deviated toward the North. To compensate this surface water movements, deep water upwells. In the Southern Ocean, the deep water formed corresponds to Antarctic Bottom Water (AABW) and Antarctic Intermediate Water (AAIW). These waters spread in the Atlantic, Indian and Pacific basin were they upwell. Surface and deep-water masses all circulate in the Antarctic Circum polar Current (ACC), making this wind driven current a keystone for modern global ocean circulation (Figure 1.2).

In a nutshell, the Atlantic meridional circulation can be sketched as a "tilted number eight" (Ferrari et al. (2014)-Figure 1.3). The surface waters from the tropical area flow

northward, mainly in the Gulf Stream surface current. Along the way to the Northern Atlantic they lose their heat and become saltier. They sink in the North Atlantic convection sites such as the Nordic seas and the Labrador Sea and form the NADW. The NADW flows southward, mainly via the DWBC and reaches the Southern Ocean. Due to strong divergence forced by the zonal winds, deep waters upwell along the isopycnals. In the Southern Ocean, deep waters are formed as well in the polynias: the AABW and the AAIW. These water masses flow out of the Southern Ocean below the NADW for AABW and closer to the surface for AAIW. The turbulent mixing due to the bottom ocean topography closes the circulation loop or the "tilted number eight" (Figure 1.3, 1.2).

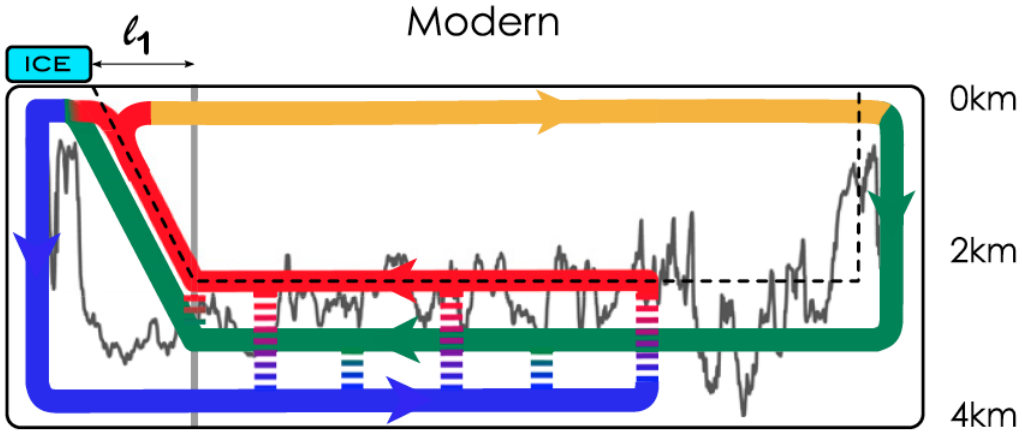

Figure 1.3 – **Schematic representation of meridional circulation in the Atlantic basin (Ferrari et al., 2014)**
The blue arrow represents the AABW, the green one the NADW, the yellow one the surface waters and AAIW, the red one the Indian and Pacific deep waters. The dashed black lines represent the isopycnals. The dashed thick lines represent the turbulent mixing of water masses induced by bottom ocean topography. The grey line indicates the most northernmost zone affected by the Antarctic Circum polar current (ACC). L1 represents the distance between this zone and the permanent sea ice extent marked in light blue box.

As a conclusion of this first section, we have seen that the ocean is a key player in the climate system. Numerous oceanographic cruises and measurements of physical and chemical properties of the water as well as passive tracers and tracking device such as "argo" floats allowed to develop a comprehensive overview of the modern circulation scheme. This modern oceanography work is still ongoing and is really important to better assess the natural variability of the ocean circulation and its current response to the ongoing anthropogenic perturbation. However, only a few decades of the past ocean circulation evolution is available from the instrumental records. Even if the available data is exceptionally complete (good geographical coverage and multiple tracers), they only provide information about the ocean circulation evolution under the modern climate state. Therefore, to fully constrain the mechanisms controlling the ocean circulation variations

(strength and geometry of the water masses), long-term observations are needed (Smeed et al., 2014). Paleoclimate records provide the opportunity to constrain the past ocean variations associated with various climate states and thus understand the role of the ocean in climate transitions. However, reconstructions of the past climate and ocean circulation rely on indirect evidence: the paleoproxies. In the following section, I present the classical tools used in this PhD thesis to reconstruct past ocean properties and in particular the sea surface temperatures, the ocean ventilation and circulation strength.

1.2 Classical Tools for paleoceanography

1.2.1 Foraminifer-based proxies

1.2.1.1 Foraminifer species used in this PhD thesis

Foraminifers are single-cell microorganisms, which produce a calcium carbonate shell, also called "test". Along their development, the shells integrate physical and chemical properties of the surrounding water. As foraminifers are really abundant in the world ocean surface waters, their tests are often preserved in the marine sediments, providing useful tools for paleoceanographers to reconstruct past water masses properties. We present here three foraminifers families that are commonly used for paleoceonagraphic reconstructions and in this PhD thesis.

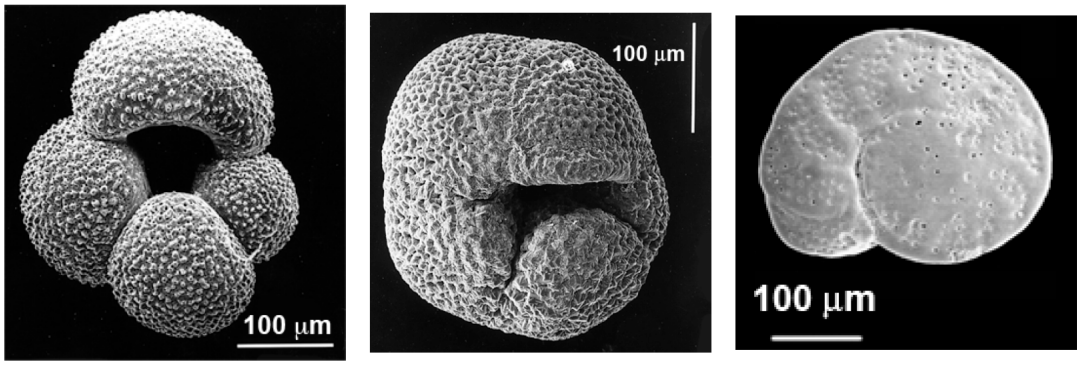

Figure 1.4 – **Comonly used foraminifera species for paleoceanographic reconstructions.**
Globigerina bulloides (left), *Neogloboquadrina pachyderma* senestral (middle), *Cibicides kullenbergi* (right). Figure from Govin (2008)

There exist two categories of foraminifera: the planktonic, living in surface or subsurface waters and the benthic, living at the water-sediment interface. Among the numerous planktonic species we cite here two remarkable ones (Figure 1.4). First, *Globigerina bulloides* is dwelling at less than 50 m depth and is particularly abundant in a wide temperature range (5-20°C) corresponding to the subpolar zones (Mortyn & Charles, 2003).

Second, *Neogloboquadrina pachyderma* senestral (hereafter NPS) are living in polar areas and dwelling between 50 up to 400 m from the surface (Mortyn & Charles, 2003). Among the benthic species, we highlight the gender Cibicides (Figure 1.4), which belongs to the epibenthic family. Contrarily to their endobenthic counterparts the epibenthics live on the top of the sediment layer and not in the upper sediment layers. All these species are commonly used by paleoceanographers to reconstruct surface and deep waters characteristics as described in the following two paragraphs.

1.2.1.2 Sea Surface Temperature reconstructions

Precise identification of foraminifer faunal assemblages allows reconstructing sea surface temperatures (SST). Among the numerous existing SST proxies based on foraminifers (*e.g.* Mg/Ca, clumped isotopes...), we rapidly explain here only the two methods that were used in this PhD thesis.

The first one is based on the determination of the percentage of NPS among the foraminifer specimens present in the sediment sample (%Nps). The method relies on the fact that NPS is a polar species which disappears from the modern foraminifer assemblages when the surface water temperatures exceeds 12°C. The %Nps can directly be used as a qualitative temperature index, the temperature increasing when the %Nps decreases. Otherwise, the %Nps can be converted into an absolute SST using regional calibration (Govin et al., 2012).

The second method requires the precise determination of the faunal assemblage composition on a representative sample aliquot (typically more than 300 specimens). A transfer function is then applied to convert this assemblage information into an absolute SST following the MAT method (Modern Analog Technique) and appropriate software such as "Paleoanalog" (Therón et al., 2004). This method consists in searching, for each reconstructed paleo-assemblage, the closest modern assemblages (so-called analogs) among the assemblages indexed into a modern core tops database such as (Waelbroeck et al., 1998). The summer, winter or annual mean temperatures are then reconstructed for each sample of the studied sites according to the best analogs temperatures recorded in the modern database.

1.2.1.3 Oxygen and carbon isotopic measurements

The benthic and planktonic foraminifer shells being made of $CaCO_3$, the O and C isotopic composition can be also studied, giving information from both oxygen and carbon composition of the water where the shell was formed. The oxygen isotopic composition is expressed in the δ notation:

$$\delta^{18}O(‰) = \left(\frac{(\frac{^{18}O}{^{16}O})_{sample}}{(\frac{^{18}O}{^{16}O})_{standard}} - 1 \right) \times 1000 \quad (1.1)$$

The standard material can be either the Standard Mean Ocean Water (SMOW) for water samples or the Pee Dee Belemnite (PDB) for carbonate samples.

The δ^{18}O of the foraminifer tests depends on the isotopic composition but also on the temperature of the seawater where the shells develop. The seawater isotopic composition is a function of the local hydrological balance (evaporation/precipitation balance) and thus the local salinity but also of the global hydrological situation (total ice volume). Indeed, during a glacial period, the ^{16}O is preferentially stored in the icecaps with light δ^{18}O signatures. The glacial ocean is thus globally heavier, containing relatively more ^{18}O atoms than its interglacial ocean counterpart. The foraminifer δ^{18}O thus represents a convoluted signal between the global ice volume and the local temperature and salinity. According to the dominant processes at play for each specific location or the foraminifer type analyzed (benhic or planktonic), the δ^{18}O can be used as a proxy for local temperature or salinity, or freshwater inputs (mainly from ice melting).

Carbon has three isotopes, two stable ones: ^{12}C which represents 98.9% of the total carbon available on Earth and ^{13}C representing only 1.1% of the total carbon; and a radioactive one: the ^{14}C (10^{-10} % of the total carbon budget) decaying with a half-life of 5730 years. In the following section we show how the study of the stable and radioactive carbon isotopes can be valuable for paleoceanography.

1.2.1.4 Benthic foraminifer δ^{13}C: a tracer for deep water mass ventilation

As for the oxygen, the ^{13}C isotopic composition is expressed with the "delta notation" using the PDB standard:

$$\delta^{13}C(‰) = \left(\frac{(\frac{^{13}C}{^{12}C})_{sample}}{(\frac{^{13}C}{^{12}C})_{standard}} - 1 \right) \times 1000 \quad (1.2)$$

The carbon isotopic composition of the epibenthic foraminifers (*i.e.* foraminifers living at the sediment-water interface) represents the isotopic composition of the dissolved inorganic carbon (DIC) of the water in which the shell was formed. This latter isotopic composition is determined by a combination of several mechanisms described below.

Isotopic fractionation during air-sea exchanges

Some carbon is exchanged s CO_2 between the atmopshere and the surface waters. This process is responsible for an isotopic fractionation of the carbon and an enrichment of the surface waters in ^{13}C by 8.5‰ on average (Siegenthaler & Münnich, 1981).

Biological isotopic fractionation

The primary producers of organic matter preferentially incorporate the ^{12}C regarding to the ^{13}C along the photosynthesis pathway. The organic matter produced in the ocean surface waters has thus a very negative $\delta^{13}C$ signature around -25‰ (Stuiver & Polach, 1977). The same fractionation mechanism also accounts for terrestrial biomass. This biological fractionation of the carbon affects the DIC in several ways (Figure 1.5).

First, major changes in vegetation cover, notably between glacial or interglacial periods can lead to substantial carbon exchange between the continental biosphere and the ocean. Across a global cooling, like it has probably been the case during the Last Glacial Maximum (LGM), part of the continental biosphere vanished and its isotopically light carbon was washed into the ocean. The $\delta^{13}C_{DIC}$ is thought to have decreased by 0.4 ‰ at the LGM compared to the modern conditions (Duplessy et al., 1988). Second, the high biological production in the photic zone tends to deplete the surface waters in ^{12}C (Volk & Hoffert, 1985). Thus, the surface waters display a very positive $\delta^{13}C_{DIC}$, around +1 or +2 ‰. The organic matter produced in the surface waters is then exported deeper in the water column where it starts to be remineralized either via biotic or abiotic oxydation. Along this process, bacteria and other organisms, feed from the organic matter and release ^{12}C atoms in the water column. Thus, the $\delta^{13}C_{DIC}$ decreases toward neutral or negative values (up to -1‰ in the Pacific Ocean (Eide et al., 2017)).

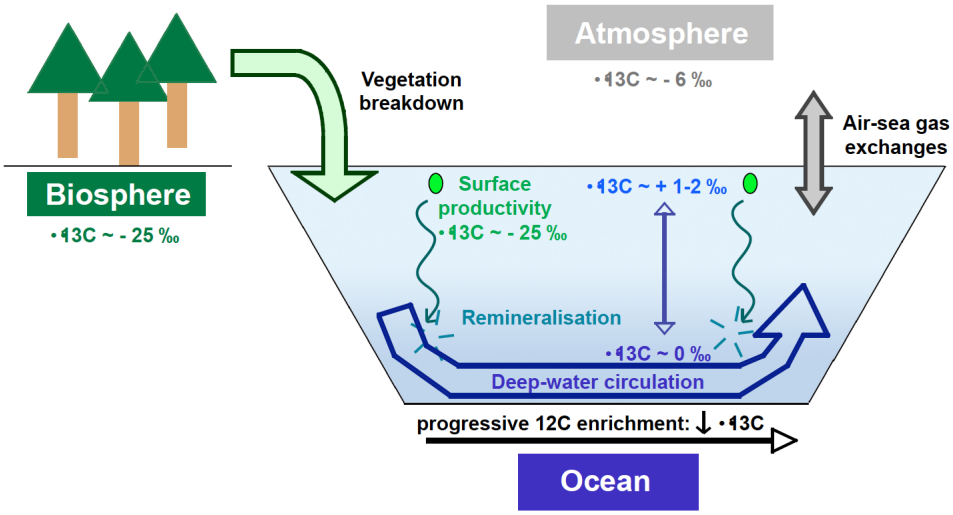

Figure 1.5 – **Simplified carbon cycle after Govin (2008)**

Deep ocean circulation

The $\delta^{13}C_{DIC}$ is not homogenous in the modern deep ocean. It varies from +1‰ in the North-Atlantic to -1‰ in North-Pacific. These variations are attributed to the modern

deep ocean circulation scheme (see section 1.1.2 for further details). Indeed, the North-Atlantic surface waters, relatively dense and depleted in ^{13}C, sink to form the NADW. Along its path in the ocean interior, the biotic or abiotic remineralization process operates, releasing ^{12}C from the organic matter in decomposition (Figure 1.5). On its way from the Atlantic basin to the Pacific basin, the water mass $\delta^{13}C_{DIC}$ increases until it reaches the Pacific signature. Thus the Atlantic deep waters are nutrient poor, ^{13}C rich and exhibit high $\delta^{13}C_{DIC}$ signature. On the contrary, the Pacific deep waters are nutrient rich and exhibit a low $\delta^{13}C_{DIC}$. The water mass "ventilation" state represents its equilibration with the atmosphere: well-ventilated water mass have equilibrated with the atmosphere and generally have higher $\delta^{13}C_{DIC}$ while poorly ventilated water masses have been isolated from the surface and generally exhibit lower $\delta^{13}C_{DIC}$ (*e.g.* Lynch-Stieglitz et al., 2007). In the modern ocean, the $\delta^{13}C_{DIC}$ has a tight relationship with the water mass apparent oxygen utilization (and nutrient content), highlighting the potential of foraminifer $\delta^{13}C$ as a proxy for past water mass ventilation and to trace changes in water masses geometry (Eide et al., 2017).

To sum up, the $\delta^{13}C_{DIC}$ of a given water mass is a convoluted signal because its absolute value depends on three parameters, which are i) the initial (preformed) $\delta^{13}C_{DIC}$ of the surface waters (that depends on the air-sea exchanges efficiency), ii) the remineralization/biological activity intensity along its path and iii) its circulation speed.

1.2.1.5 Benthic radiocarbon content as a tracer for deep-water ventilation

^{14}C production in the upper atmosphere

^{14}C is formed in the upper atmosphere by interaction between cosmic rays and ^{14}N. Cosmic rays are mainly made of protons when they enter the atmosphere (90%), but after several collisions, they become secondary neutrons or slow neutrons. Those secondary neutrons have a concentration peak between 12 and 16 km height allowing the following reaction to take place in this altitude band:

$$^{14}N + neutron \rightarrow ^{14}C + ^{1}H \tag{1.3}$$

The secondary neutrons density, which conditions this reaction, depends on the Earth magnetic field intensity and geometry, as well as on the solar activity. Indeed, when the strength of the planetary magnetic field is increased, the cosmic rays penetrate less in the atmosphere, resulting in a decrease of the ^{14}C production. When the solar activity increases, enhanced solar winds tend to deflect the cosmic rays from Earth's atmosphere and thus decrease the ^{14}C production. The secondary neutrons density is thus a function of the latitude and the longitude of the considered position due to spatial variations of

the magnetic field, but also a function time because of variations of both solar activity and Earth's magnetic field strength. On average, the radiocarbon production is estimated to be equal to 2.25 ±0.1 atom.cm^{-2}.s^{-1} but it can vary between 1 and 6 atom.cm^{-2}.s^{-1} between the equator and the poles. The solar activity can modulate the ^{14}C production by a factor of 4.

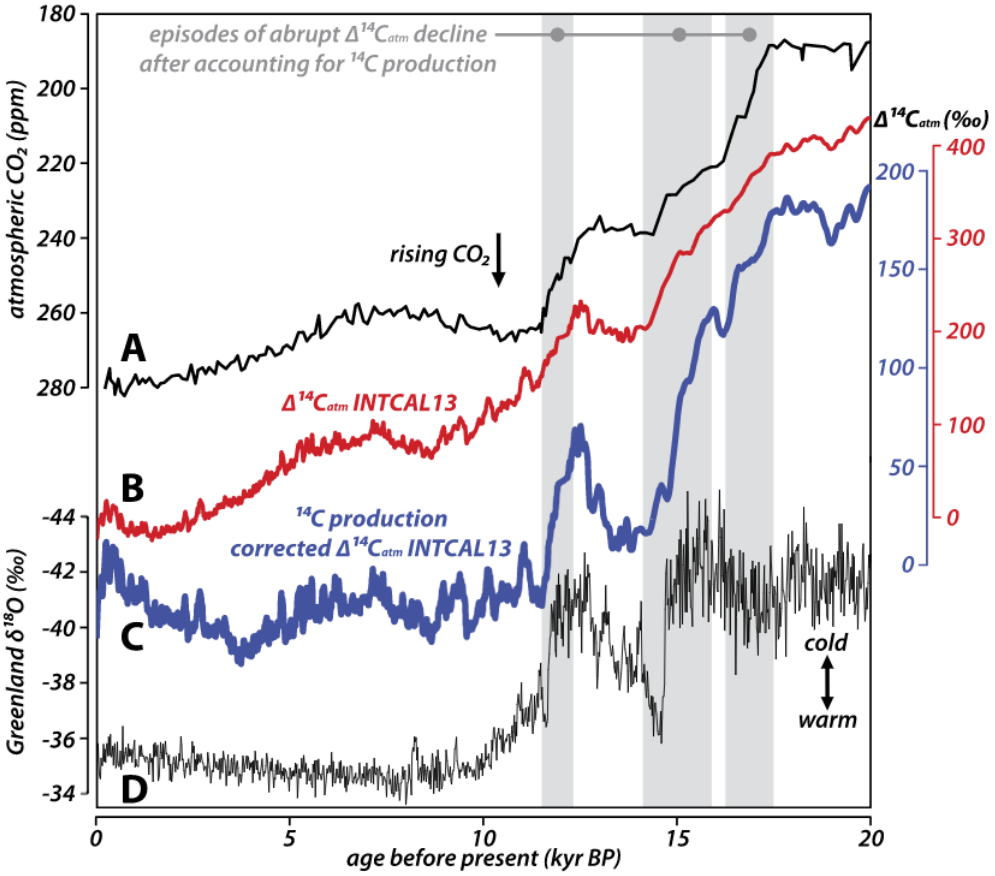

Figure 1.6 – **Evolution of the atmospheric radiocarbon and CO_2 content over the last 20 ky**
Figure from Hain et al. (2014) A. Atmospheric CO_2 (Monnin et al. (2001),Lemieux-Dudon et al. (2010)) B. Atmospheric $\Delta^{14}C$ (Reimer et al., 2013), C. Reconstructed ^{14}C production and D. NGRIP δ^{18}O (Andersen et al. (2006), Rasmussen et al. (2006), Vinther et al. (2006))

Over the last 25 ka, the evolution of ^{14}C production in the atmosphere is relatively well-constrained thanks to the work of the IntCal community (Reimer et al., 2013) (Figure 1.6). The 12 500 first years of data were obtained using terrestrial archives containing large amounts of carbon such as wood that can be independently dated through dendrochronology. The oldest part of the record consists in a compilation of ^{14}C measurements on marine samples such as corals independently dated using the U-Th geochemical chronometer. The ^{14}C content is often expressed as:

$$\Delta^{14}C(‰) = \delta^{14}C - 2(\delta^{13}C + 25)\left(1 + \frac{\delta^{14}C}{1000}\right) \quad (1.4)$$

The value of 25 corresponds to the -25‰ of the mean δ^{13}C measured in the wood due to biological fractionation (Stuiver & Polach, 1977). The atmospheric ^{14}C history over the last 25 ka is shown in (Figure 1.6). Notably, the atmospheric Δ^{14}C decreased from 450‰ to 0‰ from the LGM to the preindustrial period. This decrease happened relatively rapidly during the Heinrich stadial 1 (HS1) and the Younger Dryas (YD). A plateau in atmospheric Δ^{14}C is observed during the Bolling- Allerod period (BA) (Figure 1.6).

The ^{14}C atoms produced from the upper atmosphere are then rapidly oxidized to form CO_2 molecules. Those molecules have a relative short residence time in the atmosphere (about 8 years) and are quickly transferred to the different carbon reservoirs such as the ocean and the terrestrial biosphere (Figure 1.7).

^{14}C in the ocean

Carbon exchanges between the ocean and the atmosphere are function of the partial CO_2 pressure at the ocean-atmosphere interface but they also depend on the water temperature. The surface waters rapidly exchange carbon with the atmosphere. Surface waters roughly contain the same quantity of carbon as the atmosphere (roughly 600 Gt) and have the highest $^{14}C/^{12}C$ ratio of the ocean. However, the air-ocean carbon exchange is not an instantaneous process and the radioactive ^{14}C atoms are constantly decaying. Thus the $^{14}C/^{12}C$ ratio of the surface waters is always lower than the $^{14}C/^{12}C$ ratio of the atmosphere with which the exchanges take place. In other words, the surface waters always look older from the radiocarbon point of view than the contemporaneous atmosphere. This radiocarbon age difference between surface waters and the atmosphere is called “surface water reservoir age”. The modern average surface reservoir age is around 400 years (Key et al., 2004) but it can vary with space and time as a function of variations in temperature, CO_2 partial pressure or inputs of radiocarbon poor waters from deep waters compartment.

Once in the ocean, the ^{14}C can be used as a passive tracer of water masses ventilation and circulation (Figure 1.7). Indeed, as soon as a water parcel is isolated from the surface layer and included in the general circulation, its ^{14}C content stops to be renewed. Thus its ^{14}C content starts to decrease by radioactive decay and the water mass starts aging. Modern radiocarbon data are consistent with the modern circulation scheme (see section 1.1.2). The ^{14}C younger water masses are found in the North Atlantic Ocean, where surface waters sink in the deep convection sites and fill the ocean interior. Contrarily, the ^{14}C older water masses, with a radiocarbon age of about 1700 years are found in the North-Pacific

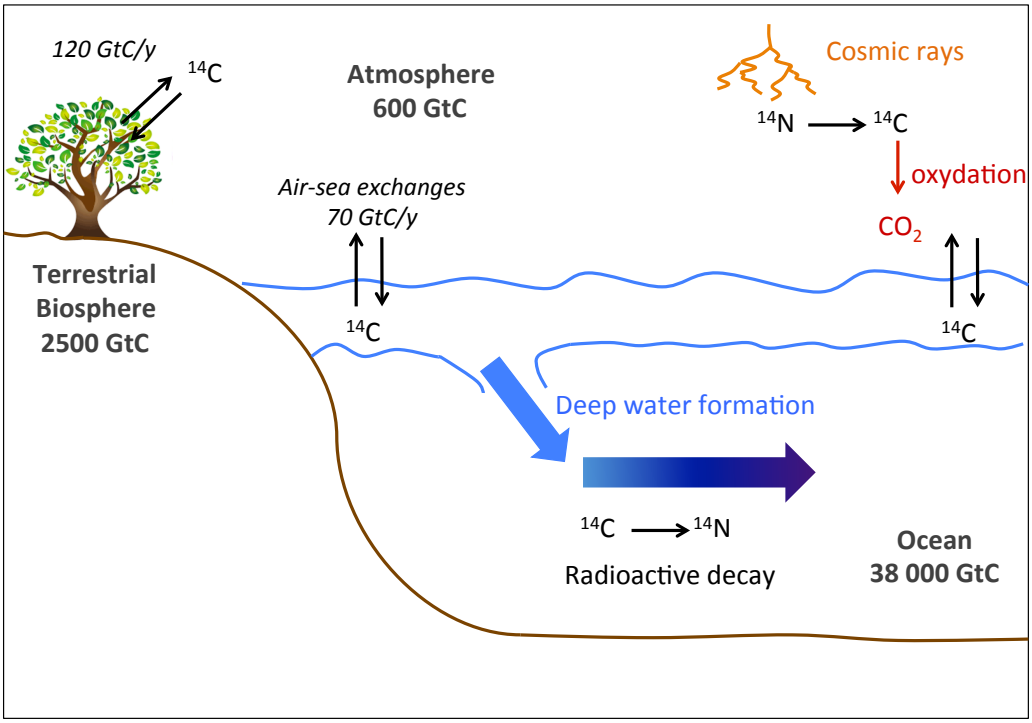

Figure 1.7 – **Simplified ocean carbon cycle showing the exchanges of ^{14}C**
Figure adapted from Mariotti (2013)

where the deep waters upwell after circulating in the global ocean. Thus, radiocarbon has the potential to be used as a tool to reconstruct past ocean ventilation/mixing as it provides indication about the mean time elapsed since a water parcel was in the mixed layer (*i.e.* the surface layer of a few hundred meters above the pycnocline that undergoes regular mixing). To reconstruct past ventilation history the water radiocarbon content can be derived from foraminifer measurements: the benthic species give the deep-water signature whereas the planktonic species measurements provide surface waters signature. Such analysis can be also conducted on other carbonate shells such as bivalves or coral, when available.

However, the ^{14}C signal of a given water parcel is again a convolution of signals. The measurable $^{14}C/^{12}C$ ratio depends also on i) the ^{14}C atmospheric concentration, ii) the initial $^{14}C/^{12}C$ ratio of the water mass that is related to the air-sea exchange conditions (temperature - CO_2 partial pressure) and iii) the extent of mixing with other ^{14}C sources (such as radiocarbon dead from hydrothermal vents or deep waters). Part of these parameters such as the initial $^{14}C/^{12}C$ ratio or the air-sea exchange conditions (which generates reservoir age variability) can be difficult to obtain for paleoapplications. However, better constraints on the reservoir ages variations through time and space and

accurate comparison with the global atmospheric radiocarbon evolution can provide keys to study ocean circulation and water masses organization changes. To reconstruct the ocean ventilation from radiocarbon, one way has been to directly compare benthic and planktonic measurements (Broecker et al., 1984). This technique gives a raw age difference between bottom and surface waters and does not require independent precise calendar age determination for the studied samples. An alternative is to include the atmospheric radiocarbon production variations, expressing ^{14}C projection ages (see Adkins & Boyle, 1997). This requires the use of well-calibrated ages and tracing the water mass sources. Finally, the deep ventilation can be expressed as Benthic – atmosphere radiocarbon age, which will give different results for different marine core age-depth relationships (see Skinner & Shackleton, 2004; Skinner et al., 2014).

1.2.2 U-series nuclides

^{231}Pa and ^{230}Th are natural radioactive isotopes derived from the decay chains of uranium. As a result of their interesting chemical behavior and particulate reactivity, they can be used to reconstruct either past ocean circulation or sedimentary fluxes (Francois et al., 2004; Francois, 2007; Yu et al., 1996). In the following paragraphs, I first describe the production of ^{231}Pa and ^{230}Th and their behavior in the water column. Then, I describe how ^{231}Pa and ^{230}Th can be used to reconstruct past circulation strength and sedimentary fluxes.

1.2.2.1 ^{231}Pa and ^{230}Th behavior in the water column

The only source of ^{231}Pa and ^{230}Th in the water column is the radioactive decay of the parent isotopes ^{235}U and ^{238}U respectively. U is a very soluble element in sea-water, thus its residence time in the ocean is very long (between 400 000 and 450 000 years - (Weyer et al., 2008)) compared to the mixing time of the oceans (1 000 to 1 600 years - (Broecker & Peng, 1982)). U is thus considered as homogeneously distributed in the ocean with a concentration of *ca* 3.3 ppb (Ku et al., 1977) and a $(^{235}U/^{238}U)_{sw}$ activity ratio of 1.1467 ($1\sigma = 0.0025$) (Robinson et al., 2004), where *sw* stands for seawater and the parenthesis denote an activity. As a results, ^{231}Pa and ^{230}Th are produced everywhere in the oceans at a constant and well-constrained rate corresponding to the activity ratio $(^{231}Pa/^{230}Th) = 0.093$ (Yu et al., 1996), hereafter referred as "production ratio".

Contrarily to U, ^{231}Pa and ^{230}Th have a much higher affinity for marine particles such as dust grains, dead plankton or organic matter. The two isotopes have slightly different behaviors though. On the one hand, ^{230}Th has only one stable oxidation state in the ocean: Th (+IV) (Santschi et al., 2006). ^{230}Th mostly exists in seawater as organic and inorganic complexes with very high particulate reactivity (Guo et al., 2002; Santschi

et al., 2006). ^{230}Th is thus extremely insoluble in seawater and sticks to colloids and particles. Consequently, its residence time in the water column is quite short: 10 years for surface waters and up to 40 years for deep waters (Henderson & Anderson, 2003). On the other hand, ^{231}Pa has several stable oxidation states in the ocean: +IV, +V and +VI. Most of the ^{231}Pa is at oxidation state +V under the form of soluble complexes associated with F^- ions. ^{231}Pa can undergo reduction reactions in the ocean, transforming Pa (+V) in Pa (+IV), which has a much higher particulate reactivity (Roberts et al., 2009). Because ^{231}Pa can have numerous oxidation states coexisting in the ocean forming various complexes with moderate particulate reactivity, ^{231}Pa is globally more soluble than ^{230}Th in the seawater. ^{231}Pa has thus a longer residence time in the water column estimated to be around 50-200 years (Henderson & Anderson, 2003).

1.2.2.2 Lateral transport of ^{231}Pa and ^{230}Th

^{231}Pa and ^{230}Th are present in the water column as dissolved and particulate phases. The dissolved isotopes are rapidly adsorbed onto the particles sinking in the water column. However, the isotopes in the particulate phase can also desorb and return in the dissolved phase (Figure 1.8). This mechanism is called reversible scavenging and is responsible for the increase of ^{231}Pa and ^{230}Th concentrations with depth in the water column (Bacon & Anderson, 1982; Nozaki & Nakanishi, 1985). The adsorption/desorption is described by a partition coefficient $K_{d,i}$ which indicates the proportion of the element i in the particulate phase compared to the dissolved phase at equilibrium ($K_{d,i} = C_{i,part}/C_{i,diss}$ – C standing for concentration). In fact, $K_d = K_{adsorp}/K_{desorp}$, K_{adsorp} being the adsorption coefficient and K_{desorp} being the desorption coefficient. At equilibrium, the desorption rate equals the adsorption rate. Besides, ^{231}Pa and ^{230}Th adsorption and desorption coefficients vary according to the particle chemistry, hence the particle chemistry has a direct influence on ^{231}Pa and ^{230}Th scavenging to the sediments (*e.g.* Chase et al., 2002, 2003). For instance, ^{231}Pa has a strong affinity for biogenic opal, increasing ^{231}Pa scavenging efficiency relative to ^{230}Th in areas where opal is the dominant particle type, such as in the Southern ocean (Walter et al., 1997).

In the modern ocean, numerous deviations to the theoretical profile of ^{231}Pa and ^{230}Th with concentrations increasing linearly with depth can be observed. To explain those differences a transport term has to be added to the equation (Francois, 2007). This lateral transport of ^{231}Pa and ^{230}Th has two main origins.The first is called "boundary scavenging" and corresponds to diffusion due to particles fluxes (which depends on the concentration and settling speed) gradient (*e.g.* Bacon, 1988). Indeed, at the margins the water column particle fluxes is increased compared to the open ocean due to inputs of terrigenous material by rivers and/or enhanced biologic primary production sustained by increased

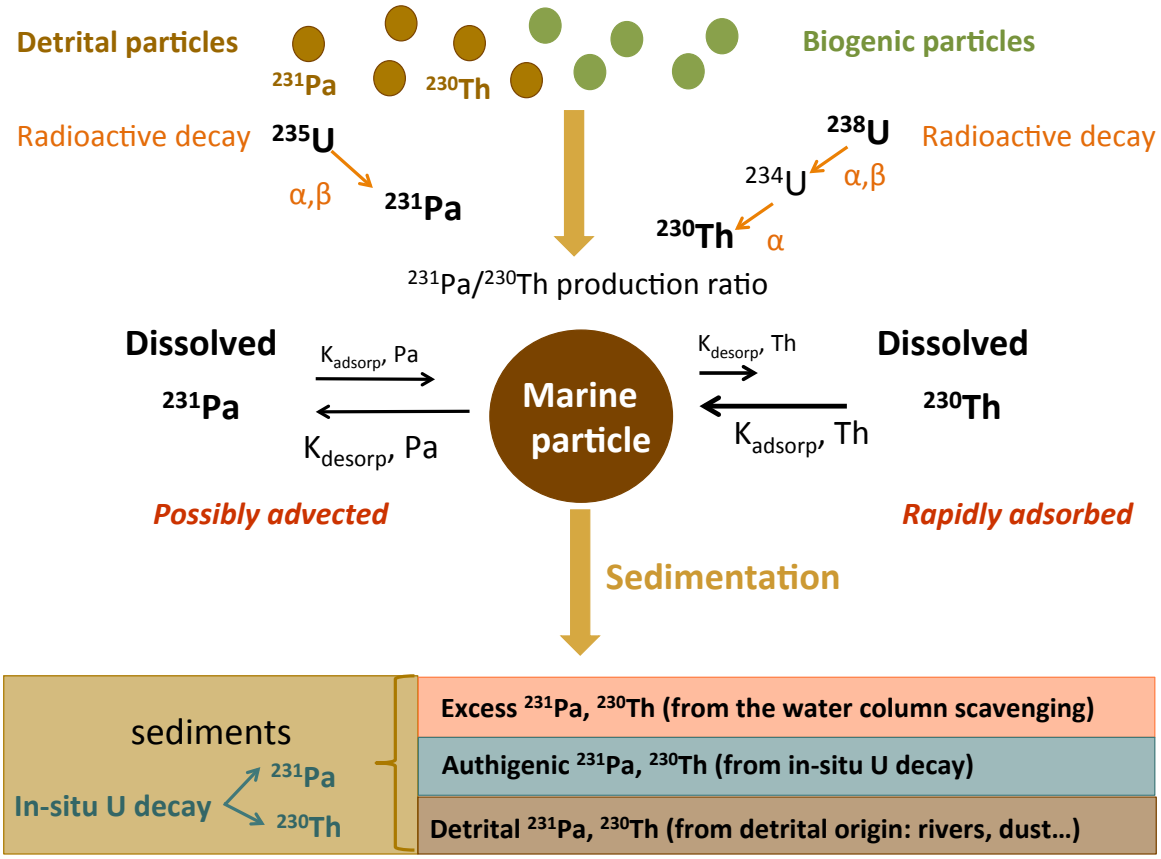

Figure 1.8 – **^{231}Pa and ^{230}Th behavior in the water column**

nutrient availability. This higher particle flux generates a more intense adsorption of ^{231}Pa and ^{230}Th onto those particles. The isotopes being produced at a constant rate, the concentrations of dissolved ^{231}Pa and ^{230}Th at this particular location are reduced. Thus, a concentration gradient is established between areas with high particle fluxes, which exhibit low dissolved concentrations (*e.g.* Eastern Equatorial Pacific) and areas with less intense particulate fluxes, which exhibit higher dissolved concentrations (*e.g.* central North Pacific). These gradients are usually compensated by the implementation of diffusive fluxes from high dissolved concentrations areas toward lower dissolved concentrations areas. The second origin of lateral isotope transport is the ocean circulation that can create new high/low concentration area.

The lateral extent of those transport processes depends on the residence time of the element in the water column. It is usually assumed that the residence time of ^{230}Th is short enough that there is almost no ^{230}Th lateral transport (Bacon, 1984) and all the ^{230}Th produced in the water column reaches the underlying sediments. On the contrary, the smaller particulate affinity of ^{231}Pa implies a substantial increase in its residence time ($\sim$ 200 years) in the water column compared to ^{230}Th ($\sim$ 40 years). Thus, the ^{231}Pa can be transported laterally much more than ^{230}Th on distances of the order of magnitude of

several thousands of kilometers (Figure 1.8).

Consequently, differences in the way ^{231}Pa and ^{230}Th are removed from the water column induce a fractionation between those two isotopes. Paleoceanographers took advantage of this fractionation to develop proxies to constrain past ocean circulation or past sedimentary fluxes as explained in details in the next two sections.

1.2.2.3 ($^{231}Pa_{xs,0}/^{230}Th_{xs,0}$) as a kinematic circulation proxy

It is estimated that in the modern ocean, about 50% of the ^{231}Pa produced in the North-Atlantic is advected by the NADW (Yu et al., 1996) and scavenged later to the sediment in the Southern ocean. Indeed, the Southern Ocean has favorable conditions for siliceous plankton such as diatoms to develop, forming an opal belt that efficiently scavenges the ^{231}Pa to the sediments (Walter et al., 1997). Contrarily, ^{230}Th reaches directly the underlying sediments due to its short residence time in the water column. Thus, hypothetically, the advection of NADW should decrease the ratio between ^{231}Pa and ^{230}Th adsorbed onto the sinking particles compared to the production ratio. This is consistent with observed sedimentary ^{231}Pa and ^{230}Th ratios for Holocene Atlantic core tops (Yu et al., 1996). Applying the same principle to past situations, weakened circulation (or advection) in the North-Atlantic should lead to decrease the proportion of ^{231}Pa exported. Consequently, the sedimentary ^{231}Pa/^{230}Th ratio should increase toward the production ratio. Thus, the ^{231}Pa/^{230}Th activity ratio derived from particle scavenging can be used as a kinematic circulation proxy in the Atlantic basin (Böhm et al., 2015; Bradtmiller et al., 2014; Burckel et al., 2015, 2016; Gherardi et al., 2009; Lippold et al., 2012; McManus et al., 2004; Yu et al., 1996).

In order to use ^{231}Pa and ^{230}Th as a past circulation proxy, one has first to extract the ^{231}Pa and ^{230}Th signal from particle scavenging (*i.e.* the ^{231}Pa and ^{230}Th in excess) from ^{231}Pa and ^{230}Th of other origins (Figure 1.8). Indeed, marine sediments are a mixture of material from detrital origin, corresponding to terrigenous inputs from rivers or dust, from authigenic origin that corresponds to Fe and Mn oxyhydroxydes grown after sediment deposition under suboxic conditions and finally a fraction derived from the water column scavenging. Thus, using bulk sediment measurements, one has to calculate first the ^{231}Pa and ^{230}Th in excess (subscript "xs"), and then correct from the radioactive decay in order to reconstruct the signal at the time of sediment deposition (subscript "0"). Finally, the ratio that represents the past circulation changes is ($^{231}Pa_{xs,0}/^{230}Th_{xs,0}$)(hereafter shortened as Pa/Th).

The excess fractions are usually determined from bulk sediment measurements, estimating the detrital and authigenic contributions using several assumptions. First, the ^{232}Th content of the sediment is assumed to be purely detrital. Then, detrital ^{230}Th is

considered to be at secular equilibrium with detrital ^{238}U, *i.e.* $(^{238}\mathrm{U})_{det} = (^{230}\mathrm{Th})_{det}$. The incorporation of authigenic uranium occurs at the time of sediment deposition at a known $(^{234}\mathrm{U}/^{238}\mathrm{U})$ activity ratio, assumed to be that of sea water: $(^{234}\mathrm{U}/^{238}\mathrm{U})_{sw}$=1.1467 ($1\sigma$=0.0025) (Robinson et al., 2004). The equations used to determine Pa and Th excess activities are the following (Henderson & Anderson, 2003):

$$(X)_{xs} = (X)_{meas} + (X)_{authi} + (X)_{det} \tag{1.5}$$

where X stands for ^{231}Pa or ^{230}Th activities, "*meas*" for the measured activity, "*det*" for the detrital fraction and "*auth*" for the authigenic fraction.

$$\begin{aligned}(^{230}Th)_{xs} = (^{230}Th)_{meas} &- \left[(^{232}Th)_{meas}\left(\frac{^{238}U}{^{232}Th}\right)_{det}\right] \\ &- \left\{\left[(^{238}U)_{meas} - (^{232}Th)_{meas}\left(\frac{^{238}U}{^{232}Th}\right)_{det}\right](1-e^{-\lambda_{230}t}) \right. \\ &\left. + \frac{\lambda_{230}}{\lambda_{230}-\lambda_{234}}(e^{-\lambda_{234}t} - e^{-\lambda_{230}t})\left[\left(\frac{^{234}U}{^{238}U}\right)_{sw} - 1\right]\right\}\end{aligned} \tag{1.6}$$

$$\begin{aligned}(^{231}Pa)_{xs} = (^{231}Pa)_{meas} &- \left[\left(\frac{^{235}U}{^{238}U}\right)_{nat}(^{232}Th)_{meas}\left(\frac{^{238}U}{^{232}Th}\right)_{det}\right] \\ &- \left[\left(\frac{^{235}U}{^{238}U}\right)_{nat}\left((^{238}U)_{meas} - (^{232}Th)_{meas}\left(\frac{^{238}U}{^{232}Th}\right)_{litho}\right)(1-e^{-\lambda_{231}t})\right]\end{aligned} \tag{1.7}$$

where λ_x is the decay constant of the considered isotope and t the age of the sediment. $(^{235}\mathrm{U}/^{238}\mathrm{U})_{nat}$=0.046 is the natural activity ratio of U isotopes. Finally, the excess activity at the time of sediment deposition ($^{231}\mathrm{Pa}_{xs,0}$, $^{230}\mathrm{Th}_{xs,0}$) can be calculated by correcting $^{231}\mathrm{Pa}_{xs}$ and $^{230}\mathrm{Th}_{xs}$ from the radioactive decay:

$$(X)_{xs,0} = (X)_{xs}e^{\lambda_x t} \tag{1.8}$$

The use of the Pa/Th ratio as a kinematic circulation proxy has been debated (*e.g.* Guo et al., 2002; Lippold et al., 2009, 2011). Indeed, as explained before, the sedimentary Pa/Th ratio relies on the differences in particulate reactivity of the ^{231}Pa and ^{230}Th. Any change in the relative scavenging intensity, for instance due to particle concentration or composition changes can bias the Pa/Th ratio, which then may not solely reflect circulation changes. Particle flux is controlled by changes in riverine inputs and/or increase in biologic productivity. Enhanced particle flux will increase the probability for ^{231}Pa to be adsorbed onto particles and scavenged to the sediments. This way, there is a posi-

tive relationship between the particle flux and the sedimentary Pa/Th. Changes in the Pa/Th ratio due to particle concentration gradients has been discovered in coastal regions, which usually have strong particle concentrations and named "boundary scavenging". This boundary scavenging is in general less important in the Atlantic Ocean than in the Pacific basin (Francois, 2007). In the Atlantic, the AMOC produces a strong southward ^{231}Pa advection, which is the dominant process, making this area ideal for the use of Pa/Th. As mentioned before, the chemical nature of the particles can also greatly influence the sedimentary Pa/Th by changing the Kd coefficients. For instance, it has been shown that the ^{231}Pa has a greater affinity for biogenic silica or opal than $CaCO_3$ (*e.g.* Chase et al., 2002; Walter et al., 1997). Moreover, ^{231}Pa is more effectively scavenged by MnO_2 (Kadko, 1980), a compound notably found in hydrothermal contexts or in suboxic basins. It has also been shown that the fractionation between ^{231}Pa and ^{230}Th was modified and their scavenging intensity increased during peaks of hydrothermal activity (Frank et al., 1994). Thus, before using the Pa/Th as a kinematic circulation proxy, it is appropriate to test evidence of changes in the scavenging intensity, *i.e.* monitor past changes in particle concentration and composition. In the literature, the past sedimentary fluxes as well as the opal content are often monitored along with Pa/Th analysis (Böhm et al., 2015; Burckel et al., 2015, 2016; Lippold et al., 2012; Waelbroeck et al., 2018) to rule any change of particle nature as a main driver of Pa/Th changes. In the case of SU90-08, the vicinity of the mid Atlantic ridge will require to investigate about the potential influences of hydrothermal activity.

As a conclusion, the different particle reactivity of ^{231}Pa and ^{230}Th scavenged to the sediments and the ensuing sedimentary Pa/Th ratio allow to derive qualitative information about the circulation strength of Atlantic water masses under broadly constant particle supply. As this proxy is based on radioactive isotopes, its validity period corresponds to roughly 5 half-lives of the shortest-lived element (Pa $T_{1/2}$=32 760 years (Firestone et al., 1998)). Thus sedimentary Pa/Th can be used over the time period 0-150 ky, which largely covers the study period of this PhD project.

1.2.2.4 Preserved sedimentary flux and past sedimentation reconstruction

The sedimentary flux corresponds to particles that settle from surface layers to the sediments. It is mostly made of biogenic export from the euphotic layer (pellets, organic matter, calcareous or siliceous shells...) or of detrital particles from dust or riverine inputs. The past sedimentary flux can be reconstructed using the very high particle reactivity of ^{230}Th and assuming that integrality of the ^{230}Th produced in a water column is rapidly transferred to the underlying sediments (Bacon, 1984). The amount of ^{230}Th produced (P_{Th}) in the water column of height Z(m) is calculated as follows (Francois,

2007):

$$P_{Th} = \beta_{Th} \times Z \tag{1.9}$$

Where β_{Th} is the production rate of ^{230}Th in the water column (=0.0267 dpm.m^{-3}.y^{-1}). This theoretical production is then compared to the measured $^{230}Th_{xs,0}$ to estimate the preserved vertical rain rate V_p or ^{230}Th-normalized flux (in g.m^{-2}.y^{-1}) (Francois, 2007):

$$V_p = \frac{Z \times \beta_{Th}}{^{230}Th_{xs,0}} \tag{1.10}$$

This ^{230}Th-normalized flux is calculated using the ^{230}Th content which was preserved in the sediments. Consequently, reconstructed paleofluxes represent the vertical rain rate reaching the sea floor minus the dissolution rate of the sediments on the sea floor. Thus,^{230}Th-normalization does not allow to evaluate the dissolution stage of considered sediment. However, ^{230}Th-normalized flux is used a basis to reconstruct past sedimentary fluxes such as $CaCO_3$ or opal fluxes. Besides, ^{230}Th-normalized flux is also used to compute ^{232}Th ^{230}Th-normalized flux (^{232}Th flux), used as a tracer for material of detrital origin (Andersen et al., 2006).

As proposed by Adkins et al. (1997), and further implemented by Bourne et al. (2012), the $^{230}Th_{xs,0}$ can be used to refine the marine cores age models by correcting the sedimentation rate inferred between two dated points using $^{230}Th_{xs,0}$ values. Indeed, as ^{230}Th has a very short residence time in the water column (∼40 years for deep waters (Francois, 2007)), one can assume that all the ^{230}Th produced in the water column rapidly reaches the underlying sediments. Thus, comparing the excess $^{230}Th_{xs,0}$ from bulk sediment measurements to the theoretical ^{230}Th amount produced in the water column gives information about sedimentation rates variations. Consequently, the $^{230}Th_{xs,0}$ is supposed to be inversely proportional to the sedimentation rate: high sedimentation rates are inferred from low $^{230}Th_{xs,0}$ concentrations, highlighting an effective dilution of the ^{230}Th by increased sediment supply as the ^{230}Th is constantly produced in the overlying water column. Conversely, high $^{230}Th_{xs,0}$ concentrations are interpreted as a reduction in the sedimentation rate. The $^{230}Th_{xs,0}$ is then used to correct the average sedimentation rate inferred from available dated points, using the following expression (Bourne et al., 2012):

$$S_i = S_a \times \frac{Th_{mean}}{Th_i} \tag{1.11}$$

With S_i: corrected sedimentation rate for interval i (i=1 to n intervals between two bracketing dated points), S_a: average sedimentation rate, Th_{mean}: weighted (over interval lengths) average of $^{230}Th_{xs,0}$ between two bracketing dated points, Th_i: $^{230}Th_{xs,0}$ of interval i. One of the main benefits of this method lies in the generally high resolution of the Th data, which leads to a high-resolution reconstruction of sedimentation rate variations.

1.2.3 Other common circulation proxies

1.2.3.1 ϵ_{Nd}

Nd is part of the Rare Earth Elements (REE) and has seven isotopes, of which ^{143}Nd is a radiogenic one coming from the α decay of parent ^{147}Sm. Sm and Nd present heterogenous distribution in the rocks of Earth's crust because they have quite different behavior across melting. Indeed, Nd is more incompatible than Sm, meaning that when partial melting occurs, the Nd goes preferentially in the liquid phase compared to Sm. Consequently, the Earth mantle is richer in Nd than the crust. Hence, volcanic rocks from deep mantle melting are richer in Nd than other types of rocks. As ^{147}Sm is radioactive, the age of the rock formation (and particularly the time when melting event occurred) accounts for the final ^{143}Nd/^{144}Nd signature. In a nutshell, across the Earth's history, rocks obtain different Sm/Nd and thus ^{143}Nd/^{144}Nd composition according to their geological nature and history. As a result, geological provinces have their own Nd signature as Nd measurements compilation highlight (Jeandel et al., 2007) (Figure 1.9).

Variations in the Nd composition being quite small, they are always reported with the ϵ_{Nd} notation:

$$\epsilon_{Nd} = \left(\frac{(\frac{^{143}Nd}{^{144}Nd})_{sample}}{(\frac{^{143}Nd}{^{144}Nd})_{CHUR}} - 1 \right) \times 10000 \tag{1.12}$$

CHUR, standing from Chondritic Uniform Reservoir and representing a modeled meteorite composition.

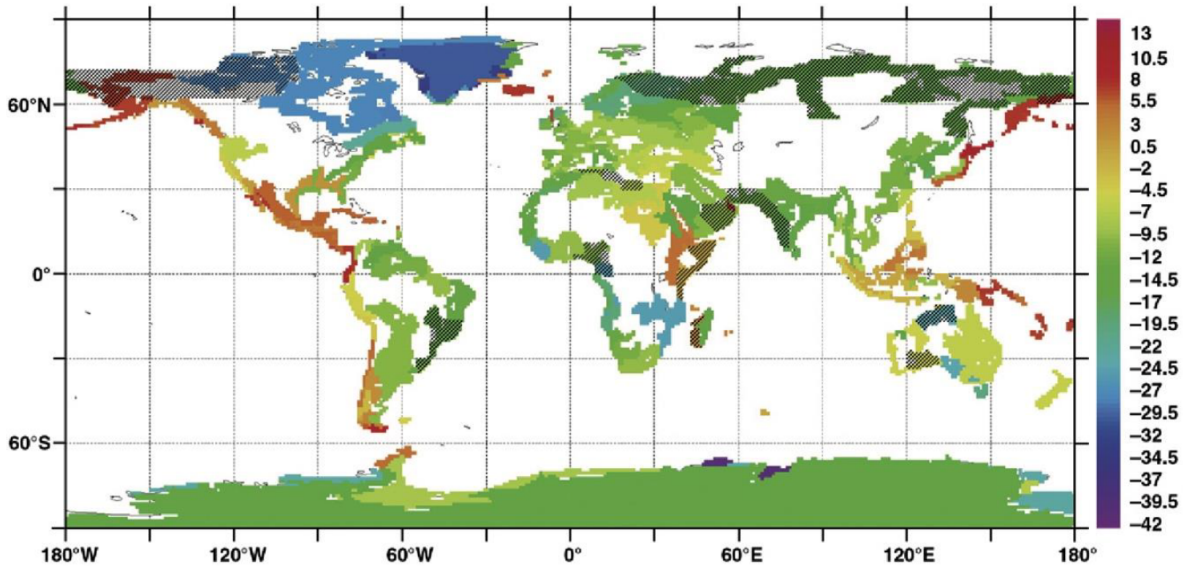

Figure 1.9 – **Compilation of rock ϵ_{Nd} with focus to the coastal areas.**
Figure from Jeandel et al. (2007)

Nd from rocks is transferred to the ocean via continental erosion by wind and rivers.

Thus, the ϵ_{Nd} of the water in a given region is clearly influenced by the composition of the surrounding rocks. Nd is considered as a quasi-conservative water mass tracer and used to identify the mixing processes and water mass provenance, especially in the Atlantic basin (Tachikawa et al., 2003). As shown in Figure 1.9, the observed diversity in crustal formations in terms of ages and geological natures results in a large range of ϵ_{Nd} around the Atlantic basin. Under modern conditions, the Canadian and Greenland old cratons deliver a very unradiogenic Nd signature resulting in ϵ_{Nd} values of about -14.2 $\pm$ 0.3 for LSW (Lambelet et al., 2016). Younger volcanic rocks of Iceland give a more radiogenic signature of around – 8.4 $\pm$1.4 for the water mass coming from the Denmark Strait (Lacan & Jeandel, 2004). The southern sourced water, AABW has a ϵ_{Nd} value around -8.5 in the Southern Ocean which is modified to reach -12.2 at 45°N after having undergone mixing with overlaying NADW. ϵ_{Nd} can then be used to reconstruct past ocean mixing and derive water mass provenance, provided that the deep water Nd signature can be extracted. This can be achieved by measuring the Nd signal of foraminifer authigenic coatings (*e.g.* Piotrowski et al. (2012)). However, this technique is quite time consuming because it requires picking an important amount (3mg) of foraminifera due to their low Nd concentration. More recently, (Blaser et al., 2016) showed that the Nd signal could also be measured directly from bulk sediments. ϵ_{Nd} signal from authigenic material either extracted from foraminifers or bulk sediment has been used and is still used to reconstruct past ocean mixing and water mass provenance over the last deglaciation (*e.g.* Pöppelmeier et al., 2018).

1.2.3.2 Grain size

Grain size distribution provides a more direct physical indication of the current strength (*e.g.* McCave et al., 1995, 2006; McCave & Hall, 2006). The method consists in measuring the mean grain size of the non-cohesive (or sortable) silt fraction (10-63 μm) of the sediment from terrigenous origin. The biogenic carbonates and opal are thus removed from the sample previous to grain size analysis in order to avoid any biological interference. The 10μm limit reflects the empirical observations that smaller particles are cohesive and tend to aggregate. Thus those particles settled as aggregates and their size distribution is not a simple function of transport and deposition; that is why they are not taken into account by this method. The grain size distribution can be measured using laser diffraction or settling velocities differences (Stokes Law). The grain size is then used as a qualitative indicator of the bottom current strength. Indeed, bottom current can sort the silts by size during events of sediment resuspension. The coarser the silts are, the greater the current speed was.

1.3 Reconstructing the Atlantic Ocean geometry and circulation over the last 40 ky

1.3.1 The Last Glacial Maximum Circulation scheme

The first attempts to reconstruct past circulation changes focused on the water masses geometry changes between the Holocene and the LGM. The compilation of δ^{13}C data from epibenthic foraminifera from cores located across the Atlantic Ocean at various water depths (*e.g.* Duplessy et al., 1988; Curry & Oppo, 2005) exhibited substantial changes in the main water masses positions under glacial and interglacial conditions (Figure 1.10). During the Holocene the well-ventilated (high δ^{13}C) NADW is flowing southward between 1000 and 3000 m while the poorly ventilated (low δ^{13}C) AABW is filling the deep basin (below 3500 m) from the Southern Ocean. At the LGM, the δ^{13}C indicates that those two water masses are still present but the AABW occupies a larger part of the basin and the NADW appears much shallower and confined to the upper 2000 m of the basin. This glacial NADW has thus been renamed as GNAIW for Glacial North Atlantic Intermediate Water.

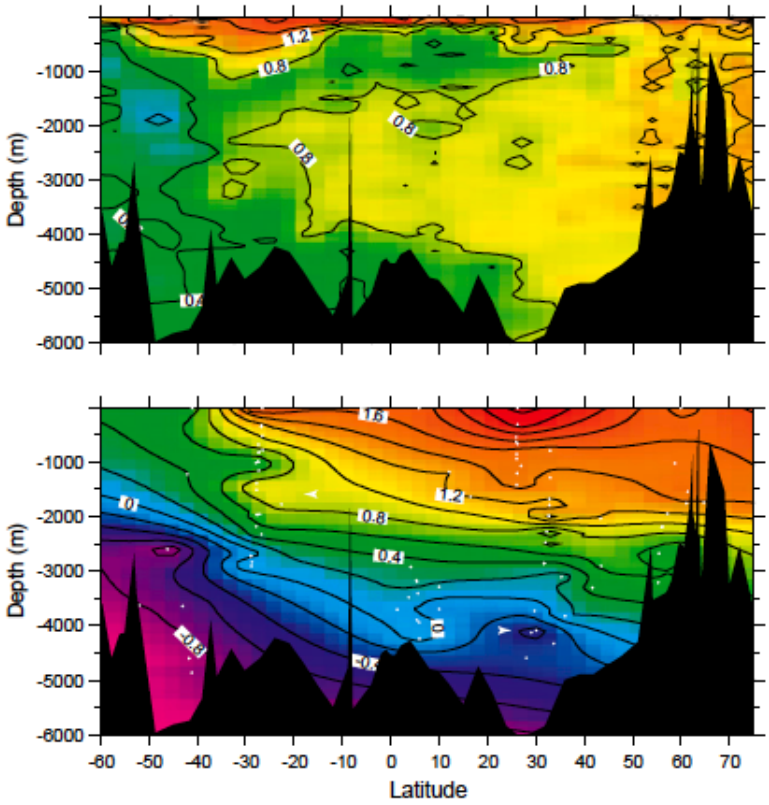

Figure 1.10 – **Atlantic δ^{13}C section reconstructed from benthic measurements** The upper panel shows the Holocene situation, the lower panel the LGM situation. Figure from Curry & Oppo (2005)

Ferrari et al. (2014) proposed a mechanism to explain the shoaling of the GNAIW invoking change in Antarctic sea-ice extent. Under modern conditions, the sub-Antarctic divergence is an area where deep waters upwell around Antarctica due to the strong winds action (Ekman pumping). Indeed around Antarctica, due to the Earth rotation, surface waters are shifted northward, perpendicularly to the wind direction (effect of Coriolis force). The resulting divergence causes the upwelling of deep-water masses. In this area, located at the edge of the sea ice extent, the upwelled waters sink again and form the AABW via the brine rejection process. Ferrari et al. (2014) argued that an increase of the sea-ice extent at the LGM would move this edge and the deep-water formation zone northward. Then as the slope of the isopycnals is conserved and because the deep water upwells along the isopycnals that form strong physical separation between water masses, the deep waters upwell from shallower depths and the AABW fills a greater part of the deep basin. Contrarily to what happens in the modern ocean, the LGM circulation scheme is then organized as two distinct loops (Figure 1.11). The first loop corresponds to the GNAIW that is formed in the North Atlantic and stays above 2000 m. When those waters reach the southern ocean, they upwell along the sub-Antarctic divergence isopycnals and return as surface waters in the North-Atlantic. The second loop corresponds to the AABW waters that are flowing northward in the deep Atlantic. Due to the roughness of the ocean floor, turbulent mixing that occurs along the AABW pathway is responsible for progressive density loss of those water parcels and thus a slow upwelling. A return current is then established in the contact zone between GNAIW and AABW because of the constant dragging applied on AABW by southward flowing GNAIW. The AABW finally returns in the Southern Ocean where it upwells along the isopycnals. This model explains the ventilation characteristics of both main Atlantic water masses.

If there is conclusive evidence from $\delta^{13}C$ for substantial changes in Atlantic water mass geometry between the modern and the LGM, all the Pa/Th studies tend to show that the circulation rate of the AMOC had globally the same strength across both time periods (see Gherardi et al., 2005, 2009; McManus et al., 2004; Yu et al., 1996). More precisely, (Bradtmiller et al., 2014; Freeman et al., 2016; Gherardi et al., 2009) showed that the active circulation depth was not the same under interglacial or glacial conditions. In the modern (interglacial) settings the circulation is more active below 2000m depth. On the contrary, under LGM (glacial) settings, the circulation is more active above 2000 m. This result is confirmed by grain size studies (Evans & Hall, 2008). Besides, Lippold et al. (2012) showed that a shallow (around 2000 m) but active overturning cell produced the best model–data agreement using glacial Atlantic Pa/Th database as well as a 2D circulation model coupled with Pa/Th module.

To sum up, the LGM circulation mode corresponds to a shallow cell of GNAIW (centered at around 2000 m), derived from the deep-water formation in the North Atlantic

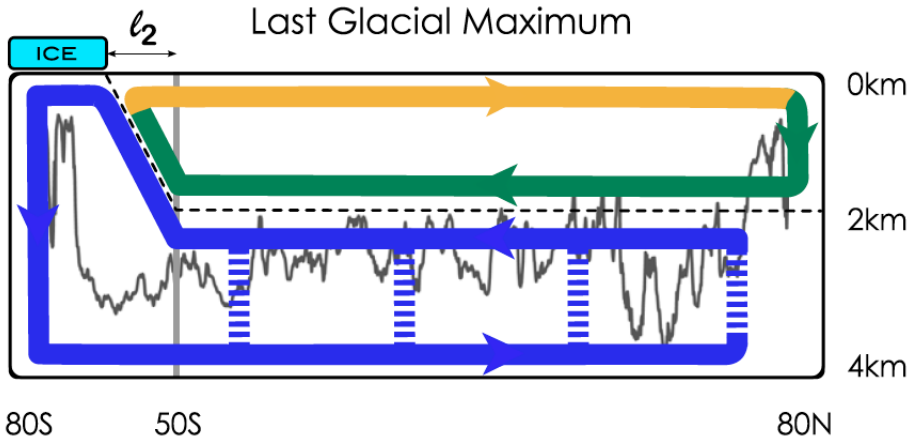

Figure 1.11 – **Conceptual model of the two loops LGM circulation scheme**
The green thick arrow represents the GNAIW, the yellow one represents the surface waters flowing toward North-Atlantic convection zones. The thick blue arrow represents the AABW. The thick dashed blue line represents the gradual upwelling of AABW due to turbulent mixing related to the roughness of the ocean topography represented by the black line. The grey line indicates the most northernmost zone affected by the Antarctic Circum polar current (ACC). L2 represents the distance between this zone and the permanent sea ice extent marked in light blue box. The sea-ice extent is determining the position of the sub-Antarctic divergence. The isopycnals along which the water masses upwell, are represented by the tilted black dashed line. Figure from Ferrari et al. (2014)

overlying the AABW cell derived from the deep-water formation in the Southern Ocean. This view is consistent with Nd isotopes data that suggest that Southern Sourced Water (SSW) bathed the deep North Atlantic during the LGM (*e.g.* Rutberg et al., 2000).

However, recent studies bring carbon isotopes (both ^{13}C and ^{14}C) as well as Nd isotopes evidence for a persisting deep water formation in the North Atlantic during the last glacial maximum (Howe et al., 2016; Keigwin & Swift, 2017). The carbon isotopic signatures observed at Corner Rise (North West Atlantic) as well as a reanalysis of the available Nd isotopic signature throughout the Atlantic basin supports the sustained deep-water production in the North Atlantic during the LGM. The Corner Rise data suggests very dense deep-water production in the Labrador Sea during the LGM with analogous brine rejections mechanisms as observed today close to Antarctica and explaining the poor ventilation observed in the deep Atlantic during this period.

Thus there is compelling evidence that the LGM circulation was different from the modern situation. Though, the exact nature of the LGM pattern in terms of water mass geometry and circulation strength is still debated.

1.3.2 Circulation changes across the millenial scale events of the last glacial

The circulation changes during the last glacial are often sketched as alternations between 3 main circulation modes (Rahmstorf, 2002) (Figure 1.12) involving Northern Sourced Water (NSW, which corresponds to NADW or GNAIW) and Southern Sourced Water (AABW and eventually AAIW). The first mode or "warm mode" corresponds to the modern circulation scheme with a deep, well-ventilated and vigorous NSW cell overlying a slow and poorly ventilated SSW cell. The second mode or "cold mode" corresponds to the LGM circulation scheme with a shallow yet vigorous and well-ventilated NSW and a slower poorly ventilated SSW. The last mode is the so-called "off mode" and corresponds to a collapse of the NSW cell, the SSW filling the entire Atlantic basin. This last mode has been proposed to be the general circulation pattern during the Heinrich events.

The last deglaciation is a relatively well studied period. To date, there is compelling evidence for drastic circulation changes during the last 20 ky, notably during the Heinrich event I and the Younger Dryas. At the first look, both events appear like reversals to glacial conditions (Figure 1.13). During those events, the water masses properties (δ^{13}C and ϵ_{Nd}) suggest a presence of SSW in the mid-latitudes of the North Atlantic (30°N-Bermuda Rise) like during the LGM. The Pa/Th records from several locations in the North West Atlantic and at the Iberian margin also display a consistent pattern with a marked Pa/Th increase during HS1 and the YD (Gherardi et al., 2009; McManus et al., 2004; Ng et al., 2018). As the Pa/Th seems to indicate a drastic reduction of the circulation in the North Atlantic during HS1, it was proposed that the NADW formation completely stopped during that period and that the AABW would fill the deep and intermediate basin (Figure 1.12).

Besides HS1 and the YD, other millennial scale climate events, referred as DO cycles and Heinrich stadials have been detected during the last glacial period. The DO cycles are characterized by a sharp temperature increase followed by gradual cooling toward glacial conditions. The Heinrich stadials correspond to Greenland stadials during which an Heinrich event occurred. The Heinrich events correspond to large iceberg discharge events in the North-Atlantic. In the marine sediments, they are recorded as occurrence of coarse detrital grains, names as Ice Rafted Debris (IRDs) in a latitudinal band called the "Ruddiman belt". The size of those grains implies that they can only have been transported to the core location by icebergs (see Hemming (2004) for a review).

There is now compelling evidence that the circulation pattern changed in the Atlantic during those Heinrich stadials (see Lynch-Stieglitz (2017) for a review), among which, HS1 is the most comprehensively studied. For a long time it has been believed that the icebergs discharges could have been the cause of those millennial scale circulation changes (*e.g.*

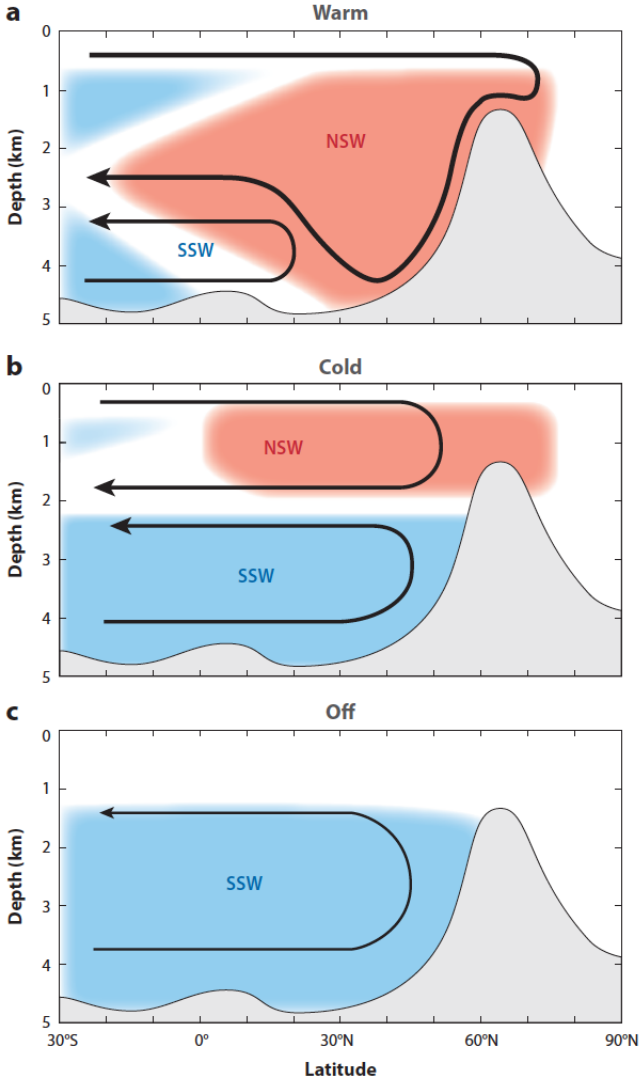

Figure 1.12 – **Three circulation modes in the Atlantic**
a. "warm mode" characterized by a vigorous and deep NADW (>2500m), b. "cold mode" characterized by vigorous but shallow upper cell (<2000 m) c. "off mode" characterized by a drastic reduction of the NADW formation, the deep water from south Atlantic filling the basin. Figure from Lynch-Stieglitz (2017)

Broecker (1994)). Indeed, iceberg melting brings fresh water to the North-Atlantic. As a result, the surface waters in this area become less dense, consequently less deep water is formed in the convection sites such as the Labrador Sea and the Nordic Seas. The impact of freshwater inputs in the North-Atlantic has been widely tested in climate models by running fresh water hosing scenarios (*e.g.* Rahmstorf, 2002; Roche et al., 2010, 2014). Those numerical experiments showed that fresh water hosing is responsible for a slowdow or shutoff of the AMOC export toward the South-Atlantic depending on the fresh water flux imposed in the model. The AMOC slowdown, then induces a surface cooling in the Northern hemisphere and a surface warming in the Southern Hemisphere. This bipolar

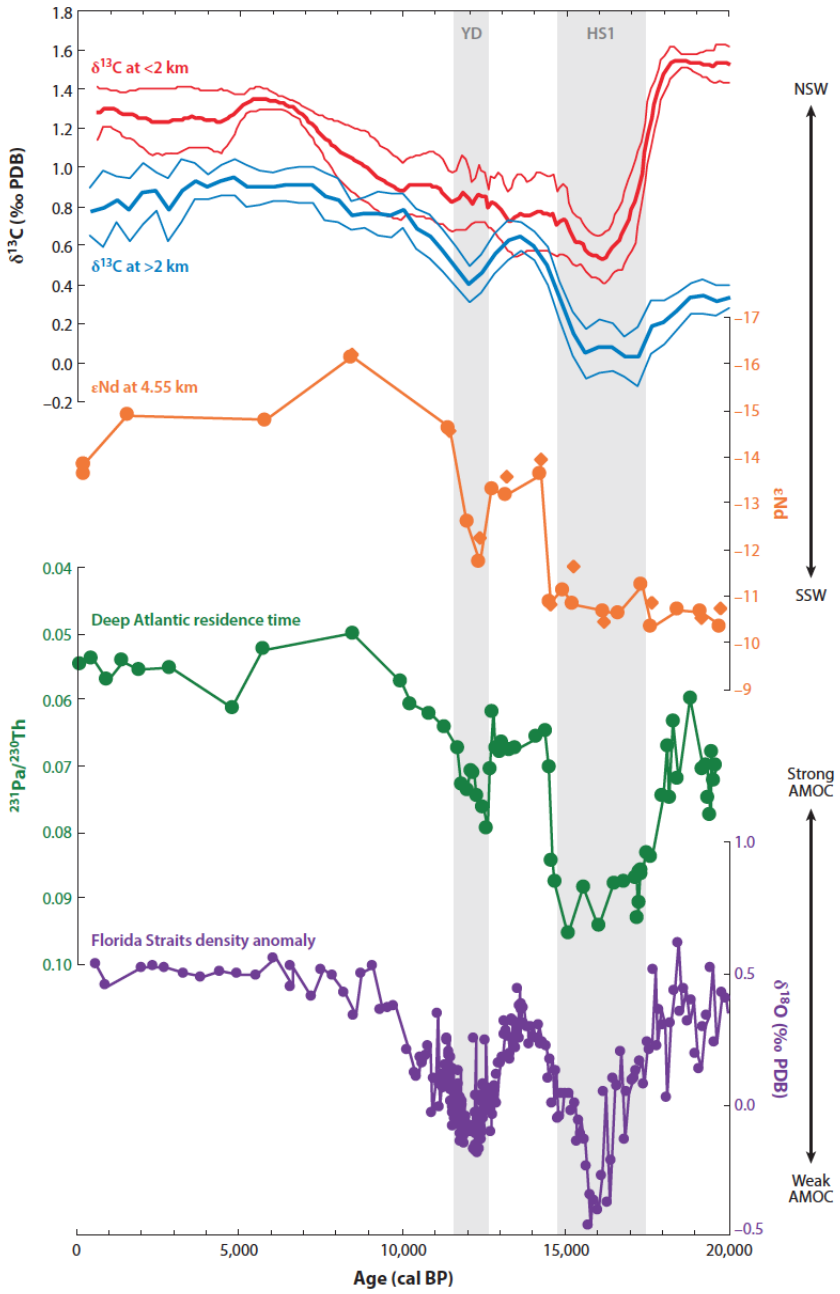

Figure 1.13 – **Time series circulation proxies compilation for the North-Atlantic during the last deglaciation**
Figure from Lynch-Stieglitz (2017)

thermal seesaw effect can be explained by the reduced heat transport from the equator toward the North-Atlantic area by the reduced AMOC and an accumulation of the heat in the Southern Atlantic basin. However, it appeared that the best model-data fit was not obtained when putting the freshwater in the Ruddiman belt area where the iceberg melting occurred. Moreover, a careful look at the relationship between reconstructed SST

changes and IRDs records evidence a systematic lag between the IRDs occurrence and the surface cooling (Barker et al., 2015). Burckel et al. (2015) and Waelbroeck et al. (2018) also showed that the AMOC reduction preceeded climatic changes such as the tropical Atlantic rainfall events. These new observations contributed to the evolution about the understanding of the Heinrich events and DO cycles underlying mechanisms. It has been proposed that the iceberg discharges are the consequence of the cooling observed during the Heinrich events rather than the cause (Barker et al., 2015) but the mechanisms at play during the Heinrich events are still a matter of debate.

The theoretical scheme of the AMOC changes related to the millennial scale events and in particular to the Heinrich is still under debate. Indeed, according to the conceptual model (Figure 1.12), the "off mode" circulation scheme is attributed to the Heinrich events. In this mode, the NSW formation has collapsed and the SSW is filling the major part of the basin, in particular above 2000m. However, the paleoproxy data available do not entirely support this model. Supporting the "off-mode" theory, a compilation of deep $\delta^{13}C$ records and ϵ_{Nd} from the Bermuda Rise ($\sim$30°N, in the Deep Western Boundary Current, $>$ 4000 m) shows persistent SSW signature across Heinrich events (Böhm et al., 2015; Lynch-Stieglitz et al., 2014). The famous Pa/Th record from the same location reaches the production ratio during HS1 (McManus et al., 2004) and other Heinrich stadials (Böhm et al., 2015). The fact that the Pa/Th ratio reaches the production ratio suggests that the Pa export in the North Atlantic completely stopped during the Heinrich events. Thus, paleoceanographers first concluded that the NADW formation completely ceased during those periods. However, other Pa/Th records show evidence of persisting AMOC through the entire glacial period including during the Heinrich events (Bradtmiller et al., 2014; Gherardi et al., 2005, 2009). Those discrepancies in the Pa/Th data argue that the Pa/Th proxy may record regional circulation or specific portions of the water column. Indeed, Thomas et al. (2006) argued that the Pa/Th does not record the Pa advection through the entire water column but rather in the 1000 m above the water-sediment interface. This way, the Pa/Th from a core retrieved at 4000 m water depth only shows what happens in the water column between 3000 and 4000 m. Thus the very deep records, such as the Bermuda Rise record cannot prove that there was no active circulation cell above 2000 m. Like some Pa/Th records, some grain size studies do not give further indication of NADW flow reduction specifically related to Heinrich events (Evans & Hall, 2008). It appears from the available data compilation that there might be substantial regional variability, especially for the upper part of the water column (above 2000m). Last, but not least, the data also supports strong differences between Heinrich events and DO cycles themselves. For instance the Pa/Th and Nd signatures appear different for different millennial scale event on the long Bermuda Rise record (Böhm et al., 2015). Those differences as well as a more comprehensive review on the (few) available data on

circulation changes during DO cycles can be found in (Lynch-Stieglitz, 2017).

1.3.3 Past ocean circulation: open questions

In the previous sections, I briefly reviewed the knowledge available from paloeceanographic data for the LGM, the last deglaciation and the millennial scale events (*i.e.* the Heinrich and the DO events). To date, the data support quite well the conceptual model presented in Figure 1.12 for the modern and glacial modes and there is clear evidence that some of the abrupt events (notably the Heinrich and the DO events) are associated with circulation changes.

However, the circulation pattern that paleoceanographers try to reconstruct for the abrupt events appears to be much more complex than the "off-mode" described above. The data suggest variability at two scales: i) regionally and ii) between the Heinrich events or DO cycles as well as complex interactions between the AMOC, the climate and the cryosphere (Lynch-Stieglitz, 2017). Further work is needed to try to answer to the following questions that arise from the current paleocirculation reconstruction state of the art:

— What are the mechanisms at play during Heinrich and DO events? What is the Atlantic water masses geometry during those events?

— What are the differences between a DO stadial and a Heinrich stadial? What are the differences between the Heinrich events/stadials themselves? What lead to the last deglaciation?

— What are the climate thresholds responsible for abrupt climate events?

These are the ongoing challenges for Paleoceanography.This PhD thesis aims at making a step further toward understanding the role of the ocean during climate transitions. To do so, I will try to quantify the Atlantic deep ocean circulation changes across the last 40 ky. In the following section, I detail the thesis strategy.

1.4 Thesis strategy

1.4.1 Multi-proxy approach

As described in section 1.2 none of the paleo-proxies available can provide complete information about past ocean circulation. Indeed, the benthic $\delta^{13}C$ represents a mixed signal from i) the preformed $\delta^{13}C$ at the deep-water formation site, ii) the remineralization intensity and iii) the ocean water mass speed and pathway. The benthic ^{14}C provides the time for which the water mass has been isolated from the surface. However, on the one hand, the ^{14}C can be biased by unconstrained changes in surface reservoir ages

and, on the other hand, it provides no information about the path followed by the water masses. Finally, the sedimentary Pa/Th is the only proxy to give more direct, though only qualitative, information about the water mass speed. In order to overcome the limitations of each proxy taken separately, I will combine the informations from the sedimentary Pa/Th and the carbon isotopes on a single sediment core.

As we have seen in the previous sections, reconstructing the past Atlantic ocean circulation changes requires a good geographical proxy data coverage. The available high resolution paleoproxy time series are still scarse, therefore it is worth to obtain new records in geographical locations that have not been explored before. In the next section, I describe the core location that has been studied in this PhD thesis and how it improves the geographical coverage of the paleo-proxy data.

1.4.2 Sediment core SU90-08

The sediment core chosen for this study, SU90-08 (43°03'1 N, 30°02'5 W, 3080m), was retrieved by the French R/V Suroît during the "Paleocinat" cruise of 1990. The core was taken on the mid Atlantic ridge flank, in the western Atlantic basin. With an average sedimentation rate of 4.6 cm/ka, the 12 meters of sediment available cover about 260 ky of climate history (Bout-Roumazeilles et al., 1999; Grousset et al., 1993). This location sits in the Ruddiman belt and is far from the coats and fluvial detrital sources. Thus it usually receives small terrigenous inputs except during the Heinrich events when iceberg discharges bring coarse detrital material at the core site. The sediment is mainly made from carbonates (foraminifera ooze and nanofossils) interbeded with clay layers (Bout-Roumazeilles et al., 1999). Levels showing accumulation of coarse detrital material from iceberg discharges, Ice Rafted Debris (IRDs), have been identified and provide a first stratigraphic guidance. For the considered time interval, Heinrich events 1, 2 and 4 have been identified. Heinrich event 3 is not observed in this marine sediment core (Bout-Roumazeilles et al., 1999; Kissel, 2005; Vidal et al., 1997). Besides, around ten ^{14}C planktonic foraminifera dates cover the last 40 ky (Vidal et al., 1997), allowing to produce a first chronology. The site displays interesting though quite complex modern settings. Because it is located on the mid-Atlantic ridge western flank, the core is on the pathway of the NADW but not in the deep western boundary current. The oceanographic setting of SU90-08 is shown in figures 1.14, and 1.15. Studying NADW variability over the last 40 ky from this location should bring a different perspective relative to the previous literature. Indeed, most of the previous studies using the sedimentary Pa/Th as a kinematic circulation proxy focused on cores located directly in the deep western boundary current. Moreover, these studies concern much deeper cores (Böhm et al., 2015; Gherardi et al., 2005; Henry et al., 2016; McManus et al., 2004) or cores with water depth around 2000

m (Burckel et al., 2015; Gherardi et al., 2009; Mulitza et al., 2017). The Pa/Th time series for cores with water depth around 3000 m are rare, the most remarkable one being SU81-18 from (Gherardi et al., 2005). Therefore, SU90-08 will bring new record from 3000 m in the western basin and will allow to investigate about potential differences between the Eastern and Western basin as well as differences between deeper cores (>4000m).

SU90-08 has been studied quite intensively in the past decades (Bout-Roumazeilles et al., 1999; Cortijo et al., 1997; Grousset et al., 1993; Guihou et al., 2010; Vidal et al., 1997) so there exists published records of SST reconstructions, planktonic foraminifera δ^{18}O, or radiocarbon dates. This data demonstrates the interest of this cores and this location for paleoceanographic reconstructions and provide precious preliminary stratigraphic information. Additionally, sedimentary Pa/Th has been measured in the past on SU90-08 section corresponding to the last glacial inception (Guihou et al., 2010). This existing data has been determinant in the choice of this core to perform multi-proxy analysis.

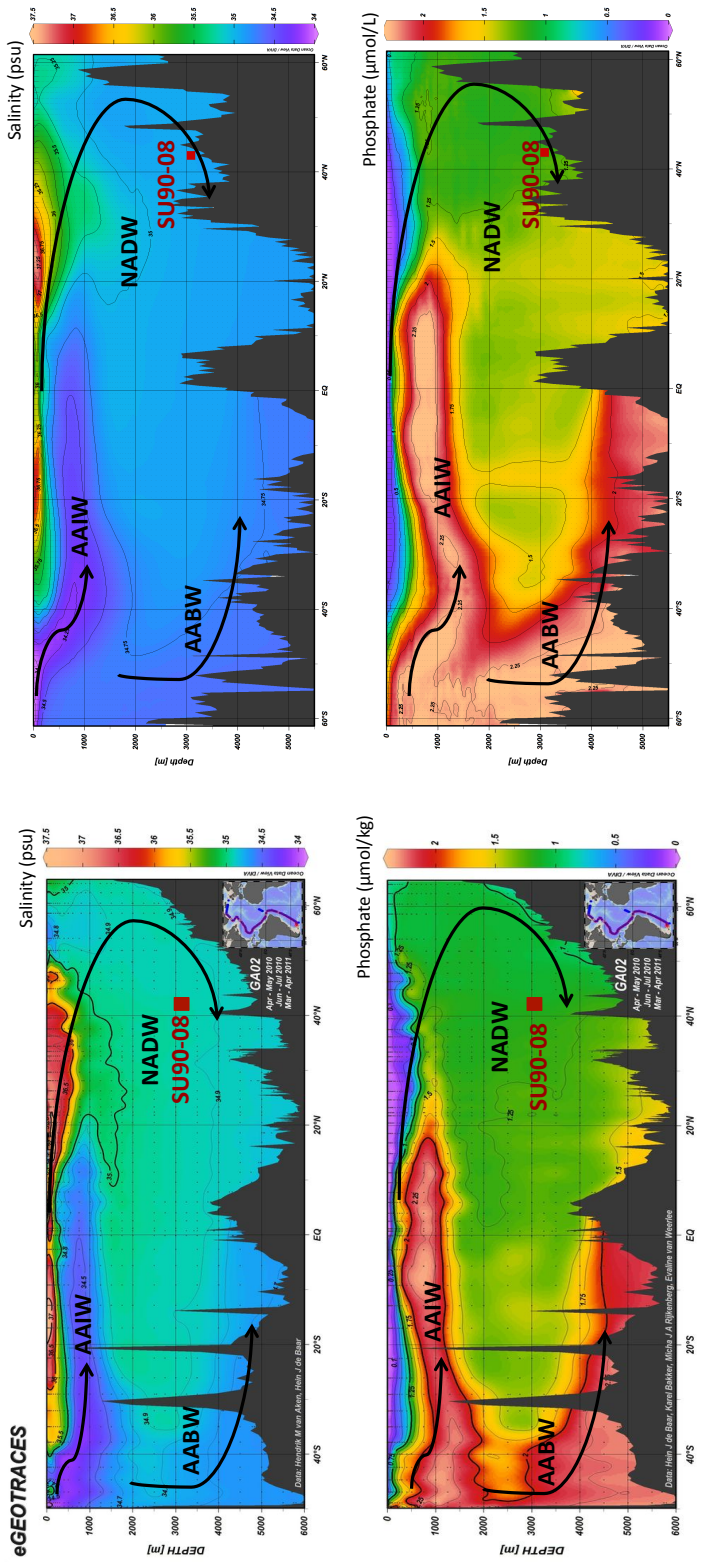

Figure 1.14 – **Atlantic Modern North-South salinity and phosphate concentration sections**
Left panel corresponds to the GEOTRACES GA02 section, Right panel corresponds to a North-South section closer to the western flank of the Mid Atlantic Ridge. Upper panels represent the salinity; lower panels represent the phosphate concentration. The position of sediment core SU90-08 is indicated by a red square. The main Atlantic water masses and their flowing directions are indicated with black arrows. eGEOTRACES sections from Schlitzer, Reiner, eGEOTRACES - Electronic Atlas of GEOTRACES Sections and Animated 3D Scenes, http://www.egeotraces.org, 2018.

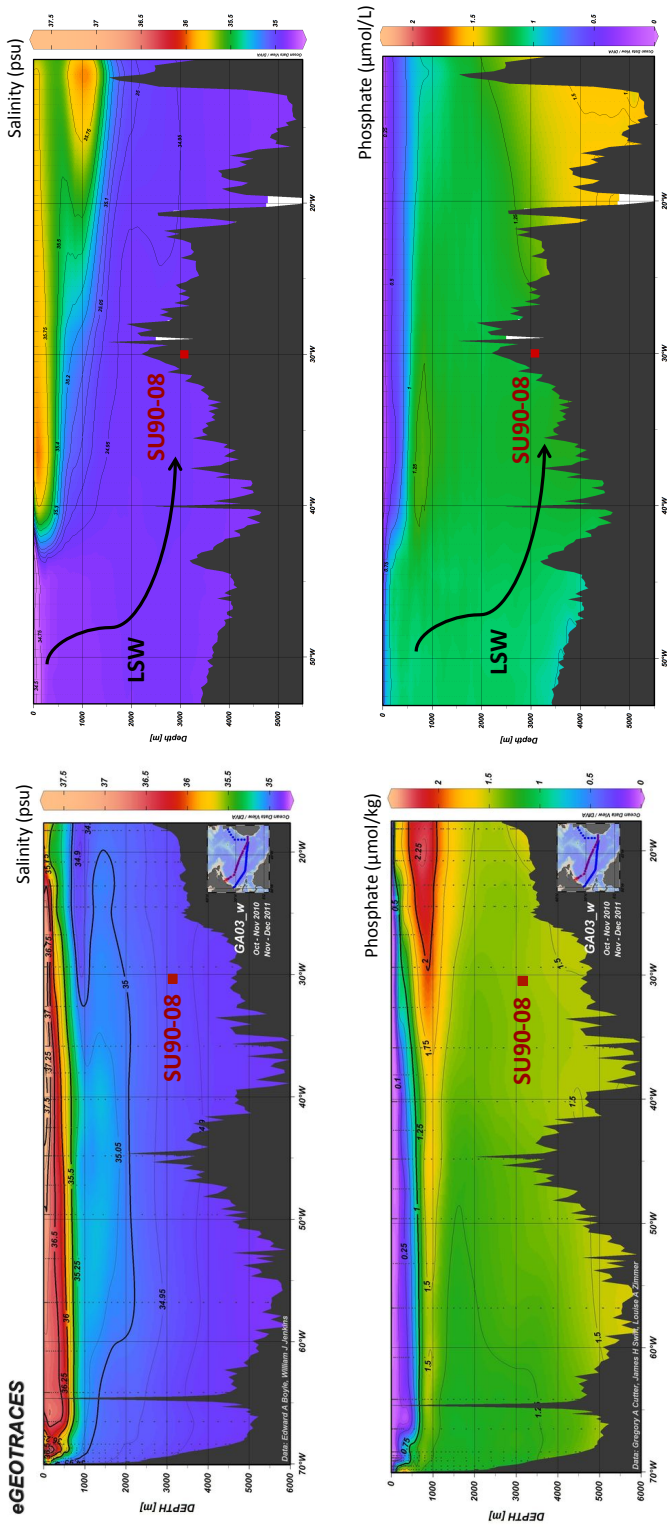

Figure 1.15 – **Atlantic modern East-West salinity and phosphate concentration sections** Left panel corresponds to the GEOTRACES GA03 section. Right panel corresponds to a East-West section passing by 43°N. Upper panels represent the salinity; lower panels represent the phosphate concentration. The position of sediment core SU90-08 is indicated by a red square. The main identifiable Atlantic water masses and their flowing directions are indicated with black arrows. eGEOTRACES sections from Schlitzer, Reiner, eGEOTRACES - Electronic Atlas of GEOTRACES Sections and Animated 3D Scenes, http://www.egeotraces.org, 2018.

1.4.3 Model-data comparison

Proxy data bring information about the climate and ocean circulation at given locations and for given time periods. In order to further investigate the physical mechanisms that drive the climate system, there is a need for modeling approach and for model-data comparison. Indeed, a climate model reproduces – to a certain extent related to its complexity level – the mechanisms taking place in the different components of the climate system (*e.g.* the ocean, the vegetation, the atmosphere) and the interactions between those components. A climate model is made of numerous physical equations that contain adjustable or "tunable" parameters. By running climate models, one can either test whether the physical mechanisms taken into account can reproduce climate events or features identified in the data or test different model versions to identify which parameter set fits best with a dataset. Climate models can also be used as tools to test hypotheses explaining features observed in the paleo-data. Last but not least, some paleo-proxies give only qualitative reconstruction of oceanic or climatic changes. Going from qualitative to quantitative information then involves climate models and model-data comparison. There exist different categories of climate models. The General Circulation Models (GCMs) try to include detailed circulation schemes, numerous interactions as well as very complex physical processes such as full nutrient cycles or the impacts of clouds in the atmosphere. These models are considered to be "state of the art" climate models but in return they are very costly in terms of computation resources: computing a few decades can require months of supercomputer calculations. Thus, those models are not adapted to run paleo simulations of several thousands of years that are needed to study the abrupt events of the last 40 ky or the last deglaciation. Instead, we use climate models of intermediate complexity that have coarser resolution and represent less physical mechanisms or interactions and/or represent those mechanisms in a simpler way. Those models can simulate a thousand of years in about 24 hours of computations. In that sense those models are better suited to study relatively long term paleoclimate variations.

The model chosen for this PhD thesis is iLOVECLIM. At the date this manuscript was written, the model contained an ocean, an atmosphere, an ice-sheet model, a vegetation model, a carbon cycle model and even sediments and permafrost model (Fig 1.16). iLOVECLIM is a model of intermediate complexity that nevertheless computes quite sophisticated ocean circulation. The resolution of the ocean 3D grid is 3° x 3° with 20 layers in the vertical direction with logarithmic spacing (the uppermost layer is 10 m thick whereas the bottom layer is 741 m thick). Before the beginning of this PhD, the model was able to simulate oceanic the $\delta^{18}O$, $\delta^{13}C$ and $\Delta^{14}C$ but not the Pa/Th.

To conclude, in this introductory chapter we have seen that the ocean was a key component of the climate system. We have also described the modern circulation patterns,

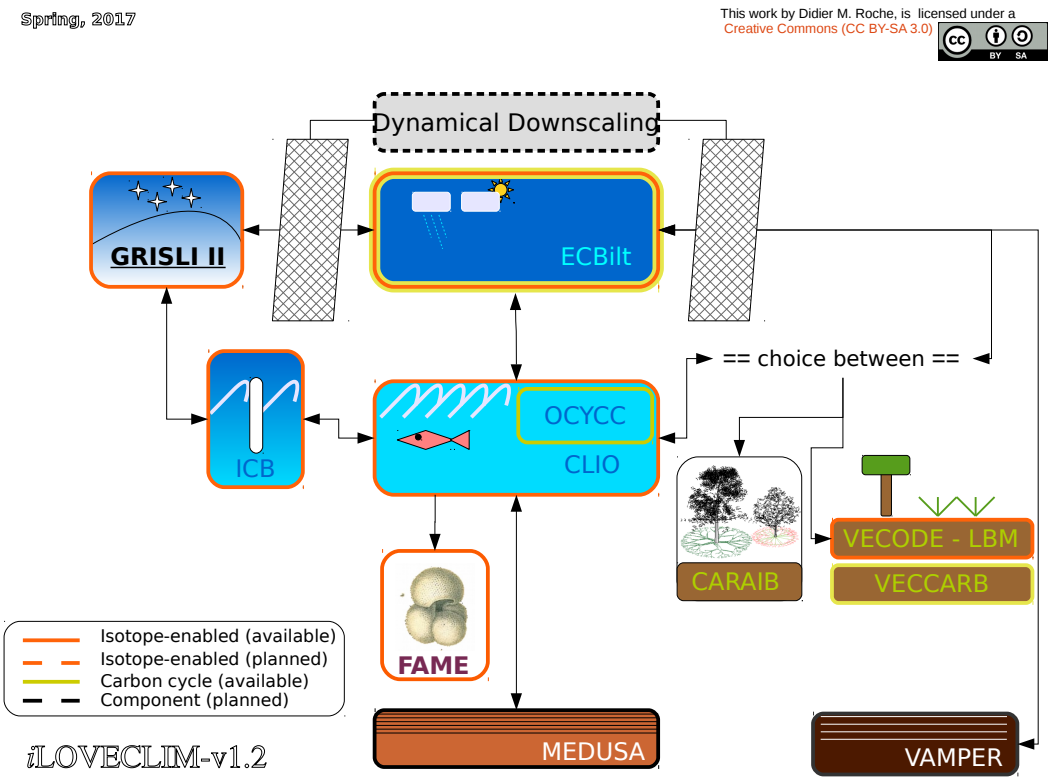

Figure 1.16 – **iLOVECLIM climate model of intermediate complexity**
Courtesy of Didier Roche

particularly in the Atlantic basin. We have described the main paleo-proxies available to reconstruct the oceanic circulation through the last 40 ka. We have then described the current knowledge about circulation changes across the abrupt climate events such as the Heinrich events, the DO cycles and the last deglaciation. Finally, we have presented the strategy for this PhD project. In the next chapter we will start to analyze the multiproxy record of SU90-08, starting with the Pa/Th data.

Chapter 2. Determination of marine sediment detrital fraction (^{238}U/^{232}Th) ratio for SU90-08, implications for sedimentary fluxes and ocean circulation reconstructions

2.1 Introduction

The first objective of this thesis is to produce a multiproxy record (in particular sedimentary Pa/Th, benthic δ^{13}C and Δ^{14}C) reflecting the ocean circulation variations over the past 40 ky for the deep sea sediment core SU90-08. The U-series related proxies, *i.e.* the ^{230}Th-normalized flux and the Pa/Th, require the calculation of the excess fractions for ^{231}Pa and/or ^{230}Th (subscript "xs") at deposition time (subscript "0"). $^{231}Pa_{xs,0}$ and $^{230}Th_{xs,0}$ thus correspond to ^{231}Pa and ^{230}Th produced in the water column by parent isotope disintegration (respectively ^{235}U and ^{238}U) that are adsorbed on particle sinking through the water column. $^{231}Pa_{xs,0}$ and $^{230}Th_{xs,0}$ are calculated from bulk sediment isotopic activities measurements of ^{231}Pa, ^{230}Th, ^{232}Th and ^{238}U, correcting from detrital and authigenic contributions. The authigenic fraction corresponds to the ^{231}Pa and ^{230}Th produced by radioactive decay of parent U accumulated in the sediment under suboxic or anoxic conditions. The authigenic correction is estimated using decay constants and detrital contribution. The detrital fraction corresponds to ^{231}Pa and ^{230}Th coming from wind, riverine inputs or more rarely, from iceberg discharge. The detrital contribution is estimated using the measured ^{232}Th activity, ^{232}Th assumed to be entirely of detrital

origin and the (^{238}U/^{232}Th) activity ratio of the sediment detrital fraction (herafter called $(U/Th)_{det}$).The sediment $(U/Th)_{det}$ is inherited from the geological parent material and varies with the parent material age and geological nature. The rock (^{238}U/^{232}Th) is highly variable around the Atlantic basin (Figure 2.1) and there is no formal compilation of the sediment $(U/Th)_{det}$ values. In the literature, the $(U/Th)_{det}$ has always been considered as constant through time. Its values is set either as a regional or local estimate (see Table 2.1).

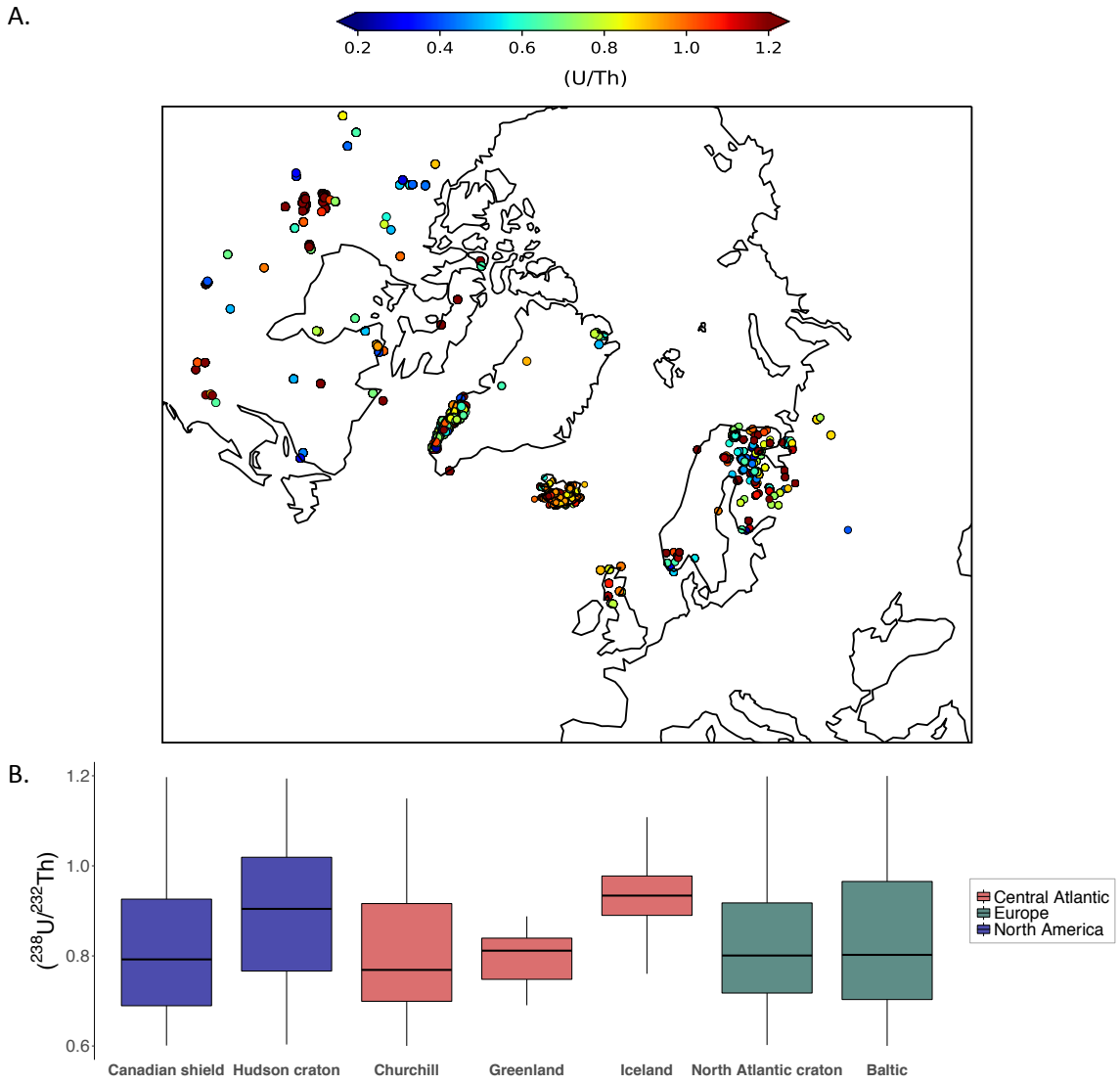

Figure 2.1 – **(^{238}U/^{232}Th) variability in rock samples for the North-Atlantic region.**
(A.) Map of (^{238}U/^{232}Th) based on the Georoc database (http://georoc.mpch-mainz.gwdg.de/georoc/) **(B.)** Same dataset as (A.) shown as boxplots for various areas around the North Atlantic. The data supports the high variability of the (^{238}U/^{232}Th) in parent materials that form the sediment detrital fraction in North-Atlantic region. Measurements from North America, Greenland, Iceland and Scandinavia display a median (^{238}U/^{232}Th) of 0.89, significantly different from the Atlantic range mentioned in Henderson & Anderson (2003) (0.6 ± 0.2).

Table 2.1 – Atlantic literature $(U/Th)_{det}$ values

Reference	**$(U/Th)_{det}$ value**	**Region**
Veiga-Pires & Hillaire-Marcel (1999)	0.58 ± 0.16	Labrador Sea
Thomson et al. (1999)	0.7 ± ?	Iberian Margin
Henderson & Anderson (2003)	0.6 ± 0.1	Atlantic
McManus et al. (2004)	0.6 ± 0.2	N-Atlantic
Gherardi et al. (2009)	0.6 ± 0.1	N-Atlantic
Guihou et al. (2010)	0.5 ± 0.1	N-Atlantic
Bourne et al. (2012)	Local value (inferred from ^{234}U)	-
Böhm et al. (2015)	0.47 ± 0.1	N-Atlantic
Burckel et al. (2016)	0.5 ± 0.1	Eq-Atlantic
Mulitza et al. (2017)	0.4 ± 0.03	Eq-Atlantic

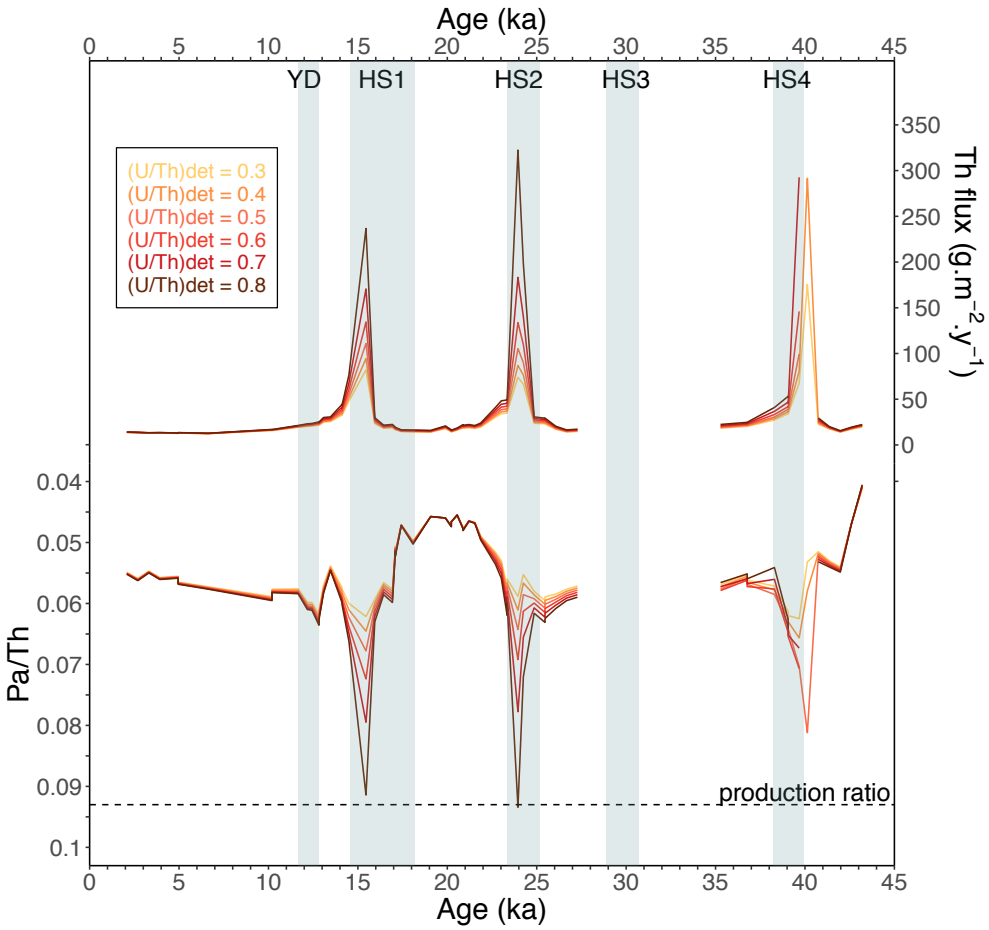

Figure 2.2 – **SU90-08 ^{230}Th-normalized flux and Pa/Th calculated for $(U/Th)_{det}$ values ranging between 0.3 and 0.8.** ka denotes ky cal BP

After performing the activities measurements of ^{231}Pa, ^{230}Th, ^{232}Th and ^{238}U for 65 levels of SU90-08 deep-sea sediment core (see appendix for details about procedures and data processing), I had no objective way to choose a value for $(U/Th)_{det}$ at SU90-08 location. Thus, I decided to perform sensitivity tests: I calculated the Pa/Th and ^{230}Th-normalized flux for $(U/Th)_{det}$ ranging from 0.3 to 0.8 with 0.1 increment (Figure 2.2), this range of $(U/Th)_{det}$ values being consistent with literature $(U/Th)_{det}$ values (see Table 2.1) These sensitivity tests highlighted that the ^{230}Th-normalized flux and the Pa/Th are very sensitive to the choice of the $(U/Th)_{det}$ value, especially of samples corresponding to SU90-08 Heinrich layers (Figure 2.2). While the Holocene and LGM values remain very stable whatever the choice of the $(U/Th)_{det}$ value, in the Heinrich layers, the ^{230}Th-normalized flux and Pa/Th increase by more than 100%. Thus the choice of (U/Th)det value seems to be a crucial parameter regulating the amplitude of ^{230}Th-normalized flux and Pa/Th changes across Heinrich events in SU90-08 deep-sea sediment core. In order to better constrain the amplitude of sedimentary fluxes and circulation changes, I decided to better constrain $(U/Th)_{det}$ temporal evolution for this particular core. This work is summarized in the sections below and presented in detail in the article entitled "Downcore variations of sedimentary detrital (^{238}U/^{232}Th) ratio: implications on the use of $^{230}Th_{xs}$ and $^{231}Pa_{xs}$ to reconstruct sediment flux and ocean circulation", published in 2018 in the journal *Geophysics, Geochemistry, Geosystems* (Missiaen et al., 2018).

2.2 Article "Downcore variations of sedimentary detrital (^{238}U/^{232}Th) ratio: implications on the use of $^{230}Th_{xs}$ and $^{231}Pa_{xs}$ to reconstruct sediment flux and ocean circulation"

2.2.1 Article and supplementary information

AGU100 ADVANCING EARTH AND SPACE SCIENCE

Geochemistry, Geophysics, Geosystems

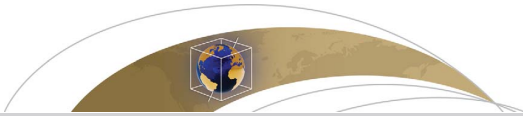

RESEARCH ARTICLE

10.1029/2017GC007410

Key Points:
- The ($^{238}U/^{232}Th$) of the sediment detrital fraction of SU90-08 varied between 0.4 and 0.7 over the last 40 ky
- The influence of varying detrital ($^{238}U/^{232}Th$) value on widely used paleoceanographic proxies can exceed the uncertainty on the proxies
- The sensitivity to the detrital ($^{238}U/^{232}Th$) value mainly depends on the detrital fraction proportion and terrigenous material supply

Supporting Information:
- Supporting Information S1
- Data Set S1
- Data Set S2
- Data Set S3
- Data Set S4
- Data Set S5
- Data Set S5

Correspondence to:
L. Missiaen,
lise.missiaen@lsce.ipsl.fr

Citation:
Missiaen, L., Pichat, S., Waelbroeck, C., Douville, E., Bordier, L., Dapoigny, A., et al. (2018). Downcore variations of sedimentary detrital ($^{238}U/^{232}Th$) ratio: Implications on the use of $^{230}Th_{xs}$ and $^{231}Pa_{xs}$ to reconstruct sediment flux and ocean circulation. *Geochemistry, Geophysics, Geosystems*, *19*. https://doi.org/10.1029/2017GC007410

Received 28 DEC 2017
Accepted 2 MAY 2018
Accepted article online 8 MAY 2018

Downcore Variations of Sedimentary Detrital ($^{238}U/^{232}Th$) Ratio: Implications on the Use of $^{230}Th_{xs}$ and $^{231}Pa_{xs}$ to Reconstruct Sediment Flux and Ocean Circulation

L. Missiaen[1], S. Pichat[1,2,3], C. Waelbroeck[1], E. Douville[1], L. Bordier[1], A. Dapoigny[1], F. Thil[1], L. Foliot[1], and L. Wacker[4]

[1]Laboratoire des Sciences du Climat et de l'Environnement, LSCE/IPSL, CEA-CNRS-UVSQ-Université Paris-Saclay, Gif-sur-Yvette, France, [2]Laboratoire de Géologie de Lyon (LGL-TPE), ENS de Lyon, Université de Lyon, Lyon, France, [3]Climate Geochemistry Department, Max Planck Institute for Chemistry, Mainz, Germany, [4]Laboratory of Ion Beam Physics, ETH Zürich, Zürich, Switzerland

Abstract Excess ^{231}Pa and ^{230}Th ($^{231}Pa_{xs}$ and $^{230}Th_{xs}$) can be used to reconstruct past oceanic sedimentation (^{230}Th-normalized flux) and circulation changes ($(^{231}Pa/^{230}Th)_{xs,0}$, hereafter Pa/Th). These quantities are determined by computing the detrital and authigenic contributions from bulk sediment measurement. The method relies on the use of a chosen constant value of the detrital ($^{238}U/^{232}Th$) activity ratio (hereafter $(U/Th)_{det}$). In this study, we have extracted the detrital fraction of the sediments from North Atlantic deep-sea core SU90-08 (43°03′1N, 30°02′5W, 3,080 m) and determined its $(U/Th)_{det}$ value over the last 40 ky. We find that $(U/Th)_{det}$ varied significantly through time with a minimum value of 0.4 during the Holocene and a maximum value of 0.7 during the Last Glacial Maximum (LGM). The sensitivity of sedimentary ^{230}Th-normalized flux and Pa/Th is tested for our study site and for other North Atlantic sites. We show that the sensitivity is highly dependent on the core location and its terrigenous material supply. The ^{230}Th-normalized flux and Pa/Th signals are very robust in cores with low detrital contributions, whereas they are very sensitive to $(U/Th)_{det}$ changes in cores with higher detrital contribution. In the latter case, changes in ^{230}Th-normalized flux and Pa/Th due to the choice of a constant $(U/Th)_{det}$ can largely exceed the uncertainty on the ^{230}Th-normalized flux and Pa/Th, inducing potential biases in the amplitude and temporal variability of reconstructed sedimentation and ocean circulation changes.

1. Introduction

The U-series nuclides, and particularly ^{231}Pa, ^{230}Th, ^{232}Th, ^{238}U, provide a powerful tool to study oceanic processes such as sedimentation or circulation (Bacon & Anderson, 1982; Bourdon et al., 2003; Henderson & Anderson, 2003; Yu et al., 1996). For instance, ^{230}Th-normalization is now widely used to reconstruct past sedimentary fluxes and sedimentation rates (François et al., 1993, 2004; Winckler et al., 2016). Depending on the ocean basin considered, the sedimentary $(^{231}Pa/^{230}Th)_{xs,0}$ ratio (hereafter Pa/Th) enables to reconstruct past export productivity (Kumar et al., 1995; Pichat et al., 2004), or past overturning rates (Burckel et al., 2016; McManus et al., 2004; Yu et al., 1996).

Both proxies are based on the determination of the nuclides excess activities (subscript "xs") at the deposition time (subscript "0"). The excess activity corresponds to the fraction of the radioisotope that is produced in the water column by U decay and transferred to the sediment by adsorption on particles sinking in the water column. $^{230}Th_{xs,0}$ and $^{231}Pa_{xs,0}$ are calculated from bulk sediment measurements by correcting from the contribution of the detrital and authigenic fractions, and in situ decay of each radioisotope after deposition (François et al., 2004; Henderson & Anderson, 2003). Both the detrital and authigenic contributions to the measured concentration of the radioisotope are estimated based on several assumptions. The authigenic contribution corresponds to the radioisotopes produced by in situ radioactive decay of the parent authigenic U, accumulated under suboxic or anoxic conditions. It is calculated using decay constants of the parent isotope and the detrital contribution. This latter is itself derived from the terrigenous content of the sediment. In most previous studies the detrital contribution has been calculated using a chosen constant value for the ($^{238}U/^{232}Th$) activity ratio of the sediment detrital fraction (hereafter $(U/Th)_{det}$) (Table 1).

Geochemistry, Geophysics, Geosystems 10.1029/2017GC007410

Table 1
Atlantic Literature $(U/Th)_{det}$ Values

References	$(U/Th)_{det}$ value	Region
Veiga-Pires and Hillaire-Marcel (1999)	0.58 ± 0.16	Labrador Sea
Thomson et al. (1999)	$0.7 \pm ?$	Iberian Margin
Henderson and Anderson (2003)	0.6 ± 0.1	Atlantic
McManus et al. (2004)	0.6 ± 0.2	N-Atlantic
Gherardi et al. (2009)	0.6 ± 0.1	N-Atlantic
Guihou et al. (2010)	0.5 ± 0.1	N-Atlantic
Bourne et al. (2012)	Local value (inferred from ^{234}U)	
Böhm et al. (2015)	0.47 ± 0.1	N-Atlantic
Burckel et al. (2016)	0.5 ± 0.1	Eq-Atlantic
Mulitza et al. (2017)	0.4 ± 0.03	Eq-Atlantic

There is actually no formal compilation of $(U/Th)_{det}$ in marine sediments and, for the Atlantic, the assumed $(U/Th)_{det}$ value and its uncertainty vary from one publication to another (Table 1). Regarding the choice of the $(U/Th)_{det}$ value, most authors used a constant value corresponding to a regional estimate as proposed in Henderson and Anderson (2003). For instance the value chosen for $(U/Th)_{det}$ was 0.6 in Gherardi et al. (2009), Henderson and Anderson (2003), and McManus et al. (2004) or 0.5 in Burckel et al. (2016) and Guihou et al. (2010). Others proposed to define local estimates of the $(U/Th)_{det}$ value. A first approach consists in using the average measured bulk ($^{238}U/^{232}Th$) (Veiga-Pires & Hillaire-Marcel, 1999). Later, Bourne et al. (2012) proposed a method to achieve a more precise estimate. ^{234}U is used as an indicator of the authigenic content and thus, enables to identify sediment levels characterized by an absence of authigenic contribution. In these levels, the measured bulk ($^{238}U/^{232}Th$) is used as the local estimate of $(U/Th)_{det}$. Finally, Böhm et al. (2015) and Mulitza et al. (2017) also attempted to use a local $(U/Th)_{det}$ estimate for their Pa/Th calculation and used, respectively, 0.47 and 0.4, corresponding to the minimum bulk ($^{238}U/^{232}Th$) of their records. They assumed that the minimum bulk ($^{238}U/^{232}Th$) value corresponds to depths where there is no authigenic contribution. Even though this approach provides a reliable upper limit for the local $(U/Th)_{det}$, it is not optimal since, in the absence of ^{234}U measurement, there is no conclusive evidence that there is no authigenic contribution at the considered levels. In addition, a temporal decreasing trend can be observed for the uncertainty associated to $(U/Th)_{det}$: while earlier studies used regional $(U/Th)_{det}$ estimates associated with relatively large uncertainties ± 0.2 (2σ) (Henderson & Anderson, 2003; McManus et al., 2004), more recent studies, still using basin-scale $(U/Th)_{det}$ estimate reduced the uncertainties to ± 0.1 (2σ) (Burckel et al., 2016; Gherardi et al., 2009; Guihou et al., 2010). Finally, the most recent study used a local estimate of $(U/Th)_{det}$, associated with an uncertainty of ± 0.03 (2σ) (Mulitza et al., 2017), i.e., more than 6 times smaller than the uncertainty used by the first studies cited above (Table 1).

Basin-scale variations in $(U/Th)_{det}$ have been reported. For instance, $(U/Th)_{det}$ has been shown to increase northward from 0.3 to 0.6 between 70°S and 45°S in the South Atlantic (Walter et al., 1997). In the equatorial Pacific, basin-scale variability has been considered (Anderson et al., 1983; Pichat et al., 2004). $(U/Th)_{det}$ values of 0.8 ± 0.2 were assumed in the east while 1.0 ± 0.3 was assumed for a core located close to Guinea based on a compilation of ($^{238}U/^{232}Th$) values of the potential detrital sources. Nevertheless, many Pa/Th studies involving cores from various Atlantic sites used a single $(U/Th)_{det}$ value (Gherardi et al., 2009; Guihou et al., 2010; Yu et al., 1996).

Overall, it is relevant to question whether the choice of the $(U/Th)_{det}$ value might significantly affect the records generated in those studies, which could be crucial when performing basin-wide or ocean-wide integrative studies based on the comparison of several records. Although some studies (Burckel et al., 2015; Lippold et al., 2016) have examined the impact of the choice of the $(U/Th)_{det}$ value on computed Pa/Th values, $(U/Th)_{det}$ has been assumed to be constant through time. However, ($^{238}U/^{232}Th$) depends on the geological nature and age of the parental material, resulting in highly variable ($^{238}U/^{232}Th$) at the Earth surface (supporting information Figure S1). The provenance of the detrital material or the relative contribution of various sources of detrital material can vary temporally, especially across climatic transitions. As shown by numerous studies, based on model experiments and/or paleoclimate proxies (Clement & Peterson, 2008; Hemming, 2004; Peterson et al., 2000; Voelker, 2002), rapid climate transitions are associated with changes

Geochemistry, Geophysics, Geosystems 10.1029/2017GC007410

in precipitation regime, wind pattern, or iceberg discharge; hence, local changes in dust and/or riverine inputs, as well as ice rafted debris (IRD) are expected. It is thus likely that modifications in detrital inputs induce changes in the $(U/Th)_{det}$ value. Particularly in the case of locations characterized by high detrital inputs (for instance, coastal areas or areas subject to IRD discharges), changes in $(U/Th)_{det}$ can lead to substantial differences in the calculated $^{230}Th_{xs,0}$ and $^{231}Pa_{xs,0,}$ and interpretation of associated proxies across climate transitions.

In this study, we investigate (i) the variations of $(U/Th)_{det}$ over the last 40 ky in a core located within the IRD Ruddiman belt in the North Atlantic and (ii) the effect of $(U/Th)_{det}$ changes on the computed ^{230}Th-normalized flux and Pa/Th, and on the interpretation of these proxies.

2. Materials and Methods

2.1. Core Location and Age Model

In order to study $(U/Th)_{det}$ variability through time, we sampled sediment core SU90-08 (43°03′1N, 30°02′5W, 3,080 m) located on the western flank of the Mid-Atlantic Ridge, within the Ruddiman belt (Figure 1). The sediment mainly consists in interbedded carbonates, foraminifera ooze, and mud (Bout-Roumazeilles et al., 1999). IRD layers containing coarse detrital material corresponding to Heinrich events 1, 2, and 4 are observed. Heinrich event 3 is not recorded in this core.

An age model has been previously established for core SU90-08 based on 10 radiocarbon dates covering the period from the Bolling-Allerod to Heinrich Stadial 4 (Vidal et al., 1997). Nevertheless, due to the core location (north of 40°N) and poorly constrained surface reservoir ages variations through the last glacial and the deglaciation (Bondevik et al., 2006; Waelbroeck et al., 2001), the age model cannot simply be derived from calibrated planktonic foraminifer ^{14}C ages beyond the Holocene. We thus constructed a new age model based on mixed pointers: ^{14}C dates for the Holocene period, where the reservoir ages are assumed to be constant and close to the current value of 400 ± 100 years, and alignment of sea surface temperature to Greenland air temperature for the glacial period (supporting information Table S1 and Figure S2). Planktonic foraminifera (*Globigerina bulloides*) were picked from four Holocene levels and radiocarbon dated using a Mini Carbon Dating System (MICADAS) with a gas introduction system (Fahrni et al., 2013; Wacker

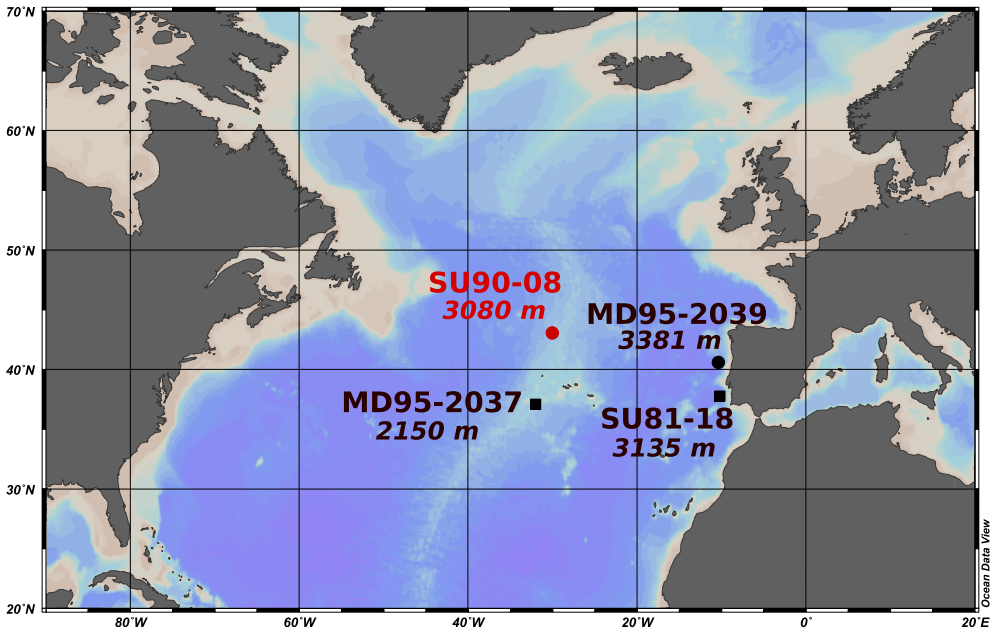

Figure 1. North Atlantic map showing the location of the cores used in this study. In red SU90-08 (new data: this study). In black, cores with published data: SU81-18 and MD95-2037 (Gherardi et al., 2009) and MD95-2039 (Thomson et al., 1999). Dots represent cores with U and Th data only; squares denote cores with U, Th, and Pa data.

Geochemistry, Geophysics, Geosystems 10.1029/2017GC007410

et al., 2013) at Eidgenössiche Technische Hochscule Zürich (ETH-Zürich). The ^{14}C ages were calibrated to calendar ages using Oxcal (online version 4.3) (Ramsey, 2009), a reservoir age of 400 ± 100 years, and the IntCal13 calibration curve (Reimer et al., 2013). Deeper in the core, a new high-resolution sea surface temperature records (based on planktonic foraminifera assemblages (see supporting information text S1) and percentage of *Neogloboquadrina pachyderma* senestral) were aligned to North-GRIP $\delta^{18}O$, a proxy for air temperature above the ice sheet (Andersen et al., 2006; Bond et al., 1993; Rasmussen et al., 2006; Svensson et al., 2006; Vinther et al., 2006). The sedimentation rate was assumed to be constant between tie-points. More information about the methodology can be found in the supporting information (Cortijo et al., 1997; Therón et al., 2004; Waelbroeck et al., 1998).

2.2. ^{238}U and ^{232}Th Analysis in SU90-08 Detrital Fraction

In the following, parentheses denote activity or activity ratio. In order to determine as precisely as possible the ($^{238}U/^{232}Th$) of the actual detrital fraction of the sediments (i.e., $(U/Th)_{det}$), we measured ^{238}U and ^{232}Th in different fractions of SU90-08 sediment samples: (i) we extracted the carbonate-free and ferromanganese-free sediment detrital fraction using a sequential leaching procedure, this fraction will be referred as the "leaching residue" in the following, (ii) we handpicked IRDs to analyze (a) bulk IRDs and (b) the detrital carbonates contained in the IRDs.

We used the sequential leaching procedure described in Pichat et al. (2014) to isolate the detrital fraction of the sediment from the carbonates and ferromanganese oxihydroxides. After the sequential leaching, the residue was digested in a mixture of concentrated HNO_3:HF (3:5 volume ratio) for 48 h at 150°C. The solution was then fumed with 2 mL $HClO_4$ at 170°C. During this procedure, beaker walls were rinsed 6 times with concentrated HNO_3. No residue was observed in the solutions after this digestion step. At near dryness, the sample was brought in 20 mL 2 N HNO_3. NH_4OH was added to precipitate Fe-oxyhydroxydes, which contain U and Th and leave the remaining fluorides in solution. The precipitate was washed 3 times with 18.2 MΩ water and finally dissolved in 5 mL 1 N HNO_3 and stored.

Because the leaching procedure removes carbonates, detrital carbonates possibly present in the sediment are also removed. However, it is known that IRDs have the potential to contain detrital carbonates (Hemming, 2004). To evaluate the impact of both IRDs and detrital carbonates contained in IRD layers on the sediment $(U/Th)_{det}$, we handpicked and measured ($^{238}U/^{232}Th$) of (a) bulk IRDs and (b) IRD detrital carbonates. For that purpose, five levels with high IRD content were selected (see supporting information Figure S3). The bulk sediment was sieved and the coarse fraction (>150 μm) rinsed with deionized water and dried.

For bulk IRD analyses, individual detritic grains from different size fractions (>350, 350–250, 250–200, and 150–200 μm) were handpicked and mixed to obtain ca. 50 mg of material. The samples were digested in a mixture of concentrated HNO_3:HF (3:5, volume ratio) for 48 h at 150°C. The solution was then fumed with 2 mL $HClO_4$ at 170°C. During this procedure, beaker walls were rinsed 6 times with concentrated HNO_3.

For IRD detrital carbonates analyses, around 50 mg of individual detrital carbonate grains (from the same levels) were handpicked and dissolved in 0.5 N HCl for 4 h. After centrifugation, the supernatant (= carbonates) was isolated. The residue was further leached in 0.5 N HCl for 4 h and the supernatants were combined. The sample (supernatant or residue) was then fully digested in a mixture of concentrated HNO_3:HF and evaporated to dryness with frequent rinsing of the beaker walls by concentrated HNO_3 to ensure full removal of fluorides prior to analysis. The samples were then evaporated to near dryness, dissolved in 1 N HNO_3 and stored.

The quality of the chemistry was assessed by preparing procedural blanks along the sample treatment. The blanks were found to represent less than 1% of the samples signals.

Bulk IRDs and leaching residues ($^{238}U/^{232}Th$) were diluted in 1 N HNO_3/0.01 N HF for analysis with addition of Re and In internal standards. The samples were measured using an Inductively Coupled Plasma Quadrupole Mass-Spectrometer (ICP-QMS, $X^{SeriesII}$ ThermoFisher) at the Laboratoire des Sciences du Climat et de l'Environnement (LSCE), France. The use of 1 N HNO_3/0.01 N HF carrier acid and of a PFA micronebulizer of 100 μL/min allowed rapid rinsing steps and high signal stability during measurements (signal variations represented about 1%) (Douville et al., 2010). U and Th concentrations were derived using an external calibration and corrected from the signal drift during the analysis using internal standard ^{185}Re monitoring. During the measurement sequence, ^{185}Re variations never exceeded 10% for the samples and 15% for home

Geochemistry, Geophysics, Geosystems 10.1029/2017GC007410

standard solutions. The measurement quality and analytical uncertainties were controlled with reference materials SL-1 (sediment, International Atomic Energy Agency, Vienna), BR1 (basalt, CRPG, France) and GSR6 (carbonate rock, National Research Center for CRMs, China) dissolutions. The values obtained with this procedure agree with the certified or published values within the error bars (see supporting information Figure S4). The analytical uncertainties (2σ) do not exceed 8% on Th concentrations, 7% on U concentrations, and 2.5% on the ratio. The variability observed in our samples largely exceeds those uncertainties, with changes in samples Th concentration, U concentration, and (U/Th) ratio, respectively, 12.5, 14.3, and 40 times larger than the analytical errors (supporting information Tables S2 and S3).

^{238}U and ^{232}Th concentrations of both the carbonate and residual fractions from IRD detrital carbonates were measured by ICP-QMS (Agilent 7900 equipped with an ISIS 3 introduction system) at the Climate Geochemistry Department of the Max Planck Institute for Chemistry, Mainz, Germany (supporting information Tables S4 and S5). The accuracy of the measurement was assessed using slate OU-6. Both measured ^{232}Th and ^{238}U concentrations of OU-6 are within errors of the certified values (Kane, 2004). The precision of the measurement is 2% (2σ) for both the U and Th concentrations (supporting information Tables S4 and S5). As for the other Q-ICP-MS measurements, we used 2% HNO_3–0.01 N HF as acid carrier and a PFA nebulizer. Indium was used as internal standard to correct for instrumental drift.

To assess the leaching quality and efficiency, standard material BR1 was prepared in the same conditions as the samples. As this material is a basalt rock, the total ^{238}U and ^{232}Th content should end up in the residue fraction. We observed about ~22% loss of material (24% for Th and 20% for U) during the leaching steps most likely due to repeated transfers of the samples to different containers necessary to perform leaching and centrifugation steps (Pichat et al., 2014). However, the ($^{238}U/^{232}Th$) ratio of the BR1 standard was practically not affected and remained stable within 6% (2σ) uncertainties, taking into account the measurement error and the uncertainties deriving from element fractionation during the leaching procedure (supporting information Figure S4).

The reproducibility of the leaching residue measurements was assessed by replicate ($^{238}U/^{232}Th$) measurements of two samples (121 and 196 cm). The results differed by 2.5% and 1.4% at 121 and 196 cm, respectively, which is lower or equivalent to the analytical standard deviation (2.5%, 2σ) for simple digestion and lower than the analytical standard deviation for leaching preparation (6%, 2σ, assessed using BR1 standard preparation as explained above). To assess the sample preparation reproducibility as well as the potential sample heterogeneity, the full procedure was applied to 2 aliquots of the level 121 cm. Based on these aliquot measurements, we evaluated the external reproducibility (difference between the two measurements) to 10% (2σ).

2.3. ^{238}U, ^{230}Th, and ^{232}Th Analysis in SU90-08 Bulk Sediment

In order to investigate the potential impact of $(U/Th)_{det}$ change on the calculation of $^{230}Th_{xs}$, we measured radioisotope ^{230}Th, ^{232}Th, and ^{238}U activities in SU90-08 bulk sediment. The analyses were performed on 53 samples following the procedure of Guihou et al. (2010). The measurements were done by isotope-dilution mass-spectrometry on a MC-ICP-MS (Neptune^{Plus} Thermo Fisher) at LSCE, France.

2.4. ^{230}Th-Normalized Flux and Pa/Th Sensitivity to $(U/Th)_{Det}$ Variations

We conducted sensitivity tests to assess (1) the impact of $(U/Th)_{det}$ changes on the ^{230}Th-normalized flux and Pa/Th calculations and (2) the potential spatial variability of this impact. We used new data on core SU90-08 (this study) and published data from two cores located on the Iberian Margin: SU81-18 (37°46′N, 10°11′W, 3,135 m) (Gherardi et al., 2005) and MD95-2039 (40°34.71′N, 10°20.91′W, 3,381 m) (Thomson et al., 1999), and one core close to the Azores archipelago and the Mid-Atlantic Ridge: MD95-2037 (37°05′N, 32°01′W, 2,150 m) (Gherardi et al., 2009) (Figure 1). The age models used for the latter three cores are the ones of the original publications.

As explained in section 1, the calculation of the excess fraction of the measured total ^{230}Th and ^{231}Pa requires corrections from other ^{230}Th and ^{231}Pa sources (detrital and authigenic). This relies on the following assumptions. First, the ^{232}Th content of the sediment is assumed to be purely detrital. Then, detrital ^{230}Th is considered to be at secular equilibrium with detrital ^{238}U, i.e., $(^{238}U)_{det} = (^{230}Th)_{det}$. The incorporation of authigenic uranium occurs at the time of sediment deposition at a known ($^{234}U/^{238}U$) ratio, assumed to be

Geochemistry, Geophysics, Geosystems 10.1029/2017GC007410

that of sea water: $(^{234}U/^{238}U)_{sw} = 1.1467$ ($1\sigma = 0.0025$) (Robinson et al., 2004). The equations used to determine Pa and Th excess activities are the following (Henderson & Anderson, 2003):

$$X_{xs} = X_{meas} - X_{det} - X_{auth} \quad (1)$$

where X stands for ^{231}Pa or ^{230}Th activities, "meas" for the measured activity, "det" for the detrital fraction, and "auth" for the authigenic fraction

$$^{230}Th_{xs} = {}^{230}Th_{meas} - \left(^{232}Th_{meas} \times (U/Th)det\right) - \left[^{238}U_{meas} - \left(^{232}Th_{meas} \times (U/Th)det\right) \times \left\{ \left(1 - e^{-\lambda 230 t}\right) + \frac{\lambda 230}{\lambda 230 - \lambda 234} \left(\left(\frac{234U}{238U}\right)_{sw} - 1 \right) \left(e^{-\lambda 234 t} - e^{-\lambda 230 t}\right) \right\} \right] \quad (2)$$

$$^{231}Pa_{xs} = {}^{231}Pa_{meas} - \left[\left(\frac{235U}{238U}\right)_{nat} \times (U/Th)det \times {}^{232}Th_{meas} \right] - \left[\left(\frac{235U}{238U}\right)_{nat} \times \left(^{238}U_{meas} - (U/Th)det \times {}^{232}Th_{meas}\right) \times \left(1 - e^{-\lambda 231 t}\right) \right] \quad (3)$$

where λ_x is the decay constant of the considered isotope and t is the age of the sediment. $(^{235}U/^{238}U)_{nat} = 0.046$ is the natural activity ratio of U isotopes.

Finally, the excess fraction at the time of sediment deposition ($^{231}Pa_{xs,0}$, $^{230}Th_{xs,0}$) can be calculated by correcting $^{231}Pa_{xs}$ and $^{230}Th_{xs}$ from the radioactive decay:

$$(X)_{xs,0} = (X)_{xs}\ e^{\lambda x t} \quad (4)$$

The preserved vertical rain rate or ^{230}Th-normalized flux (in g m^{-2} yr^{-1}) of sediment is given by

$$\frac{Z \times \beta\ Th}{^{230}Th_{xs,0}}$$

where Z is the water depth at the core location in meters and β_{Th} is the production rate of ^{230}Th in the water column (= 0.0267 dpm m^{-3} yr^{-1}).

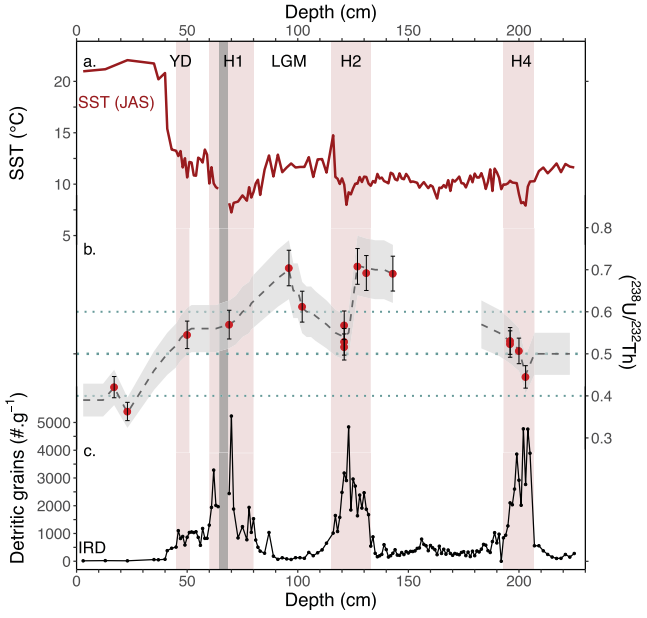

Figure 2. SU90-08 downcore variations. (a) Summer sea surface temperature (SST) reconstructed from planktonic foraminifera assemblages (see supporting information). (b) $(^{238}U/^{232}Th)$ of the leaching residues (red dots, see text section 2.2 for details) and associated standard deviation (2σ), interpolated $(U/Th)_{det}$ time series (dashed line) and associated uncertainty (2σ) (grey envelope). The dotted blue lines correspond to the most commonly used $(U/Th)_{det}$ and associated uncertainty. (c) Ice Rafted Debris content expressed as the number of >150 μm detritic grains per gram of dry sediment. The Younger Dryas and Heinrich layers are highlighted by red bands based on IRDs abundances. The vertical grey band corresponds to a sediment perturbation between 65 and 69 cm evidenced by reversals in ^{14}C ages as well as reversals in planktonic and benthic $\delta^{18}O$ and $\delta^{13}C$ signals. The data corresponding to the affected levels were systematically removed.

3. Results

3.1. Leaching Residues

The $(^{238}U/^{232}Th)$ ratio measured on SU90-08 leaching residues ranges from 0.36 ± 0.04 to 0.71 ± 0.07 (Figures 2 and 3, supporting information Table S2) and exhibits clear temporal variations. A major shift is observed between the Holocene period, where $(^{238}U/^{232}Th) \approx 0.4$, and the LGM period, where $(^{238}U/^{232}Th) \approx 0.7$. During the Younger Dryas (YD) and Heinrich events 1, 2, and 4, marked by relatively high IRD abundances, the $(^{238}U/^{232}Th)$ ratio is around 0.53, except for two points at the beginning of Heinrich layer 2. The observed temporal variations largely exceed the external reproducibility uncertainty (10%, 2σ) (Figure 2).

3.2. Handpicked Material

The $(^{238}U/^{232}Th)$ ratio of handpicked bulk IRDs and detrital carbonates is presented in Figure 3. Additionally, the maximal value of $(U/Th)_{det}$ was calculated assuming that the total measured ^{230}Th activity in the bulk sediment is of detrital origin, i.e., $(^{230}Th)_{meas} = (^{230}Th)_{det}$ (see equations (1) and (2)). The comparison of the sediment components $(^{238}U/^{232}Th)$ at a given depth (Figure 3) shows that (i) $(^{238}U/^{232}Th)$

Geochemistry, Geophysics, Geosystems 10.1029/2017GC007410

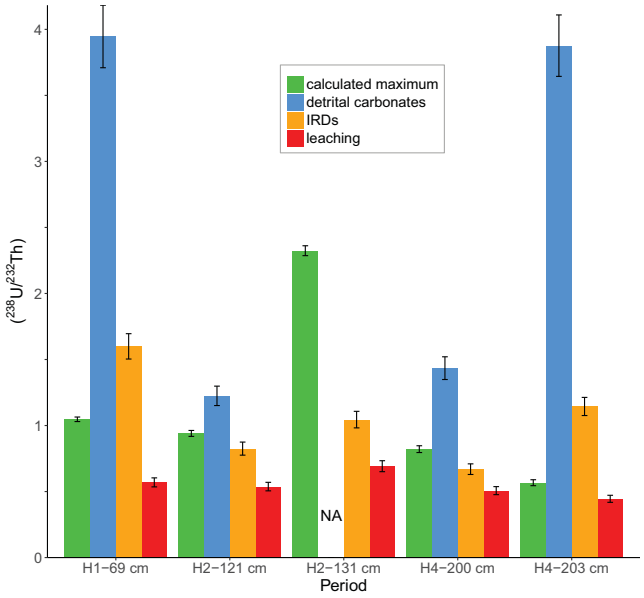

Figure 3. Comparison of the $(^{238}U/^{232}Th)$ ratio measured in leaching residue (red) and handpicked material (bulk IRD (orange) and detrital carbonates (blue)) with calculated maximum $(U/Th)_{det}$ (green) for five IRD levels in SU90-08. The calculated maximum $(U/Th)_{det}$ was obtained from the total (^{230}Th) and (^{232}Th) activities under the hypothesis that the sediment is purely detrital (see equation (1)). The high calculated maximum $(U/Th)_{det}$ obtained at 131 cm compared to the other depths is due to the lower IRD abundance at that level. Consequently the proportion of the excess and/or authigenic fractions is larger at that level. "NA" stands for "not available": not enough detrital carbonates were found in level 131 cm to analyze the detrital carbonates $(^{238}U/^{232}Th)$ signature.

measured in leaching residues is 2–9 times lower than that of detrital carbonates; (ii) the $(^{238}U/^{232}Th)$ of bulk IRDs is up to 3 times higher than that of leaching residues; (iii) the detrital carbonate $(^{238}U/^{232}Th)$ is always significantly higher than the calculated maximum $(U/Th)_{det}$.

4. Discussion

4.1. Constraining the Actual $(U/Th)_{det}$ Value

Figure 3 shows that the $(^{238}U/^{232}Th)$ ratio measured in handpicked IRDs (i.e., detrital carbonates and bulk IRDs) is significantly different from the $(^{238}U/^{232}Th)$ ratio measured in the leaching residues. Actually, none of the three measured components truly represents the detrital fraction of the sediment. Instead, we argue below that the $(^{238}U/^{232}Th)$ of detrital carbonates on the one hand, and of leaching residues on the other hand, can be seen as end-members values bracketing the actual $(U/Th)_{det}$ value.

On the one hand, detrital carbonates only represent a part of the total sediment detrital fraction. On the other hand, the handpicked material (bulk IRDs and detrital carbonates) only represents the coarser fraction of the sediment (>150 μm), the finer fraction having been eliminated along the sieving step. The finer detrital fraction might indeed represent an important portion of the total sediment detrital fraction. Finally, the leaching residue contains the fine fraction but misses the detrital carbonates that are removed during the leaching procedure. Consequently, none of these three components is representative of the actual sediment detrital fraction. Additionally, it is important to note that none of the fractions measured in this study (bulk sediments, leaching residues, bulk IRDs, and detrital carbonates) present remarkably low (^{238}U) or (^{232}Th) activities compared to the other fractions (see supporting information Tables S2–S6). Therefore, it is not possible to conclude that one of these fractions would not significantly affect the actual $(^{238}U/^{232}Th)$ of the true detrital fraction.

Detrital carbonates have systematically higher $(^{238}U/^{232}Th)$ than the leaching residue (Figure 3). Thus, because the leaching residue misses the detrital carbonate fraction, the $(^{238}U/^{232}Th)$ ratio measured on the leaching residues yields an underestimated detrital fraction $(^{238}U/^{232}Th)$ value compared to the actual $(U/Th)_{det}$. Also, for a given depth, the $(^{238}U/^{232}Th)$ ratio of the detrital carbonates is always much higher than the calculated maximum $(U/Th)_{det}$ (Figure 3). The calculated maximum $(U/Th)_{det}$ could be biased because it is determined on subsamples of only 200 mg that might not be representative of the total sample if the latter contains big IRD grains, like in the case of levels 200 and 203 cm. Despite this possible bias, the systematic and significant difference between the detrital carbonates $(^{238}U/^{232}Th)$ and the calculated maximum $(U/Th)_{det}$ is consistent with the fact that detrital carbonates do not represent a large portion of the total detrital fraction. This is confirmed by the observation of levels 200 and 203 cm, which are characterized by very high IRD content (71% and 93% of the grains (foraminifera and IRDs) counted in the >150 μm size fraction, respectively). Examined under the binocular, these levels appeared to be almost entirely made of detrital material and contained very few foraminifera. For those levels, the leaching steps removed a very small fraction of the sediment, corresponding to biogenic (e.g., foraminifera) and detrital carbonates. For those levels, the leaching $(^{238}U/^{232}Th)$ ratio is very close to the calculated maximum $(U/Th)_{det}$ and very different from the detrital carbonates $(^{238}U/^{232}Th)$. Thus, detrital carbonates must represent a very small portion of the detrital fraction for the levels 200 and 203 cm. This is also the case for the rest of the core, as attested by the systematic and significant difference between the detrital carbonates and calculated maximum $(^{238}U/^{232}Th)$. The low amount of detrital carbonates in the sediment is indeed consistent with the core location, relatively far from the sources of detrital carbonates (Andrews & Tedesco, 1992; Jennings et al., 2015). Consequently, our leaching residue $(^{238}U/^{232}Th)$ measurements should be close to the actual $(U/Th)_{det}$ in SU90-08.

Geochemistry, Geophysics, Geosystems 10.1029/2017GC007410

In cores with large detrital carbonate content (for instance cores closer to detrital carbonates sources), the leaching residue ($^{238}U/^{232}Th$) could be significantly lower than the actual $(U/Th)_{det}$ value. Consequently, the leaching residue ($^{238}U/^{232}Th$) could underestimate the actual $(U/Th)_{det}$ when the detrital carbonates represent an important part of the detrital fraction. In conclusion, the true $(U/Th)_{det}$ lies on a mixing line between detrital carbonates high ($^{238}U/^{232}Th$) and leaching residue low ($^{238}U/^{232}Th$) values. Moreover, in SU90-08, the true $(U/Th)_{det}$ should be close to the measured leaching residues ($^{238}U/^{232}Th$).

The range of ($^{238}U/^{232}Th$) values measured in SU90-08 leaching residues (Figure 2) is overall consistent with the ($^{238}U/^{232}Th$) values measured in the literature for the Atlantic basin (Veiga-Pires & Hillaire-Marcel, 1999; Walter et al., 1997). However, the downcore variability of leaching residue ($^{238}U/^{232}Th$) in SU90-08 (0.36 ± 0.04 to 0.71 ± 0.07) largely exceeds the $(U/Th)_{det}$ range assumed in the studies after 2004 (Table 1) that considered a constant $(U/Th)_{det}$ value and an error range ≤ 0.1 (2σ). Since the choice of $(U/Th)_{det}$ has the potential to affect the $^{231}Pa_{xs,0}$ and $^{230}Th_{xs,0}$ signals, variations of $(U/Th)_{det}$ with time could be considered, which has not been done in previous studies.

In conclusion, although the leaching residue misses the detrital carbonates, the leaching residue ($^{238}U/^{232}Th$) values are close (slightly underestimated) to the real $(U/Th)_{det}$ values because the detrital carbonates are representing only a small fraction of the total detrital fraction. Consequently, the ($^{238}U/^{232}Th$) range observed in the leaching residues of SU90-08 samples ($0.4–0.7 \pm 0.1$) is representative of the actual $(U/Th)_{det}$ range in these samples and a suitable basis for testing the sensitivity of excess fraction related proxies to $(U/Th)_{det}$ variations.

4.2. Impact of $(U/Th)_{det}$ Variations on the Estimation of Sedimentary Flux and Ocean Circulation Strength

We calculated the ^{230}Th-normalized flux (Figure 4) and Pa/Th ratio (Figure 5) using $(U/Th)_{det}$ values varying between 0.3 and 0.8, with a 0.1 increment, for the 4 cores presented in section 2.4 (Figure 1). For SU90-08, we compared these six ^{230}Th-normalized flux records with the ^{230}Th-normalized flux record obtained using a $(U/Th)_{det}$ value that varied with time as derived from leaching residue ($^{238}U/^{232}Th$) measurements (Figure 2b).

In order to calculate realistic uncertainties on the ^{230}Th-normalized flux and Pa/Th accounting for all sources of uncertainties, we performed Monte Carlo simulations (see supporting information text S2). In the two following sections, we assess whether changes in $(U/Th)_{det}$ can bias ^{230}Th-normalized fluxes or Pa/Th by comparing the uncertainty on ^{230}Th-normalized flux or Pa/Th ratio computed using Monte Carlo simulations with the range of variations in ^{230}Th-normalized flux or Pa/Th obtained using the two extreme $(U/Th)_{det}$ values of 0.3 and 0.8.

4.2.1. Assessing the Impact of $(U/Th)_{Det}$ Variations on ^{230}Th-Normalized Fluxes

We have identified three types of responses of the ^{230}Th-normalized flux to changes in $(U/Th)_{det}$ (Figure 4). Some cores are marginally affected, as exemplified by core MD95-2037 near the Azores, where an increase of $(U/Th)_{det}$ from 0.3 to 0.8 leads to a minor 6.6% increase of the ^{230}Th-normalized flux (median value) over the length of the record. The second type of behavior corresponds to cores for which the ^{230}Th-normalized flux is significantly affected by $(U/Th)_{det}$ changes only during specific time periods as illustrated by core SU90-08, near the Mid-Atlantic Ridge, where the ^{230}Th-normalized flux is mainly affected during Heinrich events. The major part of the downcore record displays a limited 18.1% (median of all values) increase in ^{230}Th-normalized flux when applying an increase in $(U/Th)_{det}$ from 0.3 to 0.8. In contrast, within Heinrich layers, the ^{230}Th-normalized flux is, on average, multiplied by almost 3. Finally, the ^{230}Th-normalized flux record can be significantly affected by $(U/Th)_{det}$ changes along the entire core as exemplified by the two Iberian margin cores, SU81-18 and MD95-2039. In these cores, the ^{230}Th-normalized flux record is homogeneously affected, with a median increase in the ^{230}Th-normalized flux of 65% and 61% for SU81-18 and MD95-2039, respectively, in response to an increase from 0.3 to 0.8 in $(U/Th)_{det}$.

The standard deviation (2σ) for the ^{230}Th-normalized flux calculated following the Monte Carlo simulation varies between the cores. For the Iberian margin cores, the average relative error ranges from 12.2% (SU81-18) to 14.4% (MD95-2039). For the Mid-Atlantic Ridge cores, it is ~3% for MD95-2037 and 4.3% for SU90-08, but it becomes much larger (19% on average) in Heinrich layers for the latter. For Mid-Atlantic Ridge core MD95-2037, the small change in ^{230}Th-normalized flux in response to an increase in $(U/Th)_{det}$ from 0.3 to 0.8 (6%) corresponds to only twice the Monte Carlo error. Therefore, in cases similar to MD95-2037, a poorly

Geochemistry, Geophysics, Geosystems 10.1029/2017GC007410

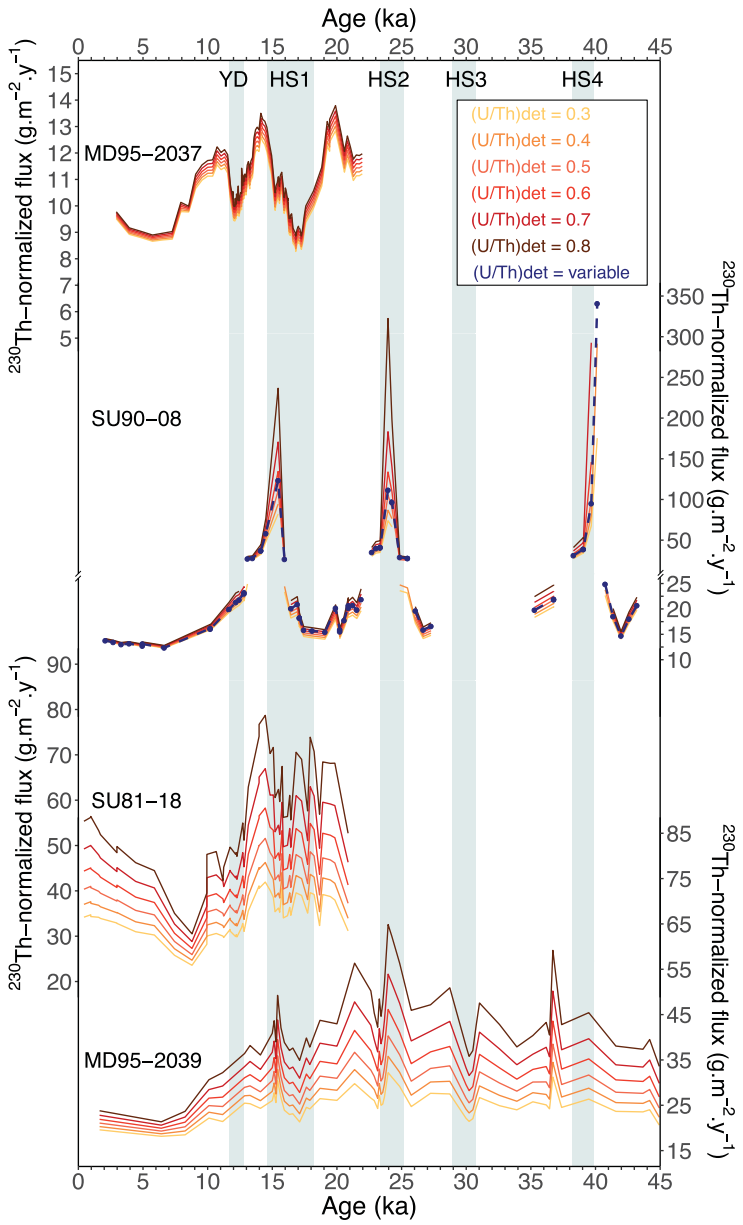

Figure 4. Sensitivity of ^{230}Th-normalized flux to $(U/Th)_{det}$ variations. The variable $(U/Th)_{det}$ corresponds to the $(U/Th)_{det}$ time series presented in Figure 2. Grey bands delineate the YD and Heinrich stadials chronozones. For SU90-08 we note that in HS4, there are missing ^{230}Th-normalized flux values for $(U/Th)_{det} = 0.7$ and 0.8. For these data points, the calculation with high $(U/Th)_{det}$ values gives computed detrital fractions above 100%. As this is physically impossible, these data points were removed (see supporting information Figure S6).

constrained $(U/Th)_{det}$ value does not enlarge too much the error on the ^{230}Th-normalized flux, the uncertainty being kept below 10%. In contrast, for Iberian margin cores (SU81-18, MD95-2039), an increase in $(U/Th)_{det}$ from 0.3 to 0.8 leads to a ~60% increase in ^{230}Th-normalized flux. This change largely exceeds the Monte Carlo error on the ^{230}Th-normalized flux (~14%). The same conclusion is valid for SU90-08, especially in Heinrich layers where the ^{230}Th-normalized flux can be multiplied by 2–3 in response to an increase from 0.3 to 0.8 in the $(U/Th)_{det}$. Thus, in SU90-08, knowing the $(U/Th)_{det}$ is necessary to correctly evaluate the increase in ^{230}Th-normalized flux during the Heinrich events (Figure 4).

Geochemistry, Geophysics, Geosystems 10.1029/2017GC007410

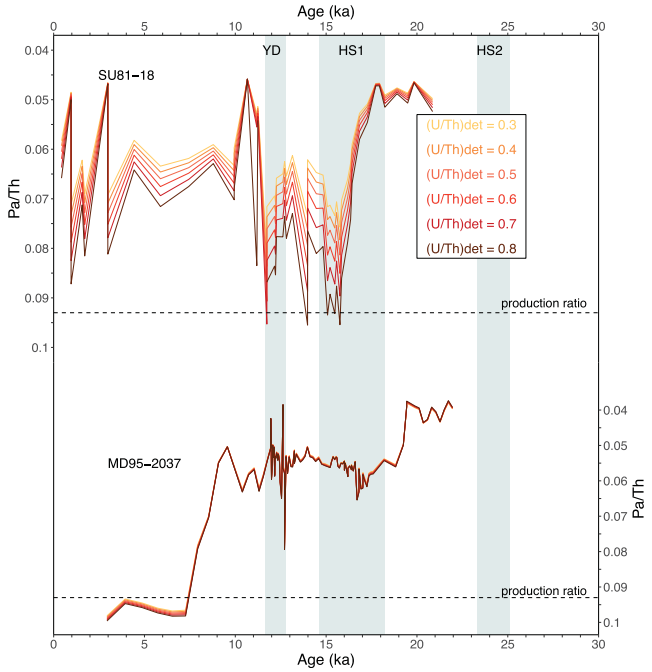

Figure 5. Sensitivity of Pa/Th to $(U/Th)_{det}$ variations. $(U/Th)_{det}$ values and grey bands as in Figure 4.

In the cases where the $(U/Th)_{det}$ is not well constrained, the consequences of the choice of a $(U/Th)_{det}$ value must be carefully examined. For example, assuming that the $(U/Th)_{det}$ variability in Iberian Margin cores is comparable to that observed in SU90-08, the ^{230}Th-normalized flux would decrease from roughly 65 to 45 g m^{-2} yr^{-1} for SU81-18, and from 45 to 30 g m^{-2} yr^{-1} for MD95-2039, from 17 to 10 ka. In both cases, it would correspond to a 30% decrease in ^{230}Th-normalized flux, with potential consequences on all the quantities derived from the ^{230}Th-normalized flux value, such as mass accumulation or sedimentation rates.

4.2.2. Assessing the Impact of $(U/Th)_{det}$ Variations on Pa/Th

For Pa/Th, we also observe different responses to changes in $(U/Th)_{det}$ (Figure 5). Mid-Atlantic Ridge core MD95-2037 shows almost no Pa/Th variations—on average 1%—for a $(U/Th)_{det}$ varying between 0.3 and 0.8. The latter Pa/Th variation is lower than the uncertainty calculated by Monte Carlo ($2\sigma = 6.5\%$). Iberian Margin core SU81-18 shows an overall greater sensitivity to $(U/Th)_{det}$ changes with an average Pa/Th variation of 15.5% for a 0.3–0.8 increase in $(U/Th)_{det}$. However, while some parts of the record, such as the LGM, only display minor (3.4%) variations, other sections, such as the Heinrich Stadial 1 (HS1), vary by up to 25%. The uncertainty on Pa/Th, calculated by Monte Carlo simulations is about 14% on average for core SU81-18. Thus, the change in Pa/Th due to variations in $(U/Th)_{det}$ is about twice as big as the uncertainty on Pa/Th for this core. Consequently, an improper estimation of the $(U/Th)_{det}$ value could lead to a misevaluation of the Pa/Th increase during HS1, interpreted as circulation slowdown (Gherardi et al., 2009). For example, assuming a constant $(U/Th)_{det}$ value of 0.7 (i.e., SU90-08 glacial value), Pa/Th would vary from 0.05 at the LGM to 0.085 during the Holocene, whereas assuming a $(U/Th)_{det}$ of 0.4 (i.e., SU90-08 Holocene value), Pa/Th would vary from 0.05 to 0.075 over the same interval. More importantly, a change of the $(U/Th)_{det}$ value through time could actually result in a bigger amplitude of the Pa/Th change or, conversely, could damp or erase the temporal variability of the Pa/Th signal obtained using a constant $(U/Th)_{det}$ value. For instance, a shift of $(U/Th)_{det}$ from 0.4 to 0.8 at the end of HS1 in Iberian Margin core SU81-18 would erase the increase in overturning rate at the end of HS1 that is derived from Pa/Th measurements when assuming a constant $(U/Th)_{det}$ value.

Interestingly, for both cores, Pa/Th is less affected than the ^{230}Th-normalized flux. Indeed, in core MD95-2037, Pa/Th is virtually not affected by changes in the $(U/Th)_{det}$ value. In SU81-18, the Pa/Th record is little affected over some time periods, such as the LGM or the late Holocene, while much larger Pa/Th variations (0.02–0.03) are calculated over other time periods, such as 16–11 ka (Figure 5). In contrast, the ^{230}Th-normalized flux record in SU81-18 is affected by $(U/Th)_{det}$ variations to a similar extent over its entire length. The lower sensitivity of Pa/Th compared to the ^{230}Th-normalized flux can be explained by the fact that the detrital correction affects both the Pa_{xs} and Th_{xs} calculations and thus partially cancels out in the Pa/Th calculation despite the different corrections applied for the two isotopes (see equations (2) and (3)).

4.3. Controls on $^{230}Th_{xs}$ and $^{231}Pa_{xs}$ Sensitivity to $(U/Th)_{Det}$

We have shown that the ^{230}Th-normalized flux and Pa/Th records do not exhibit the same sensitivity to changes in $(U/Th)_{det}$ in different cores. Here we discuss the impact of the core location (water depth, coastal area versus open ocean) and nature of the terrigenous supply (e.g., IRD contribution, river inputs, etc.) on this sensitivity.

^{230}Th-normalized flux and Pa/Th are calculated using excess ^{231}Pa and ^{230}Th, i.e., the ^{231}Pa and ^{230}Th produced in the water column and scavenged to the sediment. Consequently, one should expect the deeper cores to have a larger proportion of $^{231}Pa_{xs}$ and $^{230}Th_{xs}$ for a given detrital contribution because the water column is thicker; hence, more excess is produced. Among the studied cores, MD95-2037 is the least sensitive to the changes in $(U/Th)_{det}$ value although it is the shallowest (2,150 m). Thus, the water depth itself

Geochemistry, Geophysics, Geosystems 10.1029/2017GC007410

does not seem to be the dominating factor controlling the ^{230}Th-normalized flux and Pa/Th sensitivity to $(U/Th)_{det}$ at the studied locations.

MD95-2037 is the core the most remote from terrigenous inputs. This is confirmed by the relatively high (^{230}Th) activity compared to (^{232}Th) activity. Indeed, it is located very far from the coasts and is consequently not significantly affected by riverine input (Figure 1). It is also too far south to receive notable IRD inputs. This is illustrated by the fact that for a given $(U/Th)_{det}$, the total calculated detrital contribution, X_{det} (equation (1)), does not exceed 10% of the measured (^{230}Th) or (^{231}Pa) signals (Figure 6). For MD95-2037, the dominant fraction is the excess fraction (Figure 6), which explains the low sensitivity of the data to the value of $(U/Th)_{det}$.

Core SU90-08 is also located far from the coasts and thus receives negligible riverine inputs. However, this core is located within the Ruddiman belt, so that its detrital content is highly influenced by IRD deposits during Heinrich events. The calculated detrital contribution for (^{230}Th) varies between 15% and 18% of the measured signal outside of the Heinrich layers but reaches 45%, 55%, and 90% during HS1, HS2, and HS4, respectively (Figure 6). Overall, in Heinrich layers, because of the significant increase of the detrital content, the excess fraction is greatly reduced and consequently, the detrital correction becomes very important. Therefore, it is critical to evaluate the $(U/Th)_{det}$ value in Heinrich layers to assess the correct detrital correction. Moreover, in the detrital-rich levels, the uncertainty on $^{230}Th_{xs}$ or $^{231}Pa_{xs}$ increases because the detrital and authigenic corrections are larger (equations (2) and (3)). In some cases, the uncertainties on $^{230}Th_{xs}$ or $^{231}Pa_{xs}$ calculations can be very large such as at 203 cm, where the calculated 2σ uncertainty on the ^{230}Th-normalized flux reached 42% (supporting information Figure S5). This data point is very uncertain but consistent with the rest of the record and should be considered with particular care in subsequent paleoceanographic interpretations.

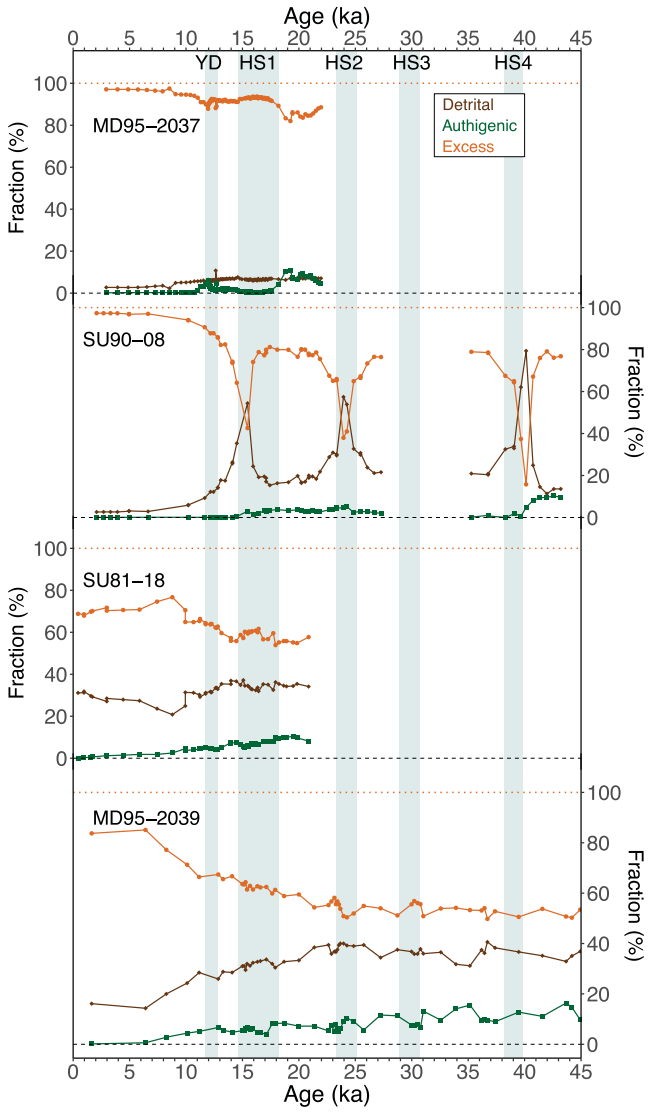

Figure 6. Computed detrital, authigenic, and excess fractions (%) for the studied cores. The fractions are computed based on equation (2). The results shown here are obtained for $(U/Th)_{det} = 0.5$ for MD95-2037, MD95-2039, and SU81-18. For SU90-08, we used $(U/Th)_{det}$ values based on our measurements as shown in Figure 2. The grey bands are as in Figures 4 and 5.

Finally, Iberian margin cores SU81-18 and MD95-2039 likely receive significant riverine or even Saharan dust inputs, as shown by average detrital contribution of 30% and 35% for SU81-18 and MD95-2039, respectively (Figure 6). In these two cores, the detrital contribution seems to have been roughly constant throughout the entire records as highlighted by a roughly constant (^{230}Th/^{232}Th) of about 1.5 downcore. This might not always be the case for all coastal records and we strongly recommend to evaluate the effect of potential detrital inputs temporal variations in coastal cores or cores strongly influenced by mineral aerosols inputs.

5. Conclusions

We have examined the influence of the sediment detrital fraction (^{238}U/^{232}Th) activity ratio, $(U/Th)_{det}$, on the calculation of two proxies that are widely used for the reconstruction of past oceanic sedimentation (^{230}Th-normalized flux) and circulation (Pa/Th) changes. We have shown that the $(U/Th)_{det}$ value varied between 0.4 and 0.7 in North Atlantic core SU90-08 over the last 40 ky. The largest measured $(U/Th)_{det}$ change was observed across the deglaciation, with values ranging from 0.7 at the LGM, to 0.4 during the Holocene. Therefore, considering a chosen constant $(U/Th)_{det}$ value associated with a ± 0.1 uncertainty (2σ), as commonly done in Pa/Th and ^{230}Th-normalized studies, cannot account for the variability observed in SU90-08.

The sensitivity of $^{230}Th_{xs}$ and $^{231}Pa_{xs}$ to changes in $(U/Th)_{det}$ was tested for core SU90-08 and three additional cores from the North

Geochemistry, Geophysics, Geosystems 10.1029/2017GC007410

Atlantic. We find that both ^{230}Th-normalized flux and Pa/Th can be sensitive to changes in $(U/Th)_{det}$ for some core locations and that this sensitivity is highly dependent on the terrigenous inputs in the considered area. For cores located in the open ocean, far from riverine inputs, and away from the influence of iceberg discharges, the terrigenous fraction represents a small proportion of the sediments, thus changes in the estimate of the $(U/Th)_{det}$ have little impact on $^{230}Th_{xs}$ and $^{231}Pa_{xs.}$ For shallow cores located close continental margins or affected by ice rafting, the detrital fraction may represent 30–90% of the signal, thus the ^{230}Th-normalized flux and Pa/Th records are much more affected by changes in the $(U/Th)_{det}$ value. For those cores, the changes in ^{230}Th-normalized flux due to the choice of a constant $(U/Th)_{det}$ value can largely exceed the uncertainty on the ^{230}Th-normalized flux. For some specific time periods, the same conclusion applies for Pa/Th. Our study shows that in some cases, misestimating $(U/Th)_{det}$ can lead to a misinterpretation of the amplitude of sediment fluxes or circulation changes. In other cases, if the temporal variations of $(U/Th)_{det}$ are not taken into account, the temporal variability of sediment fluxes or circulation changes may not be correctly reconstructed. In both cases, misevaluating $(U/Th)_{det}$ can be critical when comparing different cores and reconstructing regional or basin-scale changes in ocean circulation.

In conclusion, when using $^{231}Pa_{xs}$ and/or $^{230}Th_{xs}$ it is recommended to (i) assess the relative proportion of the detrital contribution at the studied locations, (ii) consider potential temporal variations of the $(U/Th)_{det}$, especially when the choice of this value has large effects on $^{230}Th_{xs}$ or $^{231}Pa_{xs}$, (iii) use uncertainties for $(U/Th)_{det}$ not lower than the $(U/Th)_{det}$ measurement external reproducibility, and (iv) evaluate the error on $^{231}Pa_{xs}$ and $^{230}Th_{xs}$ accounting for the uncertainty on the $(U/Th)_{det}$ value at the studied location. Future work is necessary to measure $(U/Th)_{det}$ in cores from different regions and evaluate the impact of $(U/Th)_{det}$ on Pa/Th and ^{230}Th-normalized flux records obtained in these different regions. It would also be of great interest to explore the potential of monitoring $(U/Th)_{det}$ temporal variations using routine measurements such as mineral characterization, major, and/or trace elements analysis.

Data availability

The data are given as Tables S1–S6 in the supporting information and are available online on Pangaea database (https://doi.pangaea.de/10.1594/PANGAEA.889695).

Competing interests

The authors declare that they have no conflict of interests.

References

Andersen, K. K., Svensson, A., Johnsen, S. J., Rasmussen, S. O., Bigler, M., Röthlisberger, R., et al. (2006). The Greenland ice core chronology 2005, 15–42 ka. Part 1: Constructing the time scale. *Quaternary Science Reviews*, *25*(2324), 3246–3257.

Anderson, R. F., Bacon, M. P., & Brewer, P. G. (1983). Removal of ^{230}Th and ^{231}Pa at ocean margins. *Earth and Planetary Science Letters*, *66*, 73–90.

Andrews, J., & Tedesco, K. (1992). Detrital carbonate-rich sediments, northwestern Labrador Sea: Implications for ice-sheet dynamics and iceberg rafting (Heinrich) events in the North Atlantic. *Geology*, *20*(12), 1087–1090.

Bacon, M. P., & Anderson, R. F. (1982). Distribution of thorium isotopes between dissolved and particulate forms in the deep sea. *Journal of Geophysical Research*, *87*(C3), 2045–2056. https://doi.org/10.1029/JC087iC03p02045

Böhm, E., Lippold, J., Gutjahr, M., Frank, M., Blaser, P., Antz, B., et al. (2015). Strong and deep Atlantic meridional overturning circulation during the last glacial cycle. *Nature*, *517*(7532), 73–76.

Bond, G., Broecker, W., Johnsen, S., McManus, J., Labeyrie, L., Jouzel, J., et al. (1993). Correlations between climate records from North Atlantic sediments and Greenland ice. *Nature*, *365*(6442), 143–147.

Bondevik, S., Mangerud, J., Birks, H. H., Gulliksen, S., & Reimer, P. (2006). Changes in North Atlantic radiocarbon reservoir ages during the Allerød and Younger Dryas. *Science*, *312*(5779), 1514–1517.

Bourdon, B., Turner, S., Henderson, G. M., & Lundstrom, C. C. (2003). Introduction to U-series geochemistry. *Reviews in Mineralogy and Geochemistry*, *52*(1), 1–21. https://doi.org/10.2113/0520001

Bourne, M. D., Thomas, A. L., Mac Niocaill, C., & Henderson, G. M. (2012). Improved determination of marine sedimentation rates using. *Geochemistry, Geophysics, Geosystems*, *13*, Q09017. https://doi.org/10.1029/2012GC004295

Bout-Roumazeilles, V., Cortijo, E., Labeyrie, L., & Debrabant, P. (1999). Clay mineral evidence of nepheloid layer contributions to the Heinrich layers in the northwest Atlantic. *Palaeogeography, Palaeoclimatology, Palaeoecology*, *146*(1–4), 211–228.

Burckel, P., Waelbroeck, C., Gherardi, J. M., Pichat, S., Arz, H., Lippold, J., et al. (2015). Atlantic Ocean circulation changes preceded millennial tropical South America rainfall events during the last glacial. *Geophysical Research Letters*, *42*, 411–418. https://doi.org/10.1002/2014GL062512

Burckel, P., Waelbroeck, C., Luo, Y., Roche, D. M., Pichat, S., Jaccard, S. L., et al. (2016). Changes in the geometry and strength of the Atlantic meridional overturning circulation during the last glacial (20–50 ka). *Climate of the Past*, *12*(11), 2061.

Acknowledgments

This is a contribution to ERC project ACCLIMATE; the research leading to these results has received funding from the European Research Council under the European Union's Seventh Framework Programme (FP7/2007–2013)/ERC grant agreement 339108. The authors thank J. Duprat for planktonic foraminifer census counts; M. Roy-Barman for expert advice on radioisotope measurements on LSCE MC-ICP-MS; and S. Moreira for his help with R programming. S. Pichat was supported by a research sabbatical (CRCT) from the ENS de Lyon. S. Pichat is thankful to S.J.G. Galer for allowing him to use the Max Planck Institute Q-ICP-MS and to K.P. Jochum for his help with standard reference material. This is LSCE contribution 6412.

Geochemistry, Geophysics, Geosystems 10.1029/2017GC007410

Clement, A. C., & Peterson, L. C. (2008). Mechanisms of abrupt climate change of the last glacial period. *Reviews of Geophysics*, *46*, RG4002. https://doi.org/10.1029/2006RG000204

Cortijo, E., Labeyrie, L., Vidal, L., Vautravers, M., Chapman, M., Duplessy, J.-C., et al. (1997). Changes in sea surface hydrology associated with Heinrich event 4 in the North Atlantic Ocean between 40 and 60 N. *Earth and Planetary Science Letters*, *146*(1–2), 29–45.

Douville, E., Sallé, E., Frank, N., Eisele, M., Pons-Branchu, E., & Ayrault, S. (2010). Rapid and accurate U-Th dating of ancient carbonates using inductively coupled plasma-quadrupole mass spectrometry. *Chemical Geology*, *272*(1–4), 1–11. https://doi.org/10.1016/j.chemgeo.2010.01.007

Fahrni, S., Wacker, L., Synal, H.-A., & Szidat, S. (2013). Improving a gas ion source for ^{14}C AMS. *Nuclear Instruments and Methods in Physics Research Section B*, *294*, 320–327.

François, R., Bacon, M. P., Altabet, M. A., & Labeyrie, L. D. (1993). Glacial/interglacial changes in sediment rain rate in the SW Indian sector of subantarctic waters as recorded by ^{230}Th, ^{231}Pa, U, and $\delta^{15}N$. *Paleoceanography*, *8*(5), 611–629. https://doi.org/10.1029/93PA00784

François, R., Frank, M., Rutgers van der Loeff, M. M., & Bacon, M. P. (2004). ^{230}Th normalization: An essential tool for interpreting sedimentary fluxes during the late Quaternary. *Paleoceanography*, *19*, PA1018. https://doi.org/10.1029/2003PA000939

Gherardi, J. M., Labeyrie, L., McManus, J. F., Francois, R., Skinner, L. C., & Cortijo, E. (2005). Evidence from the Northeastern Atlantic basin for variability in the rate of the meridional overturning circulation through the last deglaciation. *Earth and Planetary Science Letters*, *240*(3–4), 710–723. https://doi.org/10.1016/j.epsl.2005.09.061

Gherardi, J. M., Labeyrie, L., Nave, S., Francois, R., McManus, J. F., & Cortijo, E. (2009). Glacial-interglacial circulation changes inferred from $^{231}Pa/^{230}Th$ sedimentary record in the North Atlantic region. *Paleoceanography*, *24*, PA2204. https://doi.org/10.1029/2008PA001696

Guihou, A., Pichat, S., Nave, S., Govin, A., Labeyrie, L., Michel, E., et al. (2010). Late slowdown of the Atlantic Meridional Overturning Circulation during the last glacial inception: New constraints from sedimentary ($^{231}Pa/^{230}Th$). *Earth and Planetary Science Letters*, *289*(3–4), 520–529.

Hemming, S. R. (2004). Heinrich events: Massive late Pleistocene detritus layers of the North Atlantic and their global climate imprint. *Reviews of Geophysics*, *42*, RG1005. https://doi.org/10.1029/2003RG000128

Henderson, G. M., & Anderson, R. F. (2003). The U-series toolbox for paleoceanography. *Reviews in Mineralogy and Geochemistry*, *52*(1), 493–531. https://doi.org/10.2113/0520493

Jennings, A., Andrews, J., Pearce, C., Wilson, L., & Ólfasdótttir, S. (2015). Detrital carbonate peaks on the Labrador shelf, a 13–7 ka template for freshwater forcing from the Hudson Strait outlet of the Laurentide Ice Sheet into the subpolar gyre. *Quaternary Science Reviews*, *107*(Suppl. C), 62–80. https://doi.org/10.1016/j.quascirev.2014.10.022

Kane, J. S. (2004). Report of the International Association of Geoanalysts on the Certification of Penrhyn Slate, OU-6. *Geostandards and Geoanalytical Research*, *28*(1), 53–80.

Kumar, N., Anderson, R. F., Mortlock, R. A., Froelich, P. N., Kubik, P., Dittrich-Hannen, B., et al. (1995). Increased biological productivity and export production in the glacial Southern Ocean. *Nature*, *378*(6558), 675.

Lippold, J., Gutjahr, M., Blaser, P., Christner, E., de Carvalho Ferreira, M. L., Mulitza, S., et al. (2016). Deep water provenance and dynamics of the (de)glacial Atlantic meridional overturning circulation. *Earth and Planetary Science Letters*, *445*, 68–78. https://doi.org/10.1016/j.epsl.2016.04.013

McManus, J. F., Francois, R., Gherardi, J.-M., Keigwin, L. D., & Brown-Leger, S. (2004). Collapse and rapid resumption of Atlantic meridional circulation linked to deglacial climate changes. *Nature*, *428*(6985), 834–837.

Mulitza, S., Chiessi, C., Schefuß, M., Lippold, E., Wichmann, J., Antz, D., et al. (2017). Synchronous and proportional deglacial changes in Atlantic Meridional Overturning and northeast Brazilian precipitation. *Paleoceanography*, *32*, 622–633. https://doi.org/10.1002/2017PA003084

Peterson, L. C., Haug, G. H., Hughen, K. A., & Röhl, U. (2000). Rapid changes in the hydrologic cycle of the tropical Atlantic during the last glacial. *Science*, *290*(5498), 1947–1951.

Pichat, S., Abouchami, W., & Galer, S. J. (2014). Lead isotopes in the Eastern Equatorial Pacific record Quaternary migration of the South Westerlies. *Earth and Planetary Science Letters*, *388*, 293–305.

Pichat, S., Sims, K. W., François, R., McManus, J. F., Brown Leger, S., & Albarède, F. (2004). Lower export production during glacial periods in the equatorial Pacific derived from $(^{231}Pa/^{230}Th)_{xs,\ 0}$ measurements in deep-sea sediments. *Paleoceanography*, *19*, PA4023. https://doi.org/10.1029/2003PA000994

Ramsey, C. B. (2009). Bayesian analysis of radiocarbon dates. *Radiocarbon*, *51*(1), 337–360.

Rasmussen, S. O., Andersen, K. K., Svensson, A., Steffensen, J. P., Vinther, B. M., Clausen, H. B., et al. (2006). A new Greenland ice core chronology for the last glacial termination. *Journal of Geophysical Research*, *111*, D06102. https://doi.org/10.1029/2005JD006079

Reimer, P. J., Bard, E., Bayliss, A., Beck, J. W., Blackwell, P. G., Ramsey, C. B., et al. (2013). IntCal13 and Marine13 radiocarbon age calibration curves 0–50,000 years cal BP. *Radiocarbon*, *55*(4), 1869–1887.

Robinson, L. F., Henderson, G. M., Hall, L., & Matthews, I. (2004). Climatic control of riverine and seawater uranium-isotope ratios. *Science*, *305*(5685), 851–854. https://doi.org/10.1126/science.1099673

Svensson, A., Andersen, K. K., Bigler, M., Clausen, H. B., Dahl-Jensen, D., Davies, S. M., et al. (2006). The Greenland ice core chronology 2005, 15–42 ka. Part 2: Comparison to other records. *Quaternary Science Reviews*, *25*(23–24), 3258–3267.

Therón, R., Paillard, D., Cortijo, E., Flores, J.-A., Vaquero, M., Sierro, F. J., et al. (2004). Rapid reconstruction of paleoenvironmental features using a new multiplatform program. *Micropaleontology*, *50*(4), 391–395.

Thomson, J., Nixon, S., Summerhayes, C. P., Schönfeld, J., Zahn, R., & Grootes, P. (1999). Implications for sedimentation changes on the Iberian margin over the last two glacial/interglacial transitions from $(^{230}Th_{excess})_0$ systematics. *Earth and Planetary Science Letters*, *165*(3–4), 255–270. https://doi.org/10.1016/S0012-821X(98)00265-9

Veiga-Pires, C. C., & Hillaire-Marcel, C. (1999). U and Th isotope constraints on the duration of Heinrich events H0-H4 in the southeastern Labrador Sea. *Paleoceanography*, *14*(2), 187–199. https://doi.org/10.1029/1998PA900003

Vidal, L., Labeyrie, L., Cortijo, E., Arnold, M., Duplessy, J., Michel, E., et al. (1997). Evidence for changes in the North Atlantic Deep Water linked to meltwater surges during the Heinrich events. *Earth and Planetary Science Letters*, *146*(1–2), 13–27.

Vinther, B. M., Clausen, H. B., Johnsen, S. J., Rasmussen, S. O., Andersen, K. K., Buchardt, S. L., et al. (2006). A synchronized dating of three Greenland ice cores throughout the Holocene. *Journal of Geophysical Research*, *111*, D13102. https://doi.org/10.1029/2005JD006921

Voelker, A. H. (2002). Global distribution of centennial-scale records for Marine Isotope Stage (MIS) 3: A database. *Quaternary Science Reviews*, *21*(10), 1185–1212.

Wacker, L., Fahrni, S., Hajdas, I., Molnar, M., Synal, H.-A., Szidat, S., et al. (2013). A versatile gas interface for routine radiocarbon analysis with a gas ion source. *Nuclear Instruments and Methods in Physics Research Section B*, *294*, 315–319.

Geochemistry, Geophysics, Geosystems 10.1029/2017GC007410

Waelbroeck, C., Duplessy, J.-C., Michel, E., Labeyrie, L., Paillard, D., & Duprat, J. (2001). The timing of the last deglaciation in North Atlantic climate records. *Nature*, *413*(6855), 548.

Waelbroeck, C., Labeyrie, L., Duplessy, J. C., Guiot, J., Labracherie, M., Leclaire, H., et al. (1998). Improving past sea surface temperature estimates based on planktonic fossil faunas. *Paleoceanography*, *13*(3), 272–283. https://doi.org/10.1029/98PA00071

Walter, H., Van der Loeff, M. R., & Hoeltzen, H. (1997). Enhanced scavenging of ^{231}Pa relative to ^{230}Th in the South Atlantic south of the Polar Front: Implications for the use of the $^{231}Pa/^{230}Th$ ratio as a paleoproductivity proxy. *Earth and Planetary Science Letters*, *149*(1–4), 85–100.

Winckler, G., Anderson, R. F., Jaccard, S. L., & Marcantonio, F. (2016). Ocean dynamics, not dust, have controlled equatorial Pacific productivity over the past 500,000 years. *Proceedings of the National Academy of Sciences of the United States of America*, *113*(22), 6119–6124. https://doi.org/10.1073/pnas.1600616113

Yu, E.-F., Francois, R., & Bacon, M. P. (1996). Similar rates of modern and last-glacial ocean thermohaline circulation inferred. *Nature*, *379*(6567), 689–694.

Geochemistry, Geophysics, Geosystems

Supporting Information for

Downcore variations of sedimentary detrital ($^{238}U/^{232}Th$) ratio: implications on the use of $^{230}Th_{xs}$ and $^{231}Pa_{xs}$ to reconstruct sediment flux and ocean circulation

Lise Missiaen[1,*], Sylvain Pichat[2,1,3] Claire Waelbroeck[1], Eric Douville[1], Louise Bordier[1], Arnaud. Dapoigny[1], François. Thil[1], Lorna. Foliot[1], Lukas. Wacker[4]

[1] Laboratoire des Sciences du Climat et de l'Environnement, LSCE/IPSL, CEA-CNRS-UVSQ-Université Paris-Saclay, F-91198 Gif-sur-Yvette, France

[2] Université de Lyon, ENS de Lyon, Laboratoire de Géologie de Lyon (LGL-TPE), F-69007 Lyon, France.

[3] Climate Geochemistry Department, Max Planck Institute for Chemistry, Mainz, Germany

[4] Laboratory of Ion Beam Physics, ETH Zürich, 8093 Zürich, Switzerland

Contents of this file

Introduction

This supporting information file contains supplementary text (2 sections), which provide more information about sea surface temperature reconstruction at SU90-08 (text S1) and the evaluation of the uncertainties for the ^{230}Th-normalized flux and Pa/Th using Monte Carlo method (text S2).
It also contains 6 supplementary figures showing variability of ($^{238}U/^{232}Th$) for rock samples taken around the North-Atlantic (Fig S1), tie points and surface records alignments with N-GRIP related to SU90-08 age model (Fig. S2), the SU90-08 levels selected for IRD analysis (Fig. S3), the U, Th concentrations as well as the U/Th ratios obtained in analyzed reference materials (Fig. S4), SU90-08 ^{230}Th-normalized flux and its Monte Carlo uncertainty (Fig S5) and finally the proportion of the computed detrital fraction for different values of $(U/Th)_{det}$ for all the studied cores (Fig.S6).
Finally, this files contains 6 tables which gather SU90-08 data presented in the main text: the age model tie points (Table S1), ^{238}U and ^{232}Th measurements on leaching residues (Table S2), ^{238}U and ^{232}Th measurements on handpicked material (Table S3 to S5) and ^{238}U, ^{232}Th and ^{230}Th activities in bulk sediment (Table S6).

Supplementary text:

S1. SU90-08 sea surface temperature reconstructions from planktonic foraminifer assemblages

High-resolution planktonic foraminifer census counts were produced in splits of the > 150 mm size fraction of core SU90-08, with the total number of specimens counted exceeding 300 in all samples but one, which contained only 171 specimens. Summer sea surface temperature were reconstructed from planktonic foraminifer assemblages, using the PaleoAnalogs program [*Therón et al.*, 2004] and the database containing 615 core tops from the North-Atlantic region described in [*Waelbroeck et al.*, 1998]. Paleo-temperatures were calculated based on the 10 nearest analogs.

S2. Evaluation of the uncertainties for the ^{230}Th-normalized flux and Pa/Th using Monte Carlo simulation.

The Monte Carlo method consists in repeating the ^{230}Th-normalized flux and Pa/Th calculations a large number of times – in the present case, 2000 – to compute mean values and uncertainties around the latter arising from all sources of uncertainties. For each calculation, the program takes a random value of the following parameters: $(^{234}U/^{238}U)_{sw}$ ($1\sigma = 0.0025$), ^{238}U, ^{232}Th, ^{230}Th, ^{231}Pa activities, age and $(U/Th)_{det}$ following a Gaussian probability distribution and its associated standard deviation (1σ). Tests have been performed to ensure that the number of draws used (n=2000) was sufficient to produce satisfactory Gaussian distributions for each of the above-cited parameters. In our computations, we defined the uncertainty on $(U/Th)_{det}$ as follows: for SU90-08, the $(U/Th)_{det}$ uncertainty was defined to be equal to the external measurement reproducibility, *i.e.* 10 % (2σ) (Fig 2). For the other cores, we assume $(U/Th)_{det} = 0.5 \pm 0.1$ (2σ), *i.e.* 20% (2σ), as commonly done in the literature. The Monte Carlo uncertainty calculated for the ^{230}Th-normalized flux or Pa/Th is thus the standard deviation (2σ) of the 2000 ^{230}Th-normalized flux or Pa/Th calculated at each depth (see for instance Fig. S4).

The following R-script was developed to perform these Monte Carlo simulations and can be used to assess error bars on ^{230}Th-normalized flux and Pa/Th.

R-script

```
------------------------------------------------------------------------------------------------------------------------
------

#-------------------------------------------------------------------------
#Programm description
#-------------------------------------------------------------------------
#This script calculates the Pa/Th value, 230Th flux and lithogenic vs authigenic contributions
# It also provides the corresponding error bars using Monte Carlo simulations.

#Author : Lise Missiaen
#Date : December 2016
#-------------------------------------------------------------------------
# Importing Core data
#-------------------------------------------------------------------------
 z<- 3080 # z is the water depth
#-------------------------------------------------------------------------
# Importing the data
#-------------------------------------------------------------------------
# Here you have to prepare an excel file summarizing the measured activities
# Be careful: in this version the detrital (238U/232Th) activity ratio and its associated error
# that you assume  must be specified in the input file
require(openxlsx)
sample_data<-read.xlsx("../data/sample_data_other.xlsx", 4, colNames=T ,startRow=1)
sample_data <- as.data.frame(sample_data)


#-------------------------------------------------------------------------
# Importing the known constants
#-------------------------------------------------------------------------
#Decay constants in kyr-1
# Note: it is assumed that the error on lambdas are neglectable
# therefore we do not include errors associated with lambdas
lambda_230 <-9.195E-03
lambda_232 <-4.933E-08
lambda_231 <-2.116E-02
lambda_234 <-2.823E-03
lambda_238 <-1.551E-07

#Known activity ratios
R_sw <- 1.1466 # enter here the value for sea water 234U/238U activity ratio
# we consider sd=0.0025, (Robinson et al 2004)
R_nat<-0.04604
# R_nat is a natural isotopic (activity) ratio, it is calculated via decay chains therefore there is
no incertitude on it


# "chemical" constants
Na<- 6.02214086E+23 #in mol-1
```

```
#-------------------------------------------------------------------------------
# Creating dataframes for each sample
#-------------------------------------------------------------------------------
# Each parameter of the Pa/Th calculation will have a column of the dataframe dedicated
# Each dataframe has 2 000 lines corresponding to 2 000 random sampling in the error bar of
each ndependant value

# initialization of an empty list
sample_list <-list()
# set the seed to have reproducible random samplings
set.seed(349875)


# Monte Carlo
# I this part we create a dataframe containing
# all the parameters needed for the subsequent calculations for the 2000 repetitions
for (i in 1:length(sample_data$Sample)){
  sample_list[[i]]<- matrix(nrow = 2000, ncol = 8)



  for (j in 1:2000) {

    sample_list[[i]][j,1] <- sample_data$Depth_cm[i]
    sample_list[[i]][j,2]<-rnorm(1, mean = sample_data$t_mean..ky.[i],
sd=((sample_data$t_max..ky. -sample_data$t_min..ky.)/2))
    sample_list[[i]][j,3]<-rnorm(1, mean = sample_data$A_238_dpm_g[i],
sd=sample_data$Sigma_238[i])
    sample_list[[i]][j,4]<-rnorm(1, mean = sample_data$A_232_dpm_g[i],
sd=sample_data$Sigma_232[i])
    sample_list[[i]][j,5]<-rnorm(1, mean = sample_data$A_230_dpm_g[i],
sd=sample_data$Sigma_230[i])
    sample_list[[i]][j,6]<-rnorm(1, mean = sample_data$A_231_dpm_g[i],
sd=sample_data$Sigma_231[i])
    sample_list[[i]][j,7]<-rnorm(1, mean = sample_data$D_U_Th[i], sd=
sample_data$D_U_Th_sigma[i])
    sample_list[[i]][j,8]<-rnorm(1, mean = R_sw, sd=0.0025)


  }
  sample_list[[i]] <- as.data.frame(sample_list[[i]])
  col_names<-c("Depth_cm", "Age_ky", "A_238_dpm_g", "A_232_dpm_g",
"A_230_dpm_g", "A_231_dpm_g", "D_U_Th", "R_sw")
  names(sample_list[[i]])<-col_names
  sample_list[[i]] <- as.data.frame(sample_list[[i]])
}

#-------------------------------------------------------------------------------
# Pa/Th calculation
```

```
#-------------------------------------------------------------------------

for (i in 1: length(sample_data$Core)){

# calculation of 238U_authigenic If negative, set authigenic U fraction to zero


sample_list[[i]]$authi_238U<- sample_list[[i]]$A_238_dpm_g -
(sample_list[[i]]$A_232_dpm_g*sample_list[[i]]$D_U_Th)



# lithogenic fraction calculation for 230Th and 231Pa
sample_list[[i]]$litho_230<- sample_list[[i]]$A_232_dpm_g*sample_list[[i]]$D_U_Th

sample_list[[i]]$litho_231<-
R_nat*sample_list[[i]]$A_232_dpm_g*sample_list[[i]]$D_U_Th


# Checking that we don't create negative lithogenic and authigenic fraction

for(j in 1:length(sample_list[[i]]$A_238_dpm_g)) {
  if (sample_list[[i]]$authi_238U[j] <= 0) {
    sample_list[[i]]$authi_238U[j]<-0
  }

  if (sample_list[[i]]$litho_230[j] <=0) {
    sample_list[[i]]$litho_230[j] <-0
  }
  if (sample_list[[i]]$litho_231[j] <=0) {
    sample_list[[i]]$litho_231[j] <-0
  }
}

# authigenic fraction calculation

  sample_list[[i]]$authi_230<- (sample_list[[i]]$authi_238U)*((1-exp(-
sample_list[[i]]$Age_ky* lambda_230)) + (lambda_230/(lambda_230-lambda_234))*(exp(-
lambda_234*sample_list[[i]]$Age_ky)-exp(-sample_list[[i]]$Age_ky* lambda_230))*(R_sw-
1))

  sample_list[[i]]$authi_231<- (R_nat*(sample_list[[i]]$authi_238U)*(1-exp(-
lambda_231*sample_list[[i]]$Age_ky)))

# percent lithogenic and authigenic

  sample_list[[i]]$percent_litho_230<-
sample_list[[i]]$litho_230/sample_list[[i]]$A_230_dpm_g*100
```

```
  sample_list[[i]]$percent_litho_231<-
sample_list[[i]]$litho_231/sample_list[[i]]$A_231_dpm_g*100

  sample_list[[i]]$percent_authi_230<-
sample_list[[i]]$authi_230/sample_list[[i]]$A_230_dpm_g*100

  sample_list[[i]]$percent_authi_231<-
sample_list[[i]]$authi_231/sample_list[[i]]$A_231_dpm_g*100

  # Excess fraction calculation

  sample_list[[i]]$xs_231 <- sample_list[[i]]$A_231_dpm_g - sample_list[[i]]$litho_231-
sample_list[[i]]$authi_231

  sample_list[[i]]$xs_230<- sample_list[[i]]$A_230_dpm_g -sample_list[[i]]$litho_230 -
sample_list[[i]]$authi_230


  # Excess fraction, 0 calculation "at the time of sediment deposition"

  sample_list[[i]]$xs_0_230 <- sample_list[[i]]$xs_230 * exp(lambda_230 *
sample_list[[i]]$Age_ky)

  sample_list[[i]]$xs_0_231 <- sample_list[[i]]$xs_231 * exp(lambda_231 *
sample_list[[i]]$Age_ky)

  # Final result : Pa/Th ratio calculation

  sample_list[[i]]$Pa_Th<- sample_list[[i]]$xs_0_231/sample_list[[i]]$xs_0_230


  # 230Th_flux calculation

  sample_list[[i]]$Th_flux <- z * 0.0267 / sample_list[[i]]$xs_0_230

}

#---------------------------------------------------------------------------
# Storing the results
#---------------------------------------------------------------------------

results<-NULL

for (i in 1: length(sample_list)){
  results$Sample[i]<-paste("L", sample_data$Sample[i], sep="_")
  results$Depth_cm[i]<-sample_list[[i]]$Depth_cm[1]
  results$Age_ky[i]<-sample_list[[i]]$Age_ky[1]
  results$Pa_Th_mean[i]<-mean(sample_list[[i]]$Pa_Th)
  results$Pa_Th_min[i]<-min(sample_list[[i]]$Pa_Th)
  results$Pa_Th_max[i]<-max(sample_list[[i]]$Pa_Th)
```

```
  results$Pa_Th_median[i]<-median(sample_list[[i]]$Pa_Th)
  results$Pa_Th_sigma[i]<-sd(sample_list[[i]]$Pa_Th)
  results$Pa_Th_mad[i]<-mad(sample_list[[i]]$Pa_Th)
  results$Th_flux[i]<- mean(sample_list[[i]]$Th_flux)
  results$Th_flux_sigma[i]<-sd(sample_list[[i]]$Th_flux)
  results$th_230_xs_0[i]<-mean(sample_list[[i]]$xs_0_230)
  results$th_230_xs_0_sigma[i]<-sd(sample_list[[i]]$xs_0_230)
  results$processing_date[i]<-date()

}
results<-as.data.frame (results)


#-------------------------------------------------------------------------------
# Exporting the results in excel
#-------------------------------------------------------------------------------

require(openxlsx)
write.xlsx(results, file="Pa_Th_mc_results.xlsx", sheetName= "feuille 1" )



-------------------------------------------------------------------------------------------------------------------
--
```

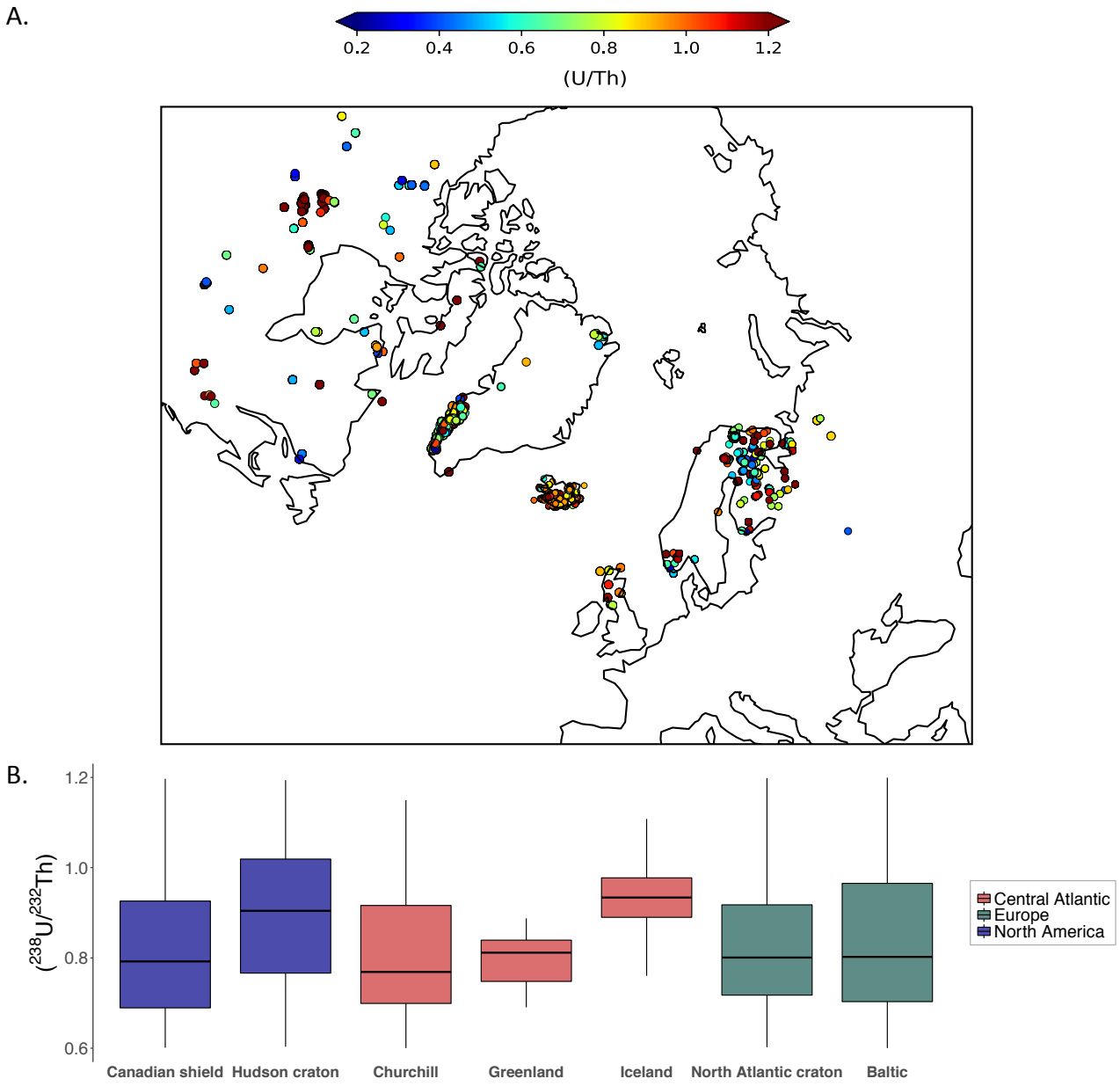

Fig. S1. ($^{238}U/^{232}Th$) variability in rock samples for the North-Atlantic region.
(**A.**) Map of ($^{238}U/^{232}Th$) based on the Georoc database (http://georoc.mpch-mainz.gwdg.de/georoc/) (**B.**) Same dataset as (**A.**) shown as boxplots for various areas around the North Atlantic.
The data supports the high variability of the ($^{238}U/^{232}Th$) in parent materials that form the sediment detrital fraction in North-Atlantic region. Measurements from North_America, Greenland, Iceland and Scandinavia display a median ($^{238}U/^{232}Th$) of 0.89, significantly different from the Atlantic range mentioned in [*Henderson and Anderson*, 2003] (0.6 ± 0.2).

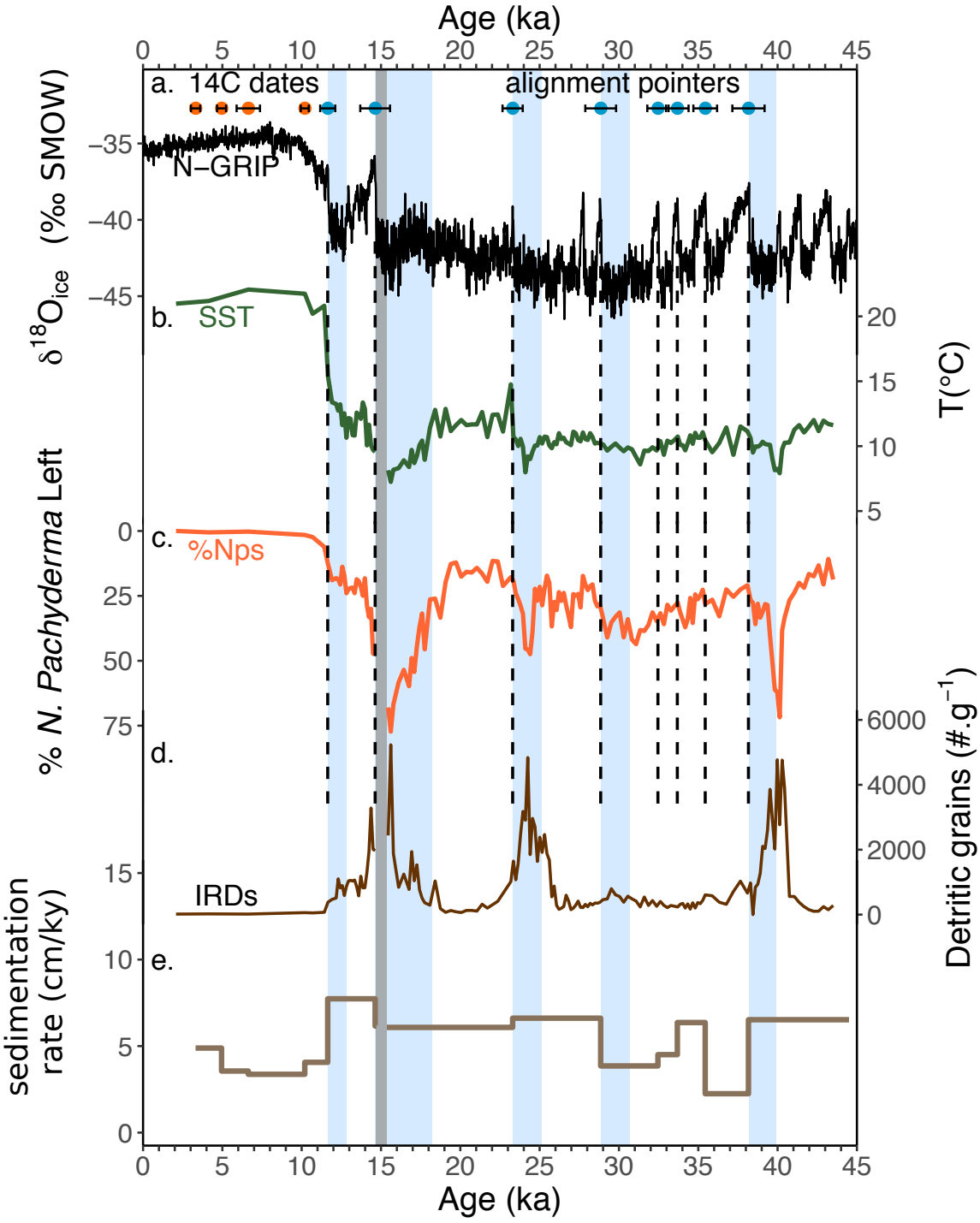

Fig. S2. SU90-08 age model. **a**. North-GRIP $\delta^{18}O$ ice [*Bond et al.*, 1993], [*Andersen et al.*, 2006], [*Rasmussen et al.*, 2006], [*Svensson et al.*, 2006], [*Vinther et al.*, 2006]. **b**. High-resolution summer Sea Surface Temperature (SST) from foraminifera assemblages (this study). **c.** High-resolution percentage of *N.Pachyderma* left (this study). **d**. IRD abundances (grains counted in the fraction > 150 µm per grain of dry sediment, this study) **e**. Sedimentation rate. The grey band corresponds to a sediment perturbation between 65 and 69 cm evidenced by reversals in ^{14}C ages planktonic and benthic $\delta^{18}O$ and $\delta^{13}C$.

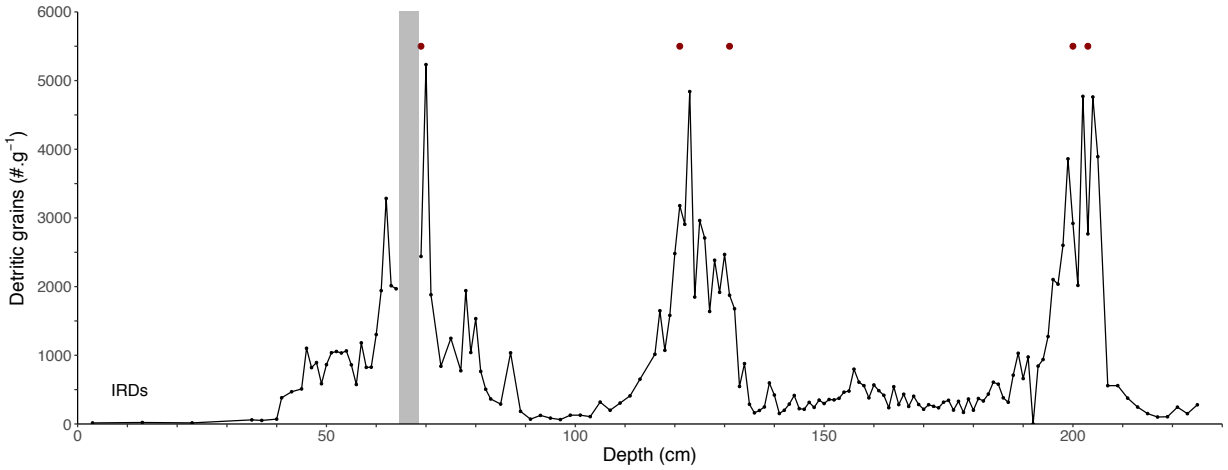

Fig. S3. **Levels selected for handpicked IRDs analyses.** We selected 4 levels in the IRD peaks (69, 121, 200 and 203 cm) and one level on the IRD peak flank (131 cm). Those levels were also analyzed for radioisotope activities. The grey band represents the sedimentary hiatus observed between 65 and 69 cm.

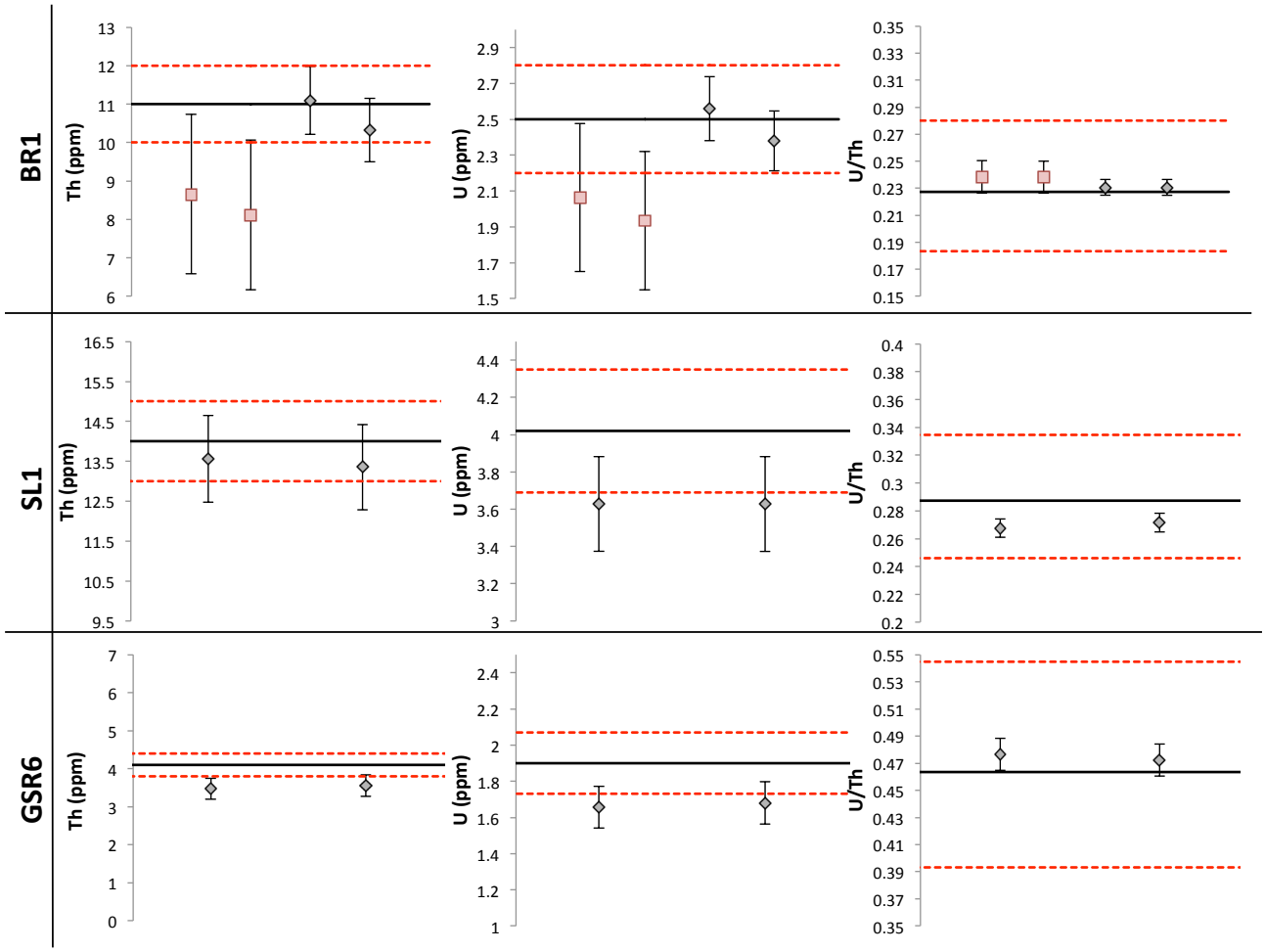

Fig. S4. U and Th concentrations, and U/Th ratios obtained for standard materials
The grey diamonds represent the values (concentration or concentration ratio) obtained for different reference materials (total digestion). In each plot the black line represents the certified value, the dashed red lines the error bars around the certified value. For BR1, the red

squares represent the values (concentration or concentration ratio) obtained for the residues of the leaching procedure. The standard deviation (2σ) obtained on total digestions is 8% for Th concentrations, 7% for U concentrations and 2.5 % for U/Th concentration ratio. The standard deviation obtained for the leaching procedure is 24 % for Th and 20 % for U most likely due to material loss during the leaching procedure (see section 2.2 for details). However it resulted in a much lower standard deviation (6%) for the (U/Th) ratio.

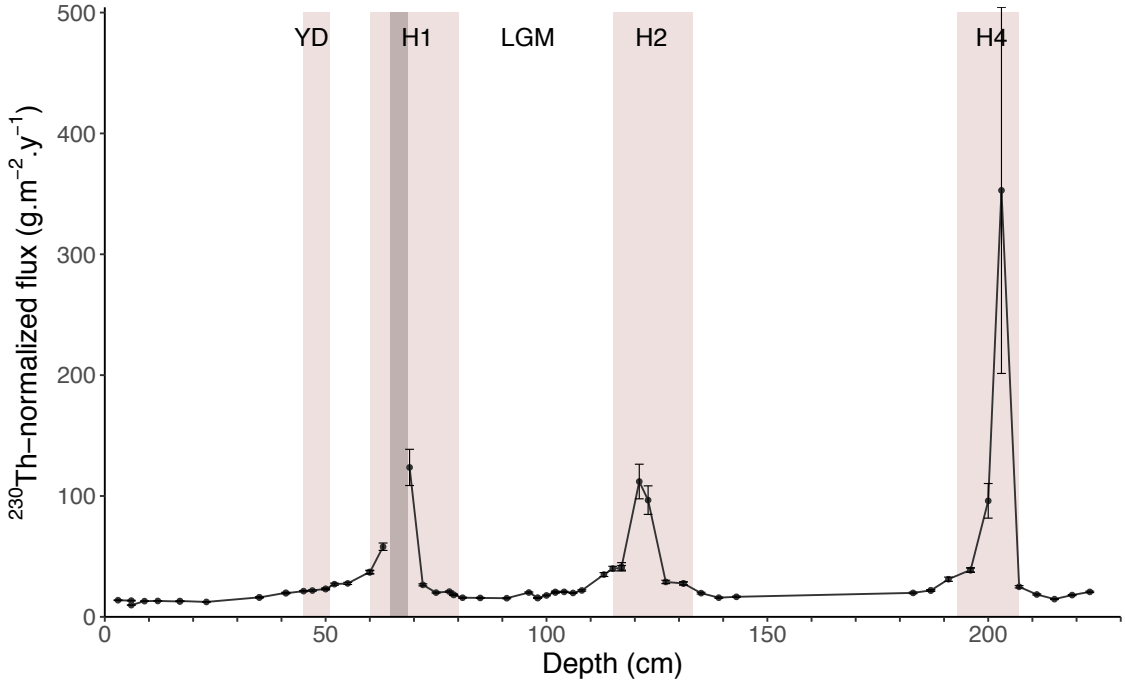

Fig. S5. ^{230}Th-normalized flux for SU90-08. The error bars represent the 2σ calculated based on the Monte Carlo simulation. It corresponds to *ca.* 3% of the ^{230}Th-normalized flux value over most of the record (error bars smaller than the point). However, in Heinrich layers, the uncertainty increases significantly due to the higher proportion of detrital material. At 203 cm, there is a spectacular increase of the uncertainty that reaches 42% (see text section 4.2.1. for details).

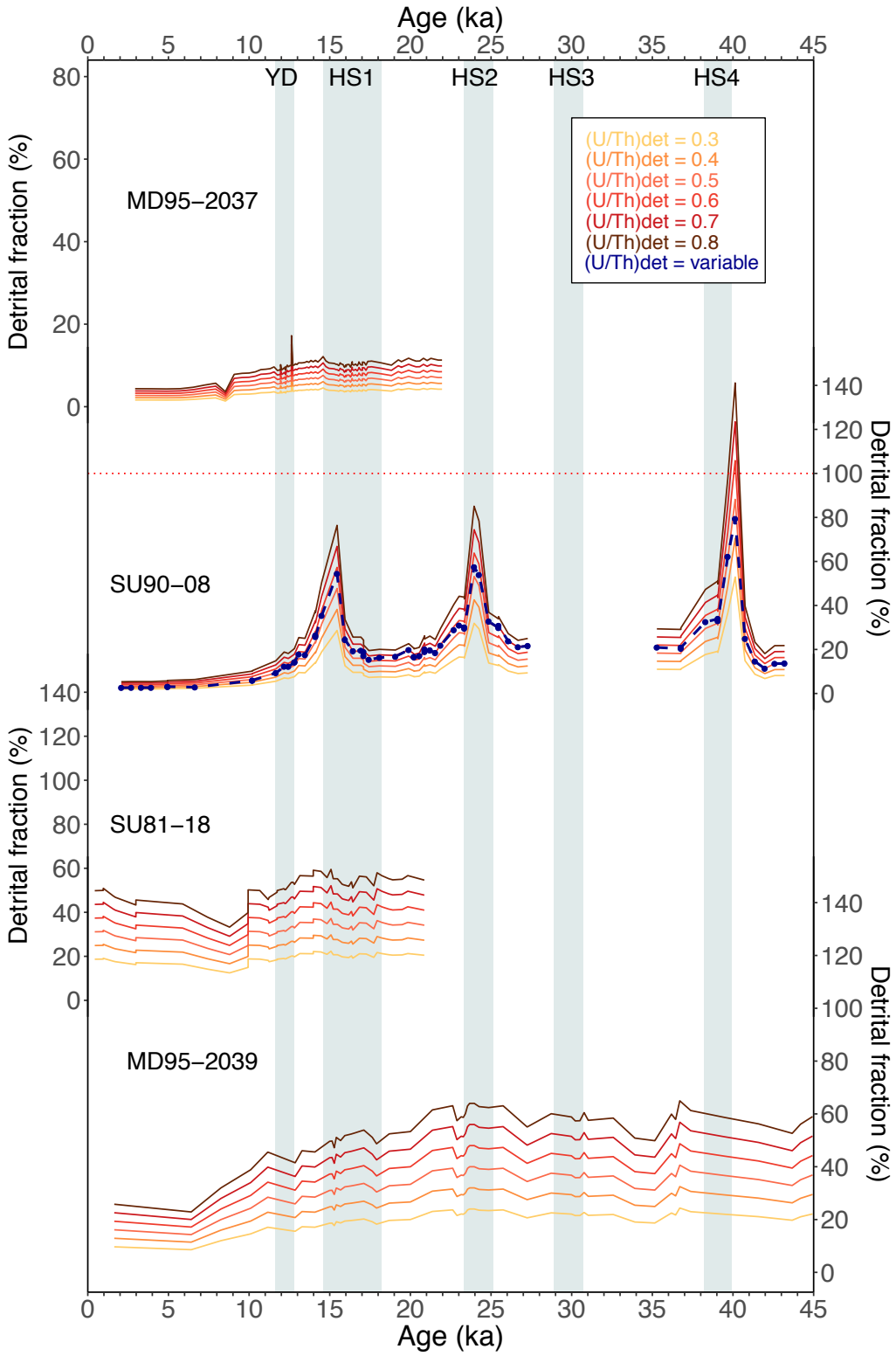

Fig S6: Time evolution of the computed detrital contribution
The detrital contribution is calculated from Eq.2. for different $(U/Th)_{det}$. It is expressed as the percentage of the total measured (^{230}Th). Similar results were obtained when computing the detrital fraction contribution from Eq.3. and expressing it as the percentage of the total measured ^{231}Pa (when available).

Table S1. SU90-08 age model. The tie points corresponding to the Holocene consist in ^{14}C ages measured on planktonic *G. bulloides* using a gas introduction system on ETH Zürich MICADAS [*Fahrni et al.*, 2013; *Wacker et al.*, 2013]. The alignments were performed using high resolution Summer Sea Surface Temperature from foraminifera assemblages (hereafter SST (HR) - this study), high resolution percentage of *N. pachyderma* left (hereafter %Nps- this study) covering the part of the record younger than HS4, as well as a low resolution SST reconstruction (hereafter SST (LR)) from [*Cortijo et al.*, 1997] for the last tie point older than HS4.

Depth (cm)	Age (ka BP)	2 σ	Type of pointer
9.0	3.312	0.292	*Planktonic ^{14}C age*
17.0	4.949	0.286	*Planktonic ^{14}C age*
23.0	6.635	0.736	*Planktonic ^{14}C age*
35.0	10.195	0.254	*Planktonic ^{14}C age*
40.9	11.641	0.475	*Alignment of SST (HR) & %Nps vs N-GRIP*
64.0	14.631	0.784	*Alignment of SST (HR) vs N-GRIP*
116.7	23.298	0.636	*Alignment of SST (HR) & %Nps vs N-GRIP*
153.4	28.848	0.970	*Alignment of SST (HR) & %Nps vs N-GRIP*
167.3	32.457	0.670	*Alignment of SST (HR) vs N-GRIP*
172.8	33.680	0.709	*Alignment of SST (HR) vs N-GRIP*
184.0	35.438	0.747	*Alignment of SST (HR) & %Nps vs N-GRIP*
190.1	38.164	1.015	*Alignment of SST (HR) & %Nps vs N-GRIP*
246.0	46.731	1.053	*Alignment of SST (LR) vs N-GRIP*

Table S2. ^{238}U and ^{232}Th measurements in SU90-08 leaching residues

Depth (cm)	($^{238}U/^{232}Th$)	2σ	U/Th	2σ	(^{238}U) (dpm.g^{-1})	2σ	(^{232}Th) (dpm.g^{-1})	2σ	Comment
17	0.421	0.050	0.136	0.008	0.113	0.008	0.270	0.022	
23	0.363	0.044	0.118	0.007	0.100	0.007	0.278	0.022	
50	0.545	0.065	0.177	0.011	0.328	0.023	0.607	0.049	
69	0.569	0.068	0.184	0.011	0.452	0.032	0.801	0.064	
96	0.704	0.084	0.228	0.014	0.558	0.039	0.798	0.064	
102	0.612	0.073	0.198	0.012	0.576	0.040	0.949	0.076	
121	0.568	0.068	0.184	0.011	0.498	0.035	0.884	0.071	Full procedure replicate
121	0.516	0.062	0.167	0.010	0.477	0.033	0.931	0.074	Replicate measurement
121	0.529	0.063	0.171	0.010	0.494	0.035	0.942	0.075	Replicate measurement
127	0.708	0.085	0.229	0.014	0.687	0.048	0.979	0.078	
131	0.692	0.083	0.224	0.013	0.713	0.050	1.039	0.083	
143	0.691	0.083	0.224	0.013	0.719	0.050	1.049	0.084	
196	0.523	0.063	0.170	0.010	0.467	0.033	0.899	0.072	Replicate measurement
196	0.531	0.064	0.172	0.010	0.484	0.034	0.919	0.074	Replicate measurement
200	0.507	0.061	0.164	0.010	0.516	0.036	1.026	0.082	
203	0.445	0.053	0.144	0.009	0.704	0.049	1.594	0.127	

Table S3. **^{238}U and ^{232}Th measurements in SU90-08 handpicked bulk IRDs** (see text section 2.2 for details)

Depth (cm)	($^{238}U/^{232}Th$)	2σ	(^{238}U) (dpm/g)	2σ	(^{232}Th) (dpm/g)	2σ
69	1.600	0.192	0.314	0.022	0.197	0.016
121	0.825	0.099	0.273	0.019	0.333	0.027
131	1.045	0.125	0.329	0.023	0.319	0.026
200	0.670	0.080	0.204	0.014	0.305	0.019
203	1.144	0.137	0.268	0.019	0.236	0.024

Table S4. **^{238}U and ^{232}Th measurements in SU90-08 handpicked detrital carbonates** (see text section 2.2 for details)

Depth (cm)	($^{238}U/^{232}Th$)	2σ	(^{238}U) (dpm/g)	2σ	(^{232}Th) (dpm/g)	2σ
69	3.946	0.237	0.514	0.010	0.130	0.003
121	1.225	0.073	0.568	0.011	0.464	0.009
200	1.434	0.086	0.256	0.005	0.178	0.004
203	3.877	0.233	0.244	0.005	0.063	0.001

Table S5. **^{238}U and ^{232}Th measurements in SU90-08 residues remaining after acid dissolution of handpicked detrital carbonates (**see text 2.2 for details**)**

Depth (cm)	($^{238}U/^{232}Th$)	2σ	(^{238}U) (dpm/g)	2σ	(^{232}Th) (dpm/g)	2σ
69	2.062	0.124	0.133	0.003	0.064	0.001
121	1.539	0.092	0.287	0.006	0.186	0.004
200	2.825	0.169	0.111	0.002	0.039	0.001
203	6.673	0.400	0.094	0.002	0.014	0.001

Table S6. **^{238}U, ^{232}Th and ^{230}Th activities measured in SU90-08 bulk samples**.
Discarded data are noted in italic blue. The discarded level at 6 cm corresponds to an outlier with respect to surrounding levels.

Depth (cm)	Age (ka BP)	2 σ	$A^{238}U$ ($dpm.g^{-1}$)	σ	$A^{232}Th$ ($dpm.g^{-1}$)	σ	$A^{230}Th$ ($dpm.g^{-1}$)	σ
3	2.08	0.292	0.262	0.0010	0.403	0.0041	6.025	0.0593
6	2.70	0.292	0.260	0.0010	0.417	0.0043	6.138	0.0613
6	*2.70*	*0.292*	*0.280*	*0.0043*	*0.584*	*0.0041*	*8.490*	*0.0291*
9	3.31	0.292	0.255	0.0010	0.429	0.0042	6.305	0.0595
12	3.93	0.289	0.266	0.0053	0.419	0.0030	6.194	0.0225
17	4.95	0.348	0.275	0.0070	0.456	0.0031	6.381	0.0221
17	4.95	0.348	0.274	0.0061	0.459	0.0032	6.193	0.0222
23	6.64	0.618	0.286	0.0011	0.513	0.0052	6.459	0.0618
35	10.20	0.367	0.334	0.0018	0.626	0.0062	4.929	0.0477
35	10.20	0.367	0.337	0.0013	0.643	0.0064	4.971	0.0476
41	11.66	0.590	0.403	0.0022	0.759	0.0076	4.089	0.0399
41	11.66	0.590	0.403	0.0016	0.745	0.0082	4.162	0.0444
45	12.17	0.663	0.419	0.0023	0.927	0.0093	3.936	0.0385
47	12.43	0.680	0.448	0.0018	0.872	0.0088	3.839	0.0376
50	12.82	0.696	0.495	0.0019	0.938	0.0095	3.671	0.0356
50	12.82	0.696	0.506	0.0020	0.954	0.0094	3.710	0.0354
52	13.08	0.711	0.548	0.0021	1.043	0.0105	3.282	0.0320
55	13.47	0.731	0.554	0.0021	0.997	0.0102	3.185	0.0312
60	14.11	0.756	0.691	0.0084	1.243	0.0084	2.641	0.0159
60	14.11	0.756	0.684	0.0069	1.215	0.0087	2.645	0.0155
63	14.50	0.777	0.749	0.0078	1.220	0.0083	1.933	0.0144
69	15.45	0.767	1.005	0.0095	1.297	0.0092	1.358	0.0145
72	15.95	0.757	1.241	0.0129	1.520	0.0104	3.620	0.0200
75	16.44	0.747	1.411	0.0133	1.431	0.0100	4.470	0.0222
78	16.93	0.739	1.691	0.0173	1.395	0.0097	4.360	0.0212
79	17.10	0.733	1.713	0.0095	1.488	0.0146	4.912	0.0472
79	17.10	0.733	1.689	0.0095	1.329	0.0131	4.824	0.0470
81	17.43	0.726	1.942	0.0075	1.329	0.0133	5.454	0.0529
85	18.08	0.712	2.095	0.0081	1.394	0.0142	5.559	0.0546
91	19.07	0.695	1.948	0.0075	1.382	0.0144	5.601	0.0567
96	19.89	0.680	1.718	0.0151	1.257	0.0085	4.441	0.0203
98	20.22	0.670	1.839	0.0219	1.379	0.0099	5.380	0.0241
98	20.22	0.670	1.847	0.0175	1.391	0.0100	5.488	0.0252
100	20.55	0.664	1.552	0.0140	1.259	0.0086	4.805	0.0212
102	20.88	0.657	1.409	0.0081	1.392	0.0137	4.249	0.0413
102	20.88	0.657	1.469	0.0187	1.337	0.0091	4.317	0.0213
104	21.21	0.650	1.477	0.0132	1.380	0.0094	4.231	0.0198
106	21.54	0.644	1.426	0.0156	1.328	0.0091	4.334	0.0201
108	21.87	0.635	1.409	0.0155	1.505	0.0104	4.075	0.0215
113	22.69	0.623	1.293	0.0052	1.429	0.0146	2.827	0.0284
115	23.02	0.614	1.261	0.0071	1.416	0.0136	2.564	0.0245
117	23.35	0.617	1.276	0.0050	1.372	0.0135	2.507	0.0241
117	23.35	0.617	1.216	0.0046	1.308	0.0320	2.436	0.0592
121	23.95	0.645	1.215	0.0047	1.659	0.0163	1.560	0.0156
123	24.25	0.675	1.272	0.0070	1.631	0.0162	1.665	0.0175
127	24.86	0.710	1.496	0.0058	1.609	0.0165	3.492	0.0345
131	25.46	0.749	1.476	0.0081	1.485	0.0146	3.503	0.0343
131	25.46	0.749	1.498	0.0056	1.545	0.0156	3.537	0.0343
135	26.07	0.788	1.589	0.0086	1.529	0.0152	4.497	0.0441
139	26.67	0.828	1.612	0.0089	1.599	0.0155	5.297	0.0508
143	27.28	0.890	1.488	0.0081	1.579	0.0155	5.051	0.0488
183	35.28	0.720	0.814	0.0044	1.398	0.0145	3.809	0.0371
187	36.77	1.090	0.802	0.0045	1.239	0.0119	3.406	0.0326
187	36.77	1.090	0.795	0.0043	1.278	0.0125	3.430	0.0336
191	38.29	1.423	0.848	0.0033	1.629	0.0164	2.755	0.0268
196	39.06	1.405	0.893	0.0035	1.466	0.0148	2.294	0.0226
196	39.06	1.405	0.894	0.0035	1.426	0.0146	2.293	0.0228
200	39.67	1.374	1.022	0.0038	1.959	0.0197	1.609	0.0165
203	40.13	1.347	0.986	0.0055	1.867	0.0184	1.058	0.0130
207	40.75	1.318	1.606	0.0062	1.684	0.0167	3.387	0.0327
211	41.36	1.287	1.632	0.0065	1.165	0.0113	3.997	0.0376
215	41.97	1.255	1.807	0.0103	1.089	0.0110	4.811	0.0476
219	42.59	1.224	1.683	0.0093	1.101	0.0106	4.054	0.0385
223	43.20	1.193	1.367	0.0076	0.948	0.0097	3.482	0.0348

2.2.2 Article summary

The first part of this article focuses on measuring the $(U/Th)_{det}$ for several SU90-08 samples covering the last 40 ky. The first challenge consisted in extracting the sediment detrital fraction. We used a sequential leaching procedure that allows dissolving and isolating the carbonate fraction first, and then the authigenic fraction made of Fe and Mn oxyhydroxydes. The leaching residue obtained after this procedure corresponds to the detrital fraction of the sediments. However, the sediments may contain some detrital carbonates and our procedure dissolves every type of carbonates during the first leaching step. In order to evaluate the impact of detrital carbonates on the total $(U/Th)_{det}$, we mechanically isolated under binocular detrital carbonates and bulk detrital grains on the fraction bigger than 150 μm, extracted by water sieving. The ^{238}U and ^{232}Th isotopic compositions analysis of detrital carbonates, bulk IRDs and leaching residues showed that:

— None of the fractions measured truly represents the detrital fraction. Instead, the actual $(U/Th)_{det}$ value should lie on the mixing line between the leaching residue and the pure detrital carbonates endmembers.

— The detrital carbonates cannot represent a significant proportion of the sediment detrital fraction for core SU90-08.

— The (^{238}U/^{232}Th) activity ratio measured on SU90-08 leaching residue is a good estimate of the actual $(U/Th)_{det}$. The leaching residue measurements allowed to reconstruct the temporal evolution of the $(U/Th)_{det}$ value at SU90-08 location over the last 40 ka. The $(U/Th)_{det}$ varies significantly between 0.4 and 0.7. The minimum value of 0.4 is reached for the Holocene period whereas the maximum value of 0.7 is reached for the LGM period. During the Heinrich events the $(U/Th)_{det}$ is close to 0.55. Therefore, considering a constant $(U/Th)_{det}$ value associated with a $\pm$ 0.1 (2σ) uncertainty as commonly done in the literature (see Table 2.1) cannot account for the variability observed in SU90-08 samples.

In the second part of this paper, we evaluate the impact of the choice of the $(U/Th)_{det}$ value on the ^{230}Th-normalized flux and Pa/Th proxies. The proxies sensitivity was tested on SU90-08 and three other North-Atlantic cores calculating the ^{230}Th-normalized flux and Pa/Th for $(U/Th)_{det}$ values ranging from 0.3 to 0.8 with 0.1 increments. To assess the significance of the proxies sensitivity, the ^{230}Th-normalized flux and Pa/Th variations related to the value of $(U/Th)_{det}$ are systematically compared to the proxy uncertainties. We observe three types of behavior:

— ^{230}Th-normalized flux and Pa/Th are not significantly affected by the choice of (U/Th)det value for the complete record

— ^{230}Th-normalized flux and Pa/Th are significantly affected by the choice of $(U/Th)_{det}$ value but only for some time periods, typically the Heinrich events for SU90-08.

— ^{230}Th-normalized flux and Pa/Th are significantly affected by the choice of $(U/Th)_{det}$ value over the entire record.

These different behaviors can be related to core location and terrigenous material supply. Indeed, cores having an important proportion of detrital material (around 30%) have lower proportion of excess fraction. Therefore, in cases of significant detrital inputs, the way the detrital fraction contribution is evaluated and the choice of the $(U/Th)_{det}$ value has a bigger impact on ^{230}Th-normalized flux and Pa/Th.

2.2.3 Article conclusions

This work brings out three main conclusions:

— $(U/Th)_{det}$ varied between 0.4 and 0.7 over the last 40 ky in sediment core SU90-08. The minimum value of 0.4 is observed for the Holocene and the maximum value of 0.7 is observed for the LGM period.

— Considering a constant $(U/Th)_{det}$ value with an uncertainty of $\pm$ 0.1 (2 σ) cannot account for the variability observed in core SU90-08.

— ^{230}Th-normalized flux and Pa/Th sensitivity to changes in $(U/Th)_{det}$ value relies mainly on the core location and terrigenous supply. On continental margins or in zones affected by iceberg discharge the detrital fraction can represent an important part of the sediment (30 to 90% in the cores studied here). In those cases, ^{230}Th-normalized flux and Pa/Th changes due to changes in $(U/Th)_{det}$ value can largely exceed the uncertainty on the proxies and thus become significant. Our study shows that an improper estimate of the $(U/Th)_{det}$ value can lead to a misinterpretation of the amplitude of sedimentary fluxes or circulation changes. Moreover, if the temporal variations of $(U/Th)_{det}$ are not accurately taken into account, the temporal variability of sediment fluxes and circulation changes may not be correctly reconstructed.

Thus, when using ^{230}Th-normalized flux and Pa/Th it is recommended to:

— Evaluate the proportion of the detrital fraction and test the sensitivity of the proxies to changes in $(U/Th)_{det}$ value.

— Consider uncertainties on $(U/Th)_{det}$ not lower than the measurement uncertainties (10 % - 2σ in this study)

— Evaluate uncertainties on ^{230}Th-normalized flux and Pa/Th accounting for the uncertainty on $(U/Th)_{det}$ at the studied location.

2.2.4 Article perspectives

We have shown that the ^{230}Th-normalized flux and Pa/Th records of two cores located on the Iberian margin, were significantly affected by changes in the $(U/Th)_{det}$ value. In order to better quantify sedimentary fluxes and circulation changes at this location, it would be interesting to actually measure the $(U/Th)_{det}$ temporal variations for at least one of the two cores. In the longer term, it could be of great interest to develop a method to monitor potential changes in $(U/Th)_{det}$ in a simpler and less time consuming way than performing sequential leachings, using for example routine measurements such as X-Ray Fluorescence (XRF) data, magnetic susceptibility or major or trace element contents.

Moreover, ^{230}Th-normalized flux can be used to refine the evaluation of sedimentation rates and thus sediment cores age-depth relationships (Bourne et al., 2012). The method consists in correcting the sedimentation rate inferred between two tie-points (^{14}C date or alignment pointer) using the $^{230}Th_{xs,0}$ value. Indeed, the short residence time of ^{230}Th allows to assume that all the ^{230}Th produced in the water column will rapidly reach the underlying sediments. From the comparison between the excess ^{230}Th measured in the sediments and corrected from the radioactive decay since deposition time and the theoretical amount of ^{230}Th produced in the water column, it is possible to infer the dilution or concentration level of ^{230}Th. This way, if the $^{230}Th_{xs,0}$ is diluted, the corrected sedimentation rate from $^{230}Th_{xs,0}$ will be increased relative to the tie-points inferred sedimentation rate and the other way around. The benefit of this method relies on the generally high-resolution of the Th data that allows considering high-resolution sedimentation rate variations. As we have shown that the $^{230}Th_{xs,0}$ can be significantly impacted by changes in the $(U/Th)_{det}$ value, it would be interesting to evaluate the impact of temporal changes of $(U/Th)_{det}$ value on age models derived from Th-normalization technique.

2.3 Conclusion

In this chapter we have shown that for SU90-08, the choice of the $(U/Th)_{det}$ value was crucial to reconstruct the correct amplitude of ^{230}Th normalized flux and Pa/Th variations across the Heinrich events. Indeed, the core is significantly affected by iceberg discharges and thus receives important terrigenous inputs during the Heinrich events. During those periods, the detrital contribution can reach up to 90% of the total sediment. Thus, the choice of the detrital correction becomes determinant to evaluate $^{230}Th_{xs,0}$ and $^{231}Pa_{xs,0}$ which are the basis of sedimentary fluxes and circulation changes evaluation. For the first time, the sediment detrital fraction was extracted and its (^{238}U/^{232}Th) signature measured. The $(U/Th)_{det}$ was found to vary through time between 0.4 (Holocene value) and 0.7 (LGM value). Such temporal variations have never been taken into account in the

previous literature and might induce significant misinterpretations in terms of amplitude and temporal trends of sedimentary fluxes and/or circulation changes reconstructions, especially for locations with high detrital contributions.

In the next chapter we focus on the construction of the age-depth relationship for SU90-08. We evaluate the potential benefits of using the Th-normalization technique for refining the core age model. We also investigate about the impact of variations of $(U/Th)_{det}$ on the chronologies derived using $^{230}Th_{xs,0}$.

Chapter 3. Improving SU90-08 age-depth relationship using ^{230}Th-normalization, implications for North Atlantic marine cores chronologies

3.1 Introduction

In the previous chapter, thanks to a better evaluation of the temporal variations of the (^{238}U/^{232}Th) activity ratio of the detrital fraction of the sediments, we have precisely reconstructed the amplitude of the ^{230}Th-normalized flux and Pa/Th changes over the last 40 ky for core SU90-08. Before looking at SU90-08 paleoproxy time series, it is necessary to generate a precise downcore age-depth relationship. Indeed, one of the main interests of this PhD thesis is to better reconstruct and quantify the ocean circulation changes across millennial scale abrupt climate events that are the Heinrich (and the DO) events. As those events only last for a few centuries up to a few millennia, producing independent and accurate chronologies for marine cores is a key aspect, especially when assessing temporal lead/lag relationships between marine and continental records, or between different marine records, possibly from different regions.

The last 40 ky is a particularly well constrained period because radiocarbon content (^{14}C) can be used as an absolute dating tool. However, there is evidence that the ^{14}C ages produced on single species planktonic foraminifers are biased in the North Atlantic because of poorly constrained changes in surface reservoir ages through space and time

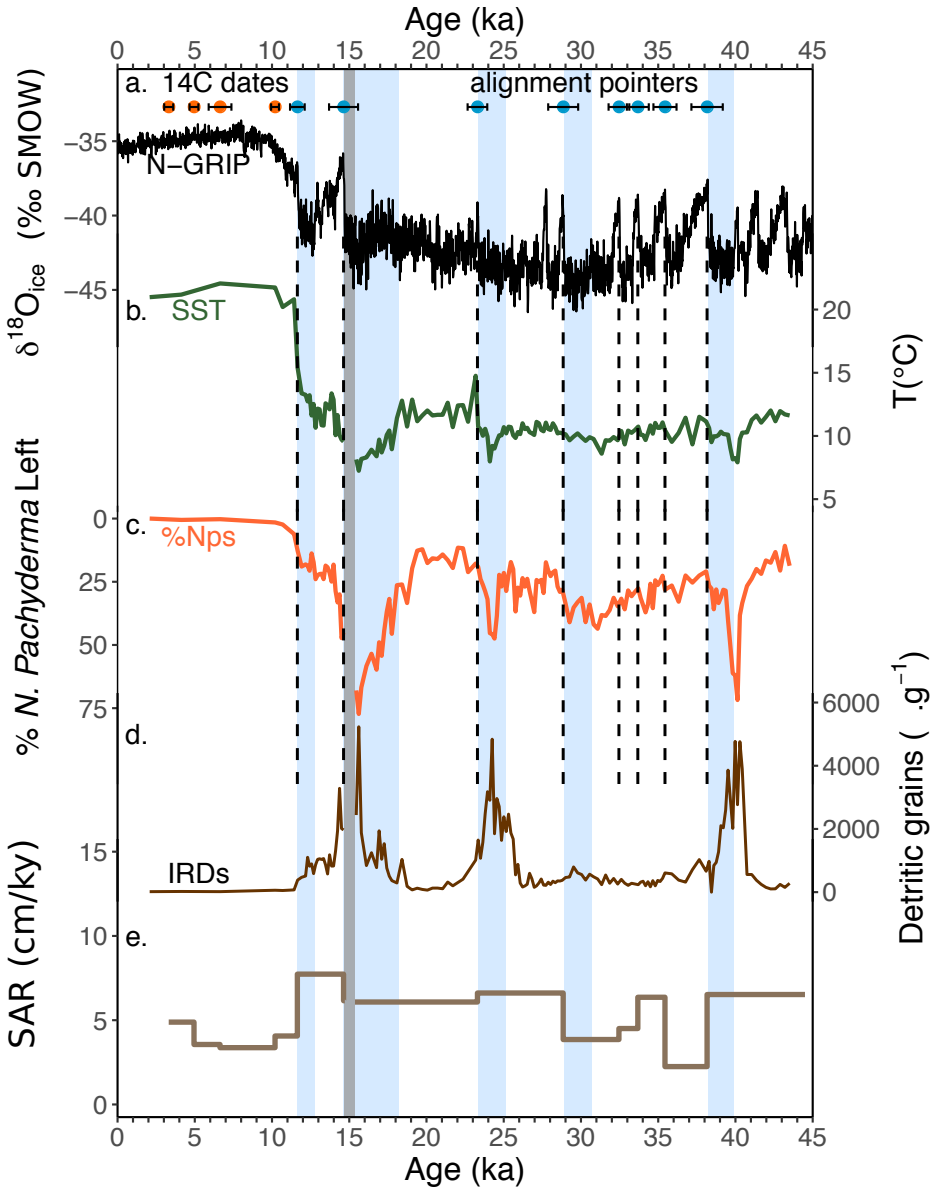

Figure 3.1 – **Surface records alignments with Greenland for SU90-08.**
a. North-GRIP $\delta^{18}O$ ice (Bond et al. (1993), Andersen et al. (2006), Rasmussen et al. (2006), Svensson et al. (2006), Vinther et al. (2006)) **b.** High-resolution summer Sea Surface Temperature (SST) from foraminifer assemblages (this study). **c.** High-resolution percentage of N. *Pachyderma* left (this study). **d.** IRD abundances (grains counted in the fraction > 150 μm per grain of dry sediment, (this study) **e.** Sediment Accumulation Rate (SAR). The grey band corresponds to a sediment perturbation between 65 and 69 cm evidenced by reversals in ^{14}C ages planktonic and benthic δ^{18}O and δ^{13}C.

(*e.g.* Thornalley et al., 2011; Waelbroeck et al., 2001), particularly for sites located north of 40°N. Thus, because of its location, it is challenging to generate accurate age-depth model for SU90-08. For North-Atlantic sediment cores, a classical approach consists in assuming that the abrupt changes in sea surface temperature (SST) are synchronous with rapid air temperature variations in Greenland (*e.g.* Austin & Hibbert, 2012). However, the SST reconstructions available for SU90-08 display limited amplitude variability rendering the alignment to Greenland records difficult. Besides, the alignments from different

SST indicators such as the %Nps and the foraminifer assemblages SST reconstruction do not exhibit fully synchronous evolution against core depth (Figure 3.1). Nevertheless, I have identified 8 tie-points corresponding to the major Greenland δ^{18}O abrupt transitions described by Wolff et al. (2010). These tie-points are consistent with the use of ^{14}C as a safeguard (Figure 3.1 and 3.2).

Yet this age model is not fully satisfactory for two major reasons. First, the core is situated in the IRD belt and the location receives important amount of detrital material from icebergs discharges during the Heinrich events as shown by the IRD record (Figure 3.1). Though, the sedimentation rate obtained by aligning the surface records to Greenland does not display significant changes across those events. This can be easily related to the limited number of tie-points, that restrict the resolution of the reconstructed sedimentation rate history. Second, the Greenland δ^{18}O record lacks of well marked, high amplitude climatic events in the interval from 27.73 to 14.64 cal ky BP (hereafter ka) that can serve as chronological tie-point for North-Atlantic marine chronologies.

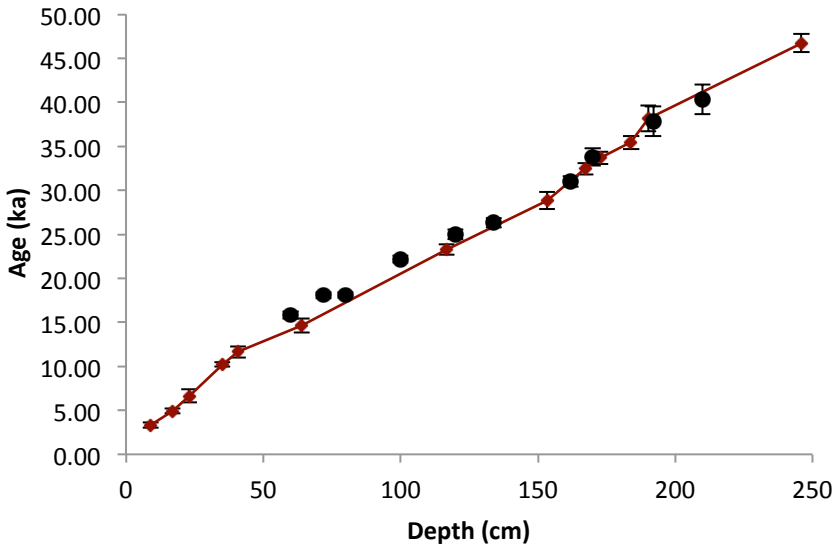

Figure 3.2 – **Evaluation of alignment tie-points for SU90-08**
The red diamonds represent the alignment tie-points (SST vs N-GRIP δ^{18}O) with 2σ uncertainty. The red line corresponds to the linear interpolation between the alignment tie-points. The black dots represent the calibrated 14C ages assuming a constant surface reservoir age of 400 ± 100 y, with 2 σ uncertainty. In principle, the alignment tie-points should be older or of the same age than the calibrated ^{14}C dates.

As proposed by Adkins et al. (1997) and further implemented by Bourne et al. (2012), the $^{230}Th_{xs,0}$ can be used as a tool to refine marine core chronologies. The sedimentation rate inferred from two consecutive dated levels (*i.e.* either calibrated ^{14}C ages or tie-points alignment) is variably adjusted using changes in $^{230}Th_{xs,0}$. $^{230}Th_{xs,0}$ data can be produced at high resolution through intervals with a limited number of tie-points, potentially improving marine core chronologies across these time periods. To date, despite its

apparent advantages, the use of Th-normalization to refine marine cores age models has been relatively limited (Adkins et al., 1997; Bourne et al., 2012). I used ^{230}Th normalization method to refine the age-depth model of SU90-08 and other North Atlantic marine cores. This work is summarized in the sections below and presented in detail in the article entitled "Improving North Atlantic marine core chronologies using ^{230}Th-normalization", under revisions in the journal *Paleoceanography and Paleoclimatology*.

3.2 Article "Improving North Atlantic marine core chronologies using ^{230}Th-normalization"

3.2.1 Article and supplementary information

Confidential manuscript submitted to Paleoceanography and Paleoclimatology

Improving North Atlantic marine core chronologies using ^{230}Th-normalization

L. Missiaen[1,*], C. Waelbroeck[1], S. Pichat[2,1,3] S. L. Jaccard[4] , F. Eynaud[5] , R. Greenop[6], A. Burke[6]

[1]Laboratoire des Sciences du Climat et de l'Environnement, LSCE/IPSL, CEA-CNRS-UVSQ-Université Paris-Saclay, F-91198 Gif-sur-Yvette, France.

[2]Université de Lyon, ENS de Lyon, Laboratoire de Géologie de Lyon (LGL-TPE), F-69007 Lyon, France.

[3]Climate Geochemistry Department, Max Planck Institute for Chemistry, Mainz, Germany.

[4]Institute of Geological Sciences and Oeschger Center for Climate Change Research, University of Bern, CH-3012 Bern, Switzerland

[5]Université de Bordeaux, UMR EPOC 5805, F-33615 Pessac, France

[6]School of Earth and Environmental Science, Irvine Building, University of St Andrews, North Street, St Andrews, KY16 9AL, United Kingdom

* Corresponding author: Lise Missiaen (lise.missiaen@lsce.ipsl.fr)

Key Points:

- We evaluated the impact of Th-normalization to refine the age models for three North Atlantic cores.
- The revised chronologies imply that the cooling at the onset of Heinrich Stadial 1 was synchronous with an increase in the Greenland dust record.
- The Greenland ice Ca^{2+} increase at 17.48 ka ± 0.21 can serve as a new tie-point for the onset of Heinrich Stadial 1 in North-Atlantic marine cores.

Abstract:

Producing independent and accurate chronologies for marine sediments is a prerequisite to understand the sequence of millennial-scale events and reveal potential temporal offsets between marine and continental records, or between different marine records, possibly from different regions. The last 40 ky is a generally well-constrained period since radiocarbon (^{14}C) can be used as an absolute dating tool. However, in the northern North Atlantic, calendar ages cannot be directly derived from ^{14}C ages, due to temporal and spatial variations of surface reservoir ages. Alternatively, chronologies can be derived by aligning Greenland ice-core time-series with marine surface records. Yet, this approach suffers from the lack of clearly defined climatic events between 14.7 and 23.3 cal ky BP (hereafter ka), a crucial period encompassing Heinrich Stadial 1 (HS1) and the onset of the last deglaciation. In this study i) we assess the benefits of ^{230}Th-normalization to refine the sedimentation history between alignment tie-points and ii) revisit the chronologies of three North Atlantic marine records. Our study supports the contention that the marked increase in dust flux (or Ca^{+}) in Greenland at 17.48 ka ± 0.21 ky (1σ) occurred within dating uncertainty of sea surface temperature cooling in the North Atlantic at the onset of Heinrich Stadial 1. This sharp feature might be useful for future chronostratigraphic alignments to remedy the lack of chronological constraint between 14.7 and 23.3 ka for North Atlantic marine records that are subject to large changes in ^{14}C surface reservoir age.

1 Introduction

Greenland ice core records have revealed abrupt climate variability during most of the last glacial cycle. Several mechanisms have been proposed to explain the origin of these abrupt climate changes, some of which involve planetary waves, sea-ice, ice-sheets dynamics or low to high latitude teleconnections (see [*Clement and Peterson*, 2008] for a review). However, the prevailing paradigm relates these abrupt climatic events to changes in the Atlantic Meridional Overturning Circulation (AMOC) [*Böhm et al.*, 2015; *Henry et al.*, 2016; *Lynch-Stieglitz*, 2017; *Rahmstorf*, 2002]. Thus, the study of water mass reorganizations and circulation changes across those abrupt climate events remains central for a better understanding of the underlying physical mechanisms. As those events only last for a few centuries up to a few millennia, producing independent and accurate chronologies for marine archives is a key aspect, especially when assessing temporal lead/lag relationships between marine and continental records, or between different marine records, possibly from different regions.

To date, several methods have been applied to establish marine record chronologies. The last 40 ky is a particularly well dated period because it corresponds to the approximate time range covered by radiocarbon dating, enabling the construction of accurate marine core chronologies through ^{14}C dating of (preferably single species) planktonic foraminifera samples. Raw radiocarbon ages are converted into calendar ages using calibration curves (*e.g.* IntCal13 [*Reimer et al.*, 2013]). A downcore age model is then derived from these dated levels, using more or less sophisticated methods. The simplest approach assumes a constant sedimentation rate between the dated levels whereas software based on Bayesian methods (*e.g.* OxCal [*Ramsey*, 2009], Bchron [*Parnell et al.*, 2008], Bacon [*Blaauw*, 2010] and Undatable [*Obrochta et al.*, 2017; *Webster et al.*, 2018]) produce more sophisticated age-depth relationships by including additional stratigraphic information and providing age

uncertainties of the dated levels using a Monte Carlo approach. The latest improvements even take into account the uncertainty of the sampling depth [*Obrochta et al.*, 2017; *Webster et al.*, 2018]. Additionally, those tools also provide the opportunity to statistically test the consistency of the ^{14}C dates and generate realistic age uncertainties that increase with the distance from the dated depth horizons, making them, at present, the best option to build robust age models.

Despite the development of sophisticated age-depth models in recent decades, there is growing evidence for further complications affecting the use of ^{14}C to robustly date marine sediments. For instance, different planktonic foraminifer species from the same sediment depth level may have significantly different radiocarbon ages in reworked sediments or in samples which have undergone recrystallization and incorporation of secondary radiocarbon [*Broecker et al.*, 2006]. It has also been shown that bioturbation, carbonate dissolution or chemical erosion could significantly influence radiocarbon-based age scales [*Bard et al.*, 1987-a; *Barker et al.*, 2007; *Mekik*, 2014; *Wycech et al.*, 2016]. Therefore, special care has to be taken when measuring radiocarbon in locations where the sediment accumulation rate is low and where there is evidence of intense bioturbation or secondary calcite crystallization. Last but not least, converting marine radiocarbon dates into calendar ages, requires knowledge about the ^{14}C age difference between the ocean surface waters and the contemporary atmosphere, commonly referred as the surface reservoir age. This surface reservoir age is quite well constrained in the modern ocean (see [*Key et al.*, 2004]) but as it depends on the kinetics of air-sea gas exchange and on the location of deep-water formation, it can vary both spatially and temporally. In particular, it has been shown that north of ~40°N in the Atlantic, surface reservoir ages have undergone large variations through time due to changes in sea ice cover or deep water formation [*Bard et al.*, 1994; *Bondevik et al.*, 2006; *Thornalley et al.*, 2011; *Waelbroeck et al.*, 2001]. To date, surface reservoir age variations

100 remain poorly constrained; therefore simply relying on ^{14}C to build accurate chronologies for
101 North Atlantic marine records, especially for those located north of ~40°N, is problematic.
102 When dating northern North Atlantic cores over the last 40 ky, a classical approach
103 consists of assuming that abrupt changes in sea surface temperature (SST) are synchronous
104 with rapid air temperature variations in Greenland (*e.g.* [*Austin and Hibbert*, 2012]). This is
105 equivalent to assuming that the equilibration time between air temperature and surface water
106 temperature is short enough to be neglected, which appears reasonable when considering the
107 currently achievable precision in marine sediment chronologies (a few hundred years at best).
108 This method has been, and still is, very valuable for North Atlantic sites, especially north of
109 ~40°N where calendar ages cannot reliably be derived from ^{14}C dates due to poorly
110 constrained variations in surface reservoir ages. However, the age models derived by aligning
111 SST to Greenland air temperature suffer from the lack of well defined, high amplitude
112 climatic events in the Greenland temperature (or ice $\delta^{18}O$) records in the interval from 27.73
113 to 14.64 ka in the GICC05 age scale [*Wolff et al.*, 2010]. During this 13 ky long interval, there
114 is only one small abrupt warming dated at 23.29 ka ± 0.4 ky [*Wolff et al.*, 2010], which might
115 be difficult to identify in marine SST records. Consequently, North Atlantic marine records,
116 located in the vicinity of deep-water formation areas and thus in key regions for studying
117 ocean circulation changes, are particularly difficult to precisely date over this time interval,
118 which includes the last two Heinrich events and the Last Glacial Maximum (LGM). Thus,
119 improving constraints on marine chronologies for this time period (0-30 ka) will help to better
120 constrain the timing of oceanic changes leading to Heinrich events and the last deglaciation.
121 Sedimentary ^{230}Th excess ($^{230}Th_{xs}$) has been widely used to reconstruct past changes
122 in the vertial particle flux (see [*François et al.*, 2004] for a review). However, in cases where
123 the sediment lateral redustribution (*i.e.* focusing or winnowing) can be either assumed to be
124 constant across the study interval [*Bourne et al.*, 2012-b] or independently estimated [*Adkins*

125 *et al.*, 1997], ^{230}Th-normalization can also be used as a tool to refine marine core
126 sedimentation rate history between independently dated levels. The sedimentation rate
127 inferred from two consecutive dated levels (*i.e.* either calibrated ^{14}C ages or tie point
128 alignment) is variably adjusted using changes in $^{230}Th_{xs}$, corrected for radioactive decay since
129 deposition (subscript "0"), $^{230}Th_{xs,0}$ (see section 2.2 for detailed method description). $^{230}Th_{xs,0}$
130 data can be produced at high resolution through intervals with a limited number of tie-points,
131 potentially improving marine core chronologies across these time periods. To date, despite its
132 apparent advantages, the use of Th-normalization to refine marine cores age models has been
133 relatively limited ([*Adkins, and Boyle*, 1997; *Bourne et al.*, 2012-a]).

134 In this study we investigate the potential benefits of the Th-normalization method to
135 determine robust age models for northern North Atlantic (north of ~40°N) marine sediment
136 cores over the last 25 ky. First, we discuss the assumptions underlying the Th-normalization
137 approach. Second, we evaluate the consistency of sedimentation rate changes inferred from
138 Th-normalization and radiocarbon dating for a core retrieved from the tropical Atlantic, which
139 has likely not undergone large variations in surface reservoir ages. Finally, we propose new
140 age models based on the integration of surface record alignments and Th-normalization for
141 three North-Atlantic records and evaluate the implications for their SST records.

142

143 **2 Material and methods**

144 **2.1 Core locations and available data**

145 Our study requires the following data to be available: high-resolution downcore SST
146 reconstructions to allow accurate alignment with ice core records, and high-resolution ^{238}U,
147 ^{230}Th, and ^{232}Th activities between dated levels. Such a combination of data was available in
148 only a few locations. Among those, we selected low latitude core MD03-2705 and North-
149 Atlantic cores SU81-18, SU90-03, and SU90-08 (Table 1 and Figure S1) because they had

high resolution $^{230}Th_{xs,0}$ records. All selected records cover the last deglaciation and the interval of particular interest from 14.64 to 23.29 ka for which no alignment tie point can be defined in Greenland ice $\delta^{18}O$ record.

Core MD03-2705 is located in the tropical Atlantic, far from fluctuating sea ice cover and deep-water formation areas, and away from coastal upwelling. Thus, at this location, surface reservoir age is assumed to have remained close to the modern value of 470 ± 120 y (GLODAP [*Key et al.*, 2004]) throughout the studied period. This core is thus particularly well suited for a comparison of the sedimentation rate history obtained from radiocarbon and Th-normalization approaches (see section 4.1.3).

Cores SU90-08, SU90-03 and SU81-18 are well-studied reference cores with numerous paleo-proxy records and thus good candidates to test the potential of the Th-normalization technique to produce improved age-depth models. Among these three cores, SU90-08, located in the IRD belt, exhibits remarkably high amplitude $^{230}Th_{xs,0}$ changes [*Missiaen et al.*, 2018] making this core a candidate for substantial age-model change with Th-normalization. For these cores (which are either close or north of 40°N), we only use the published radiocarbon dates younger than 10 ka as chronological markers because the surface reservoir ages are likely to have significantly varied before the Holocene (see Text S1- Figure S2), To constrain the older part of the age-depth relationships, we establish a set of tie-points based on the alignment of the SST records to NGRIP ice $\delta^{18}O$ [*Andersen et al.*, 2006; *Rasmussen et al.*, 2006; *Svensson et al.*, 2006; *Vinther et al.*, 2006] using the AnalySerie software [*Paillard et al.*, 1996] and assuming synchronicity of rapid warming in both archives during the events defined by [*Wolff et al.*, 2010]. We verified the alignment tie-points using radiocarbon dates. To do so, we converted the published raw radiocarbon ages into calendar ages using Oxcal (online version 4.3) [*Ramsey*, 2009], the IntCal13 calibration curve [*Reimer et al.*, 2013] and the modern reservoir age corresponding to each location extracted from

GLODAP [*Key et al.*, 2004] (400 ± 100 y for SU90-08 and SU90-03 and 500 ± 100 y for SU81-18). We then verified that for a given depth level, the assigned calendar age (derived from the alignment age model) was either younger or within error of the calendar age derived from ^{14}C measurements assuming that the reservoir age has been constant and identical to the modern value at the considered location (see Figure 1). In other words, we are checking to ensure that the reservoir ages implied by our Greenland tie points in the pre-Holocene northern North Atlantic are not younger than modern.

Figure 2 compares the age-depth relationships derived by the two methods: i) assuming constant sedimentation rate between tie-points; and ii) using the $^{230}Th_{xs,0}$ measurements to compute sedimentation rate changes between tie-points. The latter method requires a set of assumptions that are described in the following section.

2.2 Th-normalization as a dating tool

The Th-normalization technique requires the determination of the 'excess' ^{230}Th activity in the sediments derived from the scavenging of ^{230}Th from the water column by sinking particles (*i.e.* ^{230}Th that is not incorporated within the mineral lattice or supported by radioactive decay from authigenic uranium) and corrected for radioactive ^{230}Th decay since sediment deposition (term 'excess' thorium ($^{230}Th_{xs,0}$)). The underlying assumptions are discussed in detail in section 4.1.1. The equations used to determine the ^{230}Th excess activities ($^{230}Th_{xs}$) are the following [*Henderson and Anderson*, 2003].

$$^{230}Th_{xs} = {}^{230}Th_{meas} - {}^{230}Th_{det} - {}^{230}Th_{auth} \quad \text{Eq.1.}$$

195 Where "meas" stands for the measured activity in the bulk sediments, "det" and "auth" for the
196 detrital and authigenic fractions respectively.

197 Eq.1. can be rewritten as:

198

$$
\begin{aligned}
{}^{230}\mathrm{Th}_{xs} = {}^{230}\mathrm{Th}_{meas} - ({}^{232}\mathrm{Th}_{meas} \times (\mathrm{U/Th})_{det}) \\
- \left[({}^{238}\mathrm{U}_{meas} \right. \\
- ({}^{232}\mathrm{Th}_{meas} \times (\mathrm{U/Th})_{det})) \\
\times \left\{ \left(1 - e^{-\lambda_{230} t}\right) + \frac{\lambda_{230}}{\lambda_{230} - \lambda_{234}} \left(\left(\frac{{}^{234}\mathrm{U}}{{}^{238}\mathrm{U}} \right)_{sw} - 1 \right) (e^{-\lambda_{234} t} \right. \\
\left. \left. - e^{-\lambda_{230} t}) \right\} \right]
\end{aligned}
\qquad \text{Eq.2.}
$$

199 where λ_x is the decay constant of the considered isotope and t the calendar age of the
200 sediments. $({}^{234}\mathrm{U}/{}^{238}\mathrm{U})$ ratio is assumed to be that of sea water: $({}^{234}\mathrm{U}/{}^{238}\mathrm{U})_{sw}$ =1.1467 (1σ =
201 0.0025) [*Robinson et al.*, 2004], $(\mathrm{U/Th})_{det}$ is the $({}^{238}\mathrm{U}/{}^{232}\mathrm{Th})$ activity ratio of the sediment
202 detrital fraction the latter being considered as either constant or variable with time (see
203 [*Missiaen et al.*, 2018]).

204 Finally, the excess fraction at the time of sediment deposition ${}^{230}\mathrm{Th}_{xs,0}$ can be calculated by
205 correcting ${}^{230}\mathrm{Th}_{xs}$ for the radioactive decay:

$$Th_{xs,0} = Th_{xs}\, e^{\lambda_{230} t} \qquad \text{Eq.3.}$$

206

207 As proposed by [*Adkins et al.*, 1997], and further developed by [*Bourne et al.*, 2012-
208 b], ${}^{230}\mathrm{Th}_{xs,0}$ can be used to refine age models by constraining the sedimentation rate inferred
209 between two dated levels. ${}^{230}\mathrm{Th}$ is produced by the decay of dissolved ${}^{234}\mathrm{U}$ in the water
210 column, where it is rapidly scavenged onto the surface of sinking particles. As ${}^{230}\mathrm{Th}$ has a

very short residence time in the water column (ranging from a few months in surface waters up to 50 y in deep waters [*François*, 2007]), all of the ^{230}Th produced in the water column is rapidly removed to the underlying sediments via particle scavenging. At a given location, the amount of ^{230}Th produced in the water column is constant through time and is controlled by the water depth. If all of the ^{230}Th produced in the water column reaches the underlying sediments, the activity of $^{230}Th_{xs,0}$ in the sediment is dependent on sediment supply and thus sedimentation rate variations. In this case, the $^{230}Th_{xs,0}$ should be inversely proportional to the sedimentation rate. Sedimentation rate increases are inferred from relative decrease of $^{230}Th_{xs,0}$, reflecting an effective dilution of the ^{230}Th. Conversely, increases of $^{230}Th_{xs,0}$ are interpreted as a reduction in the sedimentation rate. $^{230}Th_{xs,0}$ can then be used to correct the average sedimentation rate inferred from available dated levels, using the following expression [*Bourne et al.*, 2012-b]:

$$S_i = S_a \frac{Th_{mean}}{Th_i} \qquad \text{Eq.4.}$$

where S_i is the corrected sedimentation rate for interval i (i= 1 to n intervals between two bracketing dated levels), S_a and Th_{mean} are the average linear sedimentation rate and weighted average of $^{230}Th_{xs,0}$ between two bracketing dated levels respectively, and Th_i is the $^{230}Th_{xs,0}$ of interval i. Importantly, this method assumes that the sediment lateral redistribution remains constant throughout the interval of time between the bracketing dated levels, and so may not be applicable to cores with large temporal variations in their sedimentary regimes. However, for cores with minimal variations of lateral redistribution relative to changes in vertical sediment accumulation, this method provides a mean to reconstruct sedimentation rate variations at a higher-resolution than what can be achieved using only the dated levels.

In this study, we revisit the chronologies of North-Atlantic cores SU81-18, SU90-03 and SU90-08 using both the published and newly generated data listed in Table 1. After aligning the SST estimates to the NGRIP $\delta^{18}O_{ice}$ record we used the Th-normalization

235 approach outlined above. From the alignment tie-points we first derive an age model by linear
236 interpolation and calculate the downcore evolution of $^{230}Th_{xs,0}$ (Eq.2 and Eq.3). Then, using
237 Eq.4, we compute a corrected sedimentation rate history and derive a revised age model. As
238 $^{230}Th_{xs,0}$ is age-model dependent, we iterate the process 20 times *i.e.* until a stable age model
239 was reached.
240

241 **2.3 ^{230}Th measurements**

242 ^{230}Th for core SU90-03 was measured by isotopic dilution using a ^{229}Th spike on a
243 single collector, sector field ICP-MS at the University of British Columbia (UBC) following
244 the procedure described by [*Choi et al.*, 2001]. In short, the samples were first acidified with
245 HCl, spiked with ^{229}Th and equilibrated for 24h. Then, the samples were fully digested with
246 an HNO_3-HF mixture. The Fe-oxyhydroxydes, that adsorb or entrain dissolved and particulate
247 Th, were precipitated by adjusting the pH to 8-9 and isolated by centrifugation. After
248 dissolving the residue, the Th fraction was extracted and then purified using two anion
249 exchange columns (AG1-X8 resin). The Th fraction was filtered prior to its measurement.
250

251 **3 Results: Impact of Th-normalization on marine core chronologies**

252 The magnitude of the age model change due to Th-normalization is very different
253 depending on the core location (Figure 2). Among the cores under investigation, the inferred
254 age changes range from less than a year to 940 y. More specifically, for cores SU81-18 and
255 SU90-03 there are negligible changes when comparing the simple linear interpolation
256 between dated levels and the Th-normalized age model, with, on average, age differences of
257 less than 100 y. However, some parts of the records are characterized by larger discrepancies,
258 120-300 y between 17.4 and 21 ka for SU81-18, and around 150 y between 15 and 21 ka for
259 SU90-03. The alignment dating uncertainty mainly arises from the difficulty in identifying

common temperature trends in the marine and Greenland ice records as well from the uncertainties in dating the Greenland reference record itself [*Wolff et al.*, 2010] (see Tables S6 to S8). For SU81-18, the (1σ) uncertainty increases from 150 y around the Younger Dryas (12.7-11.7 ka) to 440 y around 23 ka. For SU90-03, the (1σ) uncertainty is generally higher (mainly because the SST transitions are less well defined) and increases from 206 y around the YD to 700 y around 23 ka. Thus, for these two cores, the age model changes due to Th-normalization remain smaller than the uncertainty on the dated levels themselves. For the interval between 23.29 and 14.64 ka the age change due to Th-normalization corresponds to about half of the dated levels uncertainty for SU90-03 and up to three-quarter of the dated levels uncertainty for SU81-18.

SU90-08 displays the largest chronological disparities, with an average age difference of about 450 y. The largest discrepancy is observed around 16.5 ka and corresponds to an age change of about 940 y. For comparison, the uncertainty on the alignment-dated levels is smaller than 400 y before 23.29 ka (Table S6). Thus, Th-normalization has a significant impact on the SU90-08 age model, especially across Heinrich layers which are characterized by the largest $^{230}Th_{xs,0}$ variations (Figure S5). During these intervals, the ^{230}Th corrected sedimentation rate is up to 4-5 times larger than the background sedimentation rate (Figure S5). In the case of SU90-08, the high variability in the $^{230}Th_{xs,0}$ record results in a drastic increase in sedimentation rate during the Heinrich events. This is indeed expected because additional detrital material would have been transported to the core site by drifting icebergs during these events.

4 Discussion

4. 1 Th-normalization validation

284 The use of radiogenic Th isotopes to reconstruct past sediment fluxes has first been
285 proposed by [*Bacon and Rosholt*, 1982] and widely used since then (*e.g.* [*Suman and Bacon*,
286 1989], see [*François et al.*, 2004] for a review). Because ^{230}Th has been found to be sensitive
287 to changes in particle size or type (*e.g.* [*Chase et al.*, 2002]), or because of necessary
288 reconsiderations of the $^{230}Th_{xs,0}$ calculation method (*e.g.* [*Bourne et al.*, 2012-b; *Missiaen et*
289 *al.*, 2018]), the use of Th-normalization to reconstruct sedimentary fluxes has remained a
290 matter of debate [*Broecker*, 2008; *Marcantonio et al.*, 2014]. However, modeling work
291 [*Henderson et al.*, 1999], sediment trap [*Yu et al.*, 2001] and marine core data [*Costa and*
292 *McManus*, 2017] indicate that Th-normalization can be used to accurately reconstruct past
293 variations in sediment accumulation.
294 In this study, we use Th-normalization to refine the sedimentation rate history between
295 dated levels, an approach, which has yet only been rarely applied (*e.g.* [*Adkins et al.*, 1997;
296 *Bourne et al.*, 2012-a]). Because of the specific use of $^{230}Th_{xs,0}$ and because our study deals
297 with high precision dating, it is worthwhile to summarize the underlying hypothesis of the
298 method first.
299
300 **4.1.1. Underlying assumptions of the Th-normalization method**
301 As highlighted in [*Bourne et al.*, 2012-b], the Th-normalization method relies on the
302 following six assumptions:
303 - 1) Lateral transport of ^{230}Th in the water column is negligible. This assumption is likely
304 valid for the cores studied here given the high particle-reactivity of ^{230}Th, and thus its short
305 residence time in the water column (from a few months up to 50 y for sluggishly-ventilated
306 deep waters [*François*, 2007]) compared to the deep ocean circulation rates.

307 - 2) The ^{232}Th content of the sediment is assumed to be entirely of detrital origin and the
308 lithogenic material is in secular equilibrium *i.e.* $(^{238}U)_{det} = (^{230}Th)_{det.}$. This hypothesis is
309 discussed in details in [*Bourne et al.*, 2012-b].
310 - 3) The incorporation of authigenic uranium occurs at the time of sediment deposition at a
311 known and constant $(^{234}U/^{238}U)$ ratio, generally assumed to be that of seawater, $(^{234}U/^{238}U)_{sw}$
312 =1.1467 ($1\sigma = 0.0025$) [*Robinson et al.*, 2004].
313 A better assessment of the initial $(^{234}U/^{238}U)$ can be obtained with ^{234}U data, but ^{234}U data
314 have rarely been published along with the Th data. In the absence of evidence for a higher
315 initial $(^{234}U/^{238}U)$, we use the seawater value in this study.
316 The estimation of the $^{230}Th_{auth}$ also assumes that the U content has been preserved since the
317 sediment deposition. Indeed, changes in the bottom water oxygenation could lead to a
318 substantial decrease of the authigenic U content by post depositional dissolution processes
319 sometimes referred as "burndown" (see [*Jacobel et al.*, 2017]). In such cases the method
320 presented here would underestimate the $^{230}Th_{auth}$ and thus overestimate the $^{230}Th_{xs,0}$,
321 especially for old sediments. However, post-depositional dissolution of authigenic U is
322 unlikely to produce significant biases in the $^{230}Th_{xs,0}$ in the studied cores over the last 25 ky
323 because i) $^{230}Th_{auth}$ represents at most 10% of the total ^{230}Th measured in these cores (see
324 [*Missiaen et al.*, 2018]) and ii) the potential ingrowth of authigenic ^{230}Th from ^{234}U (half-life
325 245 ky) would not be substantial over the last 25 ky.
326 - 4) A well-constrained age model established by accurately defined dated levels. Indeed, as
327 explained in section 2.2, the method does not alter the age of the dated levels but refines the
328 sedimentation rate and age model in between. The dated levels used in this study are shown in
329 Figure 1 (see supplementary material for further information).

330 - 5) The value of $(U/Th)_{det}$, which represents the ($^{238}U/^{232}Th$) activity ratio of the detrital
331 fraction, and its temporal evolution are sufficiently constrained [*Missiaen et al.*, 2018]. This
332 assumption is discussed in further detail in section 4.1.2.
333 - 6) Sediment focusing is constant between tie-points
334 This last assumption mainly implies that the sedimentary environment would have
335 remained broadly stable through time. In other words, the changes in material inputs to the
336 core location due to lateral sediment redistribution (*i.e.* focusing or winnowing) would be
337 limited compared to vertical sediment flux.
338 Assessing changes in lateral sediment redistribution through time is however not
339 straightforward. [*Bourne et al.*, 2012-b] proposed either (i) to check the sediment composition
340 to track potential changes in sediment type, or (ii) to carry out sortable silt and magnetic
341 properties measurements to retrieve independent constraints on sediment transport by deep
342 currents and grain size variability. However, none of these measurements is a direct indicator
343 of lateral sediment redistribution. Indeed, changes in those sediment properties such as
344 composition or grain size can also be due to changes in vertical inputs, related either to
345 changes in biologic productivity or dust supply.
346 The lateral sediment redistribution can also be assessed using the ^{230}Th data itself by
347 calculating the focusing factor ψ (see text S2 for detailed explanation and [*François et al.*,
348 2004] for a review). First, in order to compute sediment focusing it is necessary to assess the
349 downcore evolution of the dry bulk density, a measurement which is not routinely done on
350 marine sediment cores and which is not available for the cores studied here. In the absence of
351 dry bulk density measurements, the latter can be derived from $\%CaCO_3$ [*Froelich*, 1991].
352 Second, the focusing factor ψ can only be calculated as an average between well-dated levels
353 and is typically a low-resolution variable. Last, the focusing factor absolute value depends on
354 the accuracy of the age model [*Kienast et al.*, 2007]. [*Adkins et al.*, 1997] proposed to use the

355 $\%CaCO_3$ as a proxy for sediment focusing. Assuming a constant (in time) linear relation
356 between ψ and $\%CaCO_3$, they calculated a Th-normalized age using the proxy-derived
357 focusing variations. This approach was not applicable to the cores studied here because i)
358 reliable Holocene radiocarbon dates are needed to constrain the slope between ψ and
359 $\%CaCO_3$ (not applicable for SU90-03- see supplementary information) and ii) this method
360 assumes that the sedimentary regime of the studied time interval is comparable to the one of
361 the Holocene, which is likely not true for the sediment cores studied here due to the presence
362 of IRDs layers.

363 Instead, in order to highlight potential lateral sediment redistribution variations
364 between tie-points, we have evaluated the focusing factor for all four cores (see
365 supplementary text S2). We have calculated the focusing factor ψ on two sets of intervals
366 defined by levels located in between the age-model tie-points (Figure 3). In general, the
367 focusing factor varies between 0.15 and 2, which may reflects changes in sedimentary regime.
368 However, the observed ψ range is much smaller than the values reported in areas
369 characterized by strong sediment redistribution on the seafloor (*e.g.* $1< \psi< 4$ [*Marcantonio et*
370 *al.*, 2010]). More importantly, for sediment cores SU90-03, SU90-08 and SU81-18 the
371 focusing factor remained broadly constant between 14.7 to 23.3 ka, irrespective of the
372 intervals on which the calculation was performed (Figure 3), accounting for an absence of
373 significant sediment lateral redistribution during this time period. The case of sediment core
374 MD03-2705 is further discussed in section 4.1.3.

375 Furthermore, based on the analysis of a compilation of magnetic properties
376 measurements for two of the cores studied here (SU81-18, at the same location as MD95-
377 2042 and SU90-08), [*Kissel*, 2005] concluded that the only significant changes in magnetic
378 properties were associated with the Heinrich events. The increases in both grain size and
379 relative concentrations of magnetic grains mostly result from lithogenic particle supply from

drifting icebergs [*Kissel*, 2005]. Thus, magnetic properties also suggest that in these cores, changes in sedimentary regime were related to changes in the vertical flux of magnetic grains, rather than lateral sediment redistribution.

4.1.2. The impact of temporal variations of $(U/Th)_{det}$

[*Missiaen et al.*, 2018], showed that the $(U/Th)_{det}$ could vary through time, which significantly affects $^{230}Th_{xs,0}$ records for cores with important detrital input, such as cores from the Iberian margin (SU81-18) or cores located in the IRD belt (SU90-08). Thus, before using Th-normalization to refine sediment core age models, we have assessed the impact of a variable $(U/Th)_{det}$ value. We tested this effect using the dataset from core SU90-08, particularly well suited for two major reasons. First, to date, SU90-08 is the only core for which $(U/Th)_{det}$ has been measured downcore; it is thus possible to compare age models obtained with the measured $(U/Th)_{det}$ value and with prescribed $(U/Th)_{det}$ values. Second, this core displays high ^{230}Th-normalized flux variations associated with the Heinrich events, which may imply significant sedimentation rate correction and thus age changes when applying the Th-normalization approach. We computed the age models keeping the same dated levels (described in Table S6) with the following $(U/Th)_{det}$ values: constant $(U/Th)_{det}$ of 0.4 or 0.8 or variable $(U/Th)_{det}$ using the values measured by [*Missiaen et al.*, 2018].

Changes in the $(U/Th)_{det}$ value have a large effect on the SU90-08 $^{230}Th_{xs,0}$ record, particularly in the Heinrich layers. [*Missiaen et al.*, 2018] showed that in the Heinrich layers the ^{230}Th-normalized flux was multiplied by 2 to 3 in response to a change in $(U/Th)_{det}$ from 0.4 to 0.8. As a result, in response to a 0.4 to 0.8 increase in $(U/Th)_{det}$, we observe a 10% change on average of the sedimentation rate obtained from Th-normalization. In the Heinrich layers, the sedimentation rates derived from Th-normalization approach can double depending on the chosen $(U/Th)_{det}$ value (Figure 4). However, changes in the $(U/Th)_{det}$ value do not

405 change the $^{230}Th_{xs,0}$ pattern which exhibits strong increases in sedimentary flux during
406 Heinrich events. Thus, even with the large changes in sedimentation rate, changes in $(U/Th)_{det}$
407 value do not produce substantial changes in the Th-normalized age model for sediment core
408 SU90-08 (Figure 4). Extreme changes in $(U/Th)_{det}$ value (*i.e.* from 0.4 to 0.8) are responsible
409 for an average age change of 65 y and a maximum age change of about 130 y (Figure 4).
410 The drastic changes in the $(U/Th)_{det}$ value applied here result in a shift in ages within
411 the uncertainty of the age model (Table S6). In short, for SU90-08, the combined
412 uncertainties of the current marine core dating techniques are larger than the uncertainty
413 resulting from the choice of $(U/Th)_{det}$ value. In the absence of a quantitative evaluation of
414 temporal variations in the $(U/Th)_{det}$ value for the other cores, the effect of the choice of
415 $(U/Th)_{det}$ value on Th-normalization based chronologies was tested for constant and variable
416 $(U/Th)_{det}$ as detailed in Table S9, Figures S6 and S7. We find that the age model produced by
417 Th-normalization is not significantly affected by the choice of the $(U/Th)_{det}$ value for core
418 SU90-03. Core SU81-18 age model is the most affected by changes in the $(U/Th)_{det}$ value,
419 which is consistent with the high terrigenous supply at this location [*Missiaen et al.*, 2018].
420 However, the overall good agreement between the radiocarbon, tie-points and Th-
421 normalization approaches (Figure 2-Figure S2) gives us confidence in the final age model we
422 produced in this study (see section 4.2).
423
424 **4.1.3. Testing the agreement between Th-normalization and ^{14}C dating for the**
425 **equatorial Atlantic core MD03-2705**
426 One approach to evaluate the robustness of the Th-normalization dating method is to
427 compare the sedimentation rate changes inferred from $^{230}Th_{xs,0}$ with the sedimentation rate
428 changes inferred from ^{14}C dates in regions where changes in surface reservoir ages can be
429 considered negligible. We calculated the Th-normalization corrected sedimentation rate for

different sets of ^{14}C dates (Figure 5) for core MD03-2705. The sedimentation rate variations based on the calibrated ^{14}C are well reproduced by Th normalization in the upper 120 cm of the core (Figure 5b and 5c). Below 120 cm, the sedimentation rates variations inferred from ^{14}C dates are not reproduced using the Th data (Figure 5d-5f) due to the absence of distinct variability in the $^{230}Th_{xs,0}$ record.

It is unclear whether the dampened variability is real or could be related to changes in lateral sediment redistribution. This might be possible because the focusing factor decreases around 120 cm (Figure 3), where the sedimentation rate change is not reproduced by Th-normalization (Figure 5). Another explanation might be that the planktonic foraminifer ^{14}C dates produce artificial sedimentation rate changes. It is indeed well known that a set of radiocarbon dates can create age reversals or artificial sedimentation rate spikes. This could be related to several phenomena, linked to the nature of the archive, such as sediment bioturbation, variations in foraminifer abundances, or changes in chemical erosion (see [*Mekik*, 2014] for a detailed review).

Further investigation is required to distinguish which of the two hypotheses is the most likely in this case. This could be achieved by measuring additional radiocarbon ages from different foraminifer species and at higher resolution.

4.2 A new tie-point for HS1 cooling?

The age-depth relationships of sediment cores located north of 40°N in the Atlantic rely on the alignment of marine surface temperature records with well-dated Greenland ice temperature records. However, there is a lack of well-defined high amplitude events in the Greenland record that can be used as a tie-point between 14.7 and 23.3 ka. Previous research (*e.g.* [*Serno et al.*, 2015])) has shown a correspondence between cold temperatures and increased dust deposition in Greenland, both on glacial-interglacial timescales and also during

455 abrupt climate events. For instance, the onsets of Greenland cold stadials are systematically
456 associated with sharp increases in Greenland dust or dust proxies such as Ca^{2+} (*e.g.* [*Serno et*
457 *al.*, 2015]). This synchronicity between temperature and dust changes in the North Atlantic
458 region is indicative of a role of atmospheric circulation in the transitions in and out of the cold
459 stadial conditions. Our revised chronologies for North Atlantic cores SU90-08, SU90-03 and
460 SU81-18 further support this link between North Atlantic marine temperature and Greenland
461 dust records at the onset of Heinrich Stadial I.

462 The three marine records on the revised chronologies consist of SST reconstructions
463 and the percentage of *N. pachyderma* sinistral (%Nps), a polar foraminifer species, which can
464 serve as a proxy of SST in the North Atlantic (see [*Govin et al.*, 2012, *Eynaud et al.*, 2009]).
465 For these three cores, the use of Th-normalization appears to be a valid approach because, i)
466 there is no evidence for significant focusing variations (see section 4.1.1) and ii) changes in
467 $(U/Th)_{det}$ should not affect the produced age models beyond the dating uncertainties (see
468 section 4.1.2). The time period for which Th-normalization has the most significant impact is
469 in the poorly constrained interval between 14.7 and 23.3 ka. Indeed, by providing additional
470 stratigraphic information between the alignment tie-points, the use of Th-normalization helps
471 to better constrain the three SST records in this interval. Within the dating uncertainties, we
472 find that the three SST records have considerable consistency in the timing of HS1 cooling
473 (Figure 6). Furthermore, the cooling marking the beginning of HS1 in the three studied North
474 Atlantic SST records is synchronous, within dating uncertainties, with the abrupt increase in
475 Greenland Ca^{2+} that can be interpreted as a major event of dust deposition ([*Seierstad et al.*,
476 2014]-Figure 6). The considered sharp increase in NGRIP Ca^{2+} starts at 17.75 ± 0.16 (1σ) and
477 ends at 17.37 ± 0.16 (1σ) ka according to the NGRIP age scale [*Andersen et al.*, 2006;
478 *Rasmussen et al.*, 2006; *Wolff et al.*, 2010].

In detail, we note that the SST transition abruptness varies between our three marine records SU81-18, SU90-08 and SU90-03. The abruptness of a marine SST transition depends on the duration of the cooling but also on the core sample spacing, sedimentation rate as well as the bioturbation level. The three studied cores have different average sedimentation rate: <6.5 cm/ka for SU90-08 and SU90-03, whereas SU81-18 has an average sedimentation rate of about 30 cm/ka. Consequently considering a typical mixed layer of 10 cm, the records from the low sedimentation rate cores SU90-08 and SU90-03 are more affected by bioturbation and likely display smoother transitions [*Bard et al.*, 1987-a]. Furthermore, the two types of SST reconstructions (foraminifera assemblages and %Nps), do not show synchronous changes at the onset of Heinrich Stadial 1: in SU90-03 the foraminifer assemblage SST reconstruction displays a progressive cooling, whereas the %Nps is characterized by a stepwise and more marked SST cooling.

Despite variations of the SST cooling abruptness in our three North Atlantic records, and within the uncertainties, the midpoint of the NGRIP Ca^{2+} record dated at 17.48 ± 0.21 (1σ) ka falls between the onset and end of the SST transition in our 3 marine records. We thus propose to use the sharp increase in Ca^{2+} dated at 17.48 ka ± 0.21 ky (1σ) as a new tie-point corresponding to the midpoint of SST decreases in the northern North Atlantic sediment cores. Filling the gap between 14.7 and 23.3 ka, this new tie-point has the potential to considerably improve North Atlantic marine chronologies based on the alignment of SST to NGRIP.

Based on the arguments above, we can assess what would be the best possible precision of northern North Atlantic core chronologies over the HS1 time interval. . To date, it is difficult to robustly evaluate the uncertainty on Th-normalization based age models since there is no available software for age model construction and uncertainty propagation including Th-normalization. To evaluate the chronological uncertainty we tested the effect of

504 changing the tie-point positions within the uncertainties described in Tables S6 to S8 (Figure
505 6). The chosen position of the tie-point within the defined uncertainties does not change the
506 above conclusions (Figure 6). Furthermore, we can estimate the dating uncertainty of our
507 new tie-point to 0.21 ky by quadratic propagation of the uncertainty of the NGRIP GICC05
508 chronology at 17.48 ka [*Wolff et al.*, 2010] and the duration of the Ca^{2+} transition. The
509 precision of marine core chronologies derived from SST alignment is limited by both the
510 temporal resolution of the SST record, and the dating uncertainties of the target tie-points.
511 The age models uncertainties associated to the onset of HS1 ranges from about 300 years in
512 the best case (SU81-18) to about 900 years for cores with low sedimentation rate and smooth
513 SST transitions (*e.g.* SU90-08 and SU90-03 (see Figure S8)).
514
515 **5 Conclusions**
516 Th-normalization provides a powerful yet underused tool to refine marine core
517 chronologies. However, the successful use of this method requires robust constraints on the
518 underlying assumptions. Among the six major assumptions, two require particular attention: i)
519 the lateral sediment redistribution should remain broadly constant over the studied climatic
520 period ii) the $(U/Th)_{det}$ temporal variations are sufficiently constrained for locations with
521 significant detrital inputs. Monitoring changes in lateral sediment redistribution is crucial
522 because untracked changes in the sedimentation regime can artificially dampen or amplify the
523 reconstructed sedimentation rate history, but to date it remains a challenge because of the lack
524 of a direct and independent proxy for focusing factor. To address the first assumption, we
525 evaluated the lateral sediment redistribution variations for our study locations looking at the
526 published magnetic properties and calculating the focusing factor based on $^{230}Th_{xs,0.}$ To
527 evaluate the second assumption, we investigated the impact of the choice and temporal
528 variations of the $(U/Th)_{det}$ value on the chronologies built using the Th-normalization

technique. Our results show that the age model changes due to variations in the $(U/Th)_{det}$ value are small compared to the uncertainties on the tie-points themselves. Finally we have found good agreement between sedimentation rate changes reconstructed from radiocarbon dates and Th-normalization technique for tropical Atlantic core MD03-2705.

Using combined information from alignment tie-points, radiocarbon dates and Th-normalization, we established comprehensive and high-resolution sedimentation rate history and chronologies for North Atlantic cores SU90-03, SU90-08 and SU81-18. Our results highlight that Th-normalization produces an increase in sedimentation rates across Heinrich events for core SU90-08, as is expected from an increased supply of detrital material from melting icebergs. Interestingly, Th-normalization has the most significant impact on SU90-08, SU90-03 and SU81-18 chronologies in the interval between 14.7 and 23.3 ka where no abrupt climate event is recorded in Greenland ice $\delta^{18}O$ or temperature reconstructions. We show that SST records from these three North-Atlantic records display great consistency. The timing of SST cooling at the onset of the HS1 appears synchronous with the Greenland Ca^{2+} record, interpreted as a proxy for dust deposition. Thus we propose the use of this event dated at 17.48 ± 0.21 (1σ) as a new tie-point corresponding to the mid-slope of HS1 cooling in North Atlantic marine SST records. The use of this new tie-point could lead to a great advance in North Atlantic age modeling as it fills the gap of tie-points between 14.7 and 23.3 ka and allows to better constrain North Atlantic records in this crucial time interval for the study of HS1 and the last deglaciation.

Future work is necessary to further test consistency between radiocarbon based chronologies and alternative dating methods such as tie-point alignment and Th-normalization. If Th-normalization becomes more broadly used as a tool to refine sedimentation rate history, including this age information in Bayesian age model software would become necessary to better evaluate the uncertainty propagation taking into account the

554 uncertainties from $^{230}Th_{xs,0}$ calculation. Finally, additional precise and comprehensive North
555 Atlantic chronologies are necessary to test the use of the NGRIP Ca^{2+} 17.48 ka event as a new
556 alignment tie-point for constraining North Atlantic sediment age models.
557

558 **Acknowledgements**

559 This is a contribution to ERC project ACCLIMATE; the research leading to these results has
560 received funding from the European Research Council under the European Union's Seventh
561 Framework Programme (FP7/2007-2013)/ERC grant agreement 339108. SLJ acknowledges
562 funding from the Swiss National Science Foundation (grants PBEZ2-111588 and
563 PP00P2_144811). SP acknowledges the support from the ENS de Lyon for a CRCT (research
564 sabbatical at the LSCE and MPIC). AB and RG were funded by NERC grant NE/M004619/1
565 awarded to AB. We thank N. Meckler and B. Malaizé for the information provided about
566 core MD03-2705, R. François for his fruitful comments about the focusing factor, M. Soon
567 for her help during SU90-03 $^{230}Th_{xs,0}$ data acquisition, and S. Moreira for his help with R
568 programming. This is LSCE contribution 6570.

569 *Competing interests:* The authors declare that they have no conflict of interests.

570 *Data availability:* The data is given as tables in the supplementary information and will be
571 available online on Pangaea database (https://www.pangaea.de/).
572

573 **Table 1: Records used in this study**
574

Core	Lat (°N)	Lon	Depth (m)	^{14}C data	Radioisotope data (^{230}Th, ^{232}Th, ^{238}U)	Foraminifer-based SST
SU90-08	43.05	30.03°W	3080	[*Vidal et al.*, 1997] [*Missiaen et al.*, 2018]	[*Missiaen et al.*, 2018]	[*Missiaen et al.*, 2018] *full dataset in supporting material*
SU90-03	40.05	32°W	2475	[*Chapman et al.*, 2000]	*This study*	[*Cortijo*, 1999]
SU81-18	37.76	10.18°W	3135	[*Bard et al.*, 1987-b; *Waelbroeck et al.*, 2001]	[*Gherardi et al.*, 2005; *Gherardi et al.*, 2009]	[*Bard et al.*, 1987-b; *Waelbroeck et al.*, 2001]
MD03-2705	18.1	21.2°E	3085	[*Matsuzaki et al.*, 2011] [*Jullien et al.*, 2007]	[*Meckler et al.*, 2013]	[*Matsuzaki et al.*, 2011]

575
576
577

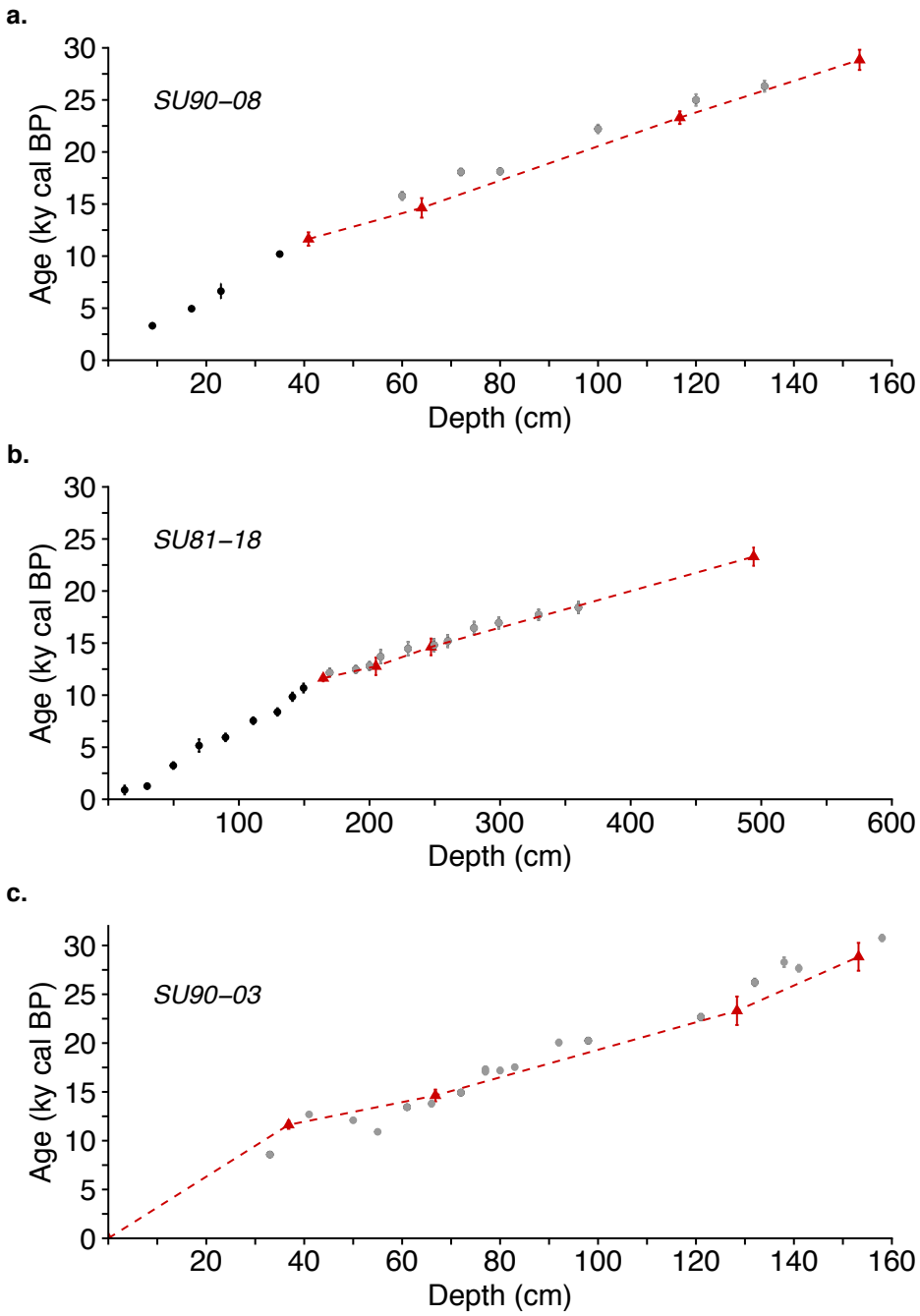

Figure 1: Evaluation of the alignment tie-points for SU90-08, SU81-18 and SU90-03. The red triangles represent the alignment tie-points (SST vs N-GRIP $\delta^{18}O$) with 2σ uncertainty. The red dashed line corresponds to the linear interpolation between the alignment tie-points. The dots represent the calibrated ^{14}C ages assuming a constant surface reservoir age (see text) with 2σ uncertainty. The black dots were used to constrain the Holocene age-depth relationships, the grey dots were not used for age model construction because of likely surface reservoir age variations.
The upper 80 cm of SU90-03 display radiocarbon age reversals and inconsistencies between radiocarbon and alignment stratigraphic information (see Figure S2). We thus chose to consider only the alignment tie-points in the final age model.

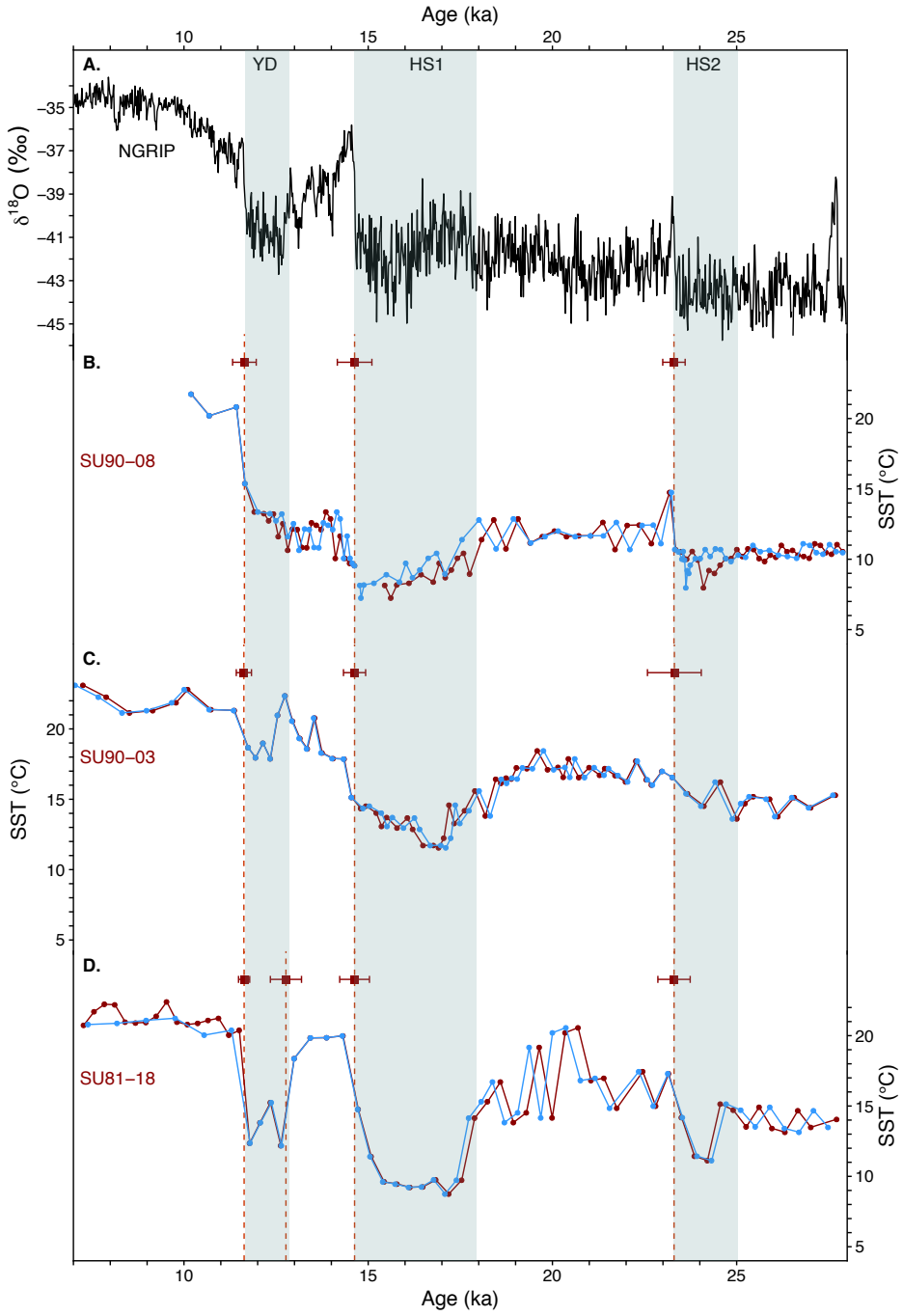

Figure 2: Impact of Th-normalization on the chronologies for SST reconstructions **A.** $\delta^{18}O$ of the ice at NGRIP [*Andersen et al.*, 2006; *Rasmussen et al.*, 2006; *Svensson et al.*, 2006; *Vinther et al.*, 2006], SST records (see Table 1) of core SU90-08 (**B**), SU90-03 (**C**), SU81-18 (**D**). For each subplot, the red squares represent the alignment tie-points and corresponding 1σ uncertainty (Tables S6 to S6), the red curve age scale is based on the alignment tie-points, the blue curve age scale is based on Th-normalization between dated levels. Grey bands represent the Younger Dryas, and Heinrich Stadial 1 and 2 chronozones.

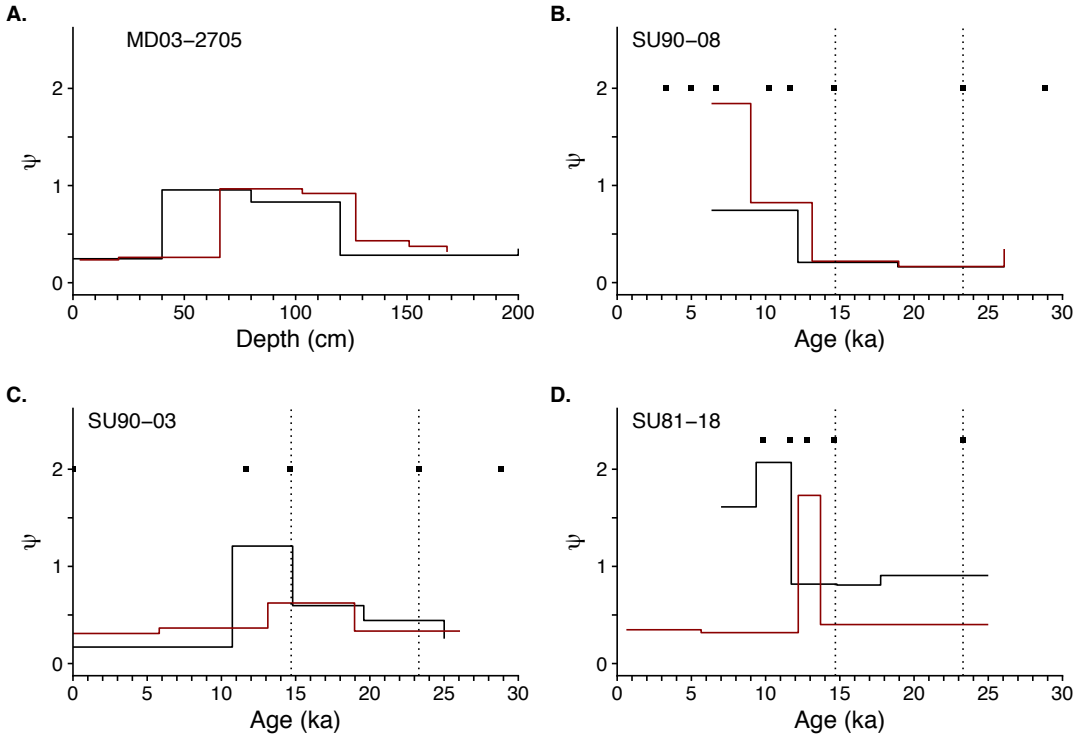

598
599
600 **Figure 3: Focusing factor (ψ) calculations.**
601 **A.** MD03-2705, **B.** SU90-08, **C.** SU90-03, **D.** SU81-18. MD03-2705 results are plotted
602 against depth as in Figure 5. SU90-03, SU90-08 and SU81-18 results are plotted against age
603 as in Figure 6.
604 The different colors represent the different focusing factor values obtained with different
605 choices of dated levels. As we aim at obtaining information about the focusing factor changes
606 between the dated levels, we calculated it on independent intervals, with the number of
607 intervals being similar to the number of intervals defined by the actual dated levels. The black
608 square represent the actual tie-points, the vertical dashed lines delimit the interval of interest
609 between 14.7 and 23.3 ka.
610
611
612
613

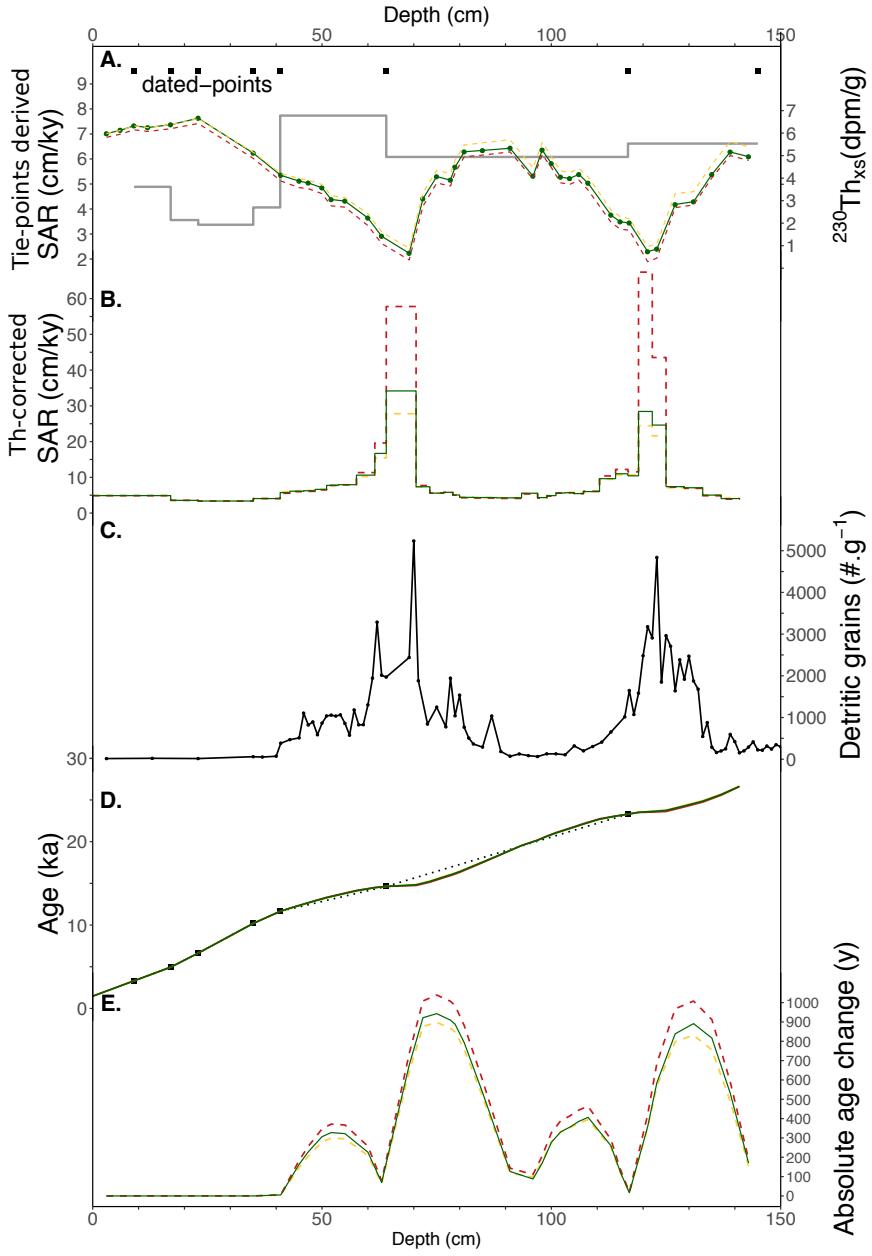

Figure 4: Impact of changes in $(U/Th)_{det}$ on the Th-normalization based chronology for SU90-08. A. Dated levels (black squares), sedimentation rate derived from the dated levels (grey line) and $^{230}Th_{xs,0}$ record **B.** corrected sedimentation rate after applying Th-normalization. **C.** IRD record showing H1 and H2 detrital peaks. **D.** Th-normalization based age model. The dotted line represents the simple age model derived from linear interpolation between dated levels **E.** Absolute change in age due tot Th-normalization with respect to the initial chronology based on dated levels.
For every subplot, the green line represents the quantity calculated using measured (and variable with time) $(U/Th)_{det}$, the orange line represents the quantity calculated with $(U/Th)_{det}$ =0.4 and the red line represents the variable calculated with $(U/Th)_{det}$ = 0.8).

626

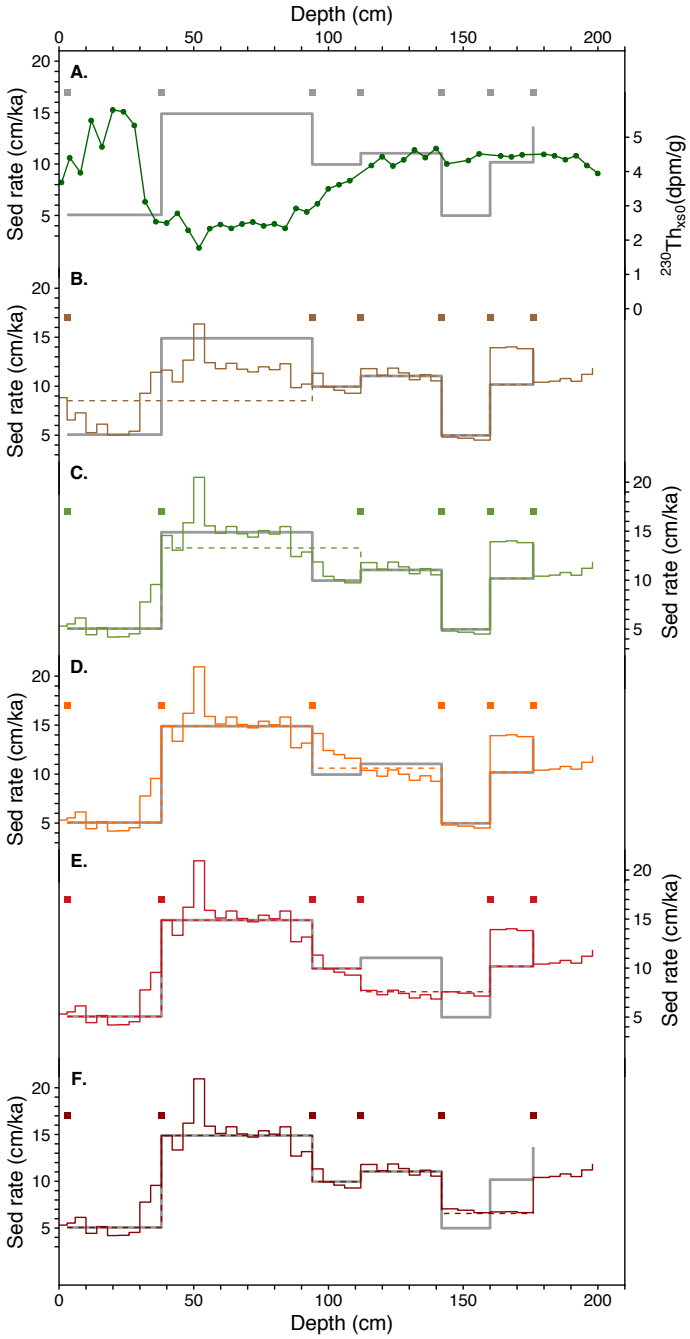

627

628 **Figure 5: Comparison of sedimentation rate changes inferred from calibrated ^{14}C dates**
629 **and Th data for MD03-2705.**
630 For each subplot, the squares indicate the used ^{14}C dates, the bold grey line represents the
631 initial sedimentation rate obtained from linear interpolation when using all the ^{14}C dates, the
632 dashed colored line represents the initial sedimentation rate obtained from linear interpolation
633 using the considered ^{14}C dates and the colored line represents the corrected sedimentation rate
634 obtained by Th-normalization. On the subplot (A), the green line corresponds to the ^{230}Th$_{xs,0}$
635 data.

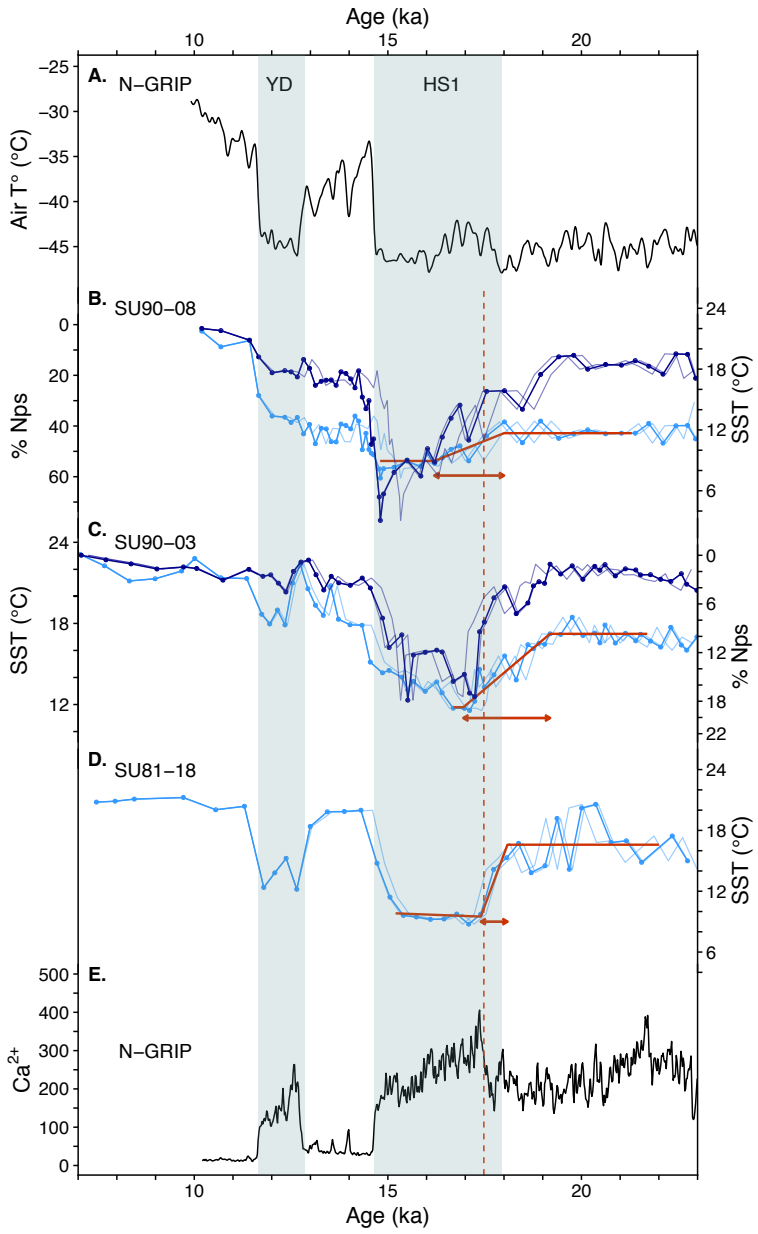

Figure 6: SST reconstructions for the cores SU90-03, SU90-08 and SU81-18 compared with NGRIP air temperature reconstruction and Ca^{2+} record.
A. NGRIP air temperature reconstruction [*Kindler et al.*, 2014] **B-D.** Summer SST reconstructions (light blue) and %N. *pachyderma* s. (dark blue) data for SU90-08 (B), SU90-03 (D), and SU81-18 (E). **E.** NGRIP Ca^{2+} record [*Seierstad et al.*, 2014]
The revised chronologies presented here are derived from radiocarbon dates (during the Holocene), alignment tie-points (for the last deglaciation) and Th-normalization (between the above cited chronological markers). The thin lines represent the envelope curves obtained when moving the alignment tie-points within the uncertainties described in Tables S6 to S8. Precise beginning and end of the cooling observed at the beginning of HS1 were evaluated for the three records using the Rampfit software [*Mudelsee*, 2000] and are represented by the bold red line. bands as in previous figures. The red vertical dashed line represents the mid-ramp of the increase in NGRIP Ca^{2+} at 17.48 ka.

650 **References**

651 Adkins, J. F., E. A. Boyle, L. Keigwin, and E. Cortijo (1997), Variability of the North
652 Atlantic thermohaline circulation during the last interglacial period, Nature, 390, 154,
653 doi: 10.1038/36540
654 https://www.nature.com/articles/36540 - supplementary-information.
655
656 Adkins, J. F., and E. A. Boyle (1997), Changing atmospheric Δ14C and the record of deep
657 water paleoventilation ages, Paleoceanography, 12(3), 337-344, doi:
658 10.1029/97PA00379.
659
660 Andersen, K. K., A. Svensson, S. J. Johnsen, S. O. Rasmussen, M. Bigler, R. Röthlisberger, U.
661 Ruth, M.-L. Siggaard-Andersen, J. P. Steffensen, and D. Dahl-Jensen (2006), The
662 Greenland ice core chronology 2005, 15–42ka. Part 1: Constructing the time scale,
663 Quaternary Science Reviews, 25(23), 3246-3257.
664
665 Austin, W. E. N., and F. D. Hibbert (2012), Tracing time in the ocean: a brief review of
666 chronological constraints (60–8 kyr) on North Atlantic marine event-based
667 stratigraphies, Quaternary Science Reviews, 36, 28-37, doi:
668 https://doi.org/10.1016/j.quascirev.2012.01.015.
669
670 Bacon, M. P., and J. N. Rosholt (1982), Accumulation rates of Th-230, Pa-231, and some
671 transition metals on the Bermuda Rise, Geochimica et Cosmochimica Acta, 46(4), 651-
672 666, doi: https://doi.org/10.1016/0016-7037(82)90166-1.
673
674 Bard, E., M. Arnold, J. Duprat, J. Moyes, and J. C. Duplessy (1987-a), Reconstruction of the
675 last deglaciation: deconvolved records of δ18O profiles, micropaleontological variations
676 and accelerator mass spectrometric14C dating, Climate Dynamics, 1(2), 101-112, doi:
677 10.1007/BF01054479.
678
679 Bard, E., M. Arnold, P. Maurice, J. Duprat, J. Moyes, and J.-C. Duplessy (1987-b), Retreat
680 velocity of the North Atlantic polar front during the last deglaciation determined by 14C
681 accelerator mass spectrometry, Nature, 328, 791, doi: 10.1038/328791a0.
682
683 Bard, E., M. Arnold, J. Mangerud, M. Paterne, L. Labeyrie, J. Duprat, M.-A. Mélières, E.
684 Sønstegaard, and J.-C. Duplessy (1994), The North Atlantic atmosphere-sea surface 14C
685 gradient during the Younger Dryas climatic event, Earth and Planetary Science Letters,
686 126(4), 275-287, doi: https://doi.org/10.1016/0012-821X(94)90112-0.
687
688 Barker, S., W. Broecker, E. Clark, and I. Hajdas (2007), Radiocarbon age offsets of
689 foraminifera resulting from differential dissolution and fragmentation within the
690 sedimentary bioturbated zone, Paleoceanography, 22(2).
691
692 Blaauw, M. (2010), Methods and code for 'classical' age-modelling of radiocarbon
693 sequences, Quaternary Geochronology, 5(5), 512-518, doi:
694 https://doi.org/10.1016/j.quageo.2010.01.002.
695
696 Böhm, E., J. Lippold, M. Gutjahr, M. Frank, P. Blaser, B. Antz, J. Fohlmeister, N. Frank, M.
697 Andersen, and M. Deininger (2015), Strong and deep Atlantic meridional overturning
698 circulation during the last glacial cycle, Nature, 517(7532), 73-76.
699

700 Bondevik, S., J. Mangerud, H. H. Birks, S. Gulliksen, and P. Reimer (2006), Changes in
701 North Atlantic radiocarbon reservoir ages during the Allerød and Younger Dryas,
702 Science, 312(5779), 1514-1517.
703
704 Bourne, M., C. Mac Niocaill, A. L. Thomas, M. F. Knudsen, and G. M. Henderson (2012-a),
705 Rapid directional changes associated with a 6.5kyr-long Blake geomagnetic excursion at
706 the Blake–Bahama Outer Ridge, Earth and Planetary Science Letters, 333-334, 21-34,
707 doi: https://doi.org/10.1016/j.epsl.2012.04.017.
708
709 Bourne, M. D., A. L. Thomas, C. Mac Niocaill, and G. M. Henderson (2012-b), Improved
710 determination of marine sedimentation rates using 230Thxs, Geochemistry, Geophysics,
711 Geosystems, 13(9).
712
713 Broecker, W. (2008), Excess sediment 230Th: Transport along the sea floor or enhanced
714 water column scavenging?, Global Biogeochemical Cycles, 22(1), doi:
715 doi:10.1029/2007GB003057.
716
717 Broecker, W., S. Barker, E. Clark, I. Hajdas, and G. Bonani (2006), Anomalous radiocarbon
718 ages for foraminifera shells, Paleoceanography, 21(2).
719
720 Chapman, M. R., N. J. Shackleton, and J.-C. Duplessy (2000), Sea surface temperature
721 variability during the last glacial–interglacial cycle: assessing the magnitude and pattern
722 of climate change in the North Atlantic, Palaeogeography, Palaeoclimatology,
723 Palaeoecology, 157(1), 1-25, doi: https://doi.org/10.1016/S0031-0182(99)00168-6.
724
725 Chase, Z., R. F. Anderson, M. Q. Fleisher, and P. W. Kubik (2002), The influence of particle
726 composition and particle flux on scavenging of Th, Pa and Be in the ocean, Earth and
727 Planetary Science Letters, 204(1), 215-229, doi: https://doi.org/10.1016/S0012-
728 821X(02)00984-6.
729
730 Choi, M. S., R. Francois, K. Sims, M. P. Bacon, S. Brown-Leger, A. P. Fleer, L. Ball, D.
731 Schneider, and S. Pichat (2001), Rapid determination of 230Th and 231Pa in seawater
732 by desolvated micro-nebulization Inductively Coupled Plasma magnetic sector mass
733 spectrometry, Marine Chemistry, 76(1), 99-112, doi: https://doi.org/10.1016/S0304-
734 4203(01)00050-0.
735
736 Clement, A. C., and L. C. Peterson (2008), Mechanisms of abrupt climate change of the
737 last glacial period, Reviews of Geophysics, 46(4).
738
739 Cortijo, E., S. Lehman, L. Keigwin, M. Chapman, D. Paillard, and L. Labeyrie (1999),
740 Changes in Meridional Temperature and Salinity Gradients in the North Atlantic Ocean
741 (30°–72°N) during the Last Interglacial Period, Paleoceanography, 14(1), 23-33, doi:
742 doi:10.1029/1998PA900004.
743
744 Costa, K., and J. McManus (2017), Efficacy of 230Th normalization in sediments from the
745 Juan de Fuca Ridge, northeast Pacific Ocean, Geochimica et Cosmochimica Acta, 197,
746 215-225, doi: https://doi.org/10.1016/j.gca.2016.10.034.
747
748 Eynaud, F., et al. (2009), Position of the Polar Front along the western Iberian margin
749 during key cold episodes of the last 45 ka, Geochemistry, Geophysics, Geosystems, 10(7),
750 doi: 10.1029/2009GC002398.
751

François, R. (2007), Paleoflux and paleocirculation from sediment 230Th and 231Pa/230Th, Proxies in late cenozoic paleoceanography. Elsevier, 681-716.

François, R., M. Frank, M. M. Rutgers van der Loeff, and M. P. Bacon (2004), 230Th normalization: An essential tool for interpreting sedimentary fluxes during the late Quaternary, Paleoceanography, 19(1), doi: 10.1029/2003PA000939.

Froelich, P. (1991), Biogenic opal and carbonate accumulation rates in the subantarctic South Atlantic: the late Neogene of Meteor Rise Site 704, Proceedings of the Ocean Drilling Program, Scientific Results, 1991, 114, 515-550.

Gherardi, J. M., L. Labeyrie, J. F. McManus, R. Francois, L. C. Skinner, and E. Cortijo (2005), Evidence from the Northeastern Atlantic basin for variability in the rate of the meridional overturning circulation through the last deglaciation, Earth and Planetary Science Letters, 240(3), 710-723, doi: https://doi.org/10.1016/j.epsl.2005.09.061.

Gherardi, J. M., L. Labeyrie, S. Nave, R. Francois, J. F. McManus, and E. Cortijo (2009), Glacial-interglacial circulation changes inferred from 231Pa/230Th sedimentary record in the North Atlantic region, Paleoceanography, 24(2), n/a-n/a, doi: 10.1029/2008PA001696.

Govin, A., et al. (2012), Persistent influence of ice sheet melting on high northern latitude climate during the early Last Interglacial, Clim. Past, 8(2), 483-507, doi: 10.5194/cp-8-483-2012.

Henderson, G. M., and R. F. Anderson (2003), The U-series toolbox for paleoceanography, Reviews in Mineralogy and Geochemistry, 52(1), 493-531, doi: 10.2113/0520493.

Henderson, G. M., C. Heinze, R. F. Anderson, and A. M. E. Winguth (1999), Global distribution of the 230Th flux to ocean sediments constrained by GCM modelling, Deep Sea Research Part I: Oceanographic Research Papers, 46(11), 1861-1893, doi: https://doi.org/10.1016/S0967-0637(99)00030-8.

Henry, L., J. F. McManus, W. B. Curry, N. L. Roberts, A. M. Piotrowski, and L. D. Keigwin (2016), North Atlantic ocean circulation and abrupt climate change during the last glaciation, Science, 353(6298), 470-474.

Jacobel, A. W., J. F. McManus, R. F. Anderson, and G. Winckler (2017), Repeated storage of respired carbon in the equatorial Pacific Ocean over the last three glacial cycles, Nature communications, 8(1), 1727.

Jullien, E., et al. (2007), Low-latitude "dusty events" vs. high-latitude "icy Heinrich events", Quaternary Research, 68(3), 379-386, doi: https://doi.org/10.1016/j.yqres.2007.07.007.

Key, R. M., A. Kozyr, C. L. Sabine, K. Lee, R. Wanninkhof, J. L. Bullister, R. A. Feely, F. J. Millero, C. Mordy, and T. H. Peng (2004), A global ocean carbon climatology: Results from Global Data Analysis Project (GLODAP), Global Biogeochemical Cycles, 18(4), doi: 10.1029/2004GB002247.

Kienast, S. S., M. Kienast, A. C. Mix, S. E. Calvert, and R. François (2007), Thorium‐230 normalized particle flux and sediment focusing in the Panama Basin region during the last 30,000 years, Paleoceanography, 22(2), doi: doi:10.1029/2006PA001357.

Kindler, P., M. Guillevic, M. Baumgartner, J. Schwander, A. Landais, and M. Leuenberger (2014), Temperature reconstruction from 10 to 120 kyr b2k from the NGRIP ice core, Clim. Past, 10(2), 887-902, doi: 10.5194/cp-10-887-2014.

Kissel, C. (2005), Magnetic signature of rapid climatic variations in glacial North Atlantic, a review, Comptes Rendus Geoscience, 337(10), 908-918, doi: https://doi.org/10.1016/j.crte.2005.04.009.

Lynch-Stieglitz, J. (2017), The Atlantic Meridional Overturning Circulation and Abrupt Climate Change, Annual Review of Marine Science, 9(1), 83-104, doi: 10.1146/annurev-marine-010816-060415.

Marcantonio, F., M. Lyle, and R. Ibrahim (2014), Particle sorting during sediment redistribution processes and the effect on 230Th‐normalized mass accumulation rates, Geophysical Research Letters, 41(15), 5547-5554, doi: doi:10.1002/2014GL060477.

Marcantonio, F., R. F. Anderson, S. Higgins, M. Stute, P. Schlosser, and P. Kubik (2010), Sediment focusing in the central equatorial Pacific Ocean, Paleoceanography, 16(3), 260-267, doi: 10.1029/2000PA000540.

Matsuzaki, K. M. R., F. Eynaud, B. Malaizé, F. E. Grousset, A. Tisserand, L. Rossignol, K. Charlier, and E. Jullien (2011), Paleoceanography of the Mauritanian margin during the last two climatic cycles: From planktonic foraminifera to African climate dynamics, Marine Micropaleontology, 79(3), 67-79, doi: https://doi.org/10.1016/j.marmicro.2011.01.004.

Meckler, A. N., D. M. Sigman, K. A. Gibson, R. François, A. Martínez-García, S. L. Jaccard, U. Röhl, L. C. Peterson, R. Tiedemann, and G. H. Haug (2013), Deglacial pulses of deep-ocean silicate into the subtropical North Atlantic Ocean, Nature, 495, 495, doi: 10.1038/nature12006 https://www.nature.com/articles/nature12006 - supplementary-information.

Mekik, F. (2014), Radiocarbon dating of planktonic foraminifer shells: A cautionary tale, Paleoceanography, 29(1), 13-29.

Missiaen, L., S. Pichat, C. Waelbroeck, E. Douville, L. Bordier, A. Dapoigny, F. Thil, L. Foliot, and L. Wacker (2018), Downcore Variations of Sedimentary Detrital (238U/232Th) Ratio: Implications on the Use of 230Thxs and 231Paxs to Reconstruct Sediment Flux and Ocean Circulation, Geochemistry, Geophysics, Geosystems, 0(ja), doi: 10.1029/2017GC007410.

Mudelsee, M. (2000), Ramp function regression: a tool for quantifying climate transitions, Computers & Geosciences, 26(3), 293-307, doi: https://doi.org/10.1016/S0098-3004(99)00141-7.

Obrochta, S. P., et al. (2017), The undatables: Quantifying uncertainty in a highly expanded Late Glacial‐Holocene sediment sequence recovered from the deepest Baltic Sea basin–IODP Site M0063, Geochemistry, Geophysics, Geosystems, 18(3), 858-871, doi: 10.1002/2016GC006697.

856
857 Paillard, D., L. Labeyrie, and P. Yiou (1996), AnalySeries 1.0: a Macintosh software for
858 the analysis of geophysical time-series, Eos, 77, 379.
859
860 Parnell, A. C., J. Haslett, J. R. M. Allen, C. E. Buck, and B. Huntley (2008), A flexible
861 approach to assessing synchroneity of past events using Bayesian reconstructions of
862 sedimentation history, Quaternary Science Reviews, 27(19), 1872-1885, doi:
863 https://doi.org/10.1016/j.quascirev.2008.07.009.
864
865 Rahmstorf, S. (2002), Ocean circulation and climate during the past 120,000 years,
866 Nature, 419, 207, doi: 10.1038/nature01090.
867
868 Ramsey, C. B. (2009), Bayesian analysis of radiocarbon dates, Radiocarbon, 51(1), 337-
869 360.
870
871 Rasmussen, S. O., K. K. Andersen, A. Svensson, J. P. Steffensen, B. M. Vinther, H. B.
872 Clausen, M. L. Siggaard‐Andersen, S. J. Johnsen, L. B. Larsen, and D. Dahl‐Jensen
873 (2006), A new Greenland ice core chronology for the last glacial termination, Journal of
874 Geophysical Research: Atmospheres, 111(D6).
875
876 Reimer, P. J., E. Bard, A. Bayliss, J. W. Beck, P. G. Blackwell, C. B. Ramsey, C. E. Buck, H.
877 Cheng, R. L. Edwards, and M. Friedrich (2013), IntCal13 and Marine13 radiocarbon age
878 calibration curves 0–50,000 years cal BP, Radiocarbon, 55(4), 1869-1887.
879
880 Robinson, L. F., G. M. Henderson, L. Hall, and I. Matthews (2004), Climatic Control of
881 Riverine and Seawater Uranium-Isotope Ratios, Science, 305(5685), 851-854, doi:
882 10.1126/science.1099673.
883
884 Seierstad, I. K., et al. (2014), Consistently dated records from the Greenland GRIP, GISP2
885 and NGRIP ice cores for the past 104 ka reveal regional millennial-scale δ18O gradients
886 with possible Heinrich event imprint, Quaternary Science Reviews, 106, 29-46, doi:
887 https://doi.org/10.1016/j.quascirev.2014.10.032.
888
889 Serno, S., G. Winckler, R. F. Anderson, E. Maier, H. Ren, R. Gersonde, and G. H. Haug
890 (2015), Comparing dust flux records from the Subarctic North Pacific and Greenland:
891 Implications for atmospheric transport to Greenland and for the application of dust as a
892 chronostratigraphic tool, Paleoceanography and Paleoclimatology, 30(6), 583-600.
893
894 Suman, D. O., and M. P. Bacon (1989), Variations in Holocene sedimentation in the North
895 American Basin determined from 230Th measurements, Deep Sea Research Part A.
896 Oceanographic Research Papers, 36(6), 869-878, doi: https://doi.org/10.1016/0198-
897 0149(89)90033-2.
898
899 Svensson, A., K. K. Andersen, M. Bigler, H. B. Clausen, D. Dahl-Jensen, S. M. Davies, S. J.
900 Johnsen, R. Muscheler, S. O. Rasmussen, and R. Röthlisberger (2006), The Greenland ice
901 core chronology 2005, 15–42ka. Part 2: comparison to other records, Quaternary
902 Science Reviews, 25(23), 3258-3267.
903
904 Thornalley, D. J., S. Barker, W. S. Broecker, H. Elderfield, and I. N. McCave (2011), The
905 deglacial evolution of North Atlantic deep convection, science, 331(6014), 202-205.
906
907 Vidal, L., L. Labeyrie, E. Cortijo, M. Arnold, J. Duplessy, E. Michel, S. Becque, and T. Van
908 Weering (1997), Evidence for changes in the North Atlantic Deep Water linked to

909 meltwater surges during the Heinrich events, Earth and Planetary Science Letters,
910 146(1), 13-27.
911
912 Vinther, B. M., H. B. Clausen, S. J. Johnsen, S. O. Rasmussen, K. K. Andersen, S. L. Buchardt,
913 D. Dahl‐Jensen, I. K. Seierstad, M. L. Siggaard‐Andersen, and J. P. Steffensen (2006), A
914 synchronized dating of three Greenland ice cores throughout the Holocene, Journal of
915 Geophysical Research: Atmospheres, 111(D13).
916
917 Waelbroeck, C., J.-C. Duplessy, E. Michel, L. Labeyrie, D. Paillard, and J. Duprat (2001),
918 The timing of the last deglaciation in North Atlantic climate records, Nature, 412(6848),
919 724.
920
921 Webster, J. M., J. C. Braga, M. Humblet, D. C. Potts, Y. Iryu, Y. Yokoyama, K. Fujita, R.
922 Bourillot, T. M. Esat, and S. Fallon (2018), Response of the Great Barrier Reef to sea-level
923 and environmental changes over the past 30,000 years, Nature Geoscience, 1.
924
925 Wolff, E. W., J. Chappellaz, T. Blunier, S. O. Rasmussen, and A. Svensson (2010),
926 Millennial-scale variability during the last glacial: The ice core record, Quaternary
927 Science Reviews, 29(21), 2828-2838.
928
929 Wycech, J., D. C. Kelly, and S. Marcott (2016), Effects of seafloor diagenesis on planktic
930 foraminiferal radiocarbon ages, Geology, 44(7), 551-554.
931
932 Yu, E. F., R. Francois, M. P. Bacon, and A. P. Fleer (2001), Fluxes of 230Th and 231Pa to
933 the deep sea: implications for the interpretation of excess 230Th and 231Pa/230Th
934 profiles in sediments, Earth and Planetary Science Letters, 191(3), 219-230, doi:
935 https://doi.org/10.1016/S0012-821X(01)00410-1.

Paleoceanography and Paleoclimatology

Supporting information for

Improving North-Atlantic marine core chronologies using Th-normalization

L. Missiaen[1,*], C. Waelbroeck[1], S. Pichat[2,1,3] S. L. Jaccard[4] , F. Eynaud[5] , R. Greenop[6], A. Burke[6]

[1]Laboratoire des Sciences du Climat et de l'Environnement, LSCE/IPSL, CEA-CNRS-UVSQ-Université Paris-Saclay, F-91198 Gif-sur-Yvette, France.

[2]Université de Lyon, ENS de Lyon, Laboratoire de Géologie de Lyon (LGL-TPE), F-69007 Lyon, France.

[3]Climate Geochemistry Department, Max Planck Institute for Chemistry, Mainz, Germany.

[4]Institute of Geological Sciences and Oeschger Center for Climate Change Research, University of Bern, CH-3012 Bern, Switzerland

[5]Université de Bordeaux, UMR EPOC 5805, F-33615 Pessac, France

[6]School of Earth and Environmental Science, Irvine Building, University of St Andrews, North Street, St Andrews, KY16 9AL, United Kingdom

* Corresponding author: Lise Missiaen (lise.missiaen@lsce.ipsl.fr)

Contents of this file

Introduction

This supporting information file contains supplementary text (2 sections), which provides more information about the comparison between alignment tie-points, the focusing factor and its estimation using $^{230}Th_{xs,0}$.
It also contains 8 supplementary figures showing the studied core locations (Fig S1), an assessment of the alignment tie-points with respect to the radiocarbon data for cores SU90-03, SU90-08 and SU81-18 (Fig S2), age reversals and radiocarbon dates selection for cores SU90-03 and SU81-18 (Fig S3 and S4), the impact of Th-normalization on SU90-08 records (Fig S5), the impact of different $(U/Th)_{det}$ patterns on the final Th-normalized age model for SU90-03 and SU81-18 (Fig S6 and S7), a test of the proposed new tie-point (Fig S8).
Finally, this file contains 9 supplementary tables gathering the U and Th activities for core SU90-03 (Table S1), the raw and calibrated ^{14}C dates for core MD03-2705, SU90-03, SU90-09 and SU81-18 (Tables S2 to Table S5), the alignment tie-points used in this study for the considered sediment cores SU90-03, SU90-08 and SU81-18 (Table S6 to Table S8) and statistical information about the effect of imposed temporal $(U/Th)_{det}$ patterns (ramp or step functions) on final Th-normalized age models for SU90-03 and SU81-18 (Table S9) .

Text S1: Comparison between alignment tie-points and calibrated ^{14}C dates

The published SST record for core MD03-2705 [*Matsuzaki et al.*, 2011] displays high noise and low amplitude variability, making it difficult to properly identify the typical northern hemisphere deglacial pattern showing an abrupt warming around 14.7 ka (Bolling-Allerod, BA) directly followed by a cooling around 12 ka (Younger Dryas, YD) and final SST rise towards the Holocene (Figure S2). Given the core location, quite far from Greenland, discrepancies with the Greenland pattern are to be expected. Thus, this location is only used to compare the sedimentation history reconstructed from radiocarbon dates and Th-normalization (section 4.1.3).

For core SU90-08, although the SST record displays small amplitude variability, three tie-points corresponding to the end of HS2, HS1 and the YD, respectively have been established [*Missiaen et al.*, 2018]. Comparing the SST evolution plotted against the two age models based on either radiocarbon dates or tie-point alignment, we observe that the ^{14}C based age model shifts the SST transitions to systematically older ages when compared to age model based on SST alignment to Greenland temperature (Figure S2). This is consistent with the core location north of 40°N where increases in surface reservoir ages have been reported for HS1 and the YD (*e.g.* [*Bard et al.*, 1994; *Thornalley et al.*, 2011; *Waelbroeck et al.*, 2001]).

For core SU90-03, the record can be divided into two parts. For the most recent part of the record, after the BA, the ^{14}C based chronology obtained assuming surface reservoir ages of 400 ± 100 y, produces younger transitions than the tie-point alignment chronology by up to 2000 y (Figure S2). This would correspond to decreases in surface reservoir ages that are considered unrealistic. However, the set of ^{14}C dates available for this core reveals an age inversion in the upper part of the record (Figure S3), possibly suggesting sedimentary disturbances. Moreover, the SST decrease, likely corresponding to the YD is much too young in the ^{14}C based chronology. We thus decided not to consider ^{14}C dating in the upper part of core SU90-03. In contrast, in the second part of the record, the SST transitions are systematically older when plotted on the ^{14}C-based chronology compared to the tie-point alignment chronology. This difference can be explained by increasing reservoir ages, which is plausible when considering the core location (~40°N).

Lastly, for core SU81-18, located on the Iberian margin, there is an overall good agreement between the two chronologies down to 20 ka (Figure S2). The ^{14}C-based chronology is rather poorly defined in the older part of the core due to several age reversals (Figure S4). In first approximation, we excluded age reversals and chose to consider the deepest ^{14}C date only.

Text S2: The focusing factor (after [*François*, 2007; *Roger François et al.*, 2004])

The sediments accumulated at one site mostly originate from the vertical settling of particles from the overlying water column. But along the sedimentation process, syndepositional sediment redistribution may occur: if sediments accumulate at the considered site due to lateral advection, there is sediment focusing, if the sediments are removed away from the considered site, there is sediment winnowing. ^{230}Th can be used to determine the level of lateral sediment redistribution. Assuming that all the ^{230}Th produced in the water column is directly scavenged to the sediments and in the absence syndepositional sediment redistribution, the ^{230}Th flux reaching the sediments is known and equal to the ^{230}Th amount produced in the water column above the considered site. From there, [*Suman and Bacon*, 1989] derive the focusing factor (ψ), which corresponds to the ratio between horizontally and vertically transported sediment at the considered site:

$$\Psi_{i,j} = \mathrm{MAR}_{i,j} \frac{[\mathrm{Th}_{xs,0}]_{i,j}}{P_{Th}(t_j - t_i)} \qquad \text{Eq.S1.}$$

Ψ is calculated on the interval [i,j], between depth levels z_i and z_j, using the following physical quantities: $MAR_{i,j}$ is the mean mass accumulation rate on the interval [i,j] and is derived from Eq.S2 using the sediment dry bulk density (DBD) and the linear mean sedimentation rate (LSR) derived from the dated levels bracketing the interval [i,j] of the core (Eq.S3.). $[Th_{xs,0}]_{i,j}$ corresponds to the average $^{230}Th_{xs,0}$ on the interval [i,j], P_{Th} corresponds to the ^{230}Th produced in the considered water column and is calculated using Eq.S4. t_i and t_j correspond to the assigned calendar age of depths levels i and j.

$$\mathrm{MAR}_{i,j} = \mathrm{DBD}_{i,j} \times \mathrm{LSR}_{i,j} \qquad \text{Eq.S2.}$$

$$\mathrm{LSR}_{i,j} = \frac{z_j - z_i}{t_j - t_i} \qquad \text{Eq.S3.}$$

$$P_{Th} = Z(\mathrm{m}) \times 0.0267 (\mathrm{dpm.m^{-3}.y^{-1}}) \qquad \text{Eq.S4.}$$

The sediment dry bulk density (DBD) is not always directly measured from the sediment but can be obtained using the $\%CaCO_3$ measured in routine on sediment cores using the following empirical equation [*Froelich*, 1991]:

$$\mathrm{DBD}\ (\mathrm{g.cm^{-3}}) = 5.313 .10^{-5} \times (\%CaCO_3)^2 + 9.346.10^{-4} \times (\%CaCO_3) + 0.3367 \qquad \text{Eq.S5.}$$

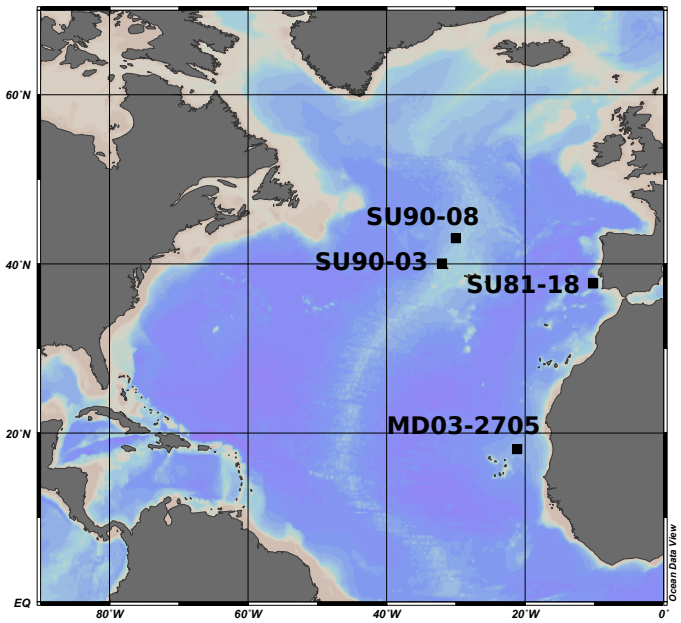

Figure S1. North-Atlantic map showing the location of the cores used in this study.

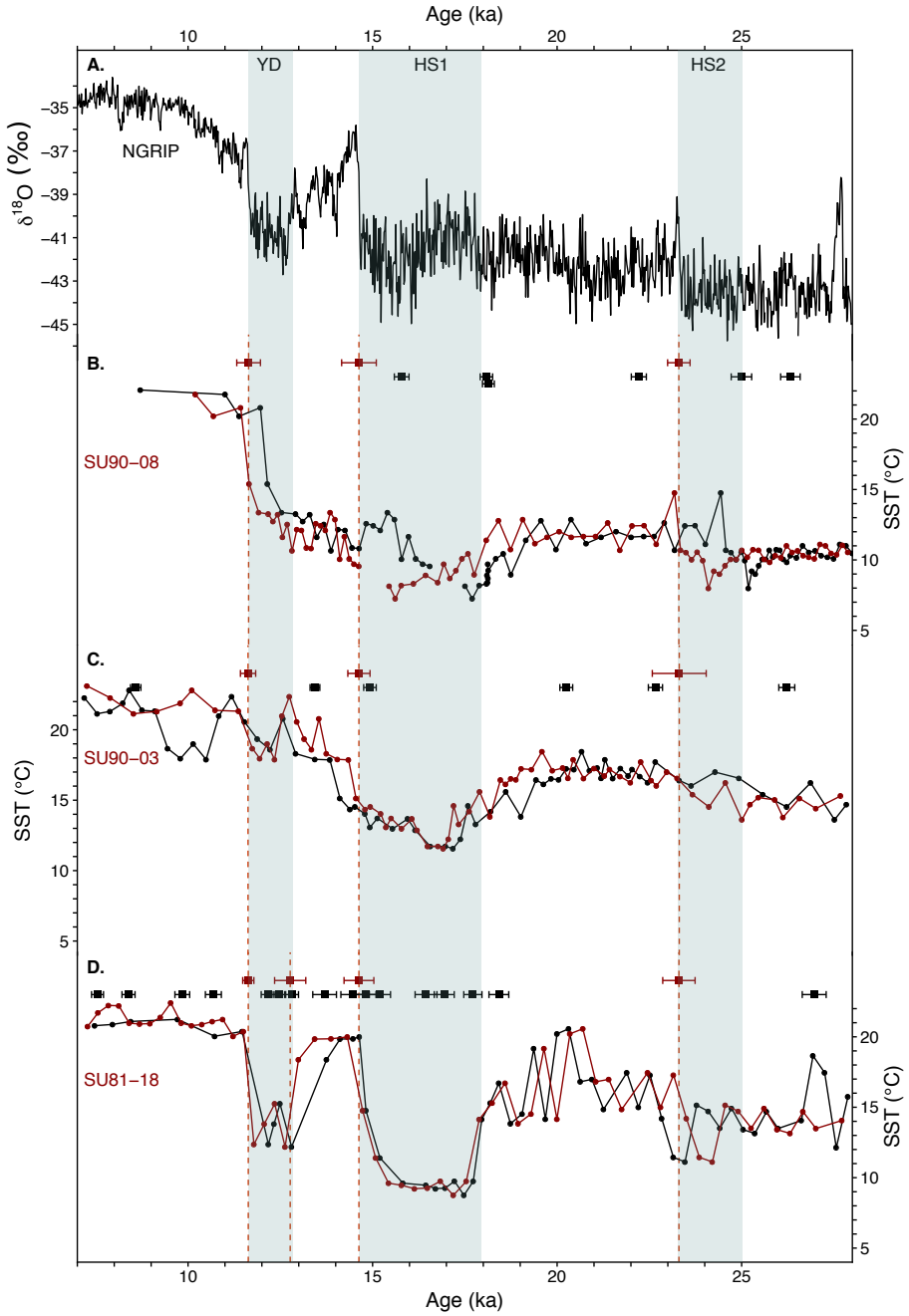

Figure S2: Sea Surface Temperature reconstructions, alignments tie-points and calibrated ^{14}C dates for the studied cores.
A. δ^{18}O of the ice at NGRIP [*Andersen et al.*, 2006; *Rasmussen et al.*, 2006; *Svensson et al.*, 2006; *Vinther et al.*, 2006] **B.** SU90-08, **C.** SU90-03, **D.** SU81-18. In each subplot, the black squares represent the calibrated ^{14}C dates (see section 2.1 for calibration details-Tables S2 to S5), the red dots correspond to the alignment tie-points (Tables S6 to S6); the black curve corresponds to the summer SST reconstructions (see Table 1) and reflects the age-depth relationship based on the calibrated ^{14}C dates, the red curve corresponds to the SST reconstructions reflecting the age-depth relationship based on the alignment tie-points. All

chronologies assume linear age interpolation between dated points (calibrated ^{14}C or alignment tie-points). Grey bands represent the Younger Dryas, and Heinrich Stadial 1 and 2 chronozones.

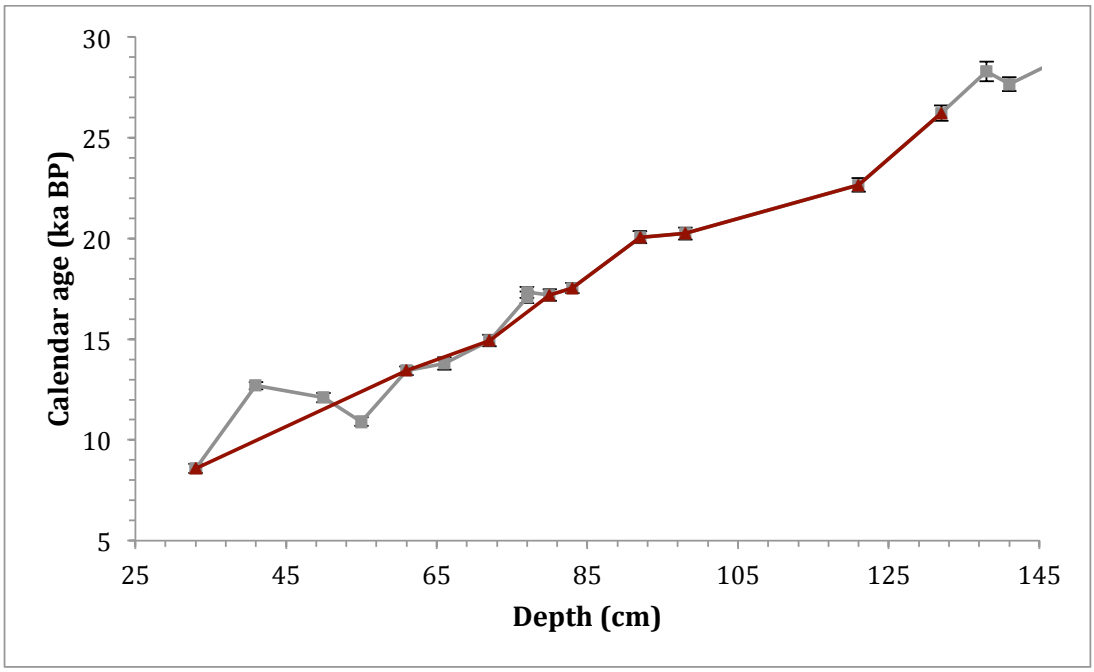

Figure S3: SU90-03 complete set of ^{14}C dates
In grey, all calibrated ^{14}C ages assuming a constant surface reservoir age of 400 ± 100 y, showing age reversals. In red, the selected calibrated ^{14}C ages, avoiding age reversals.

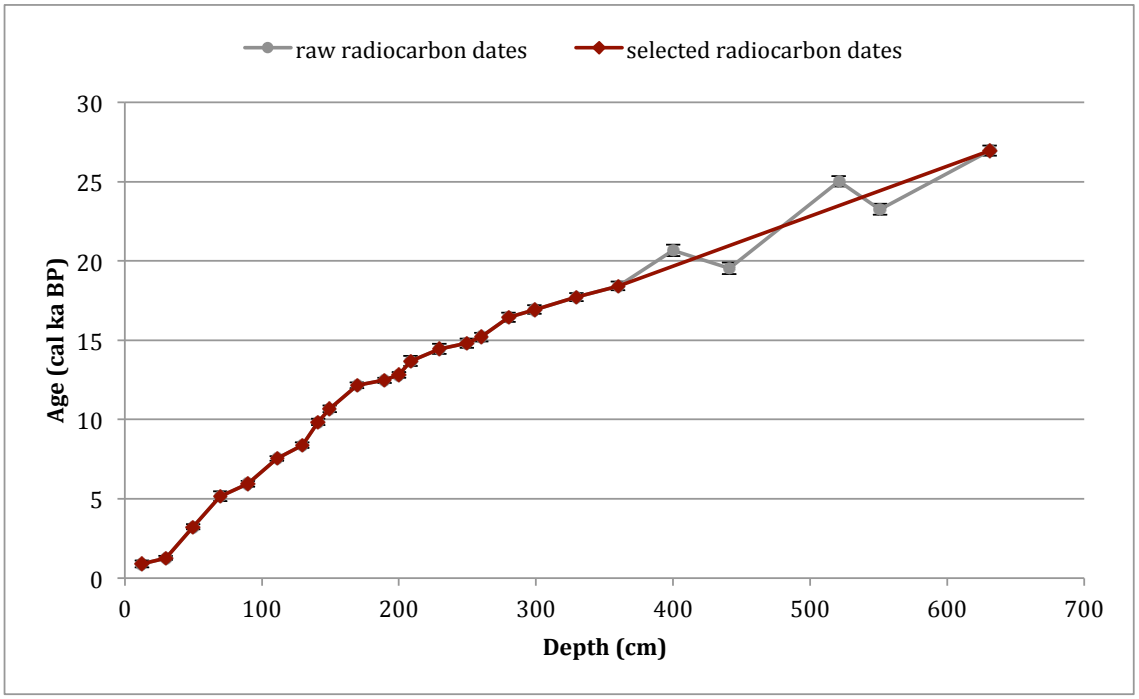

Figure S4: SU81-18 complete set of ^{14}C dates
Grey and red symbols and lines as in Fig. S4.

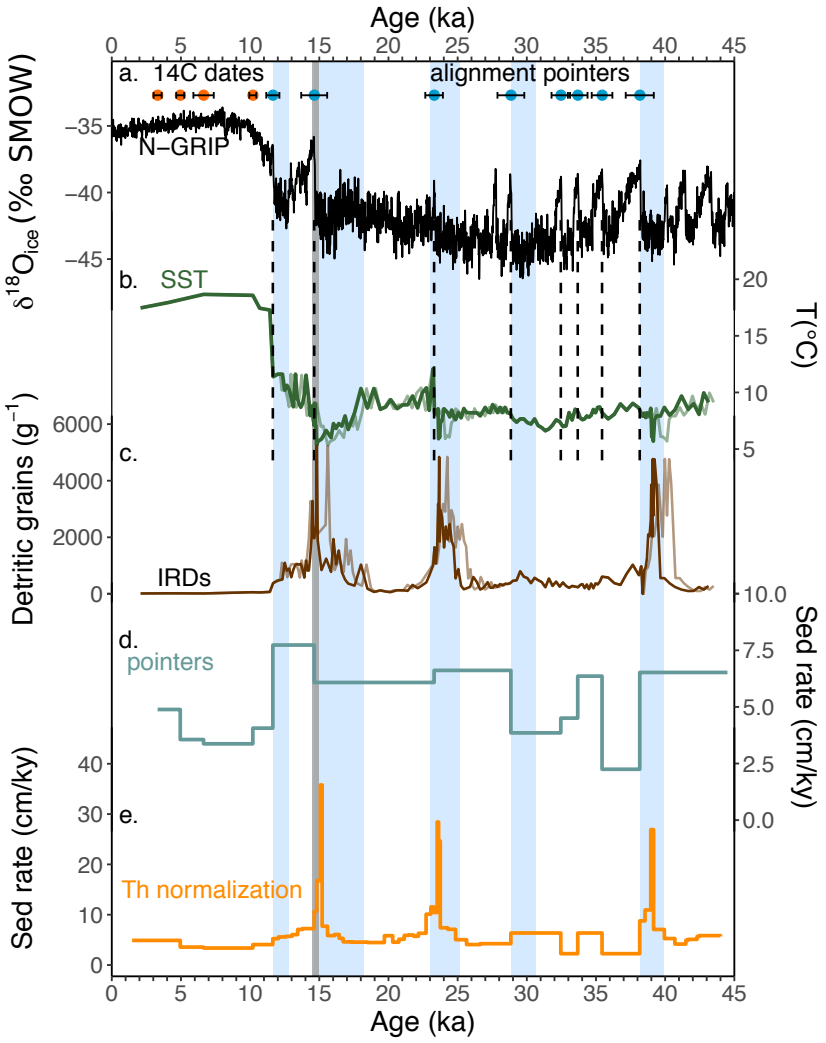

Figure S5: SU90-08 age model evolution with Th-normalization.
a. NGRIP $\delta^{18}O$ and SU90-08 tie-points. **b.** Summer SST reconstruction from planktonic foraminifera assemblages. **c.** Ice Rafted Debris (IRD) record. **d.** Initial sedimentation rate obtained from dated levels (^{14}C dates and alignment tie-points). **e.** Corrected sedimentation rate by Th-normalization. Blue bands correspond to Heinrich Stadials 1 to 4 and Younger Dryas chronozones.

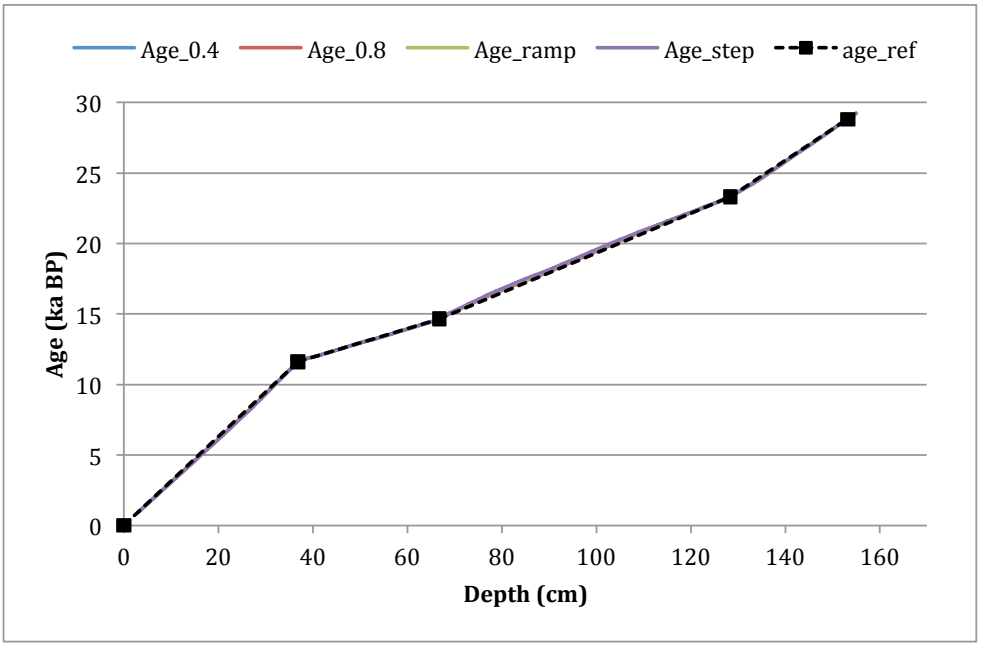

Fig. S6 Impact of the $(U/Th)_{det}$ value on the Th-normalized age model for SU90-03
Age model for different assigned $(U/Th)_{det}$ patterns presented in Table S9. The reference age model (in black) stands for the linear interpolation between dated levels.

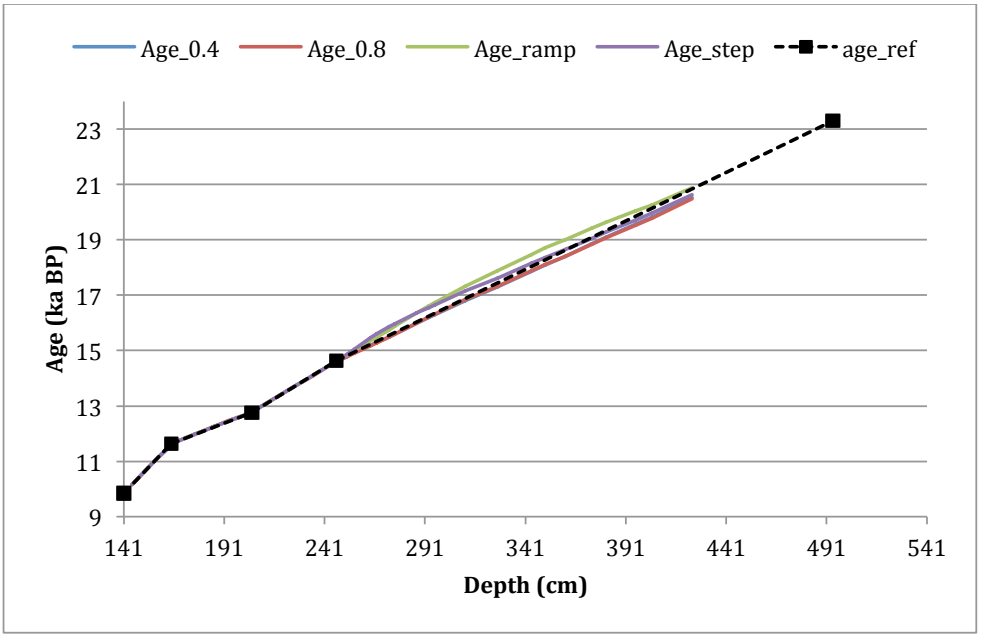

Fig. S7: Impact of the $(U/Th)_{det}$ value on the Th-normalized age model for SU81-18
Age model for different assigned $(U/Th)_{det}$ patterns presented in Table S9. The reference age model (in black) stands for the linear interpolation between dated levels.

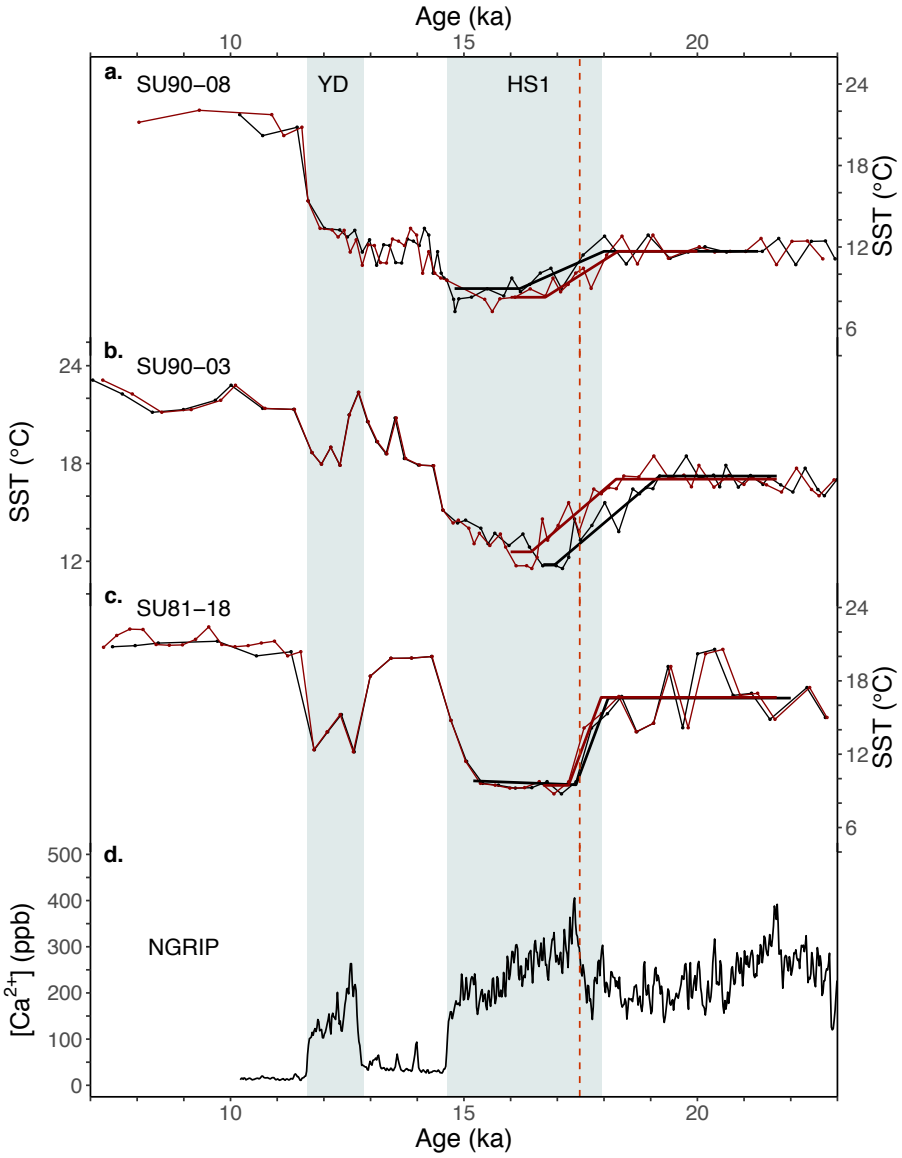

Fig S8: Testing the new tie-point at 17.48 ka ± 0.21
a-c. Summer SST reconstructions SU90-08 (b), SU90-03 (c), and SU81-18 (d) plotted against the revised chronology based on radiocarbon and alignment tie-points and Th-normalization (black), linear interpolation between radiocarbon and alignment tie-points including the new tie-point at 17.48 ± 0.21 ky (red). **d.** NGRIP Ca^{2+} record [*Seierstad et al.*, 2014]
Precise beginning and end of the cooling observed at the beginning of HS1 were evaluated for the three records using the Rampfit software [*Mudelsee*, 2000] and are represented by the bold lines (colors represent the corresponding age model). Bands as in previous figures. The red vertical dashed line represents the mid-ramp of the increase in NGRIP Ca^{2+} at 17.48 ka.
The dating uncertainties of chronologies based on this new tie point depend on both the uncertainty on the targeted tie-point (0.21 ky) and the abruptness of the SST transition (core-dependent). In this case, the uncertainties vary from around 300 years for SU81-18 (high sedimentation rate - 30 cm/ky) to 900 years or more for SU90-08 and SU90-03 (low sedimentation rate < 6 cm/ky).

Table S1: ^{238}U, ^{232}Th and ^{230}Th activities measured in SU90-03 bulk sediment samples.

Depth (cm)	$A^{238}U$ (dpm.g^{-1})	σ	$A^{232}Th$ (dpm.g^{-1})	σ	$A^{230}Th$ (dpm.g^{-1})	σ
3	0.294	-	0.370	-	5.070	0.080
7	0.291	-	0.370	-	5.050	0.060
11	0.293	-	0.380	-	5.100	0.060
15	0.289	-	0.380	-	4.940	0.050
17	0.305	-	0.380	-	4.840	0.100
19	0.284	-	0.380	-	4.850	0.050
21	0.293	-	0.390	-	4.760	0.070
23	0.304	-	0.420	-	5.010	0.100
27	0.315	-	0.460	-	5.060	0.060
29	0.329	-	0.550	-	5.380	0.090
31	0.340	-	0.515	-	5.295	0.090
35	0.348	-	0.560	-	5.160	0.070
37	0.367	-	0.620	-	5.250	0.070
39	0.361	-	0.650	-	5.410	0.090
41	0.360	-	0.630	-	5.260	0.050
43	0.355	-	0.630	-	5.150	0.070
45	0.366	-	0.640	-	5.200	0.070
47	0.337	-	0.600	-	5.180	0.070
49	0.325	-	0.590	-	5.120	0.060
51	0.330	-	0.610	-	5.140	0.080
53	0.356	-	0.690	-	5.300	0.060
55	0.341	-	0.640	-	5.040	0.080
57	0.343	-	0.660	-	5.170	0.080
59	0.356	-	0.680	-	5.200	0.070
61	0.334	-	0.670	-	5.290	0.070
63	0.358	-	0.710	-	5.410	0.070
65	0.388	-	0.770	-	5.540	0.070
67	0.410	-	0.790	-	5.370	0.090
69	0.418	-	0.770	-	4.840	0.070
71	0.451	-	0.770	-	4.390	0.060
73	0.531	-	0.800	-	4.150	0.060
75	0.613	-	0.790	-	4.500	0.070
77	0.797	-	0.790	-	4.030	0.060
79	0.988	-	0.890	-	4.180	0.060
81	1.207	-	0.950	-	4.260	0.060
83	1.371	-	0.940	-	4.030	0.050
85	1.688	-	1.020	-	3.860	0.070
87	2.203	-	1.060	-	3.940	0.090
89	2.418	-	0.720	-	4.200	0.110
91	2.681	-	0.890	-	4.600	0.100
93	2.692	-	0.880	-	4.620	0.120
95	2.742	-	0.830	-	4.420	0.100
97	2.724	-	0.830	-	4.420	0.110
99	3.012	-	0.760	-	4.260	0.090
101	3.304	-	0.750	-	4.630	0.080
103	3.279	-	0.680	-	4.320	0.100
105	3.337	-	0.800	-	4.760	0.090
107	2.887	-	0.710	-	4.110	0.100
109	2.698	-	0.720	-	4.090	0.100
111	2.641	-	0.690	-	4.010	0.090
113	2.327	-	0.650	-	3.980	0.090
115	2.477	-	0.690	-	3.810	0.070
117	2.537	-	0.790	-	4.050	0.120
119	2.227	-	0.710	-	3.890	0.090
121	2.502	-	0.780	-	4.060	0.110
123	2.145	-	0.740	-	4.100	0.090
125	2.107	-	0.720	-	3.920	0.110
127	2.114	-	0.780	-	4.070	0.120
129	1.999	-	0.760	-	3.970	0.090
131	2.083	-	0.870	-	4.100	0.080
133	2.095	-	0.850	-	3.960	0.115

Table S2: ^{14}C dates used in this study for core SU81-18
Raw ^{14}Cages from [Bard et al., 1987-b; Waelbroeck et al., 2001] calibrated ages from this study.

Depth (cm)	^{14}C age (ky)	1σ	Calibrated ^{14}C age (cal ky BP)	1σ
12.5	1.440	0.190	0.892	0.212
29.75	1.810	0.080	1.265	0.129
49.75	3.450	0.100	3.240	0.160
69.5	4.940	0.240	5.162	0.302
89.75	5.640	0.140	5.948	0.183
111	7.190	0.140	7.547	0.162
129.5	7.990	0.120	8.387	0.177
141	9.160	0.130	9.844	0.200
149.5	9.760	0.130	10.686	0.216
169.5	10.790	0.130	12.170	0.188
189.5	11.080	0.140	12.476	0.169
200	11.410	0.170	12.805	0.188
208.5	12.160	0.200	13.700	0.321
229.5	12.660	0.170	14.465	0.324
249.5	12.860	0.150	14.803	0.289
260	13.100	0.170	15.199	0.287
280	13.980	0.190	16.448	0.296
299	14.350	0.180	16.941	0.271
329.5	14.990	0.190	17.717	0.246
360	15.630	0.220	18.422	0.268
631	23.250	0.330	26.966	0.324

Table S3: ^{14}C dates used in this study for core SU90-03
Raw ^{14}C ages from [*Chapman et al.*, 2000], calibrated ages from this study.

Depth (cm)	^{14}C age (ky)	1σ	Calibrated ^{14}C age (cal ky BP)	1σ
33	8.080	0.070	8.581	0.141
61	11.950	0.080	13.438	0.132
72	12.850	0.070	14.929	0.170
98	17.110	0.100	20.248	0.174
121	19.140	0.120	22.664	0.192
132	22.360	0.140	26.223	0.216

Table S4: ^{14}C dates used in this study for core MD03-2705
Raw ^{14}C ages from [*Jullien et al.*, 2007; *Matsuzaki et al.*, 2011], calibrated ages from this study.

Depth (cm)	^{14}C age (ky)	1σ	Calibrated ^{14}C age (cal ky BP)	1σ
3	4.880	0.040	5.134	0.140
38	10.650	0.070	12.053	0.172
94	13.510	0.080	15.813	0.181
112	14.880	0.040	17.621	0.145
142	17.240	0.060	20.337	0.161
160	20.300	0.100	23.948	0.193
176	21.710	0.120	25.521	0.173
302	31.270	0.350	34.750	0.379

Table S5: ^{14}C dates used for core SU90-08
Raw ^{14}C ages from [*Vidal et al.*, 1997], calibrated ages from this study.

Depth (cm)	^{14}C age (ky)	1σ	Calibrated ^{14}C age (cal ky BP)	1σ
60	13.440	0.110	15.788	0.199
72	15.230	0.110	18.084	0.168
80	15.280	0.100	18.138	0.160
100	18.730	0.150	22.214	0.204
120	21.100	0.210	24.994	0.277
134	22.450	0.200	26.321	0.264
162	27.480	0.330	31.018	0.315
170	30.090	0.510	33.785	0.481
192	33.850	0.660	37.825	0.845
210	36.130	0.880	40.319	0.829

Table S6: Alignment tie points for SU90-08 [*Missiaen et al.*, 2018]

Depth (cm)	Start (cm)	End (cm)	Age (ka BP)	1 σ
40.9	41	37	11.641	0.237
64.0	70	58	14.631	0.392
116.7	123	116	23.298	0.318
153.4	160	151	28.848	0.485
167.3	169	166	32.457	0.335
172.8	176	172	33.680	0.355
184.0	186	183	35.438	0.374
190.1	198	187	38.164	0.508
246.0	248	244	46.731	0.527

Table S7: Alignment tie points for SU90-03 (this study)

Depth (cm)	Start (cm)	End (cm)	Age (ka BP)	1 σ
36.8	40	36	11.626	0.206
66.8	68	64	14.630	0.300
128.4	132	126	23.309	0.730
153.2	157	152	28.839	0.714

Table S8: Alignment tie points for SU81-18 (this study)

Depth (cm)	Start (cm)	End (cm)	Age (ka BP)	1 σ
164.6	170	160	11.633	0.151
204.9	210	190	12.768	0.423
247.1	262	240	14.630	0.404
494.1	509	491	23.300	0.438

Table S9: Impact of temporal variations of $(U/Th)_{det}$ on Th-normalization based chronologies for the studied cores

The impact of the choice of the $(U/Th)_{det}$ value was tested comparing the age model obtained with extreme constant $(U/Th)_{det}$ values (0.4 and 0.8) with variable patterns (ramp and step). "Ramp" stands for $(U/Th)_{det}$ changing with time as a ramp function from 0.4 in the Holocene to 0.8 in the glacial. "Step" stands for $(U/Th)_{det}$ changing with time as a step function from 0.4 in the Holocene to 0.8 in the glacial. The reference is the age model derived by linear age interpolation between the dated levels.

Core	Age change (y)	[0.4 –Ref]	[0.8 - ref]	[Ramp – ref]	[Step –ref]
SU90-03	mean	93	88	112	123
	median	99	92	107	111
	minimum	0	0	0	0
	maximum	220	202	262	319
SU81-18	mean	77	83	154	110
	median	27	32	51	38
	minimum	2	2	2	2
	maximum	317	353	454	324

3.2.2 Article summary

As this study focuses on a specific use of the Th-normalization that has rarely been used in the past and deals with high precision dating, the first part of this article discusses the underlying assumptions of the Th-normalization approach.
The first major point is to verify that the changes in sedimentary material inputs to the core location due to lateral sediment redistribution (*i.e.* focusing or winnowing) are limited compared to vertical sediment flux. However, this is not straightforward as, to date, there is no direct proxy for sediment lateral redistribution. The study of magnetic properties measurements suggests that for the considered cores, the changes in sedimentary regime were mainly related to changes in the vertical flux of magnetic grains, notably across the Heinrich events. Moreover, it is possible to calculate a focusing factor from $^{230}Th_{xs,0}$ values themselves. The values calculated between the dated levels for the cores considered suggest that the focusing factor has remained broadly constant across the studied intervals. Thus the Th-normalization method should be relevant and reliable for the studied cores.
The second major point is to evaluate the impact of the changes in the $(U/Th)_{det}$ value on the Th-normalization based chronologies. Indeed, we have seen in chapter 2 that the $(U/Th)_{det}$ value could vary through time and substantially impact the $^{230}Th_{xs,0}$ records in locations with high terrigenous inputs such as the Iberian margin or the IRD belt. The effect of the choice of $(U/Th)_{det}$ value on Th-normalization based chronologies was tested for constant and variable $(U/Th)_{det}$ for the studied cores. In general the combined uncertainties of the current marine core dating techniques (*e.g.*alignment of SST to Greenland temperature, radiocarbon dating, Th-normalization...) are larger than the uncertainty resulting from the choice of $(U/Th)_{det}$ value.
The last point was to compare the sedimentation rate changes inferred from $^{230}Th_{xs,0}$ with the sedimentation rate changes inferred from ^{14}C dates in a region where changes in surface reservoir ages can be considered negligible such as equatorial Atlantic. The sedimentation rates variations from ^{14}C are well reproduced by Th-normalization on the upper part of the core. On the lower part, the absence of notable variability in the $^{230}Th_{xs,0}$ record explains the discrepancies between the two methods. It is unclear though whether this discrepancy is mainly related to changes in sediment lateral redistribution affecting the $^{230}Th_{xs,0}$ record or related to artificial sedimentation rate changes produced by the ^{14}C dates themselves. The ^{14}C can indeed reflect to a certain extent processes such as the sediment bioturbation, the variability in foraminifer abundances, changes in chemical erosion more than the actual accumulation rate evolution.

In the second part of this article, the SST records of three North-Atlantic cores are analyzed using the comprehensive chronologies based on Th-normalization. Interestingly,

the three records display remarkable consistency in the timing of HS1 cooling. This cooling seems synchronous with an abrupt increase in Greenland Ca^{2+}, usually interpreted as major event of dust deposition. This Greenland Ca^{2+} event is thus proposed as a new chronological marker to remedy the general lack of chronological constraints between 14.7 and 23.3 ka for North Atlantic marine records subject to large changes in ^{14}C surface reservoir age.

3.2.3 Article conclusions

This work shows that Th-normalization provides a powerful, yet underused, tool to refine marine core chronologies. However, the successful application of this method requires robust constraints on the underlying assumptions. Among the six major assumptions, two require particular attention: i) the lateral sediment redistribution should remain broadly constant over the studied climatic period ii) the $(U/Th)_{det}$ temporal variations are sufficiently constrained for locations with significant detrital inputs. Interestingly, Th-normalization has the most significant impact on three North Atlantic cores chronologies in the interval between 14.7 and 23.3 ka, where no abrupt climate event is recorded in Greenland ice $\delta^{18}O$ or temperature reconstructions (Wolff et al., 2010). The SST records of these three cores display great consistency and the cooling recorded at the onset of HS1 seems to be synchronous with an abrupt event in Greenland Ca^{2+} dated at 17.48 ka $\pm$ 0.21 (1 σ). We propose to use this event as a new tie-point to fill the gap of chronological marker between 14.7 and 23.3 ka and allow better constraining North Atlantic records in this crucial time interval for the study of HS1 and the last deglaciation.

3.2.4 Article perspectives

The direct perspective of this work is to test the validity of the proposed tie-point by looking at SST records from various sediment cores across the North Atlantic. Additionally, to date it is difficult to evaluate the uncertainty of Th-normalization based chronologies because, on the one hand, there is a lot of uncertainty in the calculation of $^{230}Th_{xs,0}$, but, on the other hand it brings precious high resolution stratigraphical constrains. In the future, if Th-normalization becomes more used to derive marine cores chronologies, including this approach into a more sophisticated age modeling software could become necessary.

3.3 Conclusion

In this chapter we have explored the potential benefits of using $^{230}Th_{xs,0}$ to refine North-Atlantic sediment cores age-depth relationships. As this is a quite rare and specific

use of Th-normalization, a careful look to the method underlying assumptions is necessary. I have shown that Th-normalization can be safely used to refine SU90-08 age-depth relationship. Thanks to this technique I reconstructed SU90-08 high-resolution sedimentation rate history, including drastic sedimentation rate increase across the Heinrich events (see Figure 3.3) as expected regarding the amount of detrital inputs from iceberg discharges. We now have reliable multi-proxy time series, which reflect the correct amplitude of Pa/Th changes (chapter 2) at the correct timing (chapter 3) for sediment core SU90-08.

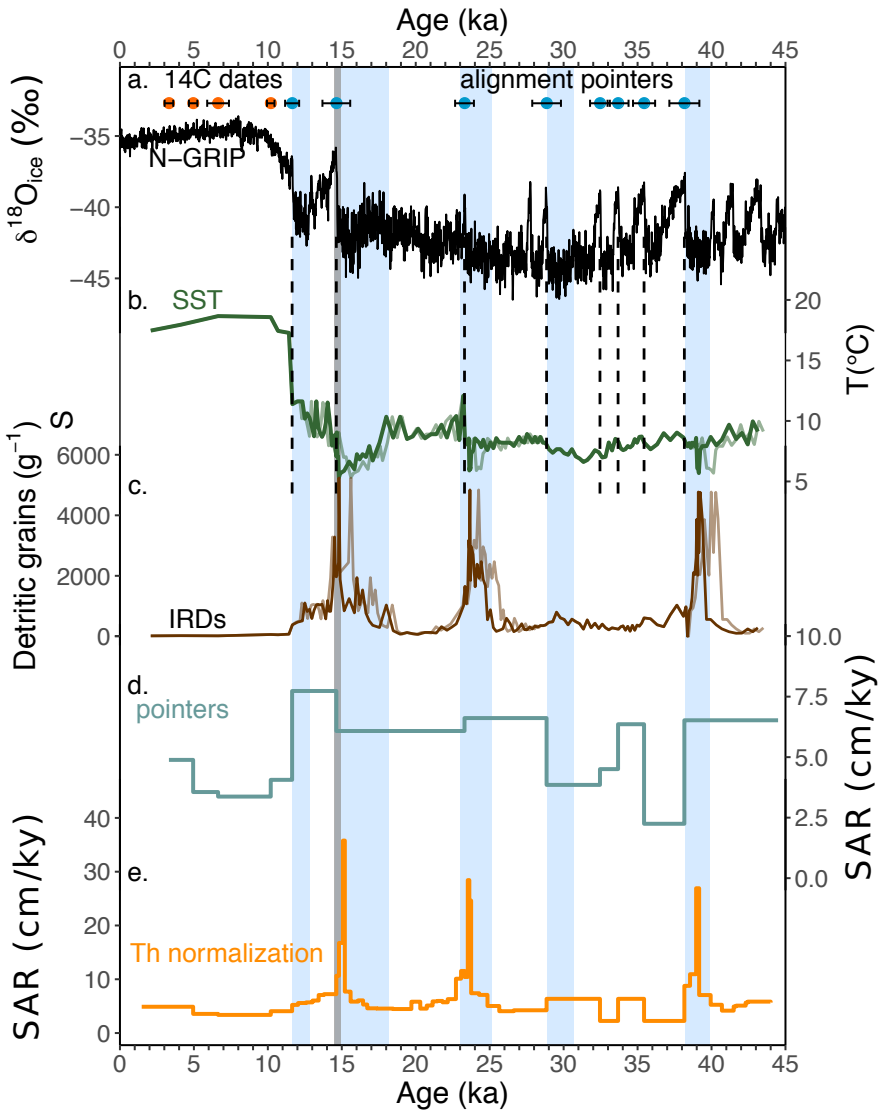

Figure 3.3 – **SU90-08 age model evolution with Th-normalization.**
a. NGRIP δ^{18}O and SU90-08 tie-points. **b.** Summer SST reconstruction from planktonic foraminifera assemblages (see 1). **c.** Ice Rafted Debris (IRD) record. **d.** Initial sediment accumulation rate (SAR) obtained from dated levels (^{14}C dates and alignment tie-points). **e.** Corrected sediment accumulation rate (SAR) by Th-normalization. Blue bands correspond to Heinrich Stadials 1 to 4 and Younger Dryas chronozones.

In the next chapter we focus on the analysis of the multiproxy time series available for SU90-08 to reconstruct past circulation changes (in particular δ^{13}C, Δ^{14}C and sedimentary

Pa/Th). As explained in details in chapter 1, each proxy provides information about different aspects of oceanic circulation such as the ventilation state of the water masses (carbon isotopes) or the overturning rate (sedimentary Pa/Th). We will evaluate the consistency of the information given by the different proxies and compare SU90-08 time series with other North-Atlantic records.

Chapter 4. Multi-proxy time series for sediment core SU90-08

4.1 Introduction

In the two previous chapters, we focused on improving SU90-08 circulation time series over the last 40 ka. Indeed, in chapter 2, we have improved the sedimentary Pa/Th record by constraining the amplitude of its variations assessing the temporal evolution of the $(U/Th)_{det}$ parameter. In chapter 3, we have improved SU90-08 age-depth relationship by combining information from radiocarbon, alignment of surface records to Greenland temperature and the use of Th-normalization technique. We can now focus on the analysis of SU90-08 circulation proxy time series (sedimentary Pa/Th, benthic $\delta^{13}C$ and benthic and planktonic radiocarbon ages) over the last 40 ky.

As explained in details in chapter 1, each proxy offers information about some aspects of temporal variations in the deep Atlantic overturning circulation. In short, the benthic $\delta^{13}C$ indicates the level of ventilation of the considered deep-water mass, which is related to the overturning rate. Though, the observed benthic $\delta^{13}C$ reflects not only the actual overturning circulation speed but also the initial surface $\delta^{13}C$ value and the organic matter mineralization efficiency. The difference between benthic and planktonic ^{14}C ages (^{14}C B-P ages) represents the ventilation of the deep water mass compared to the surface waters. However, the fluctuations of the radiocarbon production in the upper atmosphere and the surface reservoir age changes through time and space complicate its interpretation in terms of circulation strength. Finally, the sedimentary Pa/Th should provide more direct information about changes in water mass speed but its calculation relies on numerous hypotheses. Moreover, taken alone, this proxy only provides qualitative circulation strength evolution history. In summary, each proxy only provides incomplete information about

past circulation changes at the considered location. We thus need to combine them in order to get a more comprehensive view of the past circulation changes at SU90-08 site. Consequently, we address in this chapter the following questions: i) what do we learn about past circulation changes at SU90-08 from each proxy taken separately? ii) Do the proxy agree or show diverging patterns and which hypothesis can we formulate to explain the observations? iii) How does SU90-08 multiproxy record compare with available North Atlantic time series?

4.2 Testing the consistentcy of multi-proxy records

4.2.1 Benthic and planktonic radiocarbon measurements

The benthic and planktonic radiocarbon measurements performed on SU90-08 samples during this thesis require careful examination before being interpreted as deep circulation changes. Indeed, because of the low amount of available microfossils, SU90-08 is a challenging location for radiocarbon measurements. The core has marked IRD layers and thus generally low foraminifer content in these sediment layers. Besides, benthic foraminifers are rare in the deglacial section, except around 50 cm, which roughly corresponds to the YD-BA period. For several sampled levels, it was not possible to gather 3 mg of foraminifers, that are usually required for the the classical Accelerator Mass Spectrometer (AMS). Therefore, we used a recent technique that requires less material: the Mini Carbon Dating System (MICADAS) coupled to a gas introduction system. Instead of being graphitized, the samples are directly acidified and analyzed as CO_2, reducing the required amount of material, processing time and contamination risks. However, this promising technique produced negative Benthic – Planktonic radiocarbon ages (^{14}C B-P ages) for the post HS1 part of SU90-08 record, which cannot easily be interpreted as circulation changes. The detailed study of this radiocarbon dataset is the topic of the article "Small sized foraminifer samples radiocarbon measurements using (ETHZ) MICADAS gas introduction system: insights into sediment archive preservation" in preparation for submission to the journal *Radiocarbon* and inserted below. Briefly, in this article, I show that the negative ^{14}C B-P ages cannot result from either an analytical issue or the imprint of hydrothermal activity on radiocarbon content, and cannot be the consequence of dissolution/recrystallization processes on the analyzed material. Instead, I argue that the observed negative ^{14}C B-P ages reflect the heterogeneity of the sediment samples, probably attributable to sediment bioturbation in a context of reduced radiocarbon age gradient between the surface and deep waters. The ventilation and oxygenation history of the location as well as idealized Monte Carlo simulations support this hypothesis (see article below for details).

Small sized foraminifer samples radiocarbon measurements using (ETHZ) MICADAS gas introduction system: insights into sediment archive preservation

L. Missiaen[1,*], L.Wacker[2], B.C. Lougheed[1], L. Skinner[3], I. Hajdas[2], J. Nouet[4], C. Waelbroeck[1]

[1]Laboratoire des Sciences du Climat et de l'Environnement, LSCE/IPSL, CEA-CNRS-UVSQ-Université Paris-Saclay, F-91198 Gif-sur-Yvette, France.

[2]Laboratory of Ion Beam Physics, ETH Zürich, 8093 Zürich, Switzerland

[3]Godwin Laboratory for Palaeoclimate Research, Department of Earth Sciences, University of Cambridge, Cambridge CB2 3EQ, United Kingdom

[4]Université Paris Sud – Paris Saclay, UMR-CNRS GEOPS 8148, Bât. 504, Rue du Belvédère, 91405 Orsay, France

to be submitted to Radiocarbon

* Corresponding author: Lise Missiaen (lise.missiaen@lsce.ipsl.fr)

Key Points:

- Gas introduction system generates radiocarbon measurements that are accurate, reproducible (within 2σ uncertainty) and comparable to standard graphite measurements.
- Despite high gas measurement quality, SU90-08 measurements produce repeated negative Benthic-Planktonic ^{14}C ages.
- In addition to stable isotope measurements, small-sized foraminifer gas ^{14}C measurements highlight marine core bioturbation.

Abstract:

Radiocarbon is an appealing tool for paleoceanographers as it can be used to build absolute chronologies and to reconstruct past ocean ventilation and carbon cycle changes over the last 40 ky (cal BP). To date, the sample size requirements have restricted the temporal resolution of marine radiocarbon records, especially in cores with limited foraminifer content, thus impeding the use of radiocarbon in the understanding of abrupt climate events. Recent developments demonstrated that radiocarbon measurements of small-sized foraminifer samples are now possible using gas introduction system at the cost of a small decrease in precision. Here we explore the potential of gas radiocarbon measurements on benthic and planktonic foraminifers from sediment core SU90-08 (43°03'1 N, 30°02'5 W, 3080m). We show that our radiocarbon gas measurements are accurate, generally reproducible within 2σ uncertainty and comparable to standard graphite measurements. However, both gas and graphite measurements produce repeated and anomalous negative ^{14}C Benthic-Planktonic ages for the post Heinrich event 1 part of the record. These negative radiocarbon age differences cannot be explained by hydrothermal imprint or by dissolution/recrystallization processes. Instead, we argue that they reflect the modern-like small radiocarbon age gradient between the deep and surface waters at this location since the end of Heinrich event 1. Due to the small surface-depth ^{14}C age gradient, any differential bioturbation effect on benthic and planktonic foraminifers may result in negative B-P ages. More so than stable isotope measurements, small-sized gas radiocarbon measurements visually highlight the mixing state of sedimentary archives, the latter being a greater obstacle for past ocean ventilation reconstructions from radiocarbon measurements than the measurements precision itself.

INTRODUCTION

Radiocarbon (^{14}C) is a versatile tool applicable on various materials such as wood, terrestrial speleothems or marine sediment cores over a time period covering the last 50 ka (ky cal BP). It has been widely used by paleoceanographers to derive age-depth relationships for marine sediment cores. Usually, a ~1-3 mg of selected monospecific planktonic foraminifers are radiocarbon dated by Accelerator Mass Spectrometry (AMS) and the radiocarbon age is converted into a calendar age using atmospheric calibration curves (*e.g.* IntCal13-[*Reimer et al.*, 2013]) and an appropriate software (*e.g.* OxCal [*Ramsey*, 2009], Bchron [*Parnell et al.*, 2008], Bacon [*Blaauw*, 2010] and Undatable [*Obrochta et al.*, 2017; *Webster et al.*, 2018]). Radiocarbon has numerous other applications in paleoceanography such as reconstructing past ocean ventilation and water mass circulation history or tracing past carbon cycle evolution, in particular oceanic CO_2 outgassing during the last deglaciation. Indeed, as radiocarbon is produced in the upper atmosphere after interaction between the cosmic rays and atmospheric ^{14}N, it enters into the ocean via air-sea exchange with surface waters. As soon as a water parcel is isolated from the surface, its ^{14}C content starts to decrease exponentially with time due to radioactive decay (half-life of ^{14}C = 5,730 ± 40 yrs). The ^{14}C content of foraminifer specimens reflects the ^{14}C content of the water mass in which the shell formed [*Stuiver and Polach*, 1977]. Thus, by determining the ^{14}C age of benthic foraminifer samples of independently known calendar age, one can reconstruct past ocean ventilation, in other words, assess the time elapsed since the tracked deep-water parcel has been isolated from the surface (e.g. [*Skinner and Shackleton*, 2004; *Thornalley et al.*, 2015]). The method has a few caveats. Due to changes in solar activity and geomagnetic field strength, the radiocarbon production rate in the upper atmosphere is not constant through time. Thus, it becomes necessary to compare reconstructed deep-water radiocarbon history with the one of the atmosphere, compiled the most recently in IntCal13 [*Reimer et al.*, 2013] and look at

benthic – atmosphere (B-atm) radiocarbon age differences (e.g. [*Chen et al.*, 2015; *Freeman et al.*, 2016; *Skinner et al.*, 2014]). Alternatively, [*Broecker et al.*, 1984] proposed to directly study the ^{14}C age difference between benthic and planktonic foraminifers giving the ventilation difference between surface and deep waters without requiring precise and independent calendar age determination. An additional benefit of this method is that it does not require the evaluation the reservoir age, the radiocarbon age difference between the surface ocean and the contemporary atmosphere, which has been shown to vary through space and time, especially in the North Atlantic region [*Bard et al.*, 1994; *Bondevik et al.*, 2006; *Thornalley et al.*, 2011; *Waelbroeck et al.*, 2001].

Radiocarbon is thus an appealing tool for paleoceanographers as it has a wide range of possible applications and the potential to elucidate highly debated questions about ocean circulation changes across millennial scale climate events and the last deglaciation [*Lynch-Stieglitz*, 2017]. However, a current limitation for the method is that the large amount of carbonate material traditionally required by the graphitization technique involves picking hundreds of foraminifera specimens for a single ^{14}C date [*Hughen et al.*, 2006]. Overcoming the sample size limitation has become necessary to study millennial scale climate events, as they require the construction of high-resolution proxy records. Millennial scale events, such as Heinrich events, are imprinted on the North Atlantic marine sediment cores in the form of coarse detrital material layers from iceberg discharges. Consequently, these sediment layers contain a very limited amount of foraminifer material, in particular benthic specimens. Hence, obtaining radiocarbon records for these samples was usually not feasible until recent technical advances. In the past decade, efforts have been made to lower the sample size for conventional graphite targets, for example by adjusting the graphitization reaction parameter, *i.e.* improving the pre-treatment and performance of the catalyst powder [*Freeman et al.*, 2016] or changing the reaction volume [*Walter et al.*, 2016] or temperature [*Santos et al.*,

2007]. Therefore, the typical sample size for conventional graphite target analysis dropped from above 10 mg to 3 mg of $CaCO_3$. New designs such as the Mini Carbon Dating System (MICADAS) allow the analysis graphite targets of less than 1 mg $CaCO_3$ (*e.g.* [*Gottschalk et al.*, 2018]). Besides, the MICADAS device enables the analysis of CO_2 targets instead of graphite targets. This technology has two major benefits: i) the sample size is reduced ii) the measurement is performed online, without the graphitization step resulting in a substantial reduction of sample preparation cost and time, as well as lower risk of contamination by modern atmospheric radiocarbon during the preparation procedure.

The possibility of analyzing ultra-small foraminiferal samples (<0.5 mg $CaCO_3$) [*Lougheed et al.*, 2012; *Wacker et al.*, 2013] and even single foraminifer (<0.1 mg $CaCO_3$) [*Lougheed et al.*, 2018; *Wacker et al.*, 2013] has been evidenced but sample material for age determination should ideally be larger than 40 µg C (~0.3 mg $CaCO_3$) in order to contain a sufficient number of individuals to reliably represent sediment level analyzed. [*Gottschalk et al.*, 2018] showed that gas ^{14}C analysis of small sized (~0.3-0.6 mg $CaCO_3$) foraminifera samples give accurate results with only a slight precision decrease (a few tens of years on radiocarbon scale) compared to conventional AMS measurements. Despite the apparent advantages, radiocarbon gas measurements have rarely been used for paleoceanographic studies and measurements are still needed to further test the accuracy and reproducibility of small sized foraminifer sample ^{14}C gas measurements.

Here we report new benthic and planktonic gas ^{14}C measurements from North-Atlantic core SU90-08 (43°03'1 N, 30°02'5 W, 3080m). We systematically measured two aliquots of gas samples and compared those results with conventional graphite measurements (n=10). The goal of this study is to i) further test the reproducibility and accuracy of small sized gas introduction radiocarbon measurements on deep-sea foraminifer samples using the

MICADAS system and ii) assess the benefits of these measurements for the study of past ocean ventilation.

STUDY SITE AND METHODOLOGY

Sample material

Sediment core SU90-08 was retrieved in 1990 by the French R/V *Suroît* during the "*Paleocinat"* cruise on the mid Atlantic ridge flank, in the western Atlantic basin (43°03'1 N, 30°02'5 W, 3080m). The sediment available cover about 260 ky of climate history and the average sedimentation rate is 4.6 cm/ky [*Bout-Roumazeilles et al.*, 1999; *Grousset et al.*, 1993]. The sediment is mainly composed of carbonates (foraminifera ooze and nanofossils) interbedded with clay layers [*Bout-Roumazeilles et al.*, 1999]. Levels showing accumulation of coarse detrital material from iceberg discharges, Ice Rafted Debris (IRDs), attributed to Heinrich events 1, 2 and 4 have been identified in the first 250 cm of the core corresponding to the last 40 ka [*Bout-Roumazeilles et al.*, 1999; *Kissel*, 2005; *Vidal et al.*, 1997].

Bulk wet sediments were oven-dried (50°C) for about 48h and then water-sieved at 150µm mesh to remove clay particles. The >150µm fraction was rinsed with de-ionized water and oven-dried (50°C) for about 24h. Benthic and planktonic foraminifers were handpicked from respectively 28 and 29 sediment levels covering the last 25 ky. The low availability of benthic foraminifers, especially within the Heinrich layers, motivated the gas introduction system analyses. Because the represented genus of benthic foraminifers changes downcore, mixed benthic species (excluding porcelaneous and agglutinate specimens) were picked. To minimize the bioturbation effect on planktonic radiocarbon dates, we only selected specimens amongst the most abundant species: *G. bulloides and N. pachyderma* sinistral for 27 and 2 levels, respectively (see Fig S1). Singles species samples of *G. ruber* (n=8) were also prepared to assess radiocarbon age difference between coexisting species (*e.g.* [*Broecker et*

149 *al.*, 1988; *Mekik*, 2014]). To assess the value of the foraminifer blank, we also picked samples
150 of radiocarbon-dead foraminifers from the core bottom (>260 ky cal BP).

151 The foraminifers selected for gas measurements were cleaned only with de-ionized
152 water. No oxidative treatment (*e.g.* H_2O_2) was applied to preserve the shell integrity and avoid
153 potential contamination with modern atmospheric CO_2. Under the binocular, the selected
154 foraminifers appeared complete and did not display dissolution feature or extraneous
155 sediment/residue attached to the outer shell. Because the small samples are more sensitive to
156 contamination as their size decreases [*Gottschalk et al.*, 2018], we targeted homogenous
157 sample size. For our gas measurements, it was 0.97 ± 0.29 (1 σ) mg $CaCO_3$. After picking and
158 weighing, each sample was put in septum sealed glass vials and flushed with He at 50
159 mL/min for 5 min in order to remove the modern CO_2 from the vials.

160 The radiocarbon analysis was carried out at the Laboratory of Ion Beam Physics at
161 ETH Zürich using MICADAS AMS [*Synal et al.*, 2007] with a helium stripping system,
162 which leads to better signal on small samples, coupled to an Ionplus carbonate handling
163 system [*Wacker et al.*, 2013].

164

165 **Reproducibility and accuracy**

166 In order to assess the reproducibility of our gas measurements, we systematically
167 replicated our planktonic and benthic ^{14}C measurements when enough material was available
168 for the deglacial section of SU90-08. Along with the samples, standard material was also
169 measured to assess the accuracy of the measurements and process the radiocarbon data with
170 normalization to standard method. Multiple measurements of the IAEA standards C2
171 (travertine, consensus $F^{14}C$ value = 0.4114 ± 0.0003, $\delta^{13}C$= -8.25 ± 0.31‰ VPDB [*Rozanski*
172 *et al.*, 1992]) and C1 (marble, consensus $F^{14}C$ = 0.0000 ± 0.0002, $\delta^{13}C$=-2.42 ±0.33 ‰ VPDB
173 [*Rozanski et al.*, 1992]) and CSTD standard (coral, $F^{14}C$ = 0.9445 ± 0.0018 [*Gao et al.*,

2014]) were performed. For the sake of consistent sample-standard comparison, the standard sizes were equivalent to the sample size (~1 mg). Additionally, the National Institute of Standards and Technology (NIST) standard oxalic acid II (OxII) was also analyzed directly as CO_2 from a purchased gas bottle (Ionplus, Switzerland). The data processing was performed with the software BATS (version 4.20 [*Wacker et al.*, 2010]) and includes the selection of the current plateau, correction for isotopic fractionation from the AMS using $\delta^{13}C$ and the blank contribution using the foraminifer blanks. Uncertainties are fully propagated for each correction.

Twelve ^{14}C gas measurements were compared with standard graphite analysis for the same depths. Graphite measurements were performed either at ETH Zürich (n=7, [*Hajdas*, 2008; *Hajdas et al.*, 2007].) or Chrono Center, Queens University Belfast (n=4).

Leaching analysis

The online gas measurement and carbonate handling system setting allows for a weak leaching prior to the total sample dissolution [*Bard et al.*, 2015]. The samples were first acidified with 100 µL of 0.02 N HCl for at least 30 min at 50°C temperature, which dissolved 120 µg of $CaCO_3$ in each sample. The CO_2 produced by the reaction is flushed into the MICADAS and analyzed as the leach fraction. Once the leaching analysis is complete, the samples are acidified with 0.1 mL 85% orthophosphoric acid (H_3PO_4) for at least 30 min at 50 °C in order to convert the remaining carbonate into CO_2. The sample was then flushed into the MICADAS and analyzed as the main fraction. This technique gives the opportunity to assess the consistency of the ^{14}C signal of the inner and outer part of the foraminifers and infer about the dissolution/recrystallization state of the shells, which are indicated by large ^{14}C age difference between the main and leach fraction.

199 **RESULTS AND DISCUSSION**

200 **Gas measurements evaluation**

201 ***Accuracy of gas measurements***

202 We tested the accuracy of our radiocarbon gas data by measuring standard materials
203 IAEA-C1, IAEA-C2, coral CSTD and foraminifer blank (foraminifers older than 260 ky)
204 along with the samples. The values obtained agreed to the consensus values within the 2σ
205 uncertainty (Table S1).

206

207 ***Reproducibility of gas measurements***

208 The reproducibility of our gas measurements upon foraminifera was assessed using 19
209 duplicated ^{14}C gas analyses for planktonic foraminifers and 17 duplicated ^{14}C gas analyses for
210 benthic foraminifers (Figure 1). There is a clear difference between the upper part of the core
211 (0-30 cm or 3-9 ky cal BP) characterized by larger radiocarbon ages differences between the
212 different replicates (poorer reproducibility) than the section below (35-135 cm or10-25 ky cal
213 BP) (Figure 1). This sharp change in reproducibility is not synchronous with one of the abrupt
214 climatic events (Younger Dryas (YD), Heinrich Stadial 1 or 2 (HS1- HS2 respectively)). It
215 occurs at the Holocene onset and seems not to represent a climatic signal.

216 The poor gas measurement reproducibility observed in the top 35 cm of SU90-08 core
217 is likely related to syn-depositional or post-depositional sediment remobilization. A first
218 hypothesis is to attribute this remobilization to in-situ bioturbation. According to the current
219 understanding of deep-sea sediment bioturbation processes, the top most layer of a given
220 sediment archive, referred as the mixed layer, is uniformly mixed by benthic life (*e.g.*
221 burrowing) [*Berger*, 1968; *Berger and Johnson*, 1978; *Berger and Killingley*, 1982; *Guinasso*
222 *and Schink*, 1975; *Peng et al.*, 1997]. Therefore, the average age of the uppermost sediment
223 should be near-identical down to the bottom of the contemporary mixed layer, which is

typically between 5 and 10 cm thick [*Trauth et al.*, 1997]. Indeed, we see uniform ^{14}C ages to ~10 cm depth (average age 3402 ^{14}C yr BP, 3287 cal yr BP) in our sediment core (Fig S2a, S2b). Below, we see that average ^{14}C ages corresponding to the historical layers increase incrementally with core depth. This suggests the presence of a typical mixed layer of 10 cm in our sediment core. The mixed layer thickness may have changed in the past according to changes in benthic life activity in relation with bottom water oxygenation and nutrient availability. Alternatively, a second hypothesis would be to attribute this remobilization to the core retrieval technique. Indeed, some recent advances in sediment coring highlighted frequent sediment distortion due to piston effect in the first tens of cm of older sediment cores.

In the bottom part of the record (i.e. below 10 ky cal BP), the reproducibility is improved by a factor of 2 compared to the top part of the core. The planktonic foraminifer ^{14}C dates have a better reproducibility than benthic foraminifer ^{14}C dates (Figure 1), contrarily to what has been reported in [*Gottschalk et al.*, 2018]. All planktonic measurements agree within the 2σ uncertainty and roughly 65 % of the measurements agree within the 1σ uncertainty. For the benthic ^{14}C gas measurements around 57 % only agree within the 2σ uncertainties and 36 % within the 1σ uncertainty. A better agreement between replicated gas measurements is reached for glacial benthic ^{14}C gas samples compared to Holocene and Bolling Allerod (BA) samples.

Comparison of Gas and graphite measurements

Generally, the gas and graphite measurements show a consistent age-depth relationship and our new measurements are consistent with existing radiocarbon data [*Vidal et al.*, 1997] (see Figure S2). In details, we compare gas and graphite measurements on *G. bulloides*, and mixed benthic foraminifers (Figure 2 A.) and gas measurements on *G.bulloides*

249 to graphite measurements on *G.ruber* (Figure 2 B.). We observe no discernable difference
250 between the gas and graphite measurements for these species. The mean standard deviation of
251 the gas and graphite measurements is 228 y ± 199 y (1σ) for mixed benthic foraminifera, 322
252 y ± 194 y (1σ) for *G.bulloides*, and 286 y ± 188 y (1σ) for *G.bulloides* and *G.ruber*.

253 In details, the agreement between gas and graphite is highly dependent on the analyzed
254 levels (Figure 2). For instance, levels 23 cm (benthic and planktonic), 35 cm (planktonic) and
255 127 cm (planktonic) exhibit very poor agreement between gas and graphite measurements
256 with mean standard deviation of gas and graphite measurements around or above 500 y. We
257 note that some levels display poor reproducibility between the gas samples, especially at 23
258 cm, thought to be in the lower sediment accumulation rate upper 30 cm of the core as
259 discussed in the previous section. For the rest of the dataset, the mean standard deviation of
260 gas and graphite measurements is 199 y ± 97 y for mixed benthic foraminifera, 194 y ± 118 y
261 for *G.bulloides*, and 188 y ± 15 y for *G.bulloides* and *G.ruber*. That is in the order of
262 magnitude reported in [*Gottschalk et al.*, 2018]. Moreover, there are only 3 measurements for
263 which none of the gas replicate agrees with the graphite value within the 2σ uncertainty.

264 We must stress that the observed agreement of foraminiferal ^{14}C measurements for gas
265 and graphite, both here and in [*Gottschalk et al.*, 2018], can be due to random sampling when
266 picking foraminifera from a natural archive, such as a sediment core, and may vary between
267 locations and time periods. The best way to test the inherent reproducibility for gas and
268 graphite methods remains, of course, the use of standard material [*Wacker et al.*, 2013].
269
270 To summarize i) the standard materials analyzed along with the samples indicate that
271 the gas measurements were accurate; ii) the reproducibility of gas measurements aged from 2
272 to 10 ka is very poor, very likely because of sediment remobilization by in-situ bioturbation or
273 because of disturbance during coring; the gas measurements replicates from 10 to 16 ka

generally agree within the 2σ uncertainty and the overall reproducibility is comparable to what has been reported in [*Gottschalk et al.*, 2018] except for 3 analyzed levels; iii) the graphite measurements generally agrees with at least one gas replicate within 2σ uncertainty or the graphite measurement corresponds to the average of the gas replicates except for 3 analyzed levels. Overall, this analysis demonstrates the reliability of SU90-09 ^{14}C gas (and graphite) dataset generated in this study. Therefore we use those measurements to generate benthic – planktonic (B-P) ventilation ages.

Post HS1 negative ^{14}C B-P ages

We calculated the possible ^{14}C B-P ages for each depth level based on the gas and graphite replicated measurements (Figure 3). We observe wide ranges (up to 1000 y) of ^{14}C B-P ages per level as well as negative values in the top part of the record, *i.e.* from HS1 to the late Holocene (Figure 3 A.). The ^{14}C B-P ages are usually expected to be positive because the deep water-masses are expected to have been isolated from the surface for a longer time than the surface waters. Negative infrequent ^{14}C B-P ages are usually discarded in paleoceanographic studies (*e.g.* [*Wan and Jian*, 2014]). In our study, however, they represent a systematic continuous signal over the entire upper section of core SU90-08. Therefore, they cannot be considered as outliers and need to be explained.

A first hypothesis to explain the negative ^{14}C B-P ages could correspond to a bias in the radiocarbon content of benthic and planktonic foraminifers due to hydrothermal activity at, or close to the core location, in the vicinity of the Mid-Atlantic Ridge. Indeed, hydrothermal vents can circulate fluids containing large proportion of radiocarbon-dead crustal material, modifying the radiocarbon age of foraminifer shells toward older values. Living benthic foraminifers are more likely to be affected than planktonic ones as hydrothermal plumes do not usually affect the entire water column. However, both benthic

and planktonic shells can be affected by hydrothermal fluid circulation after sediment deposition. While SU90-08 is not directly located in a documented modern hydrothermal activity area [*German et al.*, 2016], this could have been the case in the past (e.g. [*German et al.*, 2016; *Hayes et al.*, 2015]). Thus, we searched for hydrothermal imprints in SU90-08. We measured elements (Al, Fe, Mn, and REE) known to be abundant in hydrothermal context in planktonic foraminifer coatings by laser-ablation ICP-MS in 16 sediment levels (see text S1 for details). Those measurements, performed on 16 sediment levels represent the bottom and pore water content (see text S1 for details). The REE pattern does not exhibit the positive Eu anomaly characteristic of vent fluids [*German et al.*, 1993; *Tostevin et al.*, 2016] (Figure S3). Furthermore, we see a negative Ce anomaly typical of seawater signature. Thus, we conclude that hydrothermal fluids have not affected SU90-08 location. Additionally, we tested if the hydrothermal vents derived particles have affected the sedimentation at SU90-08 location by evaluating the correlation between the $^{230}Th_{xs,0}$, an indicator of the sedimentation and the elements enriched in hydrothermal particles and fluids (Al, Fe and Mn). Indeed, particle content enriched in those elements can enhance the scavenging of ^{230}Th and thus increase the $^{230}Th_{xs,0}$ [*Hayes et al.*, 2015]. First, it is worth to notice that SU90-08 $^{230}Th_{xs,0}$ record primarily reflects increased sedimentary flux across Heinrich events at SU90-08 location [*Kissel*, 2005; *Missiaen et al.*, 2018]. Additionally, we observe no significant correlation between either Al, Fe and Mn in foraminifer coatings with $^{230}Th_{xs,0}$ (Figure S4). The foraminifer coating content directly reflects the composition of the sediments pore water, which is influenced by the sediment composition itself. Hence, if the sediment would have been enriched in Fe, Mn or Al particles derived from a distant hydrothermal vents, the pore water composition would also have been enriched in those elements. Therefore, the absence of correlation we observe between the $^{230}Th_{xs,0}$ and the pore water Fe, Mn and Al content supports that the sedimentation was not driven by hydrothermal processes at SU90-08 over the last 30 ky cal

BP. Consequently, we conclude that the radiocarbon pattern does not reflect hydrothermal activity changes in SU90-08 sediment core and that hydrothermal activity is thus unlikely to explain the observed negative ^{14}C B-P ages.

A second classical hypothesis to explain negative ^{14}C B-P ages is the bad preservation of the sample material that would then exhibits a dissolution/recrystallization signal [*Mekik*, 2014; *Wycech et al.*, 2016]. Indeed, the lysocline depth is susceptible to change through time and waters in which the $CaCO_3$ tends to dissolve may bath the upper sediments layers across the sediment history. Consequently the foraminifer shells can be partly dissolved and recrystallized with secondary calcite, displaying an altered radiocarbon composition. In particular, it has been shown that frosty and recrystallized shells appear older in the radiocarbon scale than transluctant and well-preserved shells [*Wycech et al.*, 2016]. In order to assess the dissolution/recrystallization state of our foraminifer samples, we i) examined some specimens on Scanning Electron Microscope (SEM) pictures (see text S2 for details) and ii) analyzed the consistency between leach and main fraction radiocarbon measurements. Generally, the foraminifers look well preserved. In details, the benthic foraminifers analyzed do not exhibit recrystallization features (see Figure S5). By contrast, some planktonic foraminifers exhibit some secondary calcite crystals with characteristic rhombohedric shape as well as dissolution features. This can be related to the more fragile shell of planktonic foraminifer shells compared to their benthic counterparts. Therefore, we cannot exclude that the planktonic foraminifers have slightly older radiocarbon ages than they should but we note that dissolution and recrystallization features are observed along the entire record on planktonic foraminifers. To summarize, the SEM pictures show that i) the benthic foraminifer are well preserved and ii) the planktonic foraminifers are slightly dissolved and recrystallized in a consistent way through the record. Therefore, it is unlikely that dissolution and recrystallization processes alone can explain SU90-08 negative ^{14}C B-P ages.

In addition, the analysis of our gas main and leach fraction radiocarbon content can also bring information about the preservation (dissolution/recrystallization) state of the foraminifer specimens that have been analyzed for radiocarbon and that could not be pictured with SEM due to sample preparation requirements. If the leaching acid dissolves always the same amount of $CaCO_3$, the nature of what is exactly dissolved is still unclear. Indeed, if some coccoliths are contaminating the surface of the foraminifers (see Figure S5), those are likely to be dissolved during the leaching step. In general, those coccoliths are expected to have the same or slightly older radiocarbon age than the foraminifers as they settle slower. In that case, the leach fraction is expected to be slightly older than the main fraction. Otherwise, the leach fraction corresponds to the outer shell of the foraminifers, directly exposed to the addition of the leaching acid. In general, this outer shell can be contaminated by young radiocarbon from the atmosphere since the core retrieval. Therefore, the leach fraction usually appears slightly younger than the inner part of the shell analyzed in the main fraction. For an altered sample, the dissolution and recrystallization processes will preferentially modify the composition of the outer shell by including old or even radiocarbon dead carbon content from the underlying sediment layers. Consequently, the altered shells should display a leach fraction radiocarbon age older than the main fraction radiocarbon age. Altered shells will also be characterized by a high difference between the outer part (leach fraction) and the inner part (main fraction). To distinguish potentially contaminated (*e.g.* by coccoliths), altered or dissolved samples we apply two different criteria: i) we discard the data for which the leach fraction is significantly older than the main fraction and ii) we discard the data for which the ^{14}C age difference between the main and the leach fraction exceeds 15% of the main fraction age. By following this procedure, we excluded 8-paired leach and main fraction ^{14}C gas measurements from our dataset (see Figure S6), representing less than 10% of our available

373 gas measurements. Interestingly, this analysis removes more benthic than planktonic samples
374 although the benthic foraminifers appeared to be better preserved on the SEM pictures.
375
376 To conclude, we observe repeated negative ^{14}C B-P ages for the post HS1 part of
377 SU90-08 record that cannot be simply considered as outliers. We show that those results can
378 neither correspond to hydrothermal imprint on the foraminifer radiocarbon content nor be the
379 result of dissolution/recrystallization of the foraminifer shells. Therefore, these negative ^{14}C
380 B-P ages have to be interpreted in terms of modern and passed oceanic ventilation changes, or
381 due to sediment dynamics and mixing of benthic and planktonic foraminifers.
382
383 **Reconciling negative B-P ages with ocean ventilation**
384 ***Sample heterogeneity highlighted by small-sized gas measurements radiocarbon ages***
385 The comparison between gas and graphite measurements as well as the leach fraction
386 analysis permits to screen the raw ^{14}C B-P ages (Figure 3.B.). Interestingly, graphite pairs of
387 ^{14}C B-P ages correspond to the average of the replicated gas ^{14}C B-P ages (Figure 3 B. from 2
388 to 9 ka) except for one depth (35 cm-10.1 ka) where the graphite pair ^{14}C B-P age is
389 completely offset compared to the gas pairs. This can be related to the sample size
390 requirement of each measurement: because the graphite analysis requires more material, the
391 sampled individuals (n>100 shells) are more likely to statistically represent the average of the
392 analyzed level than the gas samples (n < 50 shells) [*Bryan C Lougheed et al.*, 2018]. We
393 observe that the screened ^{14}C B-P ages record obtained by discarding potentially altered
394 measurements and averaging the replicated ^{14}C B-P ages for each level, contain less negative
395 ^{14}C B-P ages (Figure 3.B.). The small sized gas samples capture the heterogeneity of the
396 foraminifer population in the considered sediment level, whereas bigger graphite
397 measurements rather represent the average radiocarbon age. Thus, it seems very important to

adapt the radiocarbon measurement technique according to the study objectives (*e.g.* average signal or insights in sample heterogeneity) and of course the material availability. Interestingly such sample heterogeneity was not highlighted in existing benthic and planktonic stable isotope records (e.g. [*Vidal et al.*, 1997]) though they require also a small number of picked and analyzed individuals (in the present case, n= 30 for planktonic isotopes and n=1 to 4 for benthic isotopes). This can be mostly attributed to the fact that Holocene stable isotope have similar values throughout the Holocene period, minimizing the effect of mixing. Additionally, as proposed by [*Lougheed et al.*, 2018], this can be attributed to the non-linear relation between ^{14}C isotopic content and radiocarbon age. Therefore, the addition of a relatively small amount of radiocarbon young material significantly shifts the final radiocarbon age toward a younger value compared to the actual average ^{14}C age of the sample.

Consistent evidence for a marked ventilation change during the last deglaciation

Despite the observed negative values, SU90-08 ^{14}C B-P ages display first order great consistency with other ventilation and oxygenation proxy (Figure 4). Indeed, among the available SU90-08 data, the benthic $\delta^{13}C$ (this study, see supplementary text S3) and the Ce anomaly (this study, see supplementary text S1) show that a poorly ventilated and oxygenated deep water mass was bathing the site until the end of HS1. Conversely, after HS1 and until the end of the record, the deep water mass was oxygenated and well ventilated. This oxygenation change is also consistent with the observed benthic species occurrence: when the deep water mass is oxygenated and ventilated, the epibenthic species living on the sediment floor are dominating the assemblages whereas the endobenthic species, living inside the first centimeters of sediment are more abundant in the assemblages when the deep water mass is poorly ventilated and oxygenated. The relatively high ventilation and oxygenation level of the

deep-water mass during the Holocene is consistent with SU90-08 modern oceanographic setting. The core is located on the western flank of the Mid Atlantic Ridge and at 3000 m water depth. Thus, the deep water mass bathing the location corresponds to well oxygenated and ventilated Labrador Sea Water mixed with lower North Atlantic Deep Water [*Paillet et al.*, 1998].

The oxygenation and ventilation history of this site can help explaining the reported negative ^{14}C B-P ages in two non-exclusive ways. First, under modern, and by extension Holocene, conditions the radiocarbon age gradient between the surface and deep waters is reduced to about 150 y [*Key et al.*, 2004]. This reduced radiocarbon age difference is hardly observable in the fossil record because it is very close to the propagated uncertainty of a ^{14}C B-P age. This is particularly true for gas measurements for which the Holocene average 1σ uncertainty is 80 y for both benthic and planktonic measurements leading to a propagated 1σ uncertainty on a gas pair of ^{14}C B-P ages of about 110 y. In the best case, the propagated 1σ uncertainty on a gas pair of ^{14}C B-P ages cannot be lower than 80 y. For comparison, the propagated uncertainty on a graphite pair of ^{14}C B-P ages is around 60 y. Second, the oxygenation and ventilation history is very likely to influence the bioturbation level of the sediment core. Indeed, it appears logical that more benthic fauna might have developed during high oxygenation periods, thus potentially enhancing the potential sediment bioturbation. This would explain why the negative ^{14}C B-P ages are observed after HS1. Additionally, even if the underlying mechanisms are still discussed, it has been shown that bioturbation has differential effects on particles depending on their size (e.g. [*Wheatcroft*, 1992; *Wheatcroft and Jumars*, 1987]). If small particles placed at the top of the sediment mixed layer have been shown to penetrate deeper in the sediments [*Wheatcroft*, 1992], [*Broecker et al.*, 1991] proposed that in a context of low sedimentation and carbonate dissolution, bioturbation would exhume material from the underlying sediments. In those circumstances, the finer fraction that

448 is reworked easier remains longer in the mixed layer than the bigger fraction. Thus the finer
449 fraction appears older. In our case, benthic foraminifer shells are bigger than planktonic ones.
450 Besides, we note some dissolution and recrystallization features on the planktonic shells.
451 Consequently, the small planktonic foraminifer shells could have stayed longer in the mixed
452 layer than their bigger benthic counterparts. This mechanism could explain that the planktonic
453 foraminifers display slightly older radiocarbon ages than the benthic shells found in the same
454 sediment layer.
455
456 ***Producing negative ^{14}C B-P ages using a simulation of bioturbated sediment***
457 We argue here that the negative ^{14}C B-P ages observed after HS1 on SU90-08 record
458 can be attributed to a bioturbation effect of benthic and planktonic foraminifer shells with
459 different abundances. Using the single foraminifera simulation developed by [*Lougheed et al.*,
460 2018], we show that it is possible to produce negative ^{14}C B-P ages for the younger periods
461 considering constant true ventilation ages and uniform sediment mixed layer depth (Figure 5).
462 The planktonic foraminifer abundance evolution chosen for the simulation show higher peaks
463 during the glacial period compared to the Holocene according to the core actual G.*bulloides*
464 abundances (Figure 5- Figure S1). Decreased abundance of planktonic species during younger
465 periods compared to older periods (pre-HS1), combined with bioturbation, lead to a bias of
466 planktonic radiocarbon ages towards older ^{14}C ages for younger periods, the bioturbation
467 moving upward material from high abundance peaks. Subsequently, if the abundance histories
468 of benthic and planktonic foraminifera are out of phase and/or significantly different (as
469 shown here), erroneous ^{14}C B-P ages can be produced. In addition, the dynamic ^{14}C history of
470 the atmosphere, combined with the delay of ^{14}C activity reaching the deep ocean, can also
471 lead to dynamics in ^{14}C B-P ages that are not necessarily related to ocean ventilation (e.g.
472 [*Lund et al.*, 2011]).

CONCLUSIONS

We have analyzed and replicated radiocarbon measurements on benthic and planktonic foraminifers from reference core SU90-08 using gas introduction system and MICADAS design. This experimental setting allows the analysis of small-sized samples opening high-resolution radiocarbon measurements possible for cores with low foraminifer content. Besides, the use of the gas introduction system reduces the samples preparation time and the contamination risk as it omits the graphitization step. Additionally the analysis of the radiocarbon content of the leach fraction corresponding to the outer foraminifer shell can bring valuable information about the dissolution/recrystallization state of the analyzed material. We have shown that the measurements obtained were accurate and that the precision was reasonably decreased compared to conventional graphite AMS measurements. The reproducibility of the gas MICADAS measurements is generally satisfactory and highly dependent on the analyzed foraminifer material. In the case of SU90-08, poor reproducibility of replicated benthic and planktonic gas ^{14}C measurements in the core top highlighted a pronounced sediment remobilization by in-situ bioturbation and/or sediment stretching during core retrieval operations. Our gas measurements generally agreed with conventional graphite measurements within 2σ uncertainty. Alternatively, the graphite measurement represented the average of the two gas replicates.

From this radiocarbon dataset we calculated ensembles of possible ^{14}C B-Pages for each considered sediment level and obtained reproducible negative ^{14}C B-P ages in the post HS1 part of the record. We showed that those negative ^{14}C B-P ages can neither be attributed to hydrothermal imprint on radiocarbon content nor to the effect of the dissolution and recrystallization of the foraminifer shells. Instead, we argue that small sized radiocarbon analysis highlight the heterogeneity of the foraminifer material contained in a single sediment

498 level. We argue that these negative ^{14}C B-P ages actually reflect potential core bioturbation in
499 a context of very low radiocarbon age gradient between the surface and deep waters. Indeed,
500 several ventilation and oxygenation proxy such as benthic $\delta^{13}C$ and the Ce anomaly indicate
501 that a poorly ventilated and oxygenated deep water bathed the site until the end of HS1. After,
502 the well-ventilated and oxygenated deep-water mass, probably partly originating from the
503 Labrador Sea bathed the site like it is the case under modern conditions. This ventilation and
504 oxygenation history is consistent with enhanced bioturbation after HS1. Because bioturbation
505 seems to affect differently small and big particles and because the benthic specimens are
506 significantly bigger than their planktonic counterparts, we argue that negative ^{14}C B-P ages
507 are the result of the conjunction of low surface-deep water radiocarbon gradient and the
508 enhanced and differential bioturbation since the end of HS1. Consequently, established
509 understanding of bioturbation, combined with dynamic changes in benthic and planktonic
510 foraminiferal abundances, help to explain the existence of negative ^{14}C B-P ages, as we show
511 using a single foraminifera simulation adapted from [*Lougheed et al.*, 2018].

512 Finally, it appears that the main limitation for small sized gas radiocarbon analysis is
513 the sediment core conservation. More so than conventional stable isotopes, replicated small
514 sized radiocarbon measurements appear to reveal the heterogeneity of the material contained
515 in a sediment level. This has two major explanations i) the replication of small sized analysis
516 gives access to the statistical composition in radiocarbon age of the sediment level content ii)
517 the radiocarbon composition has an exponential (and not linear) relation with time, which
518 makes it more sensitive to mixing. Finally, in some cases like SU90-08, the archive
519 conservation and bioturbation state generates uncertainty/heterogeneity on gas radiocarbon
520 measurements that largely overcomes the precision decrease between gas and graphite
521 measurements. This case study highlights that the uncertainty on radiocarbon measurements
522 given from machine error propagation can underestimate the noise/uncertainty related to the

archive conservation. Special care has to be taken while interpreting very small ^{14}C B-P ages as they could reflect not major paleoceanographic changes but method artifacts such as bioturbation, slight dissolution/recrystallization effect or just changes in atmospheric radiocarbon compositions.

Acknowledgements

This is a contribution to ERC project ACCLIMATE; the research leading to these results has received funding from the European Research Council under the European Union's Seventh Framework Programme (FP7/2007-2013)/ERC grant agreement 339108. We thank E. Michel for fruitful discussion and S. Moreira for his help with R programming. This is LSCE contribution XXXXX.

Competing interests: The authors declare that they have no conflict of interests.

Data availability: The data will be available online on Pangaea database (https://www.pangaea.de/).

Figures:

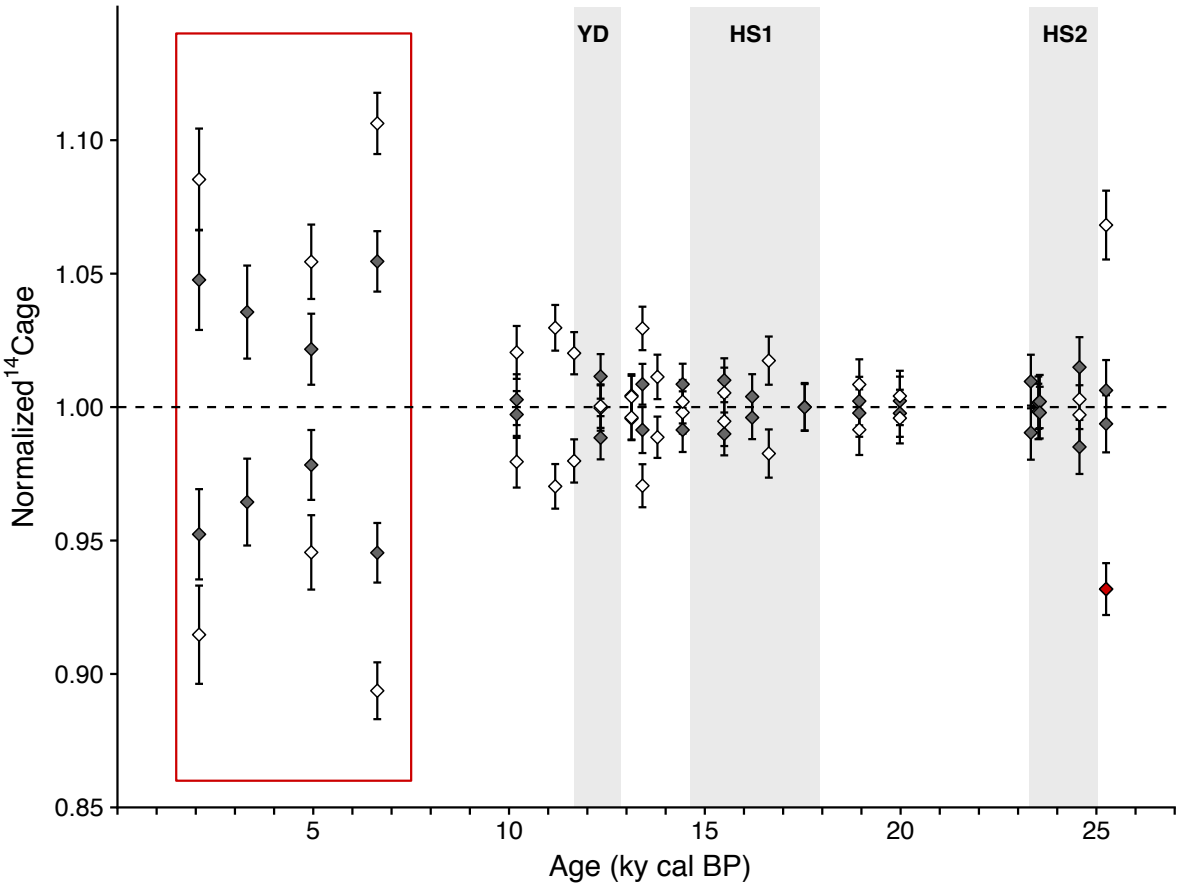

Figure 1: Reproducibility of the benthic and planktonic ^{14}C gas measurements
For each level, the "normalized ^{14}C age" corresponds to the ^{14}C age of each replicate normalized by the mean ^{14}C age of the two replicated gas measurements available for this level. The open symbols represent benthic measurements, the filled symbols the planktonic measurements. The represented uncertainty is 1 σ. In the ideal case of perfect reproducibility, the samples should fall on the dashed line. Age model following [Missiaen et al, Paleoceanography and Paleoclimatology, submitted]. The red rectangle highlights the poor gas radiocarbon reproducibility of the upper 35 cm of the core. The grey bands indicate the cold stadials (Younger Dryas, Heinrich Stadials 1 and 2). The red diamond highlights an off-trend benthic radiocarbon measurement (see Figure S2.A)

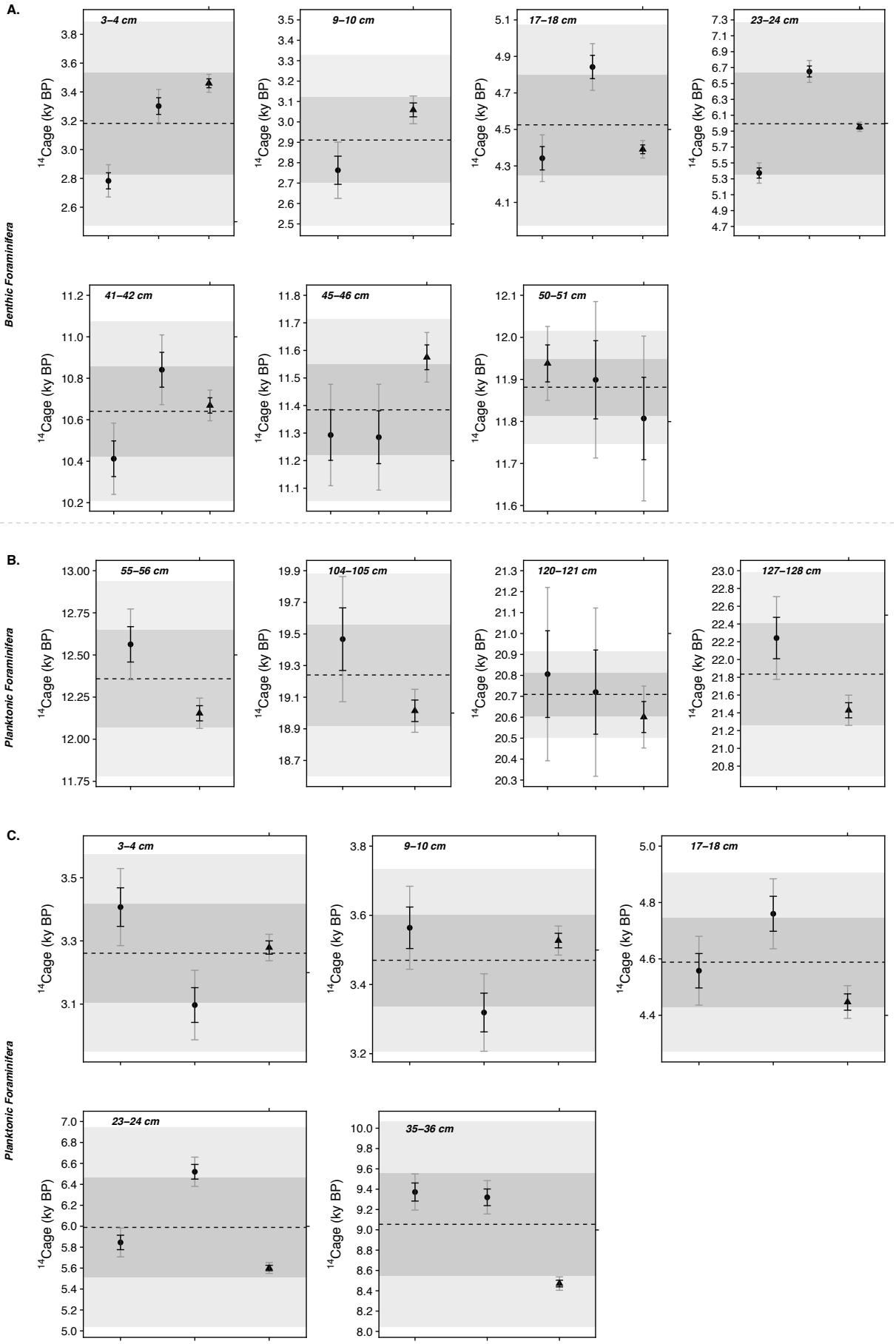
A.
Benthic Foraminifera
3–4 cm
9–10 cm
17–18 cm
23–24 cm
41–42 cm
45–46 cm
50–51 cm
B.
Planktonic Foraminifera
55–56 cm
104–105 cm
120–121 cm
127–128 cm
C.
Planktonic Foraminifera
3–4 cm
9–10 cm
17–18 cm
23–24 cm
35–36 cm
14Cage (ky BP)

554

555
556 **Figure 2: Comparison between gas and graphite for benthic and planktonic**
557 **foraminifera.**
558 Comparison between gas and graphite measurements for **A.** mixed benthic species. **B.**
559 *G.bulloides* and **C.** different planktonic species (*i.e. G.bulloides* for gas measurements and
560 *G.ruber* for graphite measurements). In each sub-plot, the gas measurements are represented
561 by triangles, the graphite measurements by squares. The 1σ uncertainty is represented in
562 black; the 2σ uncertainty is represented in grey. The dashed line represents the mean of all
563 measurements. The horizontal dark grey (light grey) band indicates the 1σ (2 σ) uncertainty
564 calculated from all available measurements.

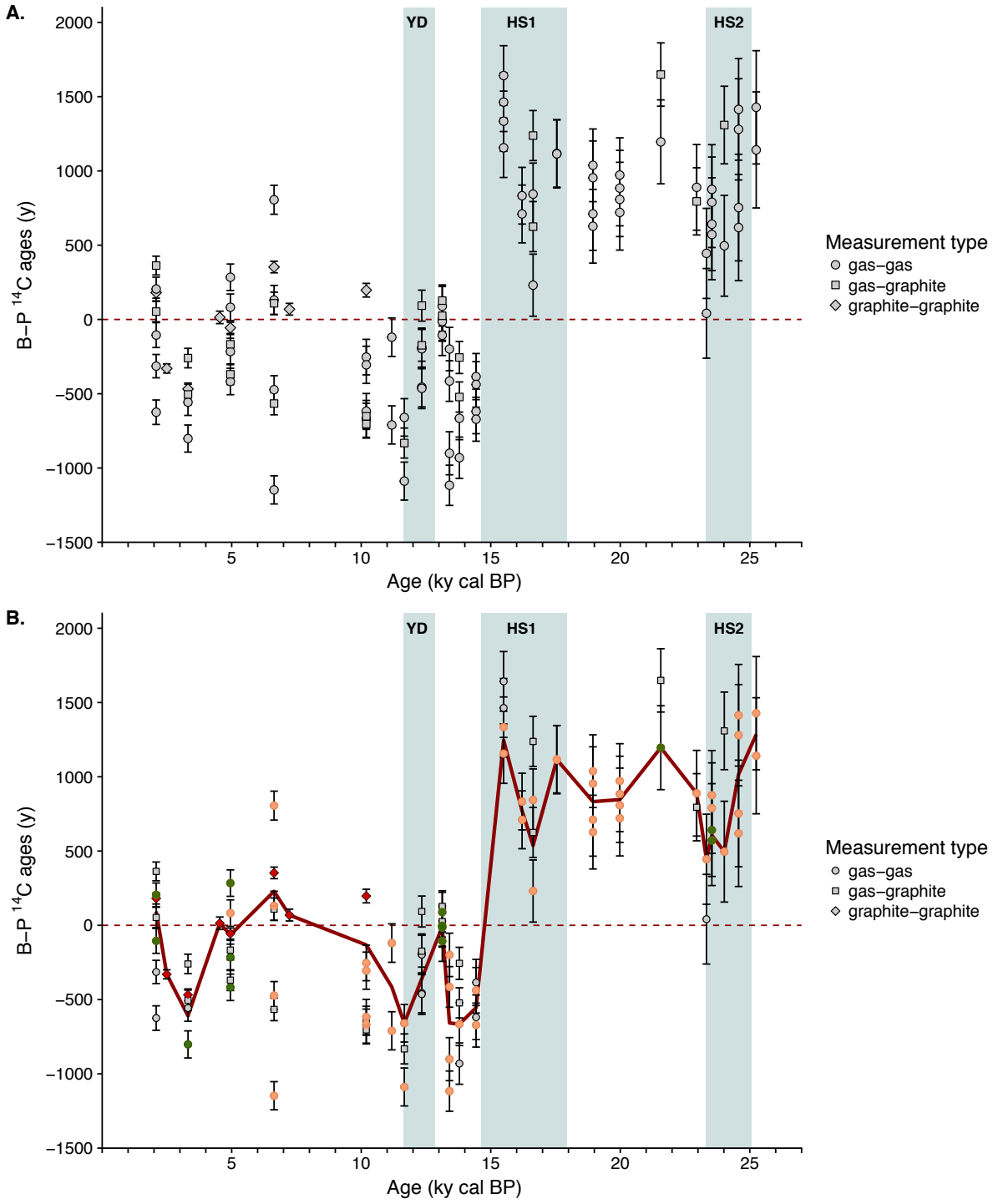

Figure 3: SU90-08 B-P ^{14}C ages time series

A. Raw B-P ^{14}C ages obtained from all pairs of measurements with the available dataset. The symbol type indicates the measurement type: gas vs gas measurements are represented by circles, gas vs graphite by squares and graphite vs graphite by diamonds. **B.** Screened B-P ^{14}C ages time series. The red symbols correspond to graphite vs graphite B-P pairs. The orange symbols correspond to the data that passed the leaching control (i.e. the leach fraction radiocarbon age should not differ by more than 15 % from the main fraction radiocarbon age and the leach fraction radiocarbon age should be younger than the main fraction- see Figure S6)). The green symbols represent pairs for which one graphite measurements agrees with one

benthic or planktonic gas measurement within 2σ uncertainty. The bold red line connects the average screened data.

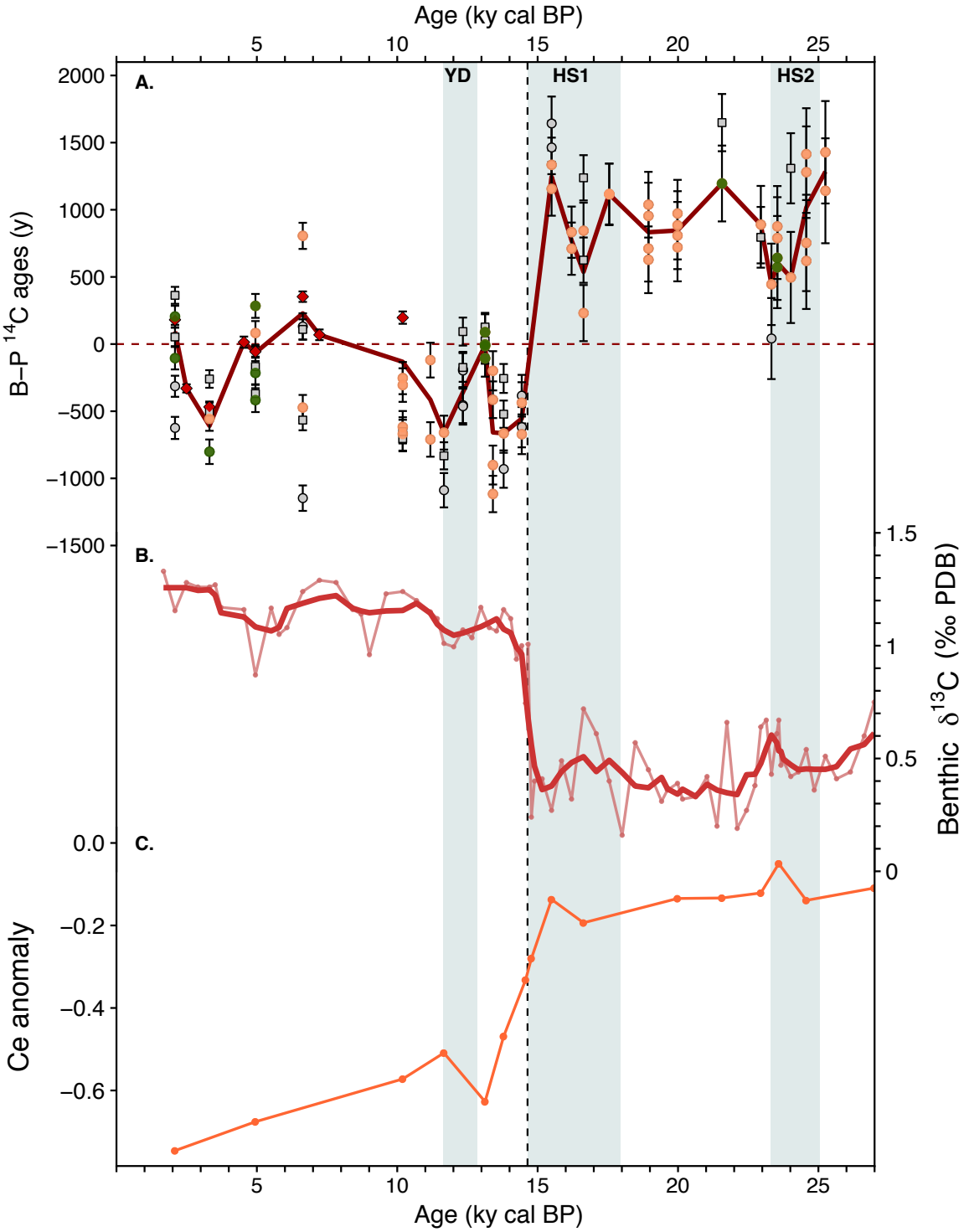

Figure 4: Ventilation and oxygenation time series for SU90-08. **A**. ^{14}C B-P record as on Figure 3, **B.** Benthic δ^{13}C record, the light red line and dots represent the raw data the bold red line represents smoothed data (running average with 5 points) **C.** Ce anomaly record. The vertical bands indicate the millennial scale events (YD, HS1 and HS2). The vertical black dashed line highlights the marked ventilation and oxygenation transition at the end of HS1.

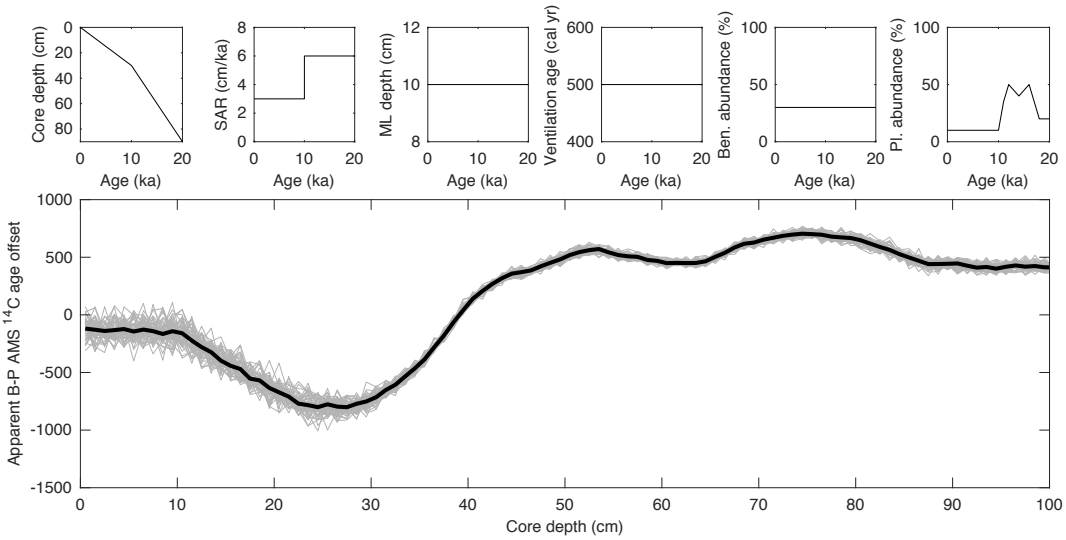

Figure 5: **Simulated B-P ^{14}C ages with constant ventilation age but changing foraminifer abundances and sedimentation rate.**

Single foraminifera sediment simulation with 10 year timesteps and 10^4 single foraminifera per cm (adapted from [*Bryan C Lougheed et al.*, 2018]) with constant mixed layer depth (10 cm) and ventilation age (500 years). At each timestep *n* new foraminifera are deposited (*n* scaled to the sedimentation accumulation rate of the timestep) and assigned a depth according to the inputted age-depth model. Each foraminifera is assigned a species type (in this case simply planktonic, benthic or other) according to the input abundance for the timestep. ^{14}C activity for each timestep is determined using *Marine13 [Reimer et al., 2013]*, with a timestep ventilation age in the case of benthic foraminifera. At each timestep, depth values in the uppermost depth (mixed layer depth- 10 cm) are uniformly mixed using random sampling of the mixed depth interval. After the end of the simulation, discrete depth benthic and planktonic expected AMS ages are calculated by taking the mean ^{14}C activity of the benthic and planktonic foraminifera for each discrete depth.

601 # References
602
603 Bard, E., T. Tuna, Y. Fagault, L. Bonvalot, L. Wacker, S. Fahrni, and H.-A. Synal (2015),
604 AixMICADAS, the accelerator mass spectrometer dedicated to 14 C recently installed in
605 Aix-en-Provence, France, Nuclear Instruments and Methods in Physics Research Section
606 B: Beam Interactions with Materials and Atoms, 361, 80-86.
607
608 Bard, E., M. Arnold, J. Mangerud, M. Paterne, L. Labeyrie, J. Duprat, M.-A. Mélières, E.
609 Sønstegaard, and J.-C. Duplessy (1994), The North Atlantic atmosphere-sea surface 14C
610 gradient during the Younger Dryas climatic event, Earth and Planetary Science Letters,
611 126(4), 275-287, doi: https://doi.org/10.1016/0012-821X(94)90112-0.
612
613 Berger W.H., H. G. R. (1968), Vertical mixing in pelagic sediments, J. Mar. Res., 26, 134-
614 143.
615
616 Berger, W. H., and R. F. Johnson (1978), On the thickness and the14C age of the mixed
617 layer in deep-sea carbonates, Earth and Planetary Science Letters, 41(2), 223-227, doi:
618 https://doi.org/10.1016/0012-821X(78)90012-2.
619
620 Berger, W. H., and J. S. Killingley (1982), Box cores from the equatorial Pacific: 14C
621 sedimentation rates and benthic mixing, Marine Geology, 45(1), 93-125, doi:
622 https://doi.org/10.1016/0025-3227(82)90182-7.
623
624 Blaauw, M. (2010), Methods and code for 'classical' age-modelling of radiocarbon
625 sequences, Quaternary Geochronology, 5(5), 512-518, doi:
626 https://doi.org/10.1016/j.quageo.2010.01.002.
627
628 Bondevik, S., J. Mangerud, H. H. Birks, S. Gulliksen, and P. Reimer (2006), Changes in
629 North Atlantic radiocarbon reservoir ages during the Allerød and Younger Dryas,
630 Science, 312(5779), 1514-1517.
631
632 Bout-Roumazeilles, V., E. Cortijo, L. Labeyrie, and P. Debrabant (1999), Clay mineral
633 evidence of nepheloid layer contributions to the Heinrich layers in the northwest
634 Atlantic, Palaeogeography, Palaeoclimatology, Palaeoecology, 146(1), 211-228.
635
636 Broecker, W., A. Mix, M. Andree, and H. Oeschger (1984), Radiocarbon measurements on
637 coexisting benthic and planktic foraminifera shells: potential for reconstructing ocean
638 ventilation times over the past 20 000 years, Nuclear Instruments and Methods in
639 Physics Research Section B: Beam Interactions with Materials and Atoms, 5(2), 331-339.
640
641 Broecker, W. S., M. Klas, E. Clark, G. Bonani, S. Ivy, and W. Wolfli (1991), The Influence of
642 CaCO3 Dissolution on Core Top Radiocarbon Ages for Deep‐Sea Sediments,
643 Paleoceanography, 6(5), 593-608.
644
645 Broecker, W. S., M. Andree, G. Bonani, W. Wolfli, M. Klas, A. Mix, and H. Oeschger (1988),
646 Comparison between radiocarbon ages obtained on coexisting planktonic foraminifera,
647 Paleoceanography, 3(6), 647-657.
648
649 Chen, T., L. F. Robinson, A. Burke, J. Southon, P. Spooner, P. J. Morris, and H. C. Ng (2015),
650 Synchronous centennial abrupt events in the ocean and atmosphere during the last
651 deglaciation, Science, 349(6255), 1537.
652

653 Freeman, E., L. C. Skinner, C. Waelbroeck, and D. Hodell (2016), Radiocarbon evidence
654 for enhanced respired carbon storage in the Atlantic at the Last Glacial Maximum,
655 Nature Communications, 7, 11998, doi: 10.1038/ncomms11998
656 https://www.nature.com/articles/ncomms11998 - supplementary-information.
657
658 Gao, P., X. Xu, L. Zhou, M. A. Pack, S. Griffin, G. M. Santos, J. R. Southon, and K. Liu (2014),
659 Rapid sample preparation of dissolved inorganic carbon in natural waters using a
660 headspace‐extraction approach for radiocarbon analysis by accelerator mass
661 spectrometry, Limnology and Oceanography: Methods, 12(4), 174-190.
662
663 German, C. R., S. Petersen, and M. D. Hannington (2016), Hydrothermal exploration of
664 mid-ocean ridges: Where might the largest sulfide deposits be forming?, Chemical
665 Geology, 420, 114-126, doi: https://doi.org/10.1016/j.chemgeo.2015.11.006.
666
667 German, C. R., N. C. Higgs, J. Thomson, R. Mills, H. Elderfield, J. Blusztajn, A. P. Fleer, and
668 M. P. Bacon (1993), A geochemical study of metalliferous sediment from the TAG
669 Hydrothermal Mound, 26° 08′ N, Mid-Atlantic Ridge, Journal of Geophysical Research:
670 Solid Earth, 98(B6), 9683-9692, doi: 10.1029/92JB01705.
671
672 Gottschalk, J., S. Szidat, E. Michel, A. Mazaud, G. Salazar, M. Battaglia, J. Lippold, and S. L.
673 Jaccard (2018), Radiocarbon Measurements of Small-Size Foraminiferal Samples with
674 the Mini Carbon Dating System (MICADAS) at the University of Bern: Implications for
675 Paleoclimate Reconstructions, Radiocarbon, 60(2), 469-491, doi: 10.1017/RDC.2018.3.
676
677 Grousset, F., L. Labeyrie, J. Sinko, M. Cremer, G. Bond, J. Duprat, E. Cortijo, and S. Huon
678 (1993), Patterns of ice‐rafted detritus in the glacial North Atlantic (40‐55 N),
679 Paleoceanography, 8(2), 175-192.
680
681 Guinasso, N. L., and D. R. Schink (1975), Quantitative estimates of biological mixing rates
682 in abyssal sediments, Journal of Geophysical Research, 80(21), 3032-3043, doi:
683 10.1029/JC080i021p03032.
684
685 Hajdas, I. (2008), Radiocarbon dating and its applications in Quaternary studies,
686 Eiszeitalter und Gegenwart Quaternary Science Journal, 57(2), 24.
687
688 Hajdas, I., G. Bonani, H. Furrer, A. Mäder, and W. Schoch (2007), Radiocarbon chronology
689 of the mammoth site at Niederweningen, Switzerland: Results from dating bones, teeth,
690 wood, and peat, Quaternary International, 164-165, 98-105, doi:
691 https://doi.org/10.1016/j.quaint.2006.10.007.
692
693 Hayes, C. T., R. F. Anderson, M. Q. Fleisher, K.-F. Huang, L. F. Robinson, Y. Lu, H. Cheng, R.
694 L. Edwards, and S. B. Moran (2015), 230Th and 231Pa on GEOTRACES GA03, the U.S.
695 GEOTRACES North Atlantic transect, and implications for modern and
696 paleoceanographic chemical fluxes, Deep Sea Research Part II: Topical Studies in
697 Oceanography, 116, 29-41, doi: https://doi.org/10.1016/j.dsr2.2014.07.007.
698
699 Hughen, K., J. Southon, S. Lehman, C. Bertrand, and J. Turnbull (2006), Marine-derived
700 14C calibration and activity record for the past 50,000 years updated from the Cariaco
701 Basin, Quaternary Science Reviews, 25(23), 3216-3227, doi:
702 https://doi.org/10.1016/j.quascirev.2006.03.014.
703

Key, R. M., A. Kozyr, C. L. Sabine, K. Lee, R. Wanninkhof, J. L. Bullister, R. A. Feely, F. J. Millero, C. Mordy, and T. H. Peng (2004), A global ocean carbon climatology: Results from Global Data Analysis Project (GLODAP), Global Biogeochemical Cycles, 18(4), doi: 10.1029/2004GB002247.

Kissel, C. (2005), Magnetic signature of rapid climatic variations in glacial North Atlantic, a review, Comptes Rendus Geoscience, 337(10), 908-918, doi: https://doi.org/10.1016/j.crte.2005.04.009.

Lougheed, B. C., B. Metcalfe, U. S. Ninnemann, and L. Wacker (2018), Moving beyond the age–depth model paradigm in deep-sea palaeoclimate archives: dual radiocarbon and stable isotope analysis on single foraminifera, Climate of the Past, 14(4), 515-526.

Lougheed, B. C., I. Snowball, M. Moros, K. Kabel, R. Muscheler, J. J. Virtasalo, and L. Wacker (2012), Using an independent geochronology based on palaeomagnetic secular variation (PSV) and atmospheric Pb deposition to date Baltic Sea sediments and infer 14C reservoir age, Quaternary Science Reviews, 42, 43-58, doi: https://doi.org/10.1016/j.quascirev.2012.03.013.

Lund, D. C., A. C. Mix, and J. Southon (2011), Increased ventilation age of the deep northeast Pacific Ocean during the last deglaciation, Nature Geoscience, 4(11), 771.
Lynch-Stieglitz, J. (2017), The Atlantic Meridional Overturning Circulation and Abrupt Climate Change, Annual Review of Marine Science, 9(1), 83-104, doi: 10.1146/annurev-marine-010816-060415.

Mekik, F. (2014), Radiocarbon dating of planktonic foraminifer shells: A cautionary tale, Paleoceanography, 29(1), 13-29.

Missiaen, L., S. Pichat, C. Waelbroeck, E. Douville, L. Bordier, A. Dapoigny, F. Thil, L. Foliot, and L. Wacker (2018), Downcore Variations of Sedimentary Detrital (238U/232Th) Ratio: Implications on the Use of 230Thxs and 231Paxs to Reconstruct Sediment Flux and Ocean Circulation, Geochemistry, Geophysics, Geosystems, 0(ja), doi: 10.1029/2017GC007410.

Obrochta, S. P., et al. (2017), The undatables: Quantifying uncertainty in a highly expanded Late Glacial ‐ Holocene sediment sequence recovered from the deepest Baltic Sea basin—IODP Site M0063, Geochemistry, Geophysics, Geosystems, 18(3), 858-871, doi: 10.1002/2016GC006697.

Paillet, J., M. Arhan, and M. S. McCartney (1998), Spreading of Labrador Sea water in the eastern North Atlantic, Journal of Geophysical Research: Oceans, 103(C5), 10223-10239.

Parnell, A. C., J. Haslett, J. R. M. Allen, C. E. Buck, and B. Huntley (2008), A flexible approach to assessing synchroneity of past events using Bayesian reconstructions of sedimentation history, Quaternary Science Reviews, 27(19), 1872-1885, doi: https://doi.org/10.1016/j.quascirev.2008.07.009.

Peng, T. H., W. S. Broecker, and W. H. Berger (1997), Rates of Benthic Mixing in Deep-Sea Sediment as Determined by Radioactive Tracers, Quaternary Research, 11(1), 141-149, doi: 10.1016/0033-5894(79)90074-7.

Ramsey, C. B. (2009), Bayesian analysis of radiocarbon dates, Radiocarbon, 51(1), 337-360.

Reimer, P. J., E. Bard, A. Bayliss, J. W. Beck, P. G. Blackwell, C. B. Ramsey, C. E. Buck, H. Cheng, R. L. Edwards, and M. Friedrich (2013), IntCal13 and Marine13 radiocarbon age calibration curves 0–50,000 years cal BP, Radiocarbon, 55(4), 1869-1887.

Rozanski, K., W. Stichler, R. Gonfiantini, E. M. Scott, R. P. Beukens, B. Kromer, and J. Van Der Plicht (1992), The IAEA 14C Intercomparison Exercise 1990, Radiocarbon, 34(3), 506-519, doi: 10.1017/S0033822200063761.

Santos, G. M., J. R. Southon, S. Griffin, S. R. Beaupre, and E. R. M. Druffel (2007), Ultra small-mass AMS 14C sample preparation and analyses at KCCAMS/UCI Facility, Nuclear Instruments and Methods in Physics Research Section B: Beam Interactions with Materials and Atoms, 259(1), 293-302, doi: https://doi.org/10.1016/j.nimb.2007.01.172.

Skinner, L. C., and N. J. Shackleton (2004), Rapid transient changes in northeast Atlantic deep water ventilation age across Termination I, Paleoceanography, 19(2), doi: 10.1029/2003PA000983.

Skinner, L. C., C. Waelbroeck, A. E. Scrivner, and S. J. Fallon (2014), Radiocarbon evidence for alternating northern and southern sources of ventilation of the deep Atlantic carbon pool during the last deglaciation, Proceedings of the National Academy of Sciences.

Stuiver, M., and H. A. Polach (1977), Discussion reporting of 14 C data, Radiocarbon, 19(3), 355-363.

Synal, H.-A., M. Stocker, and M. Suter (2007), MICADAS: a new compact radiocarbon AMS system, Nuclear Instruments and Methods in Physics Research Section B: Beam Interactions with Materials and Atoms, 259(1), 7-13.

Thornalley, D. J., S. Barker, W. S. Broecker, H. Elderfield, and I. N. McCave (2011), The deglacial evolution of North Atlantic deep convection, science, 331(6014), 202-205.

Thornalley, D. J. R., H. A. Bauch, G. Gebbie, W. Guo, M. Ziegler, S. M. Bernasconi, S. Barker, L. C. Skinner, and J. Yu (2015), A warm and poorly ventilated deep Arctic Mediterranean during the last glacial period, Science, 349(6249), 706-710, doi: 10.1126/science.aaa9554.

Tostevin, R., G. A. Shields, G. M. Tarbuck, T. He, M. O. Clarkson, and R. A. Wood (2016), Effective use of cerium anomalies as a redox proxy in carbonate-dominated marine settings, Chemical Geology, 438, 146-162, doi: https://doi.org/10.1016/j.chemgeo.2016.06.027.

Trauth, M. H., M. Sarnthein, and M. Arnold (1997), Bioturbational mixing depth and carbon flux at the seafloor, Paleoceanography, 12(3), 517-526, doi: 10.1029/97PA00722.

Vidal, L., L. Labeyrie, E. Cortijo, M. Arnold, J. Duplessy, E. Michel, S. Becque, and T. Van Weering (1997), Evidence for changes in the North Atlantic Deep Water linked to meltwater surges during the Heinrich events, Earth and Planetary Science Letters, 146(1), 13-27.

809 Wacker, L., M. Christl, and H. A. Synal (2010), Bats: A new tool for AMS data reduction,
810 Nuclear Instruments and Methods in Physics Research Section B: Beam Interactions
811 with Materials and Atoms, 268(7), 976-979, doi:
812 https://doi.org/10.1016/j.nimb.2009.10.078.
813
814 Wacker, L., J. Lippold, M. Molnár, and H. Schulz (2013), Towards radiocarbon dating of
815 single foraminifera with a gas ion source, Nuclear Instruments and Methods in Physics
816 Research Section B: Beam Interactions with Materials and Atoms, 294, 307-310, doi:
817 https://doi.org/10.1016/j.nimb.2012.08.038.
818
819 Wacker, L., S. Fahrni, I. Hajdas, M. Molnar, H.-A. Synal, S. Szidat, and Y. Zhang (2013), A
820 versatile gas interface for routine radiocarbon analysis with a gas ion source, Nuclear
821 Instruments and Methods in Physics Research Section B: Beam Interactions with
822 Materials and Atoms, 294, 315-319.
823
824 Waelbroeck, C., J.-C. Duplessy, E. Michel, L. Labeyrie, D. Paillard, and J. Duprat (2001),
825 The timing of the last deglaciation in North Atlantic climate records, Nature, 412(6848),
826 724.
827
828 Walter, S. R., A. R. Gagnon, M. L. Roberts, A. P. McNichol, M. C. L. Gaylord, and E. Klein
829 (2016), Ultra-Small Graphitization Reactors for Ultra-Microscale 14C Analysis at the
830 National Ocean Sciences Accelerator Mass Spectrometry (NOSAMS) Facility,
831 Radiocarbon, 57(1), 109-122, doi: 10.2458/azu_rc.57.18118.
832
833 Wan, S., and Z. Jian (2014), Deep water exchanges between the South China Sea and the
834 Pacific since the last glacial period, Paleoceanography, 29(12), 1162-1178.
835 Webster, J. M., J. C. Braga, M. Humblet, D. C. Potts, Y. Iryu, Y. Yokoyama, K. Fujita, R.
836 Bourillot, T. M. Esat, and S. Fallon (2018), Response of the Great Barrier Reef to sea-level
837 and environmental changes over the past 30,000 years, Nature Geoscience, 1.
838
839 Wheatcroft, R. A. (1992), Experimental tests for particle size‐dependent bioturbation
840 in the deep ocean, Limnology and Oceanography, 37(1), 90-104.
841 Wheatcroft, R. A., and P. A. Jumars (1987), Statistical re-analysis for size dependency in
842 deep-sea mixing, Marine geology, 77(1-2), 157-163.
843 Wycech, J., D. C. Kelly, and S. Marcott (2016), Effects of seafloor diagenesis on planktic
844 foraminiferal radiocarbon ages, Geology, 44(7), 551-554.

Supporting information for

Small sized foraminifer samples radiocarbon measurements using (ETHZ) MICADAS gas introduction system: insights into sediment archive preservation

L. Missiaen[1,*], L.Wacker[2], B.C. Lougheed[1], L. Skinner[3], I. Hajdas[2], J. Nouet[4], C. Waelbroeck[1] …

[1]Laboratoire des Sciences du Climat et de l'Environnement, LSCE/IPSL, CEA-CNRS-UVSQ-Université Paris-Saclay, F-91198 Gif-sur-Yvette, France.

[2]Laboratory of Ion Beam Physics, ETH Zürich, 8093 Zürich, Switzerland

[3] Godwin Laboratory for Palaeoclimate Research, Department of Earth Sciences, University of Cambridge, Cambridge CB2 3EQ, United Kingdom

[4]Université Paris Sud – Paris Saclay, UMR-CNRS GEOPS 8148, Bât. 504, Rue du Belvédère, 91405 Orsay, France

Contents of this file

Text S1 to S3

Figures S1 to S6

Tables S1 to S2

Introduction

This supporting information file contains 3 supplementary texts detailing the measurements of REE concentrations and the calculation of the Ce anomaly (Text S1), technical aspect of SEM pictures acquisition (Text S2) and the procedure followed for benthic $\delta^{13}C$ measurements (Text S3). It also contains 6 supplementary figures showing selected planktonic foraminifer abundances and sampled levels for radiocarbon analysis (Figure S1), SU90-08 radiocarbon age-depth relationship for benthic and planktonic foraminifers (Figure S2), SU90-08 REE patterns normalized to chondrites and PAAS (Figure S3), correlation tests between the $^{230}Th_{xs,0}$ and Al, Fe and Mn (Figure S4), selected SEM pictures of benthic and planktonic specimens (Figure S5) and the radiocarbon data screening through the leaching test (Figure S6). Finally, it contains 2 Tables showing the standard material results and the benthic $\delta^{13}C$ values measured in this study in SU90-08.

Text 1: Laser ablation measurements and Ce anomaly

Laser ablation measurements were performed on 16 sediments levels of core SU90-08. For each level, a dozen of planktonic foraminifer specimens (G.bulloides) were selected and prepared for laser ablation analysis. The shells were disposed in a receptacle containing methanol and dissected into chambers using clean scalpel. The material was then washed for a few seconds in ultrasonic bath to remove the clay inside the chambers that could not have been removed across the previous cleaning steps. Next, clean chamber fragments were disposed on carbon strips to expose the outer shell. REE concentrations of Foraminifer shell coatings were measured at the Godwin Laboratory, using the ANALYTE G2 excimer laser coupled with Thermo ICap-Q ICP-MS. NIST612 standard was used to optimize the ICM-MS sensitivity. In this study, the elements measured by the mass spectrometer are ^{55}Mn, ^{56}Fe, ^{88}Sr, ^{89}Y, ^{137}Ba, ^{139}La, ^{140}Ce, ^{141}Pr, ^{146}Nd, ^{147}Sm, ^{151}Eu, ^{153}Eu, ^{157}Gd, ^{159}Tb, ^{163}Dy, ^{165}Ho, ^{166}Er, ^{169}Tm, ^{172}Yb, ^{175}Lu. Data reduction, made with Iolite software, involves the subtraction of the background noise, internal standardization to ^{43}Ca and external standardization using NIS612 standard. NIST614 standard is run every 45 samples in order to calibrate and correct the instrumental drift. Raw REE concentrations are normalized against chondrite or Post Archean Australian Shale (PAAS) compositions [*Taylor and McLennan*, 1995] to remove the natural variations in absolute concentration and display the samples REE patterns (Figure S4). The analysis of the pattern allows investigating about the processes at the origin of the REE sediment content (*e.g.* hydrothermalism fluid or sea water circulations, [*Tostevin et al.*, 2016]).

Several anomalies can then be defined to quantify the amount of one element compared to his direct neighbors. For instance, the Ce anomaly is expressed with the following formula [*Wilde et al.*, 1996], all concentrations being normalized to the PAAS:

$$Ce^* = \log\left(\frac{2 \times Ce}{La+Pr}\right)$$

Ce anomaly can successfully reconstruct the oxygenation history of the sediments as the incorporation of Ce in sediment Fe-Mn oxides depends on the oxygen concentration [*Tostevin et al.*, 2016]. SU90-08 Ce anomaly record is presented in Figure 4.

Text S2: SEM pictures of SU90-08 benthic and planktonic foraminifers

Four or five benthic and planktonic foraminifera shells from 8 SU90-08 depth levels were picked and mounted on a cone using double-sided carbon tape. Then they were coated using a E5100 (Polaron) cool sputter coater equipped with a Au/Pd target. Scanning Electron Microscopy (SEM) observations were carried out on a Pro X (Phenom) bench microscope, equipped with a Back-Scattered Electron Detector (BSE) and operated at 10 keV and 3 mm working distance. A selection of the SEM images obtained is shown in Figure S5.

Text S3: Benthic $\delta^{13}C$ measurements

Epifaunal benthic foraminifers of the *Cibicides wuellerstorfi* species were handpicked in the >150 mm size fraction every 2 cm. Core SU90-08 *C. wuellerstorfi* $^{13}C/^{12}C$ ($d^{13}C$, expressed in ‰ versus Vienna Pee-Dee Belemnite, VPDB) was measured at the LSCE on Finnigan Δ+ and Elementar Isoprime mass spectrometers on samples of 1 to 3 specimens. VPDB is defined with respect to NBS-19 calcite standard ($d^{18}O$ = -2.20 ‰ and $d^{13}C$ = +1.95 ‰). The mean external reproducibility (1σ) of carbonate standards is ± 0.03 ‰ for $d^{13}C$; measured NBS-18 $d^{18}O$ is -23.27 ± 0.10 and $d^{13}C$ is -5.01 ± 0.03 ‰ VPDB. The results are presented in Table S1.

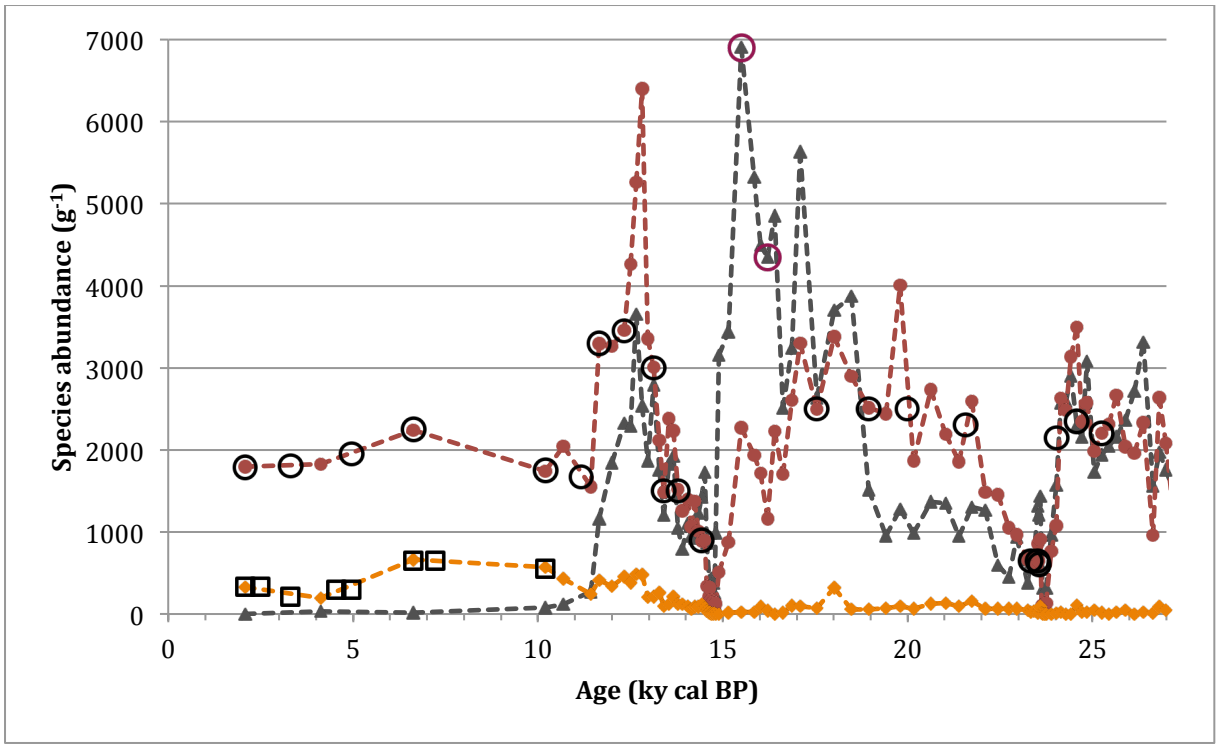

Figure S1: Downcore evolution of planktonic foraminifer abundances
The red dashed line represents the evolution of G.bulloides absolute abundance, the grey dashed line, the evolution of N. pachyderma senestral, the orange dashed line, the evolution of G. ruber. The red and black circles represent the sampled levels for gas ^{14}C analysis, the black squares represent the levels sampled for graphite analysis.

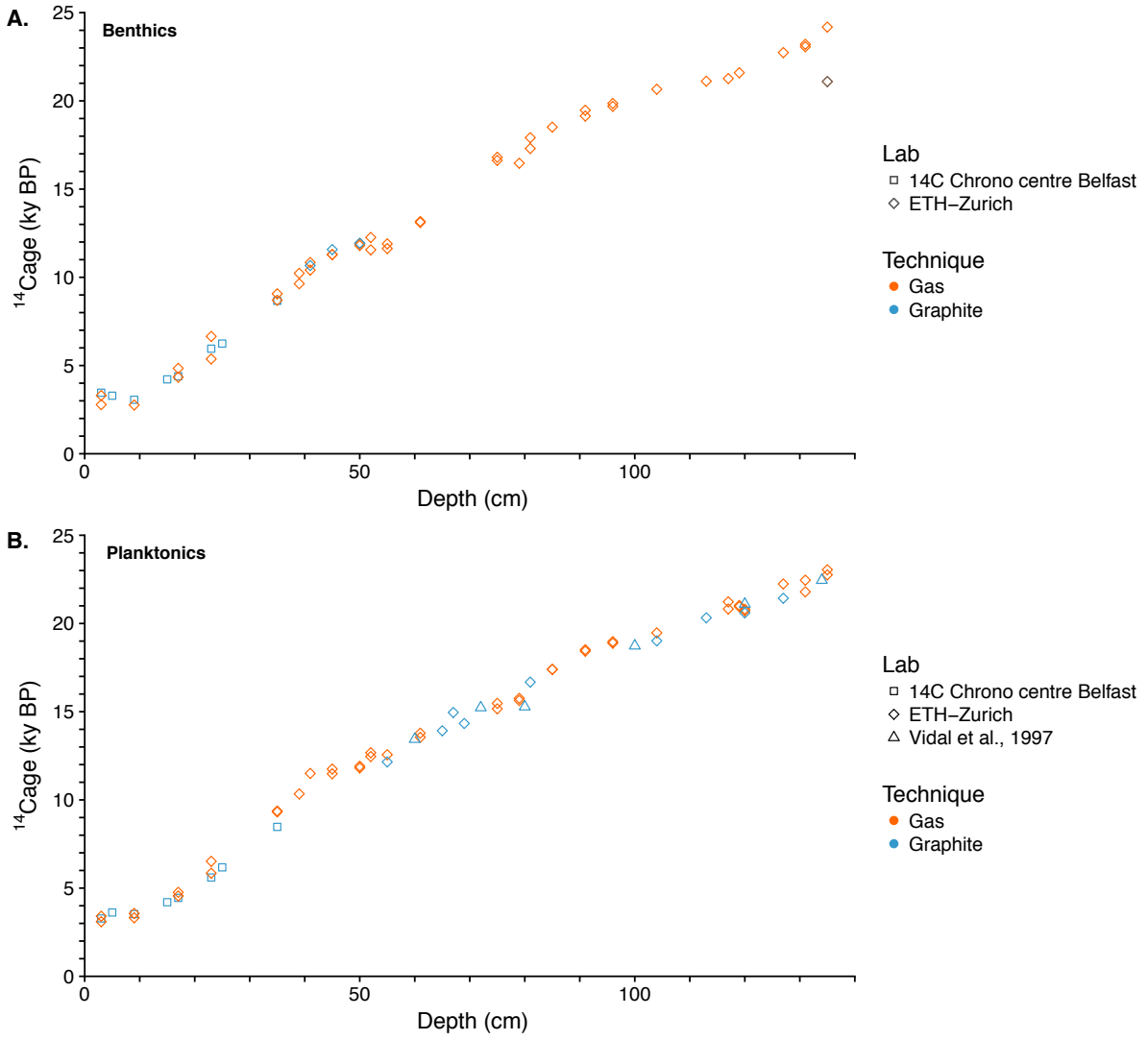

Figure S2: ^{14}C age-depth relationship for sediment core SU90-08 A. benthic and B. planktonic foraminifers.
The orange symbols represent the gas measurements while the blue symbols represent the graphite measurements. The grey point of the top panel corresponds to an off-trend benthic measurement and was thus excluded from the subsequent interpretations.

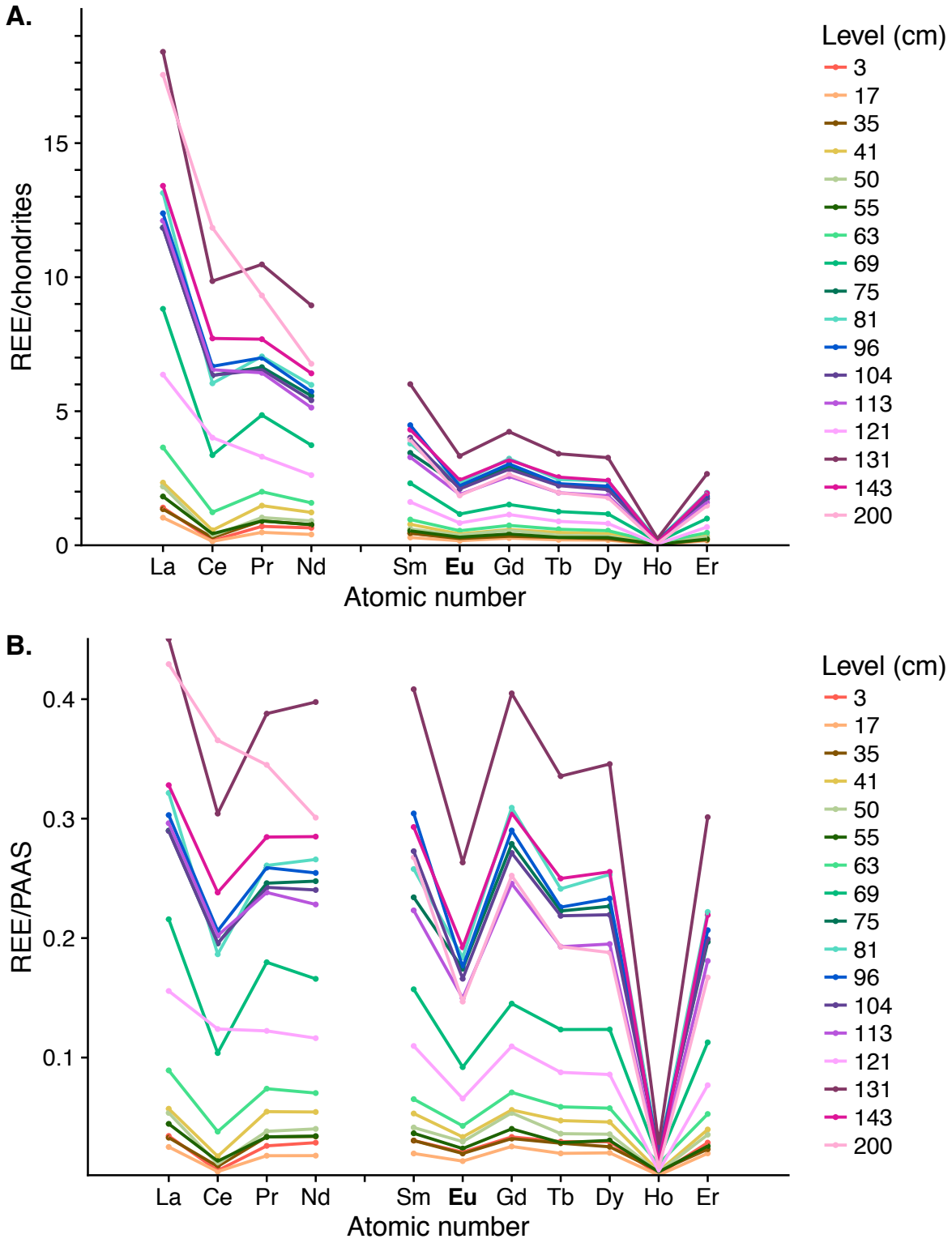

Figure S3: SU90-08 REE Patterns. A. Normalization against chondrite composition (REF) **B.** Normalization against Post Archean Australian Shale (REF)

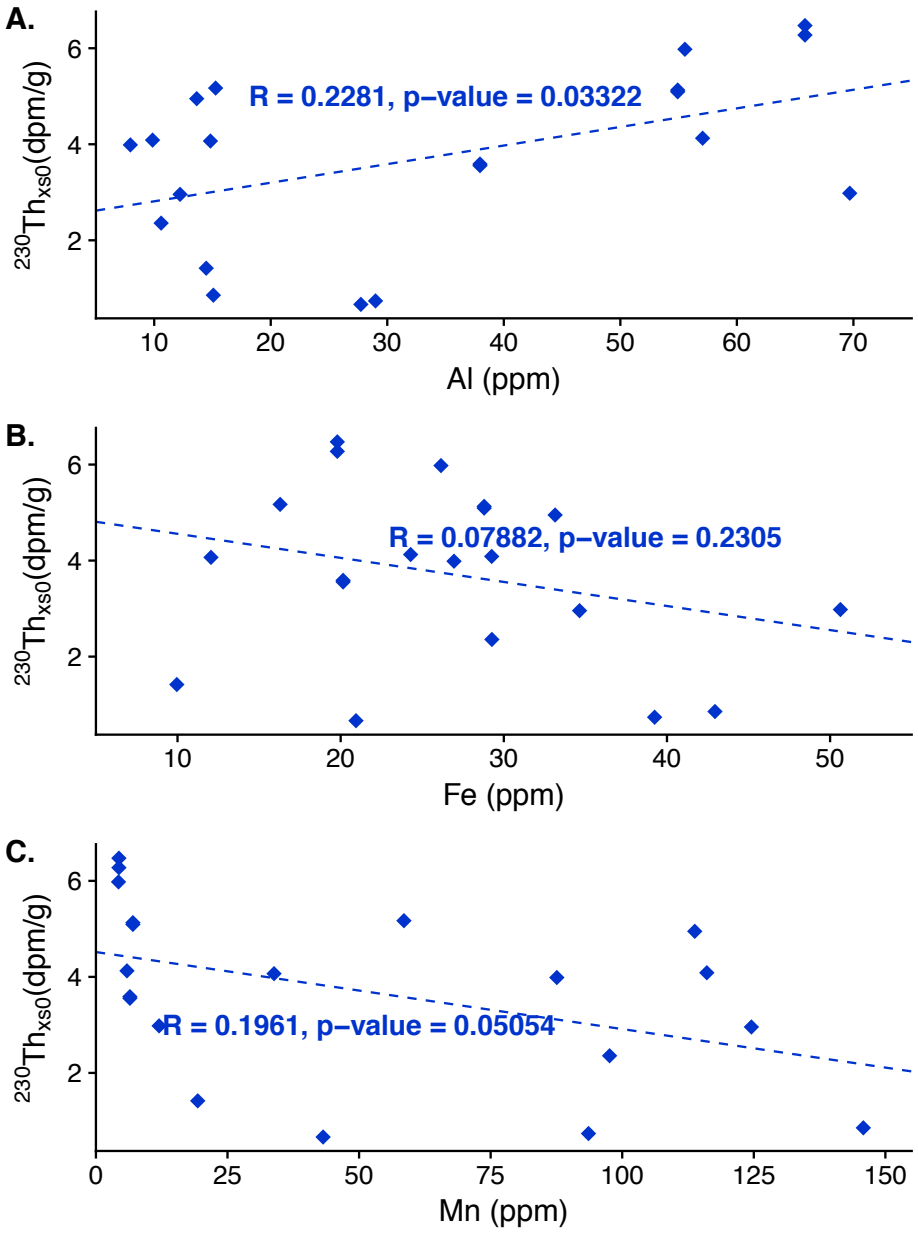

Figure S4: Evaluation of the correlation between $^{230}Th_{xs,0}$ and A. Al, B. Fe and C. Mn.

A.

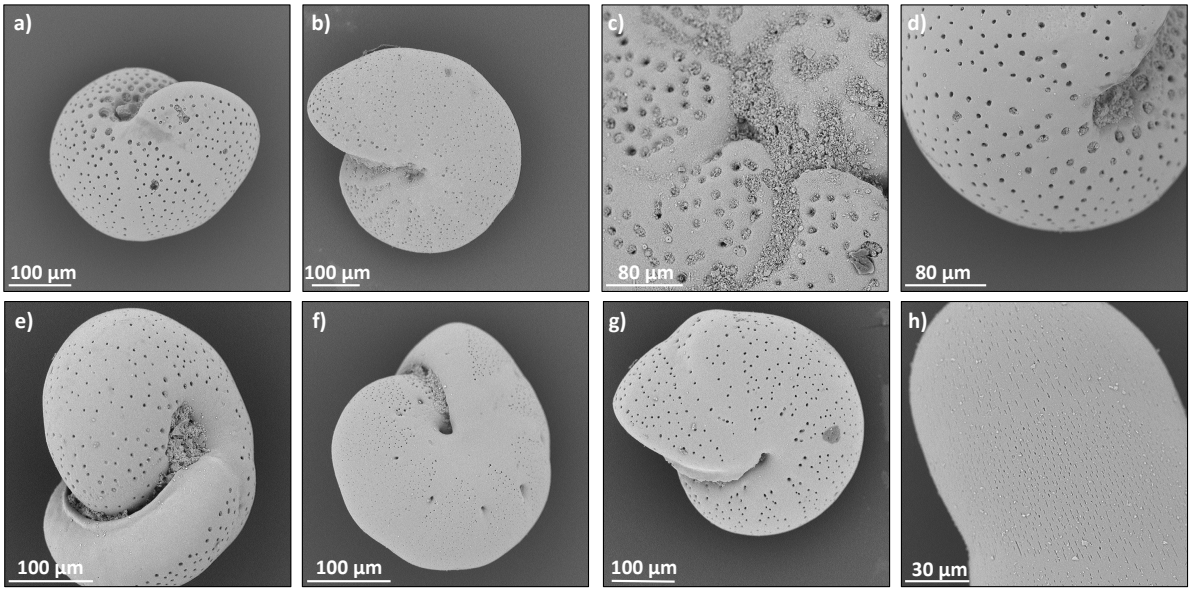

B.

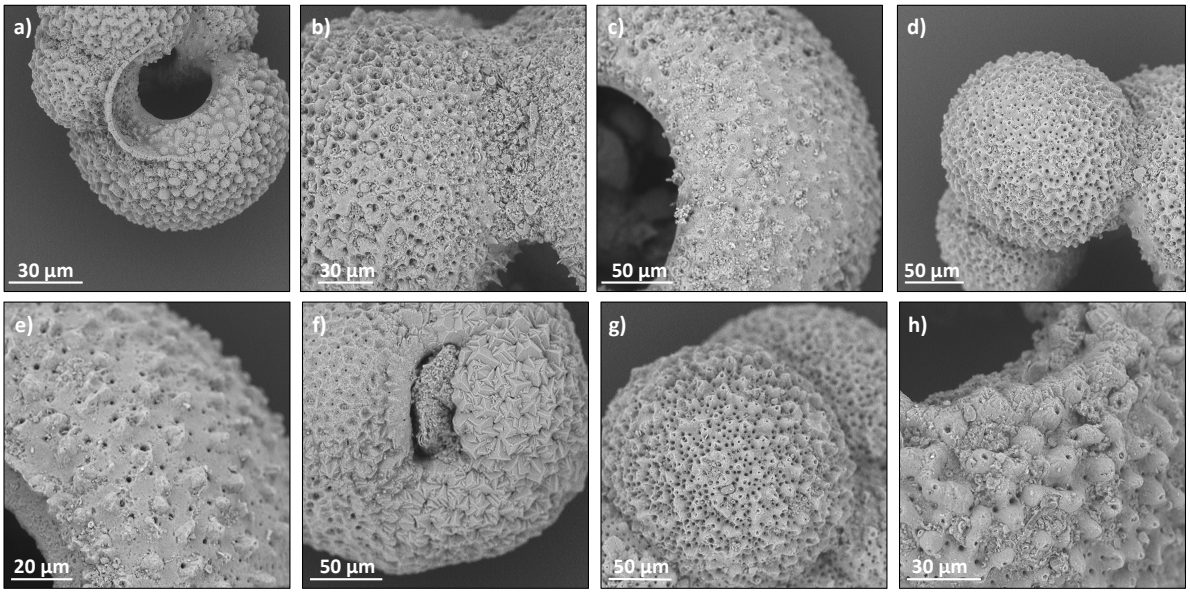

Figure S5: SEM pictures of SU90-08 benthic (A.) and planktonic (B.) foraminifers
a) 35-36 cm, b) 41-42 cm, c) 50-51 cm, d) 52-53 cm, e) 61-62 cm, f) 79-80 cm, g) 96-97 cm, h) 131-132 cm.
Planktonic foraminifers display some dissolution features as well as recrystallization of secondary calcite (especially in b) and f)). However, no drastic change in the foraminifer conservation is observed between the upper part of the core (0 to 65 cm) and the lower part of the core (65 to 135 cm).

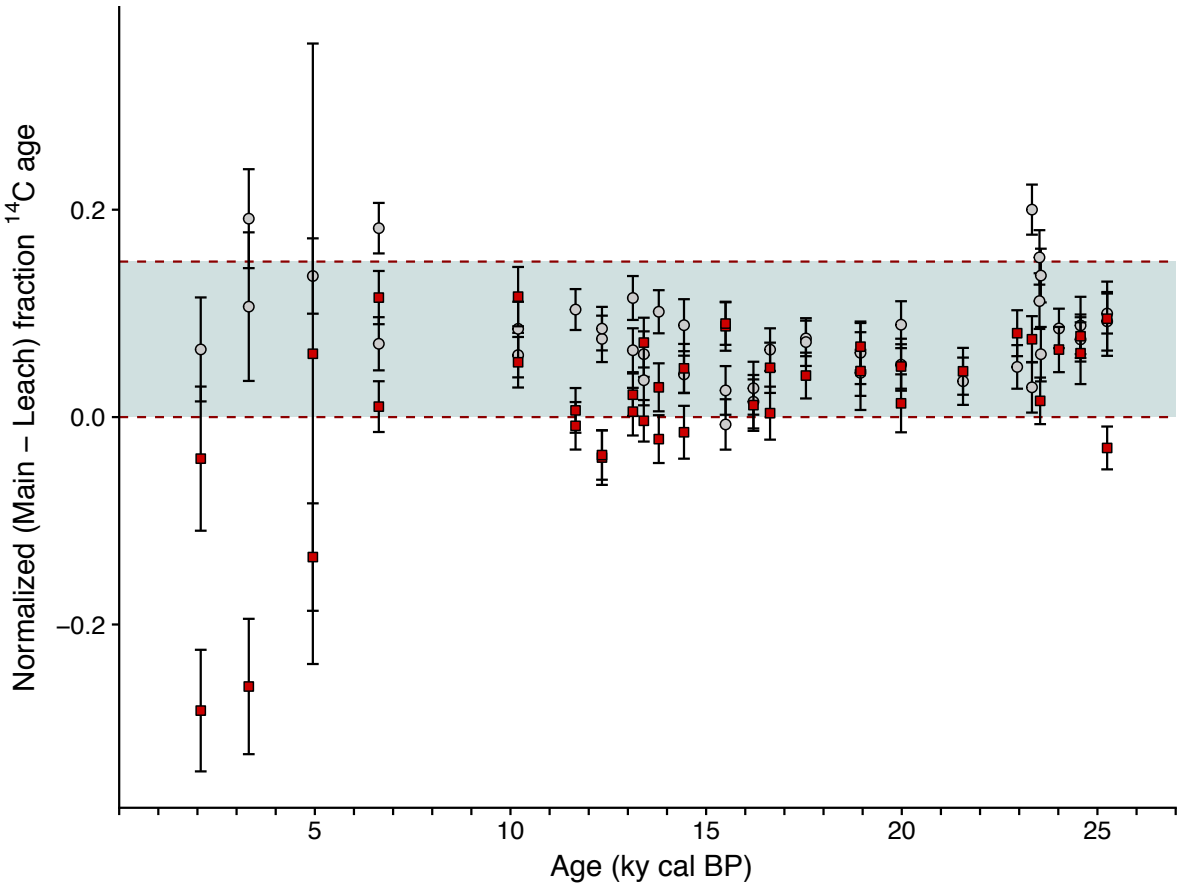

Figure S6: Leaching test. The grey dots correspond to planktonic measurements, the red squares to benthic measurements. The y axis correspond to the difference between the main and leach fraction ^{14}C age normalized by the main fraction age. The two dashed red lines correspond to thresholds. The leach fraction should not be older than the main fraction and the radiocarbon age difference between the leach and the main fraction should not exceed 15% of the reference main fraction age (see main text). All the data out of the green rectangle within the given 1σ uncertainties were rejected of our analysis: 2 data points for the planktonic foraminifers and 6 data points for the benthic foraminifers.

Table S1: Standard material radiocarbon measurements
^{14}C-free foraminifera were measured on mono-specific planktonic (G.bulloides) and mixed benthic samples hand-picked from sediments older than 260 ky of core SU90-08.

Material/standard	Reference $F^{14}C$	Measured $F^{14}C$	Uncertainty (1σ)
CSTD	0.9445 ± 0.0018	0.9461	0.0074
CSTD	0.9445 ± 0.0018	0.9287	0.0123
CSTD	0.9445 ± 0.0018	0.9414	0.0083
CSTD	0.9445 ± 0.0018	0.9371	0.0122
IAEA-C2	0.4114 ± 0.0003	0.4088	0.0040
IAEA-C2	0.4114 ± 0.0003	0.4170	0.0041
IAEA-C2	0.4114 ± 0.0003	0.4024	0.0045
IAEA-C2	0.4114 ± 0.0003	0.4305	0.0073
IAEA-C2	0.4114 ± 0.0003	0.4094	0.0045
IAEA-C2	0.4114 ± 0.0003	0.4277	0.0074
IAEA-C1	0.0000 ± 0.0002	0.0034	0.0005
IAEA-C1	0.0000 ± 0.0002	0.0038	0.0005
IAEA-C1	0.0000 ± 0.0002	0.0036	0.0006
IAEA-C1	0.0000 ± 0.0002	0.0024	0.0004
IAEA-C1	0.0000 ± 0.0002	0.0044	0.0005
IAEA-C1	0.0000 ± 0.0002	0.0121	0.0013
^{14}C free foraminifer (benthic)	-	0.0053	0.0004
^{14}C Free foraminifer (planktonic)	-	0.0050	0.0004

Table S2: SU90-08 benthic $\delta^{13}C$ measurements

Depth (cm)	Benthic $\delta^{13}C$ (‰ PDB)
1	1.33
3	1.16
5	1.28
7	1.26
9	1.26
10	1.27
11	1.17
15	1.16
17	0.87
19	1.17
20	1.05
21	1.08
23	1.24
25	1.29
27	1.28
29	1.16
30	1.14
31	0.96
33	1.23
35	1.24
37	1.20
39	1.15
40	1.12
41	1.01
43	1.00
45	1.07
47	1.04
49	1.17
51	1.08
53	1.07
55	1.16
57	1.12
59	0.94
61	1.00
63	0.75
65	1.01
69	0.24
71	0.40
73	0.41
75	0.27
77	0.49
79	0.32
81	0.72
83	0.61
85	0.40
87	0.16
89	0.57
91	0.45
93	0.31
94	0.36
96	0.39
97	0.32
99	0.33
101	0.42
103	0.20
105	0.66
107	0.19
109	0.27
111	0.38
113	0.64
115	0.67
117	0.43
119	0.61
121	0.67
123	0.47
125	0.49
127	0.42
129	0.44
131	0.54
133	0.36
135	0.51

137	0.41
139	0.44
141	0.60
143	0.75
145	0.61
147	0.66
149	0.67
151	0.94
153	1.16
155	0.87
157	0.93
159	0.83
161	1.07
163	1.01
165	0.86
167	0.80
169	1.09
170	1.09
171	1.33
172	1.20
173	1.24
174	1.07
175	0.97
176	0.95
177	1.03
178	1.15
179	1.14
181	1.03
183	1.15
185	1.04
187	1.23
189	1.29
191	1.12
193	1.26
195	0.78
197	1.11
199	1.22
205	0.86
207	1.10
209	1.29
211	1.23
213	1.32
215	1.35
217	1.13
219	1.28
221	1.18
223	1.21
225	1.08
227	1.22
229	0.90
231	1.32
233	1.08
235	1.26
237	1.12
239	1.00

References

Taylor, S. R., and S. M. McLennan (1995), The geochemical evolution of the continental crust, Reviews of Geophysics, 33(2), 241-265, doi: 10.1029/95RG00262.

Tostevin, R., G. A. Shields, G. M. Tarbuck, T. He, M. O. Clarkson, and R. A. Wood (2016), Effective use of cerium anomalies as a redox proxy in carbonate-dominated marine settings, Chemical Geology, 438, 146-162, doi: https://doi.org/10.1016/j.chemgeo.2016.06.027.

Wilde, P., M. S. Quinby-Hunt, and B.-D. Erdtmann (1996), The whole-rock cerium anomaly: a potential indicator of eustatic sea-level changes in shales of the anoxic facies, Sedimentary Geology, 101(1), 43-53, doi: https://doi.org/10.1016/0037-0738(95)00020-8.

4.2.2 The sedimentary Pa/Th

By construction, the sedimentary Pa/Th is driven both by the strength of water advection and the composition and intensity of particles fluxes (see chapter 1 for details). Therefore, before interpreting SU90-08 sedimentary Pa/Th as circulation changes, several tests have to be run to ensure that the proxy variations are not primarily controlled by particles changes. To perform these tests, I adopted here the approach generally followed in the literature (*e.g.* Böhm et al., 2015; Burckel et al., 2016, 2015; Lippold et al., 2012; Waelbroeck et al., 2018). In particular, it has been shown that ^{231}Pa has a high affinity for opal compared to other particles (Chase et al., 2002). As a consequence, high Pa/Th ratios are observed in areas with high opal concentration, irrespective of the local advection rate. Similarly, in regions with high particle flux, high Pa/Th values have been reported (Lippold et al., 2012). Finally, it has also been shown that hydrothermal fluids released from the mid Atlantic ridge are rich in Fe and Mn oxides, for which ^{231}Pa has high affinity. Hence, hydrothermal activity can affect ^{231}Pa and ^{230}Th cycles in the water column and ultimately the sedimentary Pa/Th (Hayes et al., 2015).

SU90-08 is located in the western North Atlantic, where many studies have shown that the sedimentary Pa/Th can be used as a proxy for AMOC changes (see Böhm et al., 2015; Lippold et al., 2012, 2016). Moreover, sedimentary Pa/Th has already successfully been used as a kinematic circulation proxy in this core for an other time period (Guihou et al., 2010). However, as described earlier in this thesis (chapter 1, 3) and shown in Figure 4.2 A., SU90-08 exhibits IRD grains layers and very large terrigenous inputs across three of the four last Heinrich events (H3 is not recorded in this core). The core is also located quite close to the mid Atlantic ridge and thus within the area potentially influenced by hydrothermal activity. Hence, we carefully evaluated the potential impact of the opal, the terrigenous flux changes and of hydrothermal activity on SU90-08 sedimentary Pa/Th record.

First, opal concentrations were measured using Fourier transform infrared spectroscopy as described in (Vogel et al., 2016). The measured opal concentrations are very low and all fall below 5wt%. Besides, there is no significant correlation between the opal flux and the sedimentary Pa/Th (Figure 4.1 A). However, two measurements within the HS1 layer have significantly higher opal flux than the rest of the samples primarily because of their high sedimentary flux (reconstructed from $^{230}Th_{xs,0}$ – Figure 4.2 A.) rather than because of their high opal content (all the samples have opal content lower than 5wt%). The opal flux of these two levels does not exceed the arbitrary limit of acceptable opal flux of 0.2 g.cm^{-2}.ky^{-1} proposed by Lippold et al. (2012). Taking those two measurements aside, there is no significant correlation between opal flux and sedimentary Pa/Th. Consequently, I conclude that the opal content cannot be the main driver of observed SU90-08

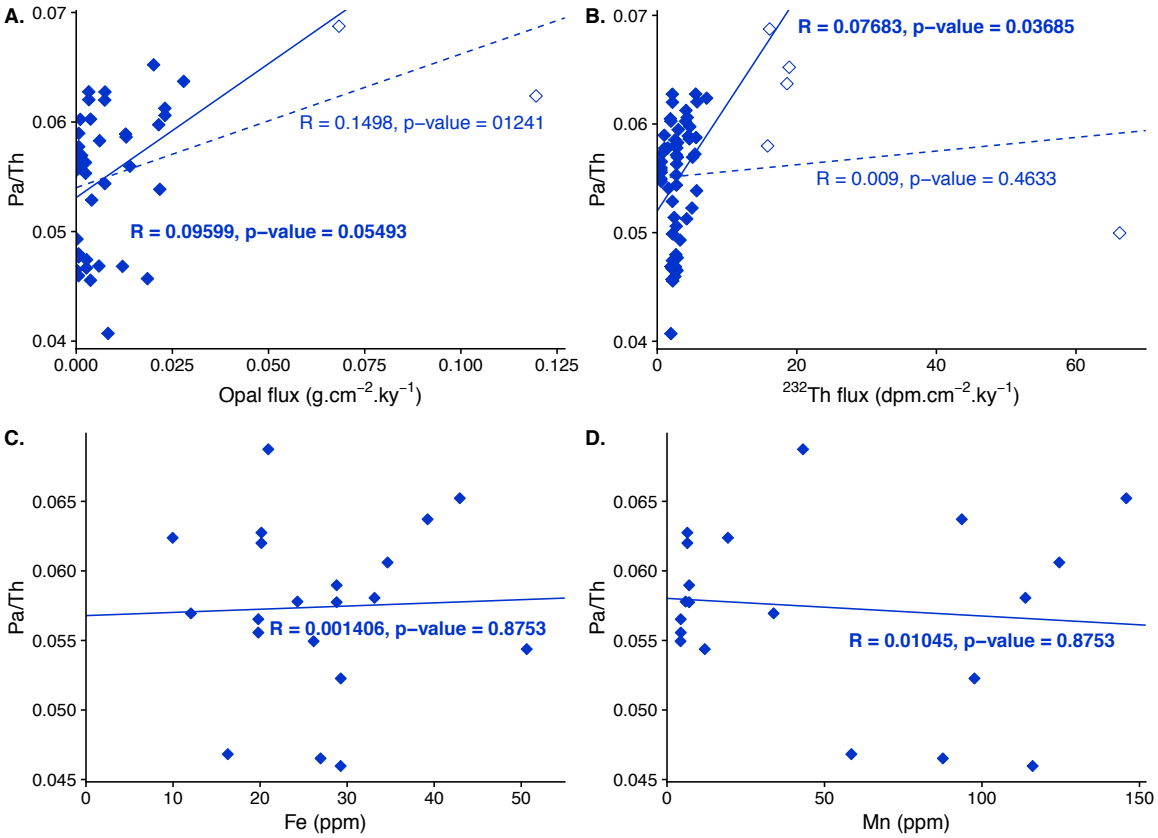

Figure 4.1 – **SU90-08 Pa/Th versus A. Opal flux, B. ^{232}Th flux, C. Fe planktonic foraminifer coating concentration and D. Mn planktonic foraminifer coating concentration.**
Open symbols correspond to levels with high particulate flux. The dashed line corresponds to the linear regression including open symbols data points. The solid line corresponds to the linear regression excluding the open symbol data points. R^2 and the p-value corresponding to each linear regression are indicated next to the corresponding regression line.

sedimentary Pa/Th variations.

Then, the vertical terrigenous flux is evaluated using the ^{232}Th-^{230}Th-normalized flux (here after the ^{232}Th flux). Five levels in the Heinrich layers have remarkably high ^{232}Th flux, above 10 dpm.cm^{-2}.ky^{-1}. Taking into account or excluding those levels does not change the general absence of correlation observed between the ^{232}Th flux and the sedimentary Pa/Th (Figure 4.1 B.). The sedimentary Pa/Th and the ^{232}Th flux display higher correlation when considering apart the data related to the Heinrich stadials (Figure 4.2 B.). I observe significant correlation between Pa/Th and the ^{232}Th flux during HS1 but no correlation during HS2 and very little correlation during HS4 (Figure 4.2 B.). However, the observed behavior of the two tracers matches with their expected change across Heinrich events 1 and 4 while the absence of correlation during HS2 can be related to the absence of marked Pa/Th variations during this time interval. Moreover, the Pa/Th does not reach the production ratio over the last 40 ky in SU90-08 record while the Pa/Th values can be largely above the production ratio in areas of high particle fluxes (*e.g.* the

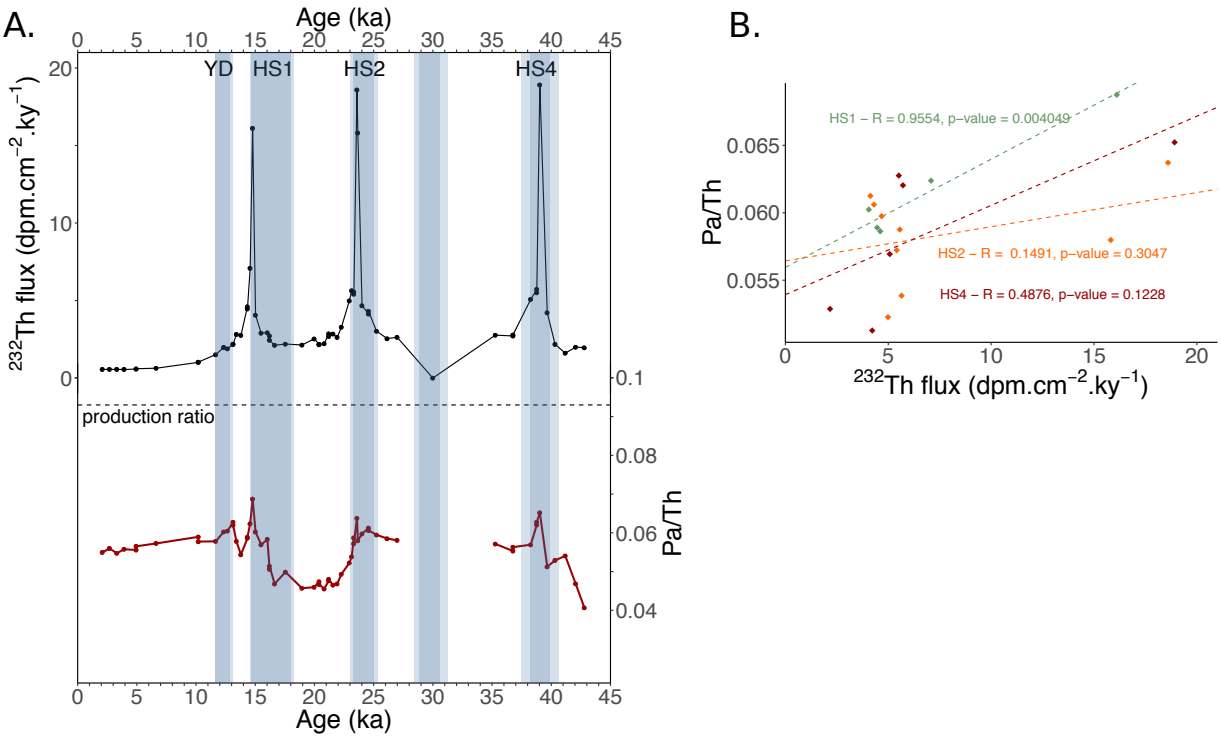

Figure 4.2 – **SU90-08 ^{232}Th flux and Pa/Th**
A. ^{232}Th flux and Pa/Th time series, **B.** Correlation between ^{232}Th flux and Pa/Th for the Heinrich stadials 1, 2 and 4

opal belt in the Southern Ocean). This argues that advection is a primary control on the Pa/Th proxy at this location during the studied time interval.

Finally, the impact of hydrothermal activity on SU90-08 sediment was tested using Fe, Mn and Rare Earth Elements (REE) content. The latter was measured by laser ablation on planktonic foraminifer (G. *bulloides*) coatings and record the bottom and pore water composition. No correlation was observed between sedimentary Pa/Th and Fe and Mn concentrations, two elements in high concentration in hydrothermal environments (Figure 4.1 C. - D.). Additionally, the REE patterns do not show the positive Eu anomaly typical of the hydrothermal vent fluids signature (Figure 4.3). Instead, the sediment displays the negative Ce anomaly, typically observed in sea-water.

In conclusion, it seems unlikely that SU90-08 sedimentary Pa/Th variations are primarily driven by change in particle nature, flux or hydrothermal activity. Instead, Pa/Th measurements reflect the circulation strength changes at SU90-08 location over the last 40 ky. During the specific periods of HS1 and HS4, the Pa/Th signal probably represents a convolution of the change in water mass advection and the increase of the particle flux that is remarkably high during those periods.

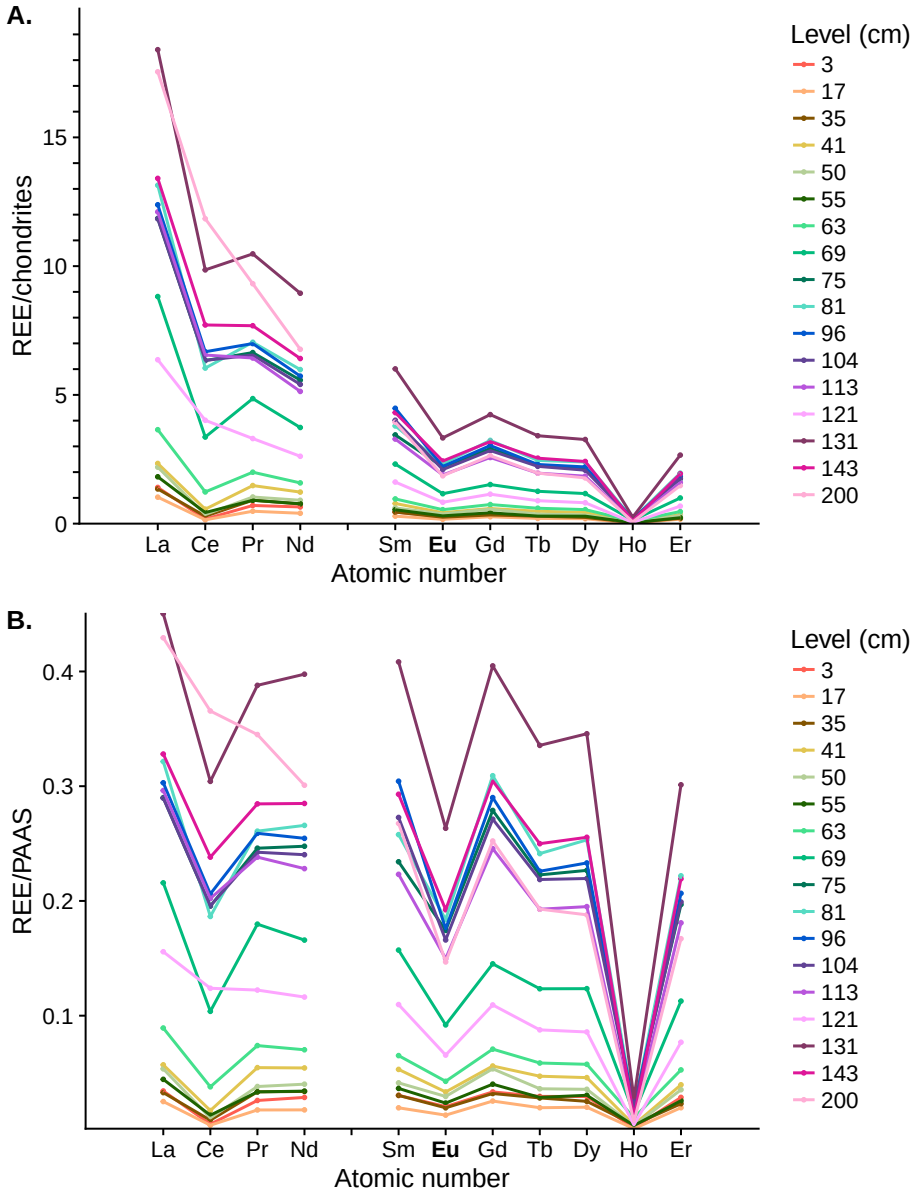

Figure 4.3 – **SU90-08 REE patterns normalized by A. chondrites REE composition and B. Post Archean Australian Shale (PAAS) composition** (Taylor & McLennan, 1995). A positive Eu anomaly is typical from hydrothermal fluid REE pattern; a negative Ce anomaly is typical from seawater REE pattern.

4.2.3 Poorly ventilated/oxygenated deep waters but active overturning at the LGM

In the previous sections, we have analyzed in details the potential biases of the radiocarbon and Pa/Th records. We have shown that i) SU90-08 deglacial ^{14}C B-P measurements can only bring first order paleoceanographic information; ii) the sedimentary Pa/Th likely faithfully capture the circulation signal. SU90-08 paleoproxy time series appear generally smoothed and contain little millennial scale variability. This can be

related to the core sedimentation rate, which is relatively low (around 3 cm/ky for the Holocene and 6 cm/ky during the glacial period) except during the Heinrich events (see chapter 3). Besides, like any other sediment core, SU90-08 is affected by bioturbation. The combination of bioturbation and low sediment accumulation accounts for the smoothing of the available paleo-proxy records. Therefore I will first focus on the analysis of the glacial-interglacial information recorded by the three proxies.

Radiocarbon data clearly differentiate a glacial mode (from HS2 to the end of HS1) and a modern-like mode (starting at the end of HS1) (Figure 4.4). The glacial mode is characterized by a greater radiocarbon age gradient between the surface and deep waters reflecting a reduced export of surface water to the ocean interior. In other words, under glacial conditions, the deep-water mass bathing SU90-08 location is poorly ventilated and poorly oxygenated and the water column appears more stratified. On the contrary, the modern-like mode corresponds to a very reduced (potentially almost inexistent) radiocarbon age gradient between the surface and the deep waters. Under modern-like conditions, the deep-water mass bathing SU90-08 location is well ventilated and well oxygenated. This radiocarbon pattern reproduces the first order benthic δ^{13}C pattern, showing good ventilation of deep-water masses from 45 ka to ∼33 ka and after the end of HS1 (from 14.7 ka to present). The deep-water ventilation decreases at SU90-08 location from 33 ka and reaches a minimum during the LGM, which lasts until 14.7 ka (Figure 4.4). Generally, the two carbon based proxy agree and show a first order pattern for deep waters alternating between modern-like, well ventilated conditions before 33 ka, then glacial and poorly ventilated conditions until the end of HS1, then well ventilated conditions again until present. This general pattern is out of phase with sedimentary Pa/Th evolution, which is not showing this three phases evolution. Instead, the Pa/Th displays low values accounting for an active overturning circulation through the entire record (Figure 4.4). The Pa/Th values are lower during the LGM compared to the Holocene. Thus, the circulation seems to have been more active during the LGM than during the Holocene. The sedimentary Pa/Th also indicates circulation reduction during HS4 and at the end of HS1 with Pa/Th values going from 0 .04 to 0.065 but not during HS2.

Consequently, to the first order, SU90-08 data show that there was an active overturning circulation that imprinted the low Pa/Th values at SU90-08 site during the LGM (25 to 14.7 ka) while the deep waters were poorly ventilated and poorly oxygenated. This result definitely contrasts with the traditional ventilation proxy interpretations that the poor ventilation of deep-water masses automatically results in sluggish/weak circulation. Besides, this result raises the question whether the different proxies sample the same water mass or distinct water masses. Indeed, the proxies have distinct carrier phases: carbon isotopes are measured on benthic and planktonic foraminifers whereas sedimentary Pa/Th is measured on the fine-size sediment (on which Pa and Th stick more efficiently). Thus,

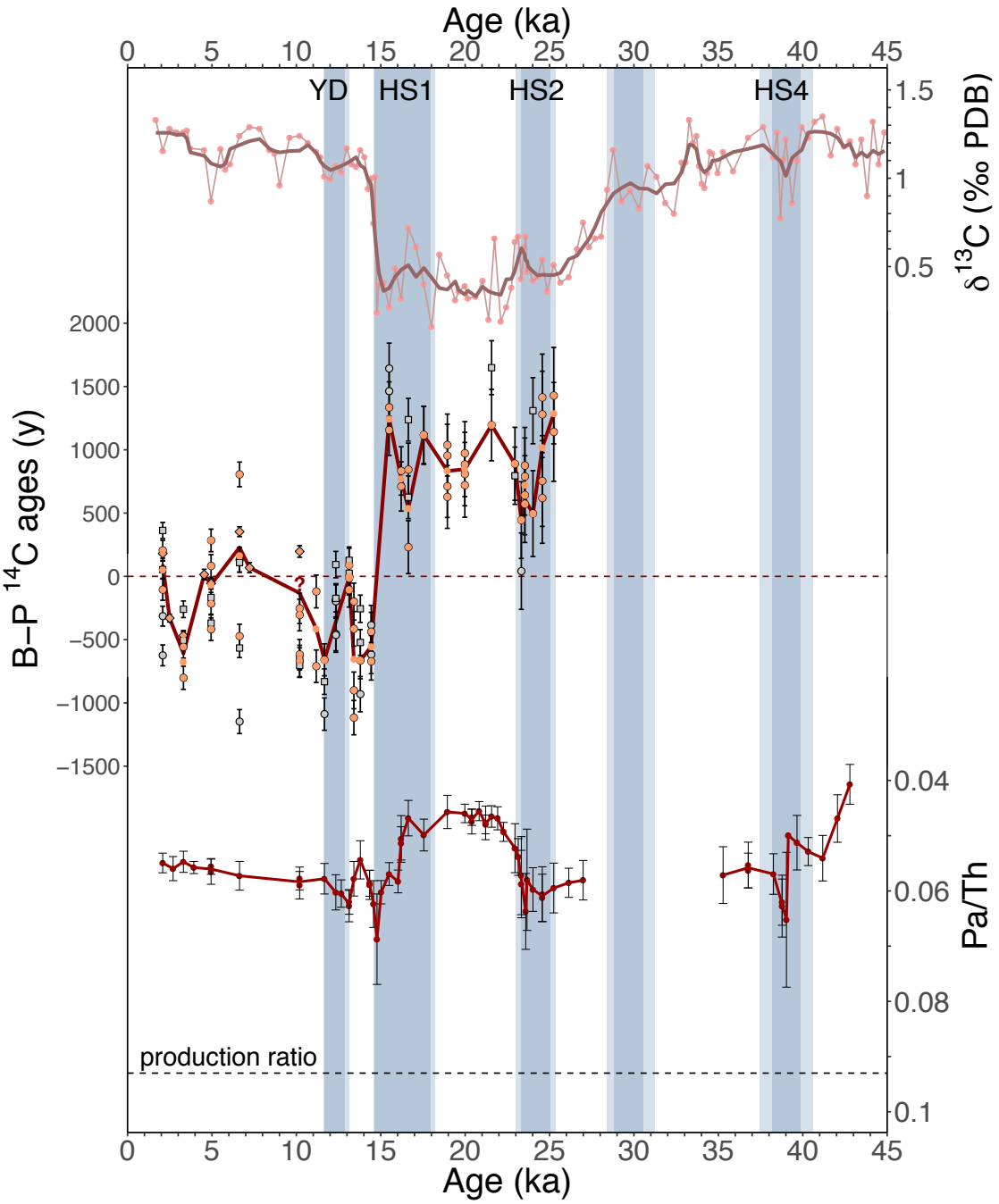

Figure 4.4 – **SU90-08 multiproxy circulation record across the last 40 ka.** From top to bottom: benthic δ^{13}C, ^{14}C B-P ages and sedimentary Pa/Th. The uncertainty represented is 1 σ for radiocarbon and 2 σ for Pa/Th. The blue vertical bands indicate the timing of abrupt climate events with their error bars. The carbon based proxies display consistent first order pattern whereas the sedimentary Pa/Th have a different pattern. The proxies account for a poorly ventilated deep-water mass but active circulation overturning during the LGM

if the carbon content reflects the composition of the surface or deep waters in which the foraminifer shells developed, the Pa/Th integrates the signature of a more extended portion of the water column, potentially corresponding to the last 1000 m above the sea

floor (Thomas et al., 2006), where the exchanges between the dissolved phase and the particulate phases are more intense. Thus, it is theoretically possible that under glacial conditions, the sedimentary Pa/Th reflects the overturning efficiency of an intermediate water mass (which could be centered around 2000 m) while the carbon isotopes capture the poor ventilation of the deep-water masses (at 3080 m).

From the study of these SU90-08 multi-proxy records, it seems difficult to determine whether the carbon isotopes and the sedimentary Pa/Th capture the signal from the same or from different water masses. However, I briefly discuss here the implications of each situation and confront it to the information comprised in the literature.
First, I consider the case in which all the proxies represent the ventilation and circulation signature of the same water mass. Under modern conditions, at this location, the entire water column has a strong imprint of the well-ventilated and oxygenated LSW even if the water mass bathing the location corresponds to a mixing of LSW and LNADW (Paillet et al., 1998). Considering that the proxy records all represent the history of this water mass, the Pa/Th indicates that the the LSW production never completely ceased over the last 40 ky and that the LSW flow rate was more intense during the LGM than during the Holocene. From 33 ka, the ventilation decrease indicates that the surface waters at the deep convection site were more isolated from the atmosphere. This could be related to the extension of ice-sheets, ice-shelves and sea-ice that occurred between 40 ka and the LGM (Argus et al., 2014; Peltier et al., 2015; Ivanovic et al., 2016; Briggs et al., 2014; Tarasov et al., 2012) and is consistent with sea level evolution reconstructions (Lambeck et al., 2014). Proxy studies using dinoflagellates and diatoms confirm that the Labrador Sea was probably completely covered by ice-shelves and permanent sea-ice during the LGM (De Vernal et al., 2005; Pflaumann et al., 2003). Under the assumption that the Labrador Sea is completely covered by sea-ice, the deep water formed in this area would have lower ^{14}C content and lower $\delta^{13}C$ value due to the absence of ^{14}C diffusion through sea-ice and the reduced biological activity. By analogy, one can consider that the deep water formed would have the same signature than the current poorly ventilated AABW that also forms under sea-ice ($\delta^{13}C$= 0.4 ‰, $\Delta^{14}C$=-100 ‰). This hypothesis is consistent with the study of Keigwin & Swift (2017), which evidences the presence of a dense and nutrient depleted water mass in the deep western North Atlantic during the LGM from $\delta^{13}C$ and $\Delta^{14}C$ measurements. However, we have to point out that this scenario requires deep-water formation under permanent sea-ice cover. In the models, sea-ice brings fresh water flux, thus reducing the deep convection. Consequently, a reduction of sea-ice export to North-Atlantic convection sites tends to increase the overturning by a few Sv (Mauritzen & Häkkinen, 1997). For example, in the climate model of intermediate complexity LOVECLIM, Menviel et al. (2017) observe that Labrador convection site is absent for various possible circulation patterns under LGM boundary conditions. Instead,

the deep-water formation sites migrated southward (generally South of Iceland). Thus in LOVECLIM, sea-ice tends to prevent/reduce deep-water convection. This result has to be nuanced because what is simulated in a model highly depends on the choices made to represent the fluid dynamics. Thus, results may be different from one model to another and do not necessary represent the real evolution of ocean circulation. To date and to my knowledge there is no clear intercomparison study on the influence of sea-ice cover on deep-water formation in the climate and ocean circulation models.
Alternatively, if we consider that the Pa/Th and carbon isotopes capture the signature of two different water masses, the ventilation decrease from 33 ka could be interpreted as a diminution of the LSW density that would not reach the ocean floor at SU90-08 location. The deep water that bath SU90-08 location would then be replaced by AABW from Antarctica as proposed in Böhm et al. (2015) and Lippold et al. (2016). The ϵNd shows a shift between the LGM and the Holocene in SU90-08 neighboring cores (*i.e.* IODP-U1313 and SU90-03 (Lippold et al., 2016; Pöppelmeier et al., 2018). Around SU90-08 location ϵNd does not reach a marked AABW signal at the LGM and potentially reflects a heavily mixed water mass. The provenance of the deep-water mass filling the Atlantic basin during the LGM is still under debate. For instance, Böhm et al. (2015), Lippold et al. (2016), Pahnke et al. (2008) and Roberts et al. (2010) interpreted that the ϵNd data showed a southern origin for the deep and intermediate Atlantic waters suring the LGM while Howe et al. (2016),Keigwin & Swift (2017) and Pöppelmeier et al. (2018) argued for a Northern sourced water filling the deep Atlantic basin. Besides, the interpretation of ϵNd as tracer of water mass provenance in the Atlantic is complicated by evidence of changes in the endmembers through the last glacial cycle. This scenario hypothesizing the presence AABW at depth at SU90-08 location is also consistent with the ice-sheets, ice-shelves and se-ice development since 40 ka in both the Arctic and Antarctic region. The extension of Arctic sea-ice could have driven the shoaling of the GNAIW by reorganization of the North-Atlantic deep-water formation zones. In that case, the AABW just mechanically filled the ocean bottom. Alternatively, the Antarctic sea-ice extension could have driven the northward shift of the sub-Antarctic divergence and thus caused the shoaling of the upper North Atlantic cell as proposed in Ferrari et al. (2014). However, from the available data it is difficult to conclude which (Arctic or Antarctic) region is driving the Atlantic circulation changes observed at SU90-08 site.

To conclude, the first order variations in the multi-proxy records at SU90-08 show a sharp circulation change across the last deglaciation. At the LGM, the deep waters were poorly ventilated but the overturning was vigorous. In contrast, the Holocene was characterized by a higher deep-water ventilation but and less vigorous overturning. These changes are probably related to the extension of the cryosphere in conjontion with sea-level decrease from roughly 30 ka toward the LGM (Lambeck et al., 2014). Integration

with other proxy record and modeling studies are necessary to investigate about the mechanisms that actually cause the apparent out of phase relation between ventilation and circulation at this particular location and water depth.

4.2.4 Moderate circulation slowdown and ventilation decrease during the Heinrich events

After having detailed the first order variations for SU90-08 multi-proxy circulation record, I focus on more muted variations corresponding to millennial scale climate events (*e.g.* YD, BA, HS, DO). Given the relatively low sedimentation rate (∼4 cm/ky in average) and the smoothing effect of bioturbation, the multi-proxy record has limited temporal resolution despite the high-resolution sampling of the sediment core (each proxy was measured approximately every 2 or 3 cm). Consequently, the record cannot provide reliable information about millennial scale events that are shorter than about 2000 years because they would be represented by insufficient number of data points. Thus I focus here on the Heinrich events that are captured in the record (HS1 and HS4) as well as the YD and BA periods.

If the carbon-based circulation proxies and the Pa/Th display first order out of phase variations, we observe subtle in phase changes during the millennial scale events. Indeed, the Pa/Th and the benthic δ^{13}C indicate slight circulation and ventilation decrease during HS4 and the second half of HS1 whereas nothing seems to happen during HS2 within the estimated proxy uncertainty. We also note that the circulation strength and the ventilation are hardly reduced during the YD. The ^{14}C B-P ages indicate a reduction of the surface to deep-water radiocarbon age gradient during HS1, HS2 and perhaps during the YD (negative data). Note that no data is available for HS4. This data suggests a reduction of the water column stratification or, in other words, more homogenous radiocarbon content between the surface and deep waters across those abrupt climate events. However, the ^{14}C B-P ages evolution during the stadial is not the same for the different stadials. For the YD, the B-P gradient is minimal at the beginning of the event and increases afterwards; for HS1 we observe an inverted W pattern and for HS2 the B-P gradient first decreases and then increases across the stadial. Variations of the B-P gradient can be obtained by changing the surface reservoir ages or the benthic reservoir ages or a combination of both. At SU90-08 site, the surface reservoir ages vary between ∼500 years during the Holocene, to ∼1000 years during the YD and up to ∼3000 years in the begining of HS1. We observe parallel changes of the benthic and surface reservoir ages: during HS1 and the YD, we observe increased radiocarbon reservoir ages while the opposite pattern is observed for HS2 (Figure 4.5).

SU90-08 multi-proxy data supports here the differences between the millennial scale

events such as the YD and the Heinrich events and between the Heinrich events that have been reported in the literature (*e.g.*Kissel (2005), Thiagarajan et al. (2014)). For instance, H3 is not recorded in this core whereas it is the case elsewhere in the Atlantic (Vidal et al., 1997). Besides, the radiocarbon surface and deep reservoir ages have different patterns during HS1 and HS2. Moreover, the Pa/Th display not clear variation during HS1 while a significant increase is recorded for HS4, HS1 and the YD. Thus, a single mechanism likely does not explain all the millennial scale climate variability. Gathering more proxy data and from various locations would help to better fingerprint each event and decipher the different mechanisms at play.

4.3 Comparison with other North-Atlantic records

We have described significant glacial-interglacial and millennial scale features in SU90-08 multi-proxy record. Now we will compare SU90-08 proxy variations with other records from North Atlantic to see if a consistent pattern emerges.

SU90-08 benthic δ^{13}C record is consistent with others North-Atlantic records [Lynch-Stieglitz et al., 2014]. Through the last 40 ky, SU90-08 δ^{13}C indicates better ventilation than very deep cores (water depth $>$ 4000 m) but lower ventilation than the intermediate cores (water depth $<$ 2000 m). The decreasing ventilation from 33 ka is also visible in other Atlantic cores as well as the reductions during the Heinrich events (Figure 4.5). The western basin seems more ventilated than the eastern basin, probably because of the western boundary current, which exports the water to the Southern Ocean more efficiently.

The reduction of the B-P radiocarbon age gradient observed at SU90-08 is quite consistent with what is reported by Thornalley et al. (2011). Besides, in the North Atlantic, a general increase of the surface reservoir ages has been documented across HS1 and the YD (*e.g.* Bondevik et al. (2006), Skinner et al. (2014), Thornalley et al. (2011)), with planktonic reservoir ages approaching 1000 years during the LGM, and up to 1800 years during HS1. Slight increase of the benthic reservoir age (B-atm radiocarbon age) is also reported in the North-Atlantic (Skinner et al., 2014). SU90-08 reservoir ages values are in the same order of magnitude but slightly than the reservoir ages reported in the literature during HS1. This may be attributed to the bioturbation effect on the radiocarbon ages. Indeed, as mentioned earlier in this chapter, we have seen that the planktonic foraminifers tend to be older on the radiocarbon scale than they should because they are partly dissolved/recrystallized and/or some specimen come from the older section of the core where the abundance was higher.

The Pa/Th changes monitored at SU90-08 location seem to be consistent with the general view of the circulation changes associated with the Heinrich event reported in the literature. Indeed, numerous studies established a marked increase of sedimentary Pa/Th

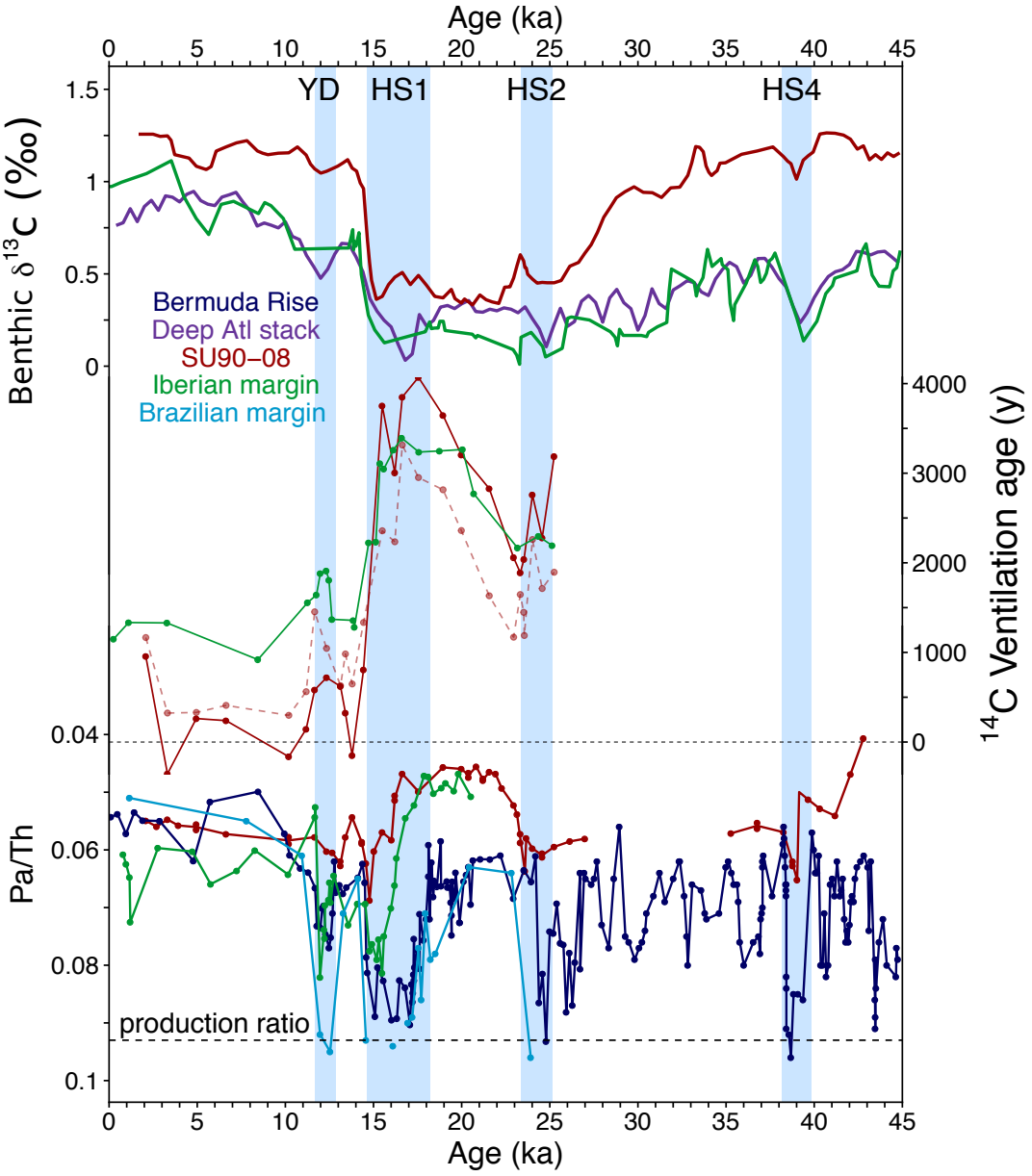

Figure 4.5 – **Comparison of SU90-08 benthic δ^{13}C (top panel), ^{14}C ventilation ages (central panel) and Pa/Th (bottom panel) records with published North Atlantic records**

SU90-08 multi-proxy record is plotted in red.In the middle pannel, the dashed red line represents SU90-08 planktonic radiocarbon ventilation ages, the plain lines represent benthic ventilation age. Literature data as detailed in Table 4.1. Deep Atlantic Stack δ^{13}C from Lynch-Stieglitz et al. (2014)

during the Heinrich events and the YD (*e.g.*Böhm et al. (2015), Gherardi et al. (2009), Henry et al. (2016), McManus et al. (2004),Mulitza et al. (2017), Waelbroeck et al. (2018)) that has been interpreted as a marked overturning decrease. The interesting point with SU90-08 Pa/Th record, is that, contrarily to the classical Bermuda rise record, it never reaches the production ratio (Figure 4.5). The small amplitude of the Pa/Th variations recorded at SU90-08 can be related to two major reasons. First, as already mentioned, the core has a relatively low sedimentation rate and the bioturbation likely smoothed all

Table 4.1 – Atlantic literature $\delta^{13}C$, $\Delta^{14}C$ and Pa/Th data

Figure code	Core name	Location	Water depth	References
Bermuda Rise	ODP 1063	33°N- 57°W	4584m	Böhm et al. (2015)
Bermuda Rise	ODP 1063	33°N- 57°W	4584m	Lippold et al. (2009)
Bermuda Rise	OCE326-GGC5	33°N- 57°W	4550m	McManus et al. (2004)
Bermuda Rise	KNR191-CDH19	33°N- 57°W	4541m	Henry et al. (2016)
Iberian Margin	SU81-18	37°N- 10°W	3135m	Gherardi et al. (2005)
Iberian Margin	MD99-2334K	37°N- 10°W	3146m	Skinner et al. (2014)
Brazilian Margin	GeoB16202-2	1°S- 41°W	2248m	Mulitza et al. (2017)

the proxy records. Besides, the amplitude of Pa/Th changes can be related to the site water depth (3000m). Indeed, in a scenario where the deep water formation has never been interrupted across the last 40 ka (*e.g.* Bradtmiller et al. (2014)) but where the upper GNAIW cell was very shallow, the deep cores (> 4000m) could not record Pa advection as the signal is not integrated through the entire water column but through the last 1000m or so. Consequently, the deep cores capture the deep circulation slowdown but shallower cores capture the remaining shallow upper circulation cell activity during Heinrich events. Interestingly, the Iberian margin core SU81-18 has the same water depth (about 3100 m) and its Pa/Th record display striking resemblance with SU90-08. For example, the Pa/Th indicates more active circulation at the LGM than during the Holocene and the absolute values for the 2 cores are quite similar (Figure 4.5). However, the sedimentary Pa/Th reaches much higher values during HS1 at the SU81-18 site than at the SU90-08 site. This may be due to the position of the core in the eastern basin. Indeed, the western boundary current of the western basin is responsible for most of the water export, form North Atlantic to the Southern ocean (Rhein et al., 1995). Thus, the sedimentary Pa/Th could reflect the more difficult water export in the eastern Atlantic basin across the Heinrich events. Alternatively, as we have seen that SU81-18 was located on a margin and receives thus important terrigenous inputs, this marked Pa/Th increase could also reflect yet poorly understood changes in particle fluxes and composition (Chapter 2). In any case, the circulation slowdown of those two cores displays striking in-phase timing that is very different from the classical Bermuda rise record. Indeed, at the Bermuda or the Brazilian margin (Böhm et al. (2015), Henry et al. (2016), McManus et al. (2004), Mulitza et al. (2017), Waelbroeck et al. (2018)), the circulation slowdown is observed at the beginning of HS1 or even before around 18 ka (Figure 4.5). In contrast, in SU90-08 and SU81-18, the circulation slowdown happens during the second half of HS1 around 16 ka and we have seen that this difference cannot be explained by uncertainties in age models (see chapter 3). It is unclear why this lag in the Pa/Th change is observed at

these 2 locations compared to the classical Pa/Th record from the western boundary current. It could be related to the fact that the 2 cores are at 3000m depth or due to the fact that their Pa/Th records capture the same water mass even though they are not in the same basin (western Atlantic vs eastern Atlantic). From the literature available about the Heinrich 1 event, we can hypothesize that the Pa/Th records reflect the ocean response to the two different phases detected in this event. During the first phase of HS1 (∼19-16.2 ky cal BP), a first reduction of the Atlantic Meridional Overturning circulation occurred, possibly driven by Fennoscandian ice sheets melting. Around 16.2, a first iceberg discharge from the Laurentide ice sheets occurred. Later, around 15.1 ky cal BP, a second iceberg discharge of smaller magnitude happened. Consequently, the early HS1 would involve freshwater fluxes from the Fennoscandian area whereas the freshwater fluxes and ice rafted debris from the Laurentide ice sheet would correspond to the late HS1 (Barker et al. (2015), Stanford et al. (2011), Hodell et al. (2017)). The study of IRD peaks from different origins in SU81-18 (Bard et al., 2000) support this hypothesis.

4.4 Conclusion

In this chapter we focused on the analysis of SU90-08 paleocirculation proxy records over the last 40 ky. First, we have seen that the ^{14}C B-P ages displayed unexpected negative values from the end of HS1. After a careful examination of the measurement quality, we demonstrated that this cannot result from hydrothermal or dissolution/recrystallization processes. We interpreted that those negative ^{14}C B-P ages mostly resulted from classical bioturbation of this sediment core with moderate sedimentation rate (< 5 cm/ky in average) in a context of reduced deep to surface radiocarbon age gradient. This hypothesis is supported by oxygenation and ventilation proxy records as well as idealized Monte Carlo simulations. Consequently, only the first order ^{14}C B-P ages variations can be interpreted in terms of circulation changes. Then, we demonstrated that the sedimentary Pa/Th was not primarily reflecting changes in particle fluxes, composition or hydrothermal processes but documents the past circulation changes. Thus, we examined the records of benthic δ^{13}C, ^{14}C B-P ages and sedimentary Pa/Th first separately and then conjointly. The carbon isotope proxies depict a well-ventilated deep-water mass except from 33 ka until the end of HS1. Meanwhile, the sedimentary Pa/Th indicates an active circulation through the entire period with increased circulation strength during the LGM compared to the Holocene. The proxies bring apparent contradictory information during the LGM, showing poorly ventilated deep-water associated with strong overturning. In greater details, the proxies display in phase relation during HS4 and the second part of HS1, depicting slightly reduced circulation and ventilation during those periods. Finally, SU90-08 multi-proxy pattern appears consistent with other Atlantic records. Interestingly,

strong similarities are observed between the records from SU90-08 and SU81-18 (Iberian margin). The two cores have a water depth of about 3100 m and display similar Pa/Th values indicating stronger circulation during the LGM than the Holocene. The two cores also indicate a circulation slowdown during HS1 that is delayed compared to the classical records of the Bermuda rise in the western boundary current.

The atypical decoupling between the benthic $\delta^{13}C$ and the Pa/Th questions whether the proxies record the signal from a single of from distinct water masses. Indeed, the proxies are not carried by the same sedimentary phase and do not rely on the same mechanisms. If the foraminifers capture the carbon signature of the water in which they developed, the sedimentary Pa/Th is more likely to integrate the last 1000 m for the water column. We have evaluated and confronted the implications in the case the proxies record the same or different water masses. However, from the proxy data itself, it is not possible to distinguish which of the two hypotheses has generated SU90-08 record.

The analysis of the multi-proxy record raises the need of modeling work for two reasons. First, using a climate model would allow to test hypothetical circulation configurations and decipher which ones that could produce Pa/Th and carbon isotopes signal to be decoupled at SU90-08 site. Then, even combined, the proxy records only provide qualitative estimation of the circulation evolution. The quantification of circulation changes in terms of flowing speed can only be achieved from a comparison of proxy data to model output in which the circulation can be extensively monitored. Besides, modelling the proxy evolutions is a necessary step for paleoceanographic research because: i) the proxy records available for the last 40 ky only provide indirect evidence for past circulation changes. The proxy mechanisms are often complex and reveal caveats across their usage history (see chapters 1, 2). ii) Even grouped in screened databases, studied marine sediment cores only represent a sparse sampling of the global ocean and there is a risk that they represent exceptions rather than the general records. Consequently reconstructing the past circulation patterns and quantifying the past circulation strength correspond to an inverse problem that requires model-data comparison to be solved.

In the next chapter, we will adopt a forward approach using the climate model of intermediate complexity iLOVECLIM. By including the computation of the ^{231}Pa and ^{230}Th tracers, we will investigate about multi-proxy response to past abrupt circulation changes.

Chapter 5. Modeling Pa/Th, δ^{13}C and Δ^{14}C response to abrupt circulation changes: implications for the study of paleoproxy records

5.1 Introduction

In the previous chapter, we have examined in details SU90-08 multiproxy records (δ^{13}C, Δ^{14}C and Pa/Th). This analysis provided insights about past circulation changes at this location but also about the signal that the proxies record. Indeed, the sedimentary Pa/Th and the carbon isotopes do not show consistent or synchronous variations through the record. Instead, during the LGM, they depict a poor ventilation of the deep-water associated with active overturning. This apparent inconsistency between the proxy records raises two questions : i) what is the nature of the signal they record? ii) which water mass does control them? Moreover, the objective of this thesis was to quantify the variations of the deep Atlantic circulation. However, none of the proxies used here can provide a quantitative reconstruction of the past circulation strength (in Sv). In this context, a modeling approach is required. First, in a model, it will be possible to fingerprint the proxy response to imposed circulation changes. Such model experiments will thus enable to investigate about potential decoupling between the Pa/Th and the carbon isotopes. Then, trying to fit the model outputs to the available paleodata will provide a way quantify the past circulation changes and convert the Pa/Th or carbon isotopes units into Sv.

To go further, we thus need a climate model able to compute the three circulation proxies (δ^{13}C, Δ^{14}C and Pa/Th) evolutions for several hundreds of years in a reasonable

computing time.
Because of its key role in the climate system, the carbon cycle has been modeled and heavily studied in the past decades (*e.g.* Friedlingstein et al. (2006), Orr et al. (2001)). More recent studies simulate the evolution of carbon isotopes under pre-industrial or glacial conditions (*e.g.* Bouttes et al. (2015); Brovkin et al. (2002), Menviel et al. (2017), Tschumi et al. (2010)).
The ^{231}Pa and ^{230}Th have also been implemented in climate models. The simplest approaches used 2D models (Luo et al. (2009), Marchal et al. (2000)) or 3D models but contained oversimplifications, notably in the particles representations (Siddall et al. (2005), Siddall et al. (2007)). The latest developments (Rempfer et al. (2017), Hulten et al. (2018)) correspond to more complex and detailed representations of the isotopes scvaneging scheme as well as the particles fluxes. However, those studies suffer from the coarse resolution of the ocean model (Rempfer et al., 2017) which contains only 36 x 36 grid cells (latitude-longitude) or conversely cannot achieve to simulate 1000 years in reasonable computation time (Hulten et al., 2018). Thus I decided to implement the Pa and Th computation in the climate model of intermediate complexity iLOVECLIM (Goosse et al., 2010). Before this PhD work, the model was already able to compute ^{13}C and ^{14}C cycles (Bouttes et al., 2015). This work is the topic of the article "Paleoproxy responses to abrupt circulation changes: a model perspective using iLOVECLIM" currently in preparation.

5.2 Article: Paleoproxy responses to abrupt circulation changes: a model perspective using iLOVECLIM

5.2.1 Article and supplementary information

Paleoproxy responses to abrupt circulation changes: a model perspective using iLOVECLIM

L. Missiaen[1,*], N. Bouttes[1], D.M. Roche[1,2], J-C. Dutay[1], A. Quiquet[1], C. Waelbroeck[1,] J-Y Peterschmidtt[1,] S. Moreira[1]…

[1]Laboratoire des Sciences du Climat et de l'Environnement, LSCE/IPSL, CEA-CNRS-UVSQ-Université Paris-Saclay, F-91198 Gif-sur-Yvette, France.

Vrije Universiteit Amsterdam, Faculty of Science, Cluster Earth and Climate, de Boelelaan 1085, 1081HV Amsterdam, The Netherlands

…

* Corresponding author: Lise Missiaen (lise.missiaen@lsce.ipsl.fr)

Abstract:

Understanding the ocean circulation changes associated with last glacial abrupt climate events is key to better assess internal climate variability and better predict future climate evolutions. Sedimentary Pa/Th, benthic $\delta^{13}C$ and $\Delta^{14}C$ are commonly used to reconstruct past circulation flow rate and ventilation. To overcome the limitations of each proxy taken separately, a common approach is to perform multi-proxy measurements on a single sediment core. Yet, the available proxy data is still too scarce to constrain the ocean circulation in 3-D across past abrupt climate events. Thus, a modeling approach is necessary to assess the geographical pattern, the timing and sequence of the multi-proxy response to abrupt circulation changes.

In this study, we have implemented the computation of the ^{231}Pa and ^{230}Th tracers into the climate model of intermediate complexity iLOVECLIM. The model produces realistic results of comparable quality with GCMs, and is able to simulate the simultaneous evolution of the Pa/Th, the $\delta^{13}C$ and $\Delta^{14}C$ in a reasonable computational time (~800 years per 24h). We have evaluated the response of these three circulation proxies to an abrupt circulation reduction obtained by freshwater addition in the Nordic seas under preindustrial boundary conditions. The proxy response follows the organization of the modern Atlantic water masses. The clearest and most coherent response is obtained in the deep (> 2000m) North West Atlantic, where $\delta^{13}C$ and $\Delta^{14}C$ significantly decrease while Pa/Th increases. This is consistent with observational data across millennial scale events of the last glacial. Interestingly, in the model the $\delta^{13}C$ and $\Delta^{14}C$ response lags the Pa/Th response by a few hundreds of years.

1. Introduction

Understanding rapid climate changes is key to predict future climate variations as they provide information about internal climate variability and climate sensitivity to perturbations. Indeed, rapid and high-amplitude temperature changes of about 8 to 15°C in less than 300 years are associated with only small changes in radiative forcing. These abrupt climate events have been related to changes in the Atlantic Meridional Overturning Circulation (AMOC) strength (see [*Lynch-Stieglitz*, 2017] for a review), but the underlying mechanisms remain elusive. Identifying the processes controlling the AMOC can only be achieved from the study of long-term variations [*Smeed et al.*, 2014] that rely on the analysis of indirect evidence (paleoproxies).

Among the numerous tracers available, the most valuable ones to reconstruct and quantify past circulation patterns and water mass flow are the sedimentary ($^{231}Pa_{xs,0}/^{230}Th_{xs,0}$ – hereafter Pa/Th) and dissolved inorganic carbon isotopes ($\delta^{13}C$, $\Delta^{14}C$).

The Pa/Th represents the activity ratio, at the deposition time, of the ^{231}Pa and ^{230}Th derived from the water column scavenging and can be used as a kinematic circulation proxy (*e.g.* [*François*, 2007; *McManus et al.*, 2004]). In short, ^{231}Pa and ^{230}Th are homogeneously produced in the water column at known rates (production ratio) and then transferred to the underlying sediments by particle scavenging (see [*François*, 2007] for a review). The two isotopes have different residence times in the water column (50-200 years for ^{231}Pa and 10-40 years for ^{230}Th [*Gideon M Henderson and Anderson*, 2003]). Thus, while ^{230}Th is rapidly transferred to the sediment, ^{231}Pa can partly be transported by water mass advection along the large-scale ocean circulation. Consequently, the sedimentary Pa/Th activity ratio can be used as a proxy of the advection rate of water-masses. In the Atlantic, low sedimentary Pa/Th ratios (*e.g.* 0.04 for the modern north Atlantic [*Yu et al.*, 1996]) are diagnostic of an active

overturning, while Pa/Th ratios close or equal to the production ratio (0.093) indicate sluggish water mass or a marked overturning circulation slowdown (*e.g.* [*Böhm et al.*, 2015; *François*, 2007; *McManus et al.*, 2004]). Yet, Pa and Th scavenging to the sediment is sensitive to changes in vertical particle flux and composition; hence the sedimentary Pa/Th circulation signal could be partly impaired by a particle-related signal (*e.g.* [*Chase et al.*, 2002; 2003; *Lippold et al.*, 2009]). In addition, sedimentary Pa/Th is derived from bulk sediment measurements and requires the estimation of the contributions of the detrital and authigenic fractions to the ^{231}Pa and ^{230}Th budgets. We have recently shown that this estimation can lead to significant uncertainties on the reconstructed patterns and amplitudes of the Pa/Th signal, especially in locations characterized by high terrigenous inputs (*e.g.* [*Missiaen et al.*, 2018]). All of this complicates the evaluation of past circulation strength from Pa/Th measurements.

The carbon isotopes measured in foraminifer shells reflect the carbon isotopic content of the water mass in which they form (see [*Stuiver and Polach*, 1977]) and provide information about past water mass ventilation (*e.g.* [*Lynch-Stieglitz et al.*, 2014; *Skinner et al.*, 2014]).

More precisely, the water mass δ^{13}C signature depends on biological, physical and chemical processes. At the surface, some carbon is exchanged between the surface waters and the atmosphere and some carbon is incorporated into the organic matter. Both processes are responsible for an isotopic fractionation between ^{12}C and ^{13}C and result in a enrichment of the surface waters in ^{13}C (see [*Siegenthaler and Münnich*; *Volk and Hoffert*, 1985]). Consequently, the surface waters δ^{13}C signature varies with air-sea exchange efficiency, sea-ice cover or biological activity intensity. At depth, remineralization of the organic matter releases ^{13}C to the water parcels, which are mixed through large-scale ocean circulation [*Duplessy et al.*, 1988]. In the modern ocean, the global δ^{13}C distribution depicts a tight relation between the apparent oxygen utilization and the δ^{13}C signature of a water mass [*Eide*

et al., 2017]. Thus, in the past, the $\delta^{13}C$ of benthic foraminifers is a robust proxy for ocean oxygen content and ventilation. However, the benthic $\delta^{13}C$ does not solely record deep ventilation changes. As mentioned above, the $\delta^{13}C$ signature of a deep water mass depends on several processes, notably the value it had before the water leaves the surface mixed layer, the intensity of the biological activity in the mixed layer, the remineralization intensity at depth and finally the circulation path and strength. Thus, the benthic $\delta^{13}C$ records multiple processes, which complicates its interpretation in terms of past deep ocean ventilation and circulation changes.

The radiocarbon is produced in the upper atmosphere and enters into the ocean via air-sea exchange with surface waters. As soon as a water parcel is isolated from the surface, its ^{14}C content starts to decrease exponentially with time due to radioactive decay (half-life of ^{14}C = 5,730 ± 40 years [*Godwin*, 1962]). Thus, by determining the ^{14}C age of benthic foraminifer samples of independently known calendar age, one can reconstruct past ocean ventilation, in other words, assess the time elapsed since the tracked deep-water parcel has been isolated from the surface (*e.g.* [*Skinner and Shackleton*, 2004; *Thornalley et al.*, 2015]). However, the interpretation of a water mass radiocarbon age is complicated by temporal variations in ^{14}C production in the upper atmosphere and air-sea exchanges efficiency. Indeed, because the radiocarbon is only produced in the atmosphere and transferred to the ocean via air-sea exchanges, the surface waters have an older radiocarbon age than the contemporaneous atmosphere. This radiocarbon age difference between the surface waters and the atmosphere (*i.e.* the surface reservoir age) can vary with space and time according to variations in air-sea exchanges efficiency, especially in the North-Atlantic region (*e.g.* [*Bard et al.*, 1994; *Bondevik et al.*, 2006; *Thornalley et al.*, 2011; *Waelbroeck et al.*, 2001]). Those variations are still poorly constrained, and complicate the interpretation of deep water radiocarbon content

(often expressed as $\Delta^{14}C$) in terms of past ocean ventilation and circulation changes (*e.g.* [*Adkins*, 1997]).

Thus, we have seen that the Pa/Th as well as benthic $\delta^{13}C$ and $\Delta^{14}C$ can provide information about past ocean circulation flow rate and ventilation. Yet, as highlighted above, each proxy has its own caveats. To overcome the limitation of each proxy taken separately and gather more detailed information about past ocean circulation, paleoceanographers started to conduct multi-proxy studies, measuring different proxy records on the same sedimentary archive. This approach also provides the chance to investigate about phase relationships between the different proxies (*e.g.* [*Burckel et al.*, 2015; *Waelbroeck et al.*, 2018]). Indeed, marine cores chronologies can be established using different methods (usually either radiocarbon or alignment tie points) but the dating uncertainty typically increases with the sediment age. For radiocarbon-based chronologies, the dating uncertainty arise from the radiocarbon measurement precision, on the number of dated levels as well as on the calibration curve (*e.g.* [*Reimer et al.*, 2013]). For chronologies based on the alignment of the sea surface temperature to Greenland air temperature, the dating uncertainty arise from the abruptness of the aligned transition and the uncertainty corresponding to the tie-points. Typically, the uncertainty of the alignment tie-point is about 50 years during around 10 ka but can rise up to 800 years around 40 ka [*Wolff et al.*, 2010]. Those dating uncertainties prevent from interpreting phase relationships between proxy records from different marine cores, hence the benefit of the multi-proxy approach.

Finally, reconstructing basin-scale ocean water-mass reorganization and circulation changes requires to compile proxy record from different locations. Despite some recent paleoproxy compilation efforts (*e.g.* [*Lynch-Stieglitz et al.*, 2014; *Ng et al.*, 2018; *Zhao et al.*,

2018]) the amount of data available remains too sparse to constrain the state and evolution of the ocean circulation in 3-D across abrupt climate events. Consequently, there is a need to investigate the spatial variations and timing of proxies response under abrupt climate change events. Such work can be achieved using climate models and could help to explain why some events are not recorded or recorded differently at a given location. Climate models are also useful as they enable to analyze how the proxy patterns change in response to different circulation configurations.

Because of its key role in the climate system, the carbon cycle has been modeled and heavily studied in the past decades (e.g. [*Friedlingstein et al.*, 2006; *Orr et al.*, 2001]). More recent studies simulate the evolution of carbon isotopes under pre-industrial or glacial conditions (*e.g.* [*Bouttes et al.*, 2015; *Brovkin et al.*, 2002; *Menviel et al.*, 2016; *Tschumi et al.*, 2010]). The ^{231}Pa and ^{230}Th tracers have also been implemented in climate models. The simplest approaches used 2D models [*Luo et al.*, 2010; *Marchal et al.*, 2000] or 3D models but contained oversimplifications, notably in the particles representations [*Siddall et al.*, 2005; *Siddall et al.*, 2007]. Latest published developments focused on improved representation of particle fluxes and scavenging scheme [*Rempfer et al.*, 2017; *van Hulten et al.*, 2018]. However, these recent developments either suffer from the coarse resolution of the ocean model [*Rempfer et al.*, 2017], which contains only 36 x 36 grid cells (latitude-longitude), or conversely cannot simulate 1000 years in reasonable computation time [*van Hulten et al.*, 2018]. To our knowledge, no simulations considered the geographical pattern and the temporal evolution of combined proxies such as Pa/Th, δ^{13}C and Δ^{14}C.

In this paper we investigate the structure of multi-proxy response to an abrupt circulation change with a climate model. For that purpose, we have implemented the production and scavenging processes of ^{231}Pa and ^{230}Th in the climate model of intermediate complexity iLOVECLIM. To date, the model is able to simulate the evolution of three ocean

157 circulation proxies: Pa/Th, $\delta^{13}C$ and $\Delta^{14}C$. We also developed an analysis method that gives
158 information about the magnitude and timing of the proxy response in the Atlantic Ocean. In
159 this study, we address the following questions. 1) What is the response of each proxy to an
160 imposed circulation change? 2) What is the timing and sequence of proxy response? How
161 does it vary with regions and water depth in the Atlantic Ocean? 3) How can the observations
162 in the modeled multi-proxy response help to interpret the paleoproxy records?
163

164 **2. Material and methods**

165 **2.1 Model description and developments**

166 In this study, we use the Earth system model of intermediate complexity
167 iLOVECLIM, which is a version/fork development of the LOVECLIM model [*Goosse et al.*,
168 2010]. The model includes a representation of the atmosphere, ocean, sea ice, terrestrial
169 biosphere vegetation, as well as the carbon cycle. The ocean component (CLIO) consists of a
170 free-surface primitive equation ocean model (3° x 3°, 20 depths layers) coupled to a dynamic-
171 thermodynamic sea-ice model. iLOVECLIM includes a land vegetation module (VECODE)
172 [*Brovkin et al.*, 1997], and a marine carbon cycle model [*Bouttes et al.*, 2015] both computing
173 the evolution of ^{13}C and ^{14}C. The model simulates modern $\delta^{13}C$ and $\Delta^{14}C$ oceanic distribution
174 in good agreement with observations [*Bouttes et al.*, 2015].

175 ^{231}Pa and ^{230}Th tracers were included in iLOVECLIM model following [*Rempfer et*
176 *al.*, 2017] 3D approach. In the model, ^{231}Pa and ^{230}Th are homogeneously produced in the
177 ocean by radioactive decay of their respective uranium parents. They are removed from the
178 water column by adsorption on settling particles (reversible scavenging). Their radioactive
179 decays are also taken into account. In its current version, iLOVECLIM does not explicitly
180 simulate the biogeochemical cycle of biogenic silica (opal), which is thought to be an
181 important scavenger for ^{231}Pa (e.g. [*Chase et al.*, 2002; *Kretschmer et al.*, 2011]). Therefore,

we used prescribed and constant particles concentration fields obtained running the PISCES biogeochemical model coupled to NEMO ocean model, which are consistent with present day observations [*van Hulten et al.*, 2018]. We considered one particle size with a unique sedimentation speed and three particles types ($CaCO_3$, POC and biogenic silica). The conservation equations for dissolved and particulate ^{231}Pa and ^{230}Th activities are the following [*Rempfer et al.*, 2017]:

$$\frac{\partial A_d^j}{\partial t} = T(A_d^j) + \beta^j + K_{desorp}^j.A_p^j - (K_{adsorp}^j + \lambda_j).A_d^j \qquad \text{Eq.1}$$

$$\frac{\partial A_p^j}{\partial t} = T(A_p^j) - \frac{\partial (w_s.A_p^j)}{\partial z} - (K_{desorp}^j + \lambda_j).A_p^j + K_{adsorp}^j.A_d^j \qquad \text{Eq.2}$$

Where A_d^j and A_p^j are respectively the dissolved and particle-bound activities ($dmp.m^{-3}.y^{-1}$) of isotope j (^{231}Pa or ^{230}Th), β^j ($dpm.m^{-3}.y^{-1}$) is the water column production of isotope j by radioactive decay of its uranium parent, λ_j (y^{-1}) is the decay constant of isotope j, w_s ($m.y^{-1}$) is the particle settling speed, K_{adsorp}^j and k_{desorp}^j (y^{-1}) are the adsorption and desorption coefficient of isotope j onto particles, respectively, T is the tracer balance evolution term ($dpm.m^{-3}.y^{-1}$) resulting from the water mass advection and diffusion terms computed by the CLIO ocean model. The values used in this study for each of the above-cited parameters are compiled in Table 1.

We chose to apply a uniform desorption coefficient denoted K_{desorp} hereafter. However, the adsorption coefficient depends in our model on the particle concentration and composition of each location and is calculated with the following equation [*Rempfer et al.*, 2017]:

$$K_{adsorp}^j(\theta,\Phi,z) = \sum_i \sigma_{i,j}.F_i(\theta,\Phi,z) \qquad \text{Eq.3}$$

Where θ is the latitude, Φ the longitude, z the water depth, $\sigma_{i,j}$ the scavenging efficiency for isotope j on particle type i ($m^2.mol^{-1}$), and F_i is the particle flux ($mol.m^{-2}.y^{-1}$).

203 **2.2 Model tuning and validation**

204 The scavenging efficiency $\sigma_{i,j}$ can be related to the partition coefficient K_d, which
205 defines the proportion of each isotope (^{231}Pa or ^{230}Th) which is lodged in the dissolved phase
206 or bound to particles. Therefore one K_d can be defined for each isotope and each particle type
207 considered in the model ($K_{d(i,j)}$, j representing the isotope Pa or Th and i the particle type).
208

$$K_{d(i,j)} = \frac{\sigma_{i,j} \times w_s \times \rho_{sw}}{M_{(i)} \times k_{desorp}} \quad \text{Eq.4}$$

209

210 Where $Kd_{(i,j)}$ is the partition coefficient for isotope i for particle type j, $\sigma_{i,j}$ is the corresponding
211 scavenging efficiency, w_s is the settling speed, K_{desorp} is the desorption coefficient, $M_{(i)}$ is the
212 molar mass of particle type i (i.e. 12 g.mol^{-1} for POC, 100.08 g.mol^{-1} for $CaCO_3$ and 67.3
213 g.mol^{-1} for opal) and ρ_{sw} is the mean density of sea water (constant fixed to 1.03 10^6 g.m^{-3}).
214 Additionally the way each particle type fractionates the Pa and the Th is defined by the
215 fractionation factor $F(Th/Pa)_j$.

$$F(Th/Pa)_j = \frac{K_{d(Th,i)}}{K_{d(Pa,i)}} = \frac{\sigma_{(Th,i)}}{\sigma_{(Pa,i)}} \quad \text{Eq.5}$$

216 K_d and fractionation factors (F(Th/Pa)) have been measured for both radionuclides in various
217 areas of the modern ocean and they show a rather large distribution (Table 2) [*Hayes et al.*,
218 2015; *Rempfer et al.*, 2017]. Consequently, these values are currently considered as tunable
219 parameters in modeling studies [*Dutay et al.*, 2009; *Marchal et al.*, 2000; *Siddall et al.*, 2005].
220 Considering three particle types for both radionuclides, there are thus six tunable $\sigma_{i,j}$
221 parameters in our model.

222 To efficiently sample our parameter space, we used a Latin Hypercube Sampling
223 (LHS) methodology (https://CRAN.R-project.org/package=lhs, [*Fyke et al*., 2014]). In order
224 to only select parameters values consistent with observed F(Th/Pa), we chose to use the

225 couples $\sigma_{Th,j}$, $F(Th/Pa)_i$ as input parameters for the LHS. The value of $\sigma_{Pa,i}$ is then deduced
226 from those two following equation (Eq. 5). The parameter ranges used in the LHS are given in
227 Table 3. It allowed a relatively good exploration of the parameter space with a relatively small
228 number of model evaluations. We performed 60 tuning simulations of 1000 years under pre-
229 industrial boundary conditions. Consistently with previous modeling studies (*e.g.* [*van Hulten*
230 *et al.*, 2018]), this simulation length was sufficient for Pa and Th to reach a quasi-equilibrium
231 state. The model performance was evaluated by comparing the model output with present day
232 particulate and dissolved water column Pa and Th measurements [*Dutay et al.*, 2009] as well
233 as sedimentary Pa/Th core tops data [*Henderson et al.*, 1999]. Table 4 presents the minimum,
234 maximum and best-fit σ_{ij} values. The model-data agreement for the best fit-simulation is
235 presented in Figure 1 to Figure 3.
236
237 **2.3 Experimental design**
238 We ran our model for 5000 years under Pre Industrial (PI) conditions from a
239 simulation with equilibrated carbon cycle [*Bouttes et al.*, 2015] in order to equilibrate the
240 Pa/Th. The result of this equilibrium simulation is used as a starting point to perform hosing
241 experiments of 1,200 years duration. Each simulation contains three phases: a control phase
242 (300 years), a hosing phase (300 years) and a recovery phase (600 years). The control phase is
243 used to assess the natural variability of the circulation and associated proxies under the PI
244 climate state. Two hosing experiments were run, differing only in the location of applied
245 positive freshwater fluxes in the North-Atlantic (the Labrador Sea and the Nordic Seas, cf.
246 Table 5). Geographical areas for the freshwater input were designed following the approach
247 described in [*Roche et al.*, 2010].
248
249

3. Results

3.1. Model-data comparison under PI conditions

We focus our evaluation on the Atlantic basin, where sedimentary Pa/Th has been used as a kinematic circulation proxy (*e.g.* [*François*, 2007; *McManus et al.*, 2004]). Figure 1 shows the simulated water column dissolved and particulate ^{231}Pa and ^{230}Th activities. Model results are presented as basin wide zonal averages and the observations are superimposed as circles. Overall, we succeed in producing a realistic range for both dissolved and particulate ^{231}Pa and ^{230}Th concentrations. These concentrations generally increase with depth, which is expected in the reversible scavenging theoretical model and consistent with observations. However, our model generally simulates lower particulate and dissolved concentrations than what is measured in the present-day ocean (Figure 3), in particular at the surface. We also observe a better model performance for Th concentrations than for dissolved or particulate Pa (Figure 1 and 3). Model to data agreement is generally better at depths > 2500 m than closer to the surface, which, together with the too low dissolved concentrations, indicate that our scheme tends to scavenge too much. In other words, Pa and Th quickly adsorb on the settling particles and are too rapidly removed from the water column. This is consistent with the Kd coefficients obtained for our PI best-fit iLOVECLIM simulation that are in the upper range of the observations (Table 2) and are significantly higher than the ones reported in [*van Hulten et al.*, 2018]. As evidenced by [*Dutay et al.*, 2009], the scavenging intensity and efficiency strongly depends on the particles concentration and settling speed (Eq 4). In this study we applied the particles concentrations from PISCES but used different settling speed. Indeed, we considered only one particle size with a settling speed of 1,000 m/y, which is close to the settling speed of the small particles considered in [*van Hulten et al.*, 2018] (2m/d ~730 m/y) but much lower than that considered for big particles (50 m/d ~18250 m/y). Using the ^{231}Pa and ^{230}Th content of suspended particles and water samples, [*Gdaniec et al.*, 2018] evaluated

the particle settling speed between 500 and 1,000 m/y which is close to the value used in our model simulations. The scavenging regime also relies on the balance between adsorption and desorption on the different particles types: $CaCO_3$, POC and opal. In an attempt to be closer to reality, we chose to represent the non-equilibrium relation between dissolved and particulate Pa and Th. Therefore, for both isotopes, we considered adsorption and desorption coefficients (K_{adsorp} and K_{desorp}) and transported both dissolved and particulate activities instead of transporting a total activity that is split into particulate and dissolved activities using partition coefficients (K_d-describing equilibrium situation). If some observations are available to constrain the K_d coefficients (*e.g.* [*Chase et al.*, 2002; *Hayes et al.*, 2015]), a wide range of K_d values have been observed in the modern ocean and to date, no consensus value is available. Concerning adsorption and desorption coefficients, even less constraints are available. Equation 4 only allows to determine a range for K_{adsorp}/K_{desorp} ratio from the available ranges of K_d coefficients. As a first approach, we chose here to consider a single and constant K_{desorp} value but there is no theoretical reason to prevent K_{desorp} to be different for POC, $CaCO_3$ or opal particles. Thus, there are six $\sigma_{i,j}$ and potentially six K_{desorp} coefficients to adjust with the available observational data (that are ranges for the six K_d and three F(Th/Pa) values). We used a LHS methodology to produce 60 sets of σ coefficients to be tested. Because of the wide ranges we specified for the three Th σ coefficients and the three F(Th/Pa), the LHS probably did not capture the right balance between the scavenging efficiency of the different particle types. Indeed, in the majority of the tested parameters sets, the $K_{d\text{-}Pa,opal}$ was greater than $K_{d\text{-}Pa\text{-}CaCO3}$ or $K_{d\text{-}Pa\text{-}POC.}$ In other words, in most of our tuning tests, opal was the main scavenger for Pa. Additionally, the model-data agreement evaluation was problematic: when calculating the Root Mean Squared Error (RMSE) for the four tracers we consider (dissolved Pa, dissolved Th, particulate Pa and particulate Th) we observed that the best simulations for Pa did not correspond to the best simulations for Th and vice versa. When trying to combine

300 the best $\sigma_{i,j}$ parameters for Pa and their counterparts for Th from 2 distinct simulations, we
301 observed that the F(Th/Pa) were out of the observation range.

302 The particle-bound Pa/Th of the deepest oceanic model grid cells is shown in Figure 2.
303 The observations from core-top data are superimposed as circles. Even if the observational
304 dataset is relatively patchy, it generally shows lower sedimentary Pa/Th ratios (0.04 or lower)
305 in the basins interiors compared to the coastal areas. Such a gradient is well captured by our
306 model, which simulates very low sedimentary Pa/Th values in the deep tropical Atlantic
307 Ocean. Another interesting feature is the high sedimentary Pa/Th values in the Southern
308 Ocean between 50 and 75°S (opal belt), where Pa is heavily scavenged to the sediments by
309 opal. Our model generates higher sedimentary Pa/Th in this region compared to the deep
310 basins interior but our modeled opal belt stands slightly northward compared to the
311 observations (Figure 2). Looking at the water column Pa and Th content in this area, we
312 observe that the dissolved concentrations simulated by our model are much too low compared
313 to the observations and the model does not reproduce the water column opal belt signal
314 (Figure 1). As particles play an important role in oceanic Pa and Th scavenging to the
315 sediments the model-data agreement is directly dependent on particle field used. Our model
316 design makes use of fixed particle fields simulated by PISCES that have previously been
317 evaluated against the most recent observations available [*van Hulten et al.*, 2018]. Even if the
318 particle fields modeled by PISCES are satisfactory overall, some discrepancies with the
319 observations have been pointed out. While the imposed particle field tends to reproduce
320 correctly the observed large-scale particles patterns, modeled concentrations are
321 underestimated for POC and $CaCO_3$ while they are overestimated for opal, especially along
322 the western margins [*van Hulten et al.*, 2018]. It is therefore expected that similar deficiencies
323 will be apparent in the simulated Th and Pa dissolved and particulate concentrations in
324 iLOVECLIM. The fact that the opal belt is poorly represented in our model can also be

related to the way the Pa is exported towards the sediments. As for Pa the highest K_d is attributed to opal, Pa is mainly retrieved from the water column and exported towards the sediments via the opal sedimentary flux throughout the global ocean. Thus, in that configuration, tests to reduce the $\sigma_{Pa,opal}$ lead to a general increase of the dissolved Pa in the water column. This deterioration of the general model-data agreement is likely a consequence of reduced Pa scavenging in the high latitude and advection of the signal elsewhere and Moreover, in the current iLOVECLIM configuration, several processes are not explicitly represented or parameterized. For instance, the lithogenic particles do not participate in Pa and Th scavenging. Besides, it has been evidenced that Pa was preferentially scavenged at the continental margins (boundary scavenging), or by resuspended particles at the bottom in nepheloid layers (*e.g.* [*Anderson et al.*, 1983; *Thomas et al.*, 2006]). Those processes are not dynamically represented in our model but participate to increase Pa scavenging in those regions, affecting the dissolved and particulate water column concentrations as well as the sedimentary Pa/Th ratio. For instance, in Northwest Atlantic between Florida and Newfoundland, PISCES underestimates $CaCO_3$ concentrations [*van Hulten et al.*, 2018] and there is evidence for an important presence of nepheloid layers [*Gardner et al.*, 2018]. In our model, in this area, we find too high sedimentary Pa/Th ratio with respect to data, likely indicating an incomplete representation of the fractionation of Pa and Th in the water column due to particles composition. Reanalysis of observational data (e.g. [*Luo and Ku*, 2004]) evidenced the important role of the lithogenic particles in the Pa and Th scavenging. In some model studies, lithogenic particles have been found unimportant (e.g. [*Siddall et al.*, 2005]), whereas in other model studies lithogenic particles carry most of the particle bound Pa and Th (e.g. [*van Hulten et al.*, 2018]). The importance of the lithogenic particles is thus model dependent and probably strongly relies on the adsorption coefficient tuning, the problem being largely underconstrained.

350 In summary, the detailed analysis of the PI control simulation provides a few insights
351 on possible future development to refine model-data agreement. Overall we have shown that
352 in its current version iLOVECLIM produces results that are comparable with GCMs outputs
353 for both water column dissolved and particulate Pa and Th concentrations, as well as
354 sedimentary Pa/Th ratio. The modeled values display the first order characteristics observed
355 in the modern ocean and the sediment core tops. In the following section, we test the
356 sensitivity of the simulated sedimentary Pa/Th to abrupt circulation slowdown (hosing
357 experiments).
358
359 **3.2 Multi proxy response to an abrupt circulation change**
360 We added a freshwater flux of 0.3 Sv in the Nordic Seas or the Labrador Sea during
361 300 years (see methods), which was sufficient to cause a circulation reduction [*Roche et al.*,
362 2010]. Under PI conditions, the maximum of the AMOC stream function oscillates between
363 15 and 20 Sv in our model. During the hosing, North Atlantic water formation drops to nearly
364 0 Sv in the case of the Nordic Seas hosing and to about 5 Sv in the case of the Labrador Sea
365 hosing (Table 5, Figure 4, see supplementary information). In the case of the "Nordic Seas
366 hosing" the North Atlantic overturning cell completely vanishes whereas a weak and shallow
367 cell persists in the case of the "Labrador Sea hosing" (Figure 4). In both cases, the AMOC
368 recovers before the end of the simulation and displays a small "overshoot" with the maximum
369 AMOC stream function exceeding 20 Sv around 900 years (Figure 7, Figure 8, supplementary
370 information).
371 We evaluate the response of Pa/Th, $\delta^{13}C$ and $\Delta^{14}C$ to the "Nordic Seas hosing",
372 producing the largest AMOC reduction. We identify for each model grid cell and each proxy,
373 the simulation periods exceeding 80 years during which the proxy values are outside of their
374 natural variability range, defined as the proxy variance (2σ) under PI conditions over the first

375 300 years of the simulation (control phase). In most cases, 0, 1 or 2 periods are detected as a
376 result of the proxy response to the oceanic circulation perturbation. In some grid-cells with
377 high proxy variability, we detect up to 4 periods of significant proxy response, which were
378 difficult to connect with the hosing or overshoot timing of our simulation. Consequently, we
379 excluded the grid cells depicting more than 3 periods of significant response from the
380 subsequent analysis.

381 For the time series containing two or less periods of interest, we call "time of
382 maximum response", the simulation year for which the absolute difference between the proxy
383 value and mean proxy value during the control phase of the simulation is maximal. The proxy
384 value at the time of maximum response is denoted "proxy response" in the following. The
385 unique or dual proxy response is compared to the control proxy value (*i.e.* the mean proxy
386 value over the 300 first years of the simulation) for the western Atlantic basin (Figure 5-
387 eastern basin in SOM). The $\delta^{13}C$ and $\Delta^{14}C$ only display one single response in the deep
388 western Atlantic whereas the Pa/Th displays one or two responses in this part of the basin.
389 Generally, the unique or the first response of each proxy has the same geographical pattern
390 (Figure 5a and b) while in the case of 2 distinct responses, the second has a radically different
391 pattern (Figure 5c). The second response corresponds in general to a $\delta^{13}C$ and $\Delta^{14}C$ increase,
392 consistent with the circulation overshoot around 900 simulated years. For the Pa/Th the first
393 and second responses display opposite patterns with increased values in the NADW cell and
394 decreased values in the AABW and AAIW cells as the first response.

395 Considering that the unique and the first responses represent the proxy response to the
396 hosing, we distinguish 3 zones in the western Atlantic basin: the surface and intermediate
397 waters (0-1500 m), the deep waters (> 2000 m), and the Southern Ocean (south of 40°S). In
398 the surface and intermediate waters the $\delta^{13}C$ and $\Delta^{14}C$ increase, reflecting a more efficient
399 ventilation of these water masses while the Pa/Th displays no clear trend. In the deep waters,

400 the $\delta^{13}C$ and $\Delta^{14}C$ decrease while the Pa/Th generally increases, responding to the reduction
401 of the NADW flow rate. In the Southern Ocean, the Pa/Th decreases while the $\delta^{13}C$ and $\Delta^{14}C$
402 display a dipole pattern increasing at the surface and decreasing at depth. For $\delta^{13}C$, the depth
403 boundary is around 1500 m while for $\Delta^{14}C$ the depth boundary is ~1500 m north of 50°S and
404 reaches 3000 m south of 50°S. In terms of magnitude, the strongest proxy response is
405 recorded in the North –West Atlantic between 60 °N and 40°N and between 1500 and 3000 m
406 for the 3 proxies.

407 Looking at the proxy response times (Figure 6), we observe significantly different
408 patterns for Pa/Th and the carbon isotopes. The $\delta^{13}C$ and $\Delta^{14}C$ response time increases with
409 depth: in the surface and intermediate waters the response occurs roughly 300 years after the
410 beginning of the fresh water addition, around 3000 m the response is delayed by 150 years
411 and towards the ocean bottom the delay increases up to 600 years. On the contrary, the Pa/Th
412 displays much smaller response times, the timing of the Pa/Th response being generally
413 synchronous with the minimum of the stream function 300 years after the beginning of the
414 freshwater addition. Consequently, in most of the western Atlantic basin, the response of the
415 carbon isotopes lags the Pa/Th response by a few hundred years, especially in the deeper
416 waters. We note that in the deep tropical southwestern Atlantic (3500-5000 m between 40°S
417 and the equator) the Pa/Th reacts very shortly after the freshwater addition. This suggests that
418 in this area, the Pa/Th displays in fact a dual response to the hosing with two phases, instead
419 of one response to the hosing and one response to the circulation overshoot. The same
420 conclusion holds for the surface and intermediate waters between 40°S and 40°N.

421 In the eastern Atlantic basin the general pattern of the proxy response is similar to that
422 of the western basin (Figure S1- Figure S2). However, we note that the $\delta^{13}C$ has frequently
423 more than a single response, especially at depths > 2000m. Besides, the Pa/Th has a more
424 complex pattern with a large increase in the arctic basin, a moderate increase in the tropical

425 basin and a decrease in the northern and southern basins through the entire water column. The
426 $\Delta^{14}C$ shows the same pattern as in the western basin, with increased values during the hosing
427 in surface and intermediate waters and lower values at depth, while the $\delta^{13}C$ displays initially
428 an opposite response followed by a return to similar patterns. Concerning the response times,
429 the same pattern as in the western ocean is observed. Interestingly, we note that the $\Delta^{14}C$ has
430 longer response times in the eastern basin compared to the western basin (Figure S2).

431 Overall, the analysis of the multi-proxy response allows the identification of 3 zones
432 with different reaction patterns:

433 i) The most obvious response concerns the North-West-Atlantic between 40°N and 60°N,
434 1000 and 5000 m. This zone generally corresponds to the North Atlantic Deep Water
435 (NADW) in our model. In this area, the $\delta^{13}C$ and $\Delta^{14}C$ display marked decrease during the
436 hosing while the Pa/Th increases. Another interesting feature is that the $\delta^{13}C$ and $\Delta^{14}C$ lag the
437 Pa/Th by about 200 y (Figure 7-A).

438 ii) In the tropical intermediate and surface waters, $\delta^{13}C$ and $\Delta^{14}C$ increase during the hosing
439 compared to the reference value while Pa/Th displays no clear reaction (Figure 7-B). This
440 zone corresponds to the Antarctic Intermediate Water mass (AAIW).

441 iii) In the Southern Ocean (south of ~30°S), below 3000 m, the $\delta^{13}C$ and $\Delta^{14}C$ (respectively
442 Pa/Th) display a prolonged decrease (resp. increase) during the hosing. No lag between the
443 Pa/Th and the carbon isotopes response is observed (Figure 7-C). This zone corresponds to
444 the Antarctic Bottom Water mass (AABW).

445 We have shown that the 3 proxies can display decoupled responses to the same
446 circulation change. In the NADW we observe a lag of a few hundred years between the Pa/Th
447 and the carbon isotopes response. Thus, in our model the three proxies considered do not
448 respond simultaneously and in a simple manner to a given oceanic circulation change. In the

449 following section we discuss how this result can be informative for paleo-data multi-proxy
450 studies that aim to reconstruct past circulation changes.
451
452 **4. Discussion**
453 **4.1. Proxies and underlying physical mechanisms**
454 An interesting feature of our simulations is that the $\delta^{13}C$ and $\Delta^{14}C$ response lags the
455 Pa/Th response by a few hundreds years, in particular in the North –West Atlantic, bathed by
456 the NADW. A potential explanation for this response time difference can be found in the
457 physical and chemical mechanisms producing $\delta^{13}C$, $\Delta^{14}C$ and Pa/Th signals. The balance
458 between those mechanisms is fundamentally different for the carbon isotopes and the
459 sedimentary Pa/Th. Indeed, on the one hand, the Pa/Th depends on the scavenging efficiency
460 and on the water mass advection by the general circulation. The ^{231}Pa and ^{230}Th have
461 relatively short residence time in the water column (50-200 years and 10-50 years
462 respectively), and thus respond promptly to a circulation perturbation. Since we fixed the
463 particles fields in our model, the scavenging efficiency for ^{231}Pa and ^{230}Th remains constant
464 through the simulation. Consequently, our modeled Pa/Th response depends only on the ^{231}Pa
465 advection and thus, on the circulation changes. On the other hand, the oceanic carbon isotopes
466 depend not only on circulation changes, but also on the biological activity and the air-sea
467 exchanges. Biological activity is perturbed by oceanic circulation changes as the latter
468 modifies nutrient availability. Air-sea gas exchange depends on various factors among which
469 the pCO_2 in seawater or sea ice, both modified by the circulation change. Additionally, the
470 different carbon reservoirs (terrestrial biosphere, ocean and atmosphere) exchange with each
471 other. Consequently, the carbon isotopes need longer time to adjust to a circulation
472 perturbation. This is consistent with the equilibration times that were required to equilibrate
473 the proxies: 10 000 years [*Bouttes et al.*, 2015] for the carbon cycle against 1000 years for the

Pa/Th (this study). In the previous studies focusing on Pa/Th modeling, the equilibration time was even reduced to 500 years [*van Hulten et al.*, 2018] and consisted to a quasi equilibrium. Thus, regarding the modeled processes on which the proxies rely, it appears logical that the Pa/Th has a shorter response time to a circulation change than the carbon isotopes.

4.2. Comparison to proxy data

4.2.1 The 8.2 ky cal BP event

The best analog for our hosing experiments applied to a PI state is the 8.2 ky cal BP event [*Alley et al.*, 1997] which is attributed to the drainage of the glacial Lake Agassiz [*Hoffman et al.*, 2012; *Wiersma and Renssen*, 2006]. This event imprinted both marine and terrestrial records, with decreased land and sea surface temperature or surface water freshening in the North Atlantic. A reduction of the AMOC has been related to this event [*Ellison et al.*, 2006; *Hoogakker et al.*, 2011; *Kleiven et al.*, 2008] using sortable silts and/or benthic $\delta^{13}C$ measurements. In a deep-sea sediment core retrieved from at 3400 m depth in the Labrador Sea, the benthic $\delta^{13}C$ drops by roughly 1 ‰ (from 1‰ to 0) during the 8.2 ky cal BP event [*Kleiven et al.*, 2008]. The closest model grid cell is located at 2307m and yields $\delta^{13}C$ values of ~1.3 ‰ under PI conditions, which drop by about 1‰ during the hosing. Thus in our model we reproduce the amplitude of the $\delta^{13}C$ drop observed in a marine core of the Labrador Sea during the 8.2 ky cal BP event with a hosing in the Labrador Sea. Note that the $\delta^{13}C$ has a strong vertical gradient. Since our modeled depth at the site is shallower, we cannot compare the absolute values.

This 8.2 ky cal BP event is of short duration (~300 years) and thus is only well recorded in marine cores with exceptionally high sedimentation rate [*Lougheed et al.*, 2018]. Besides, to date there is no existing Pa/Th record with sufficient temporal resolution to capture this event.

499 **4.2.2 The millennial scale climate variability (Heinrich events and DO cycles)**

500 The Heinrich events and DO-cycles are good candidates to compare with our hosing
501 experiments because they are strongly related to freshwater fluxes in North-Atlantic (*e.g.*
502 [*Broecker et al.*, 1990; *Hemming*, 2004; *Marcott et al.*, 2011]) and associated with circulation
503 changes that are well documented in $\delta^{13}C$, $\Delta^{14}C$ and Pa/Th records (*e.g.* [*Böhm et al.*, 2015;
504 *Henry et al.*, 2016; *Lynch-Stieglitz*, 2017; *Waelbroeck et al.*, 2018]). However, the millennial
505 scale climate changes of the last glacial cycle are not direct analogs of our hosing experiments
506 because i) they occurred under glacial conditions whereas our simulations were run under PI
507 conditions ii) the Heinrich and DO events have distinct proxy patterns and can not be entirely
508 explained by a simple fresh water addition in the North Atlantic. Besides, the sequence of
509 mechanisms involved in Heinrich stadials is still under debate (*e.g.* [*Barker et al.*, 2015;
510 *Broecker*, 1994]) and these periods were likely subdivided in several distinct phases (*e.g.* [*Ng*
511 *et al.*, 2018; *Stanford et al.*, 2011]).

512 The available paleoproxy data is relatively sparse and the extensive time series are
513 rare. To date there is no published combined Pa/Th, benthic $\delta^{13}C$ and $\Delta^{14}C$ record available
514 for the same sediment core. However, remarkably comprehensive multiproxy records are
515 available for the Iberian margin ([*Gherardi et al.*, 2005; *Skinner and Shackleton*, 2004]), the
516 Brazilian margin ([*Burckel et al.*, 2015; *Burckel et al.*, 2016; *Mulitza et al.*, 2017;
517 *Waelbroeck et al.*, 2018]) and the Bermuda Rise ([*Böhm et al.*, 2015; *Henry et al.*, 2016;
518 *McManus et al.*, 2004]). A classical working hypothesis is to assume that these records
519 represent the proxy evolution of the surrounding basin. Besides, some recent compilations
520 (*e.g.* [*Lynch-Stieglitz et al.*, 2014; *Ng et al.*, 2018; *Zhao et al.*, 2018]) bring some insight about
521 the evolution of Pa/Th, benthic $\delta^{13}C$ and $\Delta^{14}C$ across the last 40 ky in the Atlantic ocean.

522 In our model, the most obvious response was obtained in the western Atlantic basin
523 (NADW), where the freshwater addition under PI boundary conditions produces a coherent

524 ventilation and circulation flow rate reduction recorded by a decrease in $\delta^{13}C$ and $\Delta^{14}C$ and a
525 Pa/Th increase. The paleodata available is consistent with this proxy evolution in the western
526 Atlantic and in the western boundary current. [*Ng et al.*, 2018] observe a consistent Pa/Th
527 pattern across the last 30 ky with a significant Pa/Th increase in the North-West deep Atlantic
528 Ocean during HS1. [*Lynch-Stieglitz et al.*, 2014] observed a ~0.4 ‰ decrease in benthic $\delta^{13}C$
529 during some of the Heinrich events in deep and intermediate waters in the Atlantic. Several
530 coral and foraminifers ^{14}C records also account for a decreased ^{14}C (decreased $\Delta^{14}C$) content
531 of deep waters and increased deep ventilation ages during HS1 [*Chen et al.*, 2015; *Skinner et*
532 *al.*, 2014]. The Brazilian margin and the Bermuda rise extensive multiproxy records are
533 located in the western boundary current and display similar proxy patterns. The Pa/Th
534 increases from ~0.06 to the production ratio (0.093) or even above while the $\delta^{13}C$ decreases
535 by ~0.5 ‰ across the Heinrich events. Similar Pa/Th and benthic $\delta^{13}C$ changes are also
536 observed for the DO cycles.

537 For comparison, we evaluated more precisely our model time series in the Bermuda
538 Rise basin (~34°N-58°W, >4300m) (Figure 8). The presented time series correspond to the
539 average of 9 model grid-cells and are representative of the time series of the Western basin
540 (see Figure 5 and Figure 7). Our simulated Pa/Th significantly increases between year 350
541 and year 850 of the simulation, consistently with the decrease of the maximum Atlantic
542 stream function (Figure 8). The simulated Pa/Th approaches the production ratio of 0.093 at
543 the year 600 of the simulation, and the maximum stream function is close to zero from y 400
544 to 600, which is consistent with a sedimentary Pa/Th reaching the production ratio in the case
545 of an AMOC shutdown. The simulated Pa/Th change has a moderate amplitude of 0.015
546 Pa/Th units (from ~0.075 to 0.090) but is significant with respect to the natural variability
547 recorded during the 300 first years of the simulation under PI conditions.

548 Our simulated $\delta^{13}C$ decreases from ~0.62 to ~0.5, reaching the minimum around year 900, i.e.
549 600 years after the beginning of the hosing. The simulated $\delta^{13}C$ decrease has a moderate
550 amplitude of ~0.12 ‰ but is significant with respect to the natural variability recorded in the
551 control first 300 years of the simulation. Although the trend of the simulated and observed
552 proxy response is the same, their absolute values differ. In our simulated record, the Pa/Th
553 value associated with the modern circulation scheme is around 0.075, which is significantly
554 higher than the value actually measured at the Bermuda Rise or Brazilian margin sites: ~0.06.
555 For both proxies, the simulated amplitude of change is much smaller than the amplitude
556 recorded in the paleodata across the Heinrich events: the modeled $\delta^{13}C$ decrease is around
557 0.12 ‰ while it is 0.5 ‰ in the paleodata; the modeled Pa/Th change is around ~0.015 Pa/Th
558 units while it is ~0.03 in the paleodata.
559 Several processes can account for the model-data mismatch. First, as mentioned before, the
560 DO cycles and the Heinrich events are not the analog of our hosing experiments.
561 Additionally, our simulation was run with fixed modeled modern particles fields, which
562 display some discrepancies with respect to the modern observations as discussed in [*van*
563 *Hulten et al.*, 2018] and in the section 3.1. Moreover, the particle fluxes and composition have
564 been shown to widely change across glacial to interglacial or millennial scale climate
565 transitions ([*Blunier et al.*, 2012; *Jacobel et al.*, 2017; *Jickells et al.*, 2005]). The ^{231}Pa and
566 ^{230}Th being very sensitive to changes in particles fluxes and concentrations (e.g. [*Chase et al.*,
567 2002]), the observed sedimentary Pa/Th likely reflects a convolution of the particle and the
568 circulation changes. Thus, by not representing the particle evolution in our model, we cannot
569 capture the integrality of the Pa/Th signal.
570 We observe a lead of Pa/Th response with respect to the $\delta^{13}C$ of about 300 years. [*Henry et*
571 *al.*, 2016; *Waelbroeck et al.*, 2018] both examined the lead/lag relationship between Pa/Th
572 and benthic $\delta^{13}C$ and found opposite results with Pa/Th leading $\delta^{13}C$ by about 200 years at the

573 Brazilian margin while Pa/Th lags $\delta^{13}C$ by about 200 years at the Bermuda Rise. [*C.*
574 *Waelbroeck et al.*, 2018] suggested that the cross-correlation method to evaluate the leads or
575 lags relationship between different proxy records in [*Henry et al.*, 2016] is not suitable to
576 analyze non-stationary climatic signals. Besides, it is important to note that both proxies are
577 not hosted by the same sediment fraction. On the one hand, Pa and Th are preferentially
578 adsorbed on the fine grain particles as they have larger adsorption surface [*Chase et al.*, 2002;
579 *van Hulten et al.*, 2018]. Thus it is reasonable to assume that the Pa/Th signal is mainly bound
580 to particles <100 μm [*Kretschmer et al.*, 2010; *Thomson*, 1993]. On the other hand, $\delta^{13}C$ and
581 $\Delta^{14}C$ are measured on foraminifer shells that correspond on larger particle sizes (> 150 μm).
582 Marine sediments usually undergo bioturbation processes. At the sediment interface, the
583 benthic life activity remobilizes the upper layer of the sediments in a layer of a few cm
584 (typically 10 cm). According to the availability of oxygen at the bottom of the water column,
585 this bioturbation intensity and thus the thickness of the mixed layer depth can vary through
586 space and time. It has been shown that bioturbation could affect different particle sizes
587 differently (*e.g.* [*Wheatcroft*, 1992]), which can affect the timing of the proxy variations in the
588 studied cores. Our model results suggest that the 280 years lead of the Pa/Th with respect to
589 $\delta^{13}C$ may be a feature of the proxy response to millennial scale variability and is not
590 necessarily an artifact due to the marine core bioturbation.

591 Our modeled also highlighted that the Pa/Th response was less clear in the eastern
592 Atlantic basin compared to the western basin. Indeed, in the eastern basin, small Pa/Th
593 amplitude variations are observed, with increasing values in the equatorial zone and
594 decreasing values elsewhere. The paleodata also accounts for ambiguous Pa/Th patterns
595 across the Heinrich event 1. If some cores located close to the Mid-Atlantic ridge and the
596 Iberian margin reproduce the amplitude of Pa/Th variations observed in the western basin,
597 two records display no millennial scale variability. In our model the low amplitude Pa/Th

598 variability accounts for an absence of strong Pa advection and thus water circulation towards
599 south Atlantic. This could be related to a poor representation of the eastern boundary current,
600 known to be the western boundary counterpart in the modern ocean (e.g. [*Paillet et al.*,
601 1998]). Alternatively, the absence of southward advection could be due to the water flux that
602 crosses Gibraltar Straight. Because the model resolution is very coarse and Gibraltar Straight
603 is represented by a full ocean grid-cell of 3 x 3 degrees, unrealistically impacting the
604 simulated eastern Atlantic circulation.
605
606 **Conclusions and perspectives**
607 We have implemented the ^{231}Pa and ^{230}Th tracers in the climate model of intermediate
608 complexity iLOVECLIM. The new Pa/Th module simulates a realistic range of dissolved and
609 particulate ^{231}Pa and ^{230}Th concentrations, increasing with depth and consistent with the
610 idealized reversible scavenging theoretical profile. In our best-fit simulation, Pa and Th tend
611 to be adsorbed on the particles and scavenged to the sediments too quickly resulting in
612 underestimated dissolved concentrations, particularly in the Southern Ocean opal belt. The
613 model represents well the open ocean sedimentary Pa/Th ratio but the opal belt and the
614 coastal regions display the largest model-data discrepancies. This could be attributed to the
615 lack of representation of processes affecting the ^{231}Pa and ^{230}Th at the ocean bottom or in
616 coastal regions. Further work to achieve better model-data agreement could be conducted in
617 two main directions i) implement representation of the missing processes such as the
618 nepheloid layers and the boundary scavenging ii) refine the scavenging coefficient tuning
619 trying to define configurations where the opal is not the main scavenger for Pa in order to
620 better represent the opal belt in the Southern ocean.
621 To date, the model is able to simulate the evolution of $\delta^{13}C$, $\Delta^{14}C$ and Pa/Th over
622 thousands of years in a reasonable computation time (~800 years per 24h). We tested and

623 fingerprinted the response of these three proxies to an imposed and abrupt circulation change
624 performing hosing experiments. We analyzed the results corresponding to significant
625 circulation reduction, associated to a freshwater input of 0.3 Sv for 300 years in the Nordic
626 Seas. For the three proxies, we detect either no, 1 or up to 4 periods during which the proxy
627 value significantly differs from its PI value. Results with more than 2 periods of significant
628 change are delicate to interpret in terms of proxy response to the freshwater forcing. Thus, we
629 focused on the analysis of the time series exhibiting 0, 1 or 2 distinct periods of significant
630 change. Our modeled Pa/Th show clear response in the western basin while in the eastern
631 basin it display low amplitude variability. Looking at the anomaly between the proxy values
632 during the hosing and the reference values under PI conditions, we show 3 distinct patterns in
633 the proxy response corresponding to the three main water masses of the Atlantic ocean:
634 NADW, AAIW and AABW. In the intermediate waters the Pa/Th and $\Delta^{14}C$ show a slight
635 increase while the $\delta^{13}C$ significantly increases. In the AABW, the three proxies display
636 consistent and synchronous response: the Pa/Th increases while the $\delta^{13}C$ and $\Delta^{14}C$ decrease,
637 corresponding to a reduced circulation and ventilation of the water mass. Finally, in the
638 NADW, the three proxies display consistent responses too, with the Pa/Th increasing and the
639 $\delta^{13}C$ and $\Delta^{14}C$ decreasing. The response time of $\delta^{13}C$ and $\Delta^{14}C$ is generally similar and
640 increases with increasing water depth, while Pa/Th displays a more homogeneous and shorter
641 response time. The maximum response of the $\delta^{13}C$ and $\Delta^{14}C$ is simulated in the NADW and
642 displays a lag of a few hundreds of years with respect to the Pa/Th response.

643 We argue that this lag between carbon isotopes and Pa/Th responses can be explained
644 by the fundamentally different mechanisms at play to produce the proxy record. Indeed, in our
645 model, because our scavenging intensity is kept constant due to the fixed particle fields, the
646 Pa/Th only depends on circulation. Besides, the Pa and Th have very short residence times in
647 the ocean water column, making the Pa/Th proxy very prompt to respond to any circulation

change. On the contrary, the carbon isotopes in the ocean interact with the carbon from other reservoirs, via air-sea exchanges and biological activity, which are processes that take time.

Even if our model results are not directly comparable with the proxy data in terms of absolute value and amplitude of change, we observe some features consistent with the available paleo proxy record: i) we observe consistency in the proxy response in the Atlantic western boundary current for Pa/Th ii) we observe distinct proxy response for intermediate and deep waters for $\delta^{13}C$ and $\Delta^{14}C$, iii) we observe significant Pa/Th increase and $\delta^{13}C$ and $\Delta^{14}C$ decrease in the deep western boundary current which are consistent with the recorded millennial scale variability of these three proxies in deep sea sediments. Besides, our model experiment suggests that there is a constitutive lag between the Pa/Th and the carbon isotopes response to a freshwater input in the North-Atlantic in the NADW water mass. Such a lag has been evidenced in one proxy record at the Brazilian margin but was attributed to a potential sediment bioturbation bias as the two proxies are carried by particles of different sizes.

The observed discrepancies between our model experiment and the proxy data in this study can be partly attributed the incomplete process representation in our model. In particular, because we have fixed particles in our model we cannot capture the integrity of the Pa/Th signal. Future work would require the evaluation of the multi-proxy response in a more realistic numerical experiment, using glacial boundary conditions and coupled/interactive particles fields. In addition, a more complete dataset containing multi-proxy records is needed to achieve a more complete model-data comparison.

Acknowledgements: This is a contribution to ERC project ACCLIMATE; the research leading to these results has received funding from the European Research Council under the European Union's Seventh Framework Programme (FP7/2007-2013)/ERC grant agreement 339108. This is a LSCE contribution XXXXX.

673 **Tables and Figures:**
674
675 Table 1: Parameters used in the Pa/Th module

Symbol	Variable	Value	Units
j	^{231}Pa or ^{230}Th	-	-
i	Particle type ($CaCO_3$, POC, opal)	-	-
A_p^j	Particle-bound activity	-	$dpm.m^{-3}.y^{-1}$
A_d^j	Dissolved activity	-	$dpm.m^{-3}.y^{-1}$
β^{Pa}	Production of ^{231}Pa from U-decay		$dpm.m^{-3}.y^{-1}$
β^{Th}	Production of ^{230}Th from - decay		$dpm.m^{-3}.y^{-1}$
λ_{Pa}	Decay constant for ^{231}Pa		y^{-1}
λ_{Th}	Decay constant for ^{230}Th		y^{-1}
K_{adsorp}^j	Adsorption coefficient	Calculated on each grid-cell	y^{-1}
k_{desorp}	Desorption coefficient	2.4	y^{-1}
$\sigma_{i,j}$	Scavenging efficiency	See Table 4	$m^2.mol^{-1}$
F_i	Particle flux	Calculated in each grid-cell Fi = [particle conc]. w_s	$mol.m^{-2}.y^{-1}$
w_s	Uniform settling speed	1000	$m.y^{-1}$

676

677 Table 2: Compilation of Kd and fractionations factors from observations and model studies

678

		Pa			Th			F(Th/Pa)		
		Kd_{POC}	Kd_{opal}	Kd_{CaCO3}	Kd_{POC}	Kd_{opal}	Kd_{CaCO3}	CaCO3	POC	Opal
obs	Chase, 2002	-	1.40E+06	2.20E+05	-	3.90E+05	9.00E+06	40.91		0.28
	Hayes, 2015 (mean value)	6.00E+05	-	9.00E+05	3.00E+06	-	3.00E+07	33.33	5	
	Hayes, 2015 (min value)	4.00E+05	-	5.00E+05	1.00E+06	-	2.60E+07	52.00	2.5	
	Hayes, 2015(max value)	8.00E+05	-	1.30E+06	5.00E+06	-	3.40E+07	26.15	6.25	
models	Sidall, 2005 (min value)	2.04E+05	2.04E+05	2.04E+05	2.04E+05	2.04E+05	2.04E+05	1	1	1
	Sidall, 2005 (mean value)	1.00E+07	1.67E+06	2.50E+05	1.00E+07	5.00E+05	1.00E+07	40	1	0.3
	Van_Hulten 2018	2.00E+06	5.00E+05	1.20E+05	5.00E+06	5.00E+05	5.00E+06	41.67	2.5	1
	Van_Hulten 2018	4.00E+05	-	-	1.00E+06	-	-		2.5	

679 Table 3: Latin Hypercube Sampling inputs and best fit parameters
680

	$F(Th/Pa)_{CaCO3}$	$F(Th/Pa)_{POC}$	$F(Th/Pa)_{opal}$	$\sigma_{Th\text{-}CaCO3}$	$\sigma_{Th\text{-}POC}$	$\sigma_{Th\text{-}opal}$
min	2.3	0.6	0.2	4.56	0.08	0.06
max	48.1	10	2.8	200	6	16
best fit	41.15	3.54	0.49	76.83	5.47	3.77

681
682
683 Table 4: Best fit $\sigma_{i,j}$ values and corresponding Kd values
684

	$\boldsymbol{\sigma_{Pa\text{-}CaCO3}}$	$\boldsymbol{\sigma_{Pa\text{-}POC}}$	$\boldsymbol{\sigma_{Pa\text{-}opal}}$	$\boldsymbol{\sigma_{Th\text{-}CaCO3}}$	$\boldsymbol{\sigma_{Th\text{-}POC}}$	$\boldsymbol{\sigma_{Th\text{-}opal}}$
Best fit	1.87	1.55	7.62	76.83	5.47	3.77
	$\boldsymbol{Kd_{Pa\text{-}CaCO3}}$	$\boldsymbol{Kd_{Pa\text{-}POC}}$	$\boldsymbol{Kd_{Pa\text{-}opal}}$	$\boldsymbol{Kd_{Th\text{-}CaCO3}}$	$\boldsymbol{Kd_{Th\text{-}POC}}$	$\boldsymbol{Kd_{Th\text{-}opal}}$
Best fit	8.01E+06	5.53E+07	4.86E+07	3.29E+08	1.96E+08	2.40E+07

685
686
687
688 Table 5: Table summarizing the experiments performed
689

Name	Hosing zone	Hosing intensity (Sv)	AMOC state during hosing
PI_control_run	-	-	-
PI_hosing_LS	Labrador Sea	0.3	off
PI_hosing_NS	Nordic Seas	0.3	very weak

690

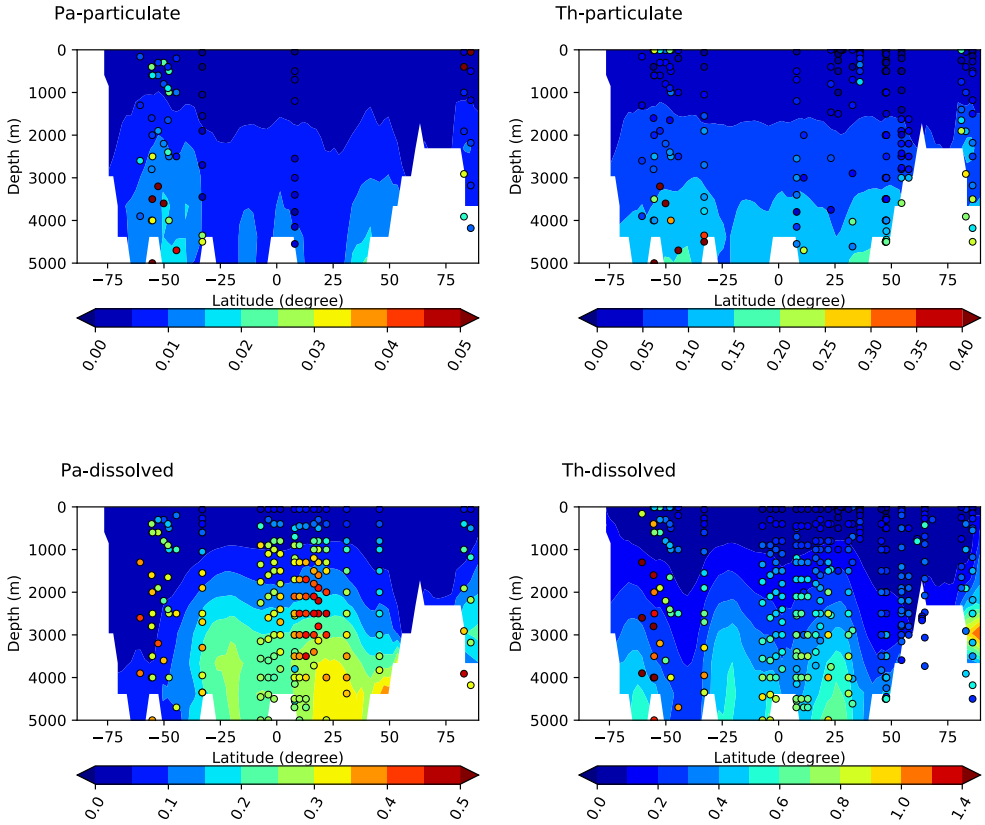

Figure 1: Atlantic sections showing water column showing dissolved and particle-bound ^{231}Pa (left panel) and ^{230}Th activities in dpm.g^{-1} (right panel) simulated by iLOVECLIM (color background) and observation data (colored dots) compiled in [*Dutay et al.*, 2009].

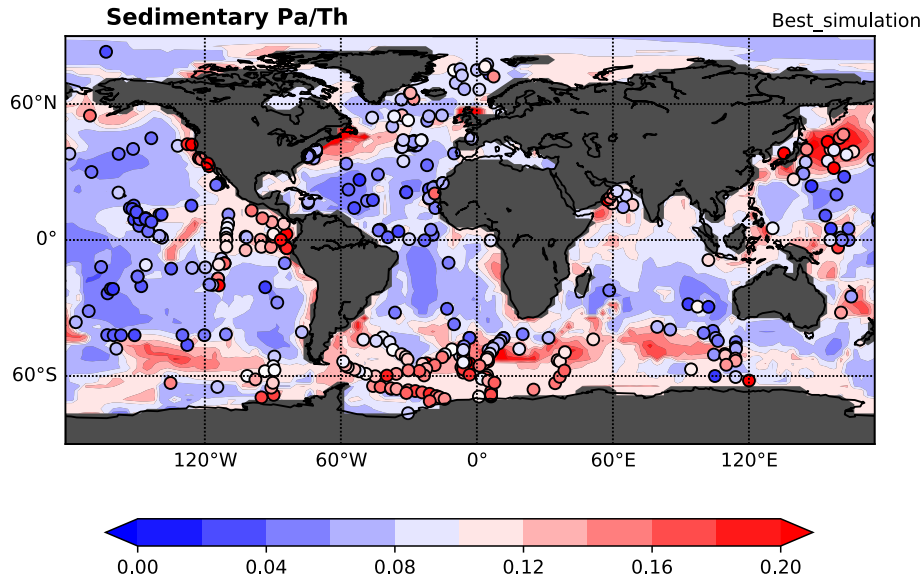

Figure 2: **Map showing the particulate ^{231}Pa/^{230}Th activity ratio of the deepest model ocean grid-cells.**
The simulated Pa/Th ratio is represented in the color background. The observations compiled in [*Henderson et al.*, 1999] are represented as circles.

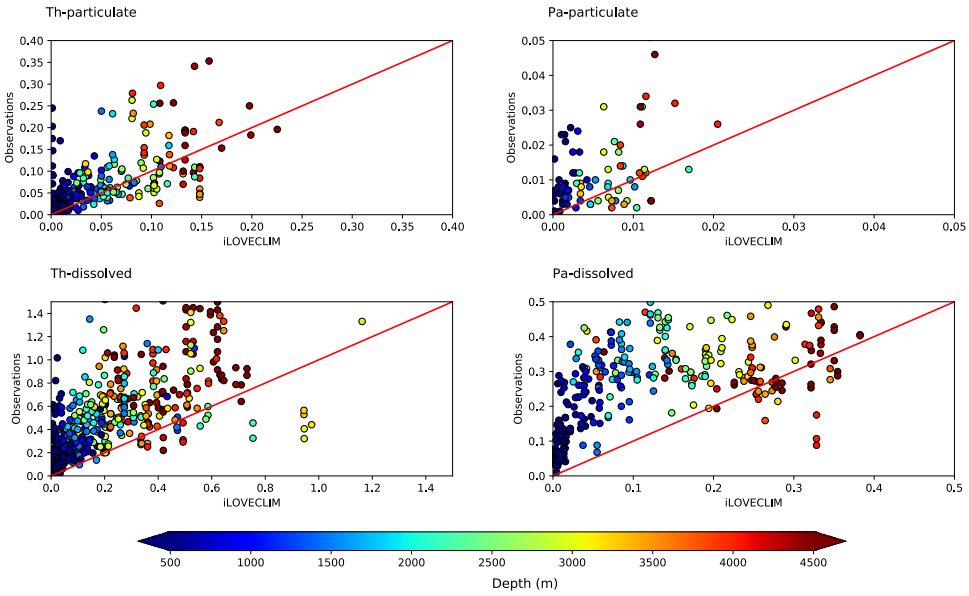

Figure 3: **Model-data agreement for ^{231}Pa and ^{230}Th dissolved and particulate water column concentrations.**
In each panel, dots represent the observed concentrations (y-axis) against the modeled concentration in the closest grid-cell (x-axis). The color of the dot represents the corresponding water depth. The red line (1:1) represents the ideal model-data agreement.

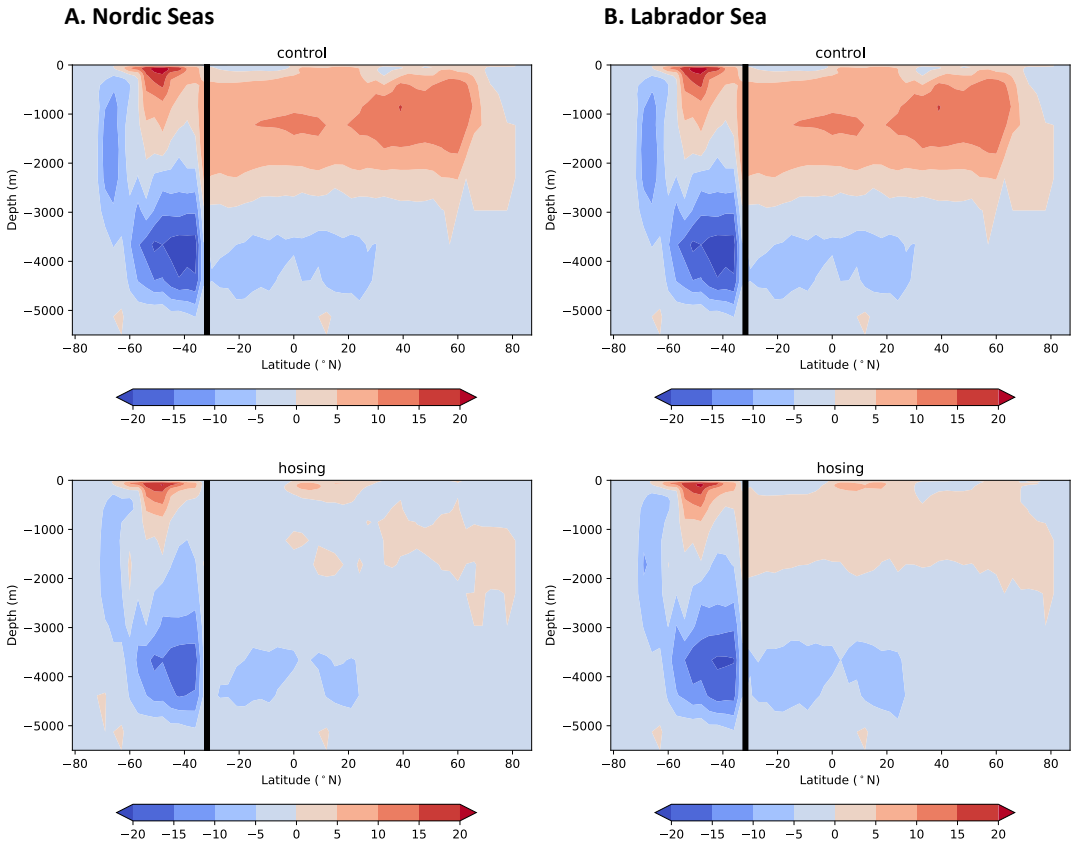

Figure 4: Atlantic zonally averaged stream function
Freshwater forcing of 0.3 Sv in **A.** the Nordic Seas or **B.** the Labrador Sea (see [*Roche et al.*, 2010]) The upper panel show the stream function during the control period of simulation (i.e. the first 300 years under PI conditions). The lower panel presents the stream function during the last 100 years of freshwater forcing (year 500 to y 600).

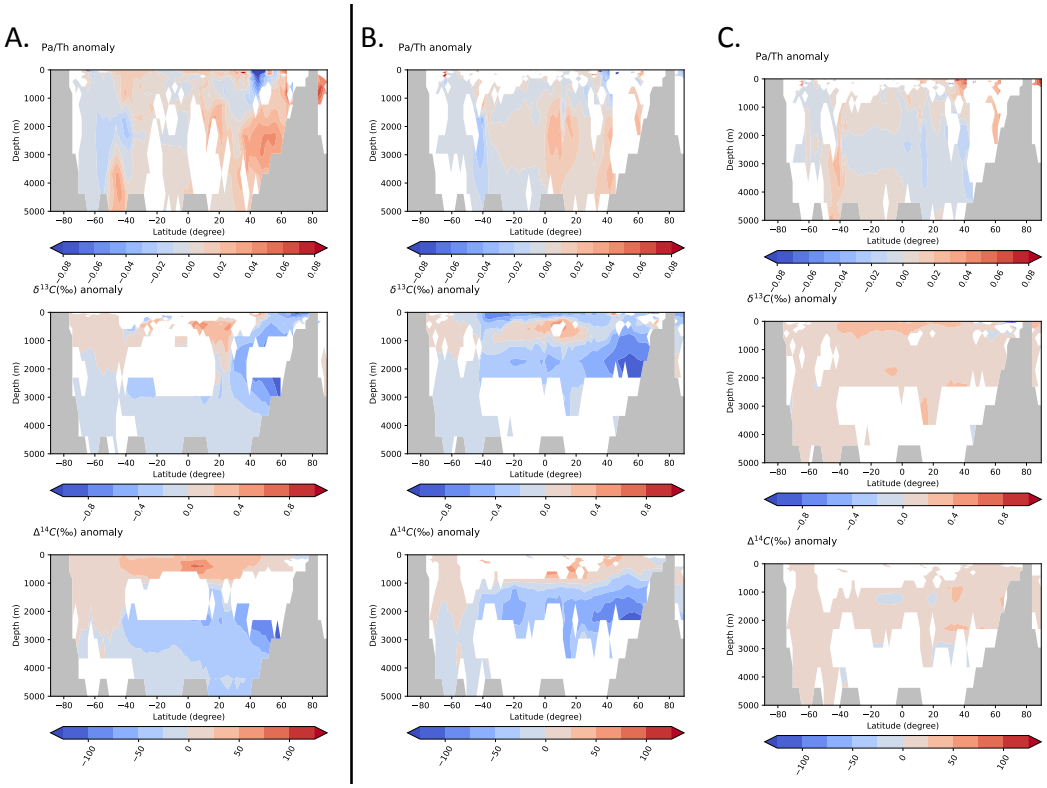

Figure 5: Zonally averaged anomalies for Pa/Th, $\delta^{13}C$ and $\Delta^{14}C$ in the western basin in the case of a freshwater input in the Nordic seas.
The anomalies are computed/defined as the proxy response minus the mean of the proxy value during the control period of 300 years under PI conditions (see text).
A. Represents the anomalies for the three proxies in the case where exactly one proxy response has been detected. In the case of two proxy responses, **B.** represents the anomaly value for the first response, **C.** represents the anomaly for the second proxy response. The zone left in blank were not showing a unique response (A.) or not showing exactly two responses (B. and C.) In each subplot, the grey contours represent the ocean bottom.

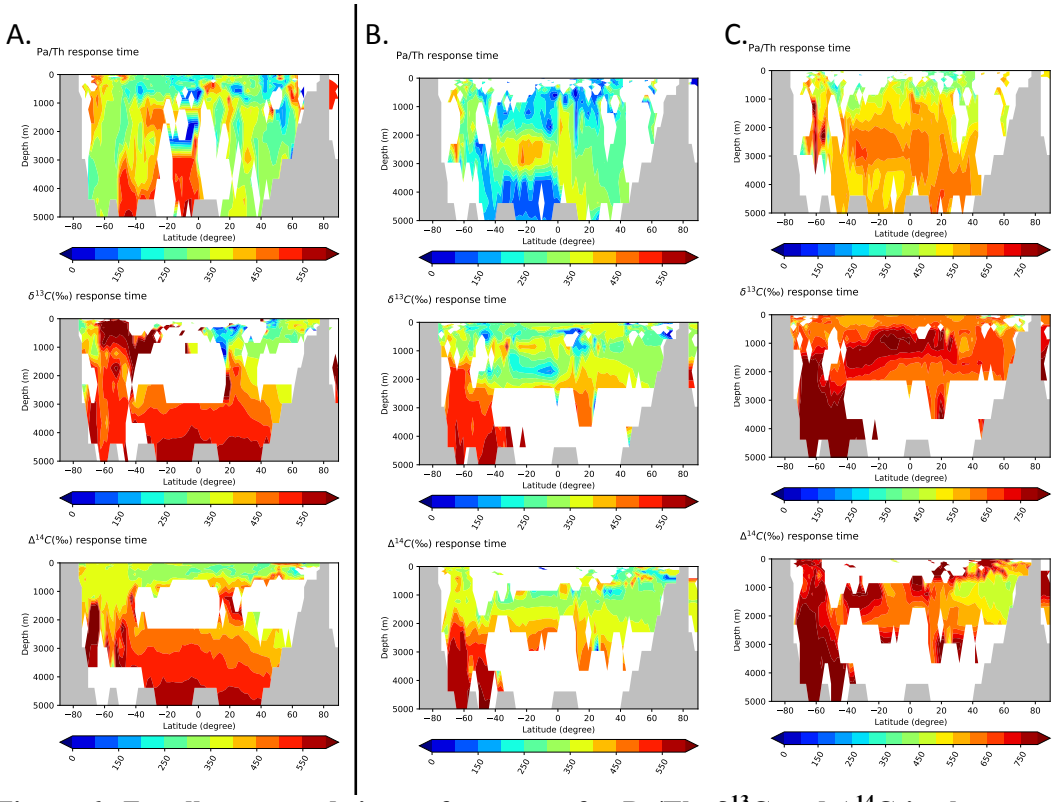

Figure 6: Zonally averaged times of response for Pa/Th, $\delta^{13}C$ and $\Delta^{14}C$ in the western basin in the case of a freshwater input in the Nordic seas.
The times of response correspond to the time of proxy maximal response (see text).
A. Response time in the case where exactly one proxy response is detected. In the case where two distinct responses are detected **B.** shows the response time of the first response and **C.** shows the response time corresponding to the second response. The zone left in blank were not showing a unique response (A.) or not showing exactly two responses (B. and C.) In each subplot, the grey contours represent the ocean bottom.

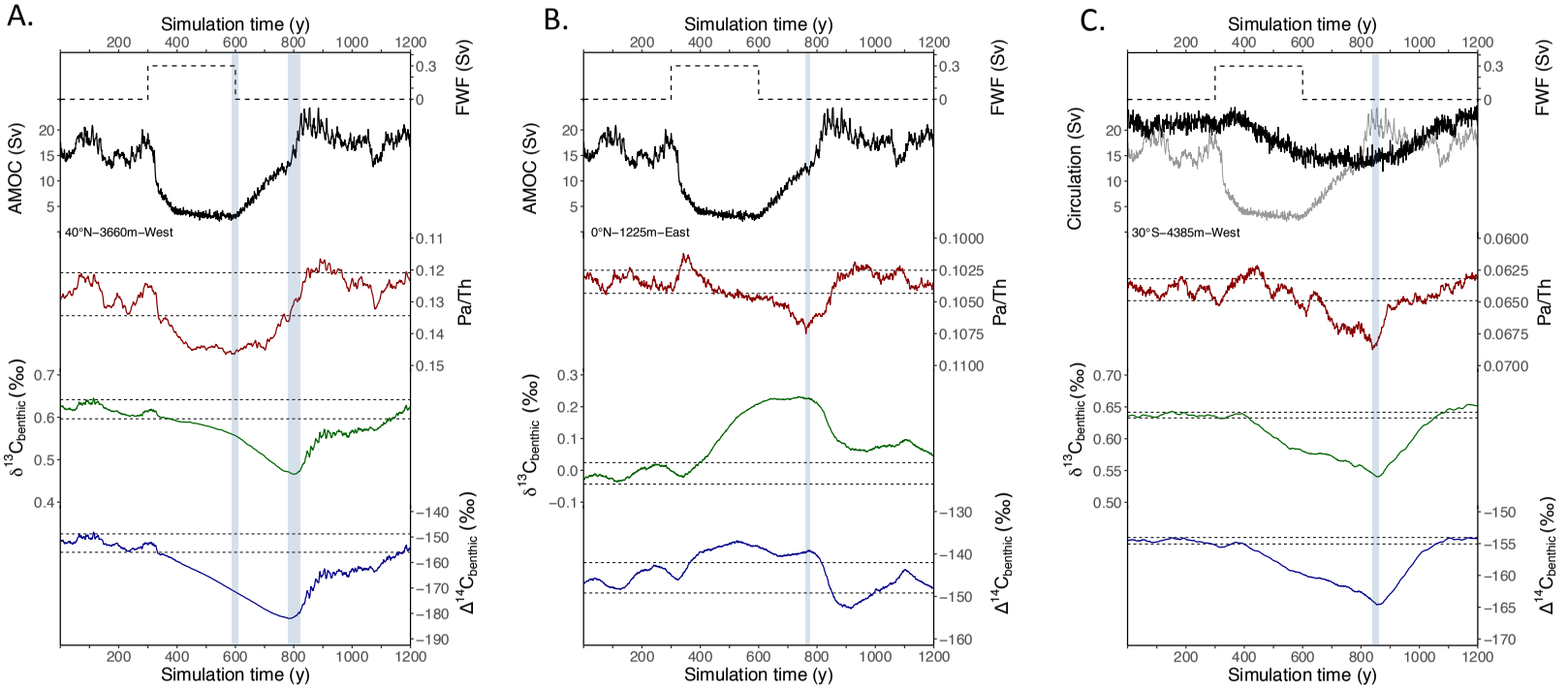

Figure 7: Selected multi-proxy time series in the case of a Nordic Seas hosing.
A. Zonally averaged on the western Atlantic basin time series at 40°N 3660 m. This time series is representative of the proxy behaviors in the NADW. **B.** Zonally averaged on the eastern Atlantic basin time series at 0°N 1225 m. This time series is representative of the intermediate waters. **C.** Zonally averaged on the western Atlantic basin time series at 30°S 4385 m. This time series is representative of the proxy response in the AABW. In the eastern basin, the $\delta^{13}C$ generally displays 2 responses, first increasing (not shown) and then decreasing (as shown).
In each subplot from top to bottom the dashed black line represent the freshwater flux applied in the Nordic Seas, the black line represents the North Atlantic Maximum stream function (A. and B.) and the Southern Ocean maximum stream function (C.), the red line represents the particulate Pa/Th, the green line represents the $\delta^{13}C$ and the blue line represents the $\Delta^{14}C$. The thin dashed black lines represent the proxy variance (2 σ) on the first 300 simulated years. The blue vertical bands indicate the timing of the proxy responses.

730

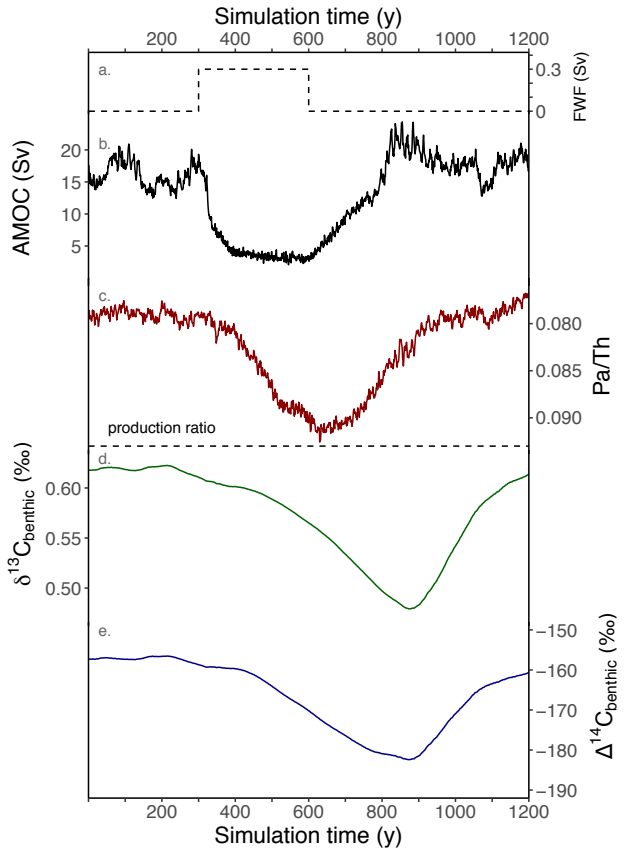

731
732 **Figure 8: Modeled multi-proxy time series at the Bermuda Rise for a hosing in the**
733 **Nordic Seas.**
734 **a.** Imposed freshwater flux, **b.** Maximum North-Atlantic Stream function (Sv) c. simulated
735 Pa/Th, d. benthic $\delta^{13}C$ (‰) and e. $\Delta^{14}C$ (‰)
736 The presented time series correspond to an average of 6 grid cells surrounding the model grid-
737 cell closest to the Bermuda Rise (34°N-58°W).
738

761 **References**

762 Adkins, J. F., and E. A. Boyle (1997), Changing atmospheric Δ14C and the record of deep
763 water paleoventilation ages, Paleoceanography, 12(3), 337-344, doi:
764 10.1029/97PA00379.
765 Alley, R. B., P. A. Mayewski, T. Sowers, M. Stuiver, K. C. Taylor, and P. U. Clark (1997),
766 Holocene climatic instability: A prominent, widespread event 8200 yr ago, Geology,
767 25(6), 483-486.
768 Anderson, R. F., M. P. Bacon, and P. G. Brewer (1983), Removal of 230 Th and 231 Pa at
769 ocean margins, Earth and Planetary Science Letters, 66, 73-90.
770 Bard, E., M. Arnold, J. Mangerud, M. Paterne, L. Labeyrie, J. Duprat, M.-A. Mélières, E.
771 Sønstegaard, and J.-C. Duplessy (1994), The North Atlantic atmosphere-sea surface 14C
772 gradient during the Younger Dryas climatic event, Earth and Planetary Science Letters,
773 126(4), 275-287, doi: https://doi.org/10.1016/0012-821X(94)90112-0.
774 Barker, S., J. Chen, X. Gong, L. Jonkers, G. Knorr, and D. Thornalley (2015), Icebergs not
775 the trigger for North Atlantic cold events, Nature, 520, 333, doi: 10.1038/nature14330
776 https://www.nature.com/articles/nature14330 - supplementary-information.
777 Blunier, T., M. L. Bender, B. Barnett, and J. C. von Fischer (2012), Planetary fertility
778 during the past 400 ka based on the triple isotope composition of O₂ in
779 trapped gases from the Vostok ice core, Clim. Past, 8(5), 1509-1526, doi: 10.5194/cp-8-
780 1509-2012.
781 Böhm, E., J. Lippold, M. Gutjahr, M. Frank, P. Blaser, B. Antz, J. Fohlmeister, N. Frank, M.
782 Andersen, and M. Deininger (2015), Strong and deep Atlantic meridional overturning
783 circulation during the last glacial cycle, Nature, 517(7532), 73-76.
784 Bondevik, S., J. Mangerud, H. H. Birks, S. Gulliksen, and P. Reimer (2006), Changes in
785 North Atlantic radiocarbon reservoir ages during the Allerød and Younger Dryas,
786 Science, 312(5779), 1514-1517.
787 Bouttes, N., D. Roche, V. Mariotti, and L. Bopp (2015), Including an ocean carbon cycle
788 model into i LOVECLIM (v1. 0), Geoscientific Model Development, 8(5), 1563.
789 Broecker, W. S. (1994), Massive iceberg discharges as triggers for global climate change,
790 Nature, 372(6505), 421.
791 Broecker, W. S., G. Bond, M. Klas, G. Bonani, and W. Wolfli (1990), A salt oscillator in the
792 glacial Atlantic? 1. The concept, Paleoceanography, 5(4), 469-477.
793 Brovkin, V., J. Bendtsen, M. Claussen, A. Ganopolski, C. Kubatzki, V. Petoukhov, and A.
794 Andreev (2002), Carbon cycle, vegetation, and climate dynamics in the Holocene:
795 Experiments with the CLIMBER‐2 model, Global Biogeochemical Cycles, 16(4), 86-81-
796 86-20.
797 Burckel, P., C. Waelbroeck, J. M. Gherardi, S. Pichat, H. Arz, J. Lippold, T. Dokken, and F.
798 Thil (2015), Atlantic Ocean circulation changes preceded millennial tropical South
799 America rainfall events during the last glacial, Geophysical Research Letters, 42(2), 411-
800 418.
801 Burckel, P., C. Waelbroeck, Y. Luo, D. M. Roche, S. Pichat, S. L. Jaccard, J. Gherardi, A.
802 Govin, J. Lippold, and F. Thil (2016), Changes in the geometry and strength of the
803 Atlantic meridional overturning circulation during the last glacial (20-50ka), Climate of
804 the Past, 12(11), 2061.
805 Chase, Z., R. F. Anderson, M. Q. Fleisher, and P. W. Kubik (2002), The influence of particle
806 composition and particle flux on scavenging of Th, Pa and Be in the ocean, Earth and
807 Planetary Science Letters, 204(1), 215-229, doi: https://doi.org/10.1016/S0012-
808 821X(02)00984-6.

809 Chase, Z., R. F. Anderson, M. Q. Fleisher, and P. W. Kubik (2003), Scavenging of 230Th,
810 231Pa and 10Be in the Southern Ocean (SW Pacific sector): the importance of particle
811 flux, particle composition and advection, Deep Sea Research Part II: Topical Studies in
812 Oceanography, 50(3), 739-768, doi: https://doi.org/10.1016/S0967-0645(02)00593-3.
813 Chen, T., L. F. Robinson, A. Burke, J. Southon, P. Spooner, P. J. Morris, and H. C. Ng (2015),
814 Synchronous centennial abrupt events in the ocean and atmosphere during the last
815 deglaciation, Science, 349(6255), 1537.
816 Duplessy, J., N. Shackleton, R. Fairbanks, L. Labeyrie, D. Oppo, and N. Kallel (1988),
817 Deepwater source variations during the last climatic cycle and their impact on the global
818 deepwater circulation, Paleoceanography, 3(3), 343-360.
819 Dutay, J. C., F. Lacan, M. Roy‐Barman, and L. Bopp (2009), Influence of particle size and
820 type on 231Pa and 230Th simulation with a global coupled biogeochemical‐ocean
821 general circulation model: A first approach, Geochemistry, Geophysics, Geosystems,
822 10(1).
823 Eide, M., A. Olsen, U. S. Ninnemann, and T. Johannessen (2017), A global ocean
824 climatology of preindustrial and modern ocean δ13C, Global Biogeochemical Cycles,
825 31(3), 515-534.
826 Ellison, C. R., M. R. Chapman, and I. R. Hall (2006), Surface and deep ocean interactions
827 during the cold climate event 8200 years ago, Science, 312(5782), 1929-1932.
828 François, R. (2007), Paleoflux and paleocirculation from sediment 230Th and
829 231Pa/230Th, Proxies in late cenozoic paleoceanography. Elsevier, 681-716.
830 Friedlingstein, P., P. Cox, R. Betts, L. Bopp, W. von Bloh, V. Brovkin, P. Cadule, S. Doney, M.
831 Eby, and I. Fung (2006), Climate–carbon cycle feedback analysis: results from the C4MIP
832 model intercomparison, Journal of climate, 19(14), 3337-3353.
833 Gherardi, J. M., L. Labeyrie, J. F. McManus, R. Francois, L. C. Skinner, and E. Cortijo (2005),
834 Evidence from the Northeastern Atlantic basin for variability in the rate of the
835 meridional overturning circulation through the last deglaciation, Earth and Planetary
836 Science Letters, 240(3), 710-723, doi: https://doi.org/10.1016/j.epsl.2005.09.061.
837 Godwin, H. (1962), Half-life of radiocarbon, Nature, 195(4845), 984-984.
838 Hemming, S. R. (2004), Heinrich events: Massive late Pleistocene detritus layers of the
839 North Atlantic and their global climate imprint, Reviews of Geophysics, 42(1).
840 Henderson, G. M., and R. F. Anderson (2003), The U-series toolbox for
841 paleoceanography, Reviews in Mineralogy and Geochemistry, 52(1), 493-531, doi:
842 10.2113/0520493.
843 Henderson, G. M., C. Heinze, R. F. Anderson, and A. M. E. Winguth (1999), Global
844 distribution of the 230Th flux to ocean sediments constrained by GCM modelling, Deep
845 Sea Research Part I: Oceanographic Research Papers, 46(11), 1861-1893, doi:
846 https://doi.org/10.1016/S0967-0637(99)00030-8.
847 Henry, L., J. F. McManus, W. B. Curry, N. L. Roberts, A. M. Piotrowski, and L. D. Keigwin
848 (2016), North Atlantic ocean circulation and abrupt climate change during the last
849 glaciation, Science, 353(6298), 470-474.
850 Hoffman, J. S., A. E. Carlson, K. Winsor, G. P. Klinkhammer, A. N. LeGrande, J. T. Andrews,
851 and J. C. Strasser (2012), Linking the 8.2 ka event and its freshwater forcing in the
852 Labrador Sea, Geophysical Research Letters, 39(18), doi: 10.1029/2012GL053047.
853 Hoogakker, B. A. A., M. R. Chapman, I. N. McCave, C. Hillaire-Marcel, C. R. W. Ellison, I. R.
854 Hall, and R. J. Telford (2011), Dynamics of North Atlantic Deep Water masses during the
855 Holocene, Paleoceanography, 26(4), doi: 10.1029/2011PA002155.

856 Jacobel, A., J. McManus, R. Anderson, and G. Winckler (2017), Climate-related response
857 of dust flux to the central equatorial Pacific over the past 150 kyr, Earth and Planetary
858 Science Letters, 457, 160-172.
859 Jickells, T., Z. An, K. K. Andersen, A. Baker, G. Bergametti, N. Brooks, J. Cao, P. Boyd, R.
860 Duce, and K. Hunter (2005), Global iron connections between desert dust, ocean
861 biogeochemistry, and climate, science, 308(5718), 67-71.
862 Kleiven, H. K. F., C. Kissel, C. Laj, U. S. Ninnemann, T. O. Richter, and E. Cortijo (2008),
863 Reduced North Atlantic deep water coeval with the glacial Lake Agassiz freshwater
864 outburst, science, 319(5859), 60-64.
865 Kretschmer, S., W. Geibert, M. M. R. van der Loeff, and G. Mollenhauer (2010), Grain size
866 effects on 230 Th xs inventories in opal-rich and carbonate-rich marine sediments, Earth
867 and Planetary Science Letters, 294(1), 131-142.
868 Lippold, J., J. Grützner, D. Winter, Y. Lahaye, A. Mangini, and M. Christl (2009), Does
869 sedimentary 231Pa/230Th from the Bermuda Rise monitor past Atlantic meridional
870 overturning circulation?, Geophysical Research Letters, 36(12).
871 Lougheed, B. C., B. Metcalfe, U. S. Ninnemann, and L. Wacker (2018), Moving beyond the
872 age–depth model paradigm in deep-sea palaeoclimate archives: dual radiocarbon and
873 stable isotope analysis on single foraminifera, Climate of the Past, 14(4), 515-526.
874 Luo, Y., R. Francois, and S. E. Allen (2010), Sediment
875 ²³¹Pa/²³⁰Th as a recorder of the rate of the Atlantic
876 meridional overturning circulation: insights from a 2-D model, Ocean Sci., 6(1), 381-400,
877 doi: 10.5194/os-6-381-2010.
878 Lynch-Stieglitz, J. (2017), The Atlantic Meridional Overturning Circulation and Abrupt
879 Climate Change, Annual Review of Marine Science, 9(1), 83-104, doi: 10.1146/annurev-
880 marine-010816-060415.
881 Lynch-Stieglitz, J., M. W. Schmidt, L. Gene Henry, W. B. Curry, L. C. Skinner, S. Mulitza, R.
882 Zhang, and P. Chang (2014), Muted change in Atlantic overturning circulation over some
883 glacial-aged Heinrich events, Nature Geoscience, 7, 144, doi: 10.1038/ngeo2045
884 https://www.nature.com/articles/ngeo2045 - supplementary-information.
885 Marchal, O., R. François, T. F. Stocker, and F. Joos (2000), Ocean thermohaline circulation
886 and sedimentary 231Pa/230Th ratio, Paleoceanography, 15(6), 625-641.
887 Marcott, S. A., P. U. Clark, L. Padman, G. P. Klinkhammer, S. R. Springer, Z. Liu, B. L. Otto-
888 Bliesner, A. E. Carlson, A. Ungerer, and J. Padman (2011), Ice-shelf collapse from
889 subsurface warming as a trigger for Heinrich events, Proceedings of the National
890 Academy of Sciences, 108(33), 13415-13419.
891 McManus, J. F., R. Francois, J.-M. Gherardi, L. D. Keigwin, and S. Brown-Leger (2004),
892 Collapse and rapid resumption of Atlantic meridional circulation linked to deglacial
893 climate changes, Nature, 428(6985), 834-837.
894 Menviel, L., J. Yu, F. Joos, A. Mouchet, K. J. Meissner, and M. H. England (2016), Poorly
895 ventilated deep ocean at the Last Glacial Maximum inferred from carbon isotopes: A
896 data-model comparison study, Paleoceanography, 32(1), 2-17, doi:
897 10.1002/2016PA003024.
898 Missiaen, L., S. Pichat, C. Waelbroeck, E. Douville, L. Bordier, A. Dapoigny, F. Thil, L.
899 Foliot, and L. Wacker (2018), Downcore Variations of Sedimentary Detrital
900 (238U/232Th) Ratio: Implications on the Use of 230Thxs and 231Paxs to Reconstruct
901 Sediment Flux and Ocean Circulation, Geochemistry, Geophysics, Geosystems, 0(ja), doi:
902 10.1029/2017GC007410.
903 Mulitza, S., C. M. Chiessi, E. Schefuß, J. Lippold, D. Wichmann, B. Antz, A. Mackensen, A.
904 Paul, M. Prange, and K. Rehfeld (2017), Synchronous and proportional deglacial changes

905 in Atlantic Meridional Overturning and northeast Brazilian precipitation,
906 Paleoceanography.
907 Ng, H. C., L. F. Robinson, J. F. McManus, K. J. Mohamed, A. W. Jacobel, R. F. Ivanovic, L. J.
908 Gregoire, and T. Chen (2018), Coherent deglacial changes in western Atlantic Ocean
909 circulation, Nature communications, 9.
910 Orr, J. C., E. Maier‐Reimer, U. Mikolajewicz, P. Monfray, J. L. Sarmiento, J. Toggweiler, N.
911 K. Taylor, J. Palmer, N. Gruber, and C. L. Sabine (2001), Estimates of anthropogenic
912 carbon uptake from four three‐dimensional global ocean models, Global
913 Biogeochemical Cycles, 15(1), 43-60.
914 Paillet, J., M. Arhan, and M. S. McCartney (1998), Spreading of Labrador Sea water in the
915 eastern North Atlantic, Journal of Geophysical Research: Oceans, 103(C5), 10223-10239.
916 Reimer, P. J., E. Bard, A. Bayliss, J. W. Beck, P. G. Blackwell, C. B. Ramsey, C. E. Buck, H.
917 Cheng, R. L. Edwards, and M. Friedrich (2013), IntCal13 and Marine13 radiocarbon age
918 calibration curves 0–50,000 years cal BP, Radiocarbon, 55(4), 1869-1887.
919 Rempfer, J., T. F. Stocker, F. Joos, J. Lippold, and S. L. Jaccard (2017), New insights into
920 cycling of 231Pa and 230Th in the Atlantic Ocean, Earth and Planetary Science Letters,
921 468, 27-37, doi: https://doi.org/10.1016/j.epsl.2017.03.027.
922 Roche, D. M., A. P. Wiersma, and H. Renssen (2010), A systematic study of the impact of
923 freshwater pulses with respect to different geographical locations, Climate Dynamics,
924 34(7), 997-1013, doi: 10.1007/s00382-009-0578-8.
925 Siddall, M., G. M. Henderson, N. R. Edwards, M. Frank, S. A. Müller, T. F. Stocker, and F.
926 Joos (2005), 231Pa/230Th fractionation by ocean transport, biogenic particle flux and
927 particle type, Earth and Planetary Science Letters, 237(1), 135-155, doi:
928 https://doi.org/10.1016/j.epsl.2005.05.031.
929 Siddall, M., T. F. Stocker, G. M. Henderson, F. Joos, M. Frank, N. R. Edwards, S. P. Ritz, and
930 S. A. Müller (2007), Modeling the relationship between 231Pa/230Th distribution in
931 North Atlantic sediment and Atlantic meridional overturning circulation,
932 Paleoceanography, 22(2), doi: 10.1029/2006PA001358.
933 Siegenthaler, U., and K. Münnich C/12 C fractionation during CO 2 transfer from air to
934 sea, Carbon Cycle Modelling. Bolin B.(ed) Wiley, New York, 249-257.
935 Skinner, L. C., and N. J. Shackleton (2004), Rapid transient changes in northeast Atlantic
936 deep water ventilation age across Termination I, Paleoceanography, 19(2), doi:
937 10.1029/2003PA000983.
938 Skinner, L. C., C. Waelbroeck, A. E. Scrivner, and S. J. Fallon (2014), Radiocarbon evidence
939 for alternating northern and southern sources of ventilation of the deep Atlantic carbon
940 pool during the last deglaciation, Proceedings of the National Academy of Sciences.
941 Smeed, D., G. McCarthy, S. Cunningham, E. Frajka-Williams, D. Rayner, W. Johns, C.
942 Meinen, M. Baringer, B. Moat, and A. Duchez (2014), Observed decline of the Atlantic
943 meridional overturning circulation 2004–2012, Ocean Science, 10(1), 29-38.
944 Stanford, J., E. J. Rohling, S. Bacon, A. Roberts, F. Grousset, and M. Bolshaw (2011), A new
945 concept for the paleoceanographic evolution of Heinrich event 1 in the North Atlantic,
946 Quaternary Science Reviews, 30(9), 1047-1066.
947 Stuiver, M., and H. A. Polach (1977), Discussion reporting of 14 C data, Radiocarbon,
948 19(3), 355-363.
949 Thomas, A. L., G. M. Henderson, and L. F. Robinson (2006), Interpretation of the
950 231Pa/230Th paleocirculation proxy: New water-column measurements from the
951 southwest Indian Ocean, Earth and Planetary Science Letters, 241(3), 493-504, doi:
952 https://doi.org/10.1016/j.epsl.2005.11.031.

953 Thomson, J., S. Colley, R. Anderson, G. T. Cook, A. B. MacKenzie, and D. D. Harkness
954 (1993), Holocene sediment fluxes in the northeast Atlantic from 230Thexcess and
955 radiocarbon measurements, Paleoceanography, 8(5), 631-650, doi:
956 10.1029/93PA01366.
957 Thornalley, D. J., S. Barker, W. S. Broecker, H. Elderfield, and I. N. McCave (2011), The
958 deglacial evolution of North Atlantic deep convection, science, 331(6014), 202-205.
959 Thornalley, D. J. R., H. A. Bauch, G. Gebbie, W. Guo, M. Ziegler, S. M. Bernasconi, S. Barker,
960 L. C. Skinner, and J. Yu (2015), A warm and poorly ventilated deep Arctic Mediterranean
961 during the last glacial period, Science, 349(6249), 706-710, doi:
962 10.1126/science.aaa9554.
963 Tschumi, T., F. Joos, M. Gehlen, and C. Heinze (2010), Deep ocean ventilation, carbon
964 isotopes, marine sedimentation and the deglacial CO2 rise, Climate of the Past, 6(5),
965 1895-1958.
966 van Hulten, M., J. C. Dutay, and M. Roy-Barman (2018), A global scavenging and
967 circulation ocean model of thorium-230 and protactinium-231 with realistic particle
968 dynamics (NEMO–ProThorP 0.1), Geosci. Model Dev. Discuss., 2017, 1-32, doi:
969 10.5194/gmd-2017-274.
970 Volk, T., and M. I. Hoffert (1985), Ocean carbon pumps: Analysis of relative strengths and
971 efficiencies in ocean‐driven atmospheric CO2 changes, The carbon cycle and
972 atmospheric CO2: natural variations Archean to present, 32, 99-110.
973 Waelbroeck, C., J.-C. Duplessy, E. Michel, L. Labeyrie, D. Paillard, and J. Duprat (2001),
974 The timing of the last deglaciation in North Atlantic climate records, Nature, 412(6848),
975 724.
976 Waelbroeck, C., et al. (2018), Relative timing of precipitation and ocean circulation
977 changes in the western equatorial Atlantic over the last 45 kyr, Clim. Past, 14(9),
978 1315-1330, doi: 10.5194/cp-14-1315-2018.
979 Wheatcroft, R. A. (1992), Experimental tests for particle size‐dependent bioturbation
980 in the deep ocean, Limnology and Oceanography, 37(1), 90-104.
981 Wiersma, A. P., and H. Renssen (2006), Model–data comparison for the 8.2kaBP event:
982 confirmation of a forcing mechanism by catastrophic drainage of Laurentide Lakes,
983 Quaternary Science Reviews, 25(1), 63-88, doi:
984 https://doi.org/10.1016/j.quascirev.2005.07.009.
985 Wolff, E. W., J. Chappellaz, T. Blunier, S. O. Rasmussen, and A. Svensson (2010),
986 Millennial-scale variability during the last glacial: The ice core record, Quaternary
987 Science Reviews, 29(21), 2828-2838.
988 Yu, E.-F., R. Francois, and M. P. Bacon (1996), Similar rates of modern and last-glacial
989 ocean thermohaline circulation inferred, Nature, 379, 689-694.
990 Zhao, N., O. Marchal, L. Keigwin, D. Amrhein, and G. Gebbie (2018), A Synthesis of
991 Deglacial Deep‐Sea Radiocarbon Records and Their (In) Consistency With Modern
992 Ocean Ventilation, Paleoceanography and Paleoclimatology, 33(2), 128-151.

Supporting information for

Paleoproxy responses to abrupt circulation changes: a model perspective using iLOVECLIM

L. Missiaen[1,*], N. Bouttes[1], D.M. Roche[1,2], J-C. Dutay[1], A. Quiquet[1], C. Waelbroeck[1,] J-Y Peterschmidtt[1,] S. Moreira[1]…

[1]Laboratoire des Sciences du Climat et de l'Environnement, LSCE/IPSL, CEA-CNRS-UVSQ-Université Paris-Saclay, F-91198 Gif-sur-Yvette, France.

Vrije Universiteit Amsterdam, Faculty of Science, Cluster Earth and Climate, de Boelelaan 1085, 1081HV Amsterdam, The Netherlands

…

* Corresponding author: Lise Missiaen (lise.missiaen@lsce.ipsl.fr)

This file contains:

Figures S… to S…

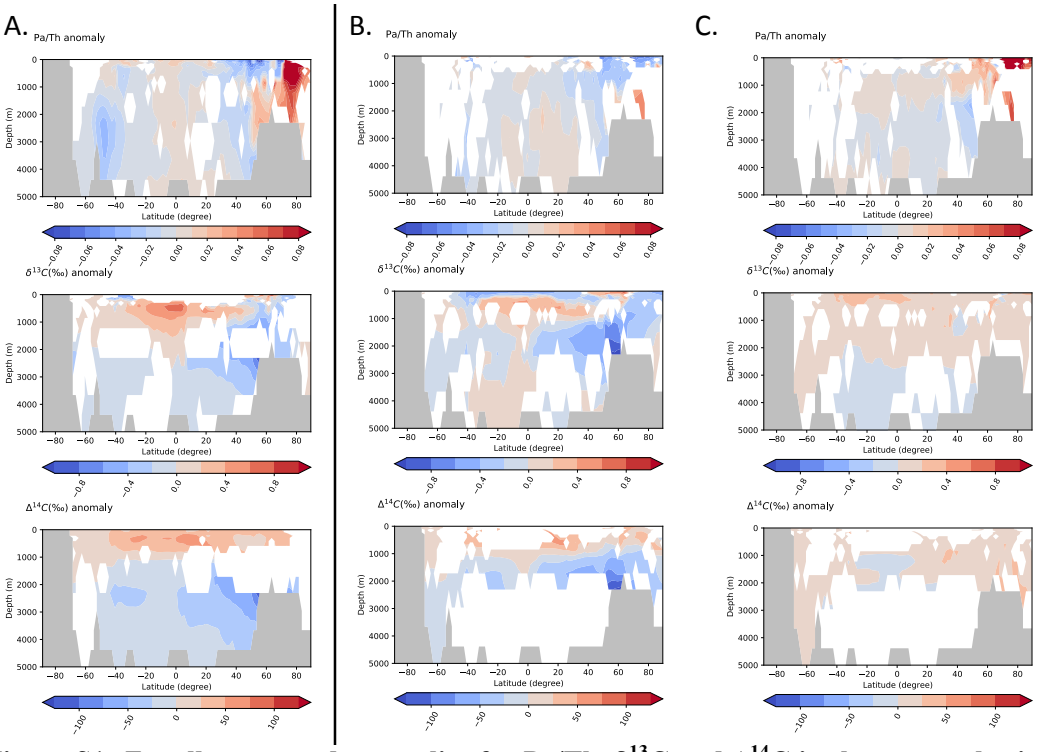

Figure S1: Zonally averaged anomalies for Pa/Th, $\delta^{13}C$ and $\Delta^{14}C$ in the eastern basin in the case of a freshwater input in the Nordic seas.
The represented anomalies correspond to the proxy value corresponding to the proxy response – the mean of the proxy value during the control period of 300 years under PI conditions. The proxy response corresponds to the simulated time where the proxy value is the most different from the mean proxy value during the first 300 years under PI condition for each period of time longer than 80 years where the proxy value has been significantly different from the PI background.
A. Represents the anomalies for the three proxies in the case exactly one proxy response has been detected. In the case of two proxy responses, **B.** represents the anomaly value for the first response, **C.** represents the anomaly for the second proxy response. In each subplot, the grey contours represent the ocean bottom.

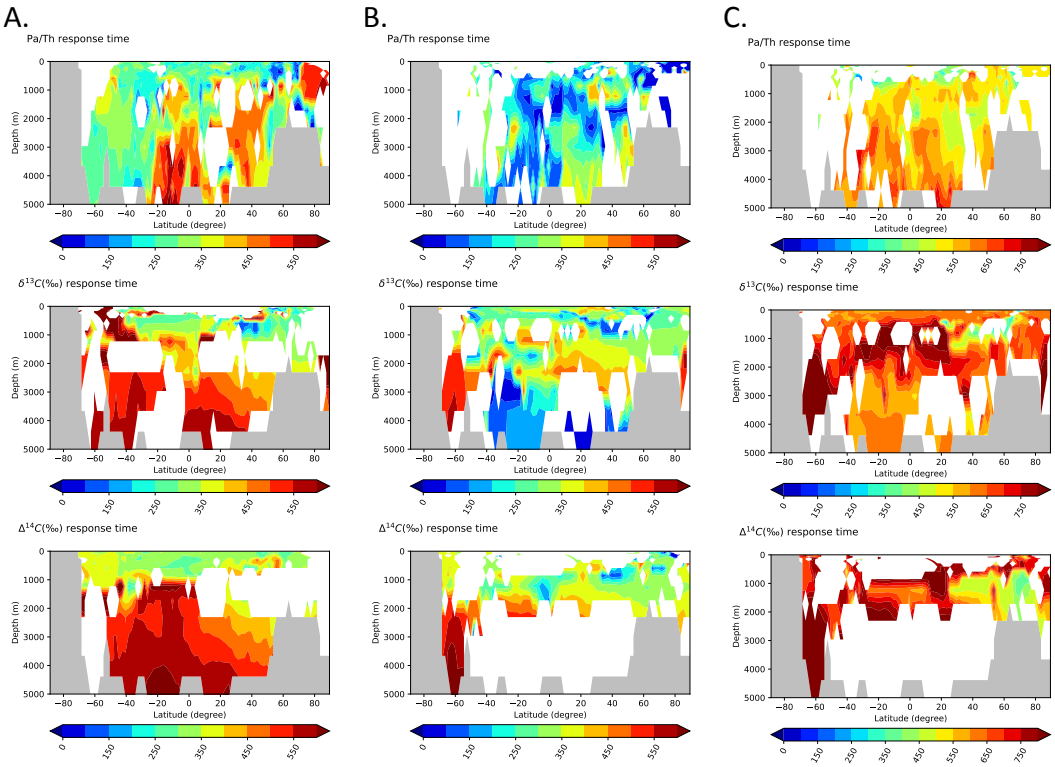

Figure S2: Zonally averaged response times for Pa/Th, $\delta^{13}C$ and $\Delta^{14}C$ in the western basin in the case of a freshwater input in the Nordic seas.
A. Response time in case of a unique response detected. In the case of two distinct responses detected **B.** shows the response time of the first response and **C.** shows the response time corresponding to the second response. The zone left in blank were not showing a unique response (A.) or not showing exactly two responses (B. and C.) In each subplot, the grey contours represent the ocean bottom.

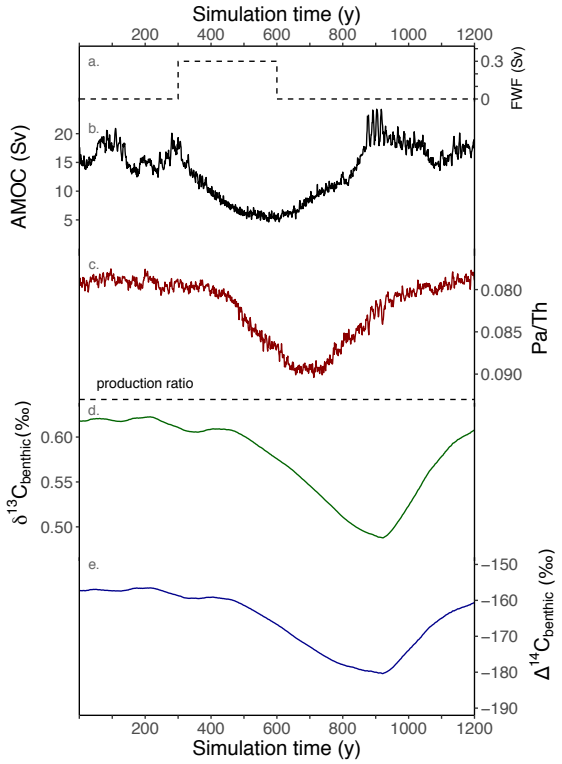

Figure S3: Modeled multi-proxy time series at the Bermuda Rise for a hosing in the Labrador Sea.

a. Imposed freshwater flux, **b.** Maximum North-Atlantic Stream function (Sv) **c.** simulated Pa/Th, **d.** benthic $\delta^{13}C$ (‰) and **e.** $\Delta^{14}C$ (‰)

The presented time series correspond to an average of 6 grid cells surrounding the model grid-cell closest to the Bermuda Rise (34°N-58°W).

5.2.2 Article summary

The first part of this article focuses on the development of the ^{231}Pa and ^{230}Th computation in the climate model of intermediate complexity iLOVECLIM. I chose to follow the approach of Rempfer et al. (2017) and considered 3 particle types ($CaCO_3$, Particulate Organic Carbon or POC and opal) and one particle size. To date, iLOVECLIM does not explicitly simulate the biogeochemical cycle of opal, which is thought to be an important scavenger for ^{231}Pa and ^{230}Th. Thus, I decided to work with fixed particles fields from the GCM (Global Circulation Model) NEMO-PISCES (Hulten et al., 2018). I considered a reversible scavenging scheme for ^{231}Pa and ^{230}Th, both isotopes having a common desorption coefficient while the adsorption coefficients depend on the particle type and concentration. The measurements of adsorption coefficients provide wide ranges of values. Thus they are usually considered as tunable parameters. In order to better sample the paramter space, I tuned the 6 adsorption coefficients (for Pa and Th and the 3 particle types) using a Latin Hypercube Sampling (LHS) methodology. I ran 60 simulations of 1000 years under Pre-Industrial (PI) conditions, which is a sufficient to reach a quasi equilibrium for Pa and Th. Then, I compared the modeled ^{231}Pa and ^{230}Th water column dissolved and particulate concentrations as well as the sediment core top Pa/Th ratio to the available observations. The new Pa/Th module simulates a realistic range of ^{231}Pa and ^{230}Th dissolved and particulate concentrations, increasing with depth and consistent with the idealized reversible scavenging theoretical profile. Our result quality is comparable with GCMs outputs. In the best-fit simulation Pa and Th tend to be adsorbed on the particles and scavenged to the sediments too quick, resulting in underestimated dissolved concentrations, particularly in the southern ocean opal belt. Additionally, in the simulations, the main scavenger for ^{230}Th is $CaCO_3$ while it is opal for ^{231}Pa. The model represents well the open ocean sedimentary Pa/Th ratio but the opal belt and the coastal regions display the highest model-data discrepancies. This could be attributed to the lack of representation of processes affecting the ^{231}Pa and ^{230}Th at the ocean bottom or in coastal regions such as nepheloid layers or boundary scavenging. The model is now able to produce realistic patterns for Pa/Th under PI conditions and simulates the evolution of the three proxies (δ^{13}C, Δ^{14}C and Pa/Th) simultaneously in a reasonable computational time ($\sim$800 years by 24 hours).

The second part of this article focuses on fingerprinting the multi-proxy (δ13C, Δ^{14}C and Pa/Th) response to an imposed abrupt circulation change under PI conditions. A marked circulation reduction is provoked in the model by adding freshwater flux of 0.3 Sv in the Nordic seas during 300 years. Consequently to this hosing, the North Atlantic circulation cell rapidly collapses and the stream function almost reaches 0 Sv shortly after the beginning of the hosing. We observe then a circulation recovery followed by a slight

overshoot (the Atlantic stream function going above the natural variability under PI conditions).
The proxy respond when their value stays out of the natural variability (assessed during a control period of 300 years) for more than 80 years. The proxies display from 0 to 4 responses to the freshwater additions. The "proxy response" corresponds to the maximum amplitude of the deviation to the mean proxy value (assessed during the control period) across each 80 years long periods. We show that the proxy response follow the pattern of the Atlantic main water masses: NADW, intermediate waters and AABW. In the intermediate waters the Pa/Th and Δ^{14}C show a slight increase while the δ13C significantly increases. In the AABW, the three proxies display consistent and synchronous response: the Pa/Th increases while the δ13C and Δ^{14}C, accounting for a reduced circulation and ventilation of the water mass. Finally, in the NADW, the three proxies display consistent response with the Pa/Th increasing and the δ13C and Δ^{14}C decreasing. The response time of δ13C and Δ^{14}C is generally similar and increasing with increasing water depth while Pa/Th display more homogeneous and quicker response time. Moreover, the δ13C and Δ^{14}C response display a lag of a few hundreds of years regarding the Pa/Th response.

5.2.3 Article conclusions

We argue that this lag between carbon isotope and Pa/Th response can be explained by the mechanisms at play to produce the proxy signal that are fundamentally different for the carbon isotopes and the Pa/Th. Indeed, in our model, because our scavenging intensity is kept constant due to the fixed particle fields, the Pa/Th only depends on circulation. Besides, the Pa and Th have very short residence time in the ocean water column, making the Pa/Th proxy very prompt to respond to any circulation change. On the contrary, the carbon isotopes in the ocean interact with the carbon from other reservoirs, via air-sea exchanges and biological activity, which are processes that take time. Even if our model results are not directly comparable with the proxy data in terms of absolute value and amplitude of change, we observe some features consistent with the available paleo proxy record: we observe consistency in the proxy response in the Atlantic western basin with significant Pa/Th increase and δ13C and Δ^{14}C decrease corresponding to the millennial scale variability recorded in deep sea sediments. Besides, our model experiment suggests that there is a constitutive lag between the Pa/Th and the carbon isotopes response to a freshwater input in the North-Atlantic in the NADW water mass. Such a lag has been evidenced in one proxy record at the Brazilian margin but was attributed to a potential sediment bioturbation bias as the two proxies are hosted by different size fraction.

5.2.4 Article perspectives

The perspectives of this work can be divided into two directions: i) refining and further developing iLOVECLIM Pa/Th module and ii) perform new modeling experiment with the multi-proxy configuration.

First refining the model tuning would perhaps allow to refine model-data agreement and potentially to better capture the opal belt signature. To do so the adsorption coefficient tuning could be improved, considering new tunable parameters such as the particle settling speed or different desorption coefficients for each particle type. In the process, it is important to take particular care to test configurations with different particle types as main scavenger. Besides, the representation of important processes such as such as boundary scavenging, nepheloid layers would also help to better capture geographical Pa/Th patterns and improve model-data agreement under PI conditions. Including a lithogenic particle class and the computation of fully prognostic particle fields could also participates to bring the model results closer to the observational data. All of these developments would increase the significance of the model-data comparison under PI conditions but also under glacial climate conditions or in transient simulations. Such developments do not require fully prognostic computation and could mainly rely on parameterization, scaling the adsorption coefficients in particular regions defined by specific masks following the approach of Rempfer et al. (2017) except for the implementation of interactive particle fields.

Some new modeling experiments can also be performed with the Pa/Th module in its current stage of development. For instance, it would be interesting to evaluate the multi-proxy response in a paelo-climate set up, using for instance glacial boundary conditions. Testing the multi-proxy pattern under different simulated glacial circulation modes following the approach of Menviel et al. (2017) could also be insightful to distinguish which simulated circulation mode corresponds the best to the past observation databases. Besides, the fact that the Pa/Th module has fixed particle fields provides a unique opportunity to test the Pa/Th sensitivity to circulation changes vs particle concentration or type changes by evaluating the amplitude of Pa/Th change in response to an imposed particle concentration change. Such a test could help to assess the significance of comparing the absolute amplitude values of Pa/Th changes at various locations having specific and different particles fields.

5.3 Conclusions

In this chapter we have described the developments that have been made on the climate model of intermediate complexity iLOVECLIM in order to implement the computation of

the ^{231}Pa and ^{230}Th. Then we have validated the model results by comparing the model output to observational water column and sediment core tops under PI conditions. To date iLOVECLIM is able to compute simultaneously the evolution of three major circulation proxies (Pa/Th, δ13C and Δ^{14}C) over several thousands of years in a reasonable computation time (800 per 24h). We have then fingerprinted the multi-proxy response to an abrupt circulation change obtained by adding sufficient freshwater forcing in the North Atlantic. We observed that the proxy response was associated with the three main Atlantic water masses: NADW, AAIW and AABW. In the NADW water mass we observed that the circulation slowdown was responsible of a decrease of the deep ventilation and circulation strength that is comparable to the observations across the millennial scale variability of the last glacial in the marine archives. However, the proxy response is not synchronous: the carbon isotopes response lags the Pa/Th by a few hundreds of years. Thus we have demonstrated that there could be a decoupling between different circulation proxies at a single location related to the mechanism driving the different proxies. It would be then interesting to perform several modeling tests with different circulation configurations in order to identify the mechanisms responsible for decoupling between ventilation and circulation strength at the LGM in SU90-08 proxy record. Such research would help to better constrain the LGM Atlantic water masses organisation.

Conclusions and perspectives

Conclusions

The general objective of this thesis was to quantify the variations of the deep Atlantic circulation across the abrupt climate events of the last 40 ky. For that purpose, I focused on the North Atlantic because, under modern conditions, this region hosts two major deep-water formation zones: the Nordic Seas and the Labrador Sea. I measured on the same deep-sea sediment core SU90-08 (43°N, 30°W, 3080m) three proxies (sedimentary Pa/Th, δ^{13}C and Δ14C) that provide complementary information about past ocean circulation changes: the carbon isotopes provide information about deep ventilation while the Pa/Th can be used as a kinematic proxy for circulation strength.

Before interpreting the multi-proxy record in terms of circulation changes two preliminary steps have been necessary.
First, it was essential to constrain the amplitude of sedimentary Pa/Th and ^{230}Th-normalized flux variations across the Heinrich events, both proxies showing particularly high sensitivity to the (^{238}U/^{232}Th) activity ratio of the sediment detrital fraction (hereafter $(U/Th)_{det}$). Indeed, the calculation of the sedimentary Pa/Th and ^{230}Th-normalized flux is generally achieved based on bulk sediment Th, Pa and U isotopic activities corrected for an estimation of the authigenic and detritic contributions. Both corrections are expressed as a function of $(U/Th)_{det}$, which is i) assumed to be constant through time, and ii) estimated based on either a regional or local value. As there is no formal $(U/Th)_{det}$ compilation in the North Atlantic and because SU90-08 Pa/Th and ^{230}Th-normalized flux records can significantly change according to the chosen $(U/Th)_{det}$, I extracted SU90-08 detrital fraction and measured its actual $(U/Th)_{det}$ value. This work demonstrated that there have been significant $(U/Th)_{det}$ temporal variations from 0.4 to 0.7 in SU90-08. Moreover, I have shown that those variations can affect the Pa/Th and ^{230}Th-normalized

flux records, potentially modifying not only the amplitude but also the timing and pattern of the reconstructed changes if the $(U/Th)_{det}$ temporal variations have not been properly evaluated.

Then, in order to be able to compare SU90-08 records to existing paleo-proxies data, I needed to establish a robust age-depth relationship. SU90-08 is indeed a challenging location because it stands North of 40°N, in an area where the radiocarbon cannot simply be used as a dating tool due to poorly constrained changes in surface reservoir ages. Thus, in this region, the marine cores chronologies usually rely on the alignment of sea surface records to Greenland air temperature records. This method required to generate high-resolution SST reconstruction for this core in order to identify as many Greenland abrupt climatic transitions as possible. Thus, I used the foraminifer assemblages and the modern analog technique to generate a new high resolution SST record for SU90-08 that I aligned to Greenland $\delta^{18}O$. The obtained age model was not fully satisfying because i) due to SU90-08 relatively low sedimentation rate, the SST record is smoothed and does not capture all the variability observed in Greenland records and ii) the inferred sedimentation rate does not increase across the Heinrich events despite the large amount of terrigenous inputs and IRD grains in the corresponding sediment layers. Moreover, the alignment method suffers from a lack of target abrupt climatic event in the Greenland ice isotopic record between 14.7 and 23.3 ky cal BP, that is the time interval encompassing the Last Glacial Maximum (LGM) and Heinrich stadial 1 (HS1). To improve SU90-08 age-depth relationship, I used the ^{230}Th normalization to refine the sedimentation rate history between alignment tie-points. The resulting chronology displays drastic sedimentation rates increases during the Heinrich events. To further validate this approach, I applied this Th-normalization technique for three North-Atlantic sediment cores in order to refine their chronologies between assumed tie-points. The method permitted to observe synchronous cooling at the onset of HS1. Additionally, this cooling is synchronous, within dating uncertainties, with an abrupt increase in dust flux dated at 17.48 ky cal BP $\pm$ 0.21 ky in the Greenland NGRIP GICC05 age scale. Therefore, I propose to use this event as a new tie-point to remedy the lack of chronological marker in Greenland record between 14.7 and 23.3 ky cal BP. The use of this new tie-point helps improving North-Atlantic marine cores chronologies in the key time period of the onset of the last deglaciation.

Obtaining SU90-08 multi-proxy record required to overcome the challenge of material availability, in particular for radiocarbon measurements. Indeed, within the Heinrich layers, the core contains up to 80% of detrital grains, hence only a few foraminifer specimens, especially for benthic species. The current limitation of radiocarbon analysis is the required sample size to perform a measurement on conventional Accelerator Mass Spectrometer (AMS) facilities. Thus, the scarcity of available material for SU90-08 led to use a new analytical technique: a Mini Carbon Dating System (MICADAS) coupled to a gas

introduction system, that is technically able to perform single foraminifer measurements. I first investigated the accuracy and reproducibility of the new SU90-08 radiocarbon measurements on paired benthic and planktonic (B-P) samples. I then analyzed the B-P ^{14}C ages. The SU90-08 dataset contains repeated negative B-P ^{14}C ages in the post HS1 part of the record. Those results are difficult to reconcile with any circulation/ventilation pattern but cannot be discarded as the signal is remarkably consistent. Because the core is located close to the mid-Atlantic ridge, I verified if an hydrothermal imprint may have affected the foraminifer radiocarbon. The analysis of the Rare Earth Elements (REE) patterns on planktonic foraminifer coatings enabled me to discard this hypothesis. Besides, dissolution and recrystallization processes can also alter foraminiferal radiocarbon signature. Thus, I looked at SEM pictures and found no significant difference between the foraminifer preservation before and after HS1. I concluded that the negative B-P ^{14}C ages represent the effect of bioturbation on a relatively low sedimentation rate archive ($\sim$4cm/ky) in a context of reduced surface to depth radiocarbon age gradient and foraminiferal abundance changes. Idealized Monte Carlo simulations showed that it is possible to produce such negative B-P ^{14}C ages. Consequently, the SU90-08 radiocarbon record appears to be partly impacted by bioturbation and can only provide first order (glacial/interglacial) paleoclimate information.

SU90-08 displays low amplitude multi-proxy variations across the last glacial abrupt climate events, notably because of the generally low sedimentation rate ($\sim$4 cm/ky) and the bioturbation that smoothed the records. However, the analysis of SU90-08 multi-proxy record contains interesting features. First, at the LGM, the carbon isotopes and sedimentary Pa/Th display apparently contradictory information, depicting low bottom water ventilation, but an active circulation, characterized by an overturning rate faster than at the Holocene. Second, during HS1, the Pa/Th values increases, indicating a decrease in the circulation strength while the benthic $\delta^{13}C$ decreases, indicating a decrease of the deep ventilation, as recorded in several other North Atlantic records. However, contrarily to the majority of North Atlantic records, the Pa/Th does not reach the production ratio during HS1 and HS4. Apart from bioturbation, one possible explanation could be that the Pa/Th does not reflect advection of the entire water column but records more efficiently the last 1000m above the water-sediment interface. In this context, SU90-08 being at 3000m water depth, the relatively low Pa/Th values recorded in SU90-08 would indicate a persisting shallow overturning cell above 3000 m during the Heinrich events. Such an overturning cell would not be recorded by the sedimentary Pa/Th of deeper cores ($>$ 4000m). Finally the other interesting feature is the timing of the Pa/Th change associated to HS1, which appears delayed at SU90-08 compared to the other cores located in the western North Atlantic basin. This late HS1 circulation slowdown is however consistent with records from the eastern North Atlantic basin. In a nutshell, SU90-08 multi-proxy record leaves

two unresolved questions i) how can we explain the apparent discrepancy between the the low Pa/Th and the low $\delta^{13}C$ values observed during the LGM ?In other words, do the proxies record the same water mass? ii) how can we explain the late circulation decrease observed in SU90-08 and other cores in the eastern North Atlantic basin? It is also clear that, taken alone, any multi-proxy record such as SU90-08 provides only qualitative information about past circulation changes. a proper quantification of past water mass flow rates in the Atlantic requires a modeling approach and the use of several records. The simultaneous computation of the above three proxies gives the opportunity to better understand their driving mechanisms and investigate about their potential decoupling, *e.g.* as observed in SU90-08.

Thus, the second objective of this thesis was to implement the ^{231}Pa and ^{230}Th production, transport and scavenging mechanisms in the climate model of intermediate complexity iLOVECLIM. The classical reversible-scavenging model was used together with three particle types ($CaCO_3$, POC and opal) and one particle size. The Pa/Th model results are comparable to previous Pa/Th modeling studies. It is now possible to simultaneously simulate the evolution of the three proxies over thousands of years in a reasonable computational time (∼800 simulated years per 24 hours). I fingerprinted/ analyzed the multi-proxy response to an imposed abrupt circulation reduction obtained by adding freshwater in the Nordic Seas, *i.e.* hosing experiment under preindustrial conditions. I showed that the proxy response reproduced the pattern of the three Atlantic main water masses: NADW, AAIW and AABW. In the NADW, the response to the hosing was an increase of the Pa/Th value and a decrease of the $\delta^{13}C$ and $\Delta^{14}C$ values. This is consistent with what is observed from marine paleoproxy records across the millennial scale events of the last glacial even if the modeled amplitude of change does not match the observations. Moreover, the simulated carbon isotope response lags the Pa/Th response by a few hundreds of years. This lag has been observed in the proxy record but was interpreted as a bioturbation artifact. In contrast, my modeling results show that it is possible to obtain a decoupling between the Pa/Th and the $\delta^{13}C$ and $\Delta^{14}C$, and that the proxies do not exhibit immediate and synchronous response to circulation changes. These modeling results have thus implications for the interpretation of marine cores multi-proxy records.

Perspectives

This PhD work raises several perspectives related to the key points highlighted above. First, as I have shown that the $(U/Th)_{det}$ could vary through time and that those variations are susceptible to affect the interpretation of the Pa/Th proxy, it would be worthwhile to evaluate the $(U/Th)_{det}$ variations at key locations. In particular, my work shows

that this is critical in areas characterized by high terrigenous inputs such as continental margins. Evaluation of the impact of temporal $(U/Th)_{det}$ variations on key Pa/Th records would enable to validate or invalidate the interpretation made so far of these records that are very often cited as indicator of the AMOC vigor evolution. Such key locations would be for example the Iberian Margin, the Brazilian Margin, or the Bermuda Rise. Additionally, it would also be valuable to establish a proxy for $(U/Th)_{det}$ variations that relies on routine analysis such as XRF data or major elements concentrations. Such proxy development would enable to assess the $(U/Th)_{det}$ variations quicker as it would avoid the expensive and time consuming extraction of the sediment detrital fraction.

Second, as I proposed a new tie-point for the beginning of HS1 cooling, it would be beneficial to test the validity of this new tie-point by comparing various SST records from North-Atlantic that are independently dated. In addition, if the Th-normalization becomes more commonly used to refine marine cores chronologies in the future, it would be worth to implement Th-normalization into age model software in order to properly estimate and propagate the age-model uncertainties of these chronologies. To date, the uncertainty related to the use of Th-normalization is difficult to assess because although Th brings precious chronological information, the $^{230}Th_{xs,0}$ calculation contains several sources of uncertainties.

Third, recent developments in radiocarbon measurements demonstrated that it is now technically possible to achieve such measurements on very small amounts of material, opening the way for more deep-sea benthic measurements. However, SU90-08 case shows that the core conservation and in particular the bioturbation level strongly affects the radiocarbon measurements. Indeed, small sized samples reveal the sample heterogeneity in terms of radiocarbon content, whereas bigger samples provide averaged radiocarbon age. In previous studies, certain radiocarbon measurements were discarded because they produced negative B-P ages that were thought to be irreconcilable with ventilation information. A reevaluation of those radiocarbon data, taking into account the potential bioturbation biases might be valuable. It would also be interesting to focus more on the analysis of the surface and benthic ventilation ages time series produced in SU90-08 and compare these results with existing North-Atlantic data. Such analysis would perhaps allow deciphering geographical patterns of surface and deep reservoir age increase across Heinrich events, providing new constrains on past circulation changes. Beside, radiocarbon could be used to trace the past carbon exchanges between the ocean and the atmosphere and investigate about oceanic carbon storage/release mechanisms across the past climate changes.

Finally, the modeling part of this study opens two main directions for future work. On one side, it would be possible to improve the representation of Pa and Th in the model in order to improve the model-data agreement and thus improve the significance of model-

data comparison. Such developments would consist in improving the adsorption coefficient tuning, considering new tunable parameters such as the particle settling speed or different desorption coefficients for each particle type. In this process, a particular attention has to be devoted to test configurations in which opal is not the main scavenger for Pa as it is probably the case in the modern ocean. Additionally, the representation of important processes such as boundary scavenging and nepheloid layers could be added. Last but not least, a major improvement of the Pa/Th computation would likely be achieved by including a new particle type (*i.e.* lithogenic particles) and the computation of fully prognostic particle fields. On the other side, interesting new modeling experiments could directly be performed with the current model development. For instance, because the Pa/Th has fixed particle fields, it provides the opportunity to test the Pa/Th sensitivity to particle changes and assess which proportion of the paleo-signal could be attributed to the circulation and the particle changes. Two distinct tests could be performed, the first by changing the particle concentrations, the second by changing the balance between particles composition. Moreover, it would also be possible to evaluate the multi-proxy response in a paleo-climate set up and test if the results found under PI conditions are repeated using glacial boundary conditions. In addition, testing the multi-proxy pattern under different simulated glacial circulation modes could also be insightful to distinguish which circulation mode produces decoupled carbon isotopes and Pa/Th records as observed in SU90-08 at the LGM. In a broader perspective, this PhD thesis contributed to go a step ahead toward the quantification of the past circulation changes. Enabling a climate model to compute directly the proxies that are measured in sediment cores has the advantage of reducing uncertainties in data-model comparison. It is thus a key step forward to characterize and quantify the past ocean circulation changes. Because my work highlighted cases of decoupling between the carbon isotopes and the Pa/Th (both in the paleo-data and in a climate model), it also demonstrates the value/interest of the multi-proxy approach to reconstruct the past ocean circulation.

Therefore, one long-term perspective would be to focus on multi-proxy records (Pa/Th, δ^{13}C, Δ^{14}C, ϵ_{Nd}) to constrain the ocean water-mass organization during past climate events such as the LGM, the Dansgaard-Oeschger (DO) cycles and the Heinrich Stadials. To do so, considering a paleo-proxy database containing enough data for each time period, one could apply a statistical approach to group the signal from different locations in clusters (k-clustering). Repeating this approach for different proxies, one could test whether the obtained clusters are consistent with putative Atlantic water-mass geometry. Such approach could also be conducted with simulated multi-proxy datasets produced with different circulation schemes. The integration of the information form both model and paleo-data studies could help constraining the past water mass geometry.

Moreover, in the literature, the past Atlantic ocean-circulation is often conceptualized

looking at North-South Atlantic sections. Recently, both model experiments and paleo-data evidenced a clear difference between the eastern and western basin. Therefore, I think the effort to constrain past circulation changes should focus on the 3D (latitide-longitude-depth) circulation changes rather than considering zonally averaged variables (stream functions in the model) or integrated variables (maximum stream function over time in the model). In the future, looking at the 3D current maps, mixed layer depth and location of deep-water formation sites and could be insightful.

Finally, there is more and more evidence that the millennial scale climate events (Heinrich Stadials, DO cycles) involve common mechanisms (*e.g.* freshwater fluxes) but have marked differences between each other. For instance, some Heinrich events are not recorded in specific regions, the event duration differ, the circulation slowdown recorded by Pa/Th has different intensities. Consequently, in order to understand why some DO stadials are associated with a Heinrich event and why some Heinrich events lead to a deglaciation, we need to consider these millennial scale climate events both as a group of events with common characteristics and also individually. This would require to precisely characterize their differences, using a multi-proxy approach, and hence to generate paleo-records with sufficient spatial coverage and temporal resolution.

List of Tables

List of Figures

Appendix

Procedures for sedimentary Pa/Th and ^{230}Th-normalized flux measurements

The calculation of the sedimentary Pa/Th ratio and ^{230}Th-normalized flux requires the measurement of the ^{238}U, ^{232}Th, ^{230}Th and ^{231}Pa isotopic concentrations. In order to perform all the measurements performed of this thesis, I used the isotope dilution method, which consists in introducing known amounts of artificial isotopes (spike) into the sediment samples in order to deduce the natural isotope concentrations. The following paragraphs detail the steps I followed to obtain the required isotopic concentrations from the wet sediment samples.

This procedure requires some training in order to safely handle unsealed radioactive sources.Numerous standard material and blanks samples were also processes along with the samples to ensure the chemical procedure absence contamination and the measurement quality. The complete procedure requires approximately 1 month of lab work for sample preparation and 1 week of MC-ICP-MS measurements per batch of 25 sediment samples. During this PhD thesis, I measured around 60 samples from sediment core SU90-08 in 3 batches.

^{233}Pa spike production

Th and U have artificial isotopes (^{229}Th and ^{236}U) with sufficiently long half-lives for establishing purchasable certified solution. Conversely, Pa has only 3 isotopes for which the half-life exceeds 2 days: ^{231}Pa ($t_{1/2}$=32 760 y), ^{233}Pa ($t_{1/2}$=26.967 days) and ^{230}Pa ($t_{1/2}$=17.4 days). Given that ^{231}Pa is a natural isotope present in the marine sediments and that ^{230}Pa has a very short half-life, the ^{233}Pa was chosen to spike the samples.

The relatively short half-life of ^{233}Pa does not allow the creation of purchasable certified solutions and imposes to produce the spike right before the sample preparation procedure. The ^{233}Pa spike production was performed following a procedure adapted from Guihou (2009) and outlined bellow. ^{233}Pa is a product of the radioactive decay of the parent isotope ^{237}Np. Before each sample preparation the ^{233}Pa is isolated from ^{237}Np using hydrated silica resin, for which ^{233}Pa has a high affinity. The procedure below describes the different steps of extraction and purification of the ^{233}Pa spike at LSCE during this thesis.

The quality of the obtained spike is tested using MC-ICP-MS by evaluating the ^{233}Pa/^{237}Np ratio because too much ^{237}Np in the final spike solution is i) dangerous (radioactive nuclide) and ii) could change the ^{233}Pa concentration in samples and thus falsify the final result. In practice, the ratio ^{237}Np/(^{233}(Pa+U) should be lower than 30. This step also allows establishing the approximate spike concentration in ^{233}Pa, which is necessary to correctly dispatch the spike into the analyzed samples. To do so, the sensitivity of the MC-ICP-MS is determined using a standard U solution.

Day 1: First silica column (Pa extraction)

Cook the 237Np solution in HNO3 8N ☐
At near dryness add 4 mL HNO3 8N ☐
Note the the activity of the Np solution (using COMO) ☐
_____ cps

Fill the column with 3mL of hydrated silica gel ☐

Column washing:
12 mL H_2O ☐
5 mL 2N HNO_3 ☐
10 mL 8N HNO_3 (2 x 5 mL) ☐

Column conditioning:
10 mL 8N HNO_3 (2 x 5 mL) ☐
Wait until the last drop comes out of the column ☐

Column loading:
Change Np beaker ☐
Load the Np solution on the column ☐
Wait until the last drop comes out of the column ☐
Rinse the beaker that contained Np solution with 1 mL 8N HNO3 and load on the column ☐
Wait until the last drop comes out of the column ☐

Evaluate the background noise with COMO _____ cps
Evaluate the activity of the colomn with COMO _____ cps
Evaluate the activity of the beaker with COMO _____ cps

Np Elution:
Elute Np with 15 mL 8N HNO3 (3 x 5 mL) ☐
Wait until the last drop comes out of the column ☐

Evaluate the activity of the colomn with COMO _____ cps
Evaluate the activity of the beaker with COMO _____ cps

Pa Elution:
Change to Pa beaker ☐
Elute pa with 12 mL 2N HNO3 + 0.13 N HF (2 x 6 mL) ☐

Evaluate the activity of the colomn with COMO _____ cps
Evaluate the activity of the beaker with COMO _____ cps

If the activity of the column is higher than the background noise continue Pa elution

---

Repeat these steps until the column activity is close to the background noise

Elute pa with 5 mL 2N HNO3 + 0.13 N HF (2 x 2.5 mL) ☐

Evaluate the activity of the colomn with COMO _____ cps
Evaluate the activity of the beaker with COMO _____ cps

Preparation of Pa fraction:

Evaporate the Pa fraction until a big drop remains ☐
Add 6 mL HNO3* and evaporate until a big drop remains ☐
Add 3 mL HNO3* and evaporate until a big drop remains ☐
Add 3 mL HNO3* and evaporate until a big drop remains ☐

Add 2.5 mL 8N HNO3 and ☐

To avoid radioactive element to be lost, the column is rinsed into the Np beaker (closed loop) and the column is thrown away into specific trash.

Day 2: Second silica column (Pa purification 1)

Note the the activity of the Pa solution (using COMO) ☐
_____ cps

Fill the column with 3mL of hydrated silica gel ☐

Column washing:
15 mL H_2O ☐
8 mL 2N HNO_3 (2 x 4 mL) ☐
10 mL 8N HNO_3 (2 x 5 mL) ☐

Column conditioning:
5 mL 8N HNO_3 ☐
Wait until the last drop comes out of the column ☐

Column loading:
Change Np beaker ☐
Load the Pa solution on the column ☐
Wait until the last drop comes out of the column ☐
Rinse the beaker that contained the solution with 1 mL 8N HNO_3 and load on the column ☐
Wait until the last drop comes out of the column ☐

Evaluate the background noise with COMO _____ cps
Evaluate the activity of the colomn with COMO _____ cps
Evaluate the activity of the beaker with COMO _____ cps

Np Elution:
Elute Np with 20 mL 8N HNO3 (4 x 5 mL) ☐
Wait until the last drop comes out of the column ☐

Evaluate the activity of the colomn with COMO _____ cps
Evaluate the activity of the beaker with COMO _____ cps

Pa Elution:
Change to Pa beaker ☐
Elute pa with 12 mL 2N HNO3 + 0.13 N HF (2 x 6 mL) ☐

Evaluate the activity of the colomn with COMO _____ cps
Evaluate the activity of the beaker with COMO _____ cps

If the activity of the column is higher than the background noise continue Pa elution

---

Repeat these steps until the column activity is close to the background noise

Elute pa with 5 mL 2N HNO3 + 0.13 N HF (2 x 2.5 mL) ☐

Evaluate the activity of the colomn with COMO _____ cps
Evaluate the activity of the beaker with COMO _____ cps

Preparation of Pa fraction:

Evaporate the Pa fraction until a big drop remains ☐
Add 6 mL HNO3* and evaporate until a big drop remains ☐
Add 3 mL HNO3* and evaporate until a big drop remains ☐
Add 3 mL HNO3* and evaporate until a big drop remains ☐

Add 2.5 mL 8N HNO3 and ☐

To avoid radioactive element to be lost, the column is rinsed into the Np beaker (closed loop) and the column is thrown away into specific trash.

Day 3: Third silica column (Pa purification 2)

Note the the activity of the Pa solution (using COMO) ☐
_____ cps

Fill the column with 2mL of hydrated silica gel ☐

Column washing:
10 mL H_2O ☐
2 mL 2N HNO_3 ☐
10 mL 8N HNO_3 (2 x 5 mL) ☐

Column conditioning:
10 mL 8N HNO_3 ☐
Wait until the last drop comes out of the column ☐

Column loading:
Change Np beaker ☐
Load the Pa solution on the column ☐
Wait until the last drop comes out of the column ☐
Rinse the beaker that contained the Pa solution with 1 mL 8N HNO3 and load on the column ☐
Wait until the last drop comes out of the column ☐

Evaluate the background noise with COMO _____ cps
Evaluate the activity of the colomn with COMO _____ cps
Evaluate the activity of the beaker with COMO _____ cps

Np Elution:
Elute Np with 12 mL 8N HNO3 (2 x 6 mL) ☐
Wait until the last drop comes out of the column ☐

Evaluate the activity of the colomn with COMO _____ cps
Evaluate the activity of the beaker with COMO _____ cps

Pa Elution:
Change to Pa beaker ☐
Elute pa with 12 mL 2N HNO3 + 0.13 N HF (2 x 6 mL) ☐

Evaluate the activity of the colomn with COMO _____ cps
Evaluate the activity of the beaker with COMO _____ cps

If the activity of the column is higher than the background noise continue Pa elution
---
Repeat these steps until the column activity is close to the background noise

Elute pa with 10 mL 2N HNO3 + 0.13 N HF (2 x 5 mL) ☐

Evaluate the activity of the colomn with COMO _____ cps
Evaluate the activity of the beaker with COMO _____ cps

Preparation of Pa fraction:

Evaporate the Pa fraction until a big drop remains ☐
Add 2 mL HNO3* and evaporate until a big drop remains ☐

Add 2 mL 8N HNO3 and ☐

To avoid radioactive element to be lost, the column is rinsed into the Np beaker (closed loop) and the column is thrown away into specific trash.

Sediment sample preparation

After the spike preparation, the sediment samples are prepared for the analysis of the ^{238}U, ^{232}Th, ^{230}Th and ^{231}Pa isotopic concentrations following the procedure described below. Beforehand, the sediment samples are oven-dried at 50°C for 48 h and an aliquot is crushed using agate mortar. The sample preparation consists of 2 major steps: the sediment digestion to destroy the mineral structure and release the elements in solution and the extraction of the U, Th and Pa fractions. For logistical reasons, some steps can only be performed with a limited number of samples obliging to split the samples in 2 groups.

Sample digestion

Day 1:

Take the spikes out of the fridge: ☐
Label the lab-book and digestion savillex (beakers): ☐
Weigh in 150-200 mg of sediments for each sample: ☐
Add HNO_3 concentrate until there is no CO2 degassing (dissolution of the carbonate fraction): ☐

Add Pa spike : ☐
Add U-Th spike (700 µL): ☐
Add Fe into the blanks and UREM (400 µL of Fe solution at 6 mg/mL) ☐

Add 2ml HNO_3 concentrate and 5ml HF concentrate: ☐
Close the beakers and leave in the ultrasonic bath for more than 30 min: ☐
Close well and heat it up to 140°C for the night: ☐

Day 2:

Take the beakers out of the hotplate. Let them cool down for 15 min ☐
Open the beakers. Let evaporate at 150°C 3 hours: ☐
Weigh in the calibration solutions of the spike and the standard of ^{231}Pa : ☐
After 3 hours (around 12h), add 2 mL $HClO_4$ and 1 mL HNO_3 concentrate per sample: ☐

Wait for 1 hour

⚠ When working with HClO4 open the window ! ⚠
No paper aroud ! If drops : use a lot of water !

Warm the hotplate at 160°C ☐
Add 1mL HNO_3 concentrate. Be careful to rinse the edge of the beakers. Wait for 1h ☐
Add 1mL HNO_3 concentrate. Be careful to rinse the edge of the beakers. ☐
Increase the hotplate temperature around 170°C: ☐

⚠ do not increase the temperature above 170°C

Once the residue is a gel add HNO_3 concentrate (around 500 µL) to re-obtain a solution. Repeat the operation 3 times (see table) : ☐
Add 4 mL HNO_3 concentrate. Heat it up for a few minutes (see table): ☐

Sample	500µL HNO3*	500µL HNO3*	500µL HNO3*	4 mL HNO3*	Transfer

Transfer the samples into falcon 50 mL tubes. Rinse the beakers with milli-Q water and add it to the tubes. ☐

Fill the tubes with milli-Q water up to 20 mL: ☐
Put the samples in the ultrasonic bath for 1h minimum ☐

If you can observe white solids in suspension, try the ultrasonic bath for an additional hour
If it is not enough, transfer the white residue of the sample into a digestion savillex and add 200 µL HNO3 and 200 µL HClO4. Evaporate everything and cook it with 1 mL HNO3*. Transfer back into the falcon tube* ☐

Day 3:

Add NH_4OH until there is a Fe precipitate (generally around 5 mL): ☐
Centrifuge 5 minutes at maximum speed (4000 rpm). Throw away the supernatant: ☐
Add 20 mL milli-Q water to suspend again the precipitate: ☐

Add a few drops of NH4OH to precipitate the Fe. Centrifuge and throw away the supernatant ☐
Add 20 ml HNO_3 2-3N. Stir to be sure the precipitates dissolves: ☐

Add NH_4OH to precipitate (around 5 mL). Centrifuge (4000 rpm 5 min)
throw away the supernatant. ☐
Add 20 mL of milli-Q water. Suspend again the precipitate. Add a few drops of NH_4OH. ☐
Centrifuge (4000 rpm 5 min), throw away the supernactant. ☐

Weigh in the calibration solutions of spikes and standard solutions. Evaporate them.
Dissolve them in 2ml HNO_3 8N : ☐

U, Th and Pa fractions extractions using ion exchange columns

Day 1:

Label the columns with sample numbers: ☐

1st column step

Add 2ml AG1 X8 hydrated in each column: ☐

Column washing:

- 5mL HNO3 8N ☐
- 3 mL H2O milli-Q ☐
- 5mL HNO3 8N ☐
- 3 mL H2O milli-Q ☐
- 5mL HNO3 8N ☐
- 3 mL H2O milli-Q ☐

Sample preparation :

- Label beakers with sample numbers ☐
- Add 500µL HNO3 concentrate to the Fe precipitate ☐
- Add 1,5 mL HNO3 8N to the samples ☐

⇨ Total volume for the samples : 2 mL

- Leave the samples in the ultrasonic bath until the solutions are transparent ☐

Conditioning:
Add 5 mL HNO3 8N to each column: ☐

Loading:
Add the samples on the columns in 2 steps: ☐ ☐

Elutions:
Add 2,5 mL HNO_3 8N on each column in 3 steps: ☐ ☐ ☐

Change to Th beakers: ☐

Add 4*5ml HCl 9N: ☐ ☐ ☐ ☐

Change to Pa beakers: ☐

Add 2*4ml HCl 9N + 0,26N HF: ☐ ☐

Change to U beakers: ☐

Add 5*5ml Milli-Q water (column volume): ☐ ☐ ☐ ☐

Evaporations:
Evaporate Pa, U and Th beakers until there is only a drop inside: ☐

⚠ Don't burn the Pa samples !!! ⚠

Day 2:

Finish to evaporate Pa fractions until there is only 1 semi-solid drop left ☐

 stop the evaporation when the drop is wet

Pa fraction preparation

Cook the Pa fractions in HNO3* :

Volume	Time/comments
2 mL	
1,5 mL	

Cook the Pa fractions in HCl* :

Volume	Time/comments
2 mL	
1,5 mL	
1,5 mL	

2nd column step (Pa)

take big columns

 Don't start the columns before the Pa fraction samples are almost ready!!

Add 2-3 mL AG1 X8 (Dowex) per column: ☐

Column washing: (put waste beaker under the column)

- 15 mL H2O milli-Q ☐
- 7 mL HCl 9N ☐

Conditioning:
Add 8ml HCl 9N to each column: ☐

Loading:
Add the Pa fraction in 2 steps: ☐☐

Add 3 mL HCl 9N in the beaker and put it on the column ☐

Elution:
Add 12*1 mL HCl 9N ☐☐ ☐☐ ☐☐ ☐☐ ☐☐ ☐☐

Change to Pa beakers: ☐

Add 15*1 mL HCl 9N + 0,13N HF per column: ☐☐ ☐☐ ☐☐ ☐☐ ☐☐ ☐☐ ☐☐

Clean the column with water: ☐

Evaporations:

Finish to evaporate all the fractions: ☐

For Th and Pa fractions:

Add a few drops 1N HNO3+ 0,01 N HF and evaporate: ☐

Add 2 mL 1N HNO3+ 0,01 N HF ☐

Filter and transfer into the Neptune tubes: ☐

For U fractions:

Add a few drops 1N HNO3 and evaporate: ☐

Add 2 mL 1N HNO3 ☐

Filter and transfer into the Neptune tubes: ☐

R programs designed during this thesis

During my PhD thesis I developed an automatized procedure to process the raw data file from the mass spectrometer (Neptune) using R software. In short, the data processing consist in obtaining Pa, Th and U activities following these steps:

— machine and chemistry blank estimation and correction

— outlier detection and elimination

— mass bias correction

— ion counter yield correction

— peak tailing correction

— hydrites correction

— spike contamination correction

Besides, I estimated the uncertainties on the U, Th and Pa activities using a Monte Carlo approach: I calculate the concentrations a large number of times (>2000) with different values for each parameter, sampled on an assumed gaussian distribution. Below are the R script I developed to calculate the Pa activities and calculate the Pa/Th ratio.

Pa activity calculation from raw Neptune Measurements

```
## ########################################################################
## reading.r
##
## R-Script for reading and preparing data files from
## Neptune Pa-Th-U analyses.
## Original data files are kept in file_NUM_name dataframes and the
## corresponding information of those files is in meta_NUM_name dataframes
## Final data frames to work are classified and stored in the lists:
## samples_data_list, blanks_data_list, and standards_data_list
## Wash files are discarded.
##
##
## Date: 2015-11-08
## Update : 2017-03-07
## Author: Santiago Moreira-Lise Missiaen
## ########################################################################

## ########################################################################
## Loading necessary packages
require(openxlsx)
```

```
## Loading required package: openxlsx
```

```
## ########################################################################
#Adjusting programm to batch parameters

# 1) Please check that the path to the DATA folder is correct:
path_data_pa<-"../DATA/Pa/"

#2) Please check the number of "header lines" to skip
skiplines_pa<- 22

# 3) Please update the file "samples_u.txt" which
#contains the names of the samples to process


#4) Please enter the lab names of the hu1 standards
names_hu1<-c("L226","L227","L246", "L247")

#5) Please enter the lab names of the Pa standards
names_pa_std<-c("L228","L229","L248", "L249")

#6) Please enter the lab names of the process blanks
names_pc_blks<-c("L216","L236")

#7) Please enter the lab names of the spiked blanks
names_spiked_blks<-c("L217","L237")

#8) Please check the file (and the path) containing all the lab info for each sample
require(openxlsx)
info_ech<-read.xlsx("../ech_juin_16.xlsx", 1,  colNames =T ,startRow=2)
```

```
## ########################################################################
## FUNCTIONS DEFINITION

## FUNCTION creating_metadata
## This functions reads and keeps the information of the top of the
## Neptune files
creating_metadata <- function(thefile){
assign(paste("metadata","_",sep=""), readLines(paste(path_data_pa,thefile,sep="")))

#assign(paste("meta_",valid_filenames_list_pa[1],sep=""),data.frame())
meta_dataframe <-NULL
title <- "NULL"
title2 <- "NULL"
filename <- "NULL"
date<- "NULL"
sample_id <- "NULL"
method_name <- "NULL"
wheel_id <- "NULL"
run_number <- "NULL"
analysis_date <- "NULL"
analysis_time <- "NULL"
operator  <- "NULL"
instrument <- "NULL"
comment     <- "NULL"
data_version <- "NULL"
export_version <- "NULL"

meta_dataframe <-data.frame(title, title2, filename, date,
                            sample_id,method_name, wheel_id,
                            run_number,analysis_date, analysis_time,
                            operator, instrument, comment, data_version,
                            export_version)

foo <- strsplit(metadata_[1],"\t")[[1]]
title <- foo[1]
meta_dataframe$title <-title


foo <- strsplit(metadata_[2],"\t")[[1]]
title2 <- foo[1]
meta_dataframe$title2 <- title2

foo <- strsplit(metadata_[3],"\t")[[1]]
foo2 <- strsplit(foo,":")[[1]]
filename <- c(foo2[1],paste(foo2[2],":",foo2[3],sep=""))
meta_dataframe$filename <- filename[2]

foo <- strsplit(metadata_[4],"\t")[[1]]
foo2 <- strsplit(foo,":")[[1]]
date <- c(foo2[1],foo2[2])
meta_dataframe$date <- date[2]
```

```
foo <- strsplit(metadata_[5],"\t")[[1]]
foo2 <- strsplit(foo,":")[[1]]
sample_id <- c(foo2[1],foo2[2])
meta_dataframe$sample_id <- sample_id[2]

foo <- strsplit(metadata_[6],"\t")[[1]]
foo2 <- strsplit(foo,":")[[1]]
method_name <- c(foo2[1],paste(foo2[2],":",foo2[3],sep=""))
meta_dataframe$method_name <- method_name[2]

foo <- strsplit(metadata_[7],"\t")[[1]]
foo2 <- strsplit(foo,":")[[1]]
wheel_id <- foo2
meta_dataframe$wheel_id <- wheel_id[2]

foo <- strsplit(metadata_[8],"\t")[[1]]
foo2 <- strsplit(foo,":")[[1]]
run_number <- foo2
meta_dataframe$run_number <- run_number[2]

foo <- strsplit(metadata_[9],"\t")[[1]]
foo2 <- strsplit(foo,":")[[1]]
analysis_date <- foo2[2]
meta_dataframe$analysis_date <-analysis_date

foo <- strsplit(metadata_[10],"\t")[[1]]
foo2 <- strsplit(foo,":")[[1]]
analysis_time <- paste(foo2[2],foo2[3],foo2[4],sep=":")
meta_dataframe$analysis_time <-analysis_time

foo <- strsplit(metadata_[11],"\t")[[1]]
foo2 <- strsplit(foo,":")[[1]]
operator <- foo2[2]
meta_dataframe$operator <-operator

foo <- strsplit(metadata_[12],"\t")[[1]]
foo2 <- strsplit(foo,":")[[1]]
instrument <- foo2[2]
meta_dataframe$instrument <-instrument

foo <- strsplit(metadata_[13],"\t")[[1]]
foo2 <- strsplit(foo,":")[[1]]
comment <-foo2[2]
meta_dataframe$comment <- comment

foo <- strsplit(metadata_[14],"\t")[[1]]
foo2 <- strsplit(foo,":")[[1]]
data_version <- foo2[2]
meta_dataframe$data_version <-data_version

foo <- strsplit(metadata_[15],"\t")[[1]]
foo2 <- strsplit(foo,":")[[1]]
export_version <- foo2[2]
```

```
meta_dataframe$export_version <-export_version

#assign(paste("meta","_",validnamefile,sep=""),meta_dataframe)
meta_dataframe

}
## END OF FUNCTION creating_metadata

## FUNCTION creating_data
## This function reads and keeps the data from each Neptune file
creating_data <-function(thefile){
  #thefile <- filenames_list_pa[147]
  data <- read.delim(paste(path_data_pa,thefile,sep=""), header=T,skip=skiplines_pa)

  data2 <- subset(data,Cycle ==1:1000)
  time <- data2[,2]
  end <- length(data2[1,]) -1
  options(digits=16)
  data2[,1] <-as.numeric(as.character(data2[,1]))

  for (i in 3:end){
    dd1 <- gsub("D","",data2[,i])
    dd2 <- gsub("X","",dd1)
    data2[,i] <-as.numeric(as.character(dd2))
  }

  data2$id<- thefile
  num <- strsplit(thefile,"-")[[1]][1]
  data2$id_num <-as.numeric(num)
  data2$num_lab<-strsplit(thefile,"-")[[1]][2]
  data2

}
## END of FUNCTION creating data


## END OF FUNCTIONS DEFINITION
## ############################################################################


## BEGINING OF SCRIPT
files <- list.files(path_data_pa) # makes a list of the files in the folder "Pa"
filenames_list_pa <- files[1:length(files)-1]# takes the last

valid_filenames_list_pa <-gsub("-","_",filenames_list_pa)
# replaces "-" by "_" to avoid problems


list_neptune_valid <- list() # initialization of empty list
pair_list_neptune <- list() # initialization of empty list

## define which labels are samples, blanks or standards
samples_l <- NULL
```

```
samples_pa <- read.table("../DATA/samples_pa.txt", header=T, quote="\"")
samples_l <- samples_pa$samples_pa

blank_l <- c("blc")
standards_l <- c("5325")
mass_bias_l <- c("bmyas")
th_h_l <-c("Th h")

samples_data_list <- list()
blanks_data_list <- list()
standard_data_list <- list()
mass_bias_list<-list()
th_h_list<-list()

s <- 1
b <- 1
t <- 1
mb <-1
th <- 1
##

## reading data and storing it in three lists of data frames:
## samples_data_list, blanks_data_list, standards_data_list
i<-1
for (i in 1:length(filenames_list_pa)){
  # for all the files in the list
  m <- creating_metadata(filenames_list_pa[i])
  # call the function "creating_metadata"
  assign(paste("meta","_",valid_filenames_list_pa[i],sep=""),m)

  d <- creating_data(filenames_list_pa[i])
  # call the function "creating_data"
  assign(paste("file","_",valid_filenames_list_pa[i],sep=""),d)

  if (strsplit(valid_filenames_list_pa[i],"_")[[1]][2] %in% blank_l){
    #if it is a blank put it in the list for blanks
    #d[d<0]<-0
    d$data_type <- "blank"
    blanks_data_list[[b]]<- d
    b <- b+1
  }

  if (strsplit(valid_filenames_list_pa[i],"_")[[1]][2] %in% samples_l){
    # if it is a sample put it in sample list
    d$correction <- FALSE # add the information that it is not blank corrected
    d$data_type <- "sample"
    samples_data_list[[s]]<- d

    s <- s+1
  }

  if (strsplit(valid_filenames_list_pa[i],"_")[[1]][2] %in% standards_l){
    d$correction <- FALSE
```

```
    d$data_type <- "standard"
    standard_data_list[[t]]<- d
    t <- t+1
  }

  if (strsplit(valid_filenames_list_pa[i],"_")[[1]][2] %in% mass_bias_l){
    d$correction <- FALSE
    d$data_type <- "standard"
    mass_bias_list[[mb]]<- d
    mb <- mb+1
  }

  if (strsplit(valid_filenames_list_pa[i],"_")[[1]][2] %in% th_h_l){
    d$correction <- FALSE
    d$data_type <- "standard"
    th_h_list[[th]]<- d
    th <- th+1
  }
}

bi <- NULL
## for every sample of the samples_data_list, look for
## the closest smaller blank sample and then, check the
## corresponding column of the blank, calculate the mean
## substract the value to the column in the sample data
for (j in 1:length(samples_data_list)){
  s1 <- samples_data_list[[j]]$id_num[1]

  for (i in 1:length(blanks_data_list)){
    bi[i]<- blanks_data_list[[i]]$id_num[1]
  }
  bbi <- which(bi < s1)[length(which(bi < s1))]
  s2 <- bi[bbi]

  d1 <- samples_data_list[[j]]
  d2 <- blanks_data_list[[bbi]]
  n1 <- names(d1)
  n2 <- names(d2)

  end_i<-which("X"==n1)-1
  for (k in 3:end_i){
    if (n1[k] %in% n2) {
      n3 <- which (n1[k] == n2)
      val <- mean(d2[,n3])
      if (val<0.0){ val<-0.0}
      samples_data_list[[j]][,k]<- samples_data_list[[j]][,k] - val
      samples_data_list[[j]]$correction <-TRUE
    }
  }
}

##############################################################################################
#Processing the Mass bias samples
```

```
#author : Lise Missiaen
#26/02/2016
################################################################################

## for every sample of the mass_bias_list, look for
## the closest smaller blank sample and then, check the
## corresponding column of the blank, calculate the mean
## substract the value to the column in the sample data
bi <- NULL
 for (j in 1:length(mass_bias_list)){
   s1 <- mass_bias_list[[j]]$id_num[1]

     for (i in 1:length(blanks_data_list)){
          bi[i]<- blanks_data_list[[i]]$id_num[1]
        }

     bbi <- which(bi < s1)[length(which(bi < s1))]
   s2 <- bi[bbi]

      d1 <- mass_bias_list[[j]]
      d2 <- blanks_data_list[[bbi]]
     n1 <- names(d1)
    n2 <- names(d2)

    end_i <- which(n1 == "X") - 1
    for (k in 3:end_i){
     if (n1[k] %in% n2) {
              n3 <- which (n1[k] == n2)
              val <- mean(d2[,n3])
              if (val<0.0){ val<-0.0}
              mass_bias_list[[j]][,k]<- mass_bias_list[[j]][,k] - val
              mass_bias_list[[j]]$correction <-TRUE
            }
      }
    }

#for each "mass bias" sample calculate R238_235 and beta
for (i in 1:length(mass_bias_list)) {
mass_bias_list[[i]]$R238_235<-mass_bias_list[[i]]$X1.238U/
  mass_bias_list[[i]]$X1.235U
mass_bias_list[[i]]$beta<-log((mass_bias_list[[i]]$R238_235)
                      /137.88)/(log(238.0507882/235.0439299))
 }

#extreme value filter
for (i in 1:length(mass_bias_list)) {
  moy<-mean (mass_bias_list[[i]]$beta)
  sigma<-sd (mass_bias_list[[i]]$beta)

  mass_bias_list[[i]]$beta_f<-mass_bias_list[[i]]$beta

  sup<-mass_bias_list[[i]]$beta >=(moy+2*sigma)
  inf<-mass_bias_list[[i]]$beta <=(moy-2*sigma)
```

```
  k<-which(sup==TRUE)
  l<-which(inf==TRUE)
  for(j in 1: length(k)){
    mass_bias_list[[i]]$beta_f[k[j]] <-NA
  }
  for(j in 1: length(l)){
    mass_bias_list[[i]]$beta_f[l[j]] <-NA
  }
}

#store the results of beta
beta_pa <-NULL
for (i in 1:length(mass_bias_list)) {
  beta_pa$std_num[i] <-i
  beta_pa$mean[i]<- mean(mass_bias_list[[i]]$beta, rm.na=T)
  beta_pa$sigma[i]<- sd(mass_bias_list[[i]]$beta)
  beta_pa$min[i]<- min(mass_bias_list[[i]]$beta, rm.na=T)
  beta_pa$max[i]<- max(mass_bias_list[[i]]$beta, rm.na=T)
  beta_pa$median[i]<- median(mass_bias_list[[i]]$beta)
}

mb_corr_pa<-NULL
mb_corr_pa$mean<-(231.035884/233.0402473)^beta_pa$mean
mb_corr_pa$sigma<-(231.035884/233.0402473)^beta_pa$sigma
mb_corr_pa$max<-(231.035884/233.0402473)^beta_pa$max
mb_corr_pa$min<-(231.035884/233.0402473)^beta_pa$min
mb_corr_pa$median<-(231.035884/233.0402473)^beta_pa$median

#for each mass bias sample calculate y_as, the yield for as
#and as, the abundance sensibility
as_pa<-NULL
for (i in 1:length(mass_bias_list)) {
  mass_bias_list[[i]]$y_as<-(mass_bias_list[[i]]$X1.238U/
                               mass_bias_list[[i]]$X1.235U)/
          (mass_bias_list[[i]]$X2.238U/(mass_bias_list[[i]]$X3.235U/62500000))

  mass_bias_list[[i]]$as <-mass_bias_list[[i]]$X4.237/62500000/
    mass_bias_list[[i]]$y_as/mass_bias_list[[i]]$X2.238U

  as_pa$mean[i]<-mean(mass_bias_list[[i]]$as)
  as_pa$sigma[i]<-sd(mass_bias_list[[i]]$as)
  as_pa$max[i]<-max(mass_bias_list[[i]]$as)
  as_pa$min[i]<-min(mass_bias_list[[i]]$as)
  as_pa$median[i]<-median(mass_bias_list[[i]]$as)
}

##############################################################################################
#Processing the Th-h samples
#author : Lise Missiaen
#03/03/2016
##############################################################################################

## for every sample of the th_h_list, look for
```

```
## the closest smaller blank sample and then, check the
## corresponding column of the blank, calculate the mean
## substract the value to the column in the sample data

bi <- NULL
for (j in 1:length(th_h_list)){
s1 <- th_h_list[[j]]$id_num[1]

for (i in 1:length(blanks_data_list)){
  bi[i]<- blanks_data_list[[i]]$id_num[1]
}

bbi <- which(bi < s1)[length(which(bi < s1))]
s2 <- bi[bbi]

d1 <- th_h_list[[j]]
d2 <- blanks_data_list[[bbi]]
n1 <- names(d1)
n2 <- names(d2)


end_i <- which(n1 == "X") - 1
for (k in 3:end_i){
  if (n1[k] %in% n2) {
    n3 <- which (n1[k] == n2)
    val <- mean(d2[,n3])
    if (val<0.0){ val<-0.0}
    th_h_list[[j]][,k]<- th_h_list[[1]][,k] - val
   th_h_list[[j]]$correction <-TRUE
  }
  }
}

#for each th-h sample calculate h
for (i in 1:length(th_h_list)) {
  th_h_list[[i]]$h<-th_h_list[[i]]$X1.233U/62500000/
    th_h_list[[i]]$X2.232Th
}

#store the h-statistics
h_pa <-NULL
for (i in 1:length(th_h_list)) {
  h_pa$std_num[i] <-i
  h_pa$mean[i]<- mean(th_h_list[[i]]$h)
  h_pa$sigma[i]<- sd(th_h_list[[i]]$h)
  h_pa$min[i]<- min(th_h_list[[i]]$h)
  h_pa$max[i]<- max(th_h_list[[i]]$h)
  h_pa$median[i]<- median(th_h_list[[i]]$h)
}
##############################################################################################
#Extracting and processing the process blanks and the spiked process blanks
#author : Lise Missiaen
#03/03/2016
```

```
#############################################################################################
#extraction of the blancs and the spiked blanks
pc_blks_list <-NULL
spk_blks_list<-NULL
k<-1
l<-1
for (i in 1:length(samples_data_list)){
  num<-samples_data_list[[i]]$num_lab[1]
  if (num %in% names_pc_blks){
    pc_blks_list[[k]]<-samples_data_list[[i]]
    k<-k+1
  } else if (num %in% names_spiked_blks){
    spk_blks_list[[l]]<-samples_data_list[[i]]
    l<-l+1
  }
}

#extraction of the process blank data
blk_231_1<-NULL #blank on 231:1
blk_231_2<-NULL # blank on 231:2
blk_233 <- NULL # blank on 233
for (i in 1:length(pc_blks_list)){
  blk_231_1$mean[i]<-mean(pc_blks_list[[i]]$X1.231Pa)
  blk_231_1$min[i]<-min(pc_blks_list[[i]]$X1.231Pa)
  blk_231_1$max[i]<-max(pc_blks_list[[i]]$X1.231Pa)
  blk_231_1$std[i]<-sd(pc_blks_list[[i]]$X1.231Pa)
  blk_231_1$median[i]<-median(pc_blks_list[[i]]$X1.231Pa)


  blk_231_2$mean[i]<-mean(pc_blks_list[[i]]$X2.231Pa)
  blk_231_2$min[i]<-min(pc_blks_list[[i]]$X2.231Pa)
  blk_231_2$max[i]<-max(pc_blks_list[[i]]$X2.231Pa)
  blk_231_2$std[i]<-sd(pc_blks_list[[i]]$X2.231Pa)
  blk_231_2$median[i]<-median(pc_blks_list[[i]]$X2.231Pa)

  blk_233$mean[i]<-mean(pc_blks_list[[i]]$X2.233U)
  blk_233$min[i]<-min(pc_blks_list[[i]]$X2.233U)
  blk_233$max[i]<-max(pc_blks_list[[i]]$X2.233U)
  blk_233$std[i]<-sd(pc_blks_list[[i]]$X2.233U)
  blk_233$median[i]<-median(pc_blks_list[[i]]$X2.233U)
}

#extraction of the contamination of 231Pa by the 233 spike
R_spike_pa <- NULL
for (i in 1:length(spk_blks_list)){
  #calculates the ratio 231/233 of the spike
  spk_blks_list[[i]]$R231_233<-(spk_blks_list[[i]]$X2.231Pa)/
    (spk_blks_list[[i]]$X2.233U)
 #calculates the yield IC4/IC5
  spk_blks_list[[i]]$y <- (spk_blks_list[[i]]$X1.231Pa)/
    (spk_blks_list[[i]]$X2.231Pa)
#corrects from the yield
 spk_blks_list[[i]]$R231_233_y_corr <-spk_blks_list[[i]]$R231_233/
```

```
   mean(spk_blks_list[[i]]$y)
#corrects from the mass bias
spk_blks_list[[i]]$R231_233_y_corr_mb_corr<-spk_blks_list[[i]]$R231_233_y_corr/
  mean(mb_corr_pa$mean)
}


#extremes values filter

for (i in 1:length(spk_blks_list)) {
moy<-mean (spk_blks_list[[i]]$R231_233_y_corr_mb_corr)
sigma<-sd (spk_blks_list[[i]]$R231_233_y_corr_mb_corr)

med<-median(spk_blks_list[[i]]$R231_233_y_corr_mb_corr)
spk_blks_list[[i]]$d_med<-abs((spk_blks_list[[i]]$R231_233_y_corr_mb_corr)-med)
mad<-median(spk_blks_list[[i]]$d_med)#mad is the median absolute distance to the median


spk_blks_list[[i]]$R231_233_f<-spk_blks_list[[i]]$R231_233_y_corr_mb_corr

sup<-spk_blks_list[[i]]$R231_233_y_corr_mb_corr >=(moy+2*sigma)
inf<-spk_blks_list[[i]]$R231_233_y_corr_mb_corr <=(moy-2*sigma)

k<-which(sup==TRUE)
l<-which(inf==TRUE)

for(j in 1: length(k)){
  spk_blks_list[[i]]$R231_233_f[k[j]] <-NA
}

for(j in 1: length(l)){
  spk_blks_list[[i]]$R231_233_f[l[j]] <-NA
}

for (j in 1: length(spk_blks_list)){
R_spike_pa$mean[j] <-mean(spk_blks_list[[i]]$R231_233_f, na.rm=T)
R_spike_pa$min[j]<-min(spk_blks_list[[i]]$R231_233_f, na.rm=T)
R_spike_pa$max[j]<-max(spk_blks_list[[i]]$R231_233_f, na.rm=T)
R_spike_pa$median[j]<-max(spk_blks_list[[i]]$R231_233_f, na.rm=T)
}

}

require(ggplot2)
```

```
## Loading required package: ggplot2
```

```
fig1a<-ggplot(spk_blks_list[[2]], aes(x=Cycle, y=R231_233_y_corr_mb_corr)) +
  geom_point()
fig2a<-  fig1a+ geom_hline(yintercept= med, color="black", size=0.7)
print(fig2a)
```

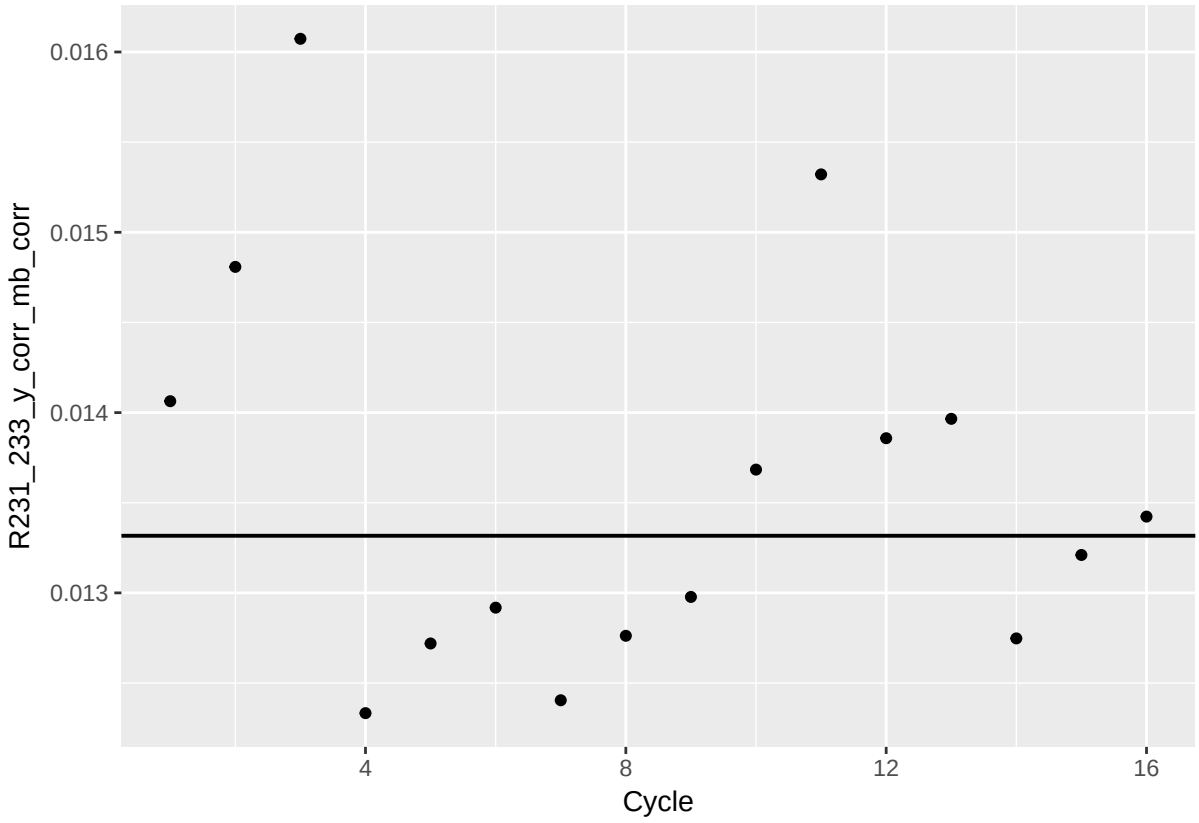


```
fig3a<- fig2a + geom_hline(yintercept=(med-2*mad), color="red", size=0.7)
fig4a<-fig3a + geom_hline(yintercept=(med+2*mad), color="red", size=0.7)
#+ geom_text("med+2 mad/med/med-2mad")
print(fig4a)
```

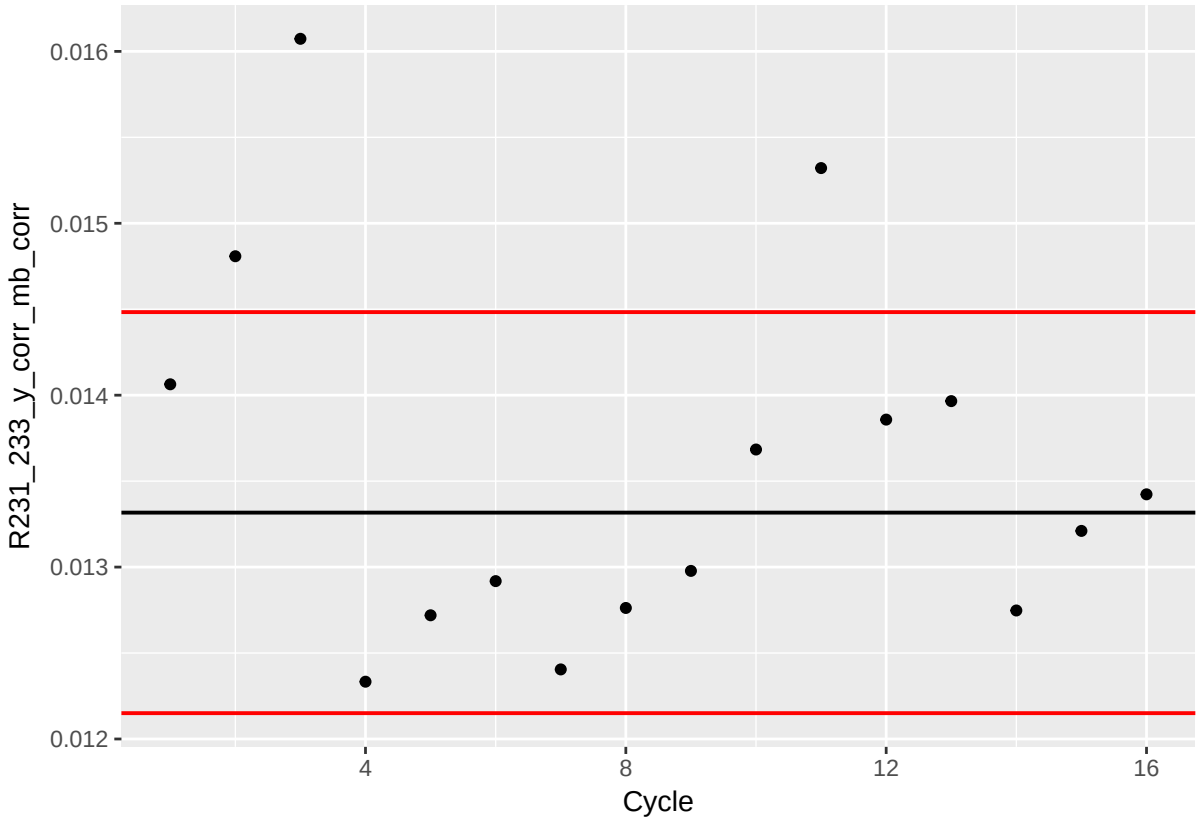


```
fig1b<-ggplot(spk_blks_list[[2]], aes(x=Cycle, y=R231_233_y_corr_mb_corr)) +
  geom_point()
fig2b<-  fig1a+ geom_hline(yintercept= moy, color="black", size=0.7)
print(fig2b)
```

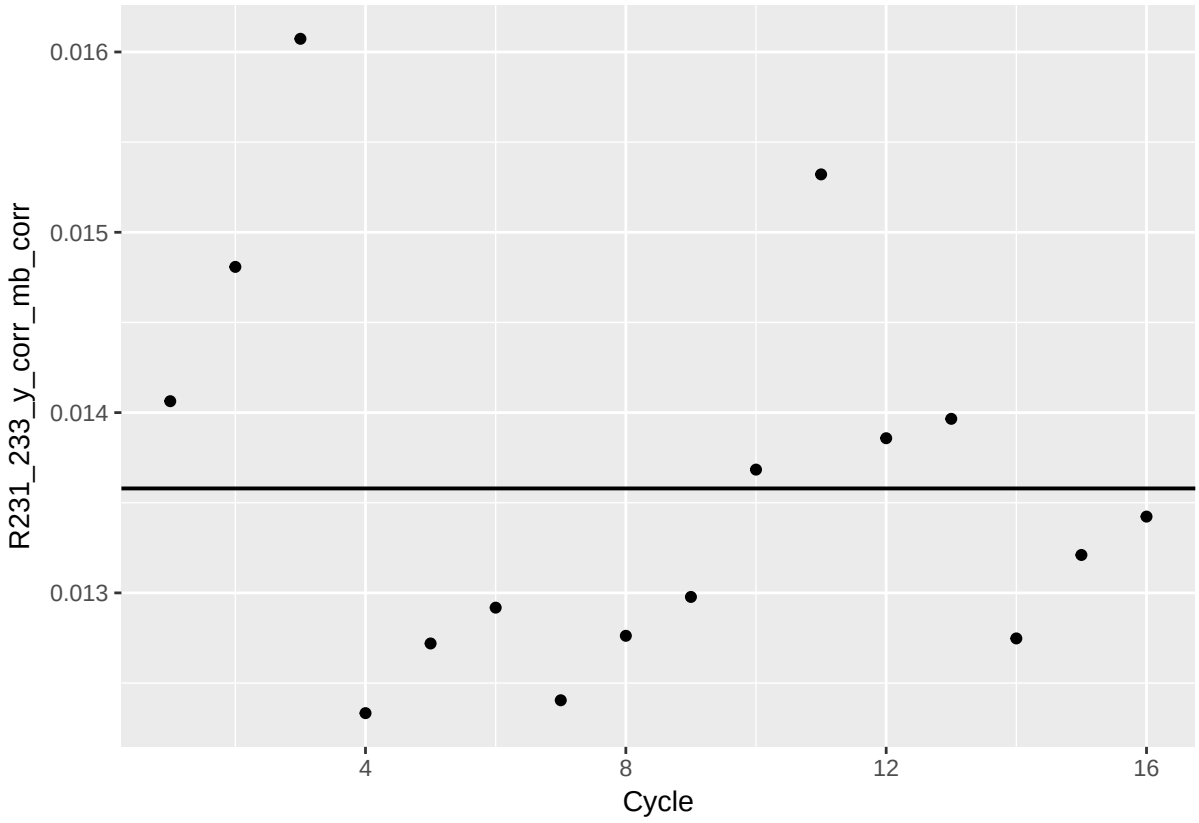


```
fig3b<- fig2b + geom_hline(yintercept=(moy-2*sigma), color="red", size=0.7)
fig4b<-fig3b + geom_hline(yintercept=(moy+2*sigma), color="red", size=0.7)
#+ geom_text("moy+2 sigma/moy/moy-2sigma")
print(fig4b)
```

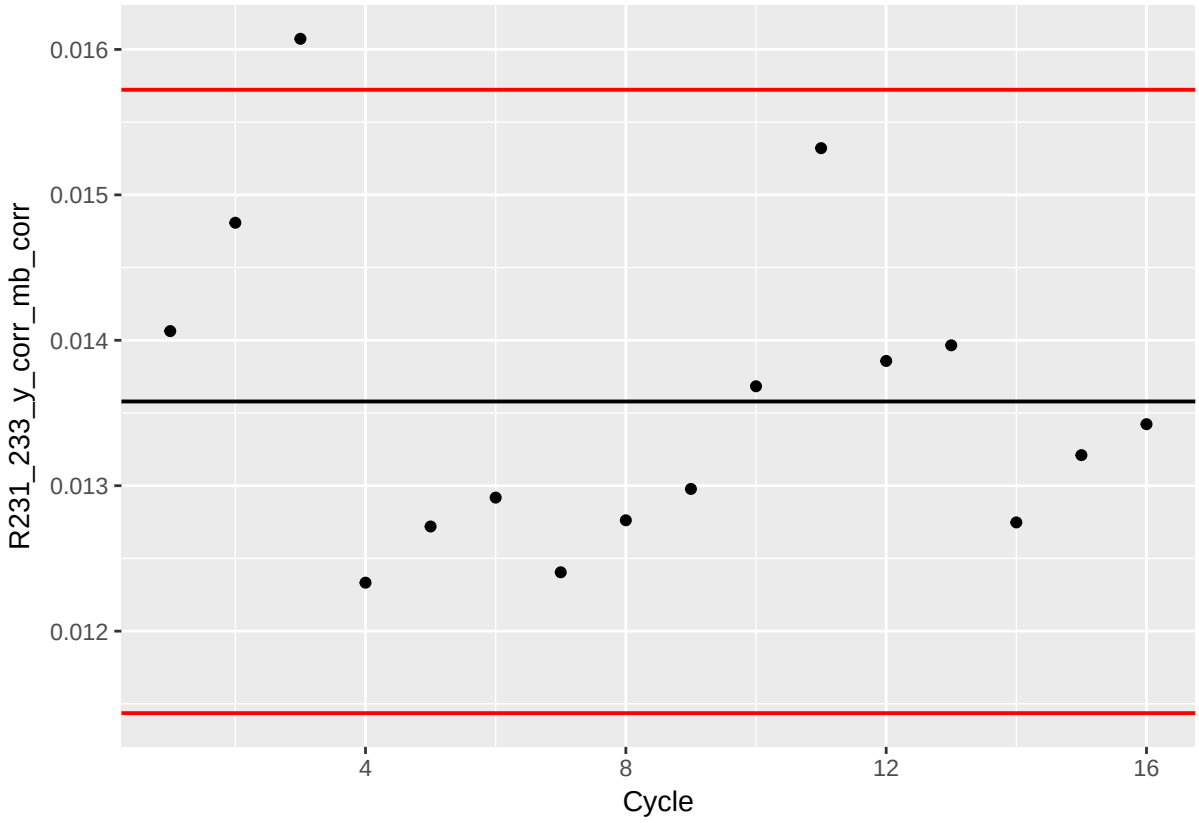


```
##############################################################################################
# 233Pa spike calibration
# 13/03/2016
##############################################################################################

# extracting the Pa standards
std_pa <-NULL #  list of Pa standards

k<-1
for (i in 1:length(samples_data_list)){
  num<-samples_data_list[[i]]$num_lab[1]
  if (num %in% names_pa_std){
    std_pa[[k]]<-samples_data_list[[i]]
    k<-k+1
  }
}

print("Pa standards processing for spike calibration : ")
```

```
## [1] "Pa standards processing for spike calibration : "
```

```
for (i in 1:length(std_pa)){
#print(i)
# correct the raw ratios from the as and hydrites
# nb the correction is done here with the mean of as calculation, we have to think about
  std_pa[[i]]$X1.231Pa_as_corr<-std_pa[[i]]$X1.231Pa -
    (std_pa[[i]]$X4.232Th * 62500000 * mean(as_pa$mean, na.rm =T))
  std_pa[[i]]$X2.231Pa_as_corr<-std_pa[[i]]$X2.231Pa -
```

```
    (std_pa[[i]]$X4.232Th * 62500000 * mean(as_pa$mean, na.rm =T))

  std_pa[[i]]$X2.233U_as_h_corr<- std_pa[[i]]$X2.233U -
    (std_pa[[i]]$X4.232Th * 62500000 * mean(h_pa$mean, na.rm=T))

#process blank correction
# nb : again correction made only with the mean...
std_pa[[i]]$X1.231Pa_blk_corr <- std_pa[[i]]$X1.231Pa_as_corr -
  mean(blk_231_1$mean, na.rm=T)

std_pa[[i]]$X2.231Pa_blk_corr <- std_pa[[i]]$X1.231Pa_as_corr -
  mean(blk_231_2$mean, na.rm=T)

std_pa[[i]]$X2.233U_blk_corr <- std_pa[[i]]$X2.233U_as_h_corr -
  mean(blk_233$mean, na.rm=T)

#spike contamination correction
#nb : again done with the mean only
std_pa[[i]]$X1.231Pa_spk_corr <- std_pa[[i]]$X1.231Pa_blk_corr -
  (std_pa[[i]]$X2.233U_blk_corr * mean(R_spike_pa$mean, na.rm=T))

std_pa[[i]]$X2.231Pa_spk_corr <-std_pa[[i]]$X2.231Pa_blk_corr -
  (std_pa[[i]]$X2.233U_blk_corr * mean(R_spike_pa$mean, na.rm=T))

# calculation of the ratio 231Pa/233Pa
std_pa[[i]]$R231_233 <- std_pa[[i]]$X2.231Pa_spk_corr/
  std_pa[[i]]$X2.233U_blk_corr

# mass bias correction
# nb : done with the mean
std_pa[[i]]$R231_233_mb_corr <- std_pa[[i]]$R231_233 /
  (mean(mb_corr_pa$mean, na.rm=T))

# yield correction
# do we calculate the yield form the raw measurments or form the corrected values
std_pa[[i]]$y<-std_pa[[i]]$X1.231Pa/std_pa[[i]]$X2.231Pa
std_pa[[i]]$R231_233_mb_y_corr <- std_pa[[i]]$R231_233_mb_corr /std_pa[[i]]$y

#extreme values test
# to do with mean/sigma or median/mad
moy<-mean(std_pa[[i]]$R231_233_mb_y_corr, na.rm = T)
sigma<-sd(std_pa[[i]]$R231_233_mb_y_corr, na.rm=T)
std_pa[[i]]$R231_233_f <-std_pa[[i]]$R231_233_mb_y_corr

sup<-std_pa[[i]]$R231_233_mb_y_corr >=(moy+(2*sigma))
inf<-std_pa[[i]]$R231_233_mb_y_corr<=(moy-(2*sigma))

k<-which(sup==TRUE)
l<-which(inf==TRUE)

for(j in 1: length(k)){
  std_pa[[i]]$R231_233_f[k[j]] <-NA
}
```

```
for(j in 1:length(l)){
  std_pa[[i]]$R231_233_f[l[j]] <-NA
}
}

# spike calibration

require(openxlsx)
info_ech<-read.xlsx("../ech_juin_16.xlsx", 1,  colNames =T ,startRow=2)
info_pa_std<-subset(info_ech, Core=="Std Pa" | Core =="std Pa")

for (i in 1:length(std_pa)){
  std_pa[[i]]$C233_pa_pg_g <- (1/std_pa[[i]]$R231_233_f)*
    (233.0402473/231.035884)* 0.0789*info_pa_std$`msed-mean`[i]/
    info_pa_std$`mspikePa-mean`[i]
}

spike_pa<-NULL
for (i in 1:length(std_pa)){
  spike_pa$sample[i]<-std_pa[[i]]$num_lab[1]
  spike_pa$series[i]<-info_pa_std$series[i]
  spike_pa$meanC233_pg_g[i]<-mean(std_pa[[i]]$C233_pa_pg_g, na.rm=T)
  spike_pa$minC233_pg_g[i]<-min(std_pa[[i]]$C233_pa_pg_g, na.rm=T)
  spike_pa$maxC233_pg_g[i]<-max(std_pa[[i]]$C233_pa_pg_g, na.rm=T)
  spike_pa$medianC233_pg_g[i]<-median(std_pa[[i]]$C233_pa_pg_g, na.rm=T)
}

spike_pa <- as.data.frame(spike_pa)


## #############  processing normal Pa samples ############################
#author : Lise Missiaen
#14/03/2016


#for all the samples in the sample list
print( "processing Pa samples : ")
```

```
## [1] "processing Pa samples : "
```

```
for (i in 1:length(samples_data_list)) {
#print(i)
  # correct the raw ratios from the as and hydrites
  # nb the correction is done here with the mean of as calculation, we have to think about
  samples_data_list[[i]]$X1.231Pa_as_corr<-samples_data_list[[i]]$X1.231Pa-
    (samples_data_list[[i]]$X4.232Th * 62500000 * mean(as_pa$mean, na.rm=T))
  samples_data_list[[i]]$X2.231Pa_as_corr<-samples_data_list[[i]]$X2.231Pa-
    (samples_data_list[[i]]$X4.232Th * 62500000 * mean(as_pa$mean, na.rm=T))

  samples_data_list[[i]]$X2.233U_as_h_corr<- samples_data_list[[i]]$X2.233U -
    (samples_data_list[[i]]$X4.232Th * 62500000 * mean(h_pa$mean, na.rm=T))

  #process blank correction
  # nb : again correction made only with the mean...
```

```
  samples_data_list[[i]]$X1.231Pa_blk_corr <- samples_data_list[[i]]$X1.231Pa_as_corr -
    mean(blk_231_1$mean, na.rm=T)

  samples_data_list[[i]]$X2.231Pa_blk_corr <- samples_data_list[[i]]$X1.231Pa_as_corr -
    mean(blk_231_2$mean, na.rm=T)

  samples_data_list[[i]]$X2.233U_blk_corr <- samples_data_list[[i]]$X2.233U_as_h_corr -
    mean(blk_233$mean, na.rm=T)

  #spike contamination correction
  #nb : again done with the mean only
  samples_data_list[[i]]$X1.231Pa_spk_corr <- samples_data_list[[i]]$X1.231Pa_blk_corr-
    (samples_data_list[[i]]$X2.233U_blk_corr * mean(R_spike_pa$mean, na.rm=T))

  samples_data_list[[i]]$X2.231Pa_spk_corr <-samples_data_list[[i]]$X2.231Pa_blk_corr-
    (samples_data_list[[i]]$X2.233U_blk_corr * mean(R_spike_pa$mean, na.rm=T))

  # calculation of the ratio 231Pa/233Pa
  samples_data_list[[i]]$R231_233 <-samples_data_list[[i]]$X2.231Pa_spk_corr/
    samples_data_list[[i]]$X2.233U_blk_corr

  # mass bias correction
  # nb : done with the mean
  samples_data_list[[i]]$R231_233_mb_corr <- samples_data_list[[i]]$R231_233/
    (mean(mb_corr_pa$mean, na.rm=T))

  # yield correction
  # do we calculate the yield form the raw measurments or form the corrected values
samples_data_list[[i]]$y<-samples_data_list[[i]]$X1.231Pa/
  samples_data_list[[i]]$X2.231Pa
samples_data_list[[i]]$R231_233_mb_y_corr <- samples_data_list[[i]]$R231_233_mb_corr/
  samples_data_list[[i]]$y

  #extreme values test
  # to do with mean/sigma or median/mad
  moy<-mean(samples_data_list[[i]]$R231_233_mb_y_corr)
  sigma<-sd(samples_data_list[[i]]$R231_233_mb_y_corr)
  samples_data_list[[i]]$R231_233_f <-samples_data_list[[i]]$R231_233_mb_y_corr

  sup<-samples_data_list[[i]]$R231_233_mb_y_corr >=(moy+(2*sigma))
  inf<-samples_data_list[[i]]$R231_233_mb_y_corr<=(moy-(2*sigma))

  k<-which(sup==TRUE)
  l<-which(inf==TRUE)

  for(j in 1: length(k)){
    samples_data_list[[i]]$R231_233_f[k[j]] <-NA
  }

  for(j in 1:length(l)){
    samples_data_list[[i]]$R231_233_f[l[j]] <-NA
  }
}
```

```
#make the plots and save them as png or pdf to have a look of data distribution...

require(ggplot2)
pdf(file="fig_extremes_mean.pdf",width=5, height=5)
for (i in 1:length(samples_data_list)){
  name<-samples_data_list[[i]]$num_lab[1]
  id<-i
  moy<-mean(samples_data_list[[i]]$R231_233_mb_y_corr)
  sigma<-sd(samples_data_list[[i]]$R231_233_mb_y_corr)

  fig1a<-ggplot(samples_data_list[[i]], aes(x=Cycle, y=R231_233_mb_y_corr)) +
    geom_point()
  fig2b<-  fig1a+ geom_hline(yintercept= moy, color="black", size=0.7)
  fig3b<- fig2b + geom_hline(yintercept=(moy-2*sigma), color="red", size=0.7)
  fig4b<-fig3b + geom_hline(yintercept=(moy+2*sigma), color="red", size=0.7)
  fig5b<-fig4b + annotate("text", x=-Inf, y=Inf, label=name, hjust=-.4, vjust=3)
  fig6b<-fig5b + annotate("text", x=-Inf, y=Inf, label=id, hjust=-.4, vjust=5)
  fig7b<-fig6b+ annotate("text", x=-Inf, y=moy, label= "mean", hjust=-.4, vjust=3)
  print(fig7b)
}
dev.off()
```

```
## pdf
##   2
```

```
pdf(file="fig_extremes_median.pdf",width=5, height=5)
for (i in 1:length(samples_data_list)){
  name<-samples_data_list[[i]]$num_lab[1]
  id<-i
  med<-median(samples_data_list[[i]]$R231_233_mb_y_corr)
  samples_data_list[[i]]$d_med<-abs(samples_data_list[[i]]$R231_233_mb_y_corr-med)
  mad<-median(samples_data_list[[i]]$d_med)

  fig1a<-ggplot(samples_data_list[[i]], aes(x=Cycle, y=R231_233_mb_y_corr)) + geom_point()
  fig2b<-  fig1a+ geom_hline(yintercept= med, color="black", size=0.7)
  fig3b<- fig2b + geom_hline(yintercept=(med-2*mad), color="red", size=0.7)
  fig4b<-fig3b + geom_hline(yintercept=(med+2*mad), color="red", size=0.7)
  fig5b<-fig4b + annotate("text", x=-Inf, y=Inf, label=name, hjust=-.4, vjust=3)
  fig6b<-fig5b + annotate("text", x=-Inf, y=Inf, label=id, hjust=-.4, vjust=5)
  fig7b<-fig6b+ annotate("text", x=-Inf, y=med, label= "median", hjust=-.4, vjust=3)
  print(fig7b)
}
dev.off()
```

```
## pdf
##   2
```

```
# Calculation of the concentration in 231Pa in samples


spike_pa_s1<-NULL
spike_pa_s2<-NULL
spike_pa_s1<-subset(spike_pa, series == 1)
spike_pa_s2 <-subset(spike_pa,series ==2)
```

```
print("Calculation of C_231 (pg/g)")
```

```
## [1] "Calculation of C_231 (pg/g)"
```

```
for (i in 1:length(samples_data_list)){
  #print(i)
sample_name<-samples_data_list[[i]]$num_lab[1]
sample_info<-subset(info_ech, sample== sample_name)

v_spk_sple<-NULL
#here we do again with the mean
if (sample_info$series[1] ==1) {
  v_spk_sple<-mean(spike_pa_s1$meanC233_pg_g, na.rm=T)
}else if (sample_info$series[1] ==2){
  v_spk_sple<-mean(spike_pa_s2$meanC233_pg_g, na.rm=T)
}

samples_data_list[[i]]$C231_pg_g<-samples_data_list[[i]]$R231_233_f*
  (231.035884/233.0402473) * sample_info$`mspikePa-mean` *
  v_spk_sple /sample_info$`msed-mean`

}


######################## calculation of the activities in 231Pa ######################
#Decay constants in kyr-1
lambda_230 <- 9.195E-03
lambda_232 <-4.933E-08
lambda_231 <-2.116E-02
lambda_234 <-2.823E-03
lambda_238 <-1.551E-07

# "chemical" constants
Na<- 6.02214086E+23 #in mol-1

print("Calculation of A_231 (dpm/g")
```

```
## [1] "Calculation of A_231 (dpm/g"
```

```
for (i in 1: length(samples_data_list)){
  #print(i)
samples_data_list[[i]]$A_231_dpm_g<-((lambda_231/(1000*365.24219*24*60)) *
                    samples_data_list[[i]]$C231_pg_g *Na)/(231.035884E+12)
}

######################## export the Pa_results as an excel file ######################
#all data exported in an excel file with 1 sample per sheet

require(xlsx)
```

```
## Loading required package: xlsx
```

```
print("writing result in Pa_samples excel file : ")
```

```
## [1] "writing result in Pa_samples excel file : "
```

```
for (i in 1:length(samples_data_list)){
  #print(i)

write.xlsx(samples_data_list[[i]], file="Pa_samples.xlsx",
           sheetName=paste(samples_data_list[[i]]$num_lab[1],
          samples_data_list[[i]]$id_num[1], sep="_") , append=TRUE)
}

# creating a dataframe with all the samples activities

# don't use summary is a command in R!

my_summary<-NULL
no<-c("L250", "L251","L216" , "L236", "L217", "L237")
for (i in 1:length(samples_data_list)){
  if (!(samples_data_list[[i]]$num_lab[1] %in% no)){
    nb<-strsplit(samples_data_list[[i]]$num_lab[1], "L")
    nb<-nb[[1]][2]
    nb<-as.numeric(nb)
    my_summary$nb[i]<-nb
    my_summary$sample[i]<-samples_data_list[[i]]$num_lab[1]
    my_summary$C_231_Pa_mean[i]<- mean(samples_data_list[[i]]$C231_pg_g, na.rm=T)
    my_summary$C_231_Pa_min[i]<-min(samples_data_list[[i]]$C231_pg_g, na.rm=T)
    my_summary$C_231_Pa_max[i]<-max(samples_data_list[[i]]$C231_pg_g, na.rm=T)
    my_summary$C_231_Pa_median[i]<-median(samples_data_list[[i]]$C231_pg_g, na.rm=T)
    my_summary$C_231_Pa_sigma[i]<-sd(samples_data_list[[i]]$C231_pg_g, na.rm=T)

    my_summary$A_231_Pa_mean[i]<- mean(samples_data_list[[i]]$A_231_dpm_g, na.rm=T)
    my_summary$A_231_Pa_min[i]<-min(samples_data_list[[i]]$A_231_dpm_g, na.rm=T)
    my_summary$A_231_Pa_max[i]<-max(samples_data_list[[i]]$A_231_dpm_g, na.rm=T)
    my_summary$A_231_Pa_median[i]<-median(samples_data_list[[i]]$A_231_dpm_g, na.rm=T)
    my_summary$A_231_Pa_sigma[i]<-sd(samples_data_list[[i]]$A_231_dpm_g, na.rm=T)
  }
}

my_summary <- as.data.frame(my_summary)
my_summary<-subset(my_summary, !is.na(sample))

order.samples<-order(my_summary$nb)

my_summary<-my_summary[order.samples, ]

#require(xlsx)
write.xlsx(my_summary, file="summary_pa.xlsx", sheetName="feuille 1")

## ###### EXCEL OUTPUT OF CORRECTIONS #################
require(xlsx)
```

```
## Loading required package: xlsx
```

```
write.xlsx(beta_pa,file="corrections_pa.xlsx",sheetName="beta_pa")
write.xlsx(as_pa,file="corrections_pa.xlsx",sheetName="as_pa",append=TRUE)
write.xlsx(mb_corr_pa,file="corrections_pa.xlsx",sheetName="mb_cor_pa",append=TRUE)
write.xlsx(h_pa,file="corrections_pa.xlsx",sheetName="h_pa",append=TRUE)
```

```
# This program calculates the activities A231 giving error bars
#produced by Monte Carlo simulation

# Known constants

#Decay constants in kyr-1
lambda_230 <-9.195E-03
lambda_238 <-1.551E-07
lambda_232 <-4.933E-08
lambda_231 <-2.116E-02
lambda_234 <- 2.823E-03


# "chemical" constants
Na<- 6.02214086E+23 #in mol-1

require(openxlsx)
info_ech<-read.xlsx("../ech_juin_16.xlsx", 1,  colNames=T ,startRow=2)

spike_pa_s1<-NULL
spike_pa_s2<-NULL
spike_pa_s1<-subset(spike_pa, series == 1)
spike_pa_s2 <-subset(spike_pa,series ==2)

##############################################################################
# PROCESSING SAMPLES
##############################################################################
set.seed(349875)
########## Processing the normal Pa samples ###########
pa_sample_data_list_2<-list()
pa_mc_results<-list()
summary_pa_mc_results<-NULL
a<-1

for (i in 1:length(samples_data_list)){


  d<-NULL

  for (o in 1:2000) {

    # correct the raw ratios from the as and hydrites
    as <- rnorm(1, mean = mean(as_pa$mean, na.rm=T), sd=sd(as_pa$mean, na.rm=T))
    h <- rnorm(1, mean = mean(h_pa$mean, na.rm=T), sd=sd(h_pa$mean, na.rm=T))

    samples_data_list[[i]]$X1.231Pa_as_corr<-samples_data_list[[i]]$X1.231Pa-
      (samples_data_list[[i]]$X4.232Th * 62500000 * as)
    samples_data_list[[i]]$X2.231Pa_as_corr<-samples_data_list[[i]]$X2.231Pa-
      (samples_data_list[[i]]$X4.232Th * 62500000 * as)

    samples_data_list[[i]]$X2.233U_as_h_corr<- samples_data_list[[i]]$X2.233U -
      (samples_data_list[[i]]$X4.232Th * 62500000 * h)
```

```
#process blank correction
 blk1 <-rnorm(1, mean = mean(blk_231_1$mean, na.rm=T), sd=sd(blk_231_1$mean, na.rm=T))
 blk2 <- rnorm(1, mean = mean(blk_231_2$mean, na.rm=T), sd=sd(blk_231_2$mean, na.rm=T))
 blk3 <- rnorm(1, mean = mean(blk_233$mean, na.rm=T), sd=sd(blk_233$mean, na.rm=T))

samples_data_list[[i]]$X1.231Pa_blk_corr<-samples_data_list[[i]]$X1.231Pa_as_corr-blk1

samples_data_list[[i]]$X2.231Pa_blk_corr<-samples_data_list[[i]]$X1.231Pa_as_corr-blk2

samples_data_list[[i]]$X2.233U_blk_corr<-samples_data_list[[i]]$X2.233U_as_h_corr-blk3

#spike contamination correction
R_spike_pa_bis <- rnorm(1, mean = mean(R_spike_pa$mean, na.rm=T),
                        sd=sd(R_spike_pa$mean, na.rm=T) )

samples_data_list[[i]]$X1.231Pa_spk_corr <- samples_data_list[[i]]$X1.231Pa_blk_corr-
  (samples_data_list[[i]]$X2.233U_blk_corr * R_spike_pa_bis)

samples_data_list[[i]]$X2.231Pa_spk_corr <-samples_data_list[[i]]$X2.231Pa_blk_corr-
  (samples_data_list[[i]]$X2.233U_blk_corr * R_spike_pa_bis)

# calculation of the ratio 231Pa/233Pa
samples_data_list[[i]]$R231_233 <-samples_data_list[[i]]$X2.231Pa_spk_corr/
  samples_data_list[[i]]$X2.233U_blk_corr

# mass bias correction
mb_corr_pa_bis <- rnorm(1, mean = mean(mb_corr_pa$mean, na.rm=T),
                        sd=sd(mb_corr_pa$mean, na.rm=T) )

samples_data_list[[i]]$R231_233_mb_corr<-samples_data_list[[i]]$R231_233/mb_corr_pa_bis

# yield correction
# do we calculate the yield form the raw measurments or form the corrected values
samples_data_list[[i]]$y<-samples_data_list[[i]]$X1.231Pa/samples_data_list[[i]]$X2.231Pa
y<- rnorm(1, mean = mean(samples_data_list[[i]]$y, na.rm=T),
          sd=sd(samples_data_list[[i]]$y, na.rm=T) )
samples_data_list[[i]]$R231_233_mb_y_corr <- samples_data_list[[i]]$R231_233_mb_corr /y

#extreme values test
# to do with mean/sigma or median/mad
moy<-mean(samples_data_list[[i]]$R231_233_mb_y_corr)
sigma<-sd(samples_data_list[[i]]$R231_233_mb_y_corr)
samples_data_list[[i]]$R231_233_f <-samples_data_list[[i]]$R231_233_mb_y_corr

sup<-samples_data_list[[i]]$R231_233_mb_y_corr >=(moy+(2*sigma))
inf<-samples_data_list[[i]]$R231_233_mb_y_corr<=(moy-(2*sigma))

k<-which(sup==TRUE)
l<-which(inf==TRUE)

for(j in 1: length(k)){
  samples_data_list[[i]]$R231_233_f[k[j]] <-NA
}
```

```
    for(j in 1:length(l)){
      samples_data_list[[i]]$R231_233_f[l[j]] <-NA
    }


  # Calculation of the concentration in 231Pa in samples

    sample_name<-samples_data_list[[i]]$num_lab[1]
    sample_info<-subset(info_ech, sample== sample_name)

    v_spk_sple<-NULL
    #here we do again with the mean
    if (sample_info$series[1] ==1) {

      v_spk_sple<-rnorm(1, mean = mean(spike_pa_s1$meanC233_pg_g, na.rm=T),
                        sd=sd(spike_pa_s1$meanC233_pg_g, na.rm=T) )

    }else if (sample_info$series[1] ==2){

      v_spk_sple<-rnorm(1, mean = mean(spike_pa_s2$meanC233_pg_g, na.rm=T),
                        sd=sd(spike_pa_s2$meanC233_pg_g, na.rm=T) )
    }

    msed <- rnorm(1, mean= sample_info$`msed-mean`,
                  sd=sample_info$`sd(msed)`)
    mspike_pa <- rnorm(1, mean=sample_info$`mspikePa-mean`,
                       sd=sample_info$`sd(mspikePa)`)

    samples_data_list[[i]]$C231_pg_g<-samples_data_list[[i]]$R231_233_f*
      (231.035884/233.0402473) * mspike_pa * v_spk_sple /msed


######################### calculation of the activity in 231Pa ########################

 samples_data_list[[i]]$A_231_dpm_g<-((lambda_231/(1000*365.24219*24*60))*
                  samples_data_list[[i]]$C231_pg_g *Na)/(231.035884E+12)


 pa_sample_data_list_2[[a]]<-samples_data_list[[i]]


    d$Process_date[o] <- date()
    d$Sample_name[o]<-samples_data_list[[i]]$num_lab[1]
    d$Monte_carlo_run[o]<-o
    d$A_231_dpm_g[o]<-mean(samples_data_list[[i]]$A_231_dpm_g, na.rm=T)
    d$Sigma_231[o]<-sd(samples_data_list[[i]]$A_231_dpm_g, na.rm=T)


    #d<-as.data.frame(d)


    a<-a+1
```

```
}

  pa_mc_results[[i]]<-d


}



for (i in 1: length(pa_mc_results)) {

  sample_name<-samples_data_list[[i]]$num_lab[1]
  sample_info<-subset(info_ech, sample==sample_name)
  depth<-sample_info$`depth.(cm)`
  depth<-as.vector(depth)
  depth<-as.numeric(depth)
  age<-sample_info$`t-mean`
  age<-as.vector(age)
  age<-as.numeric(age)

  summary_pa_mc_results$Processing_date[i]<-date ()
  summary_pa_mc_results$Sample_name[i]<-pa_mc_results[[i]]$Sample_name[1]
  summary_pa_mc_results$Depth_cm[i]<- depth
  summary_pa_mc_results$Age_ky[i]<-sample_info$`t-mean`
  summary_pa_mc_results$A_231_dpm_g[i]<-mean(pa_mc_results[[i]]$A_231_dpm_g)
  summary_pa_mc_results$Sigma_231[i]<-sd(pa_mc_results[[i]]$A_231_dpm_g)


}

summary_pa_mc_results$Sigma_231_percent<-summary_pa_mc_results$Sigma_231/
  summary_pa_mc_results$A_231_dpm_g *100

require(xlsx)
```

```
## Loading required package: xlsx
```

```
write.xlsx(summary_pa_mc_results, file="summary_pa_mc_results.xlsx",
           sheetName= "feuille 1" )
```

Pa/Th calculation with Monte Carlo error propagation

```
#-------------------------------------------------------------------------
#Programm description
#-------------------------------------------------------------------------
#This script calculates the Pa/Th value, 230Th flux and lithogenic
# vs authigenic contributions
#Author : Lise Missiaen
#Date : December 2016

# In this version there is no error bars calculation
# and 238U/232Th detritic activity ratio is constant

#-------------------------------------------------------------------------
# Importing Core data
#-------------------------------------------------------------------------
 z<- 3135 # z is the water depth in m
#-------------------------------------------------------------------------
# Importing the data
#-------------------------------------------------------------------------
# Here you have to prepare an excel file summarizing the activities obtained
# using Neptune files
# Be careful in this version the 238U/232Th activity ratio must be
# specified in the input file

require(openxlsx)
```

```
## Loading required package: openxlsx
```

```
sample_data<-read.xlsx("input.xlsx", 3, colNames=T ,startRow=1)
sample_data <- as.data.frame(sample_data)

#-------------------------------------------------------------------------
# Importing the known constants
#-------------------------------------------------------------------------
#Decay constants in kyr-1
# Note: it is assumed that the error on lambdas are neglectable
# therefore we do not include errors associated with lambdas
lambda_230 <-9.195E-03
lambda_232 <-4.933E-08
lambda_231 <-2.116E-02
lambda_234 <-2.823E-03
lambda_238 <-1.551E-07

#Known activity ratios
R_sw <- 1.1466 # enter here the value for sea water 234U/238U activity ratio
# we consider sd=0.0025, (Robinson et al 2004)
R_nat<-0.04604
# R_nat is a natural isotopic (activity) ratio, it is calculated via decay chains
# therefore there is no incertitude on it

# "chemical" constants
 Na<- 6.02214086E+23 #in mol-1
```

```
#-------------------------------------------------------------------------------
# Creating dataframes for each sample
#-------------------------------------------------------------------------------
# Each parameter of the Pa/Th calculation will have a column of the dataframe
# dedicated
# Each dataframe has 2 000 lines corresponding to 2 000 random sampling in the
# error bar of each ndependant value

# initialization of an empty list
sample_list <-list()
# set the seed to have reproducible random samplings
set.seed(349875)


# Monte Carlo
# I this part we create a dataframe containing
# all the parameters needed for the subsequent calculations for the 2000 repetitions
for (i in 1:length(sample_data$Sample)){sample_list[[i]]<- matrix(nrow = 2000, ncol = 8)

      for (j in 1:2000) {
               sample_list[[i]][j,1] <- sample_data$Depth_cm[i]
               sample_list[[i]][j,2]<-rnorm(1, mean = sample_data$t_mean..ky.[i],
                                            sd=(sample_data$age_sigma))
               sample_list[[i]][j,3]<-rnorm(1, mean = sample_data$A_238_dpm_g[i],
                                            sd=sample_data$Sigma_238[i])
               sample_list[[i]][j,4]<-rnorm(1, mean = sample_data$A_232_dpm_g[i],
                                            sd=sample_data$Sigma_232[i])
               sample_list[[i]][j,5]<-rnorm(1, mean = sample_data$A_230_dpm_g[i],
                                            sd=sample_data$Sigma_230[i])
               sample_list[[i]][j,6]<-rnorm(1, mean = sample_data$A_231_dpm_g[i],
                                            sd=sample_data$Sigma_231[i])
               sample_list[[i]][j,7]<-rnorm(1, mean = sample_data$D_U_Th[i],
                                            sd= sample_data$D_U_Th_sigma[i])
               sample_list[[i]][j,8]<-rnorm(1, mean = R_sw, sd=0.0025)

                        }
sample_list[[i]] <- as.data.frame(sample_list[[i]])
col_names<-c("Depth_cm", "Age_ky", "A_238_dpm_g", "A_232_dpm_g",
             "A_230_dpm_g", "A_231_dpm_g", "D_U_Th", "R_sw")
names(sample_list[[i]])<-col_names
sample_list[[i]] <- as.data.frame(sample_list[[i]])
 }

#-------------------------------------------------------------------------------
# Pa/Th calculation
#-------------------------------------------------------------------------------

for (i in 1: length(sample_data$Core)){

  # calculation of 238U_authigenic If negative, set authigenic U fraction to zero
```

```
sample_list[[i]]$authi_238U<- sample_list[[i]]$A_238_dpm_g-
  (sample_list[[i]]$A_232_dpm_g*sample_list[[i]]$D_U_Th)



# lithogenic fraction calculation for 230Th and 231Pa
sample_list[[i]]$litho_230<- sample_list[[i]]$A_232_dpm_g*
  sample_list[[i]]$D_U_Th

sample_list[[i]]$litho_231<- R_nat*
  sample_list[[i]]$A_232_dpm_g*sample_list[[i]]$D_U_Th


# Checking that we don't create negative lithogenic and authigenic fraction

for(j in 1:length(sample_list[[i]]$A_238_dpm_g)) {
  if (sample_list[[i]]$authi_238U[j] <= 0) {
    sample_list[[i]]$authi_238U[j]<-0
  }

  if (sample_list[[i]]$litho_230[j] <=0) {
    sample_list[[i]]$litho_230[j] <-0
  }
  if (sample_list[[i]]$litho_231[j] <=0) {
    sample_list[[i]]$litho_231[j] <-0
  }
}

# authigenic fraction calculation

sample_list[[i]]$authi_230<- (sample_list[[i]]$authi_238U)*
  ((1-exp(-sample_list[[i]]$Age_ky* lambda_230)) +
     (lambda_230/(lambda_230-lambda_234))*
     (exp(-lambda_234*sample_list[[i]]$Age_ky)-
        exp(-sample_list[[i]]$Age_ky*lambda_230))*(R_sw-1))

sample_list[[i]]$authi_231<- (R_nat*(sample_list[[i]]$authi_238U)*
                      (1-exp(-lambda_231*sample_list[[i]]$Age_ky)))

# percent lithogenic and authigenic
sample_list[[i]]$percent_litho_230<- sample_list[[i]]$litho_230/
  sample_list[[i]]$A_230_dpm_g*100

sample_list[[i]]$percent_litho_231<-sample_list[[i]]$litho_231/
  sample_list[[i]]$A_231_dpm_g*100

sample_list[[i]]$percent_authi_230<-sample_list[[i]]$authi_230/
  sample_list[[i]]$A_230_dpm_g*100

sample_list[[i]]$percent_authi_231<-sample_list[[i]]$authi_231/
  sample_list[[i]]$A_231_dpm_g*100

# Excess fraction calculation
```

```
  sample_list[[i]]$xs_231 <- sample_list[[i]]$A_231_dpm_g -
    sample_list[[i]]$litho_231- sample_list[[i]]$authi_231

  sample_list[[i]]$xs_230<- sample_list[[i]]$A_230_dpm_g -
    sample_list[[i]]$litho_230 -sample_list[[i]]$authi_230


  # Excess fraction, 0 calculation "at the time of sediment deposition"
  sample_list[[i]]$xs_0_230 <- sample_list[[i]]$xs_230 *
    exp(lambda_230 * sample_list[[i]]$Age_ky)

  sample_list[[i]]$xs_0_231 <- sample_list[[i]]$xs_231 *
    exp(lambda_231 * sample_list[[i]]$Age_ky)

  # Final result : Pa/Th ratio calculation
  sample_list[[i]]$Pa_Th<- sample_list[[i]]$xs_0_231/sample_list[[i]]$xs_0_230


  # 230Th_flux calculation
  sample_list[[i]]$Th_flux <- z * 0.0267 / sample_list[[i]]$xs_0_230
}

#-------------------------------------------------------------------------------
# Storing the results
#-------------------------------------------------------------------------------
results<-NULL

for (i in 1: length(sample_list)){
  results$Sample[i]<-paste("L", sample_data$Sample[i], sep="_")
  results$Depth_cm[i]<-sample_list[[i]]$Depth_cm[1]
  results$Age_ky[i]<-sample_list[[i]]$Age_ky[1]
  results$Pa_Th_mean[i]<-mean(sample_list[[i]]$Pa_Th)
  results$Pa_Th_min[i]<-min(sample_list[[i]]$Pa_Th)
  results$Pa_Th_max[i]<-max(sample_list[[i]]$Pa_Th)
  results$Pa_Th_median[i]<-median(sample_list[[i]]$Pa_Th)
  results$Pa_Th_sigma[i]<-sd(sample_list[[i]]$Pa_Th)
  results$Pa_Th_mad[i]<-mad(sample_list[[i]]$Pa_Th)
  results$Th_flux[i]<- mean(sample_list[[i]]$Th_flux)
  results$Th_flux_sigma[i]<-sd(sample_list[[i]]$Th_flux)
  results$th_230_xs_0[i]<-mean(sample_list[[i]]$xs_0_230)
  results$th_230_xs_0_sigma[i]<-sd(sample_list[[i]]$xs_0_230)
  results$processing_date[i]<-date()

}
results<-as.data.frame (results)

#-------------------------------------------------------------------------------
# Exporting the results in excel
#-------------------------------------------------------------------------------

require(openxlsx)
write.xlsx(results, file="Pa_Th_mc_results_SU81°18.xlsx", sheetName= "feuille 1" )
```

Co-authored article

Clim. Past, 14, 1315–1330, 2018
https://doi.org/10.5194/cp-14-1315-2018

Climate of the Past
Open Access
EGU

Relative timing of precipitation and ocean circulation changes in the western equatorial Atlantic over the last 45 kyr

Claire Waelbroeck[1], Sylvain Pichat[2,3], Evelyn Böhm[1], Bryan C. Lougheed[1], Davide Faranda[1], Mathieu Vrac[1], Lise Missiaen[1], Natalia Vazquez Riveiros[1,4], Pierre Burckel[5], Jörg Lippold[6], Helge W. Arz[7], Trond Dokken[8], François Thil[1], and Arnaud Dapoigny[1]

[1]LSCE/IPSL, Laboratoire CNRS-CEA-UVSQ, 91198 Gif-sur-Yvette, France
[2]Laboratoire de Géologie de Lyon (LGL-TPE), Ecole Normale Supérieure de Lyon, Université de Lyon, CNRS UMR5276, 69007 Lyon, France
[3]Climate Geochemistry Department, Max Planck Institute for Chemistry, Mainz, Germany
[4]Ifremer, Unité de Geosciences Marines, 29280 Plouzané, France
[5]IPGP, Université Sorbonne, 75238 Paris, France
[6]Institute of Earth Sciences, Heidelberg University, Im Neuenheimer Feld 234, 69120 Heidelberg, Germany
[7]Leibniz-Institute for Baltic Sea Research Warnemünde, Seestrasse 15, 18119 Rostock, Germany
[8]Uni Research and Bjreknes Centre for Climate Research, Nygårdsgaten 112, 5008 Bergen, Norway

Correspondence: Claire Waelbroeck (claire.waelbroeck@lsce.ipsl.fr)

Received: 2 March 2018 – Discussion started: 19 March 2018
Revised: 1 August 2018 – Accepted: 27 August 2018 – Published: 18 September 2018

Abstract. Thanks to its optimal location on the northern Brazilian margin, core MD09-3257 records both ocean circulation and atmospheric changes. The latter occur locally in the form of increased rainfall on the adjacent continent during the cold intervals recorded in Greenland ice and northern North Atlantic sediment cores (i.e., Greenland stadials). These rainfall events are recorded in MD09-3257 as peaks in ln(Ti / Ca). New sedimentary Pa / Th data indicate that mid-depth western equatorial water mass transport decreased during all of the Greenland stadials of the last 40 kyr. Using cross-wavelet transforms and spectrogram analysis, we assess the relative phase between the MD09-3257 sedimentary Pa / Th and ln(Ti / Ca) signals. We show that decreased water mass transport between a depth of ∼ 1300 and 2300 m in the western equatorial Atlantic preceded increased rainfall over the adjacent continent by 120 to 400 yr at Dansgaard–Oeschger (D–O) frequencies, and by 280 to 980 yr at Heinrich-like frequencies.

We suggest that the large lead of ocean circulation changes with respect to changes in tropical South American precipitation at Heinrich-like frequencies is related to the effect of a positive feedback involving iceberg discharges in the North Atlantic. In contrast, the absence of widespread ice rafted detrital layers in North Atlantic cores during D–O stadials supports the hypothesis that a feedback such as this was not triggered in the case of D–O stadials, with circulation slowdowns and subsequent changes remaining more limited during D–O stadials than Heinrich stadials.

1 Introduction

Rapid changes in ocean circulation and climate have been observed in marine sediments and polar ice cores over the last glacial and deglacial period (e.g., Johnsen et al., 1992; Vidal et al., 1997). These observations demonstrate that the ocean's current mode of circulation is not unique and can rapidly switch between dramatically different states, in conjunction with climate changes. Furthermore, these observations highlight the non-linear character of the climate system.

Documenting the precise timing and sequence of events in proxy records is a prerequisite for understanding the processes responsible for rapid climate changes and improving climate models' predictive skills. However, the task is complicated by the difficulty of deriving precise age models for marine sediment cores. When marine cores are radiocarbon

dated, uncertainties can arise from bioturbation biases (e.g., Lougheed et al., 2018) and changes in past surface reservoir ages (Waelbroeck et al., 2001; Thornalley et al., 2011). In the best cases, when changes in past surface reservoir ages and bioturbation biases remain limited, dating uncertainties mainly derive from the calibration of radiocarbon ages into calendar ages.

In these cases, errors are less than 150 yr for the time interval spanning 0–11 calendar kyr BP (noted ka), about 400 yr for the 11–30 ka interval, and 600 to 1100 yr for the 30–40 ka interval (Reimer et al., 2013). Thus, minimum relative dating errors between records from different marine sediment cores, or between marine and ice cores records, reach 500 yr at the end of the last deglaciation and increase from 500 to 1500 yr, for increasing ages between 11 and 40 ka. Therefore, it is not possible to quantify leads or lags of less than 500 yr between records from different marine cores, or between marine and ice core records.

Here we take advantage of the fact that the northern Brazilian margin core MD09-3257 records both ocean circulation and atmospheric changes. On the one hand, we reconstruct ocean circulation changes based on new sedimentary Pa / Th data and on epifaunal benthic isotopic ratios. On the other hand, sediment Ti / Ca measured by X-ray fluorescence reflects past changes in rainfall on the adjacent continent (Arz et al., 1998; Jaeschke et al., 2007). Because Pa / Th and Ti / Ca are recorded in the same core, their relative phasing can be examined with virtually no relative dating uncertainty.

We first present the new sedimentary Pa / Th data and their relation to changes in mid-depth water transport in the western equatorial Atlantic over the last 45 kyr. We then precisely assess the relative phasing between the changes in rainfall and ocean circulation recorded in core MD09-3257.

2 Material and methods

2.1 Core locations

Core MD09-3257 (04°14.7′ S, 36°21.2′ W, 2344 m) was recovered in 2009 from the northern Brazilian margin during the R/V *Marion Dufresne* cruise MD173/RETRO3 at approximately the same position as core GeoB3910-2 (04°14.7′ S, 36°20.7′ W, 2362 m) (Arz et al., 2001; Jaeschke et al., 2007). The improved recovery of deep-sea sediments with little or no deformation of sediment layers was achieved thanks to the systematic use of the CINEMA software (Bourillet et al., 2007; Woerther and Bourillet, 2005). This software computes the amplitude and duration of the aramid cable elastic recoil, as well as the piston displacement throughout the coring phase, accounting for the length of the cable (water depth) and total weight of the coring system.

At present, the northern Brazilian margin is bathed by southward flowing upper North Atlantic Deep Water (NADW) at these depths (Lux et al., 2001; Schott et al., 2003; Rhein et al., 2015) (Fig. 1). The southward advection of dense waters formed at higher northern latitudes is channeled through the western boundary current (Rhein et al., 2015), meaning that our sediment cores are ideally located to detect changes in the transport of northern-sourced waters above a depth of 2500 m.

2.2 X-ray fluorescence spectrometry

Elemental composition was measured by employing nondestructive, profiling X-ray fluorescence (XRF) spectrometry. The measurements were made using an AVAATECH XRF core scanner at the Bjerkness Centre for Climate Research, Bergen (Norway) at intervals of 0.5 mm on core MD09-3257, and using a CORTEX XRF scanner at the Bremen Integrated Ocean Drilling Program core repository at intervals of 0.4 cm on core GeoB3910-2 (Jaeschke et al., 2007). This automated scanning method allows for a rapid qualitative determination of the geochemical composition of the sediment at very high resolution (Croudace and Rothwell, 2015).

2.3 Chronology

Ti / Ca records from core MD09-3257 and core GeoB3910-2 exhibit marked peaks corresponding to increased terrigenous input due to enhanced precipitation and runoff from the continent (Arz et al., 1998; Jaeschke et al., 2007) (Fig. 2). These precipitation events are also recorded in South American speleothems, and have been shown to correspond to North Atlantic cold stadial periods (Cheng et al., 2013). The core GeoB3910-2 radiocarbon (^{14}C) age model shows that increases in sedimentary Ti / Ca are indeed synchronous with decreases in South American speleothem δ^{18}O (Burckel et al., 2015). Based on the observed synchronicity, composite age models of core MD09-3257 and GeoB3910-2 have been developed using ^{14}C dating for the past 35 kyr, combined with the alignment of sediment Ti / Ca increases with decreases in speleothem δ^{18}O for the older portion of the cores (Vazquez Riveiros et al., 2018); thus, speleothem ages beyond 35 ka could be transferred to the marine cores. The chronology of core GeoB3910-2 is based on 17 monospecific radiocarbon dates between 0 and 31 ka (Burckel et al., 2015; Jaeschke et al., 2007). The Ti / Ca record of core GeoB3910-2 was aligned to that of core MD09-3257 in order to transfer the radiocarbon dates of GeoB3910-2 over the interval from 12 to 36 ka to this nearby core. In addition, five monospecific radiocarbon dates over 1–21 ka were directly obtained from core MD09-3257. Speleothem tie points were used to derive the chronology of this core over the period from 38 to 48 ka (Tables S1 and S2 in the Supplement) (Vazquez Riveiros et al., 2018). All radiocarbon dates were converted to calendar dates using the OxCal 4.2 software, the IntCal13 calibration curve (Reimer et al., 2013), and a surface water reservoir age of 550 ± 50 yr over 0–18 ka (Key et al., 2004), and of 750 ± 250 yr over 18–31 ka (Freeman et al., 2016). The final age models of cores GeoB3910-2 and MD09-3257 were ob-

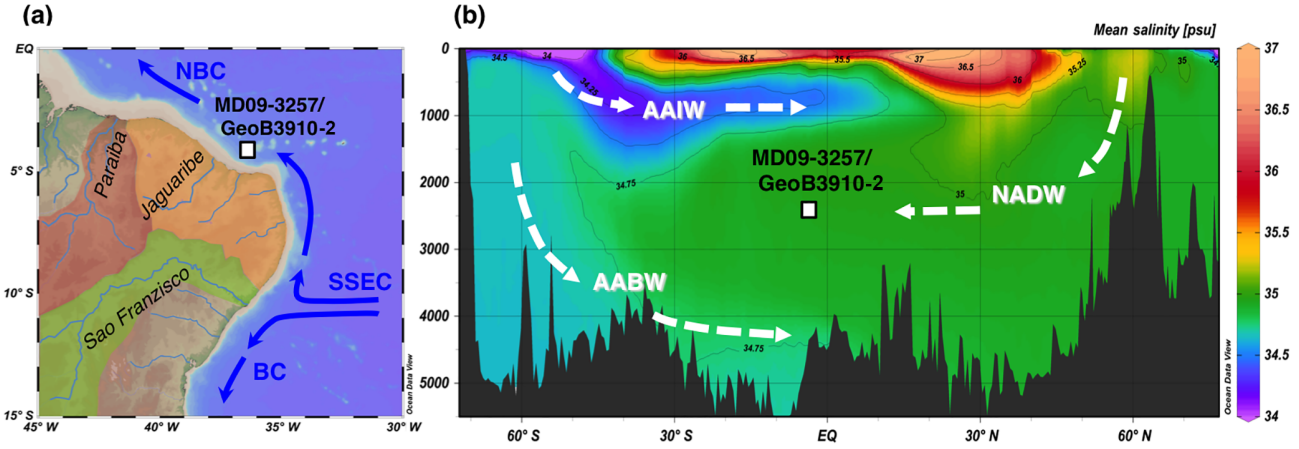

Figure 1. **(a)** Map showing the position of the main Brazilian rivers and surface currents that could influence the terrigenous input at the study site; the study site is indicated by a white square. The orange area represents the catchment area of the local rivers directly delivering sediments to the study site, and the green area represents the catchment area of the Sao Franzisco River (Milliman et al., 1975). NBC stands for North Brazil Current, SSEC stands for Southern South Equatorial Current and BC stands for Brazil Current. **(b)** Salinity section showing the core site and the main water masses in the modern Atlantic Ocean. NADW stands for North Atlantic Deep Water, AAIW stands for Antarctic Intermediate Water and AABW stands for Antarctic Bottom Water.

tained using a P_Sequence depositional model (Bronk Ramsey, 2008), i.e., a Bayesian algorithm producing posterior probability distributions for each core depth (Tables S1 and S2) (Vazquez Riveiros et al., 2018).

In the present study, the GeoB3910-2 age scale for the 32–50 ka interval was further adjusted by precise alignment of GeoB3910-2 XRF to the MD09-3257 XRF signal (Fig. S1 in the Supplement), which produced a composite record from these two nearby cores. Given that both XRF signals are virtually identical and measured at very high resolution (sampling step ≤ 0.5 cm), the mean relative dating uncertainty between the two cores is extremely small (less than 105 yr; Fig. S1).

Here, we use XRF ln(Ti / Ca) rather than Ti / Ca because log-ratios provide a unique measure of sediment composition, in contrast to simple ratios, which are asymmetric (i.e., conclusions based on evaluation of A/B cannot be directly translated into equivalent statements about B/A) and suffer from statistical intractability (Weltje and Tjallingii, 2008). We adopt the same terminology as Burckel et al. (2015) and define the larger ln(Ti / Ca) peaks as precipitation events PE0 to PE5, with PE0 occurring during the Younger Dryas, and PE1 to PE5 occurring during Heinrich stadials 1 to 5 (Fig. 2). What we refer to as Heinrich stadials are strictly those stadials characterized by the occurrence of iceberg discharges in the mid- to high-latitude North Atlantic. We refer to smaller ln(Ti / Ca) peaks corresponding to D–O stadials using the Greenland stadial numbering system, as defined by Rasmussen et al. (2014).

2.4 Benthic isotopes

Epifaunal benthic foraminifers of the *Cibicides wuellerstorfi* species were handpicked in the >150 µm size fraction (Vazquez Riveiros et al., 2018). Core MD09-3257 *C. wuellerstorfi* ^{13}C / ^{12}C ($\delta^{13}C$, expressed in ‰ versus Vienna Pee Dee Belemnite, VPDB) was measured at the LSCE on Finnigan DELTAplus and Elementar Isoprime mass spectrometers on samples of one to three specimens. VPDB is defined with respect to the NBS-19 calcite standard ($\delta^{18}O = -2.20$ and $\delta^{13}C = +1.95$ ‰). The mean external reproducibility (1σ) of carbonate standards is ±0.03 ‰ for $\delta^{13}C$; measured NBS-18 $\delta^{18}O$ is -23.27 ± 0.10 and $\delta^{13}C$ is -5.01 ± 0.03 ‰ VPDB. Core GeoB3910-2 *C. wuellerstorfi* $g\delta^{13}C$ was measured at the University of Bremen, Germany, on a Finnigan MAT 252 mass spectrometer on samples of one to five specimens (Heil, 2006), with a mean external reproducibility (1σ) for carbonate standards of ±0.05 ‰ for $\delta^{13}C$. A composite high-resolution benthic isotopic record was generated by combining isotopic data from the upper 294 cm of core MD09-3257 (covering the last 32 kyr) with isotopic data from the interval from 246 to 451 cm in core GeoB3910-2 for the older part of the record (Vazquez Riveiros et al., 2018).

The $^{13}C/^{12}C$ isotopic ratio ($\delta^{13}C$, expressed in per mil – ‰ – versus VPDB) of the epifaunal benthic foraminifer *C. wuellerstorfi* has been shown to record the $\delta^{13}C$ of bottom-water dissolved inorganic carbon (DIC) with minor isotopic fractionation (Duplessy et al., 1984; Zahn et al., 1986; Schmittner et al., 2017). A water mass' initial DIC isotopic concentration is governed by surface productivity in its formation region (i.e., the preferential consumption of ^{12}C by primary productivity, which increases dissolved $\delta^{13}C$), as

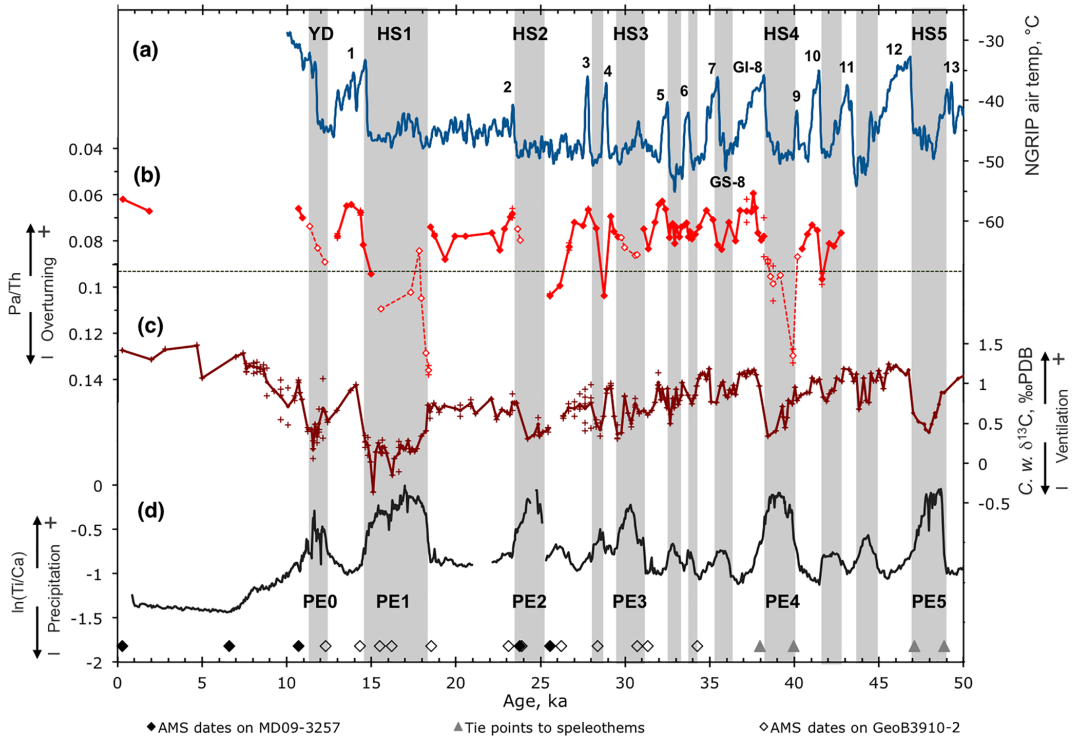

Figure 2. MD09-3257 Pa / Th, ln(Ti / Ca) and composite *C. wuellerstorfi* δ^{13}C ($\delta^{13}C_{Cw}$) records versus MD09-3257 age scale, independent from the North Greenland Ice Core Project (NGRIP) age scale. **(a)** NGRIP air temperature versus the Greenland Ice Core Chronology 2005 (GICC05) age scale (Kindler et al., 2014), transposed from kyr b2k (before 2000) to ka. Greenland interstadials are numbered according to Rasmussen et al. (2014). To avoid overcrowding the figure, Greenland stadials (GS) and interstadials (GI) are only explicitly named in the case of GS-8 and GI-8. **(b)** The MD09-3257 core Pa / Th record. Empty symbols denote data points that may be affected by terrigenous fluxes and should be interpreted with caution; crosses denote replicate measurements; the red line connects average values (filled symbols). Pa / Th could not be measured over the first half of PE2 because of the occurrence of two small sand layers (Burckel et al., 2015). **(c)** The MD09-3257 core and GeoB3910-2 core composite $\delta^{13}C_{Cw}$ record (Vazquez Riveiros et al., 2018); crosses denote replicate measurements. **(d)** MD09-3257 ln(Ti / Ca). Diamonds above the *x* axis indicate calibrated radiocarbon dates in MD09-3257 (filled symbols) and GeoB3910-2 (empty symbols). Triangles indicate alignment tie points to South American speleothem δ^{18}O (Vazquez Riveiros et al., 2018). Grey bands delineate precipitation events recorded in MD09-3257 ln(Ti / Ca).

well as temperature dependent air–sea exchanges (Lynch-Stieglitz et al., 1995). DIC δ^{13}C subsequently decreases as deep water ages, due to the progressive remineralization at depth of relatively ^{13}C-depleted biogenic material. As a result, DIC δ^{13}C largely follows water mass structure and circulation in the modern ocean, and *C. wuellerstorfi* δ^{13}C ($\delta^{13}C_{Cw}$ hereafter) has been used to trace water masses and as a proxy of bottom-water ventilation (Duplessy et al., 1988 and numerous subsequent studies). A recent study further highlighted that DIC δ^{13}C more faithfully follows water oxygen content than phosphate content (Eide et al., 2017), lending strong support to the use of $\delta^{13}C_{Cw}$ as a proxy for bottom-water ventilation – the term ventilation here refers to the transmission of oxygen-rich, atmosphere-equilibrated water to the ocean interior.

2.5 New sedimentary Pa / Th data

New sedimentary ($^{231}Pa_{xs,0}/^{230}Th_{xs,0}$) measurements (excess activity ratio at the time of deposition, Pa / Th hereafter) were produced in core MD09-3257 in order to extend the Pa / Th record of Burckel et al. (2015) and to cover the entire time interval from 10 to 43 ka (Table S3). The excess activity corresponds to the fraction of each radioisotope produced in the water column by uranium (U) decay and is transferred to the sediment by adsorption onto particles sinking in the water column. ^{230}Th and ^{231}Pa excess activities are calculated from bulk sediment measurement by correcting for the contribution of the detrital and authigenic fractions (François et al., 2004; Henderson and Anderson, 2003) using a detrital (^{238}U / ^{232}Th) value of 0.5 ± 0.1 (2σ) (Missiaen et al., 2018). These excess activities are then further corrected for radioactive decay since the time of sediment deposition. Bulk sediment measurements were performed by isotopic dilution mass spectrometry on the LSCE MC-ICP-

MS (Neptune^{Plus}, Thermo Fisher), following a method derived from Guihou et al. (2010). Error bars (2 standard deviations) on Pa / Th measurements were computed by Monte Carlo runs (Missiaen et al., 2018), accounting for the uncertainties in Pa, Th and U measurements, as well as those of the detrital (^{238}U / ^{232}Th) value, spike calibrations and dating.

Sedimentary Pa / Th can be used to reconstruct changes in the renewal rate of water masses overlying the core site. This tracer has been successfully used to reconstruct past changes in deep Atlantic circulation intensity (Burckel et al., 2015 and references therein). ^{231}Pa and ^{230}Th are produced at a constant Pa / Th activity ratio of 0.093 by dissolved uranium, which is homogeneously distributed in oceans. ^{230}Th is much more particle reactive than ^{231}Pa, as reflected by their respective residence time in the ocean (30–40 yr for ^{230}Th and 100–200 yr for ^{231}Pa, François, 2007). Therefore, ^{230}Th is rapidly removed from the water column to the underlying sediment, while ^{231}Pa can be advected by oceanic currents. Thus, when averaged over an entire ocean basin, high (low) flow rates result in high (low) ^{231}Pa export and a low (high) sedimentary Pa / Th ratio. In contrast to $\delta^{13}C_{Cw}$, which records the DIC δ^{13}C of bottom waters at the core site, sedimentary Pa / Th does not reflect the flow rate at the seabed but that of a water layer of a few hundreds to more than 1000 m above the seafloor (Thomas et al., 2006).

Several potential caveats of the proxy were tested. In particular, ^{231}Pa has a higher affinity for opal than for the other types of particles (Chase et al., 2002), meaning that high opal fluxes can result in high sedimentary Pa / Th values even in the presence of lateral advection. Similarly, areas of very high vertical particle flux, such as the Atlantic off western Africa, are characterized by high Pa / Th values (Yu et al., 1996; François, 2007; Lippold et al., 2012). Recent studies have shown that the caveats that may apply to this proxy in some areas do not apply to the western tropical Atlantic region. More specifically, a study including core top material from the western tropical Atlantic margin and using a 2-D model (Luo et al., 2010) showed that the measured Pa / Th vertical profile is consistent with a dominant role of the overturning circulation, rather than particle scavenging; this demonstrates that Pa / Th can be used to record changes in water mass overturning rates in that region (Lippold et al., 2011). However, because there are large increases in terrigenous material deposition on the northeastern Brazilian margin during the last glacial, we carefully evaluated/assessed if increased terrigenous deposition may have impacted Pa / Th values.

The ^{230}Th-normalized ^{232}Th flux, hereafter simply referred to as the ^{232}Th flux, is indicative of the vertical terrigenous flux to the core site. As ^{232}Th is a trace element that is mostly contained in the continental crust (Taylor and McLennan, 1985), it is commonly used as a geochemical tracer for material of detrital origin (e.g., Anderson et al., 2006). Besides the main precipitation events PE0 to PE4, there is no significant correlation between the Pa / Th ratio and the ^{232}Th flux ($r = 0.21$, $p = 0.07$) (Figs. S2 and S3). In contrast, because the correlation between Pa / Th and the ^{232}Th flux becomes significant ($r = 0.57$, $p \ll 0.001$) when including the main precipitation events (Fig. S3), the high Pa / Th values observed during PE0 to PE4 could be partly caused by increased terrigenous flux and should be interpreted with caution (empty symbols in Fig. 2). Note that a possible terrigenous influence during the main precipitation events does not preclude that the high Pa / Th values during these periods reflect an almost halted oceanic circulation above the core site. Indeed, Pa scavenging by boundary scavenging can be intensified in times of reduced overturning circulation due to boundary scavenging becoming the main control on sedimentary Pa / Th.

Another source of possible biases in Pa / Th results from variations in opal flux (Chase et al., 2002). However, the northern Brazilian margin is known for its low siliceous primary production (Arz et al., 1998). This is confirmed by ^{230}Th-normalized opal flux measurements in MD09-3257, which are below 0.06 g cm^{-2} kyr^{-1} (Fig. S3). Moreover, outside of precipitation events PE0 to PE4, there is no correlation between Pa / Th and opal flux (Fig. S3). In conclusion, we may consider that outside of the main precipitation events, our Pa / Th record can be interpreted in terms of changes in the strength of overturning circulation above the MD09-3257 coring site.

2.6 Cross-correlation and wavelet analysis

Assuming that there is a constant phase shift between two time series over their entire length, one can perform a simple cross-correlation analysis and compute how the correlation coefficient between the two time series varies as a function of the time lag between the two series (e.g., Davis, 1986).

We normalized (i.e., subtracted the mean and divided by the standard deviation) and resampled the time series Pa / Th, $\delta^{13}C_{Cw}$ and ln(Ti / Ca) to a common age scale using scenarios with constant time steps varying between 50 and 500 yr. We then used the *R* function cor.test (R package stats version 3.2.2) for correlation between paired series (R script in Supplement) to compute the Spearman correlation coefficient between all pairs of the three time series, after having shifted one with respect to the other by increments of the time step.

Another approach consists of classical spectral analysis methods that examine the coherence and phase between two time series in frequency space, such as Fourier transforms. Fourier transforms involve decomposing a signal into infinite-length oscillatory functions (such as sine waves). As such, these methods also rely on the assumption that the decomposition of each signal into characteristic frequencies is valid over its entire length, i.e., that the underlying processes are stationary in time.

In contrast, wavelet analysis can be used to decompose a time series into "time–frequency" space, rather than fre-

quency space, that is, to determine both the dominant modes of variability and how these modes vary in time (Torrence and Compo, 1998). To do so, the wavelet transform decomposes the signal into a sum of small wave functions of finite length that are highly localized in time. Thus, wavelet transform can describe changes in frequencies along the studied time series and are particularly relevant for dealing with climatic signals, since they are in essence not stationary in time, but in constant evolution in response to external forcing (i.e., insolation changes), and as a result of internal climate variability.

Given two times series X and Y, with wavelet transforms W^X and W^Y, the cross-wavelet spectrum is defined as $W^{XY} = W^X W^{Y*}$, where W^{Y*} is the complex conjugate of W^Y (Torrence and Compo, 1998). Similarly to Fourier coherency, which is used to identify frequency bands in which two time series are related, the wavelet coherency was developed to identify both frequency bands and time intervals over which the two time series are related. The wavelet coherence between two time series is defined as the square of the smoothed cross-wavelet spectrum normalized by the smoothed individual wavelet power spectra (Torrence and Webster, 1999). This definition resembles that of a traditional correlation coefficient, i.e., wavelet coherence ranges between 0 and 1, and may be viewed as a localized correlation coefficient in time–frequency space (Grinsted et al., 2004).

Analogous to Fourier cross-spectral analysis, the phase difference between two time series can also be computed using a cross-wavelet spectrum. The complex argument $\arg(W^{XY})$ can be interpreted as the local relative phase between X and Y in time–frequency space (Grinsted et al., 2004).

In the present study we use the software developed by Grinsted et al. (2004) to compute the cross-wavelet spectrum, coherence and relative phase between our time series that were normalized and resampled as previously described. To test for the persistence of regions of high cross-wavelet coherence, we ran all cross-wavelet analyses 1000 times for each dataset pair (i.e., a Monte Carlo approach). For each of the 1000 runs, each time data point was randomly sampled, whereby a Gaussian distribution of each data point's value (based on the measurement uncertainty) was used to weight the random sampling. Mean and standard deviation values for the coherence and phase direction were calculated using the 1000 runs.

3 Results

3.1 Ocean circulation proxy records

The Pa / Th record of core MD09-3257 now covers the entire 10–43 ka time interval, encompassing the Younger Dryas (YD) and the last four Heinrich stadials (Fig. 2). We have increased its temporal resolution over the time interval from 31 to 38 ka comprising Dansgaard–Oeschger (D–O) events 5 to 8, with respect to the rest of the study period, in order to examine Atlantic circulation dynamics during D–O events.

Pa / Th data exhibit systematic increases in conjunction with stadials, even if Pa / Th data points that are potentially biased towards elevated values by increased terrigenous input (empty symbols) are discarded. Thus, Pa / Th data indicate that the renewal rate of the water mass overlying the site decreased during stadials. More specifically, transport of the overlying water mass decreased not only during the YD and Heinrich stadials, but also during practically all D–O stadials. Among D–O stadials, the Pa / Th increase is well marked for GS-7, GS-8 and GS-11, but the signal is too noisy to provide a clear picture for GS-6. This noisy Pa / Th signal is very likely due to sediment reworking, given that the $\delta^{13}C_{Cw}$ record is also noisy over this section of the core. Also, it is noteworthy that no precipitation event is recorded in MD09-3257 or GeoB3910-2 during GS-10 (Fig. 2). There is no clear decrease in the well-dated El Condor (Cheng et al., 2013) speleothem $\delta^{18}O$ records associated with GS-10 either, which is in contrast with the other Greenland stadials (Burckel et al., 2015). It would seem that there was no apparent increase in precipitation during GS-10 over tropical South America, in contrast with all other GS of the past 40 kyr. Overall, longer stadials seem to be associated with larger increases in Pa / Th than shorter stadials.

The $\delta^{13}C_{Cw}$ composite record varies in concert with Pa / Th, with high values indicating the presence of well-ventilated waters during the Holocene and interstadials, and low values indicating a marked reduction in water ventilation during stadials at $\sim$ 2350 m in the western equatorial Atlantic (Vazquez Riveiros et al., 2018).

3.2 Relative timing of Pa / Th, $\delta^{13}C_{Cw}$ and Ti / Ca

Pa / Th, $\delta^{13}C_{Cw}$ and Ti / Ca are recorded in the same core or in two cores from the same location, which could be precisely aligned through high resolution XRF signals. This situation provides ideal conditions to examine the relative phasing of one proxy with respect to another. Pa / Th and Ti / Ca are recorded in the same core, so their relative phasing can consequently be examined with the smallest possible relative dating uncertainty, whereby the only remaining source of uncertainty is bioturbation. The situation is practically the same when examining $\delta^{13}C_{Cw}$ versus Ti / Ca or $\delta^{13}C_{Cw}$ versus Pa / Th. Apart from the unavoidable uncertainty introduced by bioturbation, the relative dating uncertainty between the $\delta^{13}C_{Cw}$ composite record and any MD09-3257 record is null over 0–32 ka, and amounts to 102 yr on average over the 32–50 ka time interval (Fig. S1).

In what follows, we assess the relative phasing between Pa / Th, $\delta^{13}C_{Cw}$ and Ti / Ca, using all Pa / Th data points (including Pa / Th values susceptible to being partially impacted by large particle fluxes or boundary scavenging resulting from slower overturning circulation) in order to have

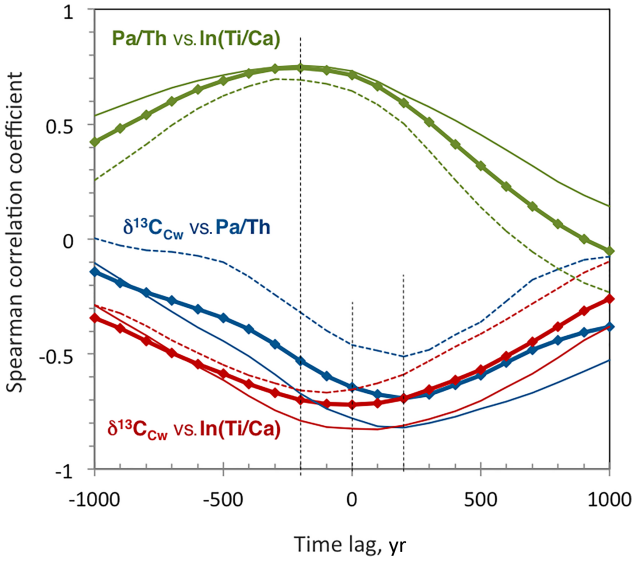

Figure 3. Spearman correlation coefficient of $\delta^{13}C_{Cw}$ versus Pa / Th (blue curves), of $\delta^{13}C_{Cw}$ versus ln(Ti / Ca) (red curves), and of Pa / Th versus ln(Ti / Ca) (green curves), as a function of the time lag. A positive time lag means that series 1 lags series 2 (e.g., $\delta^{13}C_{Cw}$ lags Pa / Th); a negative time lag means that series 1 leads series 2 (e.g., Pa / Th leads ln(Ti / Ca)). Bold lines correspond to the calculation over the entire time interval from 10.6 to 42.6 ka, thin lines to the calculation over the time interval from 10.6 to 26.6 ka, and thin dashed lines to the calculation over the time interval from 26.6 to 42.6 ka. Vertical dashed lines indicate the time lags corresponding to the maximum correlation coefficients for the three pairs of series over the entire time interval.

sufficient data to examine periodicities ranging from 1000 to 6000 yr. In doing so, we assume that changes in particle fluxes may affect the amplitude of the Pa / Th changes, rather than the timing of these changes. In the following text, we show that excluding the Pa / Th values susceptible to being partially impacted by large particle fluxes does not change our conclusions concerning D–O periodicities (i.e., 1000 to 3000 yr).

3.2.1 Average relative phases

We first apply the simple stationary cross-correlation approach to examine how the correlation coefficients of Pa / Th versus ln(Ti / Ca), of $\delta^{13}C_{Cw}$ versus ln(Ti / Ca), and of $\delta^{13}C_{Cw}$ versus Pa / Th, vary as a function of the lag between the different time series (Fig. 3). Prior to computing the correlation coefficients, the three time series were resampled with a time step of 100 yr and normalized.

Taken at face value, these results indicate that Pa / Th leads ln(Ti / Ca) (or Ti / Ca) by 200 ± 100 yr, that there is no significant phase shift between $\delta^{13}C_{Cw}$ and Ti / Ca, and that $\delta^{13}C_{Cw}$ lags Pa / Th by 200 ± 100 yr (Table S4). The uncertainty of ± 100 yr directly results from the adopted sampling step of 100 yr. In addition, in order to assess the robustness of these results, we applied the same approach to the upper half and lower half of the records. In all cases, we obtained $\delta^{13}C_{Cw}$ lags over Pa / Th of 200 yr, and Pa / Th leads over ln(Ti / Ca) of 200 or 300 yr, while the phase shift between $\delta^{13}C_{Cw}$ and Ti / Ca remained between -100 and $+100$ yr.

Although this simple method has been applied to climatic time series in previous studies (Langehaug et al., 2016; Henry et al., 2016), such results must be interpreted with caution, as the method has been designed for signals that are stationary in time and is therefore not suitable for climatic signals.

3.2.2 Wavelet transforms

The non-stationary character of climatic signals over the last 40–45 kyr is particularly pronounced. Different typical pseudo-periodicities can be identified for Heinrich and D–O stadials. In the case of Heinrich stadials (corresponding to our main precipitation events), the interval from 11.7 to 49 ka comprises five pseudo-cycles that are $\sim$ 6 to 9 kyr long (Fig. 2), such that Heinrich stadials over the studied interval are characterized by an average pseudo-periodicity of about 7 kyr. Concerning D–O events, the interval located between HS3 and HS4 (32.5–38.1 ka) comprises three pseudo-cycles that are $\sim$ 1.2, 1.5 and 3 kyr long (Fig. 2), yielding an average pseudo-periodicity of about 1.8 kyr.

We computed the cross-wavelet spectrum, coherence and phase between ln(Ti / Ca) and Pa / Th (Fig. 4), between $\delta^{13}C_{Cw}$ and Pa / Th (Fig. 5), and between $\delta^{13}C_{Cw}$ and ln(Ti / Ca) (Fig. 6), using the software from Grinsted et al. (2004). The 95 % confidence level against red noise is shown as a thick contour line. Relative phases are only plotted for coherences higher than 0.5 (<0.5 is masked as dark blue). Note that the shaded areas in Figs. 4–6 correspond to the region of the wavelet transform graphs where the edge effects due to the finite length of the time series limit the ability to carry out cross-wavelet analysis. These regions are not considered in our interpretations.

To assess the robustness of our results, we repeated the cross-wavelet transform for different interpolation resolutions ranging from 50 to 500 yr; therefore, we could verify that the features corresponding to the 95 % confidence level against red noise for a time step of 100 yr are still present at roughly the same time and frequency for other time steps (e.g., see Fig. S4 for results obtained for a time step of 400 yr).

Moreover, we ran a spectrogram analysis in order to confirm our wavelet results and avoid any overinterpretation (see Fig. S5 and explicative caption). Unlike the wavelet, the spectrogram analysis is based on a finite time Fourier transform that spans different periods. Therefore, it provides an alternative base to check wavelet-based results. These tests confirmed the wavelet results for periods between 1 and 6 kyr. Beyond 6 kyr, wavelet results could not be confirmed by spectrograms due to the short duration of the analyzed

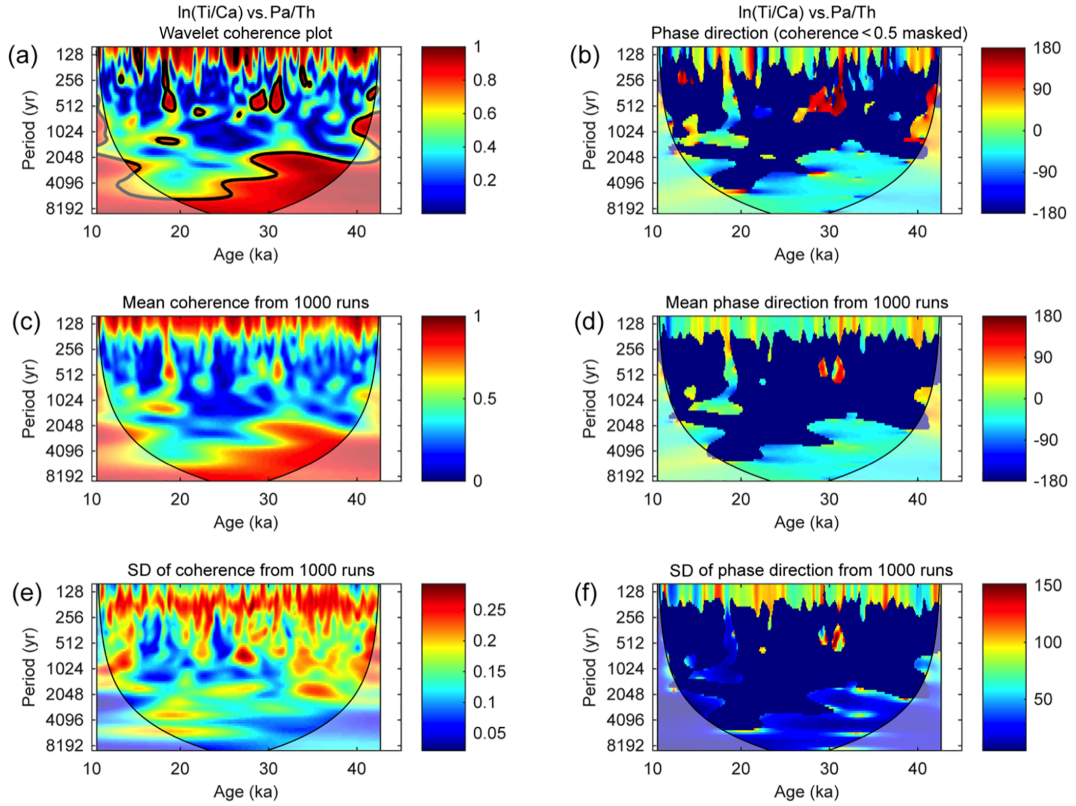

Figure 4. Cross-wavelet transform of MD09-3257 ln(Ti / Ca) versus Pa / Th. **(a, b)** Wavelet coherence and phase direction computed using Grinsted et al. (2004) software. The thick contour line corresponds to the 95 % confidence level against red noise. Phase direction is only computed for coherences higher than 0.5. **(c, d)** Mean coherence and phase direction computed from 1000 Monte Carlo simulations. **(e, f)** Standard deviation around the mean coherence and phase direction computed from these 1000 Monte Carlo simulations.

Table 1. Relative phases over regions of the cross-wavelet graphs corresponding to coherences > 0.5.

	Time interval	Period range	Perio-dicity	Phase (°)	1σ (°)	Phase (yr)	1σ (yr)	Comment
ln(Ti / Ca) vs. Pa / Th (Fig. 4)	28–40 ka*	1000–3000	2000	−46.7	25.2	−259	140	Pa / Th leads ln(Ti / Ca)
	15–40 ka*	4000–6000	5000	−45.4	24.8	−631	345	Pa / Th leads ln(Ti / Ca)
$\delta^{13}C_{Cw}$ vs. Pa / Th (Fig. 5)	28–40 ka	1000–3000	2000	−50.2	39.7	−279	244	Pa / Th leads $\delta^{13}C_{Cw}$
	15–40 ka	4000–6000	5000	−14.1	37.1	−196	525	Not significant
$\delta^{13}C_{Cw}$ vs. ln(Ti / Ca) (Fig. 6)	28–40 ka	1000–3000	2000	17	24.3	94	171	Not significant
	15–40 ka	4000–6000	5000	10.8	42.9	150	606	Not significant

* Within these time intervals, only results from the unshaded region of the wavelet graphs are taken into account.

records. Thus, we do not discuss periodicities longer than 6 kyr in what follows.

With this in mind, the following regions of significant mean coherence and well-defined mean relative phases can be identified in the cross-wavelet graphs between Pa / Th and ln(Ti / Ca) produced by 1000 Monte Carlo runs (Fig. 4, middle panels): a coherence higher than 0.5 is found for periodicities around 2000 yr (ranging from ∼ 1000 to 3000 yr) over the time interval from ∼ 28 to 40 ka, and for periodicities around 5000 yr (∼ 4000 to 6000 yr) over ∼ 25–40 ka. Computing the average phases over each of these two regions, we find that Pa / Th leads ln(Ti / Ca) by 259 ± 140 yr (1σ) for periodicities of 1000 to 3000 yr over 28–40 ka, and by 631 ± 345 yr (1σ) for periodicities of 4000 to 6000 yr over 15–40 ka (Table 1).

The cross-wavelet graph between $\delta^{13}C_{Cw}$ and Pa / Th displays slightly different regions of high mean coherence (Fig. 5, middle panels). Examining the same frequency bands as for Pa / Th versus ln(Ti / Ca), we find mean coherences higher than 0.5 for periodicities around 2000 yr over ∼ 28–

40 ka, and for periodicities around 5000 yr over ∼ 15–40 ka. Average phases for these regions indicate that $\delta^{13}C_{Cw}$ lags Pa / Th by 279 ± 244 yr (1σ) for periodicities of 1000 to 3000 yr over 28–40 ka, but that the lag of $\delta^{13}C_{Cw}$ with respect to Pa / Th for periodicities of 4000 to 6000 yr over ∼ 15–40 ka is not significant (Table 1).

Finally, the regions characterized by mean coherences higher than 0.5 between $\delta^{13}C_{Cw}$ and ln(Ti / Ca) are similar to those observed in the graph for Pa / Th and ln(Ti / Ca) (Fig. 6, middle panels). However, the average phases between $\delta^{13}C_{Cw}$ and ln(Ti / Ca) over these regions are not significantly different from zero (Fig. 6d and Table 1), indicating that decreases in $\delta^{13}C_{Cw}$ are in phase with increases in ln(Ti / Ca) within uncertainties.

The uncertainties of the leads and lags (Table 1) are computed assuming Gaussian error propagation of the two following independent uncertainties: (i) the standard deviation of the mean relative phases over the given time–frequency region (Figs. 4–6d), and (ii) the median value of the standard deviation computed by 1000 Monte Carlo runs over the same time–frequency region (Figs. 4–6f). In the case of relative phases between Pa / Th or ln(Ti / Ca) and $\delta^{13}C_{Cw}$, we also accounted for the additional error due to the combining of the MD09-3257 and GeoB3910-2 $\delta^{13}C_{Cw}$ records.

Finally, we applied the aforementioned cross-wavelet method to the subset of Pa / Th data points not affected by large particle fluxes. For the periodicities between ∼ 1000 and 4000 yr, the results obtained using this subset (Fig. S6) are virtually unchanged with respect to the results obtained using the entire dataset. For longer periodicities, coherence decreases as expected because the suppressed data points are all located in the main precipitation events (i.e., the YD and Heinrich stadials).

4 Discussion

4.1 Reconstructed ocean circulation changes over the last 45 kyr

Oceanographic studies have shown that the southward transport of northern-sourced waters in the equatorial Atlantic mainly takes place between a depth of ∼ 1300 and 4000 m in a ∼ 100 km wide Deep Western Boundary Current (DWBC) (Lux et al., 2001; Rhein et al., 2015). Using hydrographic, geochemical and direct velocity measurements acquired in 1993 to inverse an ocean circulation model, Lux et al. (2001) estimated that the volumetric flow of upper NADW occupying water depths between ∼ 1300 and 2300 m at 4.5° S within the DWBC is 11.2 Sv ($1\,\mathrm{Sv} = 10^6\,\mathrm{m^3\,s^{-1}}$). This estimate is in good agreement with the 10.9 Sv estimated by Schott et al. (2003) based on data from 13 shipboard current-profiling sections taken during the World Ocean Circulation Experiment period (1990–2002).

Our data show that outside of the main precipitation events, the total vertical particle flux did not vary much (remaining within $25.1 \pm 3.6\,\mathrm{g\,m^{-2}\,yr^{-1}}$, 1σ) (Fig. S2). The Pa / Th values of these interstadials are similar or slightly higher than those of the late Holocene (Fig. 2), suggesting that the transport of the water mass overlying the MD09-3257 core site was also ∼ 10 Sv during these interstadials.

It is more difficult to translate the observed increases in Pa / Th during stadials into quantified decreases in water mass transport. However, our new data bring additional observational constraints on the Atlantic circulation changes associated with last glacial millennial climate changes. Two recent studies have indicated that decreases in northern-sourced deep water flow took place during each stadial. On the one hand, increases in Pa / Th during each stadial of the last glacial have been observed at a very deep western North Atlantic site located at ∼ 42° N and a depth of 4500 m (Henry et al., 2016). On the other hand, reconstructions of water corrosiveness in a South Atlantic core located at ∼ 44° S and a depth of 3800 m indicate the absence of northern-sourced deep water at that site during stadials, whereas nearly all interstadials of the last 60 kyr are characterized by incursions of northern-sourced deep water into the deep South Atlantic (Gottschalk et al., 2015). Together with these independent results, our results indicate that decreases in both the flow rate and extension of northern-sourced deep waters during stadials were not limited to very dense waters circulating at 3800 m or deeper, but also affected water mass transport above 2350 m in the western equatorial Atlantic.

4.2 Relative timing of Pa / Th, $\delta^{13}C_{Cw}$ and Ti / Ca

4.2.1 Stationary cross-correlation versus cross-wavelet results

At the MD09-3257 site, cross-wavelet graphs (Figs. 4–6) show that significant coherence and well-defined relative phases between $\delta^{13}C_{Cw}$, Pa / Th and Ti / Ca can only be identified in some regions of the time–frequency space. For instance, when examining the relative phase between $\delta^{13}C_{Cw}$ and Pa / Th over the interval from 10 to 43 ka, a meaningful relative phase can only be identified over ∼ 28–40 ka at D–O frequencies (i.e., periodicities of 1000 to 3000 yr) (Fig. 5, Table 1). Furthermore, cross-wavelet results indicate that $\delta^{13}C_{Cw}$ lags Pa / Th by 279 ± 244 yr at D–O frequencies, and that decreases in $\delta^{13}C_{Cw}$ are in phase with increases in Pa / Th for periodicities of 4000 to 6000 yr (i.e., closer to Heinrich periodicities). This is in contrast with the constant 200 ± 100 lag of $\delta^{13}C_{Cw}$ with respect to Pa / Th obtained by cross-correlation between the two same time series (Fig. 3), and confirms that the latter method yields imprecise and unreliable results when applied to non-stationary climatic signals.

Nevertheless, cross-correlation has recently been applied to climatic signals (Langehaug et al., 2016), including Pa / Th and $\delta^{13}C_{Cw}$ records from the last glacial (Henry et al., 2016). In the latter study, cross-correlation between ma-

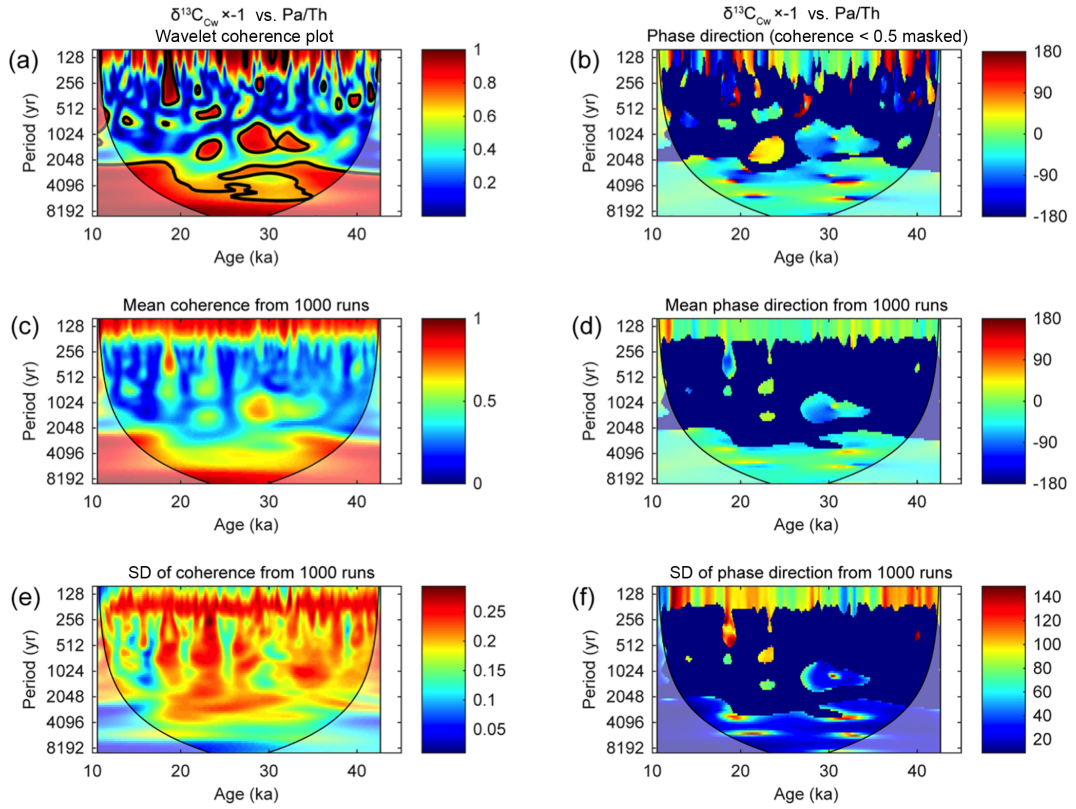

Figure 5. Cross-wavelet transform of $\delta^{13}C_{Cw}$ composite record versus MD09-3257 Pa / Th. $\delta^{13}C_{Cw}$ values have been multiplied by -1 to allow a straightforward reading of the relative phase between a decrease in $\delta^{13}C$ and an increase in Pa / Th. **(a)**–**(f)** as in Fig. 4.

rine records from two deep Bermuda Rise cores and the NGRIP ice oxygen isotopic record was used to infer that deep Bermuda Rise $\delta^{13}C_{Cw}$ led NGRIP by approximately two centuries, and that Pa / Th was approximately in phase with NGRIP over the interval from 25 to 60 ka (Henry et al., 2016). The authors further inferred that Pa / Th lags $\delta^{13}C_{Cw}$ by two centuries at their deep Bermuda Rise site. However, as shown here, cross-correlation is not a suitable method to analyze non-stationary climatic signals such as those of the last glacial. Moreover, the inferred relative phases between the marine and NGRIP records are much smaller than the dating error for each individual time series; therefore they are also much smaller than the relative dating error of one time series with respect to the other. In summary, the application of stationary cross-correlation techniques and incomplete consideration of geochronological uncertainty casts doubt on the conclusions of the aforementioned studies.

4.2.2 Lead of Pa / Th with respect to ln(Ti / Ca)

Our cross-wavelet results show that MD09-3257 Pa / Th leads ln(Ti / Ca) by 259 ± 140 yr (1σ) for periods of 1000 to 3000 yr during the $\sim$ 28–40 ka time interval, and by 631 ± 345 yr (1σ) for periods of 4000 to 6000 yr during $\sim$ 15–40 ka (Table 1). Periods of 1000 to 3000 yr correspond to pseudo-periodicities typical of D–O stadials, while periods of 4000 to 6000 yr are close to those of Heinrich stadials. It can be noted that the cross-wavelet results for D–O periodicities are only significant for the $\sim$ 28–40 ka time interval, which indeed corresponds to the interval of our records for which D–O events are best recorded.

It is important to examine if the observed relative phases could be an artifact due to bioturbation. It has been shown that smaller particles are more likely to be transported by bioturbation than larger particles (Wheatcroft, 1992; McCave, 1988; DeMaster and Cochran, 1982), and that this results in fine particles having apparent younger ages than coarse particles from the same depth in a core (Brown et al., 2001; Sepulcre et al., 2017).

Sedimentary Pa / Th is measured on bulk sediment samples, with dissolved Pa and Th being more readily adsorbed on small particles because of their higher surface to volume ratio (Chase et al., 2002). It has been shown that 50 %–90 % of ^{230}Th excess inventory is found in particles smaller than 10 µm (Kretschmer et al., 2010; Scholten et al., 1994; Thomson et al., 1993). Therefore, it is reasonable to assume that the Pa / Th signal is mostly carried by small particles (< 100 µm).

Assessing the size fraction corresponding to the Ti / Ca signal is more complicated. XRF measurements show that the marked changes in ln(Ti / Ca) recorded in MD09-3257

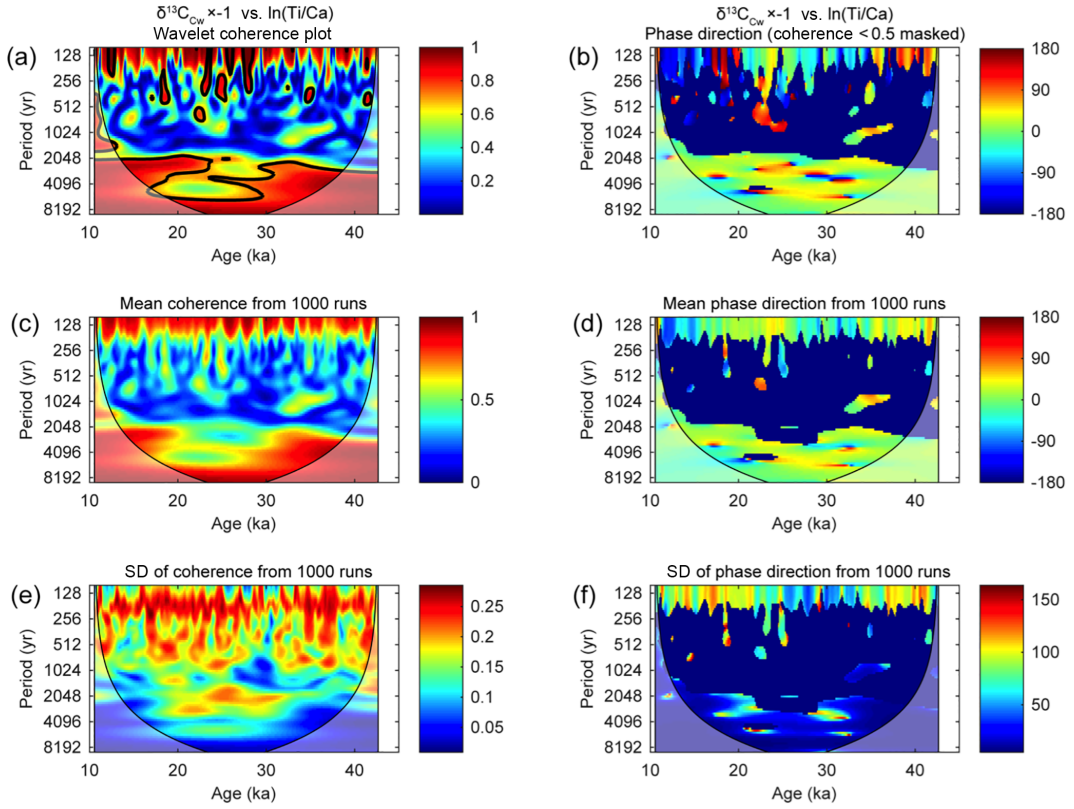

Figure 6. Cross-wavelet transform of $\delta^{13}C_{Cw}$ composite record versus MD09-3257 ln(Ti / Ca). $\delta^{13}C_{Cw}$ values have been multiplied by -1 to allow a straightforward reading of the relative phase between a decrease in $\delta^{13}C$ and an increase in ln(Ti / Ca). **(a–f)** as in Figs. 4 and 5.

result from sharp changes in both Ca and Ti concentration in the sediment. Ca is a component of marine calcite and aragonite, and is thus mainly carried by large size fractions of the sediment (> 60 µm). However, previous studies have shown that changes in marine carbonate production and dissolution between 2000 and 3000 m in the western tropical Atlantic were relatively small over the last glacial (Rühlemann et al., 1996; Gerhardt et al., 2000). Therefore, the sharp decreases in Ca concentration during stadials result from the dilution of marine carbonates by the increased input of terrigenous material. Therefore, the ln(Ti / Ca) is driven by changes in terrigenous input, rather than changes in marine carbonate production or dissolution. It is difficult to assess in which particle size fraction Ti is mostly concentrated. Knowing that Rb and K are typical constituents of clays, and thus characteristic of small grain sizes, we verified if a phase shift could be detected between the XRF Ti signal and the XRF Rb and K signals. We found no relative offset between Ti and Rb and almost no relative offset between Ti and K, with the inflexion point in the K signal taking place 0.05 cm deeper than in the Ti signal. Given that core MD09-3257 sedimentation rates range from 6 to 14 cm kyr^{-1}, 0.05 cm corresponds to 5 to 10 yr; thus, it is completely negligible with respect to the observed phase shifts between ln(Ti / Ca) and Pa / Th. Therefore, we may consider that ln(Ti / Ca) and Pa / Th are both carried by small particles and that the observed phase shifts between these two signals are not the result of bioturbation.

Finally, if, against all likelihood, bioturbation were responsible for a lead of Pa / Th with respect to ln(Ti / Ca), such a lead would be independent of the examined periodicity. Therefore, we may reasonably assume that the observed lead of Pa / Th with respect to ln (Ti / Ca) is not an artifact resulting from bioturbation.

We compute a 631 ± 345 yr (1σ) lead for Pa / Th over ln(Ti / Ca) by cross-wavelet analysis for frequencies close to those characterizing Heinrich stadials. This lead is comparable to the relative phase previously estimated between MD09-3257 Pa / Th and Ti / Ca at the onset of HS4 (690 ± 180 yr) and HS2 (1420 ± 250 yr), respectively, based on the identification of the transition in the Pa / Th and Ti / Ca signals at the beginning of these two stadials (Burckel et al., 2015). The large lead of Pa / Th with respect to ln(Ti / Ca) is clearly visible for the YD and all Heinrich stadials, except HS1 (Fig. 2). The apparent synchronicity of the Pa / Th and ln(Ti / Ca) signals at the onset of HS1 in core MD09-3257, as also recently observed in another core from the northern Brazilian margin (Mulitza et al., 2017), suggests that the sequence of events was different at the beginning of HS1 from those at the beginning of the YD and other Heinrich stadials. Such a different sequence of events seems to indicate that

the increase in rainfall over tropical South America during HS1 was not a response to a decrease in Atlantic overturning circulation. Instead, a southward shift of the low-latitude atmospheric convection zone (Intertropical Convergence Zone, ITCZ), along with its associated maximum in precipitation, could have occurred in response to extended Northern Hemisphere ice sheets and sea ice cover without any change in ocean circulation (Chiang et al., 2003). This atmospheric mechanism would have prevailed at the beginning of HS1 because ice sheets reached their maximum extent around that time.

Our results also indicate that a significant lead of Pa / Th with respect to ln(Ti / Ca) is present at D–O frequencies. Moreover, the lead of Pa / Th with respect to ln(Ti / Ca) is markedly shorter at D–O frequencies (259 ± 140 yr) than at Heinrich frequencies (631 ± 345 yr).

Climate models simulate a southward shift of the ITCZ in response to a slowdown of the Atlantic meridional overturning circulation (AMOC), but after just a few years (Dong and Sutton, 2002). In contrast, our results indicate that rainfall increases in the region adjacent to MD09-3257 occurred several hundred years after the increase in sedimentary Pa / Th at our core site. Furthermore, this lead of sedimentary Pa / Th over ln(Ti / Ca) should be taken as a minimum lead of AMOC over ln(Ti / Ca) because a change in AMOC does not instantaneously translate into a change in sedimentary Pa / Th. A delay between a change in AMOC and the resulting change in sedimentary Pa / Th is indeed expected, which depends on the propagation time of the circulation change to the core site and on the response time of dissolved Th and Pa in the water column overlying the core site (i.e., 30–40 for ^{230}Th and 100–200 yr for ^{231}Pa, François, 2007). However, increases or decreases in sedimentary Pa / Th should be measurable before the dissolved Th and Pa have fully adjusted to the new circulation regime, especially at sites with high sedimentation rates such as our study site. Thus, we expect this additional delay to be less than 100 yr and much smaller than the computed lead of MD09-3257 sedimentary Pa / Th over ln(Ti / Ca).

A mechanism has been proposed by Burckel et al. (2015) to explain the large lead of AMOC slowdowns during Heinrich and D–O stadials with respect to precipitation events over tropical South America. In this scenario, AMOC slowdowns are progressively amplified through a positive feedback linking the decrease in deep water formation to subsurface warming at high northern latitudes (Mignot et al., 2007; Alvarez-Solas et al., 2013), leading in the case of Heinrich stadials, to erosion of ice shelves and iceberg discharges, which in turn reinforce the initial AMOC slowdown. In contrast, AMOC slowdowns associated with D–O stadials would not trigger such a positive feedback loop and would consequently remain limited.

Alternatively, or in addition to an actual lead of the changes in AMOC with respect to precipitation events over tropical South America, another factor could induce a lead of Pa / Th with respect to ln(Ti / Ca) in core MD09-3257. It has been shown that the North Brazil Current (NBC) is able to transport terrigenous material laterally (Allison et al., 2000). Also, different studies have shown that a weakening of the AMOC is associated with a decrease of NBC transport, taking place not only on decadal timescales (Zhang et al., 2011), but also during the YD and HS1 (Arz et al., 1999; Wilson et al., 2011). Based on this evidence, a recent study suggested that a reduced NBC during HS1 allowed the enhanced input of terrigenous material to settle on the continental margin offshore of northeastern Brazil, instead of being transported northward (Zhang et al., 2015). Thus, it seems possible that terrestrial input would be deviated northward as long as the NBC was vigorous and reached the core site only once the NBC and AMOC were sufficiently reduced, thereby yielding a time-delayed peak in ln(Ti / Ca). If this were the case, the lag of the terrestrial input signal with respect to the Pa / Th signal would be partially or totally caused by the impact of the NBC on terrigenous material deposition (Zhang et al., 2015). Therefore, the exceptional synchronicity of the onset of terrigenous influx and AMOC slowdown at the beginning of HS1 could be due to the exceptionally large fluxes of large grain size material eroded from the proximal exposed shelf during low eustatic sea level, which would have rained down through the water column, even before full reduction of the NBC.

However, in the absence of direct measurements of the NBC velocity and vertical particle flux on the northeastern Brazilian margin, the actual delay of terrestrial input with respect to NBC slowdown remains speculative.

4.2.3 Lag of $\delta^{13}C_{Cw}$ with respect to Pa / Th

Our cross-wavelet results show that $\delta^{13}C_{Cw}$ lags Pa / Th by 279 ± 244 yr (1σ) at D–O frequencies over $\sim$ 28–40 ka at the MD09-3257 site (Table 1).

$\delta^{13}C_{Cw}$ is measured using > 150 µm foraminifera; thus, it is carried by much larger particles than the Pa / Th signal. Therefore, differential bioturbation mixing processes would lead to Pa / Th being carried by sediment material younger than the epibenthic foraminifera sampled within the same depth interval. Thus, bioturbation may induce an artificial lead of Pa / Th with respect to $\delta^{13}C_{Cw}$. Knowing that the sedimentation rates of MD09-3257 and GeoB3910-2 vary between 6 and 14 cm over the interval from 28 to 40 ka, a 280 yr lead translates to a downward shift of 2 to 4 cm in the sediment column, which seems plausible for the effect of differential bioturbation.

In conclusion, the lag of $\delta^{13}C_{Cw}$ with respect to Pa / Th at D–O frequencies during $\sim$ 28–40 ka is likely an artifact resulting from the differential bioturbation of fine and coarse particles. The same differential bioturbation processes likely also affect the relative phase between $\delta^{13}C_{Cw}$ and ln (Ti / Ca). Thus, we will not discuss the results of the cross-wavelet analyses involving $\delta^{13}C_{Cw}$ any further.

5 Conclusions

New sedimentary Pa / Th data from core MD09-3257 located on the northern Brazilian margin (∼ 4° S, 36° W) at a depth of ∼ 2350 m indicate decreases in water mass transport above the core site during all Greenland stadials of the last 45 kyr. Together with two other recent studies (Gottschalk et al., 2015; Henry et al., 2016), these results demonstrate that all stadials of the last 45 kyr were not only characterized by decreases in flow rate and extension of northern-sourced waters below a depth of 3800 m, but also by decreases in mid-depth water mass transport in the western equatorial Atlantic.

Due to its exceptional location, core MD09-3257 records both ocean circulation and atmospheric changes. Ocean circulation changes induce changes in sedimentary Pa / Th and $\delta^{13}C_{Cw}$, whereas changes in precipitation over the adjacent continent induce changes in marine sediments Ti / Ca.

Using cross-wavelet transforms and spectrogram analysis, we were able to precisely and robustly assess the relative phase between MD09-3257 sedimentary Pa / Th and ln(Ti / Ca) signals over the interval from 10 to 43 ka with minimal uncertainty. This is owing to the fact that both signals are recorded in the same sediment core. We show that Pa / Th leads ln(Ti / Ca) by 259 ± 140 yr (1σ) at D–O frequencies over 28–40 ka, and by 631 ± 345 yr (1σ) for periodicities close to Heinrich periodicities (4000 to 6000 yr) over 15–40 ka.

In other words, our cross-wavelet transforms and spectrogram analysis results show that changes in water mass transport between a depth of ∼ 1300 and 2300 m in the western equatorial Atlantic (i.e., within a ∼ 1000 m water layer above MD09-3257 core site) preceded changes in precipitation over the adjacent continent by 110 to 400 yr at D–O frequencies, and by 280 to 980 yr at Heinrich-like frequencies.

We suggest that the large lead of ocean circulation changes with respect to tropical South American precipitation changes at Heinrich-like and D–O frequencies is likely related to the action of a positive feedback in the case of Heinrich stadials, in agreement with Burckel et al. (2015). In that case, an AMOC slowdown would lead to subsurface warming at high northern latitudes, inducing ice-sheet calving and iceberg discharges that would in turn reinforce the initial AMOC slowdown. In contrast, the absence of marked ice rafted detritus layers in North Atlantic sediments during D–O stadials suggests that in the case of D–O stadials, AMOC slowdowns did not trigger such a positive feedback and, consequently, remained limited (Burckel et al., 2015).

Finally, the relative lead of Pa / Th over ln(Ti / Ca) is visible for the YD and for all Heinrich stadials, except HS1. In the case of HS1, the southward shift of the ITCZ may have been an atmospheric response to the maximum extent in northern high-latitude ice sheets and sea ice cover (Chiang et al., 2003) around that time, rather than a progressive response to a slowdown of the AMOC, as is the case for the other stadials. These different atmospheric and oceanic scenarios remain to be tested by numerical experiments performed over several thousands of years in glacial conditions, whereby climate models compute water and calcite $\delta^{18}O$, DIC $\delta^{13}C$ and sedimentary Pa / Th.

Data availability. Data related to this article are available as a Supplement file and on Pangaea.

The Supplement related to this article is available online at https://doi.org/10.5194/cp-14-1315-2018-supplement.

Author contributions. CW and SP designed the research. EB, PB, JL, FT and AD performed the sedimentary Pa / Th measurements. BCL performed the wavelet analyses. DF and LV contributed expert advice on statistical results and performed the spectrogram analyses. LM produced the sedimentary Pa / Th values and error bars from MC-ICP-MS output. NVR improved the age models of the two cores. CW, NVR and TD participated in the 2009 RETRO coring cruise. HWA contributed expert knowledge on the Brazilian margin. CW and TD obtained funding. CW and BL wrote the manuscript.

Competing interests. The authors declare that they have no conflict of interest.

Acknowledgements. This is a contribution to the ACCLIMATE ERC project; the research leading to these results has received funding from the European Research Council under the European Union's Seventh Framework Programme (FP7/2007-2013)/ERC grant agreement no. 339108. Core MD09-3257 was collected on board R/V *Marion Dufresne* during the 2009 RETRO coring cruise, supported by IPEV, ANR project ANR-09-BLAN-0347 and the ESF EUROMARC project "RETRO". We thank the IPEV team, crew members of R/V *Marion Dufresne* and all scientists who participated in the 2009 RETRO cruise. We also thank Matthieu Roy-Barman for advice regarding Pa / Th measurements from the LSCE MC-ICP-MS. We acknowledge Vincent Scao and Jørund Strømsøe for XRF measurements, Christophe Moreau, Jean-Pascal Dumoulin, and the UMS ARTEMIS for AMS ^{14}C dates, as well as Gülay Isguder, Lucile Mauclair and Fabien Dewilde for invaluable technical assistance. We are grateful to Roger François and one anonymous reviewer for their helpful comments on an earlier version of this article. This paper is LSCE contribution 6408.

Edited by: Luc Beaufort
Reviewed by: Roger Francois and one anonymous referee

References

Allison, M. A., Lee, M. T., Ogston, A. S., and Aller, R. C.: Origin of Amazon mudbanks along the northeastern coast of South America, Mar. Geol., 163, 241–256, 2000.

Alvarez-Solas, J., Robinson, A., Montoya, M., and Ritz, C.: Iceberg discharges of the last glacial period driven by oceanic circulation changes, P. Natl. Acad. Sci. USA, 110, 16350–16354, https://doi.org/10.1073/pnas.1306622110, 2013.

Anderson, R., Fleisher, M., and Lao, Y.: Glacial–interglacial variability in the delivery of dust to the central equatorial Pacific Ocean, Earth Planet. Sc. Lett., 242, 406–414, 2006.

Arz, H. W., Pätzold, J., and Wefer, G.: Correlated Millennial-Scale Changes in Surface Hydrography and Terrigenous Sediment Yield Inferred from Last-Glacial Marine Deposits off Northeastern Brazil, Quaternary Res., 50, 157–166, 1998.

Arz, H. W., Pätzold, J., and Wefer, G.: The deglacial history of the western tropical Atlantic as inferred from high resolution stable isotope records off northeastern Brazil, Earth Planet. Sc. Lett., 167, 105–117, 1999.

Arz, H. W., Gerhardt, S., Pätzold, J., and Röhl, U.: Millennial-scale changes of surface- and deep-water flow in the western tropical Atlantic linked to Northern Hemisphere high-latitude climate during the Holocene, Geology, 29, 239–242, 2001.

Bourillet, J.-F., Damy, G., Dussud, L., Sultan, N., Woerther, P., and Migeon, S.: Behaviour Of A Piston Corer From Accelerometers And New Insights On Quality Of The Recovery., Proc. 6th Int. Off shore Site Investig, Geotech. Conf., Confronting New Challenges Shar, Knowledge, 11–13 September 2007, London, UK, available at: http://archimer.ifremer.fr/doc/00071/18198/ (last access: 14 September 2018), 2007.

Bronk Ramsey, C.: Deposition models for chronological records, Quaternary Sci. Rev., 27, 42–60, 2008.

Brown, L., Cook, G. T., MacKenzie, A. B., and Thomson, J.: Radiocarbon age profiles and size dependency of mixing in northeast Atlantic sediments, Radiocarbon, 43, 929–937, 2001.

Burckel, P., Waelbroeck, C., Gherardi, J.-M., Pichat, S., Arz, H., Lippold, J., Dokken, T., and Thil, F.: Atlantic Ocean circulation changes preceded millennial tropical South America rainfall events during the last glacial, Geophys. Res. Lett., 42, 411–418, 2015.

Chase, Z., Anderson, R. F., Fleisher, M. Q., and Kubik, P. W.: The influence of particle composition and particle flux on scavenging of Th, Pa and Be in the ocean, Earth Planet. Sc. Lett., 204, 215–229, 2002.

Cheng, H., Sinha, A., Cruz, F. W., Wang, X., Edwards, R. L., d'Horta, F. M., Ribas, C. C., Vuille, M., Stott, L. D., and Auler, A. S.: Climate change patterns in Amazonia and biodiversity, Nat. Commun., 4, 1411–1417, https://doi.org/10.1038/ncomms2415, 2013.

Chiang, J. C. H., Biasutti, M., and Battisti, D. S.: Sensitivity of the Atlantic Intertropical Convergence Zone to Last Glacial Maximum boundary conditions, Paleoceanography, 18, 1–18, https://doi.org/10.1029/2003PA000916, 2003.

Croudace, I. W. and Rothwell, R. G. (Eds.): Micro-XRF Studies of Sediment Cores: Applications of a non-destructive tool for the environmental sciences, Dev. in Paleoenviron. Res., Springer, 17, 656 pp., 2015.

Davis, J. C.: Statistics and data analysis in geology, J. Wiley, New York, 646 pp., 1986.

DeMaster, D. J. and Cochran, J. K.: Particle mixing rates in deep-sea sediments determined from excess ^{210}Pb and ^{32}Si profiles, Earth Planet. Sc. Lett., 61, 257–271, 1982.

Dong, B. W. and Sutton, R.: Adjustment of the coupled ocean–atmosphere system to a sudden change in the thermohaline circulation, Geophys. Res. Lett., 29, 18-1–18-4, 2002.

Duplessy, J.-C., Shackleton, N. J., Matthews, R. K., Prell, W., Ruddiman, W. F., Caralp, M., and Hendy, C. H.: ^{13}C record of benthic foraminifera in the last interglacial ocean: implications for the carbon cycle and the global deep water circulation, Quaternary Res., 21, 225–243, 1984.

Duplessy, J.-C., Shackleton, N. J., Fairbanks, R. G., Labeyrie, L., Oppo, D., and Kallel, N.: Deepwater source variations during the last climatic cycle and their impact on the global deepwater circulation, Paleoceanography, 3, 343–360, 1988.

Eide, M., Olsen, A., Ninnemann, U. S., and Johannessen, T.: A global ocean climatology of preindustrial and modern ocean δ^{13}C, Global Biogeochem. Cy., 31, 515–534, 2017.

François, R.: Chapter Sixteen Paleoflux and Paleocirculation from Sediment ^{230}Th and ^{231}Pa / ^{230}Th, Dev. Mar. Geol., 1, 681–716, 2007. s

François, R., Frank, M., Rutgers van der Loeff, M. M., and Bacon, M. P.: ^{230}Th normalization: An essential tool for interpreting sedimentary fluxes during the late Quaternary, Paleoceanography, 19, 1–16, 2004.

Freeman, E., Skinner, L. C., Waelbroeck, C., and Hodell, D.: Radiocarbon evidence for enhanced respired carbon storage in the Atlantic at the Last Glacial Maximum, Nat. Commun., 7, 1–8, https://doi.org/10.1038/ncomms11998, 2016.

Gerhardt, S., Groth, H., Rühlemann, C., and Henrich, R.: Aragonite preservation in late Quaternary sediment cores on the Brazilian Continental Slope: implications for intermediate water circulation, Int. J. Earth Sci., 88, 607–618, 2000.

Gottschalk, J., Skinner, L. C., Misra, S., Waelbroeck, C., Menviel, L., and Timmermann, A.: Abrupt changes in the southern extent of North Atlantic Deep Water during Dansgaard–Oeschger events, Nat. Geosci., 8, 950–954, https://doi.org/10.1038/ngeo2558, 2015.

Grinsted, A., Moore, J. C., and Jevrejeva, S.: Application of the cross wavelet transform and wavelet coherence to geophysical time series, Non. Proc. Geophys., 11, 561–566, 2004.

Guihou, A., Pichat, S., Nave, S., Govin, A., Labeyrie, L., Michel, E., and Waelbroeck, C.: Late slowdown of the Atlantic Meridional Overturning Circulation during the Last Glacial Inception: new constraints from sedimentary (^{231}Pa / ^{2303}Th), Earth Planet. Sc. Lett., 289, 520–529, 2010.

Heil, G.: Abrupt climate shifts in the western tropical to subtropical Atlanic region during the last glacial, PhD Thesis, Bremen University, 121 pp., 2006.

Henderson, G. M. and Anderson, R. F.: The U-series toolbox for paleoceanography, Rev. Mineral. Geochem., 52, 493–531, 2003.

Henry, L., McManus, J. F., Curry, W. B., Roberts, N. L., Piotrowski, A. M., and Keigwin, L. D.: North Atlantic ocean circulation and abrupt climate change during the last glaciation, Science, 353, 470–474, 2016.

Jaeschke, A., Rühlemann, C., Arz, H., Heil, G., and Lohmann, G.: Coupling of millennial-scale changes in sea surface temperature

and precipitation off northeastern Brazil with high-latitude climate shifts during the last glacial period, Paleoceanography, 22, PA4206, https://doi.org/10.1029/2006PA001391, 2007.

Johnsen, S., Clausen, H. B., Dansgaard, W., Fuhrer, K., Gundestrup, N., Hammer, C. U., Iversen, P., Jouzel, J., and Stauffer, B.: Irregular glacial interstadials recorded in a new Greenland ice core, Nature, 359, 311–313, 1992.

Key, R. M., Kozyr, A., Sabine, C. L., Lee, K., Wanninkhof, R., Bullister, J. L., Feely, R. A., Millero, F. J., Mordy, C., and Peng, T. H.: A global ocean carbon climatology: Results from Global Data Analysis Project (GLODAP), Global Biogeochem. Cy., 18, 1–23, 2004.

Kindler, P., Guillevic, M., Baumgartner, M., Schwander, J., Landais, A., and Leuenberger, M.: Temperature reconstruction from 10 to 120 kyr b2k from the NGRIP ice core, Clim. Past, 10, 887–902, https://doi.org/10.5194/cp-10-887-2014, 2014.

Kretschmer, S., Geibert, W., van der Loeff, M. M. R., and Mollenhauer, G.: Grain size effects on ^{230}Th xs inventories in opal-rich and carbonate-rich marine sediments, Earth Planet. Sc. Lett., 294, 131–142, 2010.

Langehaug, H., Mjell, T., Otterå, O., Eldevik, T., Ninnemann, U., and Kleiven, H.: On the reconstruction of ocean circulation and climate based on the "Gardar Drift", Paleoceanography, 31, 399–415, 2016.

Lippold, J., Gherardi, J.-M., and Luo, Y.: Testing the ^{231}PA / ^{230}Th paleocirculation proxy: A data versus 2D model comparison, Geophys. Res. Lett., 38, 1–7, https://doi.org/10.1029/2011GL049282, 2011.

Lippold, J., Mulitza, S., Mollenhauer, G., Weyer, S., Heslop, D., and Christl, M.: Boundary scavenging at the East Atlantic margin does not negate use of ^{231}PA / ^{230}Th to trace Atlantic overturning, Earth Planet. Sc. Lett., 333, 317–331, 2012.

Lougheed, B. C., Metcalfe, B., Ninnemann, U. S., and Wacker, L.: Moving beyond the age–depth model paradigm in deep-sea palaeoclimate archives: dual radiocarbon and stable isotope analysis on single foraminifera, Clim. Past, 14, 515–526, https://doi.org/10.5194/cp-14-515-2018, 2018.

Luo, Y., Francois, R., and Allen, S. E.: Sediment ^{231}PA / ^{230}Th as a recorder of the rate of the Atlantic meridional overturning circulation: insights from a 2-D model, Ocean Sci., 6, 381–400, https://doi.org/10.5194/os-6-381-2010, 2010.

Lux, M., Mercier, H., and Arhan, M.: Interhemispheric exchanges of mass and heat in the Atlantic Ocean in January–March 1993, Deep-Sea Res. Pt. I, 48, 605–638, 2001.

Lynch-Stieglitz, J., Stocker, T., Broecker, W. S., and Fairbanks, R. G.: The influence of air-sea exchange on the isotopic composition of oceanic carbon: Observations and modeling, Global Biogeochem. Cy., 9, 653–665, 1995.

McCave, I.: Biological pumping upwards of the coarse fraction of deep-sea sediments, J. Sediment. Res., 58, 148–158, 1988.

Mignot, J., Ganopolski, A., and Levermann, A.: Atlantic subsurface temperatures: Response to a shutdown of the overturning circulation and consequences for its recovery, J. Clim., 20, 4884–4898, 2007.

Milliman, J. D., Summerhayes, C. P., and Barretto, H. T.: Quaternary sedimentation on the Amazon continental margin: a model, Geol. Soc. Am. Bull., 86, 610–614, 1975.

Missiaen, L., Pichat, S., Waelbroeck, C., Douville, E., Bordier, L., Dapoigny, A., Thil, F., Foliot, L., and Wacker, L.: Downcore variations of sedimentary detrital (^{238}U / ^{232}Th) ratio: implications on the use of ^{230}Thxs and ^{231}Paxs to reconstruct sediment flux and ocean circulation, Geochem. Geophy. Geosy., 19, 1–14, https://doi.org/10.1029/2017GC007410, 2018

Mulitza, S., Chiessi, C. M., Schefuß, E., Lippold, J., Wichmann, D., Antz, B., Mackensen, A., Paul, A., Prange, M., and Rehfeld, K.: Synchronous and proportional deglacial changes in Atlantic Meridional Overturning and northeast Brazilian precipitation, Paleoceanography, 32, 622–633, 2017.

Rasmussen, S. O., Bigler, M., Blockley, S. P., Blunier, T., Buchardt, S. L., Clausen, H. B., Cvijanovic, I., Dahl-Jensen, D., Johnsen, S. J., and Fischer, H.: A stratigraphic framework for abrupt climatic changes during the Last Glacial period based on three synchronized Greenland ice-core records: refining and extending the INTIMATE event stratigraphy, Quaternary Sci. Rev., 106, 14–28, 2014.

Reimer, P., Bard, E., Bayliss, A., Beck, J. W., Blackwell, P. G., Bronk Ramsey, C., Buck, C. E., Cheng, H., Edwards, R. L., Friedrich, M., Grootes, P. M., Guilderson, T. P., Haflidason, H., Hajdas, I., Hatté, C., Heaton T. J., Hoffmann, D. L., Hogg, A. G., Hughen, K. A., Kaiser, K. F., Kromer, B., Manning, S. W., Niu, M., Reimer, R. W., Richards, D. A., Scott, E. M., Southon, J. R., Staff, R. A., Turney, C. S. M., and van der Plicht, J.: IntCal13 and Marine13 radiocarbon age calibration curves 0–50,000 years cal BP, Radiocarbon, 55, 1869–1887, 2013.

Rhein, M., Kieke, D., and Steinfeldt, R.: Advection of North Atlantic Deep Water from the Labrador Sea to the southern hemisphere, J. Geophys. Res.-Ocean., 120, 2471–2487, 2015.

Rühlemann, C., Frank, M., Hale, W., Mangini, A., Mulitza, S., Müller, P., and Wefer, G.: Late Quaternary productivity changes in the western equatorial Atlantic: Evidence from ^{230}Th-normalized carbonate and organic carbon accumulation rates, Mar. Geol., 135, 127–152, 1996.

Schmittner, A., Bostock, H. C., Cartapanis, O., Curry, W. B., Filipsson, H. L., Galbraith, E. D., Gottschalk, J., Herguera, J. C., Hoogakker, B., Jaccard, S. L., Lisiecki, L. E., Lund, D. C., Martínez-Méndez, G., Lynch-Stieglitz, J., Mackensen, A., Michel, E., Mix, A. C., Oppo, D. W., Peterson, C. D., Repschläger, J., Sikes, E. L., Spero, H. J., and Waelbroeck, C.: Calibration of the carbon isotope composition (δ^{13}C) of benthic foraminifera, Paleoceanography, 32, 512–530, https://doi.org/10.1002/2016PA003072, 2017.

Scholten, J., Botz, R., Paetsch, H., and Stoffers, P.: 230Thex flux into Norwegian-Greenland Sea sediments: Evidence for lateral sediment transport during the past 300,000 years, Earth Planet. Sc. Lett., 121, 111–124, 1994.

Schott, F. A., Dengler, M., Brandt, P., Affler, K., Fischer, J., Bourles, B., Gouriou, Y., Molinari, R. L., and Rhein, M.: The zonal currents and transports at 35 W in the tropical Atlantic, Geophys. Res. Lett., 30, 1–4, 2003.

Sepulcre, S., Durand, N., and Bard, E.: Large ^{14}C age offsets between the fine fraction and coexisting planktonic foraminifera in shallow Caribbean sediments, Quaternary Geochronol., 38, 61–74, 2017.

Taylor, S. and McLennan, S.: The continental crust: its composition and evolution, Oxford, Blackwell Press, 312 pp., 1985.

Thomas, A. L., Henderson, G. M., and Robinson, L. F.: Interpretation of the ^{231}Pa / ^{230}Th paleocirculation proxy: New water-

column measurements from the southwest Indian Ocean, Earth Planet. Sc. Lett., 241, 493–504, 2006.

Thomson, J., Colley, S., Anderson, R., Cook, G., MacKenzie, A., and Harkness, D.: Holocene sediment fluxes in the northeast Atlantic from ^{230}Thexcess and radiocarbon measurements, Paleoceanography, 8, 631–650, 1993.

Thornalley, D. J. R., Barker, S., Broecker, W. S., Elderfield, H., and McCave, I. N.: The Deglacial Evolution of North Atlantic Deep Convection, Science, 331, 202–205, 2011.

Torrence, C. and Compo, G. P.: A practical guide to wavelet analysis, B. Am. Meteorol. Soc., 79, 61–78, 1998.

Torrence, C. and Webster, P. J.: Interdecadal changes in the ENSO–monsoon system, J. Clim., 12, 2679–2690, 1999.

Vazquez Riveiros, N., Waelbroeck, C., Roche, D. M., Moreira, S., Burckel, P., Dewilde, F., Skinner, L., Böhm, E., Arz, H. W., and Dokken, T.: Northern origin of western tropical Atlantic deep waters during Heinrich Stadials, submitted, 2018.

Vidal, L., Labeyrie, L., Cortijo, E., Arnold, M., Duplessy, J. C., Michel, E., Becqué, S., and van Weering, T. C. E.: Evidence for changes in the North Atlantic Deep Water linked to meltwater surges during the Heinrich events, Earth Planet. Sc. Lett., 146, 13–26, 1997.

Waelbroeck, C., Duplessy, J.-C., Michel, E., Labeyrie, L., Paillard, D., and Duprat, J.: The timing of the last deglaciation in North Atlantic climate records, Nature, 412, 724–727, 2001.

Weltje, G. J. and Tjallingii, R.: Calibration of XRF core scanners for quantitative geochemical logging of sediment cores: theory and application, Earth Planet. Sc. Lett., 274, 423–438, 2008.

Wheatcroft, R. A.: Experimental tests for particule size-dependent bioturbation in the deep ocean, Limnol. Oceanogr., 37, 90–104, 1992.

Wilson, K. E., Maslin, M. A., and Burns, S. J.: Evidence for a prolonged retroflection of the North Brazil Current during glacial stages, Palaeogeogr. Palaeocl., 301, 86–96, 2011.

Woerther, P. and Bourillet, J. F.: Exploitation des mesures faites avec les accéléromètres sur le carottier CAPYPSO-Mission SEDICAR4-ALIENOR, Ifremer, Brest, 47 pp., 2005.

Yu, E.-F., François, R., and Bacon, M.: Similar rates of modern and last-glacial ocean thermohaline circulation inferred from radiochemical data, Nature, 379, 689–694, 1996.

Zahn, R., Winn, K., and Sarnthein, M.: Benthic foraminiferal δ^{13}C and accumulation rates of organic carbon: Uvigerina peregrina group and Cibicidoides wuellerstorfi, Paleoceanography, 1, 27–42, 1986.

Zhang, D., Msadek, R., McPhaden, M. J., and Delworth, T.: Multi-decadal variability of the North Brazil Current and its connection to the Atlantic meridional overturning circulation, J. Geophys. Res.-Ocean., 116, 1–9, 2011.

Zhang, Y., Chiessi, C. M., Mulitza, S., Zabel, M., Trindade, R. I., Hollanda, M. H. B., Dantas, E. L., Govin, A., Tiedemann, R., and Wefer, G.: Origin of increased terrigenous supply to the NE South American continental margin during Heinrich Stadial 1 and the Younger Dryas, Earth Planet. Sc. Lett., 432, 493–500, 2015.

Bibliography

Adkins, J. F. & Boyle, E. A. 1997 Changing atmospheric δ14c and the record of deep water paleoventilation ages. *Paleoceanography* **12**, 337–344.

Adkins, J. F., Boyle, E. A., Keigwin, L., & Cortijo, E. 1997 Variability of the north atlantic thermohaline circulation during the last interglacial period. *Nature* **390**, 154.

Andersen, K. K., Svensson, A., Johnsen, S. J., Rasmussen, S. O., Bigler, M., Röthlisberger, R., Ruth, U., Siggaard-Andersen, M.-L., Steffensen, J. P., Dahl-Jensen, D., & others 2006 The greenland ice core chronology 2005, 15–42ka. part 1: Constructing the time scale. *Quaternary Science Reviews* **25**, 3246–3257.

Argus, D. F., Peltier, W., Drummond, R., & Moore, A. W. 2014 The antarctica component of postglacial rebound model ice-6g_c (vm5a) based on gps positioning, exposure age dating of ice thicknesses, and relative sea level histories. *Geophysical Journal International* **198**, 537–563.

Austin, W. E. & Hibbert, F. D. 2012 Tracing time in the ocean: a brief review of chronological constraints (60–8 kyr) on north atlantic marine event-based stratigraphies. *Quaternary Science Reviews* **36**, 28–37.

Bacon, M. 1988 Tracers of chemical scavenging in the ocean: boundary effects and large-scale chemical fractionation. *Phil. Trans. R. Soc. Lond. A* **325**, 147–160.

Bacon, M. P. 1984 Glacial to interglacial changes in carbonate and clay sedimentation in the atlantic ocean estimated from 230th measurements. *Chemical geology* **46**, 97–111.

Bacon, M. P. & Anderson, R. F. 1982 Distribution of thorium isotopes between dissolved and particulate forms in the deep sea. *Journal of Geophysical Research: Oceans* **87**, 2045–2056.

Bard, E., Rostek, F., Turon, J.-L., & Gendreau, S. 2000 Hydrological impact of heinrich events in the subtropical northeast atlantic. *Science* **289**, 1321–1324.

Barker, S., Chen, J., Gong, X., Jonkers, L., Knorr, G., & Thornalley, D. 2015 Icebergs not the trigger for north atlantic cold events. *Nature* **520**, 333.

Blaser, P., Lippold, J., Gutjahr, M., Frank, N., Link, J. M., & Frank, M. 2016 Extracting foraminiferal seawater nd isotope signatures from bulk deep sea sediment by chemical leaching. *Chemical Geology* **439**, 189 – 204.

Bond, G., Broecker, W., Johnsen, S., McManus, J., Labeyrie, L., Jouzel, J., & Bonani, G. 1993 Correlations between climate records from north atlantic sediments and greenland ice. *Nature* **365**, 143.

Bondevik, S., Mangerud, J., Birks, H. H., Gulliksen, S., & Reimer, P. 2006 Changes in north atlantic radiocarbon reservoir ages during the allerød and younger dryas. *Science* **312**, 1514–1517.

Bourne, M. D., Thomas, A. L., Mac Niocaill, C., & Henderson, G. M. 2012 Improved determination of marine sedimentation rates using 230thxs. *Geochemistry, Geophysics, Geosystems* **13**.

Bout-Roumazeilles, V., Cortijo, E., Labeyrie, L., & Debrabant, P. 1999 Clay mineral evidence of nepheloid layer contributions to the heinrich layers in the northwest atlantic. *Palaeogeography, Palaeoclimatology, Palaeoecology* **146**, 211–228.

Bouttes, N., Roche, D., Mariotti, V., & Bopp, L. 2015 Including an ocean carbon cycle model into iloveclim (v1. 0). *Geoscientific Model Development* **8**, 1563–1576.

Bradtmiller, L. I., McManus, J. F., & Robinson, L. F. 2014 231pa/230th evidence for a weakened but persistent atlantic meridional overturning circulation during heinrich stadial 1. *Nature communications* **5**.

Briggs, R. D., Pollard, D., & Tarasov, L. 2014 A data-constrained large ensemble analysis of antarctic evolution since the eemian. *Quaternary Science Reviews* **103**, 91–115.

Broecker, W., Mix, A., Andree, M., & Oeschger, H. 1984 Radiocarbon measurements on coexisting benthic and planktic foraminifera shells: potential for reconstructing ocean ventilation times over the past 20 000 years. *Nuclear Instruments and Methods in Physics Research Section B: Beam Interactions with Materials and Atoms* **5**, 331–339.

Broecker, W. & Peng, T. 1982 Tracers in the sea, 690 pp. *Lamont-Doherty Geol. Obs., Palisades, NY.*

Broecker, W. S. 1994 Massive iceberg discharges as triggers for global climate change. *Nature* **372**, 421.

Brovkin, V., Bendtsen, J., Claussen, M., Ganopolski, A., Kubatzki, C., Petoukhov, V., & Andreev, A. 2002 Carbon cycle, vegetation, and climate dynamics in the holocene: Experiments with the climber-2 model. *Global Biogeochemical Cycles* **16**, 86–1.

Buckley, M. W. & Marshall, J. 2016 Observations, inferences, and mechanisms of the atlantic meridional overturning circulation: A review. *Reviews of Geophysics* **54**, 5–63.

Burckel, P., Waelbroeck, C., Gherardi, J. M., Pichat, S., Arz, H., Lippold, J., Dokken, T., & Thil, F. 2015 Atlantic ocean circulation changes preceded millennial tropical south america rainfall events during the last glacial. *Geophysical Research Letters* **42**, 411–418.

Burckel, P., Waelbroeck, C., Luo, Y., Roche, D. M., Pichat, S., Jaccard, S. L., Gherardi, J., Govin, A., Lippold, J., & Thil, F. 2016 Changes in the geometry and strength of the atlantic meridional overturning circulation during the last glacial (20–50 ka). *Climate of the Past* **12**, 2061–2075.

Böhm, E., Lippold, J., Gutjahr, M., Frank, M., Blaser, P., Antz, B., Fohlmeister, J., Frank, N., Andersen, M., & Deininger, M. 2015 Strong and deep atlantic meridional overturning circulation during the last glacial cycle. *Nature* **517**, 73–76.

Cess, R. D. & Goldenberg, S. D. 1981 The effect of ocean heat capacity upon global warming due to increasing atmospheric carbon dioxide. *Journal of Geophysical Research: Oceans* **86**, 498–502.

Chase, Z., Anderson, R. F., Fleisher, M. Q., & Kubik, P. W. 2002 The influence of particle composition and particle flux on scavenging of th, pa and be in the ocean. *Earth and Planetary Science Letters* **204**, 215–229.

Chase, Z., Anderson, R. F., Fleisher, M. Q., & Kubik, P. W. 2003 Scavenging of 230th, 231pa and 10be in the southern ocean (sw pacific sector): The importance of particle flux, particle composition and advection. *Deep Sea Research Part II: Topical Studies in Oceanography* **50**, 739–768.

Cortijo, E., Labeyrie, L., Vidal, L., Vautravers, M., Chapman, M., Duplessy, J.-C., Elliot, M., Arnold, M., Turon, J.-L., & Auffret, G. 1997 Changes in sea surface hydrology associated with heinrich event 4 in the north atlantic ocean between 40 and 60 n. *Earth and Planetary Science Letters* **146**, 29–45.

Curry, W. B. & Oppo, D. W. 2005 Glacial water mass geometry and the distribution of $\delta^{13}C$ of ΣCo_2 in the western atlantic ocean. *Paleoceanography* **20**.

De Vernal, A., Eynaud, F., Henry, M., Hillaire-Marcel, C., Londeix, L., Mangin, S., Matthiessen, J., Marret, F., Radi, T., Rochon, A., & others 2005 Reconstruction of sea-surface conditions at middle to high latitudes of the northern hemisphere during the last glacial maximum (lgm) based on dinoflagellate cyst assemblages. *Quaternary Science Reviews* **24**, 897–924.

Duplessy, J., Shackleton, N., Fairbanks, R., Labeyrie, L., Oppo, D., & Kallel, N. 1988 Deepwater source variations during the last climatic cycle and their impact on the global deepwater circulation. *Paleoceanography* **3**, 343–360.

Eide, M., Olsen, A., Ninnemann, U. S., & Johannessen, T. 2017 A global ocean climatology of preindustrial and modern ocean δ13c. *Global Biogeochemical Cycles* **31**, 515–534.

Evans, H. K. & Hall, I. R. 2008 Deepwater circulation on blake outer ridge (western north atlantic) during the holocene, younger dryas, and last glacial maximum. *Geochemistry, Geophysics, Geosystems* **9**.

Ferrari, R., Jansen, M. F., Adkins, J. F., Burke, A., Stewart, A. L., & Thompson, A. F. 2014 Antarctic sea ice control on ocean circulation in present and glacial climates. *Proceedings of the National Academy of Sciences* **111**, 8753–8758.

Firestone, R., [Firestone, & Shirley], V. 1998 *Table of Isotopes, 2 Volume Set*.

Francois, R. 2007 Chapter sixteen paleoflux and paleocirculation from sediment 230 th and 231 pa/230 th. *Developments in Marine Geology* **1**, 681–716.

Francois, R., Frank, M., Rutgers van der Loeff, M. M., & Bacon, M. P. 2004 230th normalization: An essential tool for interpreting sedimentary fluxes during the late quaternary. *Paleoceanography* **19**.

Frank, M., Eckhardt, J.-D., Eisenhauer, A., Kubik, P. W., Dittrich-Hannen, B., Segl, M., & Mangini, A. 1994 Beryllium 10, thorium 230, and protactinium 231 in galapagos microplate sediments: Implications of hydrothermal activity and paleoproductivity changes during the last 100,000 years. *Paleoceanography* **9**, 559–578.

Freeman, E., Skinner, L. C., Waelbroeck, C., & Hodell, D. 2016 Radiocarbon evidence for enhanced respired carbon storage in the atlantic at the last glacial maximum. *Nature communications* **7**, 11998.

Friedlingstein, P., Cox, P., Betts, R., Bopp, L., von Bloh, W., Brovkin, V., Cadule, P., Doney, S., Eby, M., Fung, I., & others 2006 Climate–carbon cycle feedback analysis: results from the c4mip model intercomparison. *Journal of climate* **19**, 3337–3353.

Gherardi, J.-M., Labeyrie, L., McManus, J., Francois, R., Skinner, L., & Cortijo, E. 2005 Evidence from the northeastern atlantic basin for variability in the rate of the meridional overturning circulation through the last deglaciation. *Earth and Planetary Science Letters* **240**, 710–723.

Gherardi, J.-M., Labeyrie, L., Nave, S., Francois, R., McManus, J. F., & Cortijo, E. 2009 Glacial-interglacial circulation changes inferred from 231Pa/230Th sedimentary record in the north atlantic region. *Paleoceanography* **24**.

Goosse, H., Brovkin, V., Fichefet, T., Haarsma, R., Huybrechts, P., Jongma, J., Mouchet, A., Selten, F., Barriat, P.-Y., Campin, J.-M., & others 2010 Description of the earth system model of intermediate complexity loveclim version 1.2. *Geoscientific Model Development* **3**, 603–633.

Govin, A. 2008 *Instabilité de la circulation océanique: réponse du climat des hautes latitudes nord et sud aux variations orbitales au cours du dernier Interglaciaire et de la dernière entrée en glaciation.* PhD thesis, Versailles-St Quentin en Yvelines.

Govin, A., Braconnot, P., Capron, E., Cortijo, E., Duplessy, J.-C., Jansen, E., Labeyrie, L., Landais, A., Marti, O., Michel, E., & others 2012 Persistent influence of ice sheet melting on high northern latitude climate during the early last interglacial. *Climate of the Past* **8**, 483–507.

Grousset, F., Labeyrie, L., Sinko, J., Cremer, M., Bond, G., Duprat, J., Cortijo, E., & Huon, S. 1993 Patterns of ice-rafted detritus in the glacial north atlantic (40–55 n). *Paleoceanography* **8**, 175–192.

Guihou, A. 2009 *Reconstitution des variations de la dynamique de la Circulation Méridienne Atlantique lors de la Dernière Entrée en Glaciation par le rapport ($^{231}Pa/^{230}Th$) des sédiments marins*. PhD thesis, Université Versailles Saint-Quentin en Yvelines.

Guihou, A., Pichat, S., Nave, S., Govin, A., Labeyrie, L., Michel, E., & Waelbroeck, C. 2010 Late slowdown of the atlantic meridional overturning circulation during the last glacial inception: new constraints from sedimentary (231pa/230th). *Earth and Planetary Science Letters* **289**, 520–529.

Guo, L., Chen, M., & Gueguen, C. 2002 Control of pa/th ratio by particulate chemical composition in the ocean. *Geophysical Research Letters* **29**.

Hain, M. P., Sigman, D. M., & Haug, G. H. 2014 Distinct roles of the southern ocean and north atlantic in the deglacial atmospheric radiocarbon decline. *Earth and Planetary Science Letters* **394**, 198–208.

Hayes, C. T., Anderson, R. F., Fleisher, M. Q., Huang, K.-F., Robinson, L. F., Lu, Y., Cheng, H., Edwards, R. L., & Moran, S. B. 2015 230 th and 231 pa on geotraces ga03, the us geotraces north atlantic transect, and implications for modern and paleoceanographic chemical fluxes. *Deep Sea Research Part II: Topical Studies in Oceanography* **116**, 29–41.

Hemming, S. R. 2004 Heinrich events: Massive late pleistocene detritus layers of the north atlantic and their global climate imprint. *Reviews of Geophysics* **42**.

Henderson, G. M. & Anderson, R. F. 2003 The U-series toolbox for paleoceanography. *Reviews in Mineralogy and Geochemistry* **52**, 493–531.

Henry, L., McManus, J. F., Curry, W. B., Roberts, N. L., Piotrowski, A. M., & Keigwin, L. D. 2016 North atlantic ocean circulation and abrupt climate change during the last glaciation. *Science* **353**, 470–474.

Hodell, D. A., Nicholl, J. A., Bontognali, T. R., Danino, S., Dorador, J., Dowdeswell, J. A., Einsle, J., Kuhlmann, H., Martrat, B., Mleneck-Vautravers, M. J., & others 2017 Anatomy of heinrich layer 1 and its role in the last deglaciation. *Paleoceanography* **32**, 284–303.

Howe, J. N., Piotrowski, A. M., Noble, T. L., Mulitza, S., Chiessi, C. M., & Bayon, G. 2016 North atlantic deep water production during the last glacial maximum. *Nature communications* **7**, 11765.

Hulten, M. v., Dutay, J.-C., & Roy-Barman, M. 2018 A global scavenging and circulation ocean model of thorium-230 and protactinium-231 with improved particle dynamics (nemo–prothorp 0.1). *Geoscientific Model Development* **11**, 3537–3556.

Ivanovic, R., Gregoire, L., Kageyama, M., Roche, D., Valdes, P., Burke, A., Drummond, R., Peltier, W. R., & Tarasov, L. 2016 Transient climate simulations of the deglaciation 21-9 thousand years before present (version 1)-pmip4 core experiment design and boundary conditions. *Geoscientific Model Development*.

Jeandel, C., Arsouze, T., Lacan, F., Techine, P., & Dutay, J.-C. 2007 Isotopic nd compositions and concentrations of the lithogenic inputs into the ocean: A compilation, with an emphasis on the margins. *Chemical Geology* **239**, 156–164.

Kadko, D. 1980 A detailed study of some uranium series nuclides at an abyssal hill area near the east pacific rise at 8n45. *Earth and Planetary Science Letters* **51**, 115 – 131.

Keigwin, L. D. & Swift, S. A. 2017 Carbon isotope evidence for a northern source of deep water in the glacial western north atlantic. *Proceedings of the National Academy of Sciences* **114**, 2831–2835.

Key, R. M., Kozyr, A., Sabine, C. L., Lee, K., Wanninkhof, R., Bullister, J. L., Feely, R. A., Millero, F. J., Mordy, C., & Peng, T.-H. 2004 A global ocean carbon climatology: Results from global data analysis project (glodap). *Global biogeochemical cycles* **18**.

Kissel, C. 2005 Magnetic signature of rapid climatic variations in glacial north atlantic, a review. *Comptes Rendus Geoscience* **337**, 908–918.

Ku, T.-L., Knauss, K. G., & Mathieu, G. G. 1977 Uranium in open ocean: concentration and isotopic composition. *Deep Sea Research* **24**, 1005–1017.

Lacan, F. & Jeandel, C. 2004 Denmark strait water circulation traced by heterogeneity in neodymium isotopic compositions. *Deep Sea Research Part I: Oceanographic Research Papers* **51**, 71–82.

Lambeck, K., Rouby, H., Purcell, A., Sun, Y., & Sambridge, M. 2014 Sea level and global ice volumes from the last glacial maximum to the holocene. *Proceedings of the National Academy of Sciences* **111**, 15296–15303.

Lambelet, M., van de Flierdt, T., Crocket, K., Rehkämper, M., Kreissig, K., Coles, B., Rijkenberg, M. J., Gerringa, L. J., de Baar, H. J., & Steinfeldt, R. 2016 Neodymium isotopic composition and concentration in the western north atlantic ocean: results from the geotraces ga02 section. *Geochimica et Cosmochimica Acta* **177**, 1–29.

Lemieux-Dudon, B., Blayo, E., Petit, J.-R., Waelbroeck, C., Svensson, A., Ritz, C., Barnola, J.-M., Narcisi, B. M., & Parrenin, F. 2010 Consistent dating for antarctic and greenland ice cores. *Quaternary Science Reviews* **29**, 8–20.

Lippold, J., Gherardi, J.-M., & Luo, Y. 2011 Testing the 231pa/230th paleocirculation proxy: A data versus 2d model comparison. *Geophysical Research Letters* **38**.

Lippold, J., Grützner, J., Winter, D., Lahaye, Y., Mangini, A., & Christl, M. 2009 Does sedimentary 231pa/230th from the bermuda rise monitor past atlantic meridional overturning circulation? *Geophysical Research Letters* **36**.

Lippold, J., Gutjahr, M., Blaser, P., Christner, E., de Carvalho Ferreira, M. L., Mulitza, S., Christl, M., Wombacher, F., Böhm, E., Antz, B., & others 2016 Deep water provenance and dynamics of the (de) glacial atlantic meridional overturning circulation. *Earth and planetary science letters* **445**, 68–78.

Lippold, J., Luo, Y., Francois, R., Allen, S. E., Gherardi, J., Pichat, S., Hickey, B., & Schulz, H. 2012 Strength and geometry of the glacial atlantic meridional overturning circulation. *Nature geoscience* **5**, 813–816.

Luo, Y., Francois, R., & Allen, S. 2009 Sediment 231 pa/230 th as a recorder of the rate of the atlantic meridional overturning circulation: insights from a 2-d model. *Ocean Science Discussions* **6**.

Lynch-Stieglitz, J. 2017 The atlantic meridional overturning circulation and abrupt climate change. *Annual review of marine science* **9**, 83–104.

Lynch-Stieglitz, J., Adkins, J. F., Curry, W. B., Dokken, T., Hall, I. R., Herguera, J. C., Hirschi, J. J.-M., Ivanova, E. V., Kissel, C., Marchal, O., & others 2007 Atlantic meridional overturning circulation during the last glacial maximum. *science* **316**, 66–69.

Lynch-Stieglitz, J., Schmidt, M. W., Henry, L. G., Curry, W. B., Skinner, L. C., Mulitza, S., Zhang, R., & Chang, P. 2014 Muted change in atlantic overturning circulation over some glacial-aged heinrich events. *Nature Geoscience* **7**, 144–150.

Marchal, O., François, R., Stocker, T. F., & Joos, F. 2000 Ocean thermohaline circulation and sedimentary 231pa/230th ratio. *Paleoceanography and Paleoclimatology* **15**, 625–641.

Mariotti, V. 2013 *Le cycle du carbone en climat glaciaire: état moyen et variabilité.* PhD thesis, Versailles-St Quentin en Yvelines.

Mauritzen, C. & Häkkinen, S. 1997 Influence of sea ice on the thermohaline circulation in the arctic-north atlantic ocean. *Geophysical Research Letters* **24**, 3257–3260.

McCave, I. & Hall, I. R. 2006 Size sorting in marine muds: Processes, pitfalls, and prospects for paleoflow-speed proxies. *Geochemistry, Geophysics, Geosystems* **7**.

McCave, I., Hall, I. R., & Bianchi, G. G. 2006 Laser vs. settling velocity differences in silt grainsize measurements: estimation of palaeocurrent vigour. *Sedimentology* **53**, 919–928.

McCave, I., Manighetti, B., & Beveridge, N. 1995 Circulation in the glacial north atlantic inferred from grain-size measurements. *Nature* **374**, 149.

McManus, J., Francois, R., Gherardi, J.-M., Keigwin, L., & Brown-Leger, S. 2004 Collapse and rapid resumption of atlantic meridional circulation linked to deglacial climate changes. *Nature* **428**, 834–837.

Menviel, L., Yu, J., Joos, F., Mouchet, A., Meissner, K., & England, M. 2017 Poorly ventilated deep ocean at the last glacial maximum inferred from carbon isotopes: A data-model comparison study. *Paleoceanography and Paleoclimatology* **32**, 2–17.

Missiaen, L., Pichat, S., Waelbroeck, C., Douville, E., Bordier, L., Dapoigny, A., Thil, F., Foliot, L., & Wacker, L. 2018 Downcore variations of sedimentary detrital (238u/232th) ratio: implications on the use of 230thxs and 231paxs to reconstruct sediment flux and ocean circulation. *Geochemistry, Geophysics, Geosystems*.

Monnin, E., Indermühle, A., Dällenbach, A., Flückiger, J., Stauffer, B., Stocker, T. F., Raynaud, D., & Barnola, J.-M. 2001 Atmospheric co2 concentrations over the last glacial termination. *Science* **291**, 112–114.

Mortyn, P. G. & Charles, C. D. 2003 Planktonic foraminiferal depth habitat and δ18o calibrations: Plankton tow results from the atlantic sector of the southern ocean. *Paleoceanography* **18**.

Mulitza, S., Chiessi, C. M., Schefuss, E., Lippold, J., Wichmann, D., Antz, B., Mackensen, A., Paul, A., Prange, M., Rehfeld, K., & others 2017 Synchronous and proportional deglacial changes in atlantic meridional overturning and northeast brazilian precipitation. *Paleoceanography* **32**, 622–633.

Ng, H. C., Robinson, L. F., McManus, J. F., Mohamed, K. J., Jacobel, A. W., Ivanovic, R. F., Gregoire, L. J., & Chen, T. 2018 Coherent deglacial changes in western atlantic ocean circulation. *Nature communications* **9**.

Nicholls, K. W., Østerhus, S., Makinson, K., Gammelsrød, T., & Fahrbach, E. 2009 Ice-ocean processes over the continental shelf of the southern weddell sea, antarctica: A review. *Reviews of Geophysics* **47**.

Nozaki, Y. & Nakanishi, T. 1985 231pa and 230th profiles in the open ocean water column. *Deep Sea Research Part A. Oceanographic Research Papers* **32**, 1209–1220.

Orr, J. C., Maier-Reimer, E., Mikolajewicz, U., Monfray, P., Sarmiento, J. L., Toggweiler, J., Taylor, N. K., Palmer, J., Gruber, N., Sabine, C. L., & others 2001 Estimates of anthropogenic carbon uptake from four three-dimensional global ocean models. *Global Biogeochemical Cycles* **15**, 43–60.

Pahnke, K., Goldstein, S. L., & Hemming, S. R. 2008 Abrupt changes in antarctic intermediate water circulation over the past 25,000 years. *Nature Geoscience* **1**, 870.

Paillet, J., Arhan, M., & McCartney, M. S. 1998 Spreading of labrador sea water in the eastern north atlantic. *Journal of Geophysical Research: Oceans* **103**, 10223–10239.

Peltier, W., Argus, D., & Drummond, R. 2015 Space geodesy constrains ice age terminal deglaciation: The global ice-6g_c (vm5a) model. *Journal of Geophysical Research: Solid Earth* **120**, 450–487.

Pflaumann, U., Sarnthein, M., Chapman, M., d'Abreu, L., Funnell, B., Huels, M., Kiefer, T., Maslin, M., Schulz, H., Swallow, J., & others 2003 Glacial north atlantic: Sea-surface conditions reconstructed by glamap 2000. *Paleoceanography* **18**.

Piotrowski, A., Galy, A., Nicholl, J., Roberts, N., Wilson, D., Clegg, J., & Yu, J. 2012 Reconstructing deglacial north and south atlantic deep water sourcing using foraminiferal nd isotopes. *Earth and Planetary Science Letters* **357**, 289–297.

Pöppelmeier, F., Gutjahr, M., Blaser, P., Keigwin, L. D., & Lippold, J. 2018 Origin of abyssal nw atlantic water masses since the last glacial maximum. *Paleoceanography and Paleoclimatology* **33**, 530–543.

Rahmstorf, S. 2002 Ocean circulation and climate during the past 120,000 years. *Nature* **419**, 207–214.

Rasmussen, S. O., Andersen, K. K., Svensson, A., Steffensen, J. P., Vinther, B. M., Clausen, H. B., Siggaard-Andersen, M.-L., Johnsen, S. J., Larsen, L. B., Dahl-Jensen, D., & others 2006 A new greenland ice core chronology for the last glacial termination. *Journal of Geophysical Research: Atmospheres (1984–2012)* **111**.

Reimer, P. J., Bard, E., Bayliss, A., Beck, J. W., Blackwell, P. G., Bronk Ramsey, C., Buck, C. E., Cheng, H., Edwards, R. L., Friedrich, M., & others 2013 Intcal13 and marine13 radiocarbon age calibration curves 0-50,000 years cal bp.

Rempfer, J., Stocker, T. F., Joos, F., Lippold, J., & Jaccard, S. L. 2017 New insights into cycling of 231pa and 230th in the atlantic ocean. *Earth and planetary science letters* **468**, 27–37.

Rhein, M., Stramma, L., & Send, U. 1995 The atlantic deep western boundary current: Water masses and transports near the equator. *Journal of Geophysical Research: Oceans* **100**, 2441–2457.

Roberts, K. A., Xu, C., Hung, C.-C., Conte, M. H., & Santschi, P. H. 2009 Scavenging and fractionation of thorium vs. protactinium in the ocean, as determined from particle–water partitioning experiments with sediment trap material from the gulf of mexico and sargasso sea. *Earth and Planetary Science Letters* **286**, 131–138.

Roberts, N. L., Piotrowski, A. M., McManus, J. F., & Keigwin, L. D. 2010 Synchronous deglacial overturning and water mass source changes. *Science* **327**, 75–78.

Robinson, L. F., Henderson, G. M., Hall, L., & Matthews, I. 2004 Climatic control of riverine and seawater uranium-isotope ratios. *Science* **305**, 851–854.

Roche, D. M., Paillard, D., Caley, T., & Waelbroeck, C. 2014 Lgm hosing approach to heinrich event 1: results and perspectives from data–model integration using water isotopes. *Quaternary Science Reviews* **106**, 247–261.

Roche, D. M., Wiersma, A. P., & Renssen, H. 2010 A systematic study of the impact of freshwater pulses with respect to different geographical locations. *Climate Dynamics* **34**, 997–1013.

Rutberg, R. L., Hemming, S. R., & Goldstein, S. L. 2000 Reduced north atlantic deep water flux to the glacial southern ocean inferred from neodymium isotope ratios. *Nature* **405**, 935.

Santschi, P. H., Murray, J. W., Baskaran, M., Benitez-Nelson, C. R., Guo, L., Hung, C.-C., Lamborg, C., Moran, S. B., Passow, U., & Roy-Barman, M. 2006 Thorium speciation in seawater. *Marine Chemistry* **100**, 250–268.

Siddall, M., Henderson, G. M., Edwards, N. R., Frank, M., Müller, S. A., Stocker, T. F., & Joos, F. 2005 231pa/230th fractionation by ocean transport, biogenic particle flux and particle type. *Earth and Planetary Science Letters* **237**, 135–155.

Siddall, M., Stocker, T. F., Henderson, G. M., Joos, F., Frank, M., Edwards, N. R., Ritz, S. P., & Müller, S. A. 2007 Modeling the relationship between 231pa/230th distribution in north atlantic sediment and atlantic meridional overturning circulation. *Paleoceanography and Paleoclimatology* **22**.

Siegenthaler, U. & Münnich, K. 1981 C/12 c fractionation during co_2 transfer from air to sea. *Carbon Cycle Modelling. Bolin B.(ed) Wiley, New York*, 249–257.

Skinner, L. & Shackleton, N. 2004 Rapid transient changes in northeast atlantic deep water ventilation age across termination i. *Paleoceanography* **19**.

Skinner, L. C., Waelbroeck, C., Scrivner, A. E., & Fallon, S. J. 2014 Radiocarbon evidence for alternating northern and southern sources of ventilation of the deep atlantic carbon pool during the last deglaciation. *Proceedings of the National Academy of Sciences*, 201400668.

Smeed, D., McCarthy, G., Cunningham, S., Frajka-Williams, E., Rayner, D., Johns, W., Meinen, C., Baringer, M., Moat, B., Duchez, A., & others 2014 Observed decline of the atlantic meridional overturning circulation 2004–2012. *Ocean Science* **10**, 29–38.

Stanford, J., Rohling, E. J., Bacon, S., Roberts, A., Grousset, F., & Bolshaw, M. 2011 A new concept for the paleoceanographic evolution of heinrich event 1 in the north atlantic. *Quaternary Science Reviews* **30**, 1047–1066.

Stuiver, M. & Polach, H. A. 1977 Discussion reporting of 14 c data. *Radiocarbon* **19**, 355–363.

Svensson, A., Andersen, K. K., Bigler, M., Clausen, H. B., Dahl-Jensen, D., Davies, S. M., Johnsen, S. J., Muscheler, R., Rasmussen, S. O., Röthlisberger, R., & others 2006 The greenland ice core chronology 2005, 15–42ka. part 2: comparison to other records. *Quaternary Science Reviews* **25**, 3258–3267.

Tachikawa, K., Athias, V., & Jeandel, C. 2003 Neodymium budget in the modern ocean and paleo-oceanographic implications. *Journal of Geophysical Research: Oceans* **108**.

Talley, L. D. 2013 Closure of the global overturning circulation through the indian, pacific, and southern oceans: Schematics and transports. *Oceanography* **26**, 80–97.

Tarasov, L., Dyke, A. S., Neal, R. M., & Peltier, W. R. 2012 A data-calibrated distribution of deglacial chronologies for the north american ice complex from glaciological modeling. *Earth and Planetary Science Letters* **315**, 30–40.

Taylor, S. R. & McLennan, S. M. 1995 The geochemical evolution of the continental crust. *Reviews of Geophysics* **33**, 241–265.

Therón, R., Paillard, D., Cortijo, E., Flores, J.-A., Vaquero, M., Sierro, F. J., & Waelbroeck, C. 2004 Rapid reconstruction of paleoenvironmental features using a new multiplatform program. *Micropaleontology* **50**, 391–395.

Thiagarajan, N., Subhas, A. V., Southon, J. R., Eiler, J. M., & Adkins, J. F. 2014 Abrupt pre-bølling–allerød warming and circulation changes in the deep ocean. *Nature* **511**, 75.

Thomas, A. L., Henderson, G. M., & Robinson, L. F. 2006 Interpretation of the 231 pa/230 th paleocirculation proxy: New water-column measurements from the southwest indian ocean. *Earth and Planetary Science Letters* **241**, 493–504.

Thomson, J., Nixon, S., Summerhayes, C., Schönfeld, J., Zahn, R., & Grootes, P. 1999 Implications for sedimentation changes on the iberian margin over the last two glacial/interglacial transitions from (230 th excess) 0 systematics. *Earth and Planetary Science Letters* **165**, 255–270.

Thornalley, D. J., Barker, S., Broecker, W. S., Elderfield, H., & McCave, I. N. 2011 The deglacial evolution of north atlantic deep convection. *science* **331**, 202–205.

Tschumi, T., Joos, F., Gehlen, M., & Heinze, C. 2010 Deep ocean ventilation, carbon isotopes, marine sedimentation and the deglacial co2 rise. *Climate of the Past* **6**, 1895–1958.

Veiga-Pires, C. & Hillaire-Marcel, C. 1999 U and th isotope constraints on the duration of heinrich events h0-h4 in the southeastern labrador sea. *Paleoceanography* **14**, 187–199.

Vidal, L., Labeyrie, L., Cortijo, E., Arnold, M., Duplessy, J., Michel, E., Becque, S., & Van Weering, T. 1997 Evidence for changes in the north atlantic deep water linked to meltwater surges during the heinrich events. *Earth and Planetary Science Letters* **146**, 13–27.

Vinther, B. M., Clausen, H. B., Johnsen, S. J., Rasmussen, S. O., Andersen, K. K., Buchardt, S. L., Dahl-Jensen, D., Seierstad, I. K., Siggaard-Andersen, M.-L., Steffensen, J. P., & others 2006 A synchronized dating of three greenland ice cores throughout the holocene. *Journal of Geophysical Research: Atmospheres (1984–2012)* **111**.

Vogel, H., Meyer-Jacob, C., Thöle, L., Lippold, J. A., & Jaccard, S. L. 2016 Quantification of biogenic silica by means of fourier transform infrared spectroscopy (ftirs) in marine sediments. *Limnology and oceanography: methods* **14**, 828–838.

Volk, T. & Hoffert, M. I. 1985 Ocean carbon pumps: Analysis of relative strengths and efficiencies in ocean-driven atmospheric co2 changes. *The carbon cycle and atmospheric CO2: natural variations Archean to present* **32**, 99–110.

Waelbroeck, C., Duplessy, J.-C., Michel, E., Labeyrie, L., Paillard, D., & Duprat, J. 2001 The timing of the last deglaciation in north atlantic climate records. *Nature* **412**, 724–727.

Waelbroeck, C., Labeyrie, L., Duplessy, J.-C., Guiot, J., Labracherie, M., Leclaire, H., & Duprat, J. 1998 Improving past sea surface temperature estimates based on planktonic fossil faunas. *Paleoceanography* **13**, 272–283.

Waelbroeck, C., Pichat, S., Böhm, E., Lougheed, B. C., Faranda, D., Vrac, M., Missiaen, L., Vazquez Riveiros, N., Burckel, P., Lippold, J., Arz, H. W., Dokken, T., Thil, F., & Dapoigny, A. 2018 Relative timing of precipitation and ocean circulation changes in the western equatorial atlantic over the last 45 kyr. *Climate of the Past* **14**, 1315–1330.

Walter, H., Van der Loeff, M. R., & Hoeltzen, H. 1997 Enhanced scavenging of 231 pa relative to 230 th in the south atlantic south of the polar front: Implications for the use of the 231 pa/230 th ratio as a paleoproductivity proxy. *Earth and Planetary Science Letters* **149**, 85–100.

Weyer, S., Anbar, A., Gerdes, A., Gordon, G., Algeo, T., & Boyle, E. 2008 Natural fractionation of 238 u/235 u. *Geochimica et Cosmochimica Acta* **72**, 345–359.

Wolff, E. W., Chappellaz, J., Blunier, T., Rasmussen, S. O., & Svensson, A. 2010 Millennial-scale variability during the last glacial: The ice core record. *Quaternary Science Reviews* **29**, 2828–2838.

Yu, E.-F., Francois, R., & Bacon, M. P. 1996 Similar rates of modern and last-glacial ocean thermohaline circulation inferred. *Nature* **379**, 689–694.

université PARIS-SACLAY
ÉCOLE DOCTORALE
Sciences de l'environnement d'île-de-France (SEIF)

Titre : Quantification des changements de la circulation océanique profonde de l'Atlantique au cours des changements climatiques rapides des derniers 40 ka

Mots clés : Paléocéanographie, Quaternaire, Atlantique Nord, évènements abrupts, géochimie, modélisation

Résumé : Au cours des derniers 40 ka, le Groenland et l'Atlantique Nord ont enregistré des oscillations de température rapides et de grande amplitude (8 à 15°C en à peine 300 ans) associées à de profondes modifications de la circulation océanique et atmosphérique. Les mécanismes à l'origine de ces changements climatiques rapides ne sont encore que partiellement élucidés. L'objectif de cette thèse est de quantifier les changements de circulation océanique qui ont accompagné ces changements climatiques abrupts. La première partie de cette thèse a consisté à combiner les informations paleocéanographiques de trois traceurs géochimiques, de manière à s'affranchir des limitations de chaque traceur pris séparément. Les rapports isotopiques du carbone des foraminifères benthiques (δ^{13}C et Δ^{14}C) et le Pa/Th sédimentaire ont été mesurés sur la carotte sédimentaire de l'Atlantique Nord SU90-08 (43°N, 30°W, 3080 m). Les proxies semblent dépeindre une situation contradictoire au cours du dernier maximum glaciaire: les isotopes du carbone indiquent une faible ventilation des masses d'eau profondes alors que le Pa/Th sédimentaire atteste d'une circulation active. Ce résultat interroge sur la nature exacte du signal enregistré par chaque proxy. Par ailleurs, le recours à la modélisation est nécessaire afin de quantifier les variations de la circulation océanique passée. La seconde partie de cette thèse a donc consisté à ajouter le calcul du Pa/Th sédimentaire dans le modèle de climat de complexité intermédiaire iLOVECLIM. Ce modèle, capable de simuler l'évolution simultanée des trois proxies, a été utilisé pour analyser la réponse de chaque proxy à des changements abrupts de circulation. Les résultats montrent que la réponse des proxies est différente dans les trois principales masses d'eau de l'Atlantique. Dans l'Atlantique Nord-Ouest profond ($>$2000 m), la réponse du Pa/Th précède celle des isotopes du carbone de quelques centaines d'années, constituant un exemple de découplage entre les différents proxies.

Title : Quantification of the Atlantic deep ocean-circulation variations during the rapid climate changes of the last 40 ky

Keywords : Paleoceanography, Quaternary, North Atlantic, abrupt events, geochemistry, climate modeling

Abstract : The last 40 ky, have been characterized by abrupt and high amplitude temperature changes (8 to 15°C in less than 300 years) in Greenland and in the North Atlantic region, associated with drastic ocean and atmospheric circulation changes. The mechanisms behind these abrupt climate changes are still debated. The objective of this thesis is to quantify the ocean circulation changes associated with these abrupt climate changes. In the first part of this thesis, I combined the information of three geochemical proxies in order to overcome the limitations of each proxy taken separately. The carbon isotopic ratios of the benthic foraminifers (δ^{13}C and Δ^{14}C), as well as the sedimentary Pa/Th ratio, have been measured in the North Atlantic sediment core SU90-08 (43°N, 30°W, 3080 m). The proxies depict an apparently inconsistent situation over the last glacial maximum: the carbon isotopes indicate that the deep water mass was poorly ventilated while the Pa/Th evidence an active overturning cell. These observations question the type of signal recorded by each proxy. Besides, in order to quantify the circulation changes, a modeling approach is required. In the second part of this thesis, I have implemented the calculation of the Pa/Th in the climate model of intermediate complexity iLOVECLIM. The model is able to simulate the simultaneous evolution of the three proxies and has been used to decipher the multi-proxy response to abrupt circulation changes. The results show that the proxy response varies in the three main Atlantic water masses. In the deep ($>$2000 m) western North Atlantic, the carbon isotopes response lags the Pa/Th response by a few hundreds of years, exemplifying/illustrating a possible decoupling between the different proxies.

Université Paris-Saclay
Espace Technologique / Immeuble Discovery
Route de l'Orme aux Merisiers RD 128 / 91190 Saint-Aubin, France